# LDRD Annual Report

## Laboratory Directed Research and Development

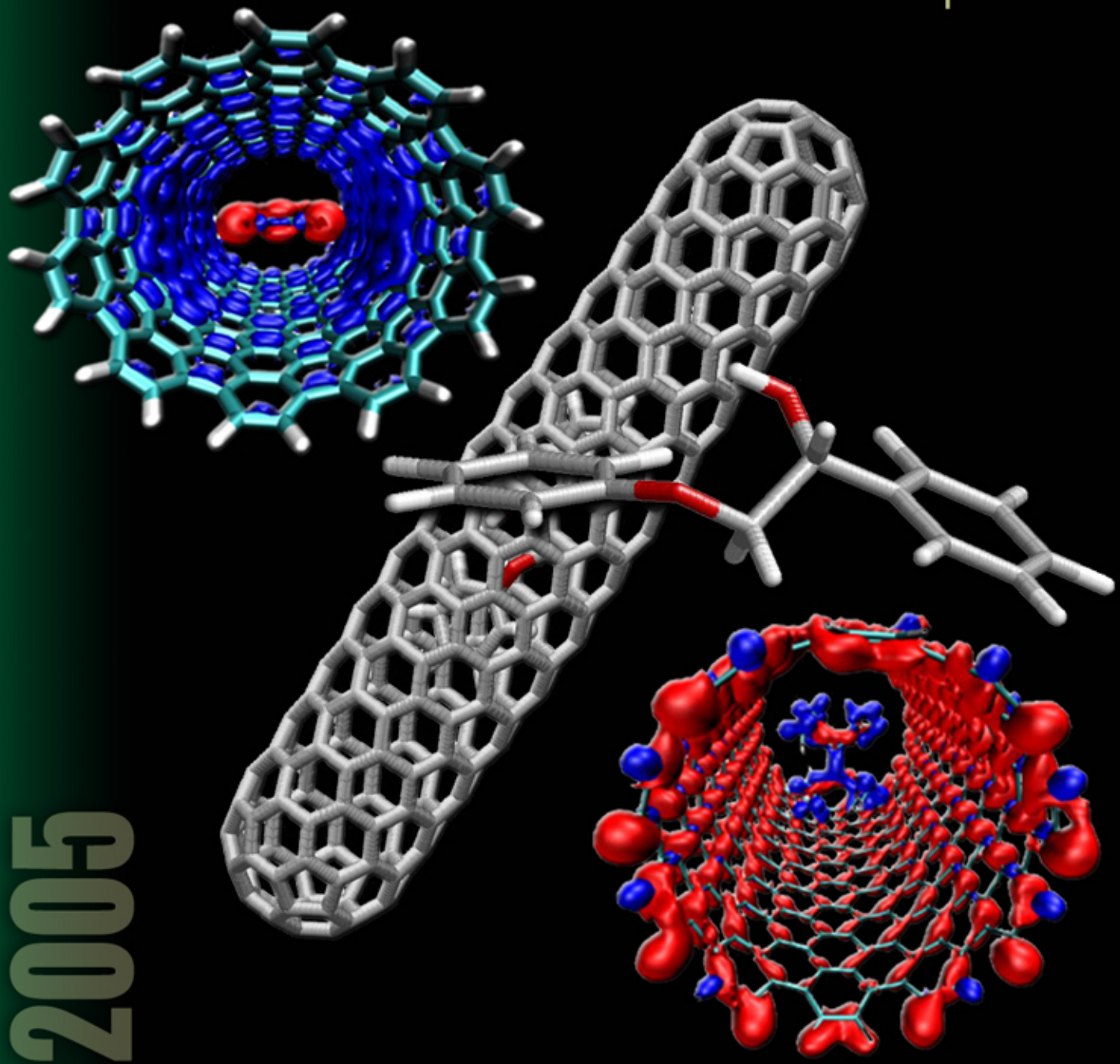

FY 2005

OAK RIDGE NATIONAL LABORATORY
MANAGED BY UT-BATTELLE FOR THE DEPARTMENT OF ENERGY

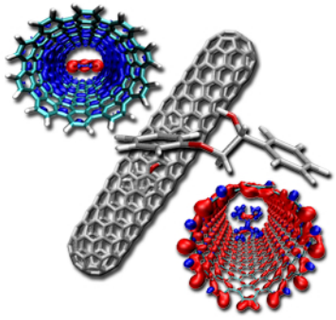

***On the cover:*** *Images from the report entitled "Nanochemistry: The Bridge from Materials to Biological Sciences" by B. G. Sumpter et al. The figures in the upper left and lower right are the results of large-scale ab initio quantum calculations investigating the effects of encapsulating organic molecules inside carbon nanotubes. The image in the center foreground is a model of α-HO phenethyl phenyl ether. When placed inside a carbon nanotube (center background), first-principles calculations show that nanoscale confinement tends to reduce the activation energy of the transition state for these types of molecular systems.*


## DOCUMENT AVAILABILITY

Reports produced after January 1, 1996,
are generally available free via the
U.S. Department of Energy (DOE)
Information Bridge:

Web site: http://www.osti.gov/bridge

Reports produced before January 1, 1996, may be purchased by members of the public from the following source:

National Technical Information Service
5285 Port Royal Road
Springfield, VA 22161
Telephone: 703-605-6000 (1-800-553-6847)
TDD: 703-487-4639
Fax: 703-605-6900
E-mail: info@ntis.fedworld.gov
Web site: http://www.ntis.gov/support/ordernowabout.htm

Reports are available to DOE employees, DOE contractors, Energy Technology Data Exchange (ETDE) representatives, and International Nuclear Information System (INIS) representatives from the following source:

Office of Scientific and Technical Information
P.O. Box 62
Oak Ridge, TN 37831
Telephone: 865-576-8401
Fax: 865-576-5728
E-mail: reports@adonis.osti.gov
Web site: http://www.osti.gov/contact.html

ORNL/PPA-2006/1

Oak Ridge National Laboratory

# LABORATORY DIRECTED RESEARCH AND DEVELOPMENT PROGRAM

# FY 2005 ANNUAL REPORT

March 2006

Prepared by
OAK RIDGE NATIONAL LABORATORY
P.O. Box 2008
Oak Ridge, Tennessee 37831-6285
managed by
UT-BATTELLE LLC
for the
U.S. DEPARTMENT OF ENERGY
under Contract DE-AC05-00OR22725

## CONTENTS

# INTRODUCTION

The Oak Ridge National Laboratory (ORNL) Laboratory Directed Research and Development (LDRD) Program reports its status to the U.S. Department of Energy (DOE) in March of each year. The program operates under the authority of DOE Order 413.2A, "Laboratory Directed Research and Development" (January 8, 2001), which establishes DOE's requirements for the program while providing the Laboratory Director broad flexibility for program implementation. LDRD funds are obtained through a charge to all Laboratory programs.

This report describes all ORNL LDRD research activities supported during FY 2005 and includes final reports for completed projects and shorter progress reports for projects that were active, but not completed, during this period. The FY 2005 ORNL LDRD Self-Assessment (ORNL/PPA-2006/2) provides financial data about the FY 2005 projects and an internal evaluation of the program's management process.

ORNL is a DOE multiprogram science, technology, and energy laboratory with distinctive capabilities in materials science and engineering, neutron science and technology, energy production and end-use technologies, biological and environmental science, and scientific computing. With these capabilities ORNL conducts basic and applied research and development (R&D) to support DOE's overarching national security mission, which encompasses science, energy resources, environmental quality, and national nuclear security. As a national resource, the Laboratory also applies its capabilities and skills to the specific needs of other federal agencies and customers through the DOE Work For Others (WFO) program. Information about the Laboratory and its programs is available on the Internet at <http://www.ornl.gov/>.

LDRD is a relatively small but vital DOE program that allows ORNL, as well as other multiprogram DOE laboratories, to select a limited number of R&D projects for the purpose of

- maintaining the scientific and technical vitality of the Laboratory,
- enhancing the Laboratory's ability to address future DOE missions,
- fostering creativity and stimulating exploration of forefront science and technology,
- serving as a proving ground for new research, and
- supporting high-risk, potentially high-value R&D.

Through LDRD the Laboratory is able to improve its distinctive capabilities and enhance its ability to conduct cutting-edge R&D for its DOE and WFO sponsors.

To meet the LDRD objectives and fulfill the particular needs of the Laboratory, ORNL has established a program with two components: the Director's R&D Fund and the Seed Money Fund. As outlined in Table 1, these two funds are complementary. The Director's R&D Fund develops new capabilities in support of the Laboratory initiatives, while the Seed Money Fund is open to all innovative ideas that have the potential for enhancing the Laboratory's core scientific and technical competencies. Provision for multiple routes of access to ORNL LDRD funds maximizes the likelihood that novel and seminal ideas with scientific and technological merit will be recognized and supported.

**Table 1. ORNL LDRD Program**

| | Seed Money Fund | Director's R&D Fund |
|---|---|---|
| Purpose | Supports core competencies | Supports laboratory initiatives |
| Year established | 1974 | 1983 |
| Funding cycle | Continuous | Annual |
| Proposal review | Proposal review committee | Initiative review committees |
| Project budget | ≤ $125,000 | ≤ $800,000 |
| Project duration | 12 to 18 months | 24 to 36 months |
| LDRD outlay | 20% | 80% |

The ORNL LDRD program recognizes that the R&D staff generally initiate new ideas, peer review of proposals is an essential component, and management has a role in fostering projects that are aligned with the strategic directions of the Laboratory. All proposals to the ORNL LDRD program undergo peer review and must be approved by the Deputy Director for Science and Technology and concurred by DOE before funding can be provided.

## Director's R&D Fund

The Director's R&D Fund is the strategic component of the ORNL LDRD program and the key tool for addressing the R&D needs of the Laboratory initiatives. The initiatives, which are the focus of the Laboratory Agenda, ORNL's strategic plan developed in collaboration

with DOE, are the critical areas on which the Laboratory must concentrate if it is to be prepared to meet future DOE and national requirements for science and technology.

The success of an initiative, which generally lasts 3–5 years, depends to a large extent on the Laboratory's ability to identify and nurture cutting-edge science and technology on which enduring capabilities can be built. To do this, ORNL uses the resources of the Director's R&D Fund to encourage the research staff to submit ideas aimed at addressing initiative-specific research goals. Each spring, after conducting a review of the initiatives with the Laboratory's senior technical managers, the Deputy Director for Science and Technology issues a call for proposals to the scientific and technical staff. The call emphasizes specific research priorities selected by management as critical to accomplishing the Laboratory's initiatives. To select the best and most strategic of the submitted ideas, the Deputy Director establishes a committee for each initiative to review the new proposals and ongoing projects associated with it. The committees are staffed by senior technical managers and subject matter experts including external members from the academic community.

Proposals to the Director's R&D Fund undergo two rounds of review. In the first round, the committees evaluate preliminary proposals and select the most promising for development into full proposals. In the second round, the committees review the new proposals and ongoing projects that are requesting second- or third-year funding. After the reviews are completed, the committees provide funding recommendations to the Deputy Director for Science and Technology, who develops an overall funding strategy and presents it for approval to the Leadership Team, ORNL's executive committee headed by the Laboratory Director. All projects selected for funding must also receive concurrence from DOE.

In FY 2005, $13.3 million was allocated to the Director's R&D Fund to support 65 projects, 36 of which were new starts (Table 2). About 90% of the fund's annual allocation is awarded to projects at the beginning of the fiscal year. The remainder, about 10%, is held in reserve primarily to support research projects of new R&D staff members being recruited to address strategic Laboratory needs.

**Table 2. FY 2004 ORNL LDRD Breakdown by Fund**

| | Director's R&D Fund | Seed Money Fund |
|---|---|---|
| Costs | $13.3 million | $3.4 million |
| Number of projects | 65 | 66 |
| Number of new starts | 36 | 37 |
| Number of continuing projects | 29 | 29 |
| Average total project budget | ~$418,000 | ~$99,000 |
| Average project duration | 24 months | 16 months |

## Research Initiatives

In requesting proposals for FY 2005, the Laboratory's senior R&D managers developed a set of research priorities for the Laboratory initiatives in advanced energy systems, advanced materials, national security, neutron sciences, systems biology, and terascale computing and simulation science. Brief descriptions of these initiatives are provided below, while Fig. 1 shows the relative levels of LDRD investment. A list of projects supported by each initiative is provided on page 359.

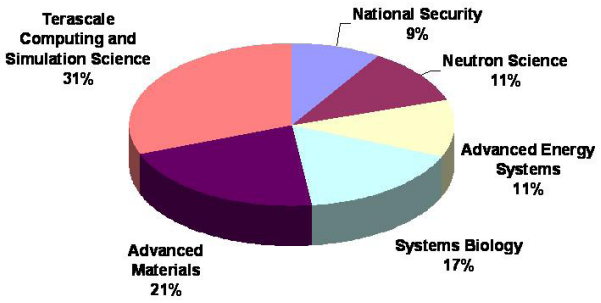


*Fig. 1. Level of Director's R&D Fund investment in the Laboratory-wide initiatives for FY 2005.*

### *Advanced Energy Systems*

The objective of this initiative is to establish ORNL as a leader in addressing problems of national importance in (1) electricity transmission, distribution, and reliability; (2) the expanded developmental use of nuclear and fusion technologies; and (3) the materials science and engineering needs for fuel cells, portable power, and hydrogen-based infrastructure and technology.

### *Advanced Materials*

The intent of advanced materials initiative is to establish ORNL as a leading interdisciplinary center for nanoscale science, engineering, and technology (NSET) performing forefront research and providing unique facilities, such as the Center for Nanophase Materials Science, for understanding the synthesis, fabrication, structure, and properties of nanoscale materials and systems.

### *National Security*

A principal thrust of the National Security initiative is to position ORNL to provide innovative technical

solutions to compelling national problems that materially improve global, national, and homeland security. Technical investments in this initiative are designed to build strong capabilities that will underpin enduring leadership roles for ORNL in meeting these security needs.

### *Neutron Sciences*

The intent of this initiative is to establish ORNL as the world's foremost center for neutron sciences, providing unprecedented capabilities for understanding the structure and properties of materials and macromolecular systems and the fundamental physics of the neutron. This initiative is focusing on three research priorities that are essential to leadership in neutron sciences: novel applications of neutron scattering, novel instrumentation concepts, and new approaches to facilitate development of higher-power spallation neutron sources.

### *Systems Biology*

The initiative in systems biology addresses the strategic needs of the DOE Genomics:GTL and related programs at other agencies that focus on gaining a molecular-level understanding of biological processes. Our intent is to strengthen ORNL's capabilities in molecular interactions, molecular complexes, interaction networks, proteomics, protein biochemistry, imaging, and computational biology.

### *Terascale Computing and Simulation Science*

The intent of terascale computing and simulation science initiative is to establish ORNL as a world leader in capability computing as a tool for scientific discovery. The initiative recognizes the importance of computing infrastructure and scientific computing in addressing key R&D issues of DOE's missions. In FY 2005, the research priorities for this initiative focused on two areas: (1) scientific applications to create new models for fusion energy, biology, nanoscience, physics, materials science, chemistry, and climate and (2) mathematics and computer science, including distributed and cluster computing, mathematical analysis, scalable numerical algorithms, mesh generation and discretization technology, petascale data analysis, and data visualization.

## Seed Money Fund

The Seed Money Fund complements the Director's R&D Fund by providing a source of funds for innovative ideas that have the potential of enhancing the Laboratory's core scientific and technical competencies. It also provides a path for funding new approaches that fall within the distinctive capabilities of ORNL but outside the more focused research priorities of the major Laboratory initiatives. Successful Seed Money Fund projects are expected to generate new DOE programmatic or Work-for-Others sponsorship at the Laboratory.

Proposals for Seed Money Fund support are accepted directly from the Laboratory's scientific and technical staff (with management concurrence) at any time of the year. Those requesting more than $20,000 ($125,000 is the maximum) are reviewed by the Proposal Review Committee (PRC), which is comprised of 11 scientific and technical staff members representing each of the Laboratory's research divisions and the LDRD manager (chair). To assist the committee, each proposal is also peer reviewed by two Laboratory staff members selected by the LDRD manager. Proposals requesting $20,000 or less are not reviewed by the PRC but are peer reviewed by a research staff member selected by the LDRD manager. All Seed Money Fund proposals receiving a favorable recommendation are forwarded to the Deputy Director for Science and Technology for approval and require DOE concurrence.

In FY 2005, $3.4 million of the LDRD program was apportioned to the Seed Money Fund to support 66 projects, 37 of which were new starts (Table 2). The distribution of Seed Money Fund support by science and technology area is shown in Fig. 2. The assignment of projects to specific areas is not meant to be definitive as many projects are cross-cutting and could be assigned to more than one category.

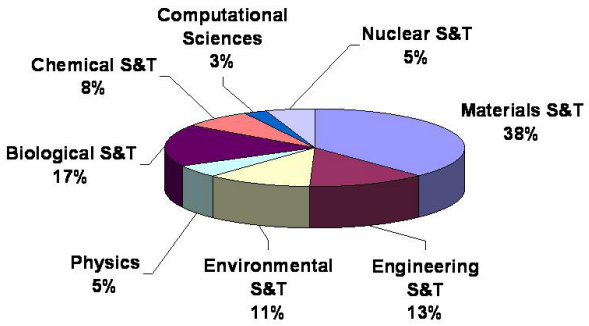


*Fig. 2. Distribution of Seed Money by science and technology area for FY 2005.*

## Report Organization

The report is divided into eight broad areas of science and technology that underlie the programmatic and Work for Others activities at ORNL. Within each of these areas, the projects are grouped by fund (i.e., either the Director's R&D Fund or the Seed Money Fund). Within each fund grouping are the final reports and progress reports in that order. A list of Director's R&D Fund projects by initiative, an author list, and a project list are included at the back of this document.

# *Materials Science and Engineering*

# *Director's R&D Fund*

# Nanorods for Energy and Photonics

D. B. Geohegan,[1] Z. Pan,[2] I. N. Ivanov,[3] B. Hu,[3] D. H. Lowndes,[1] J. W. Mays,[2]
A. A. Puretzky,[3] S. Dai,[2] S. Jesse,[3] and V. Meunier[4]
[1]*Condensed Matter Sciences Division*
[2]*Chemical Sciences Division*
[3]*The University of Tennessee*
[4]*Computer Science and Mathematics Division*

This project concentrated upon methods for the synthesis and application of quasi-one-dimensional nanocrystals called nanorods which are emerging as essential building blocks for nanoscale photonics and energy generation/storage. The project focused synthesis efforts on transparent ZnO and $SnO_2$ nanorods which can be doped to be electrically conductive, and on processing approaches to disperse and characterize nanorods inside polymers. Modeling efforts were undertaken to understand how nanorods percolate electrical current through the networks they form inside polymers using scanning electron microscope images obtained with a novel new electric-field-induced contrast imaging technique. Organic light-emitting devices (OLEDs) were made using single-wall carbon nanotubes (SWNTs) inside the conducting polymer MEH-PPV. The nanotube network was found to greatly increase the brightness compared with the polymer alone, as well as reduce the turn-on voltage and enable the injection of both electrons and holes, providing a mechanism for alternating current OLED operation. The project succeeded in new methods for nanorod synthesis, including methods for the deterministic placement of ZnO nanorods on substrates, the dispersion and characterization of nanorods inside polymers, the development of modeling frameworks to understand nanorod percolation networks, and the construction of prototype nanorod-polymer OLEDs with improved photonic properties.

## Introduction

This project focused on developing methods for the controlled synthesis of nanorods, and methods for their optical and electrical characterization, focusing primarily on applications in photonic devices. Nanorods are among the most scientifically interesting nanostructures and the most important technologically since (unlike quantum dots) the confined transport of electrons, ions, and photons over long (microns) distances permits crucial addressability for microscale electronics and photonics and efficient charge migration over long distances for energy-related applications. Nanorods are typically less than 100 nanometers in width and include not only carbon nanotubes but also many types of III-V and II-VI semiconductors. Of special interest are transparent, conducting oxide nanorods such as ZnO and $SnO_2$ since they may be used as transparent, conducting electrodes in photovoltaic and organic light-emitting devices (OLEDs). Nanorods may be grown either deterministically onto electrodes used in devices or in loose form, then purified, processed, and assembled as membranes or dispersed within polymers.

This project expanded fundamental understanding of nanorod growth, leading to the development of techniques for deterministic synthesis of ZnO nanorods, as well as methods of growing and processing loose nanorods into devices. The project succeeded in developing methods for controlled synthesis of ZnO and $SnO_2$ nanorods by CVD and laser-CVD techniques. Methods for optical characterization of band structures of as-synthesized nanostructures resolution and correlation with nanostructure and stoichiometry were developed. New methods for the characterization of nanorod networks inside polymers were achieved, and models were developed to understand local conductivity within these networks from scanning electron microscope images. Finally, the project succeeded in fabricating prototype photonic devices with enhanced light-emitting properties using nanorods and conducting polymers and in studying the charge transfer dynamics at the nanorod/polymer interface.

## Technical Approach

The overall approach involved the synthesis of transparent nanorods and their doped variants, the development of rapid optical characterization techniques to survey their electronic structure and photonic properties, and the processing and modeling of networks of these nanorods in protoype photonic devices.

The growth of crystalline nanorods of ZnO, $In_2O_3$, $SnO_2$, and their doped variants were investigated by the vapor-liquid-solid (VLS) technique and by catalyst-free methods. VLS growth involves precipitation from a high-temperature nanoparticle in which the material of choice has some solubility (e.g., gold nanoparticles can dissolve zinc and, in the presence of oxygen, can grow ZnO nanorods). Tasks involved the growth of (1) loose nanorods, (2) attached nanorod forests, and (3) attached determinsitic nanorods.

Like carbon nanotubes, loose nanorods of conducting transparent oxides are envisioned to be produced in bulk quantities and incorporated into polymers or plastics to lend conductivity, strength, and photonic capabilities (e.g., electrochromic window materials). Forests of vertically aligned nanorods that are attached to substrates can be utilized for high-surface-area electrodes for high-brightness lighting sources. Deterministically grown nanorods, precisely and individually placed at discrete addressable locations, are envisioned for arrays of nanoscale light sources (e.g., nanolasers), biophotonic probes, and many other applications. Deterministic, vertical growth is by far the most difficult task since factors determining the crystal type and orientation of the nanorod depend first on processing conditions (temperature, pressure, etc.) as well as on the substrate crystal orientation and composition and its effects on the catalyst crystal orientation and purity. For these reasons, nanorods are usually grown first as loose materials to understand their optimal processing conditions without detrimental effects to the substrate. Then desirable nanorods are attempted to be reproduced as attached nanorod forests and deterministic nanorods.

Techniques for optical assessment of nanorod properties were targeted as a task for three reasons. First, the electronic energy levels of nanorods are directly revealed by their optical absorption spectra, which yield clues to their composition and structure (e.g., via doping and defects). Second, the desirable properties of nanorods in this project—electrical conductivity and fluorescence—were directly probed via these techniques. Thus, these optical probing techniques—once calibrated—can be used to assess and help control nanorod synthesis for functional properties. These techniques are essential to help develop processing methods for the dispersion and incorporation of nanowires into polymers for composites.

Finally, direct use of nanorods as additives to enhance the electrical and photonic performance of polymers was investigated. A novel new SEM-based technique was used to image and characterize the morphology of conducting nanorod networks inside polymers during current-voltage measurements. This electric-field-induced contrast imaging technique provides voltage maps within the polymer induced by the nanorod network and permits modeling of the conductive pathways. A novel model was developed which utilizes the SEM-imaged network to derive junction resistances of the embedded nanorods. Charge transfer measurements utilizing nanotubes inside conducting MEH-PPV polymer was performed, and the device performance improvement of OLEDs was demonstrated.

## Results and Discussion

Three different methods were explored for nanorod growth of transparent conducting oxides in useful morphologies. Loose nanowires, nanorings, nanoribbons, whiskers, and comb structures were grown by evaporation of oxide powders at high temperature. For example, ZnO and $In_2O_3$ powders were co-evaporated at 1450ºC in a tube furnace and nanostructures were formed in a wide region of temperatures ranging from 1200ºC to 800ºC. Structures ranging from In-doped ZnO nanobelts, rings and nanobelts, to Zn-doped $In_2O_3$ whiskers could be grown, depending upon the temperature. This catalyst-free growth of doped nanoribbons and rings takes advantage of differential growth rates along different crystal orientations.

Similar experiments were carried out for ZnO nanowire growth in the presence of various dopants (e.g., gallium and germanium). In general, a great variety of quasi-one-dimensional structures could be achieved. These nanorods were structurally characterized by SEM and TEM, and compositionally analyzed by EDX. Their photonic properties were characterized by optical absorption spectroscopy, photoluminescence, and fluorometry.

Catalyst-free growth of loose nanorods is promising for the large-scale synthesis of novel nanowires for use in photonic and electronic functional composites. However, growth of nanorods on substrates from vapor-deposited or prepositioned catalysts—either in aligned forests, or deterministically placed—is important for functional coatings or sensors.

For the catalytic growth of ZnO nanowire forests, an entirely new strategy was developed which involved the first use of a semiconductor, germanium, as the catalyst (Fig. 1). ZnO powder was carbothermally reduced by carbon black in a tube furnace, and the germanium catalyst was provided either from the vapor generated by carbothermal reduction of $GeO_2$ powder, or by patterning germanium dots on a $SiO_2$-coated silicon wafer using photolithography. Several alumina, silicon, or sapphire wafer strips acted as nanowire growth substrates inside an alumina tube heated to 900ºC in 250 Torr Ar ambient for 30 min. The reactant vapors (Zn, Ge, CO, and O species) were transported by flowing argon to the substrates where ZnO nanowires grew. Uniform forests of quasi-aligned ZnO nanowires tipped with large germanium particles were synthesized by this technique. High-resolution TEM confirmed the single-crystal nature of the hexagonally

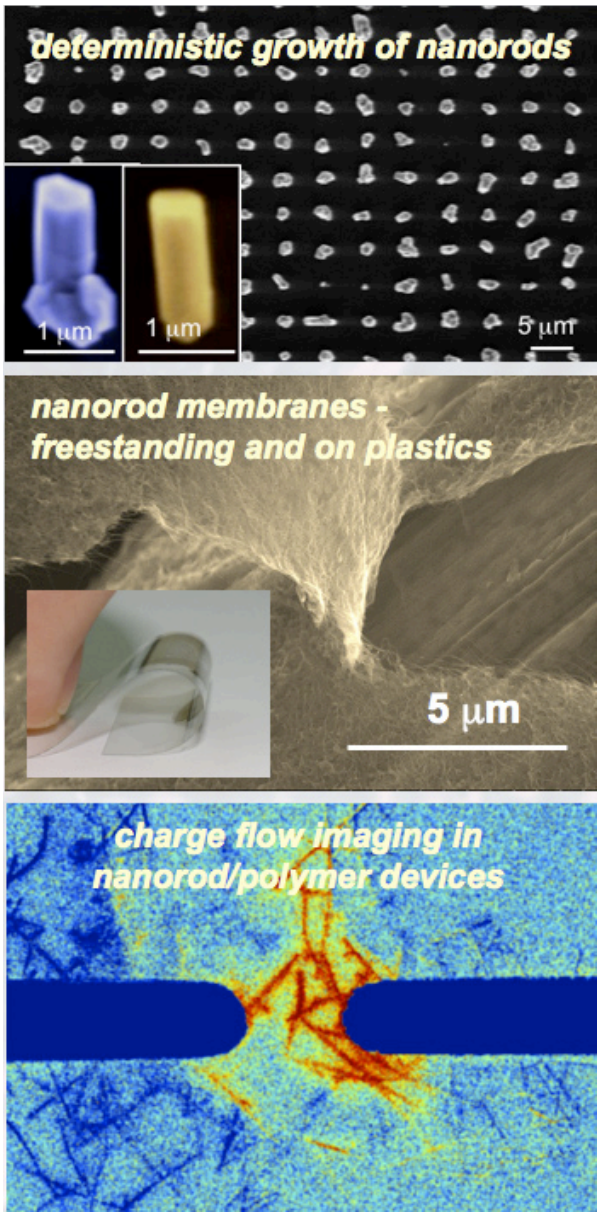


*Fig. 1. Varieties of nanorod structures (primarily ZnO) grown during this project, including single-crystal nanowires of ZnO grown using the first semiconductor catalyst (germanium).*

faceted nanowires. These nanowires contrast with metal-catalyst-grown nanowires (using mainly Au or Fe), since the diameter of the germanium particles (0.5–4 μm) is about 5–15 times that of the associated ZnO nanowires (50–400 nm). The ZnO nanowires are very long (up to 200 μm), nearly perfectly straight, quasi-aligned, structurally uniform, single crystals. Finally, germanium-catalyzed ZnO nanowires grow at a high rate, up to 400 μm/h, 1–2 orders of magnitude faster than gold-catalyzed growth.

In addition, laser vaporization was applied to controllably provide tin vapor for the growth of $SnO_2$ nanowires. Nd:YAG laser vaporization of a tin target placed just outside a tube furnace was used to grow nanowires on pre-patterned gold films on silicon. Dense mats of very small (20-nm-diam) nanowires were synthesized by this technique, which utilizes the roughening of very thin metal films to provide catalyst particles.

From the knowledge of germanium-catalyzed ZnO growth, deterministic growth of ZnO nanorods was achieved on substrates through the use of electron-beam lithography to create 75-nm-thick germanium-dot patterns on silicon with a 1-μm-thick $SiO_2$ layer. The germanium-dot patterned substrates were then loaded on a 20-cm-long graphite crucible filled with equal amounts of ZnO powder and carbon black, with the catalyst side facing down and the vertical distance between the zinc source and substrates of about 3–5 mm. The growth was conducted at 900ºC for 1 h in an argon flow. Rodlike ZnO nanostructures were grown only on the germanium-dot patterns located in the region having temperatures of ~650–800ºC, about 150ºC higher than the non-patterned growths described above. Below ~650ºC, no ZnO nanorods were grown and the Ge-dot patterns seemed unchanged. Above ~800ºC, however, the Ge dots were completely evaporated and thus no nanorods were formed.

The development of photonic composite materials utilizing loose nanorods requires methods for dispersion of the materials in solvents and polymers and methods for their blending into composites. Dispersion in solvents, followed by co-dissolution of polymers, is a technique which simultaneously permits the optical spectroscopy of the nanostructures to be measured. The most challenging case is that of single wall carbon nanotubes (SWNTs), where aggregation of the SWNTs into large ropes by van der Waals forces requires vigorous methods to debundle them. For this purpose, high shear mixing (HSM) was implemented (rather than horn sonication) to disperse and de-bundle SWNTs in surfactant solutions. The efficacy of the debundling treatments was assessed using optical absorption spectroscopy via sharpening of van Hove optical transitions. Moreover, kinetic profiles of the debundling were measured for different chiralities of SWNTs. This discovery of different kinetics of NT de-bundling and amorphous carbon separation from nanotube bundle may lead to development of a new technology of nanotube purification.

Using colloids of dispersed nanorods, processing technology was developed to produce percolation networks of thin, semitransparent, conducting window coatings and freestanding membranes. The technique involves filtration of nanorod solutions onto dissolvable filters. This permits transferral to any surface. Current research is focusing on perfecting this technique, and custon-designed electrode assemblies are being fabricated to permit in situ optical absorption spectroscopy of these

deposited nanorod networks during current-voltage measurements to assess the effects of current flow on electrochromic properties of the window.

Rapid optical characterization techniques for the photonic properties of nanorods were developed in this project. Experimentally, a great variety in nanostructures (rods, flakes, belts, ribbons, etc.) are grown as a function of doping level and temperature. Using excitation photoluminescence spectra, the mechanism of green emission from germanium-doped-ZnO nanostructures morphologies (observed by SEM) were correlated with their crystal structure using X-ray diffraction.

Prototype organic light emitting diodes (OLEDs) incorporating SWNTs in MEH-PPV polymer were made in planar geometry to investigate the charge injection of nanotubes on OLED performance. OLEDs and photovoltaics using conducting polymers were targeted in this project due to the emerging importance of plastic electronics in lighting and energy production for follow-on funding. At optimal SWNT loadings (less than percolation threshold concentrations), carbon nanotubes were found to have beneficial impact on the internal quantum efficiency of the devices, doubling the efficiency of the devices in forward bias mode and permitting reverse electroluminescence for the first time. Operation of the device now occurs in both forward and reverse bias modes. Carbon nanotubes permit the injection of both electrons and holes and appear to serve as recombination centers, resulting in increased electroluminescence. In addition, a reduction in turn-on voltage for prototype OLED devices was observed (from 8 V to 0.5 V with 0.16 wt % SWNTs), permitting lower-voltage-device operation and indicating that direct charge injection occurs under both forward and reverse bias conditions. In addition to providing conducting pathways to inject carriers over distances much greater than their characteristic diffusion lengths, photoinduced absorption measurements revealed clear transfer of electrons from the nanotubes to the valence band of the polymer chains. The latter results in 40% reduction in absorbance for 0.16% SWNT-MEH-PPV composite, compared to 56% reduction for pure MEH-PPV in photo-induced absorption experiment. These encouraging results provide the basis for expectations that nanotubes and other nanostructured additives can significantly enhance the efficiency, brightness, turn-on voltage, and other factors affecting the IQE of OLEDs without significantly affecting their processing methodology.

A model of electronic transport through nanorod networks was developed. The model uses our unique SEM-based experimental technique to spatially image biased nanorod networks inside polymers that determines which nanorods participate in electronic transport. This new method of SEM imaging—electric-field-induced contrast—provides sufficient experimental input for the first time to develop models of electronic conduction through nanorod networks and compare their electronic properties. The framework for a generalized model of electronic transport through nanorod networks was developed which promises to determine solutions for individual nanorod electrical characteristics and their interconnects. This model is unique to our knowledge and promises to give ORNL a major advantage for competitive follow-on funding in nanorod-polymer electronics (for plastic electronics, large-area photovoltaics, and functional fiber applications).

## Benefits

This project benefited DOE in several ways. First, it established a coordinated effort at ORNL in the synthesis, characterization, processing, and device development utilizing nanorods. This effort was necessary to prepare ORNL and the DOE for upcoming research utilizing transparent conductive nanorods in energy applications including photovoltaics and organic electronics. Second, it established a core capability for the new Center for Nanophase Materials Sciences, which will serve users through the capabilities established in this project. Third, the work in this project was identified by Battelle Memorial Institute (BMI) as one of the key application areas for future commercialization after their survey of technology development at ORNL. Meetings were held with BMI representatives at ORNL, and transparent conductive nanorod coatings was identified as the area for a funds-in CRADA. Thus, through involvement with BMI this project has begun collaborations with four other DOE national laboratories working in similar areas through Battelle's Nanotechnology Innovation Network. Transparent conductive coatings lend functionality to every application from OLEDs to military cockpits to floor coatings. Thus, the fundamental research in this project will be of use to military and other government agencies such as DARPA, AFRL, and NASA. Portions of the research in this project will be used in upcoming follow-on funding projects (e.g., with DARPA on their Prosthetics Program). In addition, our exciting OLED results—coupled with the idea of novel vertically integrated nanorod electrode architectures to increase the brightness of existing OLED's (VINE-OLEDs)—were submitted in two proposals to DOE's NETL call for Solid State Lighting.

# A Revolutionary Infrared Nanoscale Processing Approach

R. D. Ott,[1] C. A. Blue,[1] D. A. Blom,[1] R. B. Dinwiddie,[1] B. Radhakrishnan,[2]
A. S. Sabau,[1] T. R. Watkins,[1] and J. W. Harrell[3]
[1]*Metals and Ceramics Division*
[2]*Computer Science and Mathematics Division*
[3]*University of Alabama*

Oak Ridge National Laboratory (ORNL) has a unique infrared processing facility that is capable of controlling diffusion of materials down to the nanometer scale and thus revolutionizing rapid thermal processing. Versions of this facility are capable of bringing a 14-in. silicon wafer from 700ºC to 1300ºC in 1 millisecond, reaching heating rates of 600,000ºC/s. This heating rate is 3000 times faster than currently available rapid thermal process systems. The capability exists to utilize this facility and a technique called pulse thermal processing (PTP) to approach heating rates of lasers but with a 4000% larger footprint (processing area), thus allowing the process to be scaled for high-rate production. We have chosen to investigate the controlled synthesis of FePt nanoparticles for ultrahigh density magnetic recording as a case study. Being able to transform disordered face-centered-cubic (fcc) FePt nanoparticles to an ordered face-centered-tetragonal (fct) $L1_0$ structure without sintering the nanoparticles could result in more than a 200-fold increase in storage density. ORNL, for the first time, has demonstrated the phase transformation of FePt nanoparticles utilizing sub-second broad-area high-density plasma arc processing. This unique processing center is a disruptive technology that will enable processing science on the nanoscale and will position ORNL as a world leader in rapid thermal processing.

## Introduction

A tremendous amount of research has focused on the synthesis of nano-phase materials, which have been shown to have unique and even unattainable properties when compared to their bulk counterparts. In order to realize these unique properties, these materials must be integrated into "functional systems" which in many cases necessitates a critical heat treatment. This holds true for magnetic media (storage and read/write), thin-film transistors, photovoltaics, thin-film batteries, and many other thin-film and nanoparticle microelectronic devices. ORNL has a unique processing capability which allows for precise control of diffusion on the nanometer scale through rapid heating rates up to 600,000ºC/s over large areas (≥300 $cm^2$) utilizing a process called Pulse Thermal Processing (PTP). This research project was focused on investigating 3.5-nm FePt nanoparticles for high density magnetic storage where the nanoparticles must undergo a disordered-to-ordered phase transformation, with little-to-no sintering, to realize the required magnetic properties to increase storage densities. Nanoparticle sintering would increase the size of the magnetic domains, thus negating the motivation for starting with such small nanoparticles. With this phase transformation, storage capacities could potentially increase 200-fold from current densities of 30–50 GBits/$in^2$ to 10 TBits/$in^2$.

ORNL, for the first time, has demonstrated the ability to control diffusion on the nanomaterial scale utilizing broad-area rapid high density plasma arc heating in order to obtain the phase transformation of FePt nanoparticles from a disordered A1 structure to an ordered $L1_0$ structure while inhibiting nanoparticle sintering. The significance of this research project lies in the ability to understand and control the diffusion within the nanoparticles system. The capability to precisely control diffusion on this scale becomes extremely important when attempting to functionalize nanomaterials such as nanoparticles and thin-films for microelectronic devices. Having the ability to control phase transformations, grain growth, grain boundary refinement, sintering and crystallization on the nanoscale is key for next-generation magnetic media storage, photovoltaics, and thin-film transistors for flat panel displays. Once knowledge of this interaction begins to be understood for one material system, the foundation is set for carrying the knowledge to other functional nanomaterial systems.

The unique ability of this rapid heating process opens up a new realm of basic science and applied research based on controlling diffusion on the nanometer scale. Thus, one of the key aspects of this research is the development of a model that encompasses real-time temperature measurements and thermodynamic and kinetic information to allow the precise control of diffusion on the nanometer scale.

## Technical Approach

As-prepared nanoparticles were microstructurally and magnetically characterized by a variety of techniques available at ORNL and the University of Alabama. The following characterization techniques were employed: particle size and particle size distribution by transmission electron microscopy (TEM) and scanning transmission electron microscopy (STEM), phase analysis by X-ray diffraction, and a variety of magnetic properties that led to quantifying nanoparticle sintering due to the variability in magnetic properties as a function of microstructure.

An experimental procedure was established to vary the PTP parameters systematically in order to determine their effects on the ability of the nanoparticles to transform to the ordered $L1_0$ phase without sintering and loss of particle positioning. The PTP parameters of interest are preheat time and temperature, pulse temperature and time, the number of pulses, and the time in between pulses. Replicate films were heat treated under conventional means to ascertain any difference among samples treated with PTP.

As part of this work, a radiant heat transfer model was established so that appropriate thermal profiles could be determined, and thus, resultant microstructures of PTP-processed materials can be predicted. The model was based on the TELLURIDE code developed at Los Alamos National Laboratory (Reddy 1997). The code was developed as a multi-phase casting simulation code, but due to its modular nature, it can be custom tailored for the analysis of materials processing under the plasma arc lamp.

## Tasks

- Task #1: Process nanoparticles for PTP and conventional annealing
- Task #2: Microstructure and magnetic properties measurements
- Task #3: Microstructure evolution model
- Task #4: PTP/temperature/materials correlation and experimental procedure development
- Task #5: Process nanoparticles with PTP and conventional methods
- Iterate and establish models for PTP heat flow process and microstructure/magnetic properties correlation

The objective of this research was to develop a better understanding of the PTP technique in order to facilitate the phase transformation of FePt nanoparticles for next-generation high density magnetic media. The processing science developed from this research will lead to nanoscale manipulation of microstructures providing a nanomanufacturing tool for processing microelectronic devices and other applications.

## Results and Discussion

Results have been extremely encouraging in showing near-complete ordering and high coercivity measurements (the coercivity is the strength an applied magnetic field must apply to coerce a materials net magnetization to go to zero). Infrared imaging was utilized to provide real-time temperatures of the surface of the nanoparticles and allowed for validation of the model. Determining the processing temperature of the nanoparticle system was critical in order to compare microstructural evolution with conventionally processed FePt nanoparticles. Unfortunately, this also proved to be the most difficult aspect of the nanoparticle processing. Although there were limitations to surface temperature measurements, efforts continued forward for developing and validating the thermal model. This model was established with finite difference methods and was based on the thermal properties of the nanoparticles, substrate, and processing environment. By an iterative process, the model has been refined and led to a better understanding of the temperature profile within the nanoparticle layer and the underlying silicon substrate. Correlation between the theoretical and real-time temperature data was strong, and $\Delta T$'s between the peak and substrate temperatures of approximately 250ºC were obtained. This led to minimal interaction of the particles with the underlying substrate material.

Figure 1 shows X-ray diffraction (XRD) patterns of a conventionally annealed specimen, an as-deposited specimen, and two high-density plasma-arc-processed specimens labeled EXP.1 and EXP.2. The degree of ordering is based on the (111) peak shifting to higher $2\theta$ followed by the formation of the (001), (110) and the shift to higher $2\theta$ of the (200) peak.While some ordering is evident in the conventionally annealed specimen, significant sintering of the nanoparticles occurred. The PTP processing led to substantially greater ordering without this sintering. Processing conditions for specimens EXP.1 and EXP.2 were as follows; preheat specimens to low-level temperature and hold for 3 seconds, then expose specimens to 5 pulses of varying amperage in order to bring and hold the surface temperature to 550ºC with the only difference being the length of time for the pulses within the individual experiments. (EXP.1 pulses lengths were 0.1 second, while those for EXP.2 were 0.25 second.) The coercivity of specimen EXP.1 and EXP.2 were 1.8k Oe and 7.3k Oe, respectively. Thin-film-based FePt systems coercivity are in the range of 7.0k Oe, which shows that, by utilizing the PTP technique, ORNL has achieved a coercivity for FePt nanoparticles equivalent to that of a thin-film-based system. This is significant in that the thin-film-based systems are not able to achieve the small nanoparticle size and tight size distribution needed for storage capacity on the order of 10 Tbit/in$^2$. At best, the grain size for thin-film-based systems are 10-12 nm

with a 25% size distribution, while nanoparticle-based systems can achieve ~4-nm particle size with a 5% distribution.The latter values will an approach to the storage capacity goal.

## Benefits

This LDRD research has paved the way for controlling microstructural evolution on the nanoscale and conducting research for developing a fundamental understanding of the mechanisms involved in the thermal processing. The benefits of this knowledge will greatly accelerate the advancement of thin film and nanoparticle microelectronics and help in developing the understanding and application of synthesis processes to manipulate microstructures on the nanometer scale as related to current and next-generation photovoltaic systems. This technology will facilitate the approach to the Department of Energy's goal of $0.5/Watt for photovoltaic module costs, which currently range from $3–$5/Watt (Zweibel 1999). This cost reduction is achieved by introducing a post-deposition annealing step that will increase the collection efficiency of photovoltaic devices while adding minimal additional cost.

## References


Reddy, A. V., D. B. Kothe, C. Beckermann, R. C. Ferrell, and K. L. Lam. 1997. Proc. Fourth Int. Conf. on Solidification Processing, The University of Sheffield, U.K.

Zweibel, K. 1999. *Solar Energy Matl. & Solar Cells* **59**, 1–18.


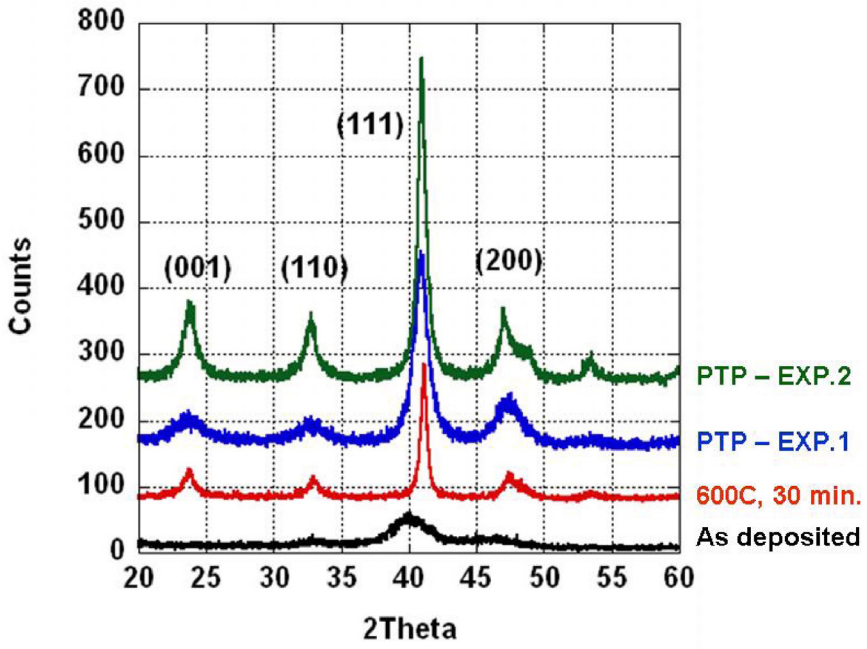


*Fig. 1. X-ray diffraction pattern for as-deposited, conventional-processed (600ºC, 30 min.) and two (EXP.1 and EXP.2) pulse thermal- processed FePt nanoparticle specimens. Specimen EXP.2 shows near-complete phase transformation from a disordered to an ordered structure.*

# Profiling Spin Injection at the Atomic Scale

J. Shen,[1] H. H. Weitering,[1] X. Zhang,[2] L. C. Feldman,[1] S. C. Erwin,[3] C.-K. Shih,[4] and M. Bode[5]
[1]*Condensed Matter Sciences Division*
[2]*Computer Science and Mathematics Division*
[3]*Naval Research Laboratory*
[4]*University of Texas at Austin*
[5]*University of Hamburg, Germany*

The grand challenge of spin-electronics or "spintronics" is to transfer spin-polarized electrons from a ferromagnetic material into a non-ferromagnetic semiconductor without substantially degrading the polarization and to provide a quantitative measure of the transfer efficiency. This proposal outlines a highly innovative experimental approach to profile spin transport across the interface using cross-sectional spin-polarized scanning tunneling microscopy (CSSP-STM). The CSSP-STM experiment simultaneously records real-space information on the local structure, electronic structure, and spin-density distribution near the cross-sectional interface with atomic precision. Fundamental physics issues as well as critical materials issues that relate directly to spin injection can be elucidated with an unprecedented level of detail and sophistication. We have successfully performed both cross-sectional and spin-polarized STM experiments. High-quality images with atomic resolution have been obtained in the cross-sectional STM, while the most difficult technical challenge for the spin polarized STM (i.e., magnetic tip preparation) has been successfully addressed. The latter has been filed for U.S. patent. In addition, we have also successfully grown and characterized various high-quality ferromagnetic/semiconductor heterostructures, which are essential for spin injection measurements by CSSP-STM. In short, the success in the CSSP-STM set-up and sample preparation has put us in an excellent position to solve the bottleneck problem in spintronics: spin injection.

## Introduction

Spintronics is widely anticipated to benefit many branches of society: information technology, strategic systems, space technology, and perimeter defense (sensors). However, researchers still face many challenges at the most fundamental level, the materials level! The greatest challenge of all is to transfer spin-polarized electrons from a ferromagnetic material into a non-ferromagnetic semiconductor without substantially degrading the polarization ("spin injection"). The second problem is to detect such spin polarization or, better yet, to obtain a complete spatial profile of the electrochemical potential of the spin-up and spin-down electrons.

Our proposal creates a novel tool that enables accurate profiling of spin polarization and injection efficiency for a wide range of materials and interfaces. We have named this cross-sectional spin-polarized scanning tunneling microscopy or CSSP-STM. Briefly, the CSSP-STM employs spin-selective tunneling as a function of position from the interface to map the chemical potentials of up and down spin with atomic precision. The CSSP-STM measurement can be analyzed without relying on input parameters that are materials dependent (such as tunneling rates and density of states). The versatility of this technique ensures applicability to a wide range of magnetic materials such as all-metal spin valves, magnetic tunnel junctions, sensors, metal/semiconductor contacts, spin MOSFETS, and magnetic polymer interfaces or "plastic spintronics."

## Technical Approach

Our goal is to achieve quantitative spin injection measurements using the CSSP-STM. The specific tasks include setting up cross-sectional STM, spin-polarized STM, and finally the combined CSSP-STM. In addition, we need to develop the synthesis capabilities for spin injection samples, and the theoretical tools for analyzing the CSSP-STM data. Cross-sectional STM and spin-polarized STM are two of the most promising recent developments in scanning probe microscopy. In cross-sectional STM, an epitaxially grown heterostructure is first cleaved in situ to create a cross sectional surface and then imaged with the STM. Both geometrical and chemical structures at interfaces can be investigated by simultaneously recording morphological and spectroscopic images at the same sample location. To achieve atomic resolution, a high-quality epitaxially grown sample is required to guarantee an atomically flat cross-sectional surface.

Spin-polarized STM is by far the most advanced technique to resolve local magnetic structures of

ferromagnetic or antiferromagnetic samples. In general the scanning tunneling tip is made of magnetic materials that have a well-defined magnetization orientation which is preferably aligned along the same axis as the sample magnetization. To view spin contrast, the tip (or the sample) magnetization is flipped 180 degree at each point. The actual magnetic signal is the difference between the tunneling signals from the two tip orientations.

While cross-sectional STM and spin-polarized STM have both been made to work by our collaborators, the combination of these two (i.e., CSSP-STM) is an absolutely unprecedented technique that will lift the characterization of the magnetic materials to a new level. The CSSP-STM method is "generic" and can be applied to all types of interfaces. Interpretation of the data does not hinge on materials-specific parameters such as band structure, density of states, or tunneling rates. Specifically, the ferromagnet/semiconductor heterostructure will be cleaved in situ to create an atomically flat cross section as the sample surface for STM. After finding the interface, a bias voltage will be applied between the ferromagnetic contact material (e.g., $Mn_5Ge_3$) and the semiconductor substrate (e.g., Ge) to allow a current passing the interface. (An early materials combination of interest is the $Mn_5Ge_3$/Ge system where our recent work has shown this to be an all-epitaxial ferromagnetic/semiconductor system, $T_c \sim 300$ K, which has convenience of fabrication and materials use.)

Furthermore, morphological and spectroscopic images will be acquired simultaneously along with the spin-dependent chemical potentials to provide information about spin polarization, lattice, and chemical structure from the same interface location. This information should deliver atomic-scale understanding of the spin injection mechanism due to the high spatial resolution of STM. In particular, we can investigate the role of interfacial tunneling barriers, Schottky barrier heights, space-charge layers, dopant profiles, and point and line defects on the injection efficiency. Many of these parameters will vary on a length scale of several nanometers up to 1 micron, and their effects on the injection efficiency can thus be elucidated from CSSP-STM investigations on a single sample. Development of this novel and unique tool will provide the definitive spin transport measure that will become the standard for developing new materials systems and understanding the effects of interface perfection on spin transfer.

## Results and Discussion

We have made outstanding progress in all these areas. High-quality images with atomic resolution have been obtained from a $Ga_{0.5}In_{0.5}As$/GaAs heterostructure in the cross-sectional STM. This involves the setup for in situ cleaving of epitaxially grown sample to create a cross-sectional surface and then imaged with the STM. For spin polarized STM, the most difficult technical challenge is to prepare magnetic tips in situ that have a controllable magnetization orientation with minimum stray field. To do this, one has to flash a nonmagnetic tungsten (W) tip at >2000ºC to create a clean, atomically flat, and nanometer-sized terrace at the very tip end (Fig. 1). Afterwards, one or two monolayers of magnetic films of choice will be deposited onto the tip end to allow a controllable magnetization orientation. Because this invention will conveniently transform the market-dominating Omicron conventional UHV VT-STMs into SP-STM, a U.S. patent has been filed by us (Li 2004a). With a coated magnetic tip, we have successfully observed magnetic domain structures in an ultrathin film of Fe grown on Cu(100) substrate.

In addition to the progress in CSSP-STM, we have also successfully grown various high-quality ferromagnetic/semiconductor heterostructures, which are essential for spin injection measurements by CSSP-STM. These include $Mn_5Ge_3$/Ge (Zeng 2003), $Mn_xGe_{1-x}$/Ge (Li 2004b), and Fe/GaAs. We have done comprehensive studies of the structural, chemical, magnetic, and transport properties of these heterostructures. Our paper on $Mn_xGe_{1-x}$/Ge (Li 2004b; Li 2004c) reports a breakthrough in understanding ferromagnetic semiconductors. During

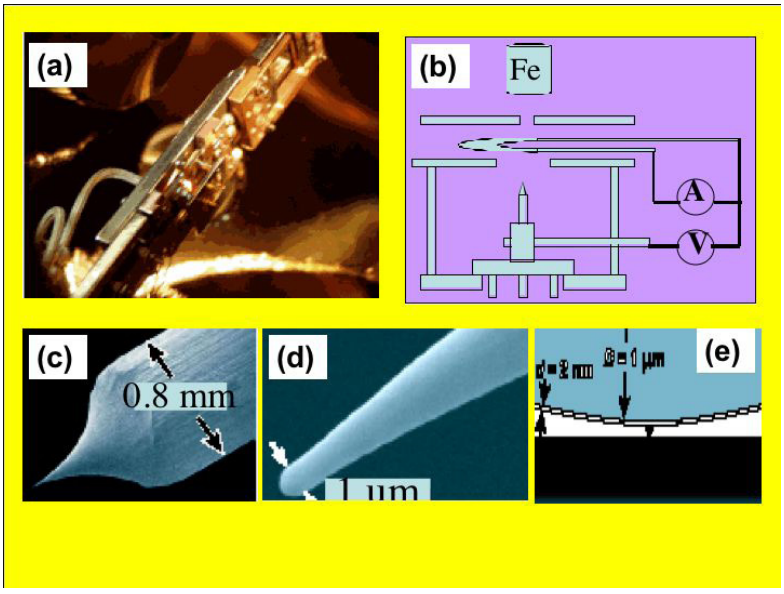


*Fig.1. SP-STM tip preparation set up in (a) and (b). SEM image of a tip before flashing (c); after flashing (d). Schematic view of monolayer magnetic film coating on the prepared tip.*

the growth, reflection high-energy electron diffraction (RHEED) is used to monitor the growth in real time. Transmission electron microscope (TEM) and ion channeling measurements (not shown here) have confirmed the high quality of the epitaxial growth.

The most remarkable achievement in the material program is that we have managed to dramatically increase the Curie temperature (Tc) of the $Mn_xGe_{1-x}$/Ge magnetic semiconductors using post-growth annealing. Based on comprehensive structural, magnetic, and transport characterizations, we have understood the underlying mechanism for the enhancement of Tc. Essentially, Mn dopants occupying interstitial sites of Ge have been driven from bulk to the surface upon thermal annealing, leaving behind those Mn ions that occupy substitutional sites in the bulk. The substitutional Mn ions contribute holes to the system and enhance the magnetic coupling strength. As a consequence, Tc of annealed $Mn_xGe_{1-x}$/Ge increases dramatically, from 20 K to above room temperature. The high Tc samples have, for the first time, made themselves useful for real applications in spintronics.

We have also measured the spin polarization of the ferromagnetic $Mn_5Ge_3$ epilayers on Ge(111) using Point Contact Andreev Reflection Spectroscopy (PCAR) and calculated the spin polarization of bulk $Mn_5Ge_3$ in the ballistic and diffusive regimes using density-functional theory (DFT). This is an important characterization step as the spin polarization of the ferromagnetic layer is essential for understanding the spin injection from a ferromagnet into a semiconductor. The spin polarization of $Mn_5Ge_3$ along the [001] direction (i.e., normal to the interface of a $Mn_5Ge_3$/Ge(111) hetero junction) was measured to be 43 ± 5%, much higher than the PDFT = 10–15% in the ballistic limit but fairly close to the PDFT = 35–50% in the diffusive limit. The agreement with the latter results must be coincidental as the measurements were done in the ballistic regime. We attribute the discrepancy between the experiment and the theory to extreme sensitivity of the DFT calculations to the crystallographic structure of $Mn_5Ge_3$, as well as possible Mn deficiency of $Mn_5Ge_3$. Overall, our results demonstrate not only that $Mn_5Ge_3$ can be lattice matched to Ge, has high mobility with a carrier mean free path of 85 nm at 1.6 K and room Curie temperature but also has higher-than-predicted spin polarization, comparable to the spin polarization of 3-d transition metals as well as MnAs. This indicates a high potential for this novel material in a variety of spintronics applications.

Finally, on the theory front, we have formulated a self-consistent procedure for calculating the band bending in a metal/semiconductor/metal sandwich, which is the effective electrostatic potential as a function of position. Our model already can account for the asymmetry of the charge accumulation due to either different metals on both sides or an applied bias voltage. The effect of the current can be included by coupling the model to the Boltzmann transport equation.

## Benefits

Spintronics is very high on the radar screen of the President's Office of Science and Technology Policy. With the dramatic diminution of basic research in industrial laboratories, the DOE nanocenters will be expected to step up their efforts in this area, in partnerships with researchers from academia. Our achievements have immediately put the ORNL Nanocenter (CNMS) on the map as the prime DOE facility for spintronics research. The technology and instrumentation is one of a kind and because of its versatility; it should become one of the most successful user facilities at CNMS. It will be an important characterization tool for a broad range of spintronic materials and devices, including semiconductor electronics, molecular electronics, soft materials ("Plastic spintronics"), radiation-hardened devices, and possibly sensors that can be utilized for perimeter defense and unexploded ordnance detection. Each of these areas is of vital interest to the U.S. economy and the security of the nation. This program is becoming a major asset for the laboratory in terms of scientific recognition.

The unique ability of profiling spin injection directly in real space across an interface means that our technique and instrumentation will be highly valuable to any company aiming to develop or optimize their spintronics devices. We foresee tremendous demand from industry for our technique, both as a user facility as well as a research partner. Many parts of this proposal contain patentable ideas. Once these ideas are verified experimentally, we will file invention disclosures and begin to actively seek industrial partners to further develop these ideas.

## References


Li, A. P., J. X. Ma, and J. Shen. 2004a. "In Situ Scanning Tunneling Microscope Tip Treatment Device For Spin Polarization Imaging." U.S. patent (pending).

Li, A. P., J. Shen, J. R. Thompson, and H. H. Weitering. 2004b. "Ferromagnetism and Polaron Percolation in MnxGe1-x Dilute Magnetic Semiconductor." *Appl. Phys. Lett.* **86**, 152507.

Li, A. P., J. F. Wendelken, J. Shen, L. C. Feldman, J. R. Thompson, and H. H. Weitering. 2004c. "Magnetism in MnxGe1-x semiconductors mediated by impurity band carriers," *Phys. Rev. B* (in press).

Zeng, C., S. C. Erwin, L. C. Feldman, A. P. Li, R. Jin, Y. Song, J. R. Thompson, and H. H. Weitering. 2003. "Epitaxial ferromagnetic $Mn_5Ge_3$ on Ge(111)," *Appl. Phys. Lett*. 83, 5002.

# Quantum Circuit Modeling for Nanoelectronics

X.-G. Zhang,[1] V. Meunier,[1] and S. T. Pantelides[2]
[1]*Computer Science and Mathematics Division*
[2]*Condensed Matter Sciences Division/Vanderbilt University*

This proposal aimed to develop the methodology and pursue initial applications for construction of "compact circuit models" that capture the key features of the nanoscale while being compatible with current industry practices in circuit modeling for ease of knowledge and technology transfer. We have studied and characterized some of the novel devices, including carbon nanotube junctions, ultrathin $SiO_2$ tunnel junctions, and Fe/MgO/Fe spin-dependent tunnel junctions. Resonant spin-dependent tunneling was discovered in the Fe/MgO/Fe/Cr junctions. Preliminary compact circuit models have also be developed based on first-principles calculations of the I-V characteristics of the device elements.

## Introduction

In recent years, nanoscale electronic devices (molecules or semiconductor nanostructures) have been extensively investigated as a new frontier beyond conventional microelectronics. The PI's and collaborators have pioneered the simulation of transport properties of individual nanodevices. Ultimately, nanodevices must be integrated as components of circuits, and the simulation of the circuit as a whole remains a key ingredient in developing applications. Here we propose a truly ground-breaking initiative to develop the fundamentals of quantum circuit modeling. The issues are strikingly different from the ones encountered in classical circuit modeling, where one assumes a simple picture of constant currents in the wires between devices, which in turn are modeled using approximate solutions of the Boltzmann transport equation (each conventional device is represented by a classical "equivalent circuit"-in-a-box, within which the relevant elements are obtained by simulating the device using the Boltzmann equation). In a quantum circuit, the wires are too short for conventional modeling to apply and should be treated by the Boltzmann equation as well, by building proper interface between the wires and the quantum devices via appropriate boundary conditions. The quantum devices themselves must be treated with full quantum mechanics.

## Technical Approach

While the quantum mechanical solution of a complete circuit is impractical and unnecessary, the rigorous quantum mechanical treatment of the device region is of utmost importance and there are sophisticated approaches available. The boundary conditions demand that the flux of electric charge at the interfaces of the quantum device is conserved and can be expressed by the transmission and reflection probabilities at the boundary. To solve the quantum mechanical problem in the device region, the most practical approach is based on the time-independent one-electron Schrödinger equation,

$$H\Psi = E\Psi .$$

The one-electron Hamiltonian $H$ is taken to have precisely the same form as the effective one-electron Hamiltonian of density functional theory (DFT), usually in the form of the Kohn-Sham (KS) formulation. In transport problems, one has to deal with open boundaries, particles injected and ejected from the device, which is most conveniently represented by "scattering" boundary conditions. Two approaches have been pursued so far: (a) the Lippmann-Schwinger (LS) equation is based on scattering theory as originally developed for high-energy physics and (b) the non-equilibrium Green's function method. Besides the calculation with these approaches, we will also use and develop a new method in which the circuit (i.e., the open system consisting of the device, the electrodes, and the battery) is modeled as a closed finite system with a source and a sink which are connected to the device. The source and the sink are modeled by imaginary Dirac delta-function potentials. A positive imaginary potential injects electrons, while a negative imaginary potential absorbs electrons. The advantage of this method is its simplicity; the existing powerful DFT computer codes can be used with little modifications to solve transport problems. It may also be more suitable for quantum circuit simulations because the source and sink terms in the boundaries directly relate the injection and ejection of the electrons from the environment to the quantum device.

The result of quantum mechanical calculations will characterize the device in terms of wave functions (or equivalently by Green's functions), and of course all physical properties of the device can be determined from this information. For an incident Bloch wave in k-th channel of the left electrode, the scattering solution is written in the following form:

$$\Phi_l^k(r) = \begin{cases} \phi_l^k(r) + \sum_{k'} r_{kk'}\phi_l^{k'}(r) & \text{(left electrode)} \\ \sum_i c_i \varphi_i(r) & \text{(device)} \\ \sum_{k'} t_{kk'}\phi_r^{k'}(r) & \text{(right electrode)}, \end{cases}$$

where $\varphi_l^k$ and $\varphi_r^k$ are Bloch states in the left and right electrodes (including evanescent modes), and $t_{kk'}$ and $r_{kk'}$ are the transmission and reflection coefficients. The wave function in the device region is written as a linear combination of linearly independent solutions $\varphi_i(r)$ (i = 1,..., N) of the device Hamiltonian obtained by the methods described in the previous sections. Matching the wave functions and their derivatives at the right and left device boundaries, one gets four sets of linear equations for the unknown transmission, reflection and coefficients. These equations, after eliminating the linearly dependent solutions by using the condition of current conservation, can be solved by simple linear algebra. The calculation of the reflection and transmission coefficients with this boundary matching approach is very efficient and accurate provided the solution in the device region satisfies the scattering boundary conditions and enough evanescent modes are included in the lead region.

In Pantelides et al. (2001), the authors perform first-principles modeling of the molecular device considered here and study the influence of the molecule-electrode link. They conclude that the I-V characteristic shape depends on the molecule orbitals and that the absolute magnitude of the current is dictated by the nature of individual atoms at the molecule-electrode contact. This result suggests that the transmission spectrum of the system can be described using an equation whose form is

$$T(E,V) = A \times DOS(E,V)$$

in which $V$ is the applied voltage, $E$ the energy, and $A$ a parameter whose physical meaning is detailed below. The form of the equation can also be justified by the following picture of the electron transport through the device (Fig. 1). The ease with which an electron travels from one electrode to the other through the molecule is determined by the symmetry of the successive orbitals the particle encounters. Biasing the system does not change this symmetry but modifies its density of states, modulating the current.

The parameter $A$ includes two contributions. The first one is the symmetry of the successive wave functions the carriers go through; the second one reflects the nature of the connecting end atoms. This means in the case of a molecule whose orbitals couple weakly with the connecting ends, the nature of the linking atoms will determine the value of the parameter $A$. This parameter could be tabulated for a given molecule embedded between electrodes of different types.

The quasi-bound state resonance of a particle within a square potential well has an energy dependence described by a Lorentzian function. Thus, we describe each peak $i$ of the molecule DOS by a Lorentzian defined by its height $H_i$, half-width $\Gamma_i$, and energy position $E_i$. As described by the equation, the general expression for the DOS is simply the sum of each peak, $n$ being the total number of states taking part in the transport over the applied bias range:

$$DOS(E,V) = \sum_{i=0}^{n} H_i(V)\left[1 + \frac{(E - E_i(V))}{1/2 \times \Gamma_i}\right]^{-1}$$

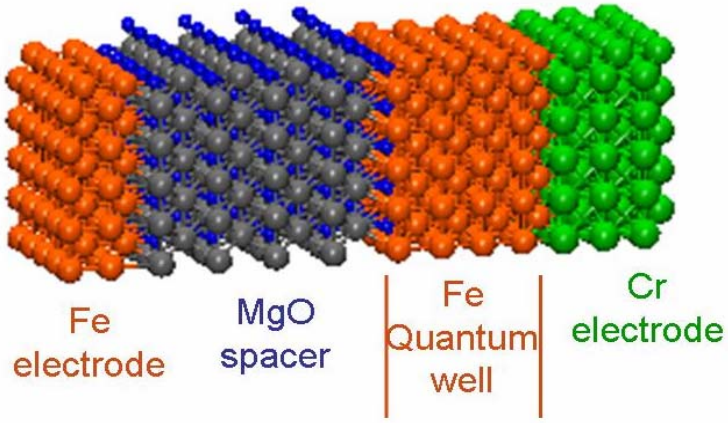


*Fig. 1. Structure of the Fe/MgO/Fe/Cr spin-dependent quantum well system.*

For each peak of the DOS, values for the three parameters at zero bias are extracted from Fig. 2, which exhibits the molecule DOS calculated from a first-principles (parameter free) density-functional method using plane waves as an orbital basis, pseudopotentials to describe the ionic cores, and periodic supercells. The relative height of each peak is extracted, as well as its half-width and energy position.

## Results and Discussion

One of the discoveries in this project was the resonant spin-dependent tunneling through metallic quantum well states in Fe/MgO/Fe/Cr tunnel junctions (Lu et al.,

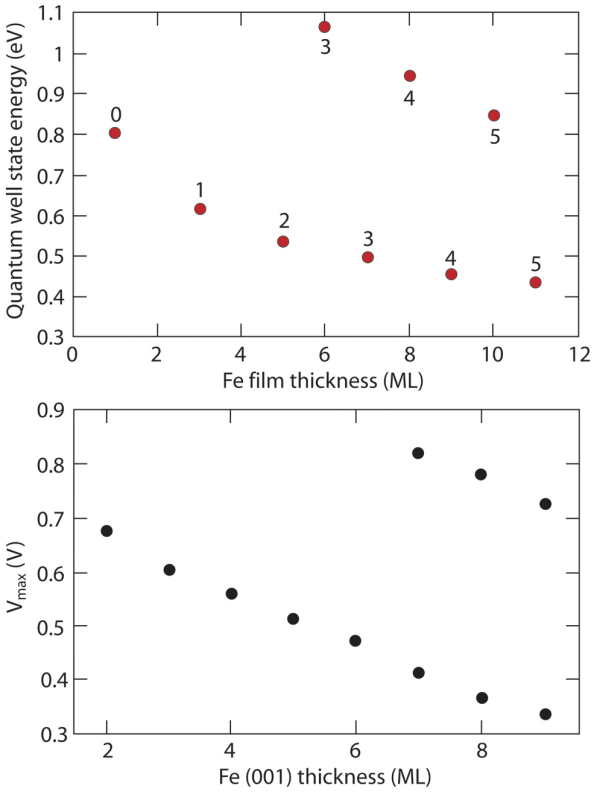


*Fig. 2. Energies of quantum well resonances compared with experiment. Top: theory (numbers above the data points indicate the number of nodes in the electron wave function); bottom: experiment.*

2005). In addition to the correct prediction of the position of the quantum well resonances, our calculation also predicts plateaus of tunneling current and large tunneling magnetoresistance resulting from these resonances.

We have made the first step in constructing a compact circuit model using parameters extracted from first-principles calculations. Table 1 summarizes the compact model, including the equations used, the necessary parameters, and the methods required to get the parameters.

**Table 1. Compact model summary**

| *Equations* | | | |
|---|---|---|---|
| | $I(V)=\frac{2e}{h}\int_{-\infty}^{+\infty}\left[f(E,E_{F,L})-f(E,E_{F,R})\right]T(E,V)dE$ | | |
| | $T(E,V)=A\times DOS(E,V)$ | | |
| | $DOS(E,V)=\sum_{i=0}^{n}H_i(V)\left[1+\frac{(E-E_i(V))}{1/2\times\Gamma_i}\right]^{-1}$ | | |
| *Parameters* | *Method for obtaining the parameter* | | |
| | *DFT w/o Jellium* | *DFT w/ Jellium* | *Fit* |
| $H_i$ | $H_i(V=0)$ | $H_i(V\neq 0)$ | |
| $E_i$ | $E_i(V=0)$ | $E_i(V\neq 0)$ | |
| $\Gamma_i$ | $\Gamma_i(V=0)$ | Not used | |
| $A$ | | | $A$ |

## Benefits

ORNL has established a foothold in the area of molecular electronics and nanoelectronics. Nano-transport is a major component of the Nano-Theory Institute of the Center for Nanophase Materials Science (CNMS). ORNL also has other ongoing projects supported by the modeling efforts in the molecular electronics area, such as the recent National Institutes of Health (NIH)–funded projects on DNA sequencing nanotechnology. This projects is the first step towards the next stage of development. Modeling on the circuit level has much greater potential due to a direct industrial need to design and simulate nanoscale circuitry before prototypes will be built. As far as we are aware, this is virgin territory with virtually no competition from our scientific peers. This is in sharp contrast to the modeling of quantum transport through individual molecules, where several codes are likely to be released publicly or become commercially available within the near future. A general quantum and semiclassical circuit model code that works for both molecular electronics and spintronics will have wide appeal with the semiconductor industry, magnetic recording industry, as well as DOD [particularly Defense Advanced Research Projects Agency (DARPA)]. Furthermore, because the application of such modeling of molecular-level circuitry requires input from large-scale, first-principles calculations, further collaborations with industry may take the form of industry-funded research efforts or user-facility-type large-scale computational tasks. Although we are still a long ways from this ultimate goal, we have made important progress in this direction. In addition to the potential industry interest, this project also established a new platform on which significant scientific breakthroughs can take place. It will allow us to model numerically complex, nonlinear dynamic systems that are also in the quantum regime.

## References

Z. Y. Lu, X.-G. Zhang, and S. T. Pantelides, "Spin-dependent resonant tunneling through quantum-well states in magnetic metallic thin films," *Phys. Rev. Lett.* **94**, 207–210 (2005).

Pantelides, S. T., M. Di Ventra, and N. D. Lang et al., Molecular Electronics by the Numbers, *IEEE Trans. on Nanotech.***1**, 86–90 (2001).

# Characterization of Spin Structure and Spin Dynamics of Nanostructure Assemblies Using In-Field Scanning Electron Microscopy with Polarization Analysis

J. F. Wendelken,[1] J. Shen,[1] S. Dai,[2] and Z. Gai[3,1]
[1]*Condensed Matter Sciences Division*
[2]*Chemical Sciences Division*
[3]*Peking University, Beijing, China*

In data storage and spintronics devices, nanostructured magnetic materials must have their magnetization direction reversed by application of an external field. The performance of the materials critically relies on the dynamics of the magnetization reversal, which can be imaged using the in-field Scanning Electron Microscope for Polarization Analysis (in-field SEMPA) developed at the MPI-Halle in Germany. Zheng Gai, who has outstanding experience in both nanoscale magnetism and instrumentation, has gained experience in the SEMPA technique by working at the MPI-Halle as a guest scientist and has now brought this experience to Oak Ridge National Laboratory (ORNL) as an employee of the Condensed Matter Sciences Division. Acquiring this expertise coincident with the purchase of the SEMPA system developed at the MPI-Halle by the Center for Nanophase Materials Sciences (CNMS) provides a major new capability at ORNL for the study of scientific issues regarding magnetization reversal and spin injection.

## Introduction

With the miniaturization of magnetic technologies, the need to understand magnetization and particularly the switching behavior on length scales below a micron is becoming increasingly important. This booming interest in micromagnetics has fueled a renaissance in both micromagnetic modeling and measurement techniques. Conversely, the development of modeling and imaging has made possible recent advances in this critical area of magnetism. On the modeling side, the rapid development of high-speed computing has had a tremendous impact on micromagnetics simulations. On the measurement side, a number of microscopes have been developed for imaging on a length scale ranging from a few to a few tens of nanometers. These include the spin polarized low-energy electron microscope (SP-LEEM), the spin polarized scanning tunneling microscope (SP-STM), the X-ray magnetic dichroism photo emission electron microscope (XMD-PEEM), and the SEMPA. Depending on the actual samples, each of these techniques has advantages and disadvantages. SP-STM has the highest spatial resolution of 1 nm or even below but yields no direct information on magnetization. SP-LEEM also has a high spatial resolution (~10 nm) but is only good for single-crystal surfaces. XMD-PEEM has elementary sensitivity but limited resolution of ~30 nm. SEMPA produces a direct image of the direction and the relative magnitude of the magnetization of the specimen, with sensitivity down to a fraction of an atomic layer and a lateral resolution of ~15 nm.

The focus of this project has been the development of the SEMPA capability at ORNL and specifically for the CNMS. In addition to acquiring necessary instrumentation, it was crucial to hire the proper expertise to make this program a success. That objective has been accomplished with the employment of Zheng Gai at ORNL. The results described briefly are the first fruits of this new program developed with the support of this LDRD project.

## Technical Approach

The SEMPA is an ultrahigh vacuum-based system that allows the investigation of magnetic domain structures of both in situ and ex situ grown samples. This SEMPA is able to acquire magnetic domain images with a spatial resolution of 30 nm or better with an incident beam size of less than 15 nm, and with monolayer sensitivity for transition metals such as Fe, Co, and Ni. The SEMPA system is equipped with a spin detector that allows the acquisition of all three orthogonal components of the vector polarization (magnetization) signal. A unique feature of this SEMPA is the capability for imaging under an external magnetic field up to 0.1 T. The coaxial Scanning Auger Microscopy (SAM) system allows the surface analytical capabilities of Auger analysis to be combined with the high spatial resolution offered by the SEM. Conventional surface science preparation and analysis facilities, including an ion-beam sputtering gun, four electron beam evaporators, quartz crystal thickness monitor, mass spectrometer, and low energy electron diffraction system, are equipped for preparation and

characterization of sample surfaces. A linear Magneto Optical Kerr Effect is also included in the preparation chamber for in situ magnetic property measurement.

In SEMPA, a well-focused high-energy ~10-keV electron beam is directed at a surface, and the spin polarization of the ejected low-energy ~eV secondary electrons is measured. The spin polarization is known to be directly proportional to the magnetization at the surface, so that the surface domain pattern may be determined. When the sample is exposed to a magnetic field, several difficulties may be incurred. First, the spot size of the primary beam could be deteriorated by aberrations. Furthermore, the spin polarization of the secondary electrons could be falsified due to spin precession, and finally, the secondary electron beam could be significantly deflected by the magnetic field so that the electrons do not reach the spin detector. These difficulties are suppressed by using our unique setup. All disturbing effects caused by a magnetic field at the sample surface may be reduced by decreasing the transit time through the magnetic field (Steierl et al. 2002). This is accomplished by using a locally confined magnetic field and an additional electric field to accelerate the slow secondary electrons directly after emission. In our setup, the magnetic field is confined to a small volume by using a magnetic circuit that ends towards the sample with a narrow gap (pole distance 120 μm) from which the magnetic field protrudes. The sample is positioned close to the magnetic pole pieces (~10–40 μm) so that the surface region near the gap can be exposed to strong magnetic fields. The accelerating electric field is generated by placing the magnetic foil and the sample at different potentials, typically several 100 V, depending on the chosen sample to magnet distance. Thus, the magnetic pole pieces serve not only as sources of the magnetic field but also as electrostatic electrodes. A subsequent electrostatic quadrupole is used to further accelerate the secondary electrons after passing the gap and to correct for small deflections induced by the magnetic field. The magnetic circuit was machined from a high permeability foil by using a laser cutter. For precise positioning, the entire assembly is mounted on a three-axes piezodriven positioner. By using the SEM mode, the positioning of the magnetic circuit with respect to the sample surface is monitored accurately.

The samples used in our experiments are either made in situ or transferred in from a load lock. The wires were grown ex situ in the Chemical Sciences Division. Those wires were attached to the clean Si or Cu substrates first. After they were transferred into our SEMPA chamber, light Ar sputtering was applied to clean the wires and substrates before the deposition of a very thin layer of Fe film. It has been found that the thin film mirrors the domain structure of the ferromagnet beneath while the newly generated surface is clean, and thus the secondary electrons are spin polarized (Oepen et al. 2002). The Fe/Cu(111) samples were grown in the SEMPA chamber, and the thickness of Fe was monitored precisely by the SAM.

## Results and Discussion

### *In-Plane Magnetic Field Reduce the Perpendicular Magnetic Anisotropy*

In magnetic ultrathin films, the study of magnetic domains is associated with the understanding of magnetic long-range order in a 2D Heisenberg system. It is known that a perpendicular uniaxial magnetic anisotropy stabilizes the magnetic long-range order in a 2D Heisenberg system, but a homogenous magnetic state is energetically unstable against the formation of magnetic stripe domains, especially at the spin reorientation transition point. Fcc Fe on Cu(001) has been a model system for the study of stripe domains. Although there are many theoretical works that have been promoted since the experimental discoveries, the limited knowledge of stripe domains within a magnetic field hinders further understanding of the stripe phase. Because of the technical difficulty of the realization of the in situ in-plane magnetic field, researchers around the world were trying to provide so-called virtual magnetic field to indirectly study the issue. A study of Co/Cu/ (Fe/Ni)/Cu(100) in which the Co magnetization provides the in-plane virtual magnetic field to the Fe/Ni stripe domains (Wu et al. 2004) has been reported. This work reveals a universal dependence of the stripe domain width on the magnetic anisotropy and on the interlayer coupling. With the unique design of our in-field imaging SEMPA, the direct observation of the in-plane field-induced stripe domain evolution of the perpendicularly magnetized Fe/Cu(001) thin film (2 ML) has been conducted. Our preliminary result in Fig. 1(a) shows that the evolution behavior of field-induced stripe domain evolution follows the same trend as the temperature, thickness of Fe, and interlayer coupling induced changes.

### *Nanometer Domains on Spinel $CoFeO_4$ Wires*

As a promising predominant magnetic and electrical resistive material, $CoFe_2O_4$ ferrite has large magnetocrystalline anisotropy with a reasonable magnetization for applications in future high-density magnetic recording media and high-performance electromagnetic and spintronic devices. The magnetic properties of the spinel $CoFe_2O_4$ nanowires (measured with SQUID magnetometry) indicate that although the Curie temperature (Tc) is well above the room temperature, the coercivity (Hc) falls at a much faster pace with increasing temperature, which reflects the fact that nanowires are approaching the superparamagnetic blocking temperature (TB) around 350 K (Zhang et al. 2005). Our SEMPA image and vector image in Fig. 1(b) shows the existence of the

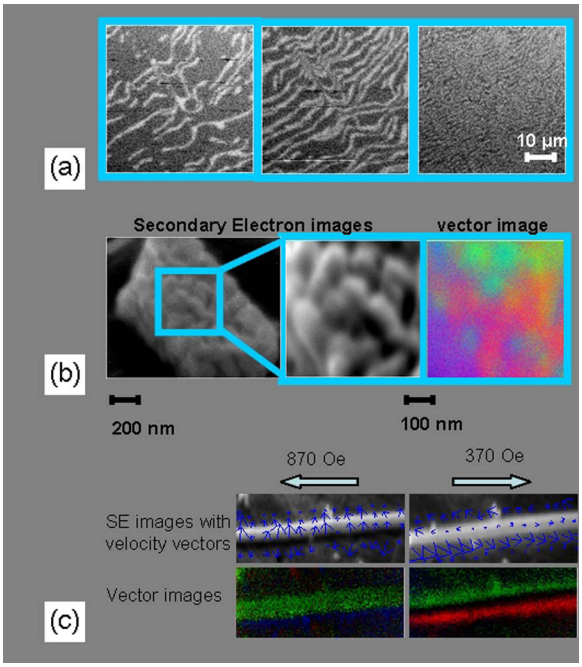


*Fig. 1. (a) Perpendicular component of SEMPA images of the stripe domains of Fe/Cu(001) under different in-plane magnetic field. The density of the domains increases while the filed increases. (b) Secondary electron (SE) images and the vector image of a $CoFeO_4$ wire. The vector image is the superimposition of the X and Y components of the domain images. (c) SE images and the vector image of a $La_{1-x}Ca_xMnO_3$ wire. Velocity vectors extracted from the vector images were superimposed on the SE images.*

magnetic domains at room temperature with a domain size as small as 50 nm. The domains remain stable in the magnetic field of 1000 Oe.

### *$La_{1-x}Ca_xMnO_3$ wires*

Recently, there has been a surge of interest in the properties of $La_{1-x}Ca_xMnO_3$ and related rare earth manganate perovskites because of the colossal magnetoresistance. For a broad range of doping, these materials have a paramagnetic-to-ferromagnetic (FM) transition upon cooling, which is accompanied by a sharp drop in the resistivity. The phase diagram of bulk LCMO shows the mixing of FM metal and CO insulator under different doping, and the transition temperatures are well below room temperature. To our surprise, the preliminary SEMPA images and vector images in Fig. 1(c) of single LCMO wire show the magnetic domain changes under external field at room temperature.

## Benefits

With the newly acquired in-field SEMPA, and in particular with the scientific expertise to exploit this capability, we are ready, for the first time, to determine the switching mechanism of individual as well as assemblies of magnetic nanostructures. This will have a great impact on both basic science and nanotechnology and will also be one of the cutting-edge tools available to users in the CNMS. Basic science will be impacted because SEMPA is an ideal tool to investigate the physics of magnetic domains. The in-field SEMPA, with its capability of imaging under magnetic field, will provide answers for many unsolved issues that are related to dynamic spin structure in reduced dimensions and magnetic quantum tunneling. It is crucial for developing theories of micromagnetic modeling by providing in-depth experimental data of magnetic structures at various fields. Nanotechnology will be impacted because with the ever-increasing density of magnetic "bits" in data storage devices, the effects of thermal fluctuations on the domain structure as well as the dynamics of magnetization reversal of the small "bit" is becoming increasingly important. By closely coupling temperature- and field-dependent measurements of switching dynamics and micromagnetic modeling of the reversal process, it can provide insight into the microscopic mechanisms that control reversal modes (coherent rotation, nucleation) and how they are affected by intrinsic materials properties as well as by particle size and shape.

The establishment of unique capabilities such as in-field SEMPA at the CNMS is one of the keys to ensure the success of the Department of Energy nanotechnology initiative. These capabilities will be available to a wide variety of users and will impact programs supported by the National Science foundation and other science and technology agencies as well as industry.

## References

Steierl, G., G. Liu, D. Iorgov, and J. Kirschner. 2002. *Rev. Sci. Inst.* **73**, 4264.

Oepen, H. P., G. Steierl, and J. Kirschner. 2002. *J. Vac. Sci. Tech. B* **20**, 2535.

Wu, Y. Z., C. Won, A. Scholl, A. Doran, H. W. Zhao, X. F. Jin, and Z. Q. Qiu. 2004. *Phys. Rev. Lett*. **93**, 117205.

Zhang, Z. T., A. J. Rondinone, J. X. Ma, J. Shen, and S. Dai. 2005. *Adv. Mater.* **17**, 1415.

# Carbon Fiber Composite Monoliths as Catalyst Supports

C. I. Contescu,[1] N. C. Gallego,[1] J. M. Pickel,[2] and T. D. Burchell[1]
[1]*Metals and Ceramics Division*
[2]*Chemical Sciences Division*

Carbon fiber composite monoliths have been studied in the Carbon Technology Group of Metals and Ceramics Division for a number of years. They are rigid, three-dimensional carbon composites that can be activated to a large surface area, have tunable porosity, and proven performance in gas separation and storage. In this project, we investigated these materials as catalyst supports. These composites are ideal as catalyst supports in applications where a rigid support with open structure and easy fluid access is desired. We developed a procedure for depositing a dispersed nanoparticulate phase of molybdenum carbide ($Mo_2C$) on carbon composite monoliths in the concentration range of 3 to 15 wt % Mo. The composition and morphology of this phase was characterized using X-ray diffraction and electron microscopy, and a mechanism was suggested for its formation. Molybdenum carbide is known for its catalytic properties that resemble those of platinum group metals, but at a lower cost. The materials obtained are expected to demonstrate catalytic activity in a series of hydrocarbon reactions involving hydrogen transfer, such as isomerization, hydrodesulfurization and hydrodenitrofication; these reactions are at the core of naphtha reforming processes. This project demonstrates the potential of carbon fiber composite monoliths as catalyst supports.

## Introduction

Industrial catalysts consist traditionally of a dispersed metal or metal oxide phase supported on a high surface area support. The preferred supports of industrial catalysts are alumina, silica, and zeolites. They have high porosity combined with large and easily accessible internal surface area, are mechanically and thermally stable, and can be shaped as required for various applications. In the 1970s, the search for better catalyst supports led to a new range of materials that combine high surface area and chemical inertness with tunable porosity, such as ordered mesoporous solids (MCM-41, SMA-15) and advanced microporous solids (zeotypes).

More recently, carbon materials became the focus of interest as catalyst supports. They combine high surface area, tunable porosity, chemical stability in acidic or basic environments, and thermal stability in non-oxidative gas environments. Carbon-based catalysts are also attractive due to easy recovering of the metal from spent catalysts. However, the research on controlled preparation of carbon-based catalysts developed slowly because the first attempts used carbon derived from natural sources, such as wood, coal, or coconut shell. Although these carbons are excellent adsorbents due to their extended surface area and are easily available at a low cost, they often display inhomogeneous texture and contain uncontrolled amounts of impurities which may adversely impact their catalytic properties. For development of catalyst supports, well-defined pure carbon materials and controlled preparation methods are indispensable. Carbon materials that do not suffer from the above-mentioned drawbacks, such as synthetic carbons, are better suited as catalyst supports. They can be produced with required texture and surface properties and in a wide variety of physical shapes.

Recent work at ORNL in the area of microporous carbons has focused on novel carbon fiber–based adsorbent monoliths (Burchell 1999). These are tri-dimensional bodies fabricated in a slurry molded process from carbon fibers and a thermosetting resin as a binder. After curing and carbonizing the resin, the resulted material can be activated into structures with tunable porosity, varying from microporous (with pores smaller than 2 nm) to mesoporous (with pores in the 2- to 50-nm range) carbons. The microporous carbon fiber composites molecular sieve (CFCMS) developed in ORNL have been proven in gas adsorption, gas separation, and gas purification applications.

The objective of this project is to investigate the possibility of using carbon fiber monoliths as catalyst supports. The monolithic structure of these carbon composites offers considerable advantage over conventional, granule-shaped activated carbons. Monoliths are less susceptible to settling, attrition, and bypass channeling than granular catalysts beds. The small diameter of carbon fibers (10–15 μm) offers kinetic advantages when these supports are used in fast sorption or desorption cycles. Moreover, the continuous carbon skeleton of carbon fiber monoliths makes them electrically conductive, allowing their use as electrocatalyst supports or regeneration by resistive electric heating. In addition, catalysts supported on carbon monoliths afford easy separation of products and fast catalyst recovery in comparison with slurry catalysts based on carbon powder supports.

We focused on the deposition and stabilization of highly dispersed molybdenum carbide on carbon fiber monoliths, and development of those surface properties that enable catalytic activity.

Highly dispersed transition metal carbides promise to be an inexpensive substitute for noble metal catalysts, with superior ability to withstand high temperatures and higher resistance to poisoning. The interest in metal carbides has grown steadily since it was noted that tungsten carbide (WC) showed catalytic properties similar to those of platinum, and molybdenum carbide ($Mo_2C$) compared to ruthenium in a series of catalytic reactions involving hydrogen: room temperature oxidation of hydrogen and hydrocarbons (Levy and Boudart 1973) as well as other more complex reactions including isomerization, hydrogenolysis, hydrogenation, dehydrogenation, hydrodenitrification (DHN) and hydrodesulphurization (DHS). Due to its high tolerance to sulfur, $Mo_2C$ supported on alumina is a promising catalyst for hydrogenation of aromatics in diesel fuel (Da Costa 2001; Da Costa 2003). Some studies suggested that the hydrogenation activity of $Mo_2C$ supported on carbon was higher than that of Co-Mo/alumina catalysts, an effect explained in terms of weak electronic interactions with the carbon support (Bridgwater 1982). In recent years, carbon-supported $Mo_2C$ catalysts were studied by several authors (Sayag et al. 2001; Mordenti et al. 1998; Liang et al. 2002) for their promising catalytic properties.

## Technical Approach

We prepared a series of carbon monoliths by slurry molding pre-activated carbon fibers (isotropic pitch fibers AP-100, AP-200, and AP-400 from Anshan E-Asia Carbon Co.) with phenolic resin as a binder. The monoliths obtained after curing and carbonizing the resin were characterized for bulk density, average Darcy permeability, BET surface area by nitrogen adsorption, and pore size distribution. The values of BET surface area of carbonized monoliths were on average 75 % of BET values of the original activated carbon fibers, showing that some extent of pore closing took place during slurry molding. Based on this characterization, we selected a monolith (NG-4) with high permeability (12 $\mu m^2$), high BET surface area (1220 $m^2/g$), and high specific pore volume (1.18 $cm^3/g$) with average pore width of about 1.2 nm. The bulk density of the monolith was 0.26 $g/cm^3$.

Molybdenum was introduced on the NG-4 carbon support by pore filling impregnation from aqueous ammonium heptamolybdate solutions (AHM), $(NH_4)_6Mo_7O_{24}$. Using a potentiometric titration technique, it was verified that the point of zero charge of the carbon support in water was at pH 9. Analysis of the proton binding isotherm revealed four distinct functional groups characterized by apparent acidity constants (pKa) of 3.7 (0.07 mmol/g); 5.4 (0.04 mmol/g); 7.7 (0.07 mmol/g); and 10.1 (0.07 mmol/g). Based on this, it was concluded that,at the pH of impregnating AHM solutions (pH 5.2), at least two surface groups on carbon are in the protonated form, which favors electrostatic adsorption of $Mo_7O_{24}^{6-}$ ions. The Mo loading in the catalysts was varied between 5 and 15 wt % Mo. A 3 wt % Mo catalyst was also prepared from a water-acetone (1:1 by volume) mixture.

All catalysts were reduced and carburized in a horizontal tube furnace using gram-sized amounts of materials. A continuous flow of 4% $H_2$ in Ar was maintained during the heating ramp and dwelling at 850ºC. In order to avoid violent re-oxidation of molybdenum and unwanted formation of molybdenum oxides, the catalysts were cooled down to room temperature after reduction under a stream of pure nitrogen and were passivated by slowly adding oxygen to the nitrogen stream before exposing them to air. The BET surface area of reduced and passivated samples was in the range of 450 $m^2/g$; as expected, catalyst porosity decreased during impregnation and $Mo_2C$ formation.

## Results and Discussion

The reduction of catalysts was studied on a thermogravimetric balance coupled with a mass spectrometer (TGMS) for simultaneous analysis of gas composition. The samples were heated up to 850ºC under a steady flow of $H_2$ (4%) in Ar. Three major weight changes were identified, in addition to the initial weight loss caused by desorption of physisorbed water or other gases. The first weight loss occurred below 200ºC and was accompanied by a significant increase of mass signals at m/e = 17 and 16 (but not at m/e = 18); the relative ratio of the mass peaks indicated the presence of $NH_3$ in the gas phase. A second weight loss occurred below 600ºC and was accompanied by an increase of mass signals at m/e = 18, 17 and 16. Although much smaller, the signal at m/e = 44 was present in the temperature range of 200–600ºC, showing that a small proportion of $CO_2$ was formed as a secondary gas product. The third weight loss occurred below 800ºC and coincided with a surge of signals at m/e = 28 and (to a much lesser extent) at m/e = 44. Based on these data, the following mechanism is proposed for the decomposition of molybdate species and their further thermochemical reduction to molybdenum carbide:

$$(NH_4)_6Mo_7O_{24} \rightarrow 7MoO_3 + 6NH_3 + 3H_2O \text{ (below 200ºC)}$$

$$MoO_3 + 3H_2 + C \rightarrow MoO_2 + CH_4 + H_2O \text{ (below 600ºC)}$$

$$MoO_2 + 5C \rightarrow Mo_2C + 4CO \text{ (below 800ºC)}$$

In the latter high-temperature transformation, the carbon support plays the double role of reducing agent for $MoO_2$ and template for $Mo_2C$ dispersion. This

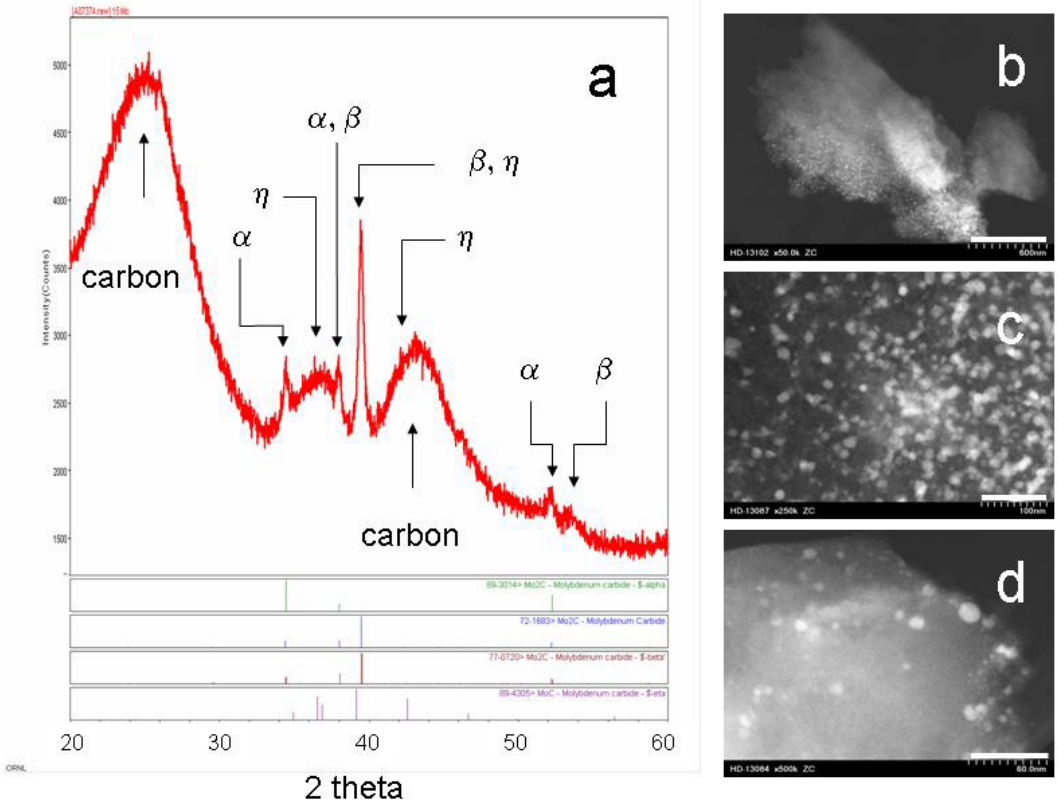


*Fig. 1. X-ray diffraction pattern (a) and Z-contrast scanning transmission electron micrographs (b-d) pictures of carbon-supported catalysts (10 and 15 % Mo) showing highly dispersed $Mo_2C$ nanoparticles. In (a) the broad peaks identified with arrows correspond to disordered graphene structures from the carbon support; the other peaks originate in α, β, and η crystalline phases of $Mo_2C$. The size bar on electron micrographs is 600 nm (b), 100 nm (c), and 60 nm (d). In (b) a compact arrangement of $Mo_2C$ particles on the 15 wt % Mo sample is shown. The size of $Mo_2C$ particles varies between 5 and 15 nm.*

carbothermal reaction with participation of reactive carbon atoms on carbon material is also the step that causes most of the carbon gasification.

The phase composition of reduced catalysts was analyzed by X-ray diffraction (Fig. 1a). In addition to two broad peaks corresponding to (002) and (100) reflections from the irregular stacking of distorted graphene structures present in the activated carbon fibers, a complex mixture of α-, β-, and η-$Mo_2C$ phases was identified. A third broad peak at 2θ = 37° may possibly originate from highly dispersed η-$Mo_2C$ particles and was observed only in the catalyst with 15 wt% Mo. The $Mo_2C$ peaks were less prominent at lower Mo concentrations, showing a higher degree of dispersion.

The morphology of supported $Mo_2C$ phase in reduced catalysts was investigated by Z-contrast scanning transmission electron microscopy (STEM). Using energy dispersion analysis (EDX), it was confirmed that, for all catalysts, the supported nanoparticles identified by STEM contained Mo and C. The micrographs of 15 and 10 wt % Mo samples showed that $Mo_2C$ nanoparticles were distributed in compact arrangements, probably at the periphery of carbon fibers; an example is shown in Fig. 1b. For the other catalysts with 3 and 5 wt % Mo, the $Mo_2C$ particles were less densely populated. In all samples impregnated from aqueous solutions, the average size of particles varied between 5 and 15 nm (Fig. 1c), and the smallest particles identified were less than 3 nm in diameter (Fig. 1d). However, much larger particles were found on the catalyst impregnated from the water-acetone solution; this shows that the wetting of carbon and the surface charge development in aqueous solution improve dispersion of the impregnated phase.

## Benefits

Literature information suggests that dispersed $Mo_2C$ has catalytic activity in hydrogen-involving reactions, including water gas shift, hydrocarbon dehydrogenation, hydrodesulphurization, and hydrodenitrification. The challenge is finding a support which can stabilize high concentrations of nanometer-size $Mo_2C$ particles and has minimal electronic interactions with them.

The results obtained at this stage demonstrate that carbon fiber monoliths can stabilize highly dispersed

molybdenum carbide particles with sizes in the 5- to 15-nm range. After reduction of molybdate-impregnated carbons in a $H_2$-Ar mixture and catalyst passivation, a series of carbon-supported $Mo_2C$ samples was obtained; in this process, carbon is both a reducing agent and a supporting template.

Removing of sulfur- and nitrogen-containing compounds from naphtha is the first process before oil is refined to gasoline. The new standards requiring lower levels of sulfur in gasoline and diesel fuels will demand new catalysts, with improved stability and poison resistance. Literature reports suggest that $Mo_2C$ supported on carbon is more active than alumina-supported catalysts, used on large scale in oil industry (Bridgwater 1982). The new catalysts based on $Mo_2C$ particles supported on carbon fiber monoliths may have a high potential in this field, a direction that deserves further investigation. In addition, carbon fiber monoliths may serve as supports for other classes of catalysts, including platinum metals and transition metal oxides. In continuation of this project, we secured funds in FY 2006 from DOE Office of Energy Efficiency for development of low-temperature selective catalytic reduction catalysts based on CFCMS materials, with promising use as vehicle exhaust after-treatment catalysts.

## Acknowledgments

We are grateful to Dr. D. A. Blom from Metals and Ceramics Division for help with STEM micrographs.

## References

Bridgwater, A. J., et al. 1982. "Carbon Supported Hydrodesulphurization Catalysts," *Appl. Catal.* **4**, 267.

Burchell, T. D. 1999. "Porous Carbon Fiber Carbon Binder Composites" in Carbon Materials for Advanced Technologies, pp. 169–204, T. D. Burchell, Ed., Elsevier Science Ltd., Oxford.

Da Costa, P., et al. 2001. "Tetralin hydrogenation catalyzed by $Mo_2C/Al_2O_3$ and $WC/Al_2O_3$ in the presence of $H_2S$," *Catalysis Today* **65**, 195.

Da Costa, P., et al. 2003. "Supported molybdenum carbides lie between metallic and sulfided catalysts for deep HDS," *Catalysis Letters* **86**, 133.

Levy, R. B. and M. Boudart. 1973. "Platinum-like behavior of tungsten carbide in surface catalysis," *Science* **181**, 547.

Liang, C., P. Ying, and C. Li. 2002. "Nanostructured β-$Mo_2C$ prepared by carbothermal hydrogen reduction on ultrahigh surface area carbon material," *Chem. Mater.* **14**, 3148.

Mordenti, D., et al. 1998. "New synthesis of $Mo_2C$ 14 nm in average size supported on a high specific surface area carbon material," *J. Solid State Chem.* **141**, 114.

Sayag, C., et al. 2001. "Effect of support activation on the kinetics of indole hydrodenitrogenation over mesoporous carbon black composite-supported molybdenum carbide," *Fuel Proc. Technology* **77–78**, 261.

# Nanostructured Superhydrophobic Materials

B. R. D'Urso,[1] J. T. Simpson,[1] and P. F. Britt[2]
[1]*Engineering Science and Technology Division*
[2]*Chemical Sciences Division*

A superhydrophobic surface is a hydrophobic material enhanced by surface microstructure or nanostructure. The surface structure effectively amplifies the hydrophobic properties of the material by suspending water on the top of the surface structure, leaving a layer of air separating most of the surface from the water. We have demonstrated and significantly improved superhydrophobic surfaces made of glass with sharp surface features. Superhydrophobic materials have numerous potential applications including drag reduction for watercraft, water-repellent windows, and microfluidic devices.

The objectives of this project are to demonstrate superhydrophobic materials with improved performance, to develop improved fabrication processes for superhydrophobic materials, and to explore potential applications of superhydrophobic materials. Completion of these objectives will increase the range of possible applications of these materials and will advance the fabrication processes of superhydrophobic materials for those applications.

The Lotus leaf can serve as a model for synthetic superhydrophobic surfaces. As with the Lotus leaf, synthetic superhydrophobic surfaces generally require a surface structure with protrusive features or high-aspect-ratio roughness. The surface may then be coated with a hydrophobic material such as a fluorinated polymer. Teflon AF®, an amorphous form of Teflon® which can be applied to a surface in solution, is a commonly used hydrophobic surface coating, as are self-assembled monolayers (SAMs). The combination of the structured protrusive surface features and the hydrophobic coating creates a superhydrophobic surface. The aspect ratio, sharpness, size, and spacing of the surface features combined with the properties of the base material determine the superhydrophobic properties of the material. The contact angle, which is a measure the hydrophobicity of the surface, is largely determined by the sharpness of the features. The pressure tolerance, or how much pressure is required to force a fluid between the surface features, is determined by the aspect ratio and spacing of the surface features.

We have concentrated our efforts on two varieties of superhydrophobic materials. The first has highly optimized surface features, such that the contact angle approaches 180 degrees and drops of water slide off of the material without noticeable friction. The second material is transparent, at the cost of having surface features less optimized for superhydrophobic properties. We are working towards producing the optimized superhydrophobic material in a hydrophobic polymer. The use of a solid hydrophobic polymer instead of a hydrophilic material with a hydrophobic coating will increase durability while potentially decreasing cost and improving manufacturability. For the transparent superhydrophobic material, we are pursuing the use of glass to produce the structure for transparency and scratch resistance.

Superhydrophobic surfaces exhibit properties with many potential applications. The most obvious property of the surface is dewetting, where water rolls of the surface, leaving it completely dry. Thus, transparent superhydrophobic materials could be used for windshields or optical windows with improved optical transmission in rainy conditions. This could be used in both defense and consumer applications. Other potential applications include drag reduction, microfluidic devices, and anti-condensation coatings. We are particularly interested in the possibility of producing a framework for microfluidics with electrically controllable superhydrophobic materials by utilizing electrowetting on dielectric (EWOD). Since water is so pervasive in our environment, the control over the interaction of materials and water provided by superhydrophobic surfaces may have broad applications.

# A Novel Thermomechanical Process for Producing Fe-3%Si Magnetic Steel Sheet for Transformers

B. Radhakrishnan,[1] G. Sarma,[1] D. B. Reister,[1] A. Goyal,[2] and J. R. Thompson[3]
[1]*Computer Science and Mathematics Division*
[2]*Metals and Ceramics Division*
[3]*Condensed Matter Sciences Division*

The current technology for making Fe-3%Si transformer core steel with sharp Goss texture is based on particle-induced secondary recrystallization that requires critical heat treatment steps that are time and energy-consuming. The resulting magnetic domains in the huge Goss grains have to be refined by an expensive laser-scribing step. We are developing a novel thermomechanical processing route based on bulk shear deformation processing that will eliminate the need for second-phase particles, secondary recrystallization, and laser scribing. During the first year, we demonstrated the ability to form sharp Goss texture by modeling the microstructure and texture evolution during shear deformation and annealing of the steel sheet.

Currently the material of choice for transformer cores is Fe-3%Si grain-oriented steel sheet with a sharp {011} <100> Goss texture that allows alignment of the applied field with <100> direction, the direction of easy magnetization in iron. The current technology for producing the core steel is based on an elaborate sequence of thermo-mechanical steps that includes an energy- and cost-intensive secondary recrystallization step that produces the Goss texture. Since the grain size after secondary recrystallization is very large, there is a need for an additional step of domain refinement by laser scribing to minimize the core losses. Based on discussions with a leading U.S. manufacturer of the grain-oriented silicon steel, it has been estimated that if secondary recrystallization and laser scribing steps could be eliminated, it would result in a saving of about 15–25% of the production cost. Increased affordability of the steel will result in more efficient transformers in the energy grid, thereby improving grid security and reliability.

The objective of the project is to develop a new processing approach that relies on bulk shear deformation to obtain the Goss orientations, and further intensifying the Goss texture through a primary recrystallization/grain growth anneal.

The optimization of the thermomechanical parameters to produce a sharp Goss texture and a desirable grain size in the final product is carried out using computational modeling of the microstructure and texture evolution in the sheet. Sensitivity analysis coupled with neural network analysis is used to identify and control the significant process variables to achieve the desired product quality. Asymmetric rolling has been chosen as the means to impart the desired shear deformation based on its potential for easy implementation in an existing plant layout.

The deformation and annealing models have been validated using experimental data generated using Fe-3%Si steel sheet supplied by the industry. The validated models were used to investigate Goss texture evolution during reversed shear deformation followed by annealing. The modeling indicated the formation of sharp Goss texture (within 5º from ideal Goss orientation) for a specific choice of the deformation parameters. Further refinement of the deformation parameters is required in order to meet the industry standard that stipulates a maximum misorientation of 2º from Goss. The grain structure has to be further optimized by controlling the number of Goss nuclei that form during primary recrystallization. Shear deformation of the steel during asymmetric rolling was modeled using the commercial finite-element code ABAQUS. The modeling results were used to specify the sizes of rolls to be used in performing the asymmetric rolling experiments. The components required to assemble an industry standard magnetic testing facility at ORNL have been identified and purchased.

Materials research in the development of improved core steel will lead to significant benefit to DOE's mission through the DOE Office of Electricity Delivery and Energy Reliability. The application of optimized shear deformation to produce unique textures will result in better formability of sheet products and will benefit DOE's Lightweight Materials Program.

# Development of Lightweight Lead-Acid Batteries

E. Lara-Curzio,[1] K. An,[1,2] B. L. Armstrong,[1] F. S. Baker,[1] N. J. Dudney,[3]
Y-I. Jang,[3] G. H. Kirby,[1,2] and C. A. Walls[1]
[1]*Metals and Ceramics Division*
[2]*Oak Ridge Associated Universities*
[3]*Condensed Matter Sciences Division*

The low specific energy of lead-acid batteries has limited their use in mobile applications. The objective of this project is to develop durable, lightweight lead-acid batteries. This objective will be achieved by using graphite fibers as current collectors, by depositing designed coatings of lead and lead oxide onto the graphite fibers, and by engineering the interface between the graphite fiber and the active materials to promote adhesion and long-term durability. The success of this project will enable the manufacture of durable, lightweight lead-acid batteries and their widespread use in portable and mobile power applications.

Processes based on electrodeposition and dipping in lead oxide suspensions were established to coat PAN- and pitch-based graphite fibers with lead and lead oxide, respectively. The values of current density, time of deposition, temperature, and concentration of $Pb(BF_4)_2$ and gelatin that yield uniform electrodeposited coatings of lead were identified. Coatings from a few tenths of a micron to several microns in thickness were obtained, and the uniformity of the coatings was found to improve with decreasing current density and longer deposition time. Optimum results were obtained at a current density of $2.5 \times 10^{-4}$ A/cm$^2$.

Lead oxide pastes containing $PbO{\cdot}PbSO_4$ (1BS), $3PbO{\cdot}PbSO_4{\cdot}H_2O$ (3BS) and $4PbO{\cdot}PbSO_4$ (4BS) were developed by combining PbO, $H_2O$, $H_2SO_4$ and other additives. Pastes with high 3BS content and low viscosity were successfully formulated by adding a polyelectrolyte-based copolymer dispersant. This dispersant has a comb-like molecular architecture with anionic, poly(acrylic acid) backbone, and uncharged, poly(ethylene oxide) teeth. The 3BS phase is a desirable phase because it is converted to the active phase $PbO_2$ with relatively small volume change during electrochemical cycling. By adjusting the initial PbO content of the paste, it was possible to modify its viscosity to coat woven graphite fibers with uniform coatings of thicknesses ranging from a few microns to ~250 μm. The addition of latex emulsions was found to improve wetting and drying behavior and cohesive strength of the dried paste.

Cyclic voltammetry measurements between -1.5 V and -0.5 V (using an $Hg/Hg_2SO_4$ reference electrode) on PAN-based graphite fibers coated with electrodeposited lead revealed the presence of a peak at -0.9 V, associated with the oxidation of lead to form $PbSO_4$, and a peak at -1.05 V, associated with the reduction of $PbSO_4$ to lead. Similarly, cyclic voltammetry measurements between 0.5 and 1.5 V on PAN-based graphite fibers coated with lead oxide deposited by dip coating revealed the existence of a peak at 1.35 V, associated with the conversion of $PbSO_4$ to $PbO_2$, and a peak at 0.9 V, associated with the inverse reaction. These are relevant findings because they demonstrate the feasibility of using lead- and lead oxide–coated graphite fibers for the fabrication of lightweight lead-acid batteries.

Galvanostatic charge-discharge cyclic measurements (up to 10 cycles) on both lead- and lead oxide–coated graphite fibers demonstrated the ability of these coating systems to accommodate the volumetric changes that result from the cyclic electrochemical conversion of the active materials.

The durability of the proposed battery system is likely to be limited by loss of electrical connectivity at the interface between the graphite fibers and the active material, in particular the positive electrode, due to cohesive failure or to the formation of an insulating, inactive phase. During FY 2006, work will be focused on the engineering of the interface between the active layers and the graphite fibers through fiber surface modifications and coating additives, for example, in order to promote adhesion and long-term durability, particularly for applications that require multiple deep-discharge cycles.

The success of this project will enable the manufacture of durable, lightweight lead-acid batteries and their widespread use in portable and mobile power applications.

# Effects of Confinement on the Statistical Physics of Nanoparticles—From Idealized Models to Real Materials: Application to Antiferromagnetic Oxides

G. M. Stocks,[1] M. Eisenbach,[1] B. Gu,[2] W. Wang,[2] and J. Shen[3]
[1]*Metals and Ceramics Division*
[2]*Environmental Sciences Division*
[3]*Condensed Matter Sciences Division*

The realization of nanostructured electronic and magnetic devices will require a deep understanding of the effects of confinement on the statistical physics of real materials. Recently it has been discovered that the magnetic properties of a wide range of antiferro-magnetic (AF) nanoparticles show indications of thermo-induced (*ferro*) magnetism (TiM) that are not explainable using theories of the bulk. In this project, we are using nanoparticles of antiferromagnetic transition metal oxides (AF-TMO) as prototype systems for developing a fundamental understanding of the effects of confinement on their statistical physics. We use an integrated experimental and theoretical approach in order to distinguish between the canonical effects of confinement and materials specific behavior.

For this project, we are using an integrated experimental and theoretical approach to study antiferromagnetic transition metal oxides (AF-TMO) nanoparticles as prototype systems for developing a fundamental understanding of the effects of confinement on their statistical physics.

We have made significant progress in understanding TiM. Our MC simulations using anisotropic Heisenberg model show that TiM does indeed exist, and that its behavior is far richer than the theory by Mørup and Frandsen originally suggested. This work has been published in *Phys. Rev. B* **72**, 140405 (2005). We have started work on spin dynamics simulations to shed light on the microscopic motion of the spins responsible for TiM. We have begun implementing the local self-interaction-corrected (L-SIC) local density approximation (LDA) within our first-principles order-N LSMS code in order to be able to treat strongly correlated TMO nanoparticles.

Based on the forced hydrolysis method, we have obtained a series of $\alpha$-$Fe_2O_3$ with size in the range of 5 to 400 nm. Dynamic light indicates that these particles can be well dispersed in aqueous suspension with relative narrow size distribution (5~15%). High-resolution TEM and Raman spectroscopy characterizations confirmed that these synthesized particles are hematite ($\alpha$-$Fe_2O_3$). We also synthesized chromium oxide ($\alpha$-$Cr_2O_3$) and nickel oxide (NiO) nanoparticles with size range from 50 to 100 nm, but more work is needed to avoid agglomeration.

We have successfully measured the properties of hematite ($\alpha$-$Fe_2O_3$) particles with diameters from 65+ nanometers down to 5nm. SQUID magnetometer has been used to measure the magnetic moment of these $\alpha$-$Fe_2O_3$ nanoparticles as a function of temperature and size. We observed that all AFM particle assemblies show *strong* evidence of an anomalous increasing moment, indicative of TiM. We have successfully grown AFM metallic nanoparticles (Cr) using cluster beam source that have a very narrow size distribution (<5%), ideal for studying TiM.

This work is directly relevant to DOE's research portfolio in basic science. It is particularly relevant to DOE initiatives in materials science, nanoscience, computational science, and high-performance computing, as well as neutron sciences. At ORNL this work is particularly relevant to stated goals of the Center for Nanophase Materials Sciences (CNMS), the National Leadership Computing Facility (NLCF), and the Spallation Neutron Scource (SNS).

# Advanced Overhead Transmission Conductors

T. Tiegs, V. Sikka, G. Ludtka, and A. Goyal
*Metals and Ceramics Division*

Electrical transmission research is important for ORNL and the nation. During the first year of this project, we examined the following areas: (1) modeling to identify the critical properties for conductors, (2) tailoring of ultra-high strength steel by microstructural texturing; (3) development of high-strength, carbon fiber reinforced-aluminum composites; and (4) assessment of ultra-high-strength copper-based alloys. During the second year, we will concentrate on Tasks 1 and 3, namely, modeling of materials property effects on conductor ampacity and development of aluminum-based conductor materials.

The electric transmission system in the United States is under ever-increasing stress, threatening both reliability and commerce. The objective of this project is to provide support for the development of advanced transmission conductors to meet the needs of the power industry.

During the first year, we examined four areas: (1) a modest modeling/analysis effort to identify the most critical mechanical requirements for conductors, (2) tailoring of ultra-high-strength conductor steel by microstructural texturing; (3) development of high-strength, carbon fiber reinforced-aluminum composites; and (4) assessment of ultra-high-strength, ultra-high-conductivity copper-based alloys.

The initial modeling showed the significant effect that some of the materials properties have on the ampacity of conductors. For example, by decreasing the coefficient of thermal expansion by 10%, a 22% increase in the amount of conductor could be realized. In a similar fashion, it was shown that by increasing the elastic modulus by 10%, a 24% improvement is possible.

The fundamental property of a material that initially defines its ability to resist elastic deformations, such as sag, is its elastic modulus. Scoping experiments to investigate the influence of magnetic field processing on texture evolution during annealing were performed on a Fe-1.1Si alloy. Various uniform magnetic field strengths were employed, and analysis of the 30-T magnetically processed specimen qualitatively indicated an increase in the {110}<001> texture component along the γ-fiber. These results provide experimental validation that magnetic fields do influence texture evolution during annealing.

Initial aluminum-carbon fiber composites exhibited poor wetting between the fibers and the aluminum and also inadequate dispersion of the fibers. Additives that were used to improve wetting include Mg, Zr, Ti, and Si. Composites were fabricated using hot pressing to obtain samples suitable for mechanical property testing. In addition, good wetting was observed between Ni-coated carbon fibers and molten aluminum. Along with the composite fabrication, the application of thin, high-emissivity coatings was investigated. Tests showed coated samples had a heat dissipation improvement of 23 to 48 % over uncoated samples for temperatures between 250°C and 50°C.

A variety of Cu alloys and Cu-alloy composites were studied and examined for their suitability for conductor application. Cu-alloy-carbon-reinforced composites, which meet the requirements of desired physical properties, were identified. These materials have high strength, elastic modulus, low thermal expansion, and high electrical conductivity.

During the second year of the LDRD project, additional modeling will look at the synergistic effect of simultaneously improving several materials properties. Development of Al-based conductor materials will examine several materials and coatings: (a) further development of Al-carbon fiber composites concentrating on fiber selection and processing issues, (b) investigation of Al-reinforced with boron-rich second phases, and (c) testing of high-emissivity coatings looking at corona effects.

Research on materials for electrical transmission is important for ORNL and the United States, and this is a very opportune time to pursue initiatives in this area. The DOE Office of Electric Delivery and Energy Reliability identified advanced electric transmission conductors as important technology.

# Interfacial Solids: Functionality from Atomic-Scale Charge Transfer at Stacked Interfaces

H. M. Christen,[1] H. N. Lee,[1] M. F. Chisholm,[1] M. Varela,[1] and C. Cantoni,[1]
L. Petit,[2] T. Schulthess,[2] and W. Temmerman[3]
[1]*Condensed Matter Sciences Division*
[2]*Computer Science and Mathematics Division*
[3]*Daresbury Laboratory, U.K.*

The creation of artificial three-dimensional materials with properties defined by two-dimensional, repeatedly stacked interfaces is pursued by a two-prong approach involving epitaxial synthesis with atomic-scale control and computational methods that correctly treat both localized and delocalized electrons in complex oxide materials. The system of lanthanum manganite/strontium titanate was identified as a test bed for this approach, and electron spectroscopy at the atomic scale has shown strong interfacial effects consistent with computational predictions. This work will allow the synthesis of completely artificial materials based on predictions from first-principle calculations.

Creating new functionalities in complex materials remains a key scientific challenge. Rather than varying the chemical composition in a spatially uniform way, the objective of this project is to modify physical properties via electronic effects at deliberately introduced, chemically abrupt interfaces, which can be stacked periodically to form a three-dimensional artificial solid with properties defined at the lower dimensionality. Furthermore, we aim to find a model system for which computational approaches can be used to predict the physical properties of the material, that is, solve the so-called inverse problem of materials by design in a specific case.

The specific approach followed consists of a simultaneous experimental and computational study of interfaces in epitaxial perovskite heterostructures grown with excellent crystalline quality using pulsed-laser deposition (PLD) and analyzed at the atomic scale using electron energy loss spectroscopy (EELS) in a scanning transmission electron microscope (STEM). Computationally, such interfaces—and their periodic stacking—can be studied using the self-interaction-corrected local spin density method (SIC-LSD), which treats localized and delocalized electrons on an equal footing.

The key result of the first-year effort of this program is the identification of the lanthanum manganite ($LaMnO_3$)—strontium titanante ($SrTiO_3$) interface as a system for which the computational method predicts the experimentally observed physical properties in both constituents, for which the PLD method yields high-quality samples, and for which STEM-EELS provides an accurate measurement of the valence state of the manganese and titanium sites. Experimentally, we observe a strong change of the manganese valence state as a function of distance from the interface, while in the strontium titanate, the electronic configuration remains unchanged as the interface is approached. Computationally, dissimilarities between different interface terminations are clearly predicted, and further experiments are currently pursued to study these structures—and periodic stackings of interfaces—in more detail.

It is clear that this project will yield results that are significant to a broad range of materials research efforts: first, we show that interfacial effects near interfaces fundamentally alter a material's physical property on a length scale of 1 nm, a finding of importance for all work on nanostructures of complex materials. Second, providing an approach to predicting materials properties illustrates the capabilities of modern computational methods and illustrates that that the inverse problem of designing materials can be solved in specific situations.

# Confocal Scanning Transmission Electron Microscopy for Three-Dimensional Atomic-Resolution In Situ Imaging

S. J. Pennycook,[1] A. R. Lupini,[1] A. Y. Borisevich,[1] M. F. Chisholm,[1] M. Varela,[1]
K. van Benthem,[1] Y. Peng,[1] and T. Gosnell[2]
[1]*Condensed Matter Sciences Division*
[2]*Pixon LLC*

It is widely appreciated that aberration-corrected scanning transmission electron microscopy (STEM) is providing enormous benefits in resolution including sensitivity to individual atoms in real materials for the first time. The higher resolution is achieved by increasing the aperture of the imaging lens, and therefore results in a reduced depth of field. For the last 70 years, electron microscope images have represented a 2D projection of a 3D structure. After aberration correction, nanometer-scale-depth resolution is obtained, opening up the possibility of 3D imaging through depth slicing. This project aims at exploring the opportunities confocal electron microscopy offers in materials, chemical, and nanoscale sciences.

The calculated depth of focus of our aberration-corrected microscope is 6 nm. It was therefore initially surprising that we were able to locate individual Hf atoms within a nm-wide $SiO_2$ layer in a next-generation high-dielectric-constant (K) device structure to an accuracy of better than 1 nm in depth, and the atoms were only visible over about a 1- to 2-nm range of focus (van Benthem et al. 2005a,b). It was found that the issue was signal-to-noise ratio, which was relatively low in this example, so that the atoms were only visible when they were well focused. A catalyst specimen comprising single heavy Pt atoms on a light carbon film did show a depth of focus in good agreement with theory. These results confirmed that the depth of field is given by the wavelength divided by the square of the radius of the imaging aperture ($\lambda/\theta^2$). It improves much more rapidly than the lateral resolution, which increases only linearly with aperture radius ($\lambda/\theta$). As a consequence, depth resolution in the next generation of aberration-corrected microscopes with larger convergence angles will be at the nm level. A new criterion for depth resolution was proposed, based on the ability to separate two objects one above the other. These results have been accepted for publication in the *Proceedings of the National Academy of Science* (Borisevich et al. 2005a). We also investigated the effects of channeling on the method, as occurs in the atomic resolution imaging of a crystal. With present correctors, channeling destroys the depth resolution but can be overcome with the next-generation correctors. Results are submitted for publication (Borisevich et al. 2005b).

We have also installed an electron energy loss spectrometer onto the 300-kV STEM in order to explore the possibility for 3D spectroscopic imaging. In theory this should show the same behavior as the image, but with lower signal levels. For optimum EELS collection efficiency, the microscope operating voltage was reduced to about 280 kV, and a realignment and recalibration of the aberration corrector was carried out. The microscope has been moved into the new Advanced Microscopy Laboratory, and instabilities in the objective lens power supply have been cured, which will allow more repeatable depth sequences to be obtained.

Initial tests of the Pixon method for three-dimensional deconvolution of the data were carried out but were unsatisfactory because of instabilities in the scan. Now the microscope is in the new building, it is hoped that the instabilities will be greatly reduced. We will also investigate other means for image reconstruction.

Significant progress has been made on the design of a new specimen stage for the VG microscopes, giving more access to the specimen for heating/cooling and allowing establishment of in situ environments such as reactive gases for catalysis studies. If successful this would also overcome several major drawbacks of the old VG designs, the lack of height variation on the 100-kV STEMs, and the poor stability of the 300-kV STEM stage.

## References

Borisevich, A. Y., A. R. Lupini, and S. J. Pennycook. 2005a. *Proc. Nat. Acad. Sci.*, in press.

Borisevich, A. Y., A. R. Lupini, S. Travaligni, and S. J. Pennycook. 2005b. *J. Electron Micros.*, submitted.

van Benthem, K., A. R. Lupini, M. Kim, H. S. Baik, S. Doh, J. H. Lee, M. P. Oxley, S. D. Findlay, L. J. Allen, J. T. Luck, and S. J. Pennycook. 2005a. *Applied Physics Letters* **87**, Art. No. 034104.

van Benthem, K., M. P. Oxley, S. D. Findlay, L. J. Allen, and S. J. Pennycook. 2005b. Ultramicroscopy, in press.

# Deformation Mechanisms in Nanocrystalline Metals

T. G. Nieh[1,2] B. Yang,[1] and M. Zhang[2]
[1]*Metals and Ceramics Division*
[2]*University of Tennessee*

Nanocrystalline tantalum was prepared by radio frequency magnetron sputtering on a glass substrate. Structure and mechanical properties of the deposited Ta film were investigated by X-ray diffraction, transmission electron microscopy, and nanoindentation. The salient feature in the present tantalum thin film with a grain size of 76.5 nm is the remarkable enhancement of hardness (11.6 GPa), about one order of magnitude higher than that of bulk coarse-grained tantalum (1.2 GPa).

Tantalum has a body-centered cubic (bcc) lattice structure. Unlike other bcc metals, Ta has an unusually low Peierls stress (frictional stress) and, thus, is ductile (>40%) at room temperature. However, the yield strength of Ta is relatively low (about 250 MPa) at room temperature, as compared with those of other bcc metals. Assuming Hall-Petch relationship is valid to nanometer scale, the yield strength of Ta with a grain size of 50 nm is estimated to be 6 GPa. With a shear modulus, G, of 65 GPa for Ta and a theoretical shear strength of about G/10, such a yield strength of Ta would be close to the theoretical strength.

In this project, nanocrystalline Ta thin film was deposited on a well-cleaned glass substrate in pure argon gas by RF magnetron sputtering from a commercial pure (99.95%) Ta target. The base pressure of sputtering chamber was kept better than $5 \times 10^{-7}$ Torr, while the working pressure was $7 \times 10^{-3}$ Torr. The substrate temperature during deposition was kept at 500°C. The sputtering power was 100 W and the deposition rate was about 3.4 nm per minute. The film was deposited for 300 min to obtain an estimated thickness of about 1 μm.

The average grain size and microstrain in the Ta film were measured using X-ray diffraction and found to be 76.5 ± 6.5 nm and 0.579 ± 0.0163%, respectively. Further using transmission electron microscopy, we observed the deposited Ta film was composed of equiaxed nanocrystalline grains. The boundaries between any two grains are irregular and arbitrarily meandering, and the majority of the grain boundaries are high-angle boundaries.

We used a nanoindentation technique to measure the hardness of the nanocrystalline Ta film and obtained the average value of 11.6 ± 0.4 GPa. This hardness value is quite remarkable and is much higher than that reported for nano-Ni (6.4 GPa) with even a smaller grain size of 14 nm. At a given nanometer scale of grain size, bcc-metals are, in general, much harder (or stronger) than face-centered cubic (fcc)-metals. The higher strength is attributable to several factors: higher melting point and more difficult for slip in bcc metals as compared to fcc metals.

A hardness value of 11.6 GPa from the nano-Ta with a grain size of 76.5 nm is by no means the highest. According to the conventional dislocation pile-up theory, the hardness of Ta with a grain size of 35 nm is anticipated to be 16.5 GPa. Experiments are planned to produce nanocrystalline Ta alloys with a finer grain size and thus higher strength. Tantalum can be alloyed with W (also a bcc metal) to form a solid-solution alloy. The W addition cannot only refine the grain size of Ta but also improve its strength. For example, the yield strength of Ta-10W with a grain size of about 20 μm is about 560 MPa. Assuming the Hall-Petch relationship is extendable to nanometer scale, the yield strength of the alloy with a grain size of 30 nm is estimated to be 20 GPa!

# High-Resolution Imaging of Biological Samples in a Wet Environment

N. de Jonge and S. J. Pennycook
*Condensed Matter Science Division*

A new high-resolution 3-dimensional scanning transmission electron microscopy (STEM) technique is being developed to image individual proteins and cells in their natural "wet" environment with a resolution down to 1 nm. The technique is a combination of confocal STEM, providing 3-dimensional information with an aberration-corrected STEM and in situ STEM, where samples in liquid are imaged in an electron microscope by using a specially designed flow cell with electron transparent windows. Immobilized biological samples, such as membrane proteins and whole cells, grown on a window of the flow cell, are imaged under life, or close to life, conditions.

One of the major goals of proteomics is to understand living systems on a molecular level. This goal requires the development of an imaging technique that provides high-resolution imaging of proteins, imaging of their assembly in whole cells under close-to-life conditions, and time-resolved imaging of the biological system in response to certain stimuli. Precisely these requirements will be met by our in situ confocal STEM technique. Success would represent a revolution in the imaging of proteins and cells and enormously enhance their understanding. This knowledge can be applied, for example, to gain a better understanding of energy-providing systems in biological organisms and to aid the development of new therapeutics.

The project requires a special flow cell for scanning transmission electron microscope (STEM) imaging of biological samples in liquid. The flow cell consists of two ultra-thin windows through which the electron beam can image a sample in liquid enclosed by these windows. The project will make use of an aberration-corrected STEM providing a large opening angle of the beam, such to enable 3-dimensional (confocal) imaging in the liquid.

Calculations were performed to design the flow cell and estimate its performance. All parts have been designed and ordered at several U.S. companies. First experiments were performed on the 3D confocal STEM imaging of stained biological cells. The results demonstrated the successful imaging with 3D sensitivity. Too large drift, or beam damage did not occur. The cells were obtained from a leading group at NIH. First successful experiments were also performed to immobilize living cells on the entrance window of the flow cell. This cell culture is on-site.

This project is relevant to DOE's Biological Sciences, Chemical Sciences, and Nanoscale Science and Technology programs. In-situ confocal STEM could revolutionize 3D imaging of biological systems on a molecular level. The project fits with DOE goal of renewable and alternative energy sources and with the first goal of the genomics for life program, to identify and characterize the molecular machines of life on a molecular level. This project will provide a new tool to image biological structures in 3D and in "wet" environment that will benefit all programs of all agencies involved in biological sciences, medicine, and drug design. Specific calls are as follows:

(1) The NIH institute, National Institute of General Medical Sciences, calls for the development of high-resolution probes for cellular imaging. The aim is to develop probes improving detection schemes by a factor of 10 to 100. The ultimate goal is to develop probes that can be used to routinely achieve single molecule sensitivity for imaging dynamic processes in living cells.

(2) The NSF has a call on instrument development for biological research. This program supports the development of novel or of substantially improved instrumentation likely to have a significant impact on the study of biological systems at any level. Proposals aimed at concept or proof-of-concept development for entirely novel instrumentation are encouraged.

# *Materials Science and Engineering*

# *Seed Money Fund*

# Alanates for High-Capacity Hydrogen Storage

J. H. Schneibel,[1] D. S. Easton,[2] S. Babu,[3] and S. A. Speakman[1]
[1]*Metals and Ceramics Division*
[2]*Consultant, Metals and Ceramics Division*
[3]*Edison Welding Institute, Columbus, Ohio*

In this work, the hydrogen storage properties of the alanates $NaAlH_4$ and $LiAlH_4$ were investigated. Mechanical alloying of $NaAlH_4$ with hydrides such as $LiAlH_4$, $NaBH_4$, and $LiBH_4$, together with a catalyst, did not change the desorption properties of the $NaAlH_4$ significantly. The desorption of $LiAlH_4$, on the other hand, was sensitive to the residual impurity content and additions of $NaAlH_4$. A previously observed "mechano-chemical" decomposition of catalyzed $LiAlH_4$ during milling at room temperature was shown to be unlikely. The decomposition is rather due to a lowering of the decomposition temperature to room temperature; that is, the milling itself is not responsible for the release of hydrogen. The results suggest that additional work on $LiAlH_4$ with precise compositional control has the potential to improve the hydrogen desorption properties of this compound. Also, this opens up the possibility that the decomposition of $Li_3AlH_6$ may be made to be reversible.

## Introduction

The Bush administration has proposed the FreedomCar (Freedom Cooperative Automotive Research) project, the goal of which is the development of technologies for hydrogen-powered fuel cell cars and trucks. One important issue that is crucial for the success of this project is the lightweight, high-capacity storage of hydrogen. Hydrogen can be stored in many different ways, for example, as a compressed gas, as a liquid, as an interstitial element in intermetallic compounds, or as a chemical compound. Among the large variety of potential chemical compounds, the alanate $NaAlH_4$ is of particular interest because it has a high hydrogen capacity (5.6 wt % when assuming final decomposition into NaH and Al) and has been shown to desorb and absorb hydrogen under modest pressure and temperature conditions. The purpose of this LDRD project was to examine alanates such as $NaAlH_4$ and $LiAlH_4$ in more detail.

## Technical Approach

Prior to 1993, the desorption/absorption kinetics of $NaAlH_4$ were considered to be too slow to make it a practical hydrogen storage material. This situation changed when Bodganovic et al. found that addition of Ti-based catalysts such as $TiCl_3$ allows desorption and absorption of hydrogen within reasonable time frames (e.g., 10 min) under modest conditions of pressure and temperature. $NaAlH_4$ releases hydrogen in a two-stage decomposition reaction; typical pairs of equilibrium temperatures and pressures for the catalyzed reactions are indicated in Eqs. (1) and (2):

$$3NaAlH_4 = Na_3AlH_6 + 2Al + 3H_2 \quad [125°C/50\ atm] \tag{1}$$

$$Na_3AlH_6 + 2Al = 3NaH + 3Al + 3/2H_2 \quad [125°C/2\ atm] \tag{2}$$

There is a critical need to further improve $NaAlH_4$ such that it desorbs/absorbs under conditions closer to ambient. Also, since higher storage capacity values than those of $NaAlH_4$ are ultimately needed, other compounds need to be examined. $LiAlH_4$ has a hydrogen capacity of 7.9 wt % when decomposing into LiH and Al. $LiAlH_4$ is not fully stable at room temperature; it tends to decompose slowly over time frames on the order of years. Also, its decomposition is not thought to be reversible. The exception to this is a publication by Chen et al. (2001) in which partial reversibility is claimed.

In this work, the strategy was to "alloy" $NaAlH_4$ with other hydrogen storage compounds in order to modify its hydrogen storage capacity and kinetics. All compositions were catalyzed with $TiCl_3$. Processing was performed by high-energy mechanical milling in a sealed capsule containing powders of hydrogen storage materials and hardened steel balls. In the case of $LiAlH_4$, experiments were conducted to determine whether the decomposition products $Li_3AlH_6$ or LiH can be recharged to form $LiAlH_4$.

## Results and Discussion

$NaAlH_4$ powder was blended with 2 mol % $TiCl_3$ and 20 mol % of $LiAlH_4$, $NaBH_4$,or $LiBH_4$ in an argon glove box. The powder mixtures were mechanically alloyed in a sealed capsule in a high-energy Spex mill

for 30 min. The hydrogen desorption of the processed materials was measured in a pressure-composition-isotherm (PCI) measurement system (Supplier: Advanced Materials Corporation). Starting at room temperature, the temperature was ramped to approximately 200°C at a rate of 1°C/min. The desorbed hydrogen flowed into a previously evacuated chamber of known volume. Its amount was determined by measuring the pressure and temperature of the chamber. Reference experiments with $NaAlH_4$-2 mol% $TiCl_3$, $LiAlH_4$-2 mol% $TiCl_3$, $NaBH_4$-2 mol % $TiCl_3$, and $LiBH_4$-2 mol % $TiCl_3$ were also carried out. The $LiBH_4$ and the $NaBH_4$ were quite stable, showing hydrogen desorption of less than 1 wt % at 200°C. The $LiAlH_4$, on the other hand, released 2 wt % hydrogen at less than 100°C. The desorption behavior of the $NaAlH_4$ powders mechanically alloyed with 20 mol % of $LiAlH_4$, $NaBH_4$, or $LiBH_4$, plus the catalyst, could be well described by a rule of mixtures. This suggests that the alloying with compounds of different stability did not produce the desired result—it did not modify the desorption properties of the $NaAlH_4$ itself. While this result is negative, it does not preclude the possibility that other substances can be found that modify the properties of $NaAlH_4$.

Work published by Balema et al. (2001) suggests that high-energy milling of $LiAlH_4$ with a $TiCl_3$ catalyst at room temperature results in the release of hydrogen due to a "mechano-chemical" effect; that is, the release will not occur at room temperature unless milling is carried out at the same time. In experiments carried out to verify this effect, a first batch of $LiAlH_4$ decomposed into $Li_3AlH_6$ after milling for 30 min. However, as described in our recent paper (Easton et al. 2005), this decomposition was presumably not due to a "mechano-chemical effect" but rather to a $TiCl_3$-induced decrease of the decomposition temperature to room temperature. Surprisingly, mechanical alloying with an addition of 20 mol% $NaAlH_4$ (plus the catalyst) prevented the decomposition. In addition, a second batch of $LiAlH_4$, purchased from the same supplier at a different time, did not decompose after milling with $TiCl_3$. Figure 1 shows the X-ray diffraction patterns of this batch collected in situ during decomposition. (It should be pointed out that such patterns could also be evaluated quantitatively; that is, the volume fraction of the different phases forming during decomposition could be determined as a function of time and temperature.) Our results show that the decomposition behavior of the $LiAlH_4$ is highly sensitive to its impurity content. Further work involving precise analyses of the chemical composition will be needed to clarify this effect. Potentially, the desorption properties of $LiAlH_4$ can be controlled within a wide range by controlling its exact composition.

For the second batch of $LiAlH_4$, it was demonstrated that a reduction in the temperature ramp rate reduced the decomposition temperature significantly. For example, the temperature for the decomposition into $Li_3AlH_6$ dropped from 70°C to 25°C, when the ramp rate was reduced from 1°C/min to 0.004°C/min. Attempts were also made to inhibit the decomposition of $LiAlH_4$ by applying hydrogen pressure. When the pressure was increased to 200 atm., the temperature for the decomposition of $LiAlH_4$ into $Li_3AlH_6$ was reduced by ~20°C, while that for the decomposition of $Li_3AlH_6$ into LiH was reduced by 50°C. Although the decomposition temperature of $LiAlH_4$ responds to the hydrogen pressure, careful experiments with discharged $LiAlH_4$ that involved ramping down the temperature extremely slowly at a hydrogen pressure of 200 atm did not show any evidence of charging. At a given pressure, the hysteresis involved in the transition between $NaAlH_4$ and $Na_3AlH_6$ is on the order of 10°C. It is suggested that the hysteresis in $LiAlH_4$ is much larger. As a result, the temperature at which LiH can be converted into $Li_3AlH_6$ at moderate hydrogen pressure (i.e., 200 atm) is likely to be so low that the kinetics of the reaction becomes too slow for the reaction to proceed. Further work involving more precise compositional control may improve this situation.

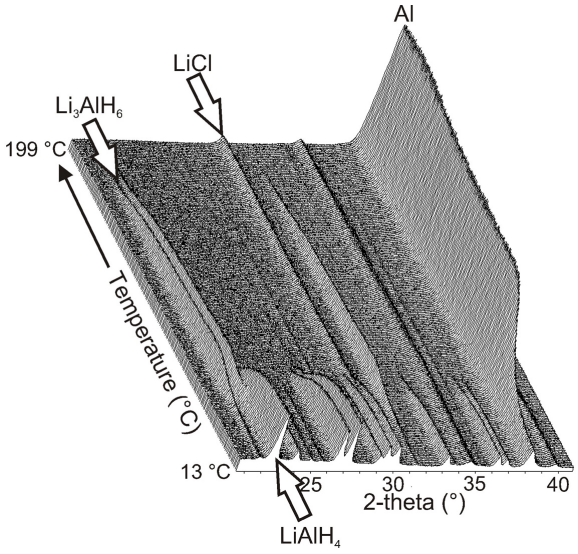


*Fig. 1. In-situ X-ray diffraction patterns collected during the decomposition of $LiAlH_4$-2 mol % $TiCl_3$ while ramping up the temperature at 0.1°C/min. The peak heights vs. temperature show clearly the increase in the amount of the reaction product Al and the initial formation, and later decomposition, of the reaction product $Li_3AlH_6$ (see also Eqs. (1) and (2), with Na replaced by Li).*

## Benefits

This work has been enabling in the sense that it has created the expertise required for the design and characterization of alanates. The importance of the exact composition (i.e., incidental or deliberate chemical additions) for the desorption properties of $LiAlH_4$ has

been shown experimentally. In order to demonstrate reversibility in this system, more work involving precise compositional control will be needed. This work has also helped to attract more funding on hydrogen storage: Energy Efficiency and Renewable Energy provided $195,000 in FY 2005 (FWP CEHI100) and is continuing this effort in FY 2006.

## References


Balema, V. P., J. W. Wiench, K. W. Dennis, M. Pruski, and V. K. Pecharsky. 2001. "Titanium catalyzed solid-state transformations in LiAlH4 during high-energy ball milling," *J. Alloys Comp*. **329**, 108.

Bogdanovic, B., and M. Schwickardi. 1997. "Ti-doped alkali metal aluminium as potential novel reversible hydrogen storage materials," *J. Alloys and Compounds* **253–254**, 1.

Chen, J., N. Kuriyama, Q. Xu, H. T. Taekshita, and T. Sakai. 2001. "Reversible hydrogen storage via titanium-catalyzed $LiAlH_4$ and $Li_3AlH_6$," *J. Phys. Chem. B* **105**, 11214.

Easton, D. S., J. H. Schneibel, and S. A. Speakman. 2005. "Factors affecting hydrogen release from lithium alanate ($LiAlH_4$)," *J. Alloys and Comp.* **398**, 245.

# Enhancing Performance of Hydrogen Storage Materials through Nanoscale Design

V. K. Sikka,[1] G. Muralidharan,[1] N. C. Gallego,[1] A. M. Clark,[1] H. M. Meyer III,[1]
N. S. Kulkarni,[1] T. M. Besmann,[1] T. J. Huxford,[1] and M. P. Paranthaman[2]
[1]*Metals and Ceramics Division*
[2]*Chemical Sciences Division*

Materials capable of reversibly storing hydrogen are of great interest for the hydrogen economy. Hurdles such as insufficient gravimetric capacities and slow hydriding/dehydriding kinetics have to be overcome to succeed in this quest. This project was focused on developing a novel approach that is based on the use of nanometer-thick films of hydrogen storage material on the interior surfaces of a mesoporous silica gel with a large surface area. If such materials could be prepared successfully, the use of thin films would result in fast reaction kinetics and allow the hydriding/dehydriding reaction to occur at temperatures lower than that observed for bulk materials. Deposition of Mg films was performed using physical and chemical vapor deposition processes. Results show that deposition of Mg-rich films can be achieved on the internal surfaces of a mesoporous silica aerogel using physical vapor deposition. Using gravimetric measurements, it was demonstrated that hydrogen uptake occurs in the mesoporous materials coated with Mg-rich films at hydrogen pressures as low as 900 Torr after appropriate pretreatments. It was also shown that the hydrogen is stored reversibly in these materials, thus establishing the feasibility of the concept. Further work is required to improve the hydrogen storage capacity and to optimize the hydriding kinetics.

## Introduction

Hydrogen storage materials are of great interest for the new national and international interest in the hydrogen economy. Based on the potential use of hydrogen storage materials in automotive applications, a storage criteria of 9 wt % of hydrogen has been set as a national goal, and there are many efforts under way to develop such materials. In addition to meeting the gravimetric capacity, such materials should also be capable of adsorbing and desorbing the hydrogen at temperatures less than 100°C at pressures of 1–10 atm. A number of metal hydrides have been studied for their potential use as hydrogen storage materials. Such studies have shown that slow kinetics of the hydriding/dehydriding reaction, high temperatures required to absorb/release the hydrogen, and/or insufficient storage capacities limit the use of metal hydrides (Schlapbach 2001; Schwarz 1999; Zaluska 2001).

Many different approaches, such as physical and chemical treatments, have been carried out to improve the hydriding and dehydriding kinetics of metal hydrides with limited success (Schlapbach 2001; Schwarz 1999; Zaluska 2001). Our approach to addressing this problem is based on developing a general scheme involving nanoscale materials for improving the hydriding/dehydriding kinetics of all hydrogen storage materials of interest. We plan to use Mg as a model material for developing and demonstrating our concept. In addition to improving the hydriding/dehydriding kinetics using this methodology, our objective is to also achieve reduced operating temperatures (in the range of 100–150°C) for hydriding and dehydriding in such films.

## Technical Approach

The core theme of our approach is the use of thin films of hydrogen storage materials with a thickness of less than 50 nm. A significant benefit in using such films is that diffusion is required only over very short distances for hydriding and dehydriding when the surfaces of the thin films are exposed to the gas. In addition, to achieve sufficient gravimetric storage capacity, the internal surfaces of a foam-like material with a large surface area and an interconnected pore structure that is permeable to the surrounding gas medium have to be coated with the thin film that can store hydrogen. Although thicker Mg films have been studied for their hydrogen storage characteristics (Léon 2002), the combined use of large-surface-area materials as a template and a thin film hydrogen storage material appears to be unique.

## Experimental Procedure

### *Materials*

Commercially available silica aerogels with a quoted surface area of 800 $m^2/g$ and with a density of 0.1 $g/cm^3$ were used as the template mesoporous material. ORNL measurements showed that the surface area in materials supplied was about 430 $m^2/g$.

### *Deposition of Thin Films*

Deposition of Mg films from the vapor phase was performed by both physical vapor deposition and chemical vapor deposition.

Physical vapor deposition (PVD) was carried out by annealing the substrates along with pieces of pure Mg or Mg-Al alloys which served as the source of magnesium vapor. Annealing was carried out at different temperatures ranging from 600 to 750°C, both in flowing $Ar/H_2$ atmosphere and in sealed $Ar/H_2$ atmosphere at a pressure of about 150 Torr at room temperature. Physical vapor deposition was carried out on both silica gels and small pieces of a Si-wafer placed along with the silica gels. The Si-wafer pieces served as the reference material for characterizing the deposited layers. Deposited materials were characterized by scanning electron microscopy and Auger electron spectroscopy. Depth profiling was carried out in the Auger electron microscope to characterize the thickness and composition of the deposited layers and the interface region.

Chemical vapor deposition (CVD) of pure Mg on various substrates was performed using a Mg precursor [Bis(cyclopentadienyl)magnesium $(C_5H_5)2Mg$]. Vapor pressure measurements of the Mg precursor as a function of temperature were initially carried out. Using thermodynamic calculations, suitable processing conditions, including the reactor temperature and pressure, and precursor temperature (hence vapor pressure) were initially identified. Based on this, CVD of Mg was carried out at a total (H + Mg precursor) pressure of 700 Torr and a temperature of 600°C. Hydrogen was used both as the carrier and reducing gas with a flow rate of 100 sccm through a bubbler containing the Mg precursor at 75°C (about 23 Torr). The deposition was carried out for a total of 6 h.

### *Adsorption-Desorption Characteristics*

Hydrogen adsorption-desorption studies were carried out on porous material treated with Mg vapor (physical vapor deposition) using gravimetric analysis. An initial bake-out treatment was performed on the coated mesoporous materials. Subsequently, the chamber was filled with gaseous hydrogen up to a maximum pressure of about 900 Torr. Sample temperatures were raised to various values between 200°C to 600°C while monitoring the changes in sample weight. Several cycles of heating and cooling were performed to see the effect of temperature changes on the interaction of the coated samples with the hydrogen atmosphere.

## Results and Discussion

### *Thin Film Deposition*

Auger electron spectra obtained from the thin films deposited on the silicon wafer and the silica gel showed the presence of Mg, confirming that Mg was indeed deposited on the surfaces. In addition to Mg, it was observed that oxygen was also present on the surface of the sample. Depth profiles show that about a 75- to 100-nm-thick layer rich in Mg was deposited on the silicon wafer under conditions used for preparing the materials whose hydriding/dehydriding characteristics are shown in Fig. 1. Auger spectra showed that oxygen was present at roughly at equi-atomic concentrations with Mg throughout the thickness of the 100-nm-thick film. Thus, it was decided that an activation step which involves heating the sample at a high temperature in a $H_2$ atmosphere needs to be performed on the coated silica aerogel samples prior to characterizing the adsorption/desorption characteristics.

X-ray photoelectron spectroscopy (XPS) analysis of the film deposited using CVD on an alumina substrate revealed a composition that was predominantly C (90–95%) with the rest Mg. However, closer to the substrate/film interface, it was found that the Mg content increased substantially while that of the C dropped. The reasons for this are not clear at the present time, but it is suggested that the kinetics of the deposition process changes as the growth proceeds. It was also discovered that CVD on the silica substrate resulted in the spallation of the film due to the formation of a number of highly reactive Mg-Si-O-C reaction products (from the XPS analysis). Hence, it was suggested that alumina is a better substrate for the CVD of Mg.

### *Adsorption-Desorption*

Figure 1 shows the weight changes in one silica aerogel sample coated with Mg using PVD techniques. This sample was prepared by subjecting the samples to magnesium vapors produced in sealed tubes with a $Ar/H_2$ atmosphere at a temperature of 665°C. It was found that the samples were extremely reactive in air (causing it to heat up) when removed from the sealed atmosphere, indicating that oxidation of Mg occurred when placed in contact with air. This is also consistent with the fact that oxygen was found in all samples that were characterized with Auger electron spectroscopy. This sample was subjected to multiple cycles of high-temperature exposure followed by cool down to room temperature in a gravimetric analyzer. The results are shown in Fig. 1. It can be noted that when the sample is heated to 250°C and 300°C and cooled down to room temperature in a hydrogen atmosphere, no weight changes are observed. As the temperature is progressively increased, increases in weight are observed both during exposure to temperature and after cool down to room temperature. Particularly prominent are the weight increases at 500°C and 550°C. At the end of the cycle, an increase of about 1% was observed during this particular sequence of exposure. It should be noted that this hydrogen uptake took place at the low hydrogen

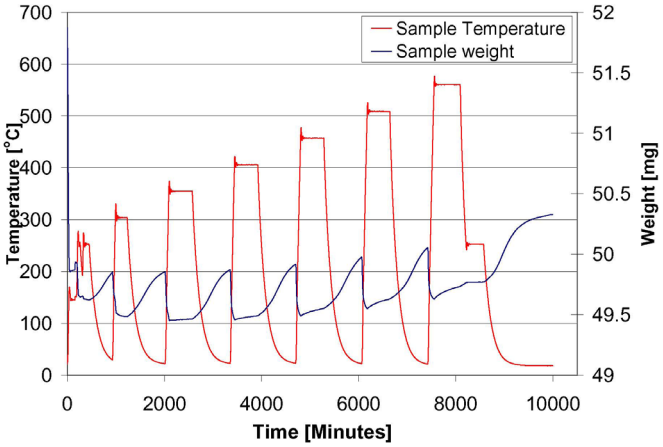


*Fig. 1. Effect of time and temperature on sample weight change in a H2 atmosphere at a pressure of about 900 Torr. Note that a weight gain (about 1 wt %) is observed after cooling down to room temperature.*

pressure of 900 Torr. Other samples prepared under different conditions have shown higher weight gains during hydrogen exposure and that the hydrogen can be released at temperatures as low as room temperature. Uncoated samples exposed to similar conditions did not show any significant adsorption of hydrogen under similar conditions, thus establishing the validity of the concept.

The seed money work has clearly outlined areas for further research. Methods must be devised to obtain better control on the thickness of the films and to optimally coat the mesoporous material to obtain higher gravimetric capacities. Work also needs to be focused on understanding the kinetics of hydrogen uptake of these materials at higher hydrogen pressures. Feasibility of using other porous template materials that would be more stable at higher temperatures should also be evaluated.

## Benefits

Hydrogen storage and delivery materials are of significant interest to DOE and other federal agencies such as Defense Advanced Research Projects Agency (DARPA). Since this scheme has been proven to be successful, engineering hydrogen storage materials based on Mg with gravimetric capacities up to 6.7 wt % (and higher capacities with more complex thin films) may be feasible, thus satisfying both the existing and future DOE criteria. The data obtained from the seed money project will be used to file an invention disclosure. This invention disclosure will be used to seek potential collaborators from the University of Missouri–Rolla, North Carolina State University, and University of Illinois in future calls for proposal. Other funding opportunities through solicitations from DOE will be explored in the future. Industrial partnerships, transfer of technology, and potential funding through Small Business Innovation Research (SBIR) and Small Business Technology Transfer (STTR) programs will also be considered.

## References

Léon, A., E. J. Knystautas, J. Huot, and R. Schulz. 2002. *Jounal of Alloys and Compounds* **345**, 158–166.

Schlapbach, L., and A. Zuttel. 2001. *Nature* **414**, 353–358.

Schwarz, R. B. 1999. *MRS Bulletin* **24**(11), 40–44.

Zaluska, A., L. Zaluska, and J. O. Strom-Olsen. 2001. *Appl. Phys. A* **72**, 157–165.

# Selectively Enhanced Adatom Diffusion

Z. Zhang, B. Wu,[1] L. C. Feldman,[2] and P. I. Cohen[3]
[1]*Condensed Matter Sciences Division*
[2]*Vanderbilt University*
[3]*University of Minnesota*

The central idea in this proposal is selectively enhanced adatom diffusion (SEAD). When a laser beam is incident on a growth system, the laser frequency can be tuned to resonantly excite a specific adatom-substrate bond. Once excited, such adatoms become more mobile and easier to desorb, consequently altering the film growth kinetics. The key feature of this excitation is its selectivity: for a system consisting of different bonds, one can tune the laser frequency to excite only the desired one, leaving the rest unchanged. The different bondings can come from multiple species in the depositing materials or distinct geometric confinements. However, the feasibility of this appealing idea is yet to be firmly established due to possible complications from other physical processes in a real growth system. The goal of this proposal is to validate the principle of SEAD with extensive theoretical modeling and calculations by focusing on a prototype model system, the chemical vapor deposition (CVD) growth of silicon. Since the system is widely used in manufacturing silicon-based devices, the success of our project will have immediate impact on real-life applications. Furthermore, once validated, the SEAD idea may find important applications in other growth systems as well.

## Introduction

In thin-film growth under laser radiation, the laser can influence the growth process in two different ways. One is laser-induced thermal excitation; that is, laser power is absorbed by the substrate and converted into thermal energy. The film growth is then affected by an increase in the substrate temperature. The other is resonant excitation (Fig. 1). This happens when the laser couples strongly to the bonding between adatom and substrate. In this case, the adatoms can be vibrationally excited to a higher level and become more mobile and easier to desorb since the diffusion barrier is effectively reduced by the photon energy. One key difference between these two mechanisms is the selectivity of resonant excitation. In a system of film growth, there can be various bondings between adatom and substrate when the deposition material consists of multiple species or when the adatoms of the same kind experience different local geometric arrangements. With resonant excitation, the laser can be tuned to selectively excite only a specific bonding between adatoms and substrate. The consequence is that only desired adatoms are excited and become more mobile and easier to diffuse along the surface while the rest are essentially unaffected. We call it selectively enhanced adatom diffusion (SEAD). The goal of this project is to demonstrate the feasibility of SEAD in film growth and its potential applications through extensive theoretical modeling and calculations. We will accomplish this by focusing on the model system of CVD growth of silicon.

## Technical Approach

This project focused on various theoretical aspects of the SEAD idea. The theoretical approaches and scientific issues addressed included the following:

(a) Rate equation analysis of the feasibility of SEAD as applied to hydrogen diffusion on and desorption from flat or vicinal Si(111) surfaces;
(b) First-principles calculations of the mobility of adsorbed silane on hydrogen-passivated Si(1111) and Si(100) surfaces, using the Venna Ab-Initio Simulation Package (VASP);
(c) Fundamental mechanisms of associative desorption of hydrogen from Si(111) at room temperature and under photon irradiation.

At the same time, a complimentary experimental investigation was carried out in collaboration with Dr. P. Cohen of the University of Minnesota and Dr. L. Feldman of Vanderbilt University. This experimental effort used the free electron laser (FEL) source located at Vanderbilt University to experimentally verify the theoretical predictions using the model system of CVD growth of Si.

## Results

### *(a) Controlling Film Growth with Selective Excitation: Chemical Vapor Deposition Growth of Silicon*

Here we proposed a method of controlling the growth mode in an epitaxial system (Wu et al. 2004). It takes advantage of differences in the vibrational frequencies

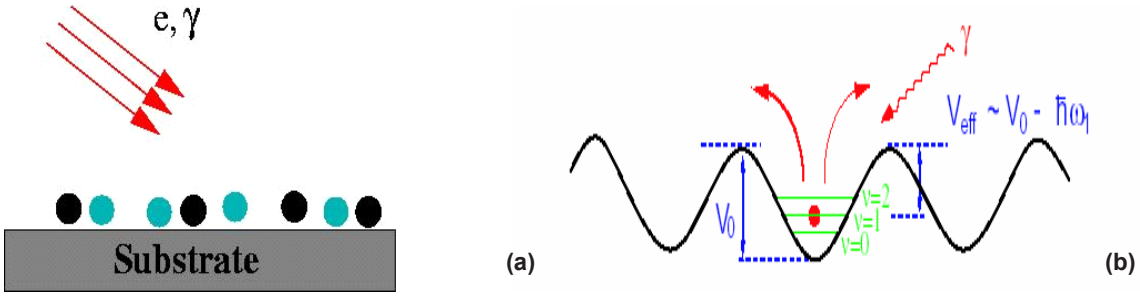


*Fig. 1. Illustration of the basic SEAD idea. (a) Light or electrons impact on the growth front of a compound material, in which the surface mobility is inherently different. The beam can only be absorbed by the slow species and thereby only enhance its mobility. (b) Once vibrationally excited, the diffusing species with lower mobility sees a lower diffusion barrier and therefore has higher mobility.*

of adatom-substrate bonds at terraces and steps. We demonstrated theoretically that, with a properly tuned infrared laser, one can selectively excite only the adatom-substrate bonds at steps and enhance the mobility of these adatoms, consequently promoting step-flow growth and reducing film roughness. The feasibility of this method is shown theoretically with respect to the prototype system of CVD growth of silicon. In the rate equation approach, we used system parameters from the literature, and the characteristics of the laser sources available in the field and at the Vanderbilt free electron laser facility.

***(b) Mobility of Adsorbed Silane on H-Passivated Si(111) and Si(100) (Huang, to be published)***

In the phenomenological model treatment of SEAD in (a), we had assumed that the desorption of H from the Si surface is the rate-limiting process for achieving potential speedy Si homoepitaxy. In doing so, we assumed that silane molecules deposited onto the H-passivated surface can easily diffuse on the surface and reach the exposed Si sites where H adatoms had been desorbed. Somewhat to our surprise, such kinetic information for the elemental diffusion processes involved in CVD growth of Si has been lacking in the literature. We carried first-principles calculations of the diffusion barriers on different surfaces of Si, and also at different H passivation coverages, using the VASP code. Our calculations show that, indeed, the silane ad-molecules can easily migrate on the H-passivated Si surfaces by overcoming potential energy barriers in the range of less than 0.05 eV, as long as the H passivation is complete. This finding ensures that the assumption of H desorption as the rate-limiting kinetic step is sound.

***(c) Fundamental Mechanisms of Associative Desorption of Hydrogen from Si(111) at Room Temperature and under Photon Irradiation (Persson et al. in preparation; Liu et al. 2006)***

In the preliminary study carried out in (a), another fundamentally intriguing and important aspect that was not addressed is the likely pairing mechanism(s) of two hydrogen adatoms on Si(111) and Si(100). There has been an active line of research debating on this problem since the late 1980's and it still remains a challenging issue. Do two H adatoms have to be nearest neighbors spatially in order to pair up and desorb? Do they pair up via quantum tunnelling, or in the classical regime (therefore thermally activated)? How the activation of one H adatom into a vibrationally excited state change the rate of pairing within either the classical or the quantum picture? What is the rate that two neighboring H adatoms are excited by the photon irradiation simultaneously? How such double excitations influence the pairing rate? What would be the isotope effects in any of the above pairing scheme? Thorough investigations of all these relevant questions would demand longer than the tenure of this project, but our theoretical studies have resulted in at least partial answers to those questions, which prove to be essential in the interpretation of the experimental data reported in the benefits and broader impacts section below.

## Benefits and Broader Impacts

This theoretical project generated two grants—one from DARPA and the other as a supplemental grant to an existing program at Vanderbilt. These grants enabled us to employ a postdoctoral researcher to experimentally verify the SEAD idea using the FEL at Vanderbilt. In this work, we made the first measurements of non-thermal, non-electronic resonant photodesorption of hydrogen from a Si(111) surface using tunable infrared radiation (Liu et al. 2006). The wavelength dependence of the desorption yield shows a peak at 0.26 eV, the energy of the Si–H vibrational stretch mode. The corresponding excitation cross section is determined to be $2.3 \times 10^{-18}$ cm$^2$. The desorption yield is quadratic in the infrared intensity and quartic in the excitation field projected in the Si–H bond direction. These observations can be rationalized with the postulate that two neighboring hydrogen adatoms, once simultaneously excited in their vibrational stretch mode, can readily desorb associatively at room temperature. The double excitation picture is supported by further tests using different isotope mixtures of H and D.

It should be noted that bond selective chemical reaction at surfaces induced by resonant light irradiation has been long sought dream in chemical physics, catalysis, and film growth, among other areas of fundamental and practical importance. The project enabled us to make a substantial step towards achieving this ultimate goal, as demonstrated using the prototype model of H desorption from Si(111). The demonstration also leads to the realization of double excitation of two neighboring H adatoms as a crucial step towards molecular hydrogen desorption.

The broader impacts of this project reside in two main spheres: sophisticated materials modification and new technology. Selective materials modification is a long-lasting promise of the interaction of radiation with matter. The concept of selectively and non-thermally removing one atomic species (among many) from a surface, or enhancing bulk diffusion of a particular species, sets a new paradigm in the control and formation of new materials and structures. The work described here provides a first example, and a technologically transferable scheme, on how this might be accomplished. A variety of technological possibilities are intrinsic to the processes being explored. For example the ability to gently uncover individual sites at low temperature is crucial to nanolithographic processes in which hydrogen is used as a mask. Thin-film semiconductor growth is also strongly connected to surface control and chemistry. In particular, step-mediated growth might be controlled through selective exposure of step sites, providing not only planar configurations but a route to atomic wires or nano-scale epitaxial features.

The results obtained so far have been gaining immediate attention in the scientific community. Several invited talks have been given by the PI and co-PIs, or have been scheduled. These included colloquiums and seminars at University of Essen and Julich Research Center (both in Germany), University of Notre Dame, Rutgers University, and Harvard University. In addition, one invited talk on theory (Wu) and one invited talk on experiment (Cohen) have been scheduled at the Fall 2006 meeting of the Materials Research Society at the symposium on nanostructure formation aided by energetic photons. One co-PI, Biao Wu, formerly a postdoctoral researcher at ORNL, has moved on to take a prestigious chair professorship at the Institute of Physics, Chinese Academy of Sciences in Beijing.

## References


Huang, L., X. G. Gong, and Z. Y. Zhang. 2006. "First-principles study of silane mobility on hydrogen-passivated Si surfaces," *Phys. Rev. B*, to be published.

Liu, Z. H., L. C. Feldman, N. H. Tolk, Z. Y. Zhang, P. I. Cohen. 2006. "Desorption of hydrogen from Si(111) by resonant excitation of the Si-H vibrational stretch mode," *Science* (2006, accepted).

Persson, B., B. Wu, and Z. Y. Zhang. 2006. "Isotope effects and pairing mechanisms of associative desorption of H from Si surfaces," *Phys. Rev. Lett.* (to be submitted).

Wu, B., P. I. Cohen, L. C. Feldman, and Z. Y. Zhang. 2004. "Controlling film growth with selective excitation: Chemical vapor deposition growth of silicon," *Appl. Phys. Lett.* **84**, 2175.

# Development of the "Ultimate Scanning Tunneling Microscopy" for the Center for Nanophase Materials Science

R. Jin,[1] J. F. Wendelken,[1] and E. W. Plummer[2,1]
[1]*Condensed Matter Sciences Division*
[2]*The University of Tennessee*

This project focused on the development of an ultra-stable, low-temperature scanning tunneling microscope (STM) in a high-magnetic-filed environment, the so-called "ultimate STM." As it will be the showcase for ORNL's Center for Nanophase Materials Science (CNMS), this requires tests of the instrument prior to the access of users. While our "ultimate STM" is being constructed, we conducted our work using the low-temperature STM in Prof. Matzdorf's group at the University of Kassel. The project demonstrated that the ultra-stable low-temperature sample environment is critical when studying fundamental problems that are of current scientific interest.

## Introduction

The fascinating advances in materials engineering at the atomic level has resulted in discoveries of new materials and new properties. To understand the special rules that control the behavior of materials at the nanoscale, the most utilized technique to visualize objects and probe properties at the nanoscale is scanning tunneling microscopy/spectroscopy (STM/S). As many novel phenomena can often only be observed in extreme conditions, a joint project between ORNL and UT focused on the development of a new ultra-stable low-temperature STM that can be operated in a high-magnetic-filed environment, the so-called "ultimate STM." Seed money was required for designing and testing the instrument. To demonstrate the usefulness and capabilities of the "ultimate STM," we conducted our work using the low-temperature STM in Prof. Matzdorf's group at the University of Kassel, while our "ultimate STM" is being constructed. The project demonstrated that the ultra-stable low-temperature sample environment is critical when studying fundamental problems that are of current scientific interest.

## Technical Approach

So far, only a few tentative steps have been made to provide the extreme STM sample environments required for the new research area. Much of the work developing and utilizing STMs that operate in the most extreme conditions of high magnetic field and low temperatures can be credited to our collaborator, Prof. Pan, at the University of Houston. Our "ultimate STM" is similar to the one in Houston, but with several more advanced features. The design specifications for this STM call for a spatial resolution of better than 0.01 Å in the z-direction and better than 0.1 Å in the x-y direction with an energy resolution of better than 100 μV. The environment of the STM will be ultra-high vacuum with a temperature range of 300 mK to 150 K and a magnetic field of –9 T to +9 T. A very unique feature of this STM will be the ability to rotate the STM and sample together by 90º with respect to the field. Perhaps the most extreme requirement is a stability level that will allow the observation and spectroscopic characterization of a single atom or molecule for a period greater than 48 h. These features will give scientists, particularly outside users, a distinct advantage in studying advanced materials at the nanoscale, such as nanostructured electronics, nanotubes, nanowires, and nanophases in correlated electron materials and will provide a very real potential for a new research thrust referred to as chemical imaging.

To achieve the extreme performance specifications outlined above requires special design considerations literally from the ground up. The system is to be mounted on a vibration isolated concrete block weighing approximately 37 tons. Then a piezoelectrically controlled active isolation stage is used to virtually eliminate any vibrations coming through the ground to the block. On top of the active isolation stage is a high stiffness table weighing approximately 1 ton that supports a three-chambered ultra-high vacuum system. A central chamber provides for sample transfer between a growth chamber, and analysis chamber, and the cryogenic, high magnetic field STM chamber. The entire system will then be enclosed in an acoustically isolated room with a design specification of less than 10 db. Ultra-low-noise electronics have also been designed and built for this system to allow very sensitive spectroscopic measurements such as single molecule vibrational spectroscopy.

During the design of the "Ultimate STM" for the Condensed Matter Sciences Division (CMSD) and the Center for Nanophase Materials Science (CNMS), it has been highly advantageous to test some of the measurement protocols on an existing low-temperature instrument prior

to construction and ultimately provide access to users. Prof. Matzdorf, who is one of the world's experts on this type of instrument, allowed us to gain experience using his instrument at the University of Kassel, while our "Ultimate STM" is being constructed. We focused on a quasi-one-dimensional $Li_{0.9}MoO_{17}$, which was prepared at ORNL as discussed below.

## Results and Discussion

The so-called purple bronze $Li_{0.9}MoO_{17}$ is a quasi-one-dimensional metal. Although it has been extensively studied since 1980s, many experimental results remain inconsistent. In particular, an extensive set of angle-resolved photoemission spectroscopy (ARPES) measurements from two groups show non-Fermi-liquid line shapes consistent with Luttinger-liquid behavior (Denlinger 1999), whereas ARPES data from other groups display Fermi-liquid line shapes (Xue 1999). Thus, the central issue of this fascinating material has been the nature of the ground state. In general, reducing the dimensionality of an electronic system increases the electron correlations, thus resulting in a Luttinger liquid as predicted for a one-dimensional gas. On the other hand, there may be many instabilities in such a system that prevent the observation of Luttinger liquid behavior, for example, a charge-density-wave (CDW) due to the coupling of the electronic system to the lattice. For $Li_{0.9}MoO_{17}$, a CDW scenario has been discussed below 25 K, at which the metal-non-metal crossover occurs. Therefore, it was argued that the Luttinger liquid behavior could only be observed at temperatures above 25 K.

To obtain information about the local structural and electronic properties above and below 25 K, we have performed in situ STM measurements between 4.9 and 55 K at the cleaved surfaces of $Li_{0.9}MoO_{17}$ single crystals. As the tunneling conductance dI/dV is directly proportional to the density of states (DOS) around the Fermi energy and the I-V characteristic is different with different ground state, STM data allow us to identify the ground state and check if there exists a CDW. The later is accompanied by an energy gap. Shown in Fig. 1(a) is the dI/dV spectrum of $Li_{0.9}MoO_{17}$ at 4.9 K. We found that (1) dI/dV varies smoothly with bias voltage with no sign of the opening of an energy gap; (2) dI/dV(V) curves can be well described by the Luttinger liquid model convoluted with a Gaussian to account for experimental resolution [see the solid red line in Fig. 1(a)]. Remarkably, the dI/dV spectrum has the same character at the elevated temperatures, as shown in Figure 1(b). This and the smooth temperature dependence of the zero-bias conductance dI/dV(V=0) [Fig. 1(c)] indicate that the electronic state remains unchanged across 25 K and can be described by the Luttinger liquid model.

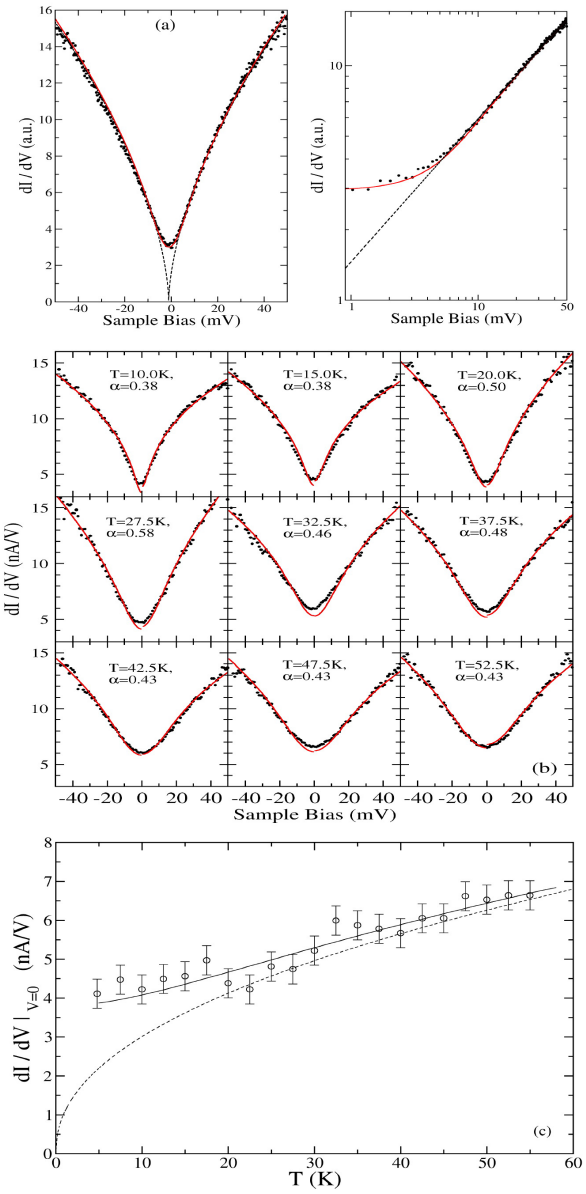


*Fig. 1 (a) The dI/dV spectrum (dots) near Fermi energy taken at 4.9 K: the solid red line is the fit of experimental data to the Luttinger-liquid model convoluted with a Gaussian to account for experimental resolution; (b) The dI/dV spectrum (dots) near Fermi energy at indicated temperatures: the solid red line is the fit of experimental data to the Luttinger-liquid model convoluted with a Gaussian to account for experimental resolution; (c) Temperature dependence of the zero-biased dI/dV: the solid line is the fit of experimental data to the Luttinger liquid model convoluted with a Gaussian to account for experimental resolution.*

The result is summarized in a paper entitled "Non-Fermi Liquid Behavior in Quasi-One-Dimensional $Li_{0.9}MoO_{17}$" that is published in *Physical Review Letters* (Hager et al. 2005).

## Benefits

The above test experiments demonstrated how a STM operating in state-of-the-art sample environments could make novel and essential contributions to physics. The low-temperature sample environment, the high stability, and resolution were crucial in determination of the ground state of $Li_{0.9}MoO_{17}$. The development of the "ultimate STM" provides a great opportunity for UT and ORNL to take a leadership role in instrumentation and nanoscale science and to build an even stronger collaboration. By providing significant advances to the state-of-the-art STM sample environments, we will be able to attract the best scientists in the world to use the instrument at ORNL's CNMS. It is anticipated that the proposed research will grow into a large research program at ORNL's CNMS and UT.

Because of its investments in the CNMS and advanced materials, ORNL is uniquely poised to play a leadership role in the nanoscience research required to advance our understanding in this important area. Construction of the "ultimate STM" along with development of the skills to fully utilize this advanced capability will be a key attraction to the best scientists in the world to bring their research to the CNMS. This anticipated success will help to ensure continued support from the DOE and to attract funding from other agencies and businesses.

## References


Denlinger, J. D., et al. 1999. *Phys. Rev. Lett.* **82**, 2540; G. –H. Gweon et al. 2000. *Phys. Rev. Lett.* **85**, 3985; G. –H. Gweon et al. 2003. *Phys. Rev. B* **68**, 195117; G. –H. Gweon et al. 2004. *Phys. Rev. B* **70**, 153103.

Hager, J., R. Matzdorf, J. He, R. Jin, D. Mandrus, M. A. Cazalilla, and E. W. Plummer. 2005. "Non-Fermi-Liquid Behavior in Quasi-One-Dimensional $Li_{0.9}MoO_{17}$," *Phys. Rev. Lett.* **95**, 186402.

Xue, J., et al. 1999. *Phys. Rev. Lett.* **83**, 1235; K. E. Smith et al., 2000. *Phys. Rev. Lett.* **85**, 3986; K. E. Smith et al. 2001. *J. Electron Spectrosc. Relat. Phenom.* **517**, 117–118.

# Real Space Imaging of High-Frequency Transport on the Nanoscale

S. V. Kalinin,[1] V. Meunier, [2] A. P. Baddorf,[1] M. B. Nardelli,[2] and D. Geohegan[1]
[1]*Condensed Matter Sciences Division*
[2]*Computer Science and Mathematics Division*

This project focuses on the development of scanning probe microscopy (SPM) techniques capable of addressing high-frequency transport behavior on the nanometer scale. The ever-shrinking size of electronic devices and the emergent field of nanoelectronics necessitate the local studies of transport behavior on small length scales and at the typical frequencies of device operation, often in the MHz and GHz ranges. The direct measurements of the high-frequency transport using force-based scanning impedance microscopy (Kalinin 2002) or current-based nanoimpedance microscopy (Shao 2002; O'Hayre 2002) are due to (a) bandwidth limitation of optical detector in SPM in force-based measurements and (b) stray cantilever-surface capacitances that dominate system response in ac current–based measurements. This project has demonstrated an approach for high-frequency transport imaging based on the detection of the frequency mixing on the (non-linear) active device interface, where the frequency of the mixed harmonic signal is chosen close to the resonant frequency of the cantilever. This technique, scanning frequency mixing microscopy, opens a new pathway to studying high-frequency transport, device characterization, and failure analysis on the nanoscale.

## Introduction

Electronic transport is the central enabling concept in the development of nanoelectronic and molecular electronic devices, chemical sensors, photovoltaic materials, and electromechanical and bioelectrical systems that has grown far beyond the borders of silicon-based technology. The major trends in this development are a decrease in the size of circuits and circuit components, as exemplified by nano- and molecular electronics, and an increase in operating frequencies, for example in photonics and microwave devices. However, the set of the experimental methods available for characterization of the new electronics has changed little in 20 years, with spatial resolution defined by the distance between microfabricated contacts and with frequency range confined below ~1 MHz. Commercial viability of nanoelectronic devices requires operation at the rates comparable or faster than traditional silicon analogues; hence, understanding the frequency-dependent transport properties in a broad frequency range from dc to MHz and GHz at nanometer length scales is vital to fulfilling the current promise of nanoscience.

## Technical Approach

We note that all semiconductor devices of interest have intrinsically non-linear current-voltage and capacitance-voltage properties which will produce frequency mixing. generalized scanning frequency mixing microscopy (SFMM), is based on spatially resolved measurements of the mixed frequency signal produced by two high frequency probing signals at frequencies $\omega$ and $\omega+\delta\omega$ applied to a device under test through macroscopic electrodes. An AFM tip is used as a moving voltage sensor to measure the spatial distribution of the amplitude and phase of the voltage oscillations at the frequency $\delta\omega$. Signals at the main ($\omega$) and higher order ($n\,\omega$, $n = 2, ..,$) of the excitation signal are also detected.

Non-linear SIM is implemented on a commercial SPM system (Veeco MultiMode NS-IIIA) equipped with a function generator and a lock-in amplifier (DS 345 and SRS 830, Stanford Research Instruments). The system is additionally equipped with external data acquisition system developed in LABVIEW/MATLAB for bias and frequency spectroscopy of interfaces and emulation of multiple data acquisition channels. A lock-in amplifier is used to determine the magnitude and phase of the cantilever response at the $n\,\omega$ or $\delta\omega$. The output amplitude and phase shift signals are stored by the external control computer as a function of frequency, dc bias applied across the device, and position on device surface, producing 2D spectroscopic maps, as illustrated in Fig. 1a and b. To ensure strong mechanical response of the cantilever for weak higher-harmonic signals while avoiding cross-talk between electrostatic and topographic data, the frequency of the ac modulation voltage was selected such that the mechanical response of the cantilever occurs at the first resonance frequency, whereas topographic imaging is performed at the second resonance frequency of the cantilever. Given that the eigenfrequencies for the cantilever are not an integral of the primary resonance frequency, this approach decouples electrostatic and mechanical signals while taking advantage of the resonance amplification for both of them. Practically, high harmonic signals can be measured for modulation voltages as small as 50 mVpp (i.e., in the true small signal limit).

The operation of NL-SIM and SFFM is illustrated using a simple model. In SFMM the modulation signal is

$V_{lat} = V_{dc} + V_1\cos(\omega t) + V_2\cos((\omega + \delta\omega)t)$ ,

and mixed frequency signal generated at the non-linear interface has the form

$V_{\delta\omega}\cos(\delta\omega t)$ .

The oscillating bias results in capacitive force acting on the dc biased tip,

$2F_{cap}(z) = C'_z(V_{tip} - V_{surf})^2$ .

Thus, the mixed frequency force signal contains intrinsic (device) and extrinsic (tip-surface junction) contributions as

$$F_{\delta\omega} \sim V_{\delta\omega}(V_{tip} - V_{0\omega}) + V_1V_2 . \quad (1)$$

In NL-SIM, application of a lateral modulation bias

$V_{lat} = V_{dc} + V_{ac}\cos(\omega t)$

across the experimental circuit in the presence of non-linear electroactive elements results in the modulation of surface potential at the harmonics of excitation signal, and the amplitude of the tip oscillations of the different harmonics is

$$F_{n\omega} \sim 2(V_{tip} - V_{0\omega})\, V_{n\omega} + V_{1\omega}V_{(n-1)\omega} . \quad (2)$$

Notice that in both cases intrinsic term is linear in tip bias, and extrinsic is tip bias independent. Hence, we extended an original SFMM concept to detect the linear component by data acquisition of several (typically 3) tip biases and detecting the slope of local response-bias curve, or using additional lock-in to determine linear component. These approaches allow explicit separation of the intrinsic and junction contributions.

As a prototype system for quantitative studies, we used Au-Si metal-semiconductor interface prepared by cross-sectioning a Schottky diode.To analyze junction effects on electronic transport in functional 1D nanostructures, SIM, non-linear SIM, and SFMM studies were performed on a set of carbon nanotube network samples embedded in polymer (Geohegan) and electroded individual $SnO_2$ nanobelts and nanobelt junctions (A. Kolmakov, Southern Illinois University). The origins of ultrahigh dielectric constant (Subramanian 2002) in polycrystalline $CaCu_3Ti_4O_{12}$ (CCTO) has been addressed (in collaboration with M. Greenblatt, Rutgers University). Finally, an extended analysis of image formation in a set of related SPM techniques using combination of DFT theory and classical electrostatics has been performed in collaboration with V. Meunier.

## Results and Discussion

The validity of SFMM approach was established on a model Au/Si junction system. Figure 1a and b demonstrate the 2D spectroscopic diagram of mixed frequency and carrier frequency signals across the interface as a function of tip position and lateral bias. The sharp bright feature observed on the $F_{\delta\omega}$ image does not have counterpart on the $F_{\omega}$ spectrum, illustrating the intrinsic origin of the data. In depth analysis of observed contrast in NL-SIM has bee reported (Shin 2005) and for SFMM is prepared for publication (Rodriguez, to be published).

In polycrytalline CCTO, combination of SIM and SSPM allowed to visualize the potential barriers at the grain boundaries at low frequencies, confirming that the origin of the ultra high dielectric constant in this material is at least partially due to the grain boundary layer limited transport (GBLL) behavior. Similar dc observations were simultaneously reported by other groups (Chung 2004). This model is further verified by the fact that at high frequencies the potential barrier is not observed due to the capacitive coupling across the interface, in agreement with impedance spectroscopy data.

In $SnO_2$ nanowire devices, the potential drops across individual electroactive elements (contacts and nanowire junction) have been observed and measured quantitatively, providing for the first time I-V characteristics and Schottky barrier heights of individual defect. It has been shown that memory effect observe din these and similar systems is often induced by the presence of the mobile surface charges with large relaxation times (~10 min), that can reversibly gate the 1D structure. The sensing activity in these systems is shown to be very sensitive to the presence of electroactive elements, thus demonstrating the development of either singe nanowire (no junctions) or multiple nanowire (statistical averaging) devices.

For polymer-nanotube composites, the SIM has allowed visualization of electronic transport pathways in the nanotube network 100–200 nm below the surface. The potential distribution along the network is shown to be controlled by the resistance of the nanotube-nanotube junctions and capacitive coupling between the nanowires and the back gate, leading to exponential decay of potential away from the electrodes. From the frequency dependence of the contrast, corresponding decay length has been determined, providing the information on RC constant of the system.

An approach to interpretation of transport data, namely changes in the electronic structure of 1D systems in the field of the tip, has been developed based on the combination of first-principles theory and continuum electrostatics, opening the pathway to quantitative interpretation of SPM data in terms of local electronic properties of individual defects.

To summarize, high-frequency transport at the nanoscale can be addressed using SFMM and related techniques. Transport imaging is possible even for the conductive nanotubes located 100–200 nm below the sample surface, overcoming traditional surface

sensitivity of SPM techniques. The image formation mechanism and surface effects on SFMM and SIM has been analyzed, and the guidelines for optimal imaging conditions are formulated. The SPM-based transport measurement techniques have allowed us to study conduction mechanisms in $SnO_2$ based nanosensor devices and establish the role of contact and junctions on sensing properties and memory effects. In polycrystalline materials, the role of grain boundaries on ultrahigh dielectric constant in $CaCu_3Ti_4O_{12}$ compound, the topic of much debate in the recent years, has been established. Finally, in-depth analysis of changes in electronic structure in nanotubes (extendable to other classes of 1D nanosystems) has been performed.

## Benefits

DOE has recently established a strong program for first-principles modeling of frequency-dependent transport properties at nanoscale dimensions. In a parallel development, synthesis and fabrication of nanoscale and particularly nanoelectronic devices is one of the central priorities for the DOE and ORNL, as clearly highlighted by the establishing of the Center for Nanoscale Materials Science and planned Chemical Imaging centers. In this perspective, development of unique scanning probe microscopy tools both contributes to the core research programs at CMSD, and creates new instrumental capabilities for CNMS. The focus of this proposal on the development of novel high-frequency transport imaging techniques is thus an important step in providing these capabilities. This proposal has attracted users (A. Kolmakov) to CNMS programs.

Spatially resolved high-frequency transport imaging provides a powerful tool for semiconductor device characterization and failure analysis in the microelectronics industry as well as in the rapidly developing fields of nanoscience and nanotechnology. Hence, the technique can be of immediate interest to electronics industry, nanotechnology companies, and AFM manufacturers. We have contacts with the leading AFM manufacturers, Veeco (Digital Instruments) and Omicron, who are potentially interested in this techniques. In addition, applications to transport in 1D structures for sensing, smart textiles, and electromechnical and electrooptical materials will benefit applications being considered by Defense Advanced Research Projects Agency's Defense Sciences Office, National Aeronautical and Space Administration NASA and Army Research Office.

## References


Kalinin, S. V., and D. A. Bonnell, *Appl. Phys. Lett.* **78**, 1306 (2001).

Shao, R., S. V. Kalinin, and D. A. Bonnell, *Appl. Phys. Lett.* **82**, 1869 (2003).

O'Hayre, R., M. Lee, and F. B. Prinz, *J. Appl. Phys.* **95**, 8382 (2004)

Subramanian, M. A., D. Li, N. Duan, B. A. Reisner, and A. W. Sleight, *J. Solid State Chem.* **151**, 323 (2000).

Chung, S. Y., I. D. Kim, and S. L. Kang, *Nature Mat.* **3**, 774 (2004).


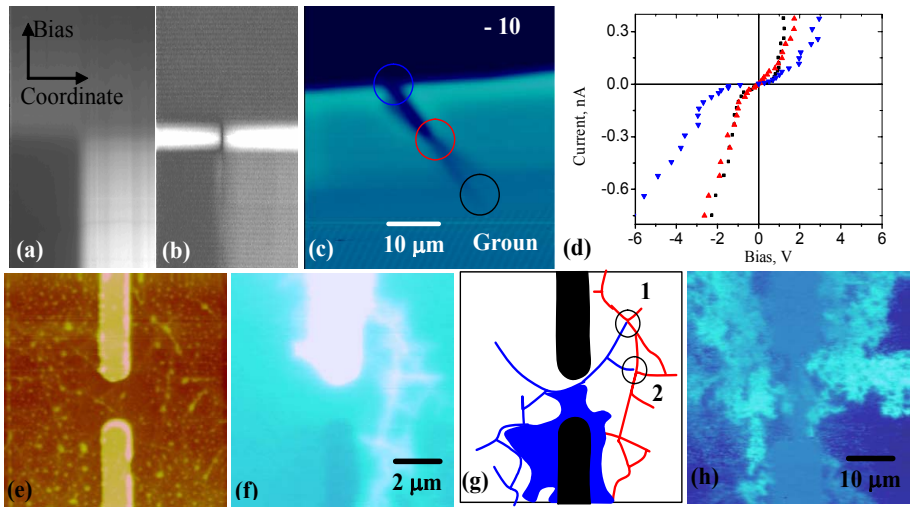


*Fig. 1. 2D spectroscopy of metal-semiconductor interface. Shown is (a) signal and driving frequency and (b) mixed frequency signal. Note the sharp resonance in the mixed frequency signal due to the interface non-linearity. (c) Potential distribution along biased $SnO_2$ nanowire. (d) I-V curves of individual defects. (e) Surface topography and (f) SIM image of carbon nanotube network in polymer. Note that biased nanotubes are clearly resolved, despite the fact that they are located below the 200-nm polymer layer. (g) The mapped conductive paths for positive (red) and negative (blue) biases, demonstrating the role of high junctions resistances on transport. (f) Phase distribution on the large scale. Gradual decay of contrast is due to the capacitive coupling to the back gate, providing information on the effective RC time constant in the network, which limits the maximal device size.*

# Novel, Tunable, Ultrafast, Nonlinear Optical Switching

W. Wang,[1] B. Gu,[1] G. E. Jellison, Jr.,[2] and R. Haglund[3]
[1]*Environmental Sciences Division*
[2]*Condensed Matter Sciences Division*
[3]*Department of Physics and Astronomy, Vanderbilt University*

We proposed to develop a new type of ultrafast optical nonlinear Bragg switch with photonic crystal materials. The goal was to fabricate metal or semiconductor quantum-dot doped silica photonic crystals, which can optically switch light in the time regime from picoseconds to several hundreds of femtoseconds. Methods were successfully developed to synthesize various metal (Ag or Au) or semiconductor (CdS)-silica composite nanoparticles with quantum dot inclusions at >10 wt %. We also were able to control the size, size distribution, and morphology of these synthesized nanoparticles. With these composite nanparticles, we successfully fabricated colloidal photonic crystals and solidified them in polymer hydrogels. These quantum dot–doped composite nanomaterials exhibited strong nonlinear responses, which provided the proof of principle that ultrafast nonlinear optical switching devices could be fabricated using techniques developed in this research. These new optical materials could potentially be used in ultra-fast optical computing, laser and laser arrays, optical bandgap materials, and sensor materials for environmental monitoring and detection.

## INTRODUCTION

Three-dimensional photonic crystals have attracted considerable interests because they offer innovative ways of controlling the propagation and emission properties of light. These photonic crystals usually are composed of plain $SiO_2$ or polymer nanospheres. In this research, we introduced nonlinear optical property of quantum dots into $SiO_2$ nanospheres to fabricate new photonic crystal materials. These semiconductor or metal quantum dot– doped silica photonic crystals can Bragg diffract light in the visible region. The use of inorganic $SiO_2$ colloids offers significant advantages because silica has a much higher damage threshold under laser pulse than most of organic polymer colloids. Our approach was to drive refractive index changes by using electronic nonlinear properties of metal or semiconductor quantum dots in $SiO_2$ colloids on the ultrafast scale from picoseconds to hundreds of femtoseconds. This creates opportunities for creating advanced photonic materials, and their novel optical nonlinear effects have potential applications in optical limiting, computing, and ultrafast optical switching devices.

## TECHNICAL APPROACH

In this research, we first developed a modified microemulsion technique to synthesize metal quantum dot–doped $SiO_2$ nanospheres with >10 wt % of silver or gold quantum dot inclusions. With systematical studies of the reaction conditions, we were able to control resulting composite particle size in the range of 50–250 nm. Particle morphologies could also be tailored; for example, silver and gold nanoparticles could be directed as a single core or as homogeneously dispersed multi-cores in the silica spheres. We also successfully synthesized semiconductor (CdS) quantum dot–doped $SiO_2$ nanoparticles in a microemulsion medium which consists of surfactant, organic solvent, and water. CdS quantum dots were first produced by mixing $Cd^{2+}$ ions and $S^{2-}$ ions in the microemulsion, and $SiO_2$ shells were then grown on CdS by hydrolyzing tetraethoxysilane (TEOS) in the presence of ammonium. Upon completion of the TEOS hydrolyzation and condensation in 24 h, CdS-$SiO_2$ composite nanoparticles were obtained. We found that the monodispersity and morphology of the resulting composite nanoparticles strongly depended on the order of added reagents and the reaction time. Another crucial step was that a silane coupling agent was needed to enhance the affinity between the CdS cores and $SiO_2$ shells. In the absence of the coupling agent, only separated CdS particles and $SiO_2$ particle formed and co-existed in the microemulsion, and no composite nanoparticles were formed. Dynamic light scattering and transmission electron microscope measurements showed that these synthesized metal- or semiconduction-silica composite nanospheres have a narrow size distribution with a polydispersity of 5–10%. Figure 1a shows a typical morphology of the synthesized composite nanoparticles. Additionally, we fabricated a limited number of photonic crystals using these quantum dot–doped silica spheres. These photonic crystals exhibited refraction properties in visible range, and results from Z-scan experiment

indicated that these quantumdot–doped silica spheres showed strong nonlinear response, as it is necessary to create optical nonlinear Bragg switches.

## RESULTS AND DISCUSSION

A method was developed to attach negatively charged acidic functional groups (e.g., $–SO_3–$ and –COO–) to the surface of metal quantum dot–silica composite nanoparticles. This process was necessary to enhance the surface charge density of synthesized CdS-, Ag-, or Au-silica nanoparticles. With highly purified colloids, strong electrostatic repulsions caused these monodispersed composite nanospheres to self-assemble into an ordered structure, that is, crystalline colloidal arrays or photonic crystals in FCC structures in pure water. These photonic crystals Bragg diffract electromagnetic radiation in the UV, visible and near-infrared spectral regions (Wang and Gu 2005).

We also developed a method to solidify the liquid photonic crystals by polymerizing them in polymer hydrogels. This was accomplished by introducing acrylamide as monomer, methylenebisacrylamide as cross-linker, and 2,2-diethoxyacetophenone as photoinitiator to produce the photonic crystal hydrogels under UV light illumination. The hydrogel photonic crystals were used to fabricate the nonlinear optical devices. Figure 1b illustrates an example of Bragg diffraction spectra of CdS quantum dot–doped $SiO_2$ photonic crystals in the hydrogel.

To fabricate ultrafast optical switching devices, we induced refractive index changes by using electronic nonlinear properties of metal or semiconductor quantum dots in $SiO_2$ colloids. With the photonic crystal materials containing nanoparticles in polymer hydrogel, we were able to match the real part (nr) of their refractive index while preserving a periodic modulation of the imaginary part (ni) of the refractive index. With a matched refractive index in a dimethyl sulfoxide (DMSO)–water mixture, the diffractions from photonic crystals disappeared and made the material transparent, as shown in Figure 1b.

In order to tune the diffraction property of these photonic crystals for ultrafast optical switching applications, it is essential to induce a refractive index difference of >0.01 between composite silica spheres and the refractive index–matched surrounding medium, and switching is then induced by manipulating electronic nonlinear properties of the quantum dots in the photonic crystals at picosecond or femtosecond time scales. We have measured a series of composite nanoparticle samples containing homogeneously dispersed quantum dots by Z-scan technique. Z-scan is a single-beam measurement of the phase distortion in the far field, which gives both the sign and magnitude of nonlinear refraction g and the nonlinear absorption b. Results showed that the Ag quantum dot–$SiO_2$ composite nanoparticles indeed gave a strong nonlinear response (Fig. 1c), which is necessary to create optical nonlinear Bragg switches. These experimental results thus provide the proof of principle

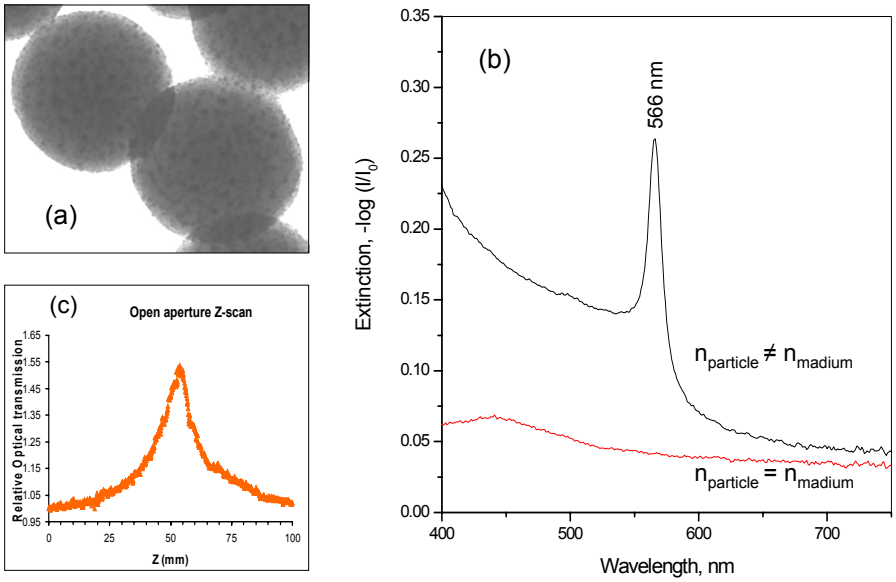


*Fig. 1 (a) SEM image of the typical morphology of quantum dot-doped silica nanospheres. (b) Transmission spectra at refractive index matched and mismatched conditions for CdS-doped silica nanoparticle photonic crystals in the polymer hydrogel. (c) The z-scan experiment showing typical optical nonlinearity from Ag quantum dot–doped silica composite nanoparticles.*

that ultrafast nonlinear optical switches can be fabricated by using these metal quantum dot-doped photonic crystal materials. However, results also indicate that the observed electronic nonlinear effects from doped quantum dots did not cause enough refractive index changes so as to control the diffraction. Further studies thus are needed in order to increase the electronic nonlinear efficiency.

In conclusion, we developed methods to synthesize metal (Ag or Au) and semiconductor (CdS)-silica composite nanoparticles with quantum dot inclusions at >10 wt %. We also were able to control the size, size distribution, and morphology of these synthesized nanoparticles. With these composite nanparticles, we successfully fabricated colloidal photonic crystals and solidified them in polymer hydrogels. These quantum dot–doped composite nanomaterials exhibited strong nonlinear responses, which provided the proof of principle that ultrafast nonlinear optical switching devices could be fabricated using techniques developed in this research. By manipulating the electronic nonlinear properties, the diffraction intensity of the photonic crystal materials may be tuned at picosecond and femtosecond time scales.

## BENEFITS

This research is closely tied to the DOE missions in basic energy sciences, nanomaterials research, and environmental detection. Many agencies in the U.S. Department of Defense also may benefit from this research. For example, Defense Advanced Research Projects Agency (DARPA) is particularly interested in the development of non-linear optical materials, and U.S. Air Force Office of Scientific Research is interested in novel lasers and laser arrays and nonlinear optical devices. These new optical materials could potentially be used in ultra-fast optical computing, laser and laser arrays, optical bandgap materials, and sensor materials for environmental monitoring and detection.

## REFERENCES

Wang, W. and Gu, B. 2005. "Self-assembly of Two- and Three-Dimensional Particle Arrays by Manipulating Hydrophobicity of Silica Nanoparticles," *J. Phys. Chem. B*, in press.

# Design and Synthesis of Oriented Guest-Host Nanostructures for Enhanced Membrane Performances

M. Z. Hu,[1] V. de Almeida,[1] I. Kosacki,[2] D. A. Blom,[2] and E. A. Payzant[2]
[1]*Nuclear Science and Technology Division*
[2]*Metals and Ceramics Division*

This project has demonstrated a novel nanomaterial design concept and a synthesis method for "guest-host"-type superionic-conducting nanocomposite membranes. This concept consists of nanophases of oxide electrolyte nanograins (guest) encapsulated inside the nanopore channels of an oxide layer matrix (host), with channels oriented perpendicular to the layer surface. Using ionic conducting YSZ (yttrium stabilized zirconia) as a special case, we have shown that the host-guest design allows orientation of a large number channels, allowing a high density of nanograin boundaries/interfaces to be built into the film to enhance cross-membrane conductivity. This structure allowed conductivity measurements with impedance spectroscopy to be performed for the first time at room temperature. Cross-membrane conductivity values at low-temperature ranges of interest are the higher than any reported values. The conductivity-enhancing mechanisms could be attributed to (1) controlled orientation and increased number density of YSZ nanograin-host interfaces and (2) creation and stabilization of YSZ nanocrystalline phases inside nanopore channels (<10-nm diam). This successful initial demonstration of host-guest nanostructures is expected to have direct impact on fuel cell technologies and may also have beneficial use in a broad range of applications such as in solar cells, sensors, chemical/gas separations, catalysis, and magnetic memory devices. This work may also lead to a new way to develop membrane technologies that offer orders-of-magnitude-higher permeability and selectivity, as well as improved thermal stability of the desirable nanocrystalline phases.

## Introduction

Oxide ionic conductors, such as oxygen- or proton-conducting ceramic membranes, are very important materials for a wide range of applications, such as in fuel cells, microbatteries, and other solid-state ionics-based devices. Solid oxide fuel cells (SOFCs) present an efficient and ecologically acceptable way to simultaneously generate heat/electricity with theoretical efficiency as high as 70%. One future development goal is to introduce intermediate-temperature solid oxide fuel cells (IT-SOFCs) by considering alternative materials (such as electrolyte and electrode) that would enable lowering the operating temperature from 1000ºC to below 800ºC without loss of performance. Lower-temperature operation will reduce the system materials requirement and cost and also avoid many undesirable interfacial reactions between electrode and electrolyte materials. At low operating temperatures, superior ionic conductivity of the oxide electrolyte layer (> $10^{-2}$ S/cm) is required for success in fuel cell applications. A technical challenge lies in the creation of a stable membrane nanostructure that offers cross-membrane conductivity far above what is available today.

Nanomaterials have been considered promising in improving materials performance for solid-state ionics and SOFCs. The objectives of this project are the following:

1. Demonstrate that novel host-guest nanocomposite membrane can be synthesized,
2. Prove that the designed nanostructure (i.e., large number density of oriented guest-host interfaces and nanocrystalline grain boundaries) can enhance cross-membrane ionic conductivity, and
3. Demonstrate improved thermal stability of nanocrystalline phases due to host nanopore confinement.

## Technical Approach

Our nanocomposite membrane design, conceptually illustrated in Fig. 1a, consists of nanocrystalline phases of oxide electrolyte (guest, that is, YSZ nanosized grains) encapsulated inside a host, which is a rigid solid ($Al_2O_3$ or $SiO_2$) matrix layer containing high-density arrays of oriented, uniform, nanopore cylinder channels (ideally <10 nm in diameter). This novel membrane approach integrates three potential conductivity-enhancement mechanisms:

1. *Oriented guest-host interfaces*, aligned parallel to the current flow direction (i.e., across the membrane layer),
2. *Large number density of nanograin boundaries and nanograin-host interfaces* via creation of nanocrystalline phases inside a host nanopore channels, and
3. *Enhanced thermal stability* of nanocrystalline phases due to confinement of grain growth inside nanopore channels.

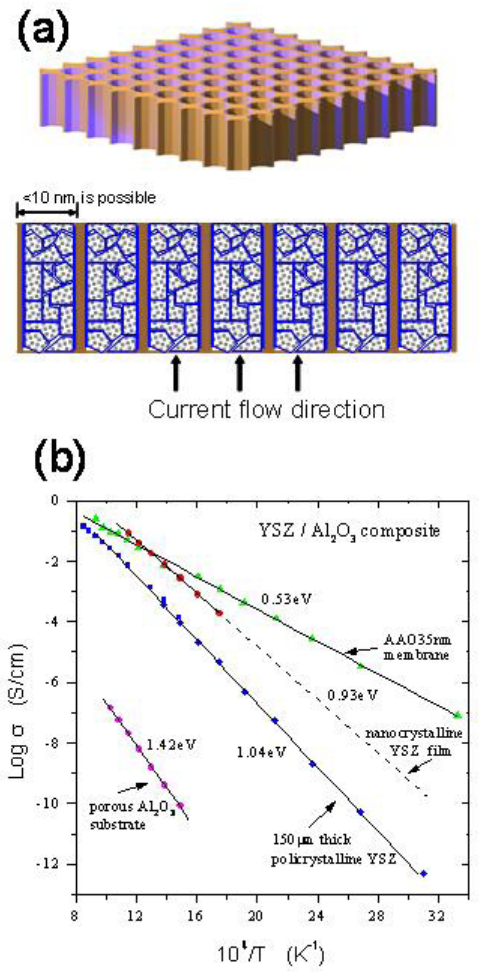


*Fig. 1. (a) Schematic illustration of the nanostructure design of oriented guest-host nanocomposite membranes. (b) The measurable room temperature ($1/T = 33 \times 10^{-4}$ $K^{-1}$) and low-temperature conductivity data provide proof-of-principle demonstration of the effects of nanostructure and orientation on the enhancement of conductivity in nanocomposite membrane (AAO35nm).*

This approach creatively allows the utilization of a large number of *oriented guest-host interfaces* as well as nanophase *grain boundaries* by stabilizing nanograins within designed nanopore channels.

Validation of conductivity enhancement through orientated crystal-substrate interfaces. This interface-orientation mechanism can be supported by the current understanding of the advantageous effect of crystal-substrate interface orientation on conductivity:

- Using a single-crystal YSZ film on MgO substrate, previous studies at ORNL have shown enhancement of ionic conductivity (measured with current flow parallel to the crystal-substrate interface) when film thickness decreased below 60 nm (Kosacki et al. 2004). A 15-nm-thick film exhibited the highest ionic conductivity ever reported, approximately 200-fold greater than that of conventional coarse-grained zirconia electrolyte at 400°C.
- Similar interface-orientation effect has been also reported for $BaF_2/CaF_2$ multilayers of epitaxial films where an increase of ionic conductivity (parallel to the layered interfaces) of over three orders of magnitude was observed relative to the bulk materials (Sata et al. 2000).
- A study in a large bulk-single-crystal YSZ clearly demonstrated the oriented interfacial effect on ionic conductivity enhancement due to dislocations (i.e., oriented interfaces of micro-cracks inside one piece of single crystal, parallel to the current flow direction) generated by plastic deformation (Otsuka et al. 2003). The conductivity increased with the increase of number density of microcracks in the crystal.

### *Justification of Conductivity Enhancement through Nanocrystalline Phases*

For nanocrystalline ceramic electrolytes, the following have been established (Kharton and Marques 2002):

- large number and volume of grain boundaries (~1019 $cm^{-3}$), resulting in a large ratio of atoms in grain boundaries to grain volume (ca. 30–60%);
- grain boundary impurity segregation, and thus considerably lower concentration of impurity phases, which blocks ionic conduction per unit of grain boundary area;
- increased contribution of space-charge effects;
- grain-size-dependent defect thermodynamics (i.e., increased vacancy concentration in the grain-boundary area; $D_{GB} >> D_B$). Ionic mobility due to a higher number density of nanograin boundaries and higher interfacial concentration of defects (oxygen vacancies) is superior to the ionic diffusion through the bulk grains.

Results from supported nanocrystalline ScSZ thin films have shown that the enhanced electrical conductivity was due to the changes of ion mobility, which occurs in grain-boundary interfaces oriented parallel to the current flow (Kosacki et al., 2001). Such an idea of interface orientation effect has been also reported for nanocrystalline $CaF_2$ (Puin et al. 2000). In addition, grain-substrate interfacial contributions are enhanced in a substrate-supported nanocrystalline film (Suzuki et al. 2002). These factors have been shown to contribute enhanced conductivity in the direction parallel to a film-substrate interface. We have aimed at a proving the concept of a nanostructured material designed to maximize the grain boundary and grain-substrate interfacial effects.

## Results and Discussion

Proof-of-principle studies have focused on development of membrane synthesis by infiltrating and growing YSZ (typically $ZrO_2$:16%Y) nanophases inside oriented nanoporous host layers of anodized alumina discs, with pore-channel diameters in the range of 10–100 nm.

### *Synthesis of Host-Guest Nanocomposite Membranes*

Initial effort to prepare ordered nanopore host materials was by an "engineered molecular assembly templated synthesis" (EMATS) (Hu et al. 2003), which allows the formation of large-area domains of hexagonally ordered cylinder channels (<10 nm), perpendicular to the layer surface. However, at this stage, oriented mesoporous silica in the form of membrane discs is difficult to make. Alternatively, we have been cooperating with Synkera Technologies and have successfully obtained anodized aluminum oxide (AAO) discs of various desirable pore channel diameters (13±2, 18±3, 35±3, 55±6, and 73±7 nm). Various methods have been attempted to infiltrate guest YSZ nanophases into host matrix. A vacuum-assisted polymer or nanoparticle precursor infiltration method has been developed to infiltrate or impregnate YSZ precursor into the host nanopore channels, followed by thermally induced crystallization and grain growth. The nanostructures of the resulting composite materials (e.g., pore channels and confined nanograins) were examined by scanning transmission electron microscope (STEM) and X-ray diffraction (XRD), showing ~ 5nm nanocrystalline grains present at typical 600ºC, 4-h calcination. Back-scatter SEM images have shown long YSZ nanowires across the channels, in some cases segmented wires.

Conductivity enhancement in oriented guest-host nanocomposite membranes. The conductivity of the nanostructured samples were measured by impedance spectroscopy (IS), which allows the separation of resistances related to grains, grain boundaries, and electrode effects. The diffusivity of ions in nanocrystalline materials corresponds to the results of conductivity measurement by impedance spectroscopy. The cross-membrane conductivity at room temperature of the materials synthesized in this study was the highest ever reported for YSZ materials; in fact, this is the first time values have been obtainable at room temperature. As shown in Fig. 1b, the oriented host-guest interfaces further enhance the conductivity beyond what grain boundaries in nanocrystalline phase can provide. It is noted that conductivity of the materials from this study is lower than other nanocrystalline YSZ at high temperatures; low guest density and nanowire discontinuity and interface segmentation at high temperatures might have contributed to this reduced performance at high temperature.

Stability and maintenance of high-conductivity nanostructures. Thermal stability of nanocrystalline phases, which is related to grain growth phenomena under relatively high-temperature processing or operation conditions, is known to be a technology bottleneck for maintaining nanophase-enhanced conductivity in conventionally supported nanocrystalline films (Dong et al. 2002). Our STEM examinations have visually proven the nanopore-confinement effect that has restricted the growth of grain size within the dimension of nanopore channels of the AAO host. In an extreme case, a single crystal nanowire may form but still provide the desirable nanograin dimension and the oriented guest-host interfaces. Therefore, this guest-host design resolves the thermal stability problem by surviving the desirable nanograin size in the nanocomposite membrane.

### *Future Work*

The demonstration of the enhanced conductivity and improved thermal stability for our nanocomposite membrane samples is expected to attract follow-on funding for further development of the membrane fabrication method for fuel cells and other applications. Future development needs to address various issues, including systematic studies of nanostructure and composition; improvement of YSZ nanophase density, homogeneity, and the contact interface between electrode and the membrane; and the effect of channel diameter, aspect ratio, channel length, and host and guest composition effect. The size of the membrane area needs to be scaled up for future practical technology development. Mechanical properties of the membrane under various temperatures need to be also evaluated.

## Benefits

The novel concept demonstrated here is not limited to ionic oxide material. Beyond fuel-cell applications, the host layer materials (if functionalized with appropriate ligands) could potentially serve as membranes for wastewater cleanup, biomolecule separation, synthesis of uniform macromolecules (dendrimers), and mining applications. Furthermore, many different kinds of nanocrystalline oxides or non-oxides (metals/alloys, nitrides) can be developed in the nanopore channels of our unique host matrix layer to take advantage of the nanocrystal confinement and oriented interfacial effects. For example, proton-conducting oxides or polymers can be prepared as guest phases confined in nanopore channels for proton membranes. Such nanocomposite membranes could also lead to a new generation of electrochemical sensor materials for $H_2$, $NO_x$, etc. The designed nanocomposite membranes could be used for solar cells,

membrane catalytic reactors (desulfurization by hosted $Mo_2N$ nanophase), hard-disk memory (magnetic recording with high signal-to-noise ratio), or for electronic/optical devices (when guests are semiconductors such as CdS). In summary, the R&D and application opportunities for our novel nanostructured membranes are very broad.

## References


Dong, J., M. Z. Hu, E. A. Payzant, T. R. Armstrong, and P. F. Becher. 2002. "Grain growth in nanocrystalline yttrium-stabilized zirconia thin films synthesized by spin coating of polymeric precursors," *J. Nanosci. Nanotechnol*. **2**, 161.

Hu, M. Z., V. de Almeida, D. A. Blom, L. Allard, S. Dai, C. Tsouris, and Z. Zhang. 2003. "Pore Channel Orientation In Self-assembled Inorganic Mesostructures," a poster presented at the Microscopy and Microanalysis 2003 Meeting, San Antonio, Texas, Aug. 3–7, 2003.

Kharton, V. V. and F. M. B. Marques. 2002. "Mixed ionic-electronic conductors: effects of ceramic microstructure on transport properties," *Current Opinion in Solid State and Materials Science* **6**, 261.

Kosacki, I., P. F. Becher, C. M. Rouleau, D. H. Lowndes, and J. Bentley. 2004. "Observation of superionic conductivity in highly oriented nanometer scale $ZrO_2$-10 mol %$Y_2O_3$ (10YSZ) film," unpublished results.

Kosacki, I., T. Suzuki, and H. U. Anderson. 2001. Proc. 7th Intern. Sym. In Solid Oxide Fuel Cells, Tsukuba, *The Electrochem. Soc. Proc.*, vol. 2001–2016, pp. 284–292.

Otsuka, K., A. Kuwabara, A. Nakamura, T. Yamamoto, K. Matsunaga, and Y. Ikuhara. 2003. "Dislocation-enahnced ionic conductivity of yttria-stabilized zirconia," *Appl. Phys. Lett.* **82**, 877.

Puin, W., S. Rodewald, R. Ramlau, P. Heitjans, J. Maimer. 2000. "Local and overall ionic conductivity in nanocrystalline $CaF_2$," *Solid State Ionics* **131**, 159.

Sata, N., K. Eberman, K. Eberl, and J. Mailer. 2000. "Mesoscopic fast ion conduction in nanometer-scale planar heterostructures," *Nature* **408**, 946.

Suzuki, T., I. Kosacki, and H. U. Anderson. 2002. "Microstructure-electrical conductivity relationships in nanocrystalline ceria thin films," *Solid State Ionics* **151**, 111.

# A Hybrid Solid-State Process for Joining High-Temperature Materials

Z. Feng, S. A. David, and E. K. Ohriner
*Metals and Ceramics Division*

Friction stir welding (FSW) is a novel joining process. Its solid-state nature allows for joining materials that are difficult to weld with existing technologies. There has been tremendous interest and need to further advance the FSW technology from aluminum alloys to high-temperature materials including titanium alloys, nickel-based alloys, oxide dispersion–strengthened (ODS) alloys, and ultra-high-strength steels. However, the application of FSW to high-temperature materials is technically challenging. A key technical issue is related to the inability of the FSW tool to generate sufficient heat to soften high-temperature material for the extensive flow and consolidation necessary to form a good joint. In this program, we demonstrated the technical feasibility of a hybrid process that combines the friction stir welding process with controllable precision auxiliary heating (laser or exothermic reaction) to improve welding productivity and minimize tool wear when joining high-temperature materials. The knowledge and intellectual property developed with the new hybrid process gives ORNL significant leverage for follow-on programs from industry partners and government funding agencies.

## Introduction

Friction stir welding (FSW) is an innovative solid-state joining process invented in the 1990s by The Welding Institute in the UK (Thomas et al. 1991). Considered as one of the most significant welding process inventions of the last two decades, the FSW process enables the advantages of solid-state joining for fabrication of continuous linear welds, the most common form of weld joint configurations. In addition, the process is being explored for localized microstructure modification for various applications including superplastic forming, casting improvement, and production of ultra-fine microstructures or even nano-structures (Mishra 2003).

Today, the FSW process is being used to join low-melting temperature materials, mostly various aluminum alloys that are difficult to fusion-weld. Well-known applications include the Delta rocket booster for the Space Shuttle of NASA, the lightweight advanced amphibious assault vehicle for the U.S. Marine Corps, high-speed express trains in Japan, superstructures for cruise liners in Europe, and nuclear waste copper alloy containers. The U.S. auto industry is also actively pursuing the application of FSW in lightweight body structures. The economical and technological benefits of FSW have been well documented for Al alloys and other low-melting temperature materials.

The economic benefits would be much more remarkable if FSW could be applied to high-performance high-melting temperature materials such as intermetallic alloys, Ni-based superalloys, Ti alloys, oxide dispersion–strengthened (ODS) alloys, and Fe-Cr-W steels. These high-performance alloys are very difficult, if not impossible, to fusion weld, and FSW is, in principle, well suited for joining these materials because of its solid-state nature. Indeed, the industry and government agencies, both nationally and internationally, have been aggressively advancing FSW technology to join high-performance high-temperature materials. Developing FSW for high-temperature materials is especially important to DOE, as many of the advanced high-temperature materials developed for the DOE mission have been difficult to weld.

## Technical Approach

Friction stir welding of high-temperature materials has been much more challenging than that for Al alloys. In order to facilitate the extensive material flow necessary to form a joint, the stir region needs to be heated to a temperature range in which the material is sufficiently soft and ductile, usually above two-thirds of the melting temperature of the material. For example, studies by the author and others (Could et al. 1996; Feng 1997; Gould 1999) have shown that FSW operates in the range of 350–450ºC for Al alloys, 850 –1150°C for Ti-6Al-4V, and 900–1300ºC for carbon steels. Thus, compared to Al alloys, FSW high-temperature materials needs to be operated at much higher temperatures. The higher process temperature dictates that more heat would have to be generated. This in turn imposes substantially higher load on the FSW tool. The combination of the reduced mechanical strength and increased mechanical load causes extensive wear and fracture of the tool.

In the present form of FSW, the rotating tool has dual functionality: it not only mechanically stirs and forges the

material to form the joint, but it also is the sole source for heat generation. Although it works well when welding Al alloys and other low temperature materials, the double-duty function of the rotating tool becomes a fundamental shortcoming when welding high-temperature materials. Our concept was to combine the FSW process with a separate or auxiliary heating system to create a new, hybrid solid-state joining process. In this new hybrid approach, the addition of the auxiliary heating source would minimize the role of the tool as a heat generator, thereby reducing the loads on the tool. This would then lead to the reduction of tool wear and premature breakdown during welding. By intelligently arranging the auxiliary heat source, the material in front of the tool can be softened properly to achieve higher welding speed. Furthermore, reducing the primary function of the tool to mechanical stirring and consolidation only would pave the way for innovative tool designs and optimizations to further increase the productivity of the process.

The objective of this seed money program was to establish the technical feasibility and to demonstrate the potential advantages of the hybrid FSW process. The research efforts focused on (1) evaluating and installing an auxiliary heating source to the FSW development system, (2) performing heat flow and stress modeling for selection of critical process parameters and determination of the effectiveness of the hybrid FSW process, and (3) conducting welding trials and post-weld microstructure and property evaluations to prove the feasibility of the hybrid FSW process.

## Results and Discussion

Two basic types of heating were investigated in this program: (1) external heating where the heat is generated by means of an external heating source, (2) internal heating through exothermic chemical reactions of a properly selected material placed at the joint interface.

For the external heating, the heating source was placed in front of the rotating tool. Three external heating methods were evaluated: Nd:YAG laser, infrared heating, and high-frequency induction heating. Experimental tests were conducted using the existing heating hardware available to the program to evaluate the performance of these heating methods in terms of speed, intensity, and heating spot size, etc., against the targeted auxiliary heating requirement as determined by welding process modeling. Based on these evaluation results, a 4-kW Nd:YAG laser was chosen for integration with the FSW machine system. The Nd:YAG laser was fiber optically delivered, allowing for flexible placement of the heating source based on the material and thickness of the plate to be welded. In addition, the size, shape, and intensity of the heating area can be easily adjusted with the laser, according to the processing needs.

Computational modeling was used to determine the hybrid process conditions (which would be quite different from the normal FSW conditions) that would produce the "suitable" temperature field around the stir region. The use of the computational modeling reduced the trials-and-errors to find the appropriate process conditions to produce good quality welds.

Experimental trials were conducted on 6-mm-thick SS304 stainless steel plates. Figure 1 shows the hybrid process in action. Under the position control operation mode, the force sensors of the FSW system recorded a substantial reduction of the weld load—the average forging force was reduced from about 6000 to 8000 lb under the normal FSW condition to about 3500 to 4500 lb under the hybrid FSW condition.

For the exothermic heating, experimental trials were performed with aluminum powder pastes and shims placed at the joint interface of SS304 stainless steel. Based on the thermodynamic calculations, when mixed with the base metal and heated above certain temperatures, the aluminum powder would form intermetallic compounds and release exothermic heat. The release of the exothermic reaction heat was triggered by the temperature increase in front of the tool as the tool is moved along the joint line. Similar to the Nd:YAG laser case, reduction of the forging load was observed with the use of exothermic heating technique.

## Benefits

The economic incentives for FSW of high-temperature materials are huge as the process would be a critical technology enabling increased use of many classes of high-performance high-temperature materials in a number of industry sectors (aerospace, automotive,

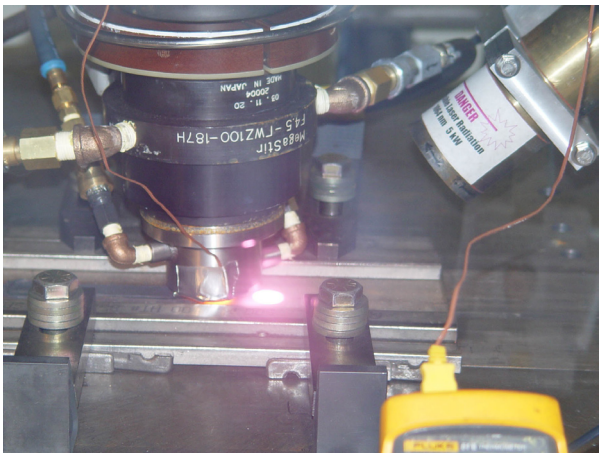

*Fig. 1. Experimental setup of the externally headed hybrid FSW process: a 4-kW fiber-optically delivered Nd:YAG laser is coupled to the friction stir welding head. Weld is made on SS304 stainless steel.*

shipbuilding, power generation—nuclear and fossil, and petrochemical) and government agencies (DOE, DOD, and NASA). Examples of potential applications of FSW include (1) joining high creep-resistant oxide dispersion strengthened steels, vanadium alloys, and dissimilar materials for fusion reactors and other high-temperature applications; (2) repair of irradiation-damaged stainless steel structures in nuclear power plants; (3) construction of ultra-high strength steel pipelines for energy (hydrogen, natural gas, and liquid petroleum) transmissions; (4) fabrication and repair of aero engine components made of Ni-based superalloys and mechanically alloyed materials; (5) titanium-alloy intensive aircraft, spacecraft, and Navy ship superstructures; (6) super austenite alloy (such as Al-6XN) for Navy ship structures; and (7) ultra-high-strength steels for lightweight, high-performance auto vehicle body-structures.

The seed money fund enabled us to evaluate the key technical concepts and the process advantages of the proposed hybrid FSW process. The successful demonstration of the hybrid FSW process has already helped ORNL to develop several programs in application of FSW to high-temperature materials. So far, we have received funding from DOE for FSW of ODS alloys, a DOD-funded program on welding of Ti alloys, and an industrial funded program on welding of nickel-based super alloys. Other programs from industry and government agencies are also being developed.

## References


Could, J. E., Z. Feng, and P. Ditzel. 1996. "Preliminary Modeling of the friction stir welding process," Int. Conf. on Advances in Welding Technology, Columbus, Ohio.

Feng, Z. 1997. *Feasibility Study of Friction Stir Welding Ti-6Al-4V to RHA Steel*, Technical Report to Army Research Laboratory, Edison Welding Institute.

Gould, J. E., and T. J. Lienert. 1999, "Friction Stir Welding of Mild Steel," First International Symposium on Friction Stir Welding, Rockwell Science Center, Thousand Oaks, California.

Mishra, R. S. 2003. "Friction stir processing technologies," *Advanced Materials & Processing* **161**(10), 43–46.

Thomas, W. M., E. D. Nicholas, J. C. Needham, M. G. Murch, P. Temple-Smith, and C. J. Dawes. 1991. "Improvements relating to friction stir welding," European Patent Specification 0615480 B1.

# An Energy Efficient Method for Semi-Solid Material Processing

Q. Han,[1] X. Jian,[2] and T. T. Meek[2]
[1]*Metals and Ceramics Division*
[2]*University of Tennessee*

This project focused on the development of a new method for semi-solid metal (SSM) processing. High-intensity ultrasonic vibrations were used for obtaining a spherical, non-dendritic solidification structure, which is ideal for SSM processing. A novel experimental apparatus was designed and built. Parameters affecting spherical grain formation were studied. These parameters included the casting temperature, the use of grain refiners, and the intensity of ultrasonic vibration. The project demonstrated that extremely small and spherical/non-dendritic grains can be obtained with ultrasonic vibration. The grain size obtained in this project was in the range of 30 to 60 μm, much smaller than 100 μm which is considered as the typical grain size in very well grain-refined aluminum alloys (Greer 2004). The mechanism of ultra-fine grain formation was also examined. Based on the scientific understanding of the grain refinement of alloys, a die caster was modified to incorporate the ultrasonic technology. Castings of high internal quality were made. The project results represent a technological opportunity for developing a unique low-cost, energy-efficient, and operationally robust method for SSM processing.

## Introduction

SSM processing is an emerging technology that offers distinct advantages over other near-net-shape manufacturing processes, such as more homogeneous microstructure, improved die filling during processing, less oxide formation, less porosity and segregation, improved mechanical properties, and less die wear (Flemings 1991). This process is ideally suited for die casting and a number of automotive components. The most widely used industrial process for high-volume production of SSM components is thixocasting (Garat 1998) using the following processing route:

Liquid → Liquid + Solid (electromagnetic stirring and direct chill casting) → Solid Billet

→ Slug (cut) → Slug (reheated) → Liquid + Solid → Solid Casting (die casting)

The energy and cost savings are enormous if the processing route can be changed to

Liquid → Liquid + Solid → Solid Casting,

which is termed rheocasting (Flemings 1976), but rheocasting has not been industrialized (Garat 1998). An ideal route for the rheocasting of SSM would consist of holding the alloy in the liquid state and then turning the liquid into a non-dendritic semi-solid structure with required solid fractions for processing. The process has to be a robust, efficient operation under various forming methods, and suitable for mass production.

In earlier research funded by the Industrial Technologies Program, the U.S. Department of Energy (DOE), we demonstrated in small-size specimens that globular grains can be obtained in aluminum alloys by injecting high-intensity ultrasonic energy into the solidifying ingot (Jian 2004). This work suggested a novel method for SSM processing using ultrasonic vibrations. The purpose of this project was to prove the feasibility of the proposed method and to demonstrate SSM processing of A356 alloys. Tasks were (1) fabrication of an experimental apparatus, (2) a parametric study of the factors affecting spherical grain formation, (3) fundamental study of spherical grain formation, and (4) demonstration of SSM processing of A356 alloy. A goals was to show that spherical grains could be obtained in ingots of 3 in. in diameter and 5 in. in height, one of the sizes of commercial SSM feed stock available in the market. We have obtained SSM castings with spherical grains using the proposed ultrasonic processing technology.

## Technical Approach

Details of the proposed method for SSM processing are described in the ORNL patent application (Han 2004). The critical step involves the use of ultrasonic vibration for the production of non-dendritic or spherical grains throughout the solidifying ingot. Technical approaches were developed based on the following phenomena for producing spherical grains in large-size ingots:

1. The injection of ultrasonic vibration into the melt generates alternating pressures within the melt. The minimum and maximum pressures are given by the following equations (Rozenberg 1973):

$$p_{max} = p_0 + \sqrt{2\rho cI} \quad (1)$$

$$p_{min} = p_0 - \sqrt{2\rho cI}\ , \quad (2)$$

where $p_0$ is the atmospheric pressure, $\rho$ and $c$ are the density and the wave velocity of the melt, respectively, and $I$ is the wave energy density.

2. The instantaneous pressure in the melt induces heterogeneous nucleation of the solid phase as well as a streaming effect that leads to the circulation of the nuclei throughout the melt.
3. The addition of grain refiners promotes heterogeneous nucleation also.
4. Spherical grains, instead of dendritic grains, can be obtained provided enough nuclei can be produced in the bulk melt (Flemings 2002).

Based on these phenomena, high-intensity ultrasonic vibrations were injected into the melt from specially designed locations (Han 2004) to generate high alternating pressure and a streaming effect; grain refiners were added in the melt to produce a maximum amount of nuclei; and metal molds were used to chill the melt to retain the small nuclei. A systematic study was carried out to investigate the parameters that affect non-dendritic grain formation in industrial size SSM feedstock (3 in. in diameter and 5 in. in height). These parameters included the casting temperature, the amount of grain refiners used, and the intensity of ultrasonic vibration. Commercial A356 alloy (Al–7.0 wt% Si–0.4wt% Mg–0.1wt% Fe) was used for the experiments.

## Results and Discussion

Experiments were first carried out using a small copper mold, which held up to 250 g of molten A356 alloy, for evaluating the effect of the intensity of ultrasonic vibration and the casting temperature on the solidification structure of the alloy.

Four ultrasonic amplitudes were tested during the experiments, namely 0% (without vibrations), 30%, 50%, and 70% of the nominal amplitude, 16 μm, of the ultrasonic radiator. Molten aluminum was cast into a copper mold at 640ºC and solidified while being subjected to ultrasonic vibration. Without the vibration, aluminum dendrites were fully developed, and the grain sizes were a few millimeters. With the increase of ultrasonic intensity, the primary aluminum grains became less dendritic, more spherical, and much smaller. Spherical, non-dendritic grains were successfully obtained when the amplitude was 70% of the nominal amplitude. Furthermore, the size and morphology of the eutectic Si phase were also altered. Rod-like silicon particles were formed under high-intensity ultrasonic vibration instead of plate-like silicon particles that formed without ultrasonic vibration, a result that has not been reported in the literature.

The effect of casting temperature on the solidification structure of A356 alloy was also evaluated. The results indicated that the size of the primary α-Al grains decreased with decreasing casting temperature, reached a minimum of about 30 μm at 630ºC, and then increased lightly with decreasing casting temperature. The results suggest that the mechanism of grain refinement is the formation of non-equilibrium nuclei at temperatures higher than the liquidus temperature of the alloy (615°C). The high instantaneous pressure induced by ultrasonic vibration contributed to the nucleation of the primary aluminum phase above the liquidus temperature of the alloy.

Based on the results obtained using a copper mold, the maximum intensity of ultrasonic vibration and a casting temperature of 630°C were chosen for processing industrial size A356 alloy ingots of about 3 in. in diameter and 5 in. in height. Image analysis was carried out to measure the size and morphology (roundness of the grains) distribution in the ingot. Results obtained in the larger ingot were consistent with that obtained in smaller casting. Non-dendritic and spherical grains were successfully obtained in the industrial size ingot. The grain sizes are in the range between 35 to 55 μm. These grains are much smaller than those obtained without the use of ultrasonic vibration. These results suggest that ultrasonic vibrations can be used for making a non-dendritic solidification structure that is ideal for SSM processing.

Thermal analysis was carried out in specimens subject to various levels of ultrasonic vibrations. The results indicated that the liquidus temperature was increased by around 6°C in specimens subjected to ultrasonic vibration, suggesting that nucleation of the solid fcc aluminum phase occurred at temperatures higher than the equilibrium liquidus temperature of the alloy. This accounted for the experimental observation that the best grain refinement effect was achieved when ultrasonic vibrations were applied to the molten metal about 10°C higher than the equilibrium liquidus temperature of the alloy. We believe that nucleation occurs at the liquid/gas interfaces of the cavitation bubbles induced by ultrasonic vibrations. During the rapid growth stage of the cavitation bubbles, the temperature within the bubble decreases sharply, resulting in localized undercooling at the bubble surfaces, while the bulk temperature of the melt is still higher than the liquidus temperature. This undercooling may be high enough for nucleation. When the cavitation bubbles collapse, nuclei formed on their surfaces will be dispersed throughout the melt. Since cavitation bubbles form and collapse at high frequencies, a large number of nuclei are generated in the melt, resulting in a significant grain refinement of the alloy.

Based on the systematic study on spherical grain formation and the fundamental understanding of the grain refinement mechanism, an experimental die caster

was modified to incorporate the ultrasonic technology for SSM processing of A356 alloy. Figure 1 shows polished sections of a die casting part with and without ultrasonic processing. The casting not subjected to ultrasonic processing contains large dendrites and large pores shown in Fig. 1(a). When ultrasonic technology was applied to the die casting process, castings made contain spherical grains and no porosity, shown in Figure 1(b). The grain size shown in Figure 1(b) is in the range of 30 to 50 μm, much smaller than the grains obtained using the thixoforming process.

## Benefits

This research will serve as the starting point for a new cost-effective and energy efficient approach for replacing the widely used thixocasting/thixoforming approach. The research will have an important impact on the commercial utilization of semi-solid technologies for the production of high-quality components for automotive applications. This research program was also important for extending the semi-solid technologies to alloys for national defense and aviation industries. Besides, the research can also serve as a starting point for fundamental research on thermodynamics and kinetics of nucleation and crystal growth processes under the influence of ultrasonic vibrations. In particular, ITP of DOE is eager to reduce the high cost and energy consumption associated with the thixoforming processes, which limits the commercial applications of the SSM processes. The DOE Office of Transportation Technology has placed significant emphasis on materials and technologies for mass reduction. High property SSM aluminum alloys will find their applications in mass reduction for automotive, aviation, and defense industries.

## References


Flemings, M. C. 2002. Personal communication with author.

Flemings, M. C. 1991. "Behavior of Metal Alloys in the Semisolid State," *Metall. Meter. Trans.* **22A**, 957–981.

Flemings, M. C., R. G. Riek, and K. P. Young. 1976. "Rheocasting," *Materials Science and Engineering* **25**, 103–117.

Garat, M., S. Blais, C. Pluchon, and W. R. Loué. 1998. "Aluminum Semi-Solid Processing: From the Billet to the Finished Part," pp. xvii–xxxi in *Proceedings 5th International Conference on Semi-Solid Processing of Alloys and Composites*, A. K. Bhasin, J. J. Moore, K. P. Young, and S. Midson, eds., Golden, Colorado, June 23–25.

Greer, A. A. 2004. "Grain Refinement of Aluminum Alloy," pp. 131–145 in *Solidification of Aluminum Alloys*, M. G. Chu, D. A. Granger, and Q. Han, eds., Warrendale, Pa., The Minerals, Metals & Materials Society .

Han, Q., X. Jian X., H. Xu, and T. T. Meek, 2004. "Method and Apparatus for Semi-Solid Material Processing," Docket No. 1372, Oak Ridge National Laboratory.

Jian, X., Q. Han, H. Xu, and T. T. Meek. 2004. "Solidification of Aluminum Alloy A356 Under Ultrasonic Vibration," pp.73–79 in *Solidification of Aluminum Alloys*, M.G. Chu, D.A. Granger, and Q. Han, eds., Warrendale, Pa., The Minerals, Metals & Materials Society, 2004.

Kirkwood, D. H. 1994. "Semisolid Metal Processing," *International Materials Reviews* **39**(5), 173–189.

Rozenbuerg, L. D. 1973. *Physical Principles of Ultrasonic Technology*, vol. 2, Plenum Press, New York, p. 166.


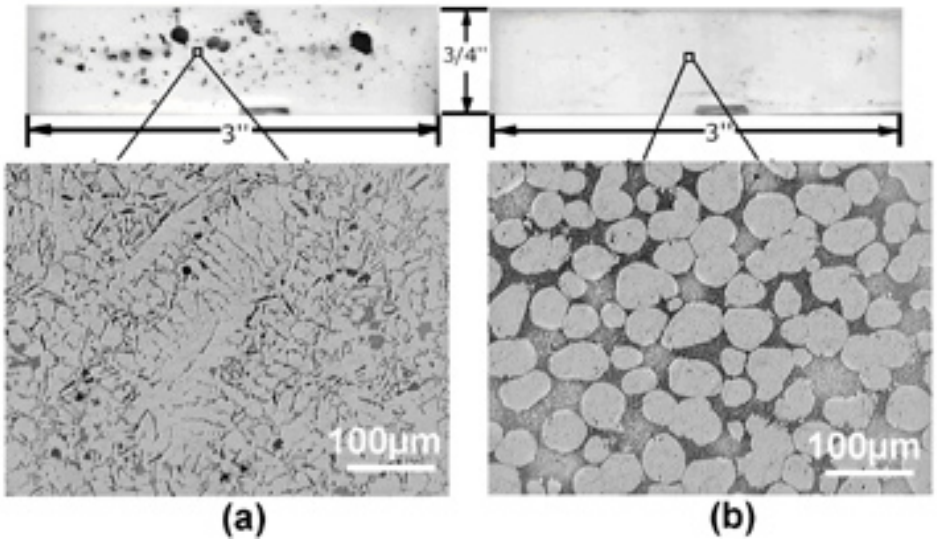


*Fig 1. Polished sections of die casting parts (3/4 in. by 3 in.) without ultrasonic vibration (a) and with ultrasonic vibration (b). The polished section of a casting is shown at the top of the figure, and its microstructure is shown below. Without ultrasonic processing, the casting is full of porosity and grains are fully dendritic. Porosity-free casting with spherical grains is produced using ultrasonic technology.*

# Direct Band Gap Semiconductors on Silicon for Solid State Lighting: Silicon-Based, Blue-Light-Emitting Diodes

R. McKee,[1] A. Janotti,[1] and F. Walker[2]
[1]*Metals and Ceramics Division*
[2]*University of Tennessee*

We seek a "cost-effective" method that will facilitate a silicon-based manufacture of high-efficiency blue, green and yellow light-emitting diodes (LEDs) for solid-state lighting (SSL). We have identified a new class of direct-gap, light-emitting semiconductor compounds that can be fabricated on Si as the materials system for the development of cost effective SSL. These compounds are tetrahedrally bonded semiconductors: $AgGaS_2$ and $CuInS_2$. They can be epitaxially stabilized on the (001) face of Si, and the band gaps are direct in the blue-to-yellow range. Unlike any other materials system that has been proposed, these compounds are chemically and structurally compatible with silicon and have tunable bandgaps.

## Introduction

Our goal has been to demonstrate proof-of-principle for silicon-based solid state lighting by growing and then getting efficient photoemission out of p-n junctions with chalcogenide heterostructures on silicon. The light will be in the blue-to-yellow wavelength range of the visible spectrum.

## Technical Approach

The blue-to-yellow wavelength range is currently covered using the wide-bandgap material GaN, a material that is both expensive to manufacture and difficult to perfect to an acceptable level for energy efficient application. We proposed that both of these problems are fixable on silicon with direct gap semiconducting heterostructures that are chemically and structurally compatible with silicon; GaN is not!

We have found two special members of the class of chalcogenide compounds (compounds out of Group VI that typically contain S, Se, or Te but not oxygen) that can be stabilized both structurally and chemically on silicon: $AgGaS_2$ and $CuGaS_2$ with indium substitutions on gallium sites to tune the band gaps. The structural matching (lattice parameter and symmetry) uniquely takes advantage of epitaxial stabilization of the CuAu and chalcopyrite polymorphs of the chalcogenide systems. The epitaxial stabilization energy is a significant energy driver for a phase-pure approach towards discriminating against competing polymorphs and defects that are responsible for the unacceptably low quantum efficiency for GaN-based systems. Our experimental approach is based on molecular beam epitaxy (MBE) growth methods and a model set of direct, wide-bandgap sulfur-based chalcogenides (I-III-VI2). As model systems they have tunable bandgaps, and two polymorphs of their basic zinc-blende structure exist: chalcopyrite and CuAu. The special feature of these model chalcogenides occurs in their CuAu structure ordering. This structure ordering gives I-III cation separation along the c-axis that manifests a modulation in local dielectric behavior in the growth direction. This cation separation can be used to modulate and screen charge at a growing surface during thin-film synthesis. A schematic of the structure and its heteroepitaxy on silicon (001) is shown in Fig. 1.

Heteroepitaxy of these compounds on the cubic silicon surface gives us two attributes: a crystal substrate that uniquely presents a standardized surface perfection for thin-film growth and an electrical platform on which to fabricate p-n junctions for electrical property measurements like doping, band offsets, and system Fermi level characterization. The structural matching (lattice parameter and symmetry) uniquely takes advantage of epitaxial stabilization of the CuAu and chalcopyrite polymorphs of the chalcogenide systems ( Fig. 2). We will discuss this in more detail in what follows, but the epitaxial stabilization energy is of the order 100 meV/4 atoms with these compounds, substantially greater than the kT of ~60 meV/4 atoms at their growth temperatures (Janotti 2001). This gives us the energy driver for a phase-pure approach that discriminates against competing polymorphs and defects that we will show to be responsible for the doping level limits in III-V and II-VI-based wide bandgap photovoltaics.

The major challenges that we face in obtaining these direct gap chalcogenides are phase-pure synthesis. The phase-pure synthesis is where strain stabilization provides the real breakthrough (Zhao 2005). Many of the compound semiconductors, GaN included, are found in nature in multiple polymorphs (variants of a basic structure type). The polymorphs develop in these covalently bonded materials basically because III-V's,

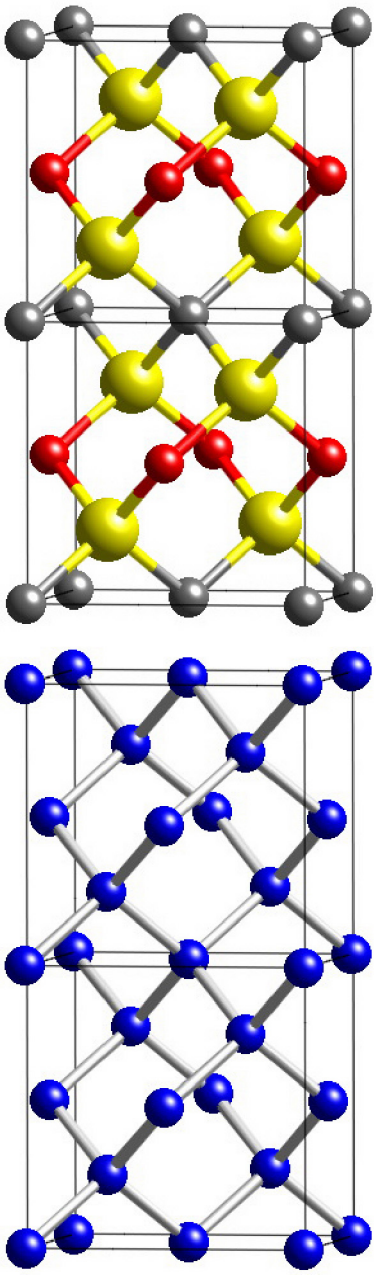

*Fig. 1. Heteoepitaxy for the Cu-Au phase of $AgGaS_2$ on (001) silicon. Yellow is sulfur, red is galium, and gray is silver. The underlying silicon unit cell is in blue.*

II-VI's or other combinations use multiple-valence-state atoms to account for the 4 electrons per atom that they mimic in the elemental Group IV semiconductors. The multiple valence states, due to the directional nature of the covalent bond, give rise to anisotropy in the bonding and drive order/disorder reactions. The order/disorder yields two polymorphs found in the chalcogenides as the chalcopyrite (CH) structure and the CuAu (CA) structure. The CA polymorph is the direct gap structure, and strain, or epitaxial stabilization of the CA structure on silicon, provides the layer-sequenced dielectric that we require for modulation of surface charge that in turn will enable the Fermi level pinning to be systematically shifted. Namely, the epitaxial constraint can be used to modulate the cation charge at a growing semiconductor surface. The energetics of this process for $AgGaS_2$ are illustrated in Fig. 2. As seen in this figure, the character and strain influence of the substrate comes through clearly. The energy of the system can be lowered and/or modulated at the surface with the silicon lattice constraint (strain stabilization); this will allow us to tune the conduction and valence bands relative to the system Fermi level. Layer sequencing in the case with indium substitution for instance is virtually assured; we expect a $\Delta E$ difference between the two polymorphs of 100 meV/4 atoms at the growth temperature. The thermal energy available for destabilization to the CH phase is only 60 meV/4 atoms. This, along with the symmetry constraint, gives a system that will lock into surface or interface phase modulation and provide tunable p-n junction architecture.

## Results and Discussion

There are two critical parts of the heteroepitaxy problem that we investigated. First, a molecular beam epitaxy (MBE) method of layer-sequencing along the [001] direction of the CuAu structured–AgGaS compound was developed. Second, we identified and solved the thermodynamic problem of interface phase stability for the sulfide/silicon system.

The first phase of our work has been to design and construct a sulfur-specific MBE machine to address these critical growth issues. Constructing this system is now complete but this task, particularly the sulfur delivery system, has dominated our experimental effort. The coupling of these two tasks can be understood by reference to Fig. 1.

As shown in Fig. 1, the heteroepitaxy for the chalcogenides on silicon, separates the silver (I) from the gallium (III) in I-III-VI2 compound. This results in charge neutrality modulation along the growth direction; the monovalent silver bonds in first sulfur layer and trivalent gallium bonds to the sulfur in the second layer. This charge separation sets up a layer-sequenced dipole whose magnitude is on the order of an eV (McKee 2003). As the semiconductor grows, however, the sign of this dipole changes, requiring a layer-by-layer modulation of the sulfur arrival rate and hence sulfur surface coverage. We accomplish this through the use of a specially designed sulfur source shown in Fig. 3.

This source controls the molecular weight of the sulfur impinging on the surface by heating the sulfur vapor at temperatures up to 2000°C (Rau 1973). The arrival rate of the sulfur is controlled by the temperature of the sulfur source ranging from 100 to 200°C and by a heated,

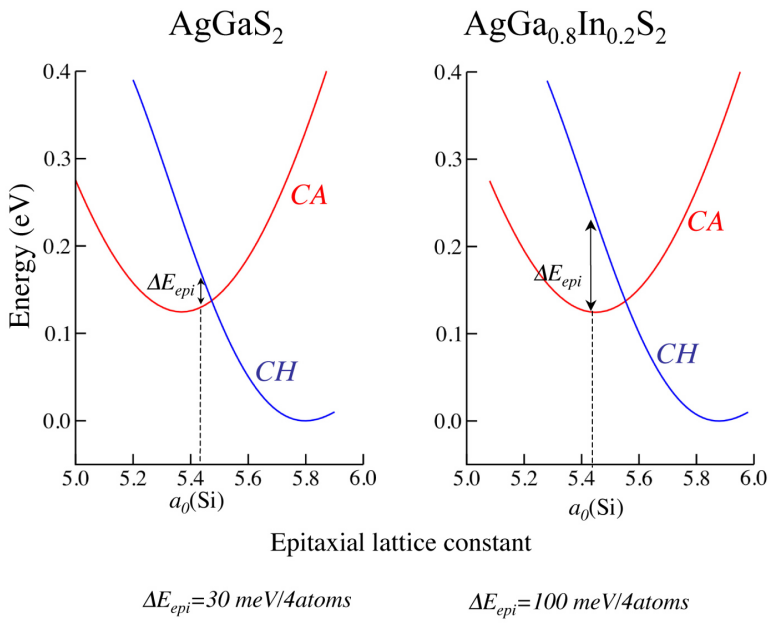


*Fig. 2. Epitaxy stabilization for the $AgGaS_2$ system. The energy gain $\Delta E_{epi}$ for the CA phase at the silicon lattice parameter, 5.43Å, is itself tunable as shown in the right panel with In addition on the Ga site.*

## References


DOE Office of Energy Efficiency and Renewable Energy. 2003. Press Release, November 2003; http://www.netl.doe.gov/ssl.

Janotti, A., S. H. Wei, S. B. Zhang, and S. Kurtz. 2001. "Structural and electronic properties of ZnGeAs2," *Phys. Rev. B* **6319**(19), art. no.-195210.

McKee, R. A., F. J. Walker, M. Buongiorno-Nardelli, W. A. Shelton, and G. M. Stocks. 2003. "The interface phase and the Schottky barrier for a crystalline dielectric on silicon," *Science* **300**(5626), 1726–1730.

Rau, H., T. R. N. Kutty, and J. R. F. Guedes-De-Carvalho. 1973. "Thermodynamics of sulfur vapor," *J. Chem. Thermodynamics* **5**, 833–844.

Zhao, Y. J. and A. Zunger. 2005. "Zinc-blende half-metallic ferromagnets are rarely stabilized by coherent epitaxy," *Phys. Rev. B* **71**(13), 132403.


mechanical valve. The output of this source can be cycled with the layer sequencing of the structure on the 0.1 to 1 monolayer rate. We can go from a sulfur-limited insulator surface to sulfur-flooded, metal surface and couple to the electrical structure of the desired surface phase. This sulfur delivery system and the growth precedure are the final outcomes of the funding used in this project and are a major step towards perfecting these materials. Follow-on funding from DOE-BES will be used to grow these compounds.

## Benefits to the DOE

DOE's Building Technologies Program (DOE 2003) has a stated goal of 50% energy conservation in electric lighting by 2010. This is a very aggressive objective. Our proposal is a silicon-integrated circuit technology, and just as the revolution that integrated circuits are to vacuum tubes, this approach to lighting replacement can be the same. This sulfides-on-silicon LED approach is the enabler for SSL and DOE's goal.

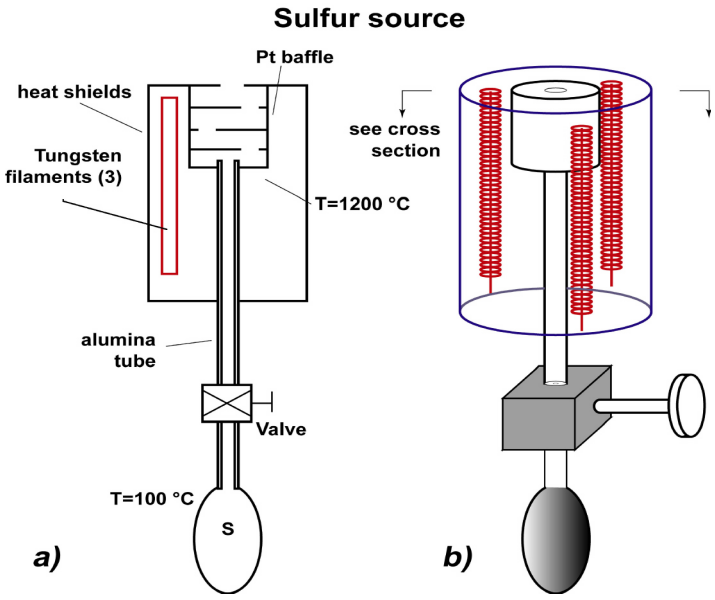


*Fig. 3. Modulated rate and species sulfur source. (a) Cross section of a sketch of the sulfur source. (b) Elements of the source consist of the solid sulfur, S, heated to temperatures between 100 and 200°C. The sulfur temperature and the metering action of the mechanical valve dynamically controls the arrival rate of sulfur. Before the sulfur can react with the metals to form the semiconductor, it must first pass through a platinum baffle heated to 1200°C in a resistively heated furnace in order to be cracked from high to low molecular weight.*

# Development of New Nanoparticle-Strengthened Ferritic and Martensitic Steels by Thermomechanical Treatment

R. L. Klueh[1] and N. Hashimoto[2]
[1]*Metals and Ceramics Division*
[2]*University of Tennessee*

Because of their excellent thermal properties, martensitic steels are preferred structural materials for elevated-temperature applications, such as fossil-fired, nuclear fission, and nuclear fusion power plants. Their use is limited by strengtn to 620ºC, and plant efficiency could be improved by operation at 650–700ºC. The objective of this project was to develop a thermo-mechanical treatment (TMT) for existing nitrogen-containing commercial steels and develop new steel compositions specifically for such a TMT that would increase the strength for use at 650–700ºC and higher. Based on the science of precipitate strengthening, a TMT was developed that increased strength at 700ºC of commercial steels and new steels designed for the TMT by up to 135 and 200% greater, respectively, than the commercial steels after a conventional heat treatment. The TMT increased strength by producing a fine distribution of nitrogen-containing precipitates in the steel matrix that were up to eight times smaller at a number density of up to four orders of magnitude greater than are present in commercial steels after a conventional heat treatment.

## Introduction

Ferritic/martensitic steels are the choice for elevated-temperature fossil-fired power plants and for several future fission nuclear reactor designs, and at present they are the only viable structural material for future fusion power plants (Masuyama 1999; Klueh 2005). A major shortcoming is high-temperature strength, which places a limit on maximum service temperature. Since higher temperatures are required for increased plant efficiency, new steels are required if the advantages of steels are to be maintained. This has led to work to develop commercial ferritic and martensitic steels with improved strength (Foldyana et al. 2001) and oxide dispersion–strengthened (ODS) steels, which are strengthened by small oxide particles (Ukai et al. 1997). However, they are produced by complicated and expensive mechanical-alloying, powder-metallurgy techniques.

The objective of this project was to develop an alternative to ODS steels by producing dispersion-strengthened steels using simpler and cheaper conventional processing (i.e., melting, casting, hot working, cold working, etc.). Based on the science of dispersion strengthening (the need for large numbers of small particles in the steel matrix) and thermodynamic modeling to choose optimum compositions, a thermomechanical treatment (TMT) was developed that increased the 0.2% yield stress of commercial nitrogen-containing 9 and 12% Cr martensitic steels with a conventional heat treatment by over 135% at 700ºC. Steels designed specifically for the TMT have yield stresses at 700ºC up to 200% greater than the commercial steels and as good as the strength of one of the strongest experimental ODS steels.

## Technical Approach

Standard 9–12% Cr transformable ferritic/martensitic steels, which could be replaced by the new steels, are typically used in the normalized-and-tempered or quenched-and-tempered condition. These heat treatments involve austenitizing by heating above the temperature where the body-centered cubic ferrite phase transforms into the face-centered cubic austenite phase. The normalizing treatment involves air cooling from the austenitization temperature; quenching involves cooling in a liquid medium. Both processes produce martensite (a body-centered tetragonal crystal structure) nucleated at the austenite grain boundaries. Because martensite is strong but brittle, it is tempered at a temperature below where ferrite transforms to austenite; a tempered martensite microstructure consists of body-centered cubic ferrite containing a distribution of precipitates.

Tempered martensite in commercial nitrogen-containing steel such as modified 9Cr-1Mo (nominal composition Fe-9.0Cr-1.0Mo-0.20V-0.08Nb-0.05N-0.10C; compositions in weight percent) consists of martensite laths (elongated subgrains ≈ 0.25–0.5 μm wide) with precipitate particles on prior-austenite grain boundaries, on lath boundaries, and in the matrix. Dominant precipitates are "large" (60–200 nm) $M_{23}C_6$ particles (M is rich in chromium with lesser amounts of other elements, i.e., Fe, Mo, etc.) located mainly on lath boundaries and prior-austenite grain boundaries along with smaller (20–80 nm) MX precipitates in the matrix at a lower number density. The M is vanadium- or niobium-rich and X is nitrogen and carbon; for vanadium-rich MX, X is high in nitrogen (nitride), and niobium-rich MX is a

carbide or carbonitride. For modified 9Cr-1Mo, average particle size and number density of $M_{23}C_6$ are typically 130–150 nm and 3–6 × $10^{19}$ $m^{-3}$, respectively, and the MX about 30–40 nm and 7–8 × $10^{18}$ $m^{-3}$, respectively (Hashimoto and Klueh 2002). It is the smaller MX particles that provide precipitate strengthening, but because of their relatively small number and large size in the modified 9Cr-1Mo, the strengthening effect is small.

A new TMT was developed that was designed to produce a high number density of nano-sized high-nitrogen precipitate particles in the matrix of nitrogen-containing steels. The TMT conditions were determined from calculations using the computational thermodynamic program JMatPro. Calculations for new steels and for existing commercial nitrogen-containing compositions were carried out to estimate the amounts of stable vanadium and niobium nitrides and carbonitrides that could be formed to produce steels with improved elevated-temperature strength.

The TMT procedure developed involves heating the steel to convert ferrite to austenite and to dissolve existing precipitates, after which the steel is cooled to a hot working temperature of 700–1000ºC. Hot working (e.g., rolling, extruding, etc.) introduces into the matrix a high density of dislocations (line defects) that act as nucleation sites for a fine distribution of MX (vanadium- and niobium-rich nitride and/or carbonitride) precipitates. Following the hot working, the steel is annealed to grow the precipitates to optimum size for hardening, after which the steel is air cooled or quenched to convert the austenite matrix into martensite. If required, the steel is tempered at 700–800ºC to improve ductility and toughness.

## Results and Discussion

For the present experiments, 25.4-mm-thick plates were hot rolled. After a modified 9Cr-1Mo steel plate was processed by the new TMTs, microstructures were dramatically different from normalized-and-tempered steel. The MX particle size was up to four times smaller (7–8 nm) and number density up to three orders of magnitude greater (2–9 × $10^{21}m^{-3}$), depending on the TMT. Transmission electron microscopy (TEM) and atom probe tomography were used to estimate precipitate size and number density and verify that the precipitates formed on dislocations. The effect of TMT can be controlled by changing (1) austenitization temperature and time (2) hot-working temperature, (3) amount of reduction by hot-working, and (4) annealing temperature and time.

A commercial 12% Cr steel (HCM12, nominal composition Fe-12.0Cr-2.0W-0.40Mo-1.0Cu-0.30Ni-0.25V-0.05Nb-0.06N-0.10C) was given a TMT at 800ºC. In contrast to modified 9Cr-1Mo steel, no fine precipitates were visible by TEM. However, after tempering 1 h at 750ºC, fine precipitates (average 4.2 nm, 2.4 × $10^{21}m^{-3}$) were detected. Evidently, the higher nitrogen concentrations in HCM12A promoted extremely fine precipitates that were too small to observe by TEM. Tempering coarsened the precipitates to the point they could be detected.

Based on thermodynamic calculations using the JMatPro computer program (Saunders et al. 2001), small (400-g) heats of new compositions were produced to maximize the effect of the TMT. To demonstrate the effect of nitrogen, a TMT was applied to two new steels with nominal composition Fe-9.0Cr-1.0Mo-1.0Ni-0.30V-0.07Nb-0.05C, one with 0.035% N, the other with 0.065% N. For both, average MX precipitate size was smaller and number density greater than for the two commercial steels: about 4.0 nm, 1.0 × $10^{22}$ $m^{-3}$ and 3.3 nm, 7.2 × $10^{22}$ $m^{-3}$ for the 0.035 and 0.065% N, respectively. Lower carbon concentrations of these new steels will result in a decrease in the amount of $M_{23}C_6$ precipitates, which will improve long-time elevated-temperature properties.

The most important properties for the new steels are elevated-temperature tensile and creep strengths. For tensile tests on modified 9Cr-1Mo steel after a TMT (hot-rolled 20% at 750ºC, no temper), the 0.2% yield stress and ultimate tensile strength from room temperature to 800ºC were considerably greater than for the normalized-and-tempered steel, with the difference increasing with increasing test temperature. For tests at 600 and 700ºC, the yield stress of the steel with the TMT was 61 and 88% greater than for the normalized-and-tempered steel. After tempering at 750ºC, the yield stress was about 7 and 69% greater at 600 and 700ºC, respectively. Total elongation of the steel with the TMT was less than that of the normalized-and-tempered steel, but given the normal trade-off of strength and ductility expected in this type of steel, ductility was excellent, with total elongation of 16 and 22% at 600 and 700ºC, respectively, and increasing further after tempering to 24 and 30%.

The 12% Cr steel HCM12A after the 800ºC TMT and 750ºC temper showed a large increase in yield stress relative to normalized-and-tempered HCM12A: 47 and 64% increases occurred at 600 and 700ºC, respectively. The strength of the HCM12A with the TMT plus temper was greater than that of the modified 9Cr-1Mo steel with just a TMT, a reflection of the smaller precipitates at a higher number density in HCM12A. The yield stress from room temperature to 700ºC was greater than that of PM 2000, the strongest commercial ODS steel available.

To demonstrate the excellent strength properties of the new steel compositions developed specifically for the new TMTs, the yield stress from a 400-g heat of a 9Cr-MoNiVNbN with 0.042% N was compared to an experimental ODS steel labeled 12YWT (Fe-12.0Cr-2.5W-0.4Ti-0.25$Y_2O_3$). This ODS steel had superior strength compared with any available commercial ODS

steel. The TMT consisting of hot rolling and annealing the 9Cr-MoNiVNbN produced yield stress values much higher than those of the normalized-and-tempered modified 9Cr-1Mo and HCM12A steels after a TMT. The strengths were comparable to those of the 12YWT up to 700ºC—the highest temperature 9Cr-MoNiVNbN was tested (Fig. 1). Ductility for 9Cr-1MoNiVNbN in the TMT condition was comparable to that of 12YWT ODS.

Finally, a commercial steel (NF616, nominal composition Fe-9Cr-1.8W-0.5Mo-0.20-V-0.05Nb-0.06N-0.07C) was given a TMT at 750ºC. This steel had a higher strength than any of the commercial steels and the small heats of new steels, and the experimental ODS steel (Fig 1).

Creep resistance is the most important mechanical property for elevated-temperature steels. Creep-rupture tests after TMTs were conducted on modified 9Cr-1Mo, HCM12A, and NF616 steels. For a stress of 138 MPa at 650ºC, rupture life for the modified 9Cr-1Mo steel given various TMTs ranged from 2092–3322 h, compared to 27 h for the normalized-and-tempered steel. Even with this large difference in strength, however, total elongation after the TMT was excellent at 21%. For HCM12A, the difference between the TMT and normalized-and-tempered steels was 2860 and 247 h, respectively, and for NF616, it was 8020 and 770 h, respectively.

Equipment was not available at ORNL to obtain nitrogen concentrations (≈0.08%N) that were calculated to give optimum strength. When the desired concentration is obtained, higher tensile and creep strengths will be possible. Since no large ingots of the new steel compositions could be produced, no creep tests were conducted on new steels.

The TEM, atom probe, and mechanical properties results indicate clearly that thermo-mechanical treatments can be devised to produce a dense dispersion of nano-scale MX precipitates in vanadium- and nitrogen-containing steels. The new TMT involves three distinct steps, each of which involves a range of experimental parameters that can be optimized to produce a favorable precipitate microstructure for high elevated-temperature strength. Along with optimization of the new TMT process, steel compositions that fully exploit the TMT have been developed. The initial efforts on the small heats produced for the new processing procedure indicated that it should be possible to develop compositions that will be significant improvements over the commercial steels with a conventional normalizing-and-tempering treatment or with the new TMT.

The high number density of precipitates produced by the new TMT using conventional processing methods is similar to particle number densities in ODS steels produced by the much more complicated and expensive powder-metallurgy and mechanical-alloying procedures. Dispersion strengthening by these nitrogen-rich MX precipitates should allow the steels to be used to

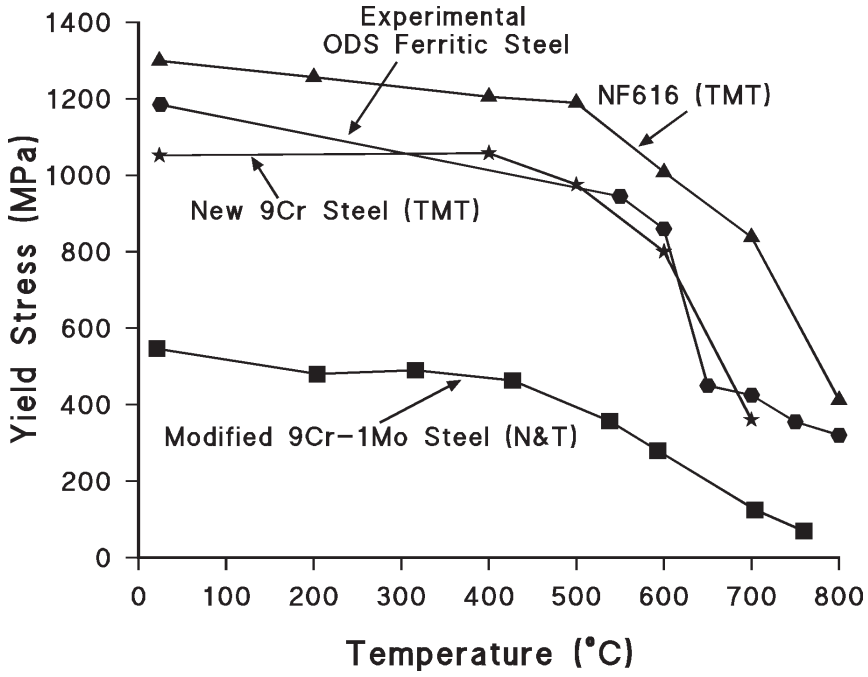


*Fig. 1. The 0.2% yield stress as a function of test temperature for a new 9Cr steel and the commercial 9Cr steel NF616 compared to the properties of an experimental ODS steel and the commercial modified 9Cr-1Mo steel after a conventional normalize-and-temper treatment.*

temperatures at 650–700ºC and higher, which would be a significant improvement over the upper-use temperature of ≈620ºC for the best commercial ferritic and martensitic steels presently available. Limitations will probably depend on corrosion resistance, which will depend on chromium concentration.

Increased operating temperatures for steel components translate directly into increased efficiencies, which for fossil-fired plants mean a more economical plant and reduced $CO_2$ and other plant emissions. Higher strength translates to thinner sections in the plant structure, meaning less steel is required, which reduces harmful emissions associated with steel production.

## Benefits

The need for greater efficiency in fossil-fired power plants requires higher operating temperatures than present plants. Because of their excellent thermal properties, the preferred structural materials are ferritic steels. Unfortunately, steels presently available have upper-temperature limits of ≈620ºC, which means materials with less favorable thermal properties will have to be used. In a similar vein, new designs for nuclear fission power plants that operate at higher temperatures than previous reactors are being planned, and steels available at present will be of limited use in many of the designs. A similar scenario applies to future fusion power plants. The new steels with their higher strength at considerably higher operating temperatures than available commercial steels would allow the favorable properties of ferritic steels to be applied at higher operating temperatures, thus improving operational efficiency. Thus the new steels should be of interest in the DOE Fossil Energy, Nuclear Energy Science and Technology, and Fusion Energy Science Programs.

In addition, Rolls Royce Ltd., Derby, UK, has expressed interest in using the material for manufacturing the shaft of the aircraft turbine engines they produce. Discussions are in progress to pursue new steels for this application.

## References


Foldyna, V., Z. Kubon, V. Vodárek, and J. Purmenský. 2001. "How to Improve Creep Rupture Strength of Advanced Chromium Steels," pp. 89–98 in *Proceedings of the 3rd EPRI Conference on Advanced Materials Technology for Fossil Plants*, Eds. R. Viswanathan, W. T. Bakker, and J. D. Parker.

Hashimoto, N. and R. L. Klueh. 2002. "Microstructural Evolution of Nickel-Doped 9Cr Steels Irradiated in HFIR," *J. Nucl. Mater.* **305**, 153.

Klueh, R. L. 2005. "Elevated-Temperature Ferritic and Martensitic Steels and Their Application to Future Nuclear Reactors," *International Materials Review* **50**, 287–311.

Masuyama, F. 1999. "New developments in steels for power generation boilers," pp. 33–48 in *Advanced Heat Resistant Steel for Power Generation*, Eds. R. Viswanathan and J. Nutting.

Saunders N., A. P. Miodownik, and J-Ph. Schillé. 2001. "Computer Modeling of Materials Properties," pp. 185–197 in *Proceedings of the Symposium on Material Design Approach and Experience*, Eds. J. –C. Zhoa et al.

Ukai, S., T. Nishida, H. Okada, T. Okuda, M. Fujiwara, and K. Asabe. 1997. "Development of Oxide Dispersion Strengthened Ferritic Steels for FBR Core Application I: Improvement of Mechanical Properties by Recrystallization Processing," *J. Nucl. Sci. & Tech.* **34**, 256–263.

# Chemical Vapor Deposition–Based Combinatorial Chemistry for New Hydrogen Storage Materials

T. M. Besmann,[1] N. S. Kulkarni,[1] J. J. Henry,[1] and R. J. Kasica[2]
[1]*Metals and Ceramics Division*
[2]*Engineering Science and Technology Division*

This project was initiated to explore the feasibility of chemical vapor deposition (CVD) for combinatorial studies in Mg-Al systems for the purpose of hydrogen storage. In the past, conventional metalorganic chemical vapor deposition (MOCVD)–based approaches for Mg deposition have been unsuccessful. The problems associated with MOCVD of Mg were overcome with the successful design, construction, and implementation of a novel combinatorial plasma-enhanced chemical vapor deposition (PE-MOCVD) system. A special feature of the system to enable continuously varying alloy compositions (e.g., Mg-Al) in the deposited thick films was also designed. To date, our present efforts have successfully demonstrated for the very first time deposition of Mg thin films by PE-MOCVD at 150ºC. At the end of FY 2005, experiments for depositing Al by PE-MOCVD were in progress, following which combinatorial films of Mg-Al were to be attempted. The successful demonstration of PE-MOCVD of Mg—a very critical element for hydrogen storage applications—will provide a suitable platform for the discovery of potential Mg-based hydrogen storage materials using combinatorial deposition and screening strategies. This work sets the stage for exploring applications of Mg-based PE-MOCVD coatings in other areas, such as coatings of anti-reflective $MgF_2$ and $MgB_2$-based high critical temperature superconductors for both of which CVD has never been demonstrated in the past.

## Introduction

High-throughout combinatorial deposition and screening approaches (MRS Bulletin 2002) have shown great potential for materials discovery in a variety of applications. Current combinatorial approaches for solid-state crystalline materials based on sputtering or electron beam evaporation are often unsuitable since equilibrium phases and compositions are difficult to achieve in the deposited thin films due to kinetic barriers, and the thicknesses are too low (in nm) to provide reliable information for screening potential hydrogen storage compositions. The proposed project was designed to demonstrate the feasibility of utilizing metalorganic chemical vapor deposition (MOCVD) for the deposition of combinatorial films (tens of μm) in a model metal alloy system (Mg-Al) followed by a screening of the vast array of compositions within such films for potential hydrogen storage materials with the aid of various characterization tools available at ORNL. Conventional MOCVD of Mg has never been possible due to the fact that at the high temperatures (>700ºC) needed for dissociation of Mg metalorganic precursors [e.g., Bis(cyclopentadienyl)Mg] and the subsequent deposition on a heated substrate, the Mg vapor pressures are too high to allow deposition. In order to use lower temperatures for Mg deposition and at the same time enable dissociation of the Mg precursor, a plasma-enhanced chemical vapor deposition (PE-MOCVD) system was required. Such a PE-MOCVD system was successfully constructed and made operational. Our present efforts have successfully demonstrated for the very first time deposition of Mg thin films using PE-MOCVD at 150ºC. A combinatorial deposition capability for depositing continuously varying compositions in the Mg-Al system was also integrated within the PE-MOCVD system. At the end of FY 2005, experiments for depositing Al by PE-MOCVD were in progress, following which combinatorial films of Mg-Al will be attempted.

## Technical Approach

The PECVD system was designed using a stainless steel 6-way vacuum cross. A cutaway of this design is shown in Fig. 1. A dc plasma system in which the plasma of a suitable gas (e.g., hydrogen) is generated between two electrodes was adopted. The dc power line for the cathode was inserted from the top port, while the anode, which also serves as the substrate, was positioned at a fixed distance from the cathode. The gap between the cathode and anode was controlled with the aid of a motion controller connected to the anode through the bottom port. Power supply to the anode heater as well as the thermocouple leads were inserted from the bottom port. A convection gauge to measure the pressure within the reactor was also included within this port assembly. The side port on the left was used for loading/unloading of a sample substrate (Si (100) wafer) on the anode. A viewing window

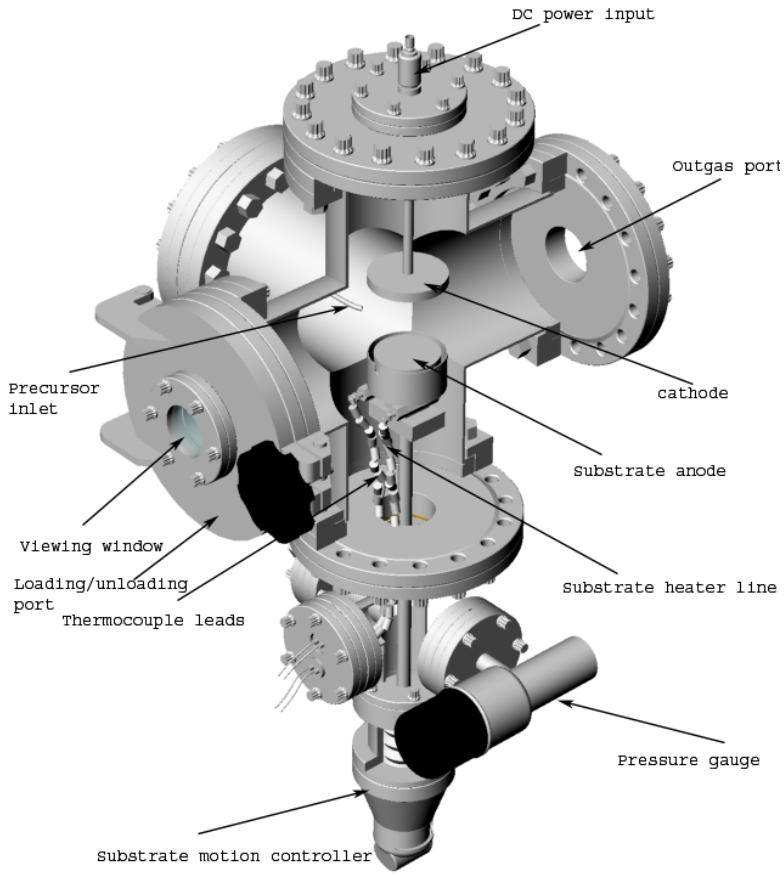


*Fig. 1. Plasma-enhanced chemical vapor deposition reactor constructed in this work for combinatorial deposition of Mg-Al films.*

permitted observation of the progress of the PE-MOCVD process within the reactor. The front and back ports were utilized for feeding the precursor gases. The inlet ports that were used to feed the precursor gases on the heated substrate were of 1/8-in. inner diameter (0.003175 m) and were positioned at different positions over the anode so as to enable combinatorial mixing and deposition. The exhaust stream was extracted through the right port. The pressure within the reactor was controlled by adjusting the inlet and outlet gas flows. A cold trap was used to collect the unreacted precursor in the exhaust stream. Digitally controlled mass flow controllers were used to bubble a controlled amount of carrier gas (hydrogen) through the precursors that were contained in stainless steel cylinders. The vapor pressure of the precursor gases over the precursors (solid or liquid forms) in the cylinders was temperature controlled, since the vapor pressure-temperature relationship for the precursors used in this study were known a priori. Since it was desired to establish a hydrogen plasma between the two electrodes prior to the introduction of the precursor gas, an excess hydrogen line was included through the bottom port.This same line was also used to flow a halocarbon gas ($CF_4$) to clean the plasma chamber prior to the start of an experiment. Ultra-pure hydrogen and argon gas was used throughout the course of this work. Gas purifiers connected to the cylinders were used to further reduce moisture levels.

The vapor pressure-temperature relationship for the Mg precursor Bis(cyclopentadienyl)magnesium or $(C_2H_5)_2Mg$ was first established using a baratron vapor pressure gauge. A temperature of approximately 40ºC was found to be adequate for providing a vapor pressure in the range of 200–300 mTorr. Thermodynamic calculations were carried out using the software FactSage™ to determine the appropriate conditions (temperature, reactor pressure, and compositions) suitable for deposition of Mg using the above-mentioned precursor. It was found that, under equilibrium conditions, Mg deposition was favored at temperatures between 150 and 300ºC for pressures greater than 1 Torr (131.6 Pa) with a Mg precursor composition that was diluted by ten times with hydrogen. At temperatures lower than 150ºC, the formation of magnesium hydride ($MgH_2$) was favored, while at temperatures greater than 300ºC, carbon is the likely product. This simple calculation confirmed the reason for the failure of Mg deposition using conventional high-temperature CVD (i.e., the formation of elemental carbon and vaporization of Mg).

## Results and Discussion

Initial Mg deposition experiments resulted in the formation of a bluish colored film with interference fringes corresponding to film thickness variations across the Si wafer. X-ray diffraction and Auger analysis confirmed that this film was in fact MgO. More rigorous leak detection was subsequently performed using He, and the cleanliness of the system was improved using annealed Cu gaskets for ensuring airtight vacuum fittings. The deposition experiments were repeated. The deposited Mg films now had a grayish-black color with interference fringes again visible. The quality of Mg films was confirmed using X-ray diffraction and Auger analysis. The successful Mg experiments performed had the following process parameters: pressure: 1100–1300 mTorr; temperature of substrate: 150ºC; DC plasma power: 100 W; precursor temperature: 40ºC; $H_2$ bubbled through precursor: 5 sccm; $H_2$ for generating plasma: 50 sccm; time of deposition: 1 h.

The demonstration of Mg deposition was followed by experiments devoted to establishing the process parameters for the deposition of Al using the liquid precursor trimethyl aluminum (TMA). Once these parameters have been established, combinatorial deposition of both Mg and Al was to be carried out. Compositions within these films could then be analyzed for hydrogen storage properties. Time and resources were insufficient to demonstrate Al and Mg-Al deposition.

## Benefits

One of the major objectives of the DOE Hydrogen Fuel Cell Initiative is to develop suitable hydrogen storage materials that meet the desired gravimetric storage and release requirements for fuel-cell powered vehicles. Achievement of this objective will be aided by high throughput experiments for discovering novel hydrogen storage compositions. The present seed project is a step in this direction. We have designed a PE-MOCVD system capable of combinatorial deposition and established that it can be used for deposition of Mg films, a feat never before accomplished. Additional combinatorial films based on Mg and other light elements can similarly be deposited using this system. These films can then be screened for their hydrogen storage properties using some of the techniques suggested previously (Olk et al. 2003). The successful deposition of Mg at low temperatures opens the possibility of depositing a coating of the superconductor $MgB_2$, and a low refractive index, anti-reflecting coating of $MgF_2$, both of which have never been successful.

The DOE EERE Program on Hydrogen Storage is expected to announce a call for proposals in the near future for which the present work, if developed further, could be of potential interest. The likelihood of extending the current work to target support from DARPA, which has previously expressed interest in multi-functional coatings and coatings for electronic and optical applications, is a strong possibility.

## References

Review articles on Combinatorial Materials Science. April 2002. *MRS Bull.* **27**(4).

Olk, C. H., G. G. Tibbetts, D. Simon, and J. J. Moleski,. 2003. "Combinatorial preparation and infrared screening of hydrogen sorbing metal alloys," *J. App. Phy*. **94**, 720 (2003).

# High-Order Ferroelectric Nanolithography: A Key to Near-Atomic-Density Information Storage and Patterning

A. P. Baddorf,[1] S. V. Kalinin,[1] H. N. Lee,[1] H. M. Christen,[1] A. L. Gruverman,[2]
E. Karapetian,[3] M. Kachanov,[3] and V. Meunier[4]
[1]*Condensed Matter Sciences Division*
[2]*North Carolina State University*
[3]*Tufts University*
[4]*Computer Sciences and Mathematics Division*

The continuing race for miniaturization of electronic components is a hallmark of our time, but costs will soon prohibit extension of current semiconductor industry approaches. This project has focused on a new paradigm: ultrahigh resolution recording and nanopatterning based on the local switching in ferroelectric materials using scanning probe microscopy (SPM) techniques. Progress was made in four directions, including growth of ferroelectric thin films, development of tools for evaluation, tip-based domain creation and switching, and theoretical understanding of the processes and dynamics. With pulsed laser deposition, we have synthesized nearly perfect epitaxial lead zirconate titanate (PZT) films, never before accomplished and thought by many to be impossible. We have developed a new SPM tool, switching spectroscopy mapping piezoresponse force microscopy, and applied SPM to write and read domains on several ferroelectric materials, including lithium niobate, polyvinylidene fluoride, and PZT and have achieved a record 30-nm domain size, corresponding to 300 Gb/in. Finally, we have published a new analysis of the thermodynamics of local switching and the kinetics of domain growth in ferroelectrics.

## Introduction

For over 50 years, ferroelectrics has been considered promising for information technology applications. The unique feature of ferroelectric materials is that the application of an electric field or mechanical stress can switch the polarization between the equivalent orientations; however, in the absence of external influences the polarization state exists indefinitely. This has led to non-volatile ferroelectric random access memories (FeRAMs), and in the last 5 years, the progress in preparation of ferroelectric thin films has rendered this technology commercially viable, for example with Motorola 64 MB non-volatile memories.

The crucial advantage of ferroelectrics is an extremely small domain wall width (~0.5 nm) which is orders of magnitude smaller than in ferromagnetics (10–100 nm) and which can allow higher density storage. Estimates suggest that ferroelectric recording can achieve a storage density two orders of magnitude higher than magnetic recording, with ~300-Tbit/in.$^2$ storage density at ~1-nm feature size!

A perspective route for ultrahigh density ferroelectric storage is based on scanning probe technology (Shin et al. 2002). Application of a high voltage to the probe tip allows local polarization switching, providing an approach to engineer and write ferroelectric domain structures at the nanoscale. At the same time, application of a periodic bias to the conductive tip in contact with a ferroelectric surface results in a periodic surface displacement due to the inverse piezoelectric effect, which provides a read-out scheme, known as piezoresponse force microscopy (PFM).

## Technical Approach

### *A. Film Preparation*

One of the most promising classes of ferroelectric materials is based on lead titanate ($PbTiO_3$) and lead zirconate titanate solid solutions (PZT). Because of their strong ferroelectric correlations, $PbTiO_3$ epitaxial thin films were shown to retain ferroelectric properties down to a 3-unit cell thickness (Streiffer et al. 2002). Combined with the high Curie temperature and the associated stability of induced-domain patterns as well as a strong electromechanical coupling, this makes $PbTiO_3$ or PZT a promising candidate for atomic density ferroelectroelastic storage. However, high lateral resolution domain patterning requires film qualities greater than previously achieved.

We have used pulsed laser deposition (PLD) and optimized the growth of epitaxial PZT films with various thicknesses on conducting $SrRuO_3$ on $SrTiO_3$ substrates. We have focused on the PZT (0/20/80) composition, since it has an in-plane lattice parameter of 0.393 nm, which is closely lattice-matched to the $SrTiO_3$ substrate (0.391 nm).

### *B. Domain Reading and Writing*

Piezoresponse force microscopy (PFM) is an application of scanning probe microscopy to electromechanical response in surfaces and thin films. Application of a periodic bias to a conductive tip in contact with a ferroelectric surface results in a periodic surface displacement due to the inverse piezoelectric effect. Mapping of the amplitude and phase of the displacement provides images of ferroelectric domain structures with ~3- to 10-nm resolution. This technique has been shown to be an ideal tool to create nanoscale domains by application of a voltage sufficient to induce local polarization reversal. In contrast to a macroscopic ferroelectric capacitor where a number of domains nucleate at the electrodes, the electric field in PFM is concentrated directly below the tip and results in nucleation of a single domain at the tip-surface junction. Domain nucleation can be controlled by varying the tip voltage, voltage duration, tip-surface separation (or force), and tip geometry. This approach can potentially be used for high-density ferroelectric storage.

## Results and Discussion

### *A. Film Preparation*

The film quality of lead-containing compounds, including PZT, is sensitive to growth conditions due to volatility of lead oxides (PbO). Therefore, growing high-quality PZT films is not trivial and requires an extensive optimization process, which includes varying the growth parameters such as the temperature, oxygen pressure, laser fluence, and laser repetition rate. By doing so, we were able to grow ultra-high-quality PZT epitaxial films with the *c*-axis aligned to the substrate normal without *a*-type domains on $SrRuO_3$/(001) $SrTiO_3$ as confirmed with four-circle X-ray diffraction. X-ray rocking curve scans of the 001 peak also confirmed the high crystallinity with a FWHM $\approx 0.03°$, comparable with that of the $SrTiO_3$ substrate. The surface of the films was very smooth with the RMS roughness ~0.4 nm over the scanned area. These films therefore meet the requirement of the present SPM work.

### *B. SPM Characterization Tools*

Applications of ferroelectrics for devices such as non-volatile memories and storage devices necessitate studies of domain structure and polarization switching phenomena on the nanoscale. Previous studies have been limited to qualitative observations; that is, no quantitative measures of local switching behavior have been obtained due to inherent limitations of PFM in the imaging mode. We have developed a new approach, named switching spectroscopy mapping piezoresponse force microscopy (SS-PFM), to address quantitatively the local switching characteristics of ferroelectric materials. To implement SS-PFM, an atomic force microscope (AFM) was configured similar to the force volume mode. The tip approaches the surface vertically in contact mode (force feedback) until the deflection set-point is achieved. Then hysteresis data is acquired with the tip fixed in space. After acquisition, the tip is moved to the next location and continued until a mesh of evenly spaced $M \times N$ points is acquired. The hysteresis curves are collected at each point as a 3D data array. The data is analyzed in real time to yield parameters describing local switching processes such as the positive and negative coercive biases, imprint voltage, saturation response, and work of switching (Jess et al. in press).

### *C. Ferroelectric Domain Switching*

Domain writing, reading, and spectroscopy was applied to several promising ferroelectric materials in search of high-quality and high-resolution response and retention.

The kinetics of sidewise domain growth in an inhomogeneous electric field have been investigated in stoichiometric $LiNbO_3$ single crystals by measuring the lateral domain size as a function of the voltage pulse magnitude and duration using PFM (Rodriguez 2005). The domain size increased linearly with the voltage magnitude, suggesting that the domain size is kinetically limited in a wide range of pulse magnitudes and durations. In spite of that, the written domains exhibited strong retention behavior.Domain kinetics could be described as an activation process by calculating the field distribution using the charged sphere model under the assumption of an exponential field dependence of the wall velocity. The activation energy required to switch domains was found to be a function of the external field.

Our best resolution writing was produced on thin films of lead zirconate titanate (PZT). Success was a product of the excellent ferroelectric properties of PZT, making it the leading material for commercial application, and the superior quality films synthesized for this project (described above).

Resolution studies were conducted by patterning a square grid with decreasing sizes as shown in the upper left panel of Fig. 1. Software for the PFM was developed to interpret such an image as a spatial map where black means to write with a negative voltage (polarization into the film) and white means to write with a positive voltage (polarization out of the film). The topography of the film, shown in the center panel on the left of the figure, remains flat. However, the film polarization imaged in the lower left reproduces the array of squares. After optimization of writing parameters, including tip voltage, tip-sample separation, and writing speed, a resolution below 30 nm was demonstrated. More complex information can also be written, as shown by the examples on the right.

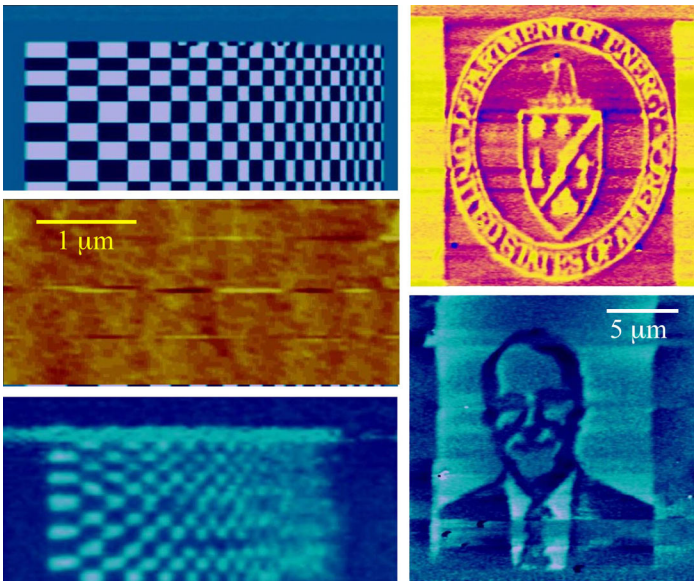


*Fig. 1. Resolution in ferroelectric domain patterning using scanning probe microscopy is demonstrated on a PZT film. On the left is the pattern of the applied voltage (top), the flat topography (middle), and the resulting ferroelectric domains (bottom). On the right are two examples of more complex images storage with nanometer-scale resolution.*

### *D. Theoretical Modeling and Interpretation*

Remarkably, a rigorous definition for lateral resolution has not existed for piezoresponse force microscopy even 10 years after its invention. Applications necessitate quantitative assessment of the ferroelectric domain structure, which can only be accomplished when PFM image formation mechanism is well characterized, allowing for resolution and contrast transfer mechanism to be defined. We have, for the first time, analyzed image formation mechanisms in PFM and demonstrated that experimental images under appropriate conditions can be represented as a convolution between instrument function, which can be determined via calibration, and ideal image reflecting materials properties. Unambiguous definitions for image resolution and minimum observable feature size were derived and compared with experimental images under different imaging conditions. Based on the linearity of the transfer function, an approach for the deconvolution of an ideal PFM image from experimental image has been developed. This contrast transfer function theory provides a quantitative basis for image interpretation and comparison of different instruments in PFM (Kalinin 2005a).

We next analyzed the frequency-dependent dynamic behavior in PFM implemented on a beam-deflection atomic force microscope using a combination of modeling and experimental measurements. The PFM signal comprises contributions from local electrostatic forces acting on the tip, distributed forces acting on the cantilever, and three components of the electromechanical response vector. These interactions result in the bending and torsion of the cantilever, detected as vertical and lateral PFM signals. The relative magnitudes of these contributions depend on geometric parameters of the system, the stiffness and frictional forces of tip-surface junction, and operation frequencies. The dynamic signal formation mechanism in PFM was analyzed and conditions for optimal PFM imaging were formulated.

We have further extended our understanding of nanoscale polarization switching in ferroelectric materials by calculation of the thermodynamics below the probe tip (Kalinin 2005b). Analysis was made in weak and strong indentation limits using exact solutions for electrostatic and electroelastic fields below the tip. This work discovered that the tip-induced domain switching can be mapped onto the Landau theory of phase transitions with domain size as an order parameter. For a point charge interacting with a ferroelectric surface, switching of both first- and second-order type is possible depending on the charge-surface separation. For a realistic tip shape, the domain nucleation process is of the first-order type in charge magnitude and polarization switching occurs only above a critical tip bias. In pure ferroelectric or ferroelastic switching, the domain size is determined by the tip charge or force only and arbitrarily large domains can be created. For higher-order ferroic switching (e.g., ferroelectroelastic), the domain size is limited by the tip-sample contact area, thus allowing precise control of ferroelectric domain size.

## References

Jesse S., A. P. Baddorf, and S. V. Kalinin, "Switching Spectroscopy Mapping Piezoresponse Force Microscopy (SS-PFM) of Ferroelectric Materials" submitted to *Appl. Phys. Lett.*

Kalinin, S. V. et al. 2005a. "Nanoelectromechanics of Polarization Switching in Piezoresponse Force Microscopy." Submitted to *Phys. Rev. Lett.*

Kalinin, S. V. et al. 2005b. "Nanoelectromechanics of polarization switching in piezoresponse force microscopy." *J. Appl. Phys.* **97**, 074305.

Rodriguez, B. J. 2005. "Domain growth kinetics in lithium niobate single crystals studied by piezoresponse force microscopy." *Appl. Phys. Lett.* **86**, 012906.

Shin, H. et al. 2002. "Read/write mechanisms and data storage system using atomic force microscopy and MEMS technology," *Ultramicroscopy* **91**, 103.

Streiffer, S. K. et al. 2002. "Observation of Nanoscale 180° Stripe Domains in Ferroelectric $PbTiO_3$ Thin Films," *Phys. Rev. Lett.* **89**, 067601.

# Pulse Thermal Processing and Characterization of Nanocrystalline Silicon Thin-Films for Photovoltaic Applications

R. D. Ott and M. J. Lance
*Metals and Ceramics Division*

The use of amorphous silicon (*a*-Si) for photovoltaic (PV) applications is growing in an effort to reduce the cost of solar cells. Current generation photovoltaics are based on single-crystal and polycrystalline silicon which yield approximately 15% and 10% efficiencies, respectively, and are costly to manufacture. The efficiencies of *a*-Si are in the range of 5% but with considerably less material and manufacturing costs. Recent interest has been directed toward nanocrystalline and microcrystalline silicon which have the ability to increase efficiencies above *a*-Si. ORNL's high density plasma arc light and a technique called Pulse Thermal Processing (PTP) were utilized to nucleate and grow a nanocrystalline silicon phase within an *a*-Si thin-film. The high-temperature and short-exposure times associated with PTP make it possible to rapidly process functional materials on a broad range of substrates, including polymers, in seconds rather than minutes or hours, dramatically increasing throughput and decreasing thermal budget. Temperatures in the range of 600C to 700ºC are required to nucleate the nanocrystallites utilizing solid phase crystallization. This research project's goal was to show proof of concept of being able to introduce a nanocrystalline phase within the amorphous silicon phase utilizing PTP, and this was accomplished.

## Introduction

Amorphous silicon utilized for photovoltaic, thin-film transistors (TFT) and other microelectronic devices is a mature technology that is economical. However, efficiency-related properties such as mobility are low compared to poly-Si (Schropp 2002). Therefore, there is a need for higher material performance in such devices without significantly increasing the cost (Zhoa 2000, Boyce 2002, Nelson 2003). Poly-Si offers the highest mobility but at a substantial cost penalty; consequently, methods for crystallizing *a*-Si have been heavily investigated using conventional furnace annealing and laser annealing.

Conventional furnace annealing is restricted by the substrate, which is usually a glass and thus limited to temperatures <600ºC (the softening point of most glasses). Also, conventional annealing takes several hours and results in a high thermal budget. Crystallization utilizing an excimer laser takes several minutes to process small areas (~1 $cm^2/s$) and can be costly to operate (Science and Technology Review 1999). However, the utilization of high density plasma arc technology allows crystallization of large areas (~300 $cm^2/s$) rapidly with relatively low operating costs.

Typical laser nanocrystallization grain sizes are equivalent to the melt zone size and are usually on the order of 10–20 nm (Guang-Sheng 2002). The PTP is a solid-phase crystallization, which allows the ability to obtain larger grains than can be achieved with laser treatment, which is advantageous due to higher atom mobilities. The high heating rates associated with PTP allow the ability to tailor the grain size during the crystallization process. It is believed that crystalline phases can be nucleated with a single pulse and the growth of the crystalline phase can be achieved via additional pulses.

## Technical Approach

A test matrix was developed around amorphous silicon (1.8 μm in thickness on glass) specimens sent from the National Renewable Energy Laboratory (NREL) in order to establish the effects PTP has on the annealing characteristics of the *a*-Si. Characterization techniques involved scanning electron microscopy (SEM) for microstructure evaluation and X-ray diffraction (XRD) and micro-Raman scattering for measuring crystallinity.

The primary research tasks for this seed money proposal were as follows:

1. Deposit *a*-Si thin-films onto quartz substrates for initial investigations.
2. Characterize as-deposited films using XRD, SEM, and micro-Raman
3. Develop test matrix to vary PTP parameters in systematic fashion to encompass multiple pulses and temperature regimes
4. Treat films using selected PTP processes
5. Characterize annealed films using XRD, SEM, micro-Raman

The objective of this research was to perform proof of concept utilizing PTP processing parameters in order to introduce a crystalline silicon phase within an amorphous

silicon phase. The work was designed to produce baseline/fundamental data needed to move forward in showing the capability of the PTP technique in processing silicon thin-film photovoltaic materials.

## Results and Discussion

The pulse thermal processing power density (heat flux) of 1400 W/cm$^2$ was chosen after processing several specimens at varying power densities with mixed results. Several of the thin film specimens peeled off the substrate because of too much heat input (too large power density). Thus, the value of 1400 W/cm$^2$ was targeted for this work. In order to determine the effects of multiple pulses on the crystalline phase, specimens were exposed to 1, 3, and 5 pulses. It is believed that the first pulse initiates nucleation sites, while the subsequent pulses grow grains that have been nucleated as well as nucleate new grains—a heterogeneous thermal nucleation and growth process. As can bee seen in the XRD (Fig. 1a) and the micro-Raman (Fig. 1b) patterns, an increasing degree of crystallinity with increasing pulse number was observed. Specifically, the XRD pattern shows the increasing intensity of the (111) peak and the formation of the (220) and (311) peaks of the crystalline silicon as the pulse number increases, as compared with the as-deposited specimens. The micro-Raman data shows a frequency shift from the amorphous 480 cm$^{-1}$ peak to the crystalline 521 cm$^{-1}$ peak. The 12 specimens that were processed, considering the limited resources for this project, yielded ample evidence to show proof of concept of utilizing PTP for the solid-phase crystallization of amorphous silicon.

## Benefits

Today, approximately 0.02% of the United States energy consumption per year is met by PV equating to about 0.02 Quads or 0.67 Gigawatt-year. Implementing and fully realizing the potential of our pulse thermal processing capability to produce lower-cost Si-based solar cells could have a significant impact on the U.S. energy production in the years to come and position ORNL as a world leader in the research on the synthesis and processing of economical, high-performance solar cells. Approximately 9–10% of the U.S. energy production could be based on PV, equating to approximately 10 Quads or 335 Gigawatt-year, by the year 2030 based on low-cost high-efficiency PV systems. The impact of developing such a low-cost high-efficiency solar cell would mean the United States would have abundant, secure, domestic reliable power and a more stable power grid in the future (Our Solar Power Future 2004). Not only would DOE benefit from such a technology breakthrough, but the Department of Homeland Security would benefit as well, given the fact that PV systems can reliably produce the same electricity cost for 30 years. Also, the ability to decentralize solar power will dramatically reduce the vulnerability of the U.S. electrical system (Our Solar Power Future 2004).

## References


Boyce, J. B., J. P. Lu, J. Ho, R. A. Street, K.van Schuylenbergh, and Y. Wang. 2002. *J. of Non-Crystalline Solids* **731**, 299–302.

Guang-Sheng, F., Y. Wei, L. She-Qiang, H. Hai-Hong, P. Ying-Cai, and H. Li. 2002. *Chinese Phy.* **12** (1), 75.

Nelson, B. P., H. M. Branz, R. S. Crandall, E. Iwaniczko, A. H. Mahan, P. Stradins, Q. Wang, and Y. Xu. 2003. *NCPV and Solar Program Review Meeting 2003*, NREL/CD-520-33586, 825.

"Our Solar Power Future: The U.S. Photovoltaics Industry Roadmap Through 2030 and Beyond." 2004.

Schropp, R. E. I., B. Stannowski, and J. K. Rath. 2002. *J. of Non-Crystalline Solids* **1304**, 299–302.

Science and Technology Review. 1999. (www.llnl.gov/str/str.html), November 1999.

Zhoa, Y., W. Wang, F. Yun, Y. Xu, X. Liao, Z. Ma, G. Yue, G. Kong. 2000. *Solar Energy Materials & Solar Cells* **62**, 143.


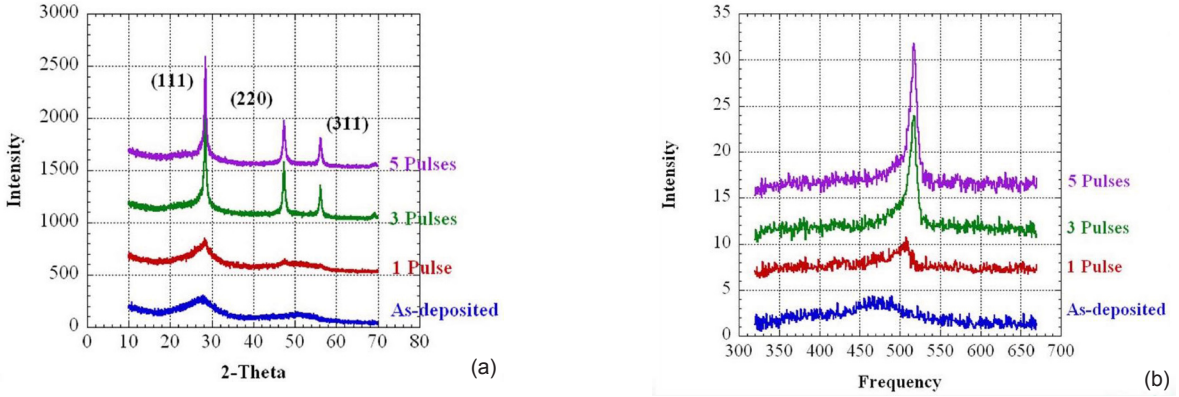


*Fig. 1 (a) XRD and (b) Micro-Raman patterns for as-deposited and 1, 3, and 5 pulses from the pulse thermal processing technique showing the increasing degree of crystallinity.*

# Quick Steps: A Fast and Cost-Effective Method of Manufacturing Carbon Single-Walled Nanotube Composites

J. Y. Howe and P. A. Menchhofer
*Metals and Ceramics Division*

The proposed study, dubbed as "Quick Steps," is designed to produce carbon single-walled nanotube (SWNT) composites in a cost-effective and fast approach. The first step is to grow SWNTs via catalyzed chemical vapor deposition (CCVD). The growth will occur at high temperature for a short time, producing short SWNTs covering metal particles with minimum carbonaceous impurities. The as-grown material can then be directly used in making metal matrix composites, after simple dispersing and mixing procedures by hot pressing. Thus, the time-consuming and labor-intensive purification step can be eliminated. Moreover, ethanol as the carbon feedstock is easy to control, low cost, and environmental friendly. The Quick Steps growth process has the potential for scaled-up, continuous production of short SWNTs grown out of metal catalyst particles.

## Introduction

After the discovery of carbon single-walled nanotubes in 1991(Iijima 1991), numerous studies have demonstrated that carbon single-walled nanotube (SWNT) composites possess superior electrical, mechanical, and thermal properties. An ideal carbon nanotube composite would have individual nanotubes as the reinforcing component, dispersed along the grain boundary in the ceramic or metal matrix. However, there are several major problems associated with the process of making such composites. Amongst all the obstacles, the most difficult engineering problem is how to disperse the bundles of the nanotubes into the matrix and ensure a good interface of the tube and matrix material. It is common knowledge that SWNTs tend to form bundles which consist of tens to hundreds of tubes due to the strong van de Waals force. Despite efforts of surface chemical modification and mechanical agitation, the dispersion problem is yet to be solved. For the composites produced to date, the carbon nanotubes remain as bundles in the matrix (Xu et al. 1999; Zhan et al. 2004). Within each bundle, the numerous SWNTs are only held together by Van de Waals force, thus becoming the weak link of the composite system. As a result, the metal or ceramic matrix nanotube composites produced so far all have inferior mechanical performance to those without the nanotubes.

## Technical Approach

The proposed study, dubbed "Quick Steps," is designed to produce carbon (SWNT) composites in a cost-effective and fast approach. The first step is to grow SWNTs via catalyzed chemical vapor deposition (CCVD). The growth will occur at high temperature for a short time, producing short SWNTs covering metal particles with minimum carbonaceous impurities. The as-grown material can then be directly used in making metal matrix composites, after simple dispersing and mixing procedures by hot pressing. Thus, the time-consuming and labor-intensive purification step can be eliminated. Moreover, ethanol as the carbon feedstock is easy to control, low cost, and environmental friendly (Maruyama et al. 2002). The "Quick Steps" growth process has the potential for scaled-up, continuous production of short SWNTs grown out of metal catalyst particles.

## Results and Discussion

A chemical vapor deposition furnace was designed, installed, and used for numerous test runs. The furnace has a quartz tube and can carry out experiments from 50 Torr to atmospheric pressure at temperatures up to 1300 K.

Four types of metal catalysts were grown on various supports at 1073 and 1123 K. The metal catalysts were Fe, Ni, Co, and Fe/Ni alloy. The size of the catalyst was from 5 to 15 nm. The support materials were quartz, silicon, and a silica surface terminated by carboxyl groups. Multi-walled carbon nanotubes were grown on the metallic substrates (Fig. 1).

## Benefits

Results from this project have set the basis for further work. We have been awarded $50K for the first 3 months of FY 2006 by the BWTX Y-12 Plant to make composites as a better machining tool material. Additional funding, $150K for the rest of FY 2006, will be secured if the work of the first quarter is successful. Benefits from this work may be exploited by further research in support of the goals of NIH/FDA in the area of health effects of nanostructured carbon and DOE's Light Weight Materials Program.

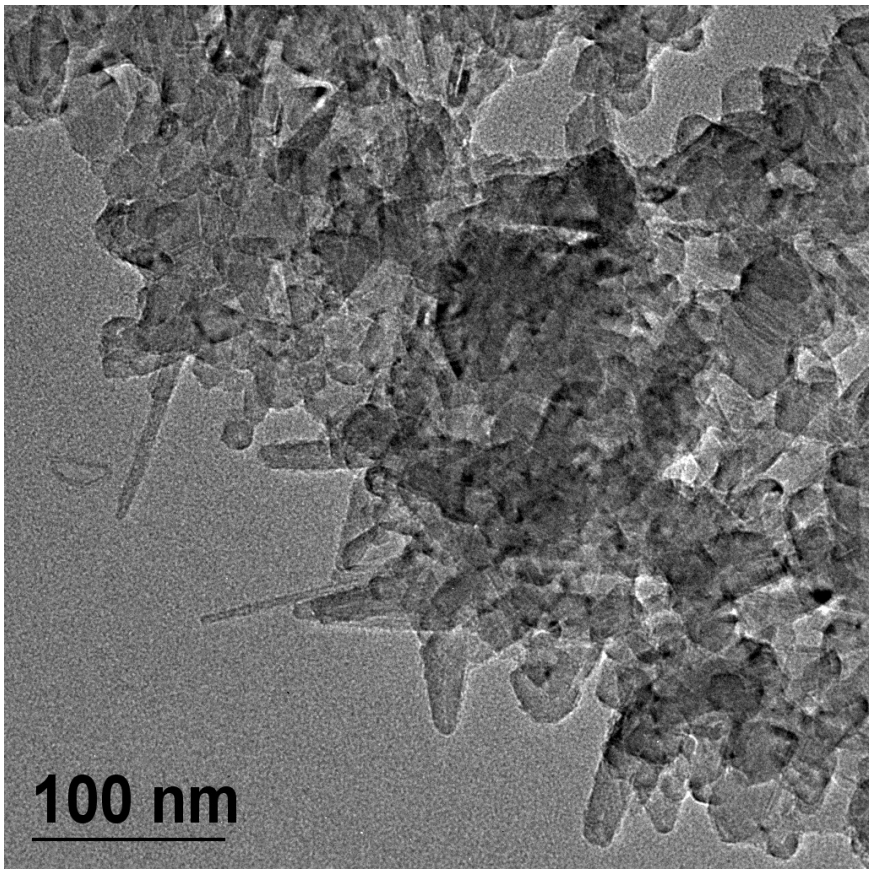


*Fig. 1. TEM micrograph of multi-walled carbon nanotubes grown on the substrate.*

An ORNL invention disclosure has been filed in July 2005 by Jane Howe, Paul Menchhofer, and Wei Wang (Environmental Science Division). A request for Technical Maturity Fund is under reviewed by the Office of Technology Transfer.

## References

Iijima, S. 1991. "Helical microtubules of graphitic carbon," *Nature* **354**, 56-58.

Maruyama, S., et al. 2002. "Low-Temperature synthesis of high-purity single-walled carbon nanotubes from alcohol," *Chem. Phy. Lett.* **360**, 229–234.

Xu, C. L., et al. 1999. "Fabrication of aluminum-carbon nanotube composites and their electrical properties," *Carbon* **37**, 855–858.

Zhan, G. D., et al. 2004. "Carbon nanotube reinforced alumina-based ceramics with novel mechanical, electrical, and thermal properties," *Int. J. Appl. Ceram. Technol.* **1**(2), 161–171.

# Modeling of Impression Creep to Characterize Superplasticity of Nanocrystalline Ceramics

C. H. Hsueh
*Metals and Ceramics Division*

Superplasticity of nanocrystalline ceramics has been the subject of research in the last decade, and conventional uniaxial creep tests are generally performed to characterize this superplastic behavior. However, nanocrystalline ceramics are often limited to a few millimeters in size because of processing difficulties. Also, many uniaxial creep tests are required to collect a complete creep data set. Hence, it is logical to establish an alternative test for use with small specimens and being able to perform multiple tests on a single specimen. The impression creep test, in which a flat-ended cylindrical indenter is loaded on the flat surface of a material, is a most attractive alternative as the indenter diameter can be scaled to test the desired sample size and/or the area of interest. To correlate the impression creep data to the uniaxial creep data, finite element analysis (FEA) has been performed to establish a semi-empirical correlation. However, this existing semi-empirical correlation is not sufficiently accurate. Hence, the purpose of this study is to establish an accurate one. For a special case of viscoelastic materials subjected to impression creep tests, the closed-form solution is also derived which serves as a checkpoint for the FEA results.

## Introduction

The impression creep test was first introduced by Chu and Li (1977). It is a modified indentation test with a flat-ended cylindrical indenter (i.e., a punch) used to characterize the deformation behavior of materials under a constant load and at elevated temperatures. By comparing the displacement versus time data between the impression creep test and the uniaxial (compressive) creep test under a constant-load condition, the following has been concluded. (i) The displacement versus time curves are similar between these two tests, having primary (decreasing creep rate) and secondary (steady-state creep rate) regions. (ii) The steady-state indenter displacement rate has the same stress exponent and temperature dependences as the uniaxial creep test. (iii) The steady-state indenter displacement rate is proportional to the diameter of the indenter.

When materials are subjected to a constant uniaxial load at elevated temperatures, they typically exhibit power-law creep, and the steady-state creep rate, $\dot{\varepsilon}$, can be related to the uniaxial stress, $\sigma$, by

$$\dot{\varepsilon} = A\sigma^n , \tag{1}$$

where $A$ is a proportional constant and $n$ is the stress exponent. For impression creep, the steady-state indenter displacement rate, $\dot{w}$, can be related to the diameter of the punch indenter, $d$, and average stress imposed by the indenter, $\sigma_i$, by

$$\dot{w}/d \propto \sigma_i^n . \tag{2}$$

The general forms to correlate $\sigma_i$ and $\dot{w}/d$ in impression creep to $\sigma$ and $\dot{\varepsilon}$ in uniaxial creep are

$$\sigma_i = \alpha\sigma , \tag{3a}$$

$$\dot{w}/d = \beta\dot{\varepsilon} , \tag{3b}$$

where $\alpha$ and $\beta$ are the correlation factors. The FEA has been performed to establish a semi-empirical correlation, such that $\alpha = 3.38$ and $\beta = 0.755$ (Hyde 1993). However, using the existing semi-empirical correlation, we found that the predicted uniaxial creep rate from the measured impression displacement rate is about 2.6 times of its theoretical value for viscous materials (i.e., $n = 1$). Hence, the purpose of the present study is to derive accurate semi-empirical equations to correlate impression creep to uniaxial creep. Both analytical modeling for the special case of viscoelastic materials and FEA for general cases are performed to analyze impression creep. While the result obtained from analytical modeling serves as a checkpoint for FEA, the results obtained from FEA are used to obtain the accurate correlation factors. Our semi-empirical correlation is shown to agree well with the analytical viscoelastic results and the existing experimental data.

## Technical Approach

The constitutive equation describing the stress-strain relation for a viscoelastic material is a time-dependent differential equation whose Laplace transform with respect to time, $t$, has been demonstrated to be of analogous form

to the governing field equation of elasticity. Hence, knowing the solutions in an elastic system, the Laplace transform of the solutions in a corresponding viscoelastic system can be formulated. Then, with the inverse Laplace transform, the viscoelastic solutions can be obtained. For elastic materials, the stress-displacement relation for impression loading is (Johnson 1985)

$$w = (1 - \nu^2)\pi d\sigma_i/4E \ , \quad (4)$$

where $E$ and $\nu$ are Young's modulus and Poisson's ratio, respectively. For viscoelastic behavior described by the Maxwell model, we have derived the general stress-displacement relation for constant impression loading, such that (Hsueh 2005)

$$w(t) = \pi d\sigma_i/16\,[t/\eta + (5 - 4\nu)/E - (1 - 2\nu)^2\exp(-Et/3\eta)/E] \ , \quad (5)$$

where $\eta$ is the shear viscosity. Differentiation of Eq. (5) with respect to time yields

$$\dot{w}(t) = \pi d\sigma_i/16\eta[1 + (1 - 2\nu)^2\exp(-Et/3\eta)/3] \ . \quad (6)$$

Both Eqs. (5) and (6) serve as checkpoints for FEA results.

Considering both the elastic and the creep components, the stress-strain relation for uniaxial loading is described by

$$\dot{\varepsilon} = \dot{\sigma}/E + A\sigma^n \ . \quad (7)$$

The stress-strain relation described by Eq. (7) is used as the input for FEA, and impression creep test is simulated using ABAQUS. The algorithm models frictionless contact between a rigid cylindrical punch and a cylindrical specimen. A 1-mm-diam punch is considered, and a constant load $P$ ranging from 1 to 5 N is applied on the punch. Sufficiently large dimensions of the specimen are used in present simulations to ensure that the simulated results are independent of the dimensions. The mesh is refined in the high stress concentration region around the contact area, and it consists of 28,369 four-node linear axisymmetric quadrilateral elements with reduced integration, accounting for a total of 29,922 nodes.

## Results and Discussion

The material properties pertinent to viscoelastic materials are considered, such that $E$ = 6 GPa, $\nu$ = 0.38, and uniaxial viscosity $\mu = 3\eta$ = 100 GPa s are used in simulations. This uniaxial viscosity datum corresponds to $A = 10^{-5}$ MPa$^{-1}$ s$^{-1}$ for $n$ = 1 in Eq. (7). For other $n$ values, $A = 10^{-5}/2^{(n-1)}$ MPa$^{-n}$ s$^{-1}$ is selected in present simulations. First, the accuracy of FEA is examined by simulating the elastic and the viscoelastic deformations under a constant impression load, and the results are checked against the analytical solutions. Then, the cases for $n$ = 1 to 8 are simulated to obtain the steady-state creep rates at different loads. This steady-state creep rate is normalized by the proportional constant $A$ as well as the punch diameter $d$, and it is then related to the average loading stress $\sigma_i$ (=$4P/\pi d^2$) by

$$\dot{w}/Ad = C\sigma_i^n \ , \quad (8)$$

where $C$ is a proportional constant. Combining Eqs. (1), (3), and (8), it can be obtained that $C$ corresponds to $\beta/\alpha^n$. Hence, the relation between $\alpha^n/\beta$ and the stress exponent $n$ can be obtained from FEA by using different values of $n$ in Eq. (7) as the input for simulations. The normalized steady-state displacement rate, $\dot{w}/Ad$, is plotted as a function of $\sigma_i$ for $n$ = 1 to 8 in Fig. 1(a). The data are then fitted by Eq. (8) for each stress exponent $n$. Both the fitting curves and the fitting parameter $C$ are also shown in Fig. 1(a), and excellent agreement is observed.

With the C value obtained for each stress exponent, $\alpha^n/\beta$ (= $1/C$) is then plotted as a function of $n$ in Fig. 1(b). The semi-empirical values of $\alpha^n/\beta$ based on Hyde et al.'s reference stress method are also included as a dashed line in Fig. 1(b) for comparison. It can be seen that good agreement in $\alpha^n/\beta$ is obtained between the present FEA and Hyde et al.'s FEA when $n > 4$; however, the results exhibit an increasing deviation as $n$ decreases below 4. Chu and Li (1977) performed both uniaxial and impression creep tests on succinonitrile at 37ºC to obtain steady-state creep rates. The stress exponent of 4 was obtained, and their experimental results were fitted by using $\alpha$ = 3.3 and $\beta$ = 1. Impression creep tests have also been performed on $\beta$-Sn single crystals in different orientations and at different temperatures (Chu 1979). By comparing to uniaxial creep data and assuming $\beta$ = 1, the following results were obtained: $n$ = 5, $\alpha$ = 3.5 at 60 ºC and $n$ = 4.5, $\alpha$ = 3.9 at 203 ºC for [110] orientation; $n$ = 4.4, $\alpha$ = 2.8 at 40ºC and $n$ = 4.3, $\alpha$ = 2.8 at 60 ºC for [001] orientation. Dorner et al. (2003) performed impression creep tests on TiAl alloy at 750ºC and compared their results to those obtained from uniaxial creep tests. The stress exponent was found to be ~7.5 and Hyde et al.'s correlation factors could be used for fitting. Based on the above empirical values of $\alpha$ and $\beta$, the corresponding values for $\alpha^n/\beta$ are also included in Fig. 1(b) for comparison, and good agreement is obtained between the semi-empirical and existing experiment values. Hence, although the present FEA result is validated by the closed-form solutions only for $n$ = 1, the agreement with existing FEA and experimental results for $n \geq 4$ makes us believe that we have determined accurately $\alpha^n/\beta$ for the range of stress exponent considered in the present study.

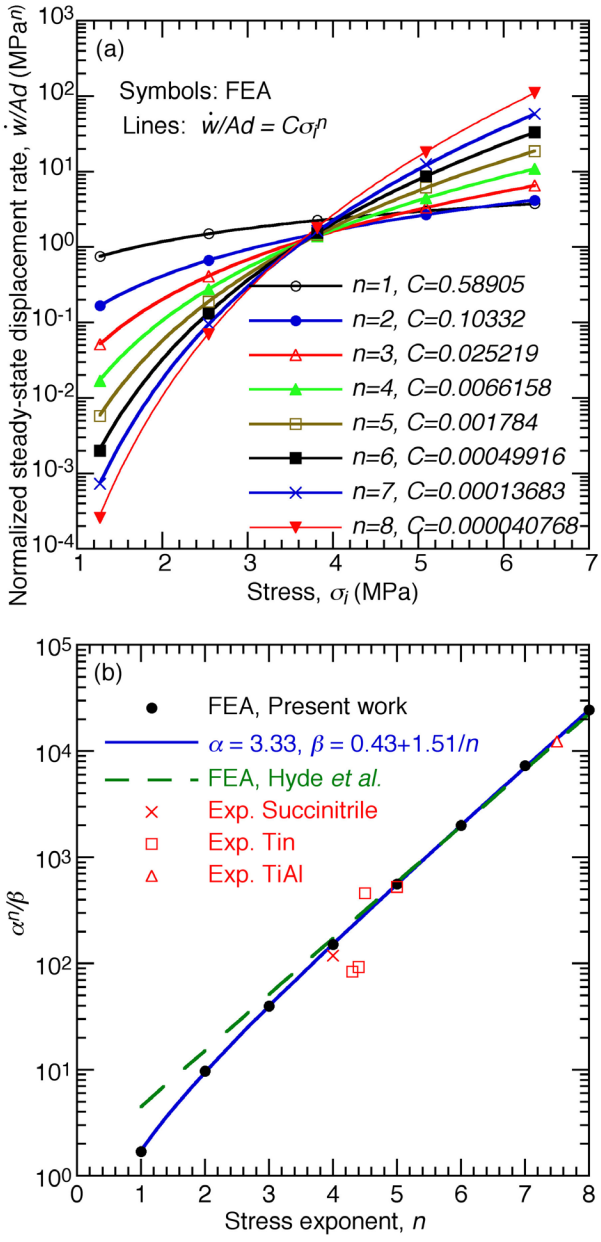


*Fig. 1. (a) FEA results (symbols) for the normalized steady-state displacement rate, $\dot{w}/Ad$, as a function of the average impression stress, $\sigma_i$, for n = 1 to 8. The best fits of the data to Eq. (8) are shown as solid lines, and (b) $\alpha^n/\beta$ as a function of n showing the comparison between present FEA results (solid circles), Hyde et al.'s semi-empirical values (dashed line), and existing experimental data (symbols). The best fit of present FEA results to Eq. (9) is also shown (solid line).*

To determine $\alpha$ and $\beta$ from the simulated $\alpha^n/\beta$ versus $n$ data, the methodology of curve fitting is described as follows. The semi-logarithm plot of the $\alpha^n/\beta - n$ relation shows nearly a straight line with a slight deviation from linearity for low $n$ values. While constant $\alpha$ and $\beta$ yield an exact straight line in the semi-logarithm plot of $\alpha^n/\beta$ versus $n$ (e.g., Hyde et al.'s results), the slight deviation from linearity for low $n$ values can be accounted for by adding an $1/n$ or $\exp(-n)$ term to a constant $\beta$. For simplicity, the $1/n$ term is adopted and the fitting equation has the following form:

$$\alpha^n/\beta = a^n/(b + c/n) \ . \qquad (9)$$

In this case, the slope of the semi-logarithm plot of the $\alpha^n/\beta - n$ relation at large $n$ values is described by $\log(\alpha)$. With curve fitting, the parameter values $\alpha = 3.33 \pm 0.04$, $\beta = 0.43 \pm 0.06$, and $c = 1.51 \pm 0.07$ yield an excellent agreement as shown in Fig. 1(b) by the solid line. Hence, it is straightforward to obtain

$$\alpha = 3.33 \ , \qquad (10a)$$

$$\beta = 0.43 + 1.51/n \ . \qquad (10b)$$

## Benefits

Research on structural nanomaterials is one of the DOE focus areas. Our closed-form solutions enable researchers to accurately characterize superplasticity of nanocrystalline materials using impression creep tests. The technique of impression creep is useful not only for cases where small volumes are available but also for cases where localized creep properties are of interest, such as welded joints. Also, nanocrystalline thin films on substrates have demonstrated variety of very unusual mechanical and transport properties. The present work can be extended to characterize superplasticity of nanocrystalline films on substrates using impression creep tests.

## References


Chu, S. N. G., and J. C. M. Li. 1977. "Impression creep; a new creep test," *J. Mater. Sci.* **12**, 2200–2208.

Chu, S. N. G., and J. C. M. Li. 1979. "Impression creep of $\beta$-tin single crystals," *Mater. Sci. Eng.* **39**, 1–10.

Dorner, D., K. Röller, B. Skrotzki, B. Stöckhert, and G. Eggeler. 2003. "Creep of a TiAl alloy: a comparison of indentation and tensile testing," *Mater. Sci. Eng.* **A357**, 346–354.

Hsueh, C. H., P. Miranda, and P. F. Becher. 2005. "Correlations between impression creep and uniaxial creep," submitted to *Phys. Rev. B.*

Hyde, T. H., K. A. Yehia, and A. A. Becker. 1993. "Interpretation of impression creep data using a reference stress approach," *Int. J. Mech. Sci.* **35**, 451–462.

Johnson, K. L. 1985. *Contact Mechanics*, Cambridge University Press, p. 59–60.

# Fundamental Growth Mechanisms of Metal Nanoparticle–Carbon Nanotube Nanocompoiste Materials

G. M. Stocks,[1] J. Zhong,[1] and D. B. Geohegan[2]
[1]*Metals and Ceramics Division*
[2]*Condensed Matter Sciences Division*

Metal nanoparticle-carbon nanotube composites are new emerging nanomaterials with a variety of potential technological applications. Currently, fabrication of these nanocomposite materials proceeds via trial and error due to the lack of fundamental understanding of their growth mechanisms. A unique structural feature of carbon nanotubes is their curved surfaces of enormous curvatures. Consequently, it is expected that the mechanisms governing nanoparticle growth on such surfaces are different from those of traditional materials growth on flat surfaces. In this project, we are using theoretical and experimental techniques to investigate the general principles governing the formation, structure, and stability of metal nanoparticles on surfaces of carbon nanotubes.

We use theory (continuum theory, classical and first-principles molecular dynamics) and experimental (growth of metallic nanoparticle on single walled nanotubes) to uncover the fundamental growth mechanisms of nanoparticles on curved surfaces.

We have made significant progress in understanding the mechanisms of growth of metal nanoparticles on carbon nanotubes. Using continuum elasticity theory we have developed a novel concept, bending-stress-induced self-organization, for predicting the shape of metal nanoparticles grown on highly curved surfaces. In work, published in *Appl. Phys. Lett.* **87**, 133105 (2005), we show that growth of a metal nanoparticle on surfaces of carbon nanotubes is three-dimensional and is described by a power law $L=aH^{0.5}$, where L (H) are the length (height) of the nanoparticle. To understand the growth process at the atomistic level, we are using simulated thermal annealing and molecular dynamics (MD) simulations. Initial results show that Au forms crystalline nanoparticles on single-wall carbon nanotubes (SWCNTs), in agreement with the prediction of the continuum theory and experimental observations. Currently, we are investigating the shape dependence of Au and Pt nanoparticles on particle size and nanotube curvature using MD and first-principles methods.

On the experimental side, we have produced SWCNTs using a pulsed-laser ablation technique and have deposited Pt, Au, Pd, and Ag metal nanoparticles on the SWCNTs in an e-beam evaporation chamber. Our high-resolution TEM and Z-contrast STEM images clearly show that uniformly distributed nanometer-sized particles form on the side walls of the SWCNTs. We have also studied the influence of post-deposition annealing on the nanoparticle size distribution and found that the mean size of nanoparticles increases with annealing temperature and the size distribution becomes greatly broadened. A power-law relationship $L = aH^b$ has been observed with $b = 0.40 \pm 0.10$ for Pt and $b = 0.316 \pm 0.024$ for Au. This power-law behavior is in agreement with the prediction given by the continuum theory but the scaling exponent is slightly different from the theoretical value 0.5. We believe that this deviation originates from the application of the continuum theory to small nanoparticles. We are currently combining MD simulations, first-principles methods, and further experimental studies to understand this power-law behavior at atomistic level.

This work is directly relevant to DOE's research portfolio in basic science. It is particularly relevant to DOE initiatives in materials science, nano-science, and hydrogen and fuel cell technologies. At ORNL this work is particularly relevant to stated goal of the Center for Nanomaterials Sciences (CNMS).

# Large-Area, Flexible, Heteroepitaxial Single-Crystal-Like Diamond Films on Low-Cost Substrates for Wide-Ranging Electronic Applications

L. Heatherly,[1] L. Wilson,[2] R. Shaw,[2] J. Li,[1] and A. Goyal[1]
[1]*Metals and Ceramics Division*
[2]*Chemical Sciences Division*

Diamond is a very attractive material for many applications including high-powered electronic devices, high-speed devices, high-temperature devices, cold cathode electron emitters for flat panel displays, and field emission diodes. For many of these applications, the diamond has to be in the form of single crystals or very highly ordered polycrystalline films. The goal of this project is to demonstrate the fabrication of large-area single-crystal-like diamond films by heteroepitaxial deposition on suitable, low-cost, single-crystal-like non-diamond substrates. If this project is successful, it could pave the way for a wide range of promising applications in the semiconductor area.

Work has progressed well with the fabrication of suitable biaxially textured substrates onto which diamond will be deposited (Task 1). Two substrates that have been explored are Ir/$Y_2O_3$/Ni-3W and Ir/YSZ/$Y_2O_3$/Ni-3W. Both result in good texture in the iridium surface layer as determined by X-ray diffraction measurements. The two-layer substrate is desirable; however, the YSZ might be necessary to prevent nickel from diffusing into the iridium during diamond deposition. Diamond will be nucleated and grown on these and other possible substrates, and the resulting films will be characterized using X-ray and electron beam techniques.

Modifications have been made to the existing hot filament-assisted CVD (FACVD) chamber which allows the bias-enhanced nucleation of diamond on the iridium surface (Task 3). Preliminary results on the biasing effect are encouraging, but the appropriate parameter space for the best nucleation density needs to be determined. Work is proceeding in this area. All the components required for the modification of the microwave-assisted CVD (MACVD) system are in house, and the modifications will be carried out as soon as access to the system can be scheduled.

Some preliminary diamond growths have been performed both in the FACVD and the MACVD, but until the suitable bias-enhancing as well as the diamond growth conditions are determined, the resulting diamond films were not always continuous or crystallographically oriented. It is realized that determining these optimal conditions will be possibly the most difficult part of the project, and a significant amount of time will be allotted to accomplishing this. We are at the point in the project when these types of experiments can be performed and evaluated, and work is proceeding in this area.

# Development of an Intermediate-Temperature Solid Oxide Fuel Cell

T. R. Armstrong,[1] E. A. Payzant,[2] and S. Speakman[2]
[1]*Energy Efficiency and Renewable Energy Program*
[2]*Metals and Ceramics Division*

Solid oxide fuel cell (SOFC) technology has been limited to operating at high temperatures (>600°C) due to the available electrolyte systems. A new inorganic proton-conducting electrolyte has been developed that only conducts protons at temperatures below 500°C. This new conductor has demonstrated the highest proton flux at the lowest temperatures ever measured in an inorganic material. The objective of this project is to fabricate and demonstrate the viability of a new class of solid oxide fuel cells operating at temperature less than 500°C utilizing this new conductor.

SOFC technology has the potential for providing high power densities, long, stable lifetimes, the ability to utilize a broad source of fuels without expensive reforming or gas cleanup, and provide high system efficiencies for a wide range of power generation applications. The critical limitations of SOFCs for small-scale power (<100 kW) are long start-up times, generally many minutes to hours, thermal cycling, seals, and cost. The long start-up times and thermal cycling have significantly impacted consideration of SOFCs for as automotive auxiliary power. A new class of fuel cells able to operate at greatly reduced temperatures has the potential to (1) reduce start-up time, (2) simplify thermal management, and (3) significantly reduce stack costs by allowing the use of inexpensive iron-base alloys for the interconnect and thin-film metallic anode and cathodes. In addition, operating below 500°C would allow direct use of renewable fuels such as ethanol and methanol as feedstocks.

The approach was a logical progression from materials synthesis to membrane development and fuel cell testing which included the evaluation of anode and cathode materials. The temperature where this new material functions (<500°C) is sufficiently lower than where current state-of-the-art anode and cathode materials operate. Thus, a large portion of the testing is being focused on the selection of candidate anode and cathode materials, with priority given to alloys, as their electrical conductivity should be significantly higher than oxides in this temperature range.

During this year, a synthesis method was developed and refined to allow large quantities, up to 1 kg, to be regularly produced. Due to the use of Mo, traditional aqueous synthesis could not be utilized. Therefore, to produce highly pure material, metal nitrates and oxalates were mixed in water, then dehydrated, and calcined. The powder produced by this method was then used to develop a tape casting process to produce thick films (≈200 μm). These tapes were than punched to size, laminated, and a series of single cell coupons were produced with thicknesses ranging from 200 to 800 μm for testing. In parallel to this effort, a single-cell test stand was designed and constructed to carry out the initial testing to determine current/voltage and power characteristics.

A fuel cell that operates below 500°C will allow the development of a rapid start fuel cell for use an auxiliary power unit in vehicular and national security applications. In addition, lower temperatures will reduce temperature swings during thermal cycling and potentially improve stack lifetimes.

# Sensing Arrays Based on Non-Nernstian Sensing Elements

F. C. Montgomery,[1] D. L. West,[2] R. J. Warmack,[2] and T. R. Armstrong[3]
[1]*Metals and Ceramics Division*
[2]*Engineering Science and Technology Division*
[3]*Energy Efficiency and Renewable Energy Program*

On-board emissions sensors are necessary in the campaign to minimize emissions from mobile power sources such as passenger car and truck engines. This is a difficult challenge as combustion exhausts are complex mixtures with time-varying concentrations of oxygen, water vapor, and pollutants such as carbon monoxide. The goal of this work is to investigate the application of sensing elements that can function at high temperature (600ºC) to meet this challenge. We are constructing and testing arrays of these sensing elements in order to determine whether this technique can circumvent the need for pure selectivity. The results to date are promising, and we are confident further testing and analysis will show that array sensing techniques can be used with these types of sensing elements to make compact and robust sensors capable of monitoring exhaust gas chemistry.

Environmental stewardship is driving the desire to reduce emissions from vehicles such as passenger cars and trucks. Towards this end, on-board sensors that can continuously monitor engine exhausts for compliance with environmental regulations are required. Further, since the exhausts from diesel and lean-burn gasoline engines are not amenable to remediation with the current generation of catalytic converters, on-board sensors may be required for control and diagnostics of proposed remediation strategies for these exhausts such as selective catalytic reduction (SCR) and the lean $NO_x$ trap (LNT).

Combustion exhausts are complex mixtures, with varying amounts of $O_2$, $H_2O$, $CO_2$, carbon monoxide (CO), hydrocarbons, and oxides of nitrogen (NO and $NO_2$). One approach that has been taken in the past to characterizing such mixtures is the use of sensing arrays (Albert et al. 2000). Sensing arrays rely on differences in response magnitudes amongst individual sensing elements in an array (as opposed to pure selectivity). These different response magnitudes will produce patterns, and if changes in the gas being sensed cause reproducible changes in the pattern output by the array, then the array can be used for characterization.

Our approach is to design arrays based on "non-Nernstian" sensing elements (Miura et al. 2000). This type of sensing element produces readily measurable DC potentials (on the order of 0.1 V) in the presence of small, yet non-equilibrium, amounts (10–1000 $ppm_V$) of reducing (e.g., CO) and/or oxidizing (e.g., $NO_2$) species. However, these elements are rarely purely selective (giving at least some response to more than one species). Thus, we have proposed to extend existing array-based techniques to these types of sensing elements. Since this is a novel approach, the first step is proof-of-principle experimentation, and the challenge of detecting ammonia ($NH_3$) in simulated diesel exhaust has been selected for this task. We should point out that the SCR technique (mentioned above) with $NH_3$ as a reagent has been proposed for diesel exhaust remediation so this proof-of-principle system could have practical applications.

There are four main components to this work, and we have made significant progress on three of them to date. The first component involved construction of a test station capable of supplying simulated exhaust mixtures to prototype sensing arrays at temperatures near 600ºC (1100ºF). These high temperatures will be encountered in practice. The second and third components consist of fabricating and testing prototype sensing arrays. The fourth and final component is data reduction wherein we will deduce what array elements are necessary in order to discriminate $NH_3$-containing mixtures.

Design and assembly of the test station is completed, and the results of testing to date are very promising. For example, we have shown that an array element consisting of a particular transition metal oxide and Pt is only weakly affected by CO but does respond very strongly to $NH_3$ and propylene ($C_3H_6$, a typical exhaust hydrocarbon). However, pairing this same oxide with a different binary oxide yields an array element that responds strongly to CO and $C_3H_6$ but is little affected by $NH_3$.

We believe as this work progresses we will discover other such "orthogonalities" that will allow for construction of a robust array that can detect $NH_3$ in diesel exhaust. This will help enable the SCR technology for diesel exhausts mentioned above. Further, since SCR with $NH_3$ is already employed at stationary power plants, this work may also yield benefits for emissions control in that area.

## References

Albert, K. J., N. S. Lewis, C. L. Schauer, G. A. Sotzing, S. E. Stitzel, T. P. Vaid, and D. R. Walt. 2000. "Cross-reactive chemical sensor arrays," *Chem. Rev.* **100**, 2595–626.

Miura, N., G. Lu, and N. Yamazoe. 2000. "Progress in mixed-potential type devices based on solid electrolyte for sensing redox gases," *Solid State Ionics* **136**, 533–42.

# Out-of-Autoclave Stabilization/Carbonization of Pitch-Based Carbon-Carbon Composites and Other Pitch Materials

J. Klett, C. Eberle, and C. Janke
*Metals and Ceramics Division*

Several pitches were characterized for their ability to be stabilized using ionizing energy. They were blended with catalyst initiators, and it was determined that the initiators caused crosslinking of the pitches such that they would not melt and bloat during carbonization. Thus, they could be processed without need for a high-temperature, high-pressure autoclave, thus dramatically reducing costs for these unique materials.

The objective of this project is to utilize ionizing energy to stabilize pitch matrices of carbon-carbon composites such that they will not melt during carbonization, thus obviating high-temperature and high-pressure autoclaves for processing.

The approach was to first characterize several types of pitches, to determine the susceptibility to ionizing energy for promoting cross-linking. Then, the pitches were exposed to the ionizing energy at various levels to characterize the response under different conditions. In addition, various catalyst initiators were blended with the pitches to determine if initiators would be required to advance the reaction and enhance the ability to stabilize the pitches.

We have determined that a cationic initiator can be utilized to successfully stabilize several different pitches, specifically coal-derived pitches as well as a petroleum-derived pitch.We evaluated five different initiators and many different ionizing conditions and determined that it is possible to stabilize pitches prior to heat treatment and prevent melting. After ionization, the pellet was fired to 1000ºC at 1ºC/min. Samples with the initiator and ionization were stabilized and cross linked and did not melt. While the sample cracked, this is due to the large shrinkages of the part during firing and would be mitigated by the fibers in the composite. In fact, this is desired as when the stabilized pitch loses mass during carbonization, it will shrink, thus opening porosity which is required so that further densifications can easily be accomplished. The density of the pellet was measured to be 1.59 g/cc (cracks included); thus, the sample densified rather well and coalesced into a very nice carbon.

Next, we discovered that the samples could be stabilized with simple thermal treatment in non-oxidizing atmospheres. While this is much slower than an ionizing treatment (hours rather than minutes), it allows faster turn around of experiments as ORNL does not have an ionizing facility on site. This advantage of thermal processing is promising as it will expand the possibilities of processing composites further. The final density of a sample just thermally processed with the initiator was 1.62 g/cc.

Clearly, it was found that pitches could be stabilized without oxygen, thus avoiding the need for autoclaves in the processing of carbon materials. To show that the addition of fibers would improve performance, we blended 25% carbon fibers into the powdered pitch with initiator and pressed into pellets, soaked, and carbonized. The pellet did not bloat and it did not crack. Thus it is believed that we had success in our first phase of the project as anticipated. However, it is also clear that the process of using initiators to cross link the pitches and either thermal or ionizing energy to start the reaction can be successful in preventing melting of pitches. The next phase of this project will be focused on producing true carbon-carbon composites with this technique to demonstrate the ability to eliminate the need for an autoclave.

By eliminating the need for an autoclave to process carbon-carbon composites, these materials can now be evaluated for many energy-saving and high-performance applications that currently do not utilize such due to very high material costs (>$5000/lb).

# Effect of Texture on High-Temperature Deformation of Nb-1%Zr Alloy

S. J. Zinkle,[1] T. G. Nieh,[1,2] T. E. McGreevy,[1] D. T. Hoelzer,[1] and Y. Cui[2]
[1]*Metals and Ceramics Division*
[2]*University of Tennessee*

Fully recrystallized samples of Nb-1%Zr with different textures were prepared by varying the cold work and annealing conditions. The texture was quantified using scanning electron microscopy, orientation image microscopy and X-ray diffraction techniques. Tensile tests were subsequently conducted at 750ºC and 1100ºC over a wide range of strain rates. To provide further identification of the deformation mechanisms, strain rate change tests were performed to evaluate the stress exponents. The texture in the recrystallized Nb-1Zr was found to significantly affect the flow stress of Nb-1%Zr at both 750 and 1100ºC.

Niobium alloys such as Nb-1%Zr are leading candidate materials for space power systems due to their good strength up to high temperatures, and good fabricability. However, large variations in the measured creep behavior of nominally identical Nb-1Zr specimens have been reported. Although crystallographic texture is known to affect the room temperature mechanical properties of refractory alloys, practically no information exists on the texture effect at high temperatures.

Nb-1Zr in the form of a 4-mm sheet was vacuum annealed at 1250ºC for 2 h, cold-rolled to 80% reduction-in-thickness, and then vacuum annealed at 1300 to 1550ºC for 2 h. The recrystallized microstructure was examined using backscattered scanning electron microscopy, and texture of the sheet was analyzed using X-ray diffraction and orientation image microscopy. The recrystallized texture was found to be highly dependent on the annealing temperature, and the recrystallized grains preferentially aligned with the {111} habit planes normal parallel to the normal direction of the sheet and the <110> crystal directions parallel to the rolling direction. Annealing at 1500 for 2 h resulted in a rotation of the grains about the {111} planes lying in the rolled plane from <110> to <121> alignment with rolling direction—that is, a 30º change in grain orientation whereby most of the grains still have the {111} habit plane parallel to the sheet but the orientation in the rolling direction rotates to <121>.

Tensile specimens from the 1500ºC annealing condition were machined at different angles to the rolling direction in order to obtain different textures relative to the tensile axis. The tensile behavior of Nb-1Zr samples oriented at 0º and 30º to the rolling direction was investigated in vacuum at 750 and 1100ºC at strain rates $3.3 \times 10^{-6}$ $s^{-1}$ to $3.3 \times 10^{-3}$ $s^{-1}$. The tensile tests performed at 750ºC did not exhibit a large strain rate dependence, whereas the tensile tests at 1100ºC exhibited increasing strength with increasing strain rate. Preliminary analysis suggests that the 750ºC deformation was controlled by dislocation glide, whereas the 1100ºC deformation was controlled by dislocation power law or diffusional creep. For tensile tests conducted at both 750 and 1100ºC at increasing strain rates, the flow stress of the 0º-oriented sample was about 20% higher than that of the 30º-oriented sample, indicating the material is stronger in the rolling direction. This strength difference was also observed in strain rate decrease tests, although the magnitude of the effect was somewhat smaller. The measured stress exponent at 1100ºC was a relatively high value of 14.8, suggesting power-law breakdown behavior. Additional tensile tests at 750 to 1250ºC are planned to obtain further insight on texture effects on the flow stress and deformation mechanisms. A single thermal creep test on each of the two orientations (0 and 30 degrees) is planned for direct experimental confirmation of texture effect, if any. These creep tests will be designed for 1000 h to reach 1% creep strain; they are equivalent to strain rates on the order of $10^{-9}$ $s^{-1}$ compared to $3 \times 10^{-6}$ $s^{-1}$ in the slowest tensile test.

# Thermoelectric Properties of Uranium Dioxide

C. E. Duty,[1] M. J. Haire,[2] J. Kiggans,[1] H. Wang,[1] and W. Porter[1]
[1]*Metals and Ceramics Division*
[2]*Nuclear Science and Technology Division*

The relative worth of thermoelectric materials is judged by a dimensionless figure of merit ($ZT = \sigma_e S^2 T/\kappa$), where $\sigma_e$ is electrical conductivity, *S* is the Seebeck coefficient, *T* is temperature, and $\kappa$ is thermal conductivity. Over the past 50 years, the best thermoelectric materials have barely achieved figure of merit above 2. Recent experimental results suggest that uranium dioxide could produce a figure of merit of ~1.3 at 450°C and ~4.2 at 800°C. The proposed research will attempt to validate this potential by fabricating $UO_2$ samples and measuring the figure of merit at 450°C.

Uranium dioxide is a strong candidate for providing a materials breakthrough in thermoelectrics. The Seebeck coefficient for $UO_2$ is ~600 μV/K at room temperature, which is more than double that of the best thermoelectric materials today. Unfortunately, uranium dioxide has not been seriously considered as a thermoelectric material due to a relatively low electrical conductivity. However, recent research by Thomas Meek and Jonathan Haire (2002) has shown that the electrical conductivity of doped $UO_2$ is four orders of magnitude higher than intrinsic, undoped $UO_2$ at room temperature. If this dramatic increase holds true at elevated temperatures and other properties change as expected, $UO_2$ could produce a figure of merit of ~1.3 at 450°C and ~4.2 at 800°C.

The current project is a small, focused mission to validate the potential of uranium dioxide as a thermoelectric material. The Metals and Ceramics Division is uniquely positioned to pursue this opportunity: The Materials Processing Group has experience processing radioactive powder material such as uranium dioxide, and the High Temperature Materials Laboratory (HTML) offers the ability to measure thermoelectric properties at elevated temperatures. Therefore, the simple research plan involves fabricating one natural and three doped $UO_2$ samples from powder and measuring the thermoelectric properties. Due to current equipment limitations, measurements will be conducted only at room temperature and 450°C. If these results warrant further investigation (i.e., a figure of merit approaching 1), a means of conducting measurements at higher temperatures will be pursued in future work with the goal of exceeding a figure of merit of 4.

To date, a small quantity of $U_3O_8$ powder has been procured and converted into $UO_2$. The powder has been doped with three different concentrations of aluminum oxide and pressed into eight sample disks. This completes the "sample fabrication" portion of the proposed research. High-temperature thermoelectric properties will be measured in FY 2006.

The development of a thermoelectric material with a high figure of merit would greatly impact direct energy conversion techniques and produce several innovative applications. Thermoelectric devices are highly reliable, silent, vibration-free, small, and lightweight. A marginal increase in the figure of merit (ZT = 2–3) would make thermoelectric devices competitive with standard vapor-compression cooling systems, while a dramatic increase would revolutionize the field of thermoelectrics and lead to their widespread use in military, space, and commercial products. The potential of uranium dioxide as a thermoelectric material was first identified in research efforts as part of DOE's Depleted Uranium Uses Research and Development Program. The U.S. Department of Defense and DARPA are also interested in thermoelectric material research and have publicly declared a figure of merit goal of 4. The Navy is also exploring the use of thermoelectric materials for power generation on submarines.

## Reference

Meek, T. T. and M. J. Haire. 2002. "Ion Implantation of UO2," Society for the Advancement of Materials and Process Engineering (SAMPE) 2002 Symposium.

# *Computer and Computational Sciences*

# *Director's R&D Fund*

# Comprehensive Fusion Simulation: Component-Based Software Engineering and Evolutionary Time Advancement

L. A. Berry,[1] D. B. Batchelor,[1] D. E. Bernholdt,[2] W. A. Houlberg,[1] E. F. Jaeger,[1]
J. A. Kohl,[2] S. Li,[3] and W. R. Elwasif[3]
[1]*Fusion Energy Division*
[2]*Computer Science and Mathematics Division*
[3]*Texas A&M, Kingsville*

Validated, predictive computer simulations of magnetic fusion plasmas that address all relevant physics have been recognized as an essential part of the fusion program as it embarks on the large International Burning Plasma Experiment (ITER). The realization of this objective requires addressing a wide range of plasma physics, applied mathematics, and computer science issues. This project addressed a subset of the these issues by developing a prototype plasma simulation using the Common Component Architecture, an approach to component-based software engineering that addresses issues of code portability, reuse, and inter-language compatibility within a high-performance computing environment. Components for the simulation were written in four different languages and comprised a mixture of new components for managing the simulation time flow and data and already developed physics modules that were encapsulated as components. High-resolution radio-frequency heating using the AORSA code was a key part of the physics in the simulation. The speed of the AORSA calculations was substantially improved through the development of a first-ever iterative solver for the electromagnetic fields.

## Introduction

The need for integrated, predictive simulation of magnetized fusion plasmas for planning and analyzing ITER experiments and for designing future fusion power reactors has been recognized in a number of studies and evaluations (Dahlberg 2001; Batchelor 2005). ITER is a ~$10B burning plasma experiment that will be built and operated by an international collaboration with the U.S. as a partner. The proposed U.S. program to address this need is called the Fusion Simulation Project (FSP). While the fusion research community has a long and successful history of using state-of-the-art computers to develop computational models for studying individual issues, the FSP poses a number of computer science, applied mathematics, and plasma physics issues that are both complex and intertwined. The objectives of this project were twofold. The first objective was to address the key computer science issues of extensibility, portability, and reuse by developing a component-based, magnetic fusion-specific simulation using the Common Component Architecture (CCA). Descriptions of CCA can be found at the Web site http://www.cca-forum.org. The second objective was to address key issues for efficiently coupling physics components with multiple time scales.

These goals were achieved through the development of a plasma simulation using the CCA that combined components written in several computer languages. The physics components were based on previously developed codes and modules that were developed in FORTRAN 77 (f77) and FORTRAN 90 (f90), while the components that controlled the overall simulation execution and provided data communications between physics components were new components that were implemented in Python and C++, respectively. The capability for efficiently integrating the fast time scales of radio frequency (RF) heating into the much slower time scales of plasma transport were increased by the development of an iterative algorithm for the All Orders Spectral Algorithm (AORSA) (Jaeger 2001) RF-plasma interaction model.

In the following, the overall simulation architecture, the function and relationships of its components, and the basis for a new iterative algorithm will be presented. A brief discussion of "lessons learned" follows these technical presentations.

## Technical Approach

A critical feature of the CCA is that it forces an upfront "design" of a simulation. The components of the simulation must be specified both in terms of their function (the methods they provide) and the data that the components use and provide. A simplified schematic of the LDRD simulation that illustrates the four-level design is shown in Fig. 1. The levels consist of a driver that controls the overall time flow of the simulation; physics components that implement physics packages and carry the main computational burden; coordinate transformation components that provide the changes in dimensionality, resolution, and coordinate systems that allow the physics components to share data; and a plasma state that stores a set of data that describe the complete simulation.

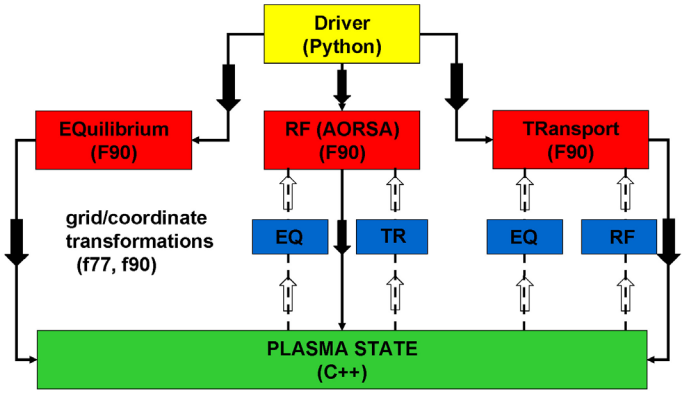


*Fig. 1. Component diagram of the CCA plasma transport simulation. The four levels of driver (yellow); physics (red); coordinate transformation (blue); and plasma state (green) are shown. The solid lines and arrows show data flowing down from the driver, through the physics components, and then to the plasma state. The dashed lines and outlined arrows show flow up from the plasma state to the transforms to the physics components. The transforms are labeled with the name of the data set on which they operate.*

The driver is the highest level component and controls the time evolution of the simulation, directs the initialization of physics components, and implements the main simulation time loop. That loop controls the order in which components are called and determines if the results of a particular calculation are acceptable and can therefore be written to the plasma state for access by other physics components. The driver was implemented in the Python computer language because of its flexibility and power as a high-level scripting language and its ability to rapidly implement changes. The usual negative of reduced computational efficiency was not a factor because the preponderance of the simulation computational load was in the physics-component layer.

The physics components at the second level were based on existing f77 and f90 code for the RF and transport components. The AORSA RF simulation was developed as part of an Oak Ridge National Laboratory (ORNL) Scientific Discovery through Advanced Computing (SciDAC) project on RF-plasma interactions, while the transport modules were based on modules that had been developed under the National Transport Code Collaboration project.

The plasma state component functioned as the central repository for the results of all physics calculations. The plasma equilibrium was assumed static for this simulation and thus could be generated externally and read in as a file and placed in the plasma state. Plasma data placed in the state was in the same form (dimensionality, coordinate system, and resolution) as it was when produced by a corresponding physics component, thus preserving its as-computed precision and mathematical properties. Two implementations for the state were developed: one without any capability of saving data to files and a second with write-through capability to same simulation data for post processing or visualization. The HDF5 package was used for creating the data files.

When data from one physics component is needed as input by another, the data typically has different dimensionalities, coordinate systems, or resolutions. For example, the RF and equilibrium components are both 2-D and utilize cylindrical coordinates, while the transport component is 1-D but in a radial flux coordinate that is derived from the equilibrium properties. Thus for an integrated simulation that incorporates a range of physics, transformations are needed to allow one physics component to utilize as input data the results from another physics components. These transformations were implemented in independent components to allow ready substitution of one algorithm for a given transformation for another that better met the data needs of a particular physics component.

The computational efficiency of the RF component is particularly important for the overall performance of transport simulations. The computer time it takes for individual solutions is acceptable for single runs, typically thousands of processor-hours on present computers. However, a time-dependent plasma simulation may require tens to ~100 such runs and thus limits the simulation's potential use. As is the case for many physics problems, obtaining the solution of a large number (in the range 105–106) of linear equations is a performance-limiting step. The needed computer time for these problems scales is the cube of the number of equations. This scaling will increase the computational cost of the increased resolution (larger number of equations) required for ITER. For many problems, the standard approach to reducing the computer time for solving linear equations is the use of iterative, rather than direct, solvers. The computer time for iterative algorithms scales is the square of the number of equations rather the cube. This more favorable scaling allows higher resolution calculations for the same amount of computer time.

Successful iterative algorithms depend either on favorable properties of the linear equations themselves or on being able to efficiently find an adequate approximate solution, or preconditioner, to the equation set. The RF equations are not well suited for iteration, and finding an adequate approximate solution required as much computational work as finding the solution itself. The time of the transport simulation provided the basis for the new algorithm. As indicated above, transport simulation requires many solutions to the RF problem. These solutions are for input variables (plasma temperatures, densities, etc.) that are closely related because of their relatively slow evolutions in time.

We successfully developed an iterative algorithm for the AORSA equations by exploiting this slow evolution, namely,

1. Obtain an AORSA solution was for an initial set of plasma parameters using a direct, non-iterative solver.
2. Advance the plasma parameters in time for a period that keeps changes in the parameters themselves small and keeps changes in the resulting (step 3) AORSA solution within an acceptable tolerance.
3. Use the AORSA solution for the initial set of plasma parameters as the preconditioner to solve for the RF fields for the plasma parameters at the current time step.

This sequence could then be repeated until the RF solver no longer converged, and a new preconditioner based on the current plasma parameters could be generated. Rapid convergence using a generalized minimum residual (GRM) iterative algorithm was found when plasma parameter changes were in the range of 20–100%, depending on the parameter. This range is typical of changes during a transport simulation and should not be overly restrictive. Net impact of this new algorithm was to speed up the AORSA calculations by a factor of 2–10, depending on the desired physics results.

The previous discussion has focused on the positive aspects of what was learned in the development of a component-based simulation. The project also illuminated issues that should be addressed in such an activity. Three stand out as most significant. First, a computational modeling project must be large enough to provide computer science support to the physicists and algorithm developers on the project. CCA imposes an incremental complexity on project implementation (while providing significant advantages) and adequate computer science support is necessary to effectively meet this need. Second, proper functioning of the CCA environment requires a stable operating system environment that is consistent with the CCA implementation. New, leadership-class computers may require a significant period of time to achieve this compatibility or may not implement all of the required operating system features on a timely basis. Third, an essential requirement for developing, maintaining, and using a complex simulation such as that described above is a computer directory structure and corresponding build environment that allows researchers to work on their individual components while maintaining compatibility with other components and the CCA infrastructure. The design for this simulation employed separate directory trees for each of the four component levels, for simulation input and output data, and for so-called legacy codes that were employed in the simulation without significant modifications. Similarly, a central repository for version control was essential for organized development by the project team.

## Benefits

As anticipated, an FY 2006 program aimed towards the FSP was initiated by DOE under the sponsorship of both OFES and OASCR. ORNL and its partners successfully proposed a simulation integration project, Simulation of Wave Interactions with MHD (SWIM). Key factors in winning the award were the utilization of the technical concepts developed in the LDRD project and the strength of the combined FED/CSM team that was greatly enhanced through their the mutual understanding of physics, computer science, and algorithm issues that resulted from the combined effort. This same experience contributed to our winning a 3-year renewal of a SciDAC project on the simulation of wave-plasma interactions and to our ability to effectively use fusion as one of the program foci for ORNL's National Leadership Computer Facility proposal.

Our future efforts for follow-on funding are focused on two areas. First, we will attempt increase the size and scope of ORNL's effort in the FSP, assuming that their will be some growth in the areas as a result of increased OFES emphasis on ITER. Second, computer science direct SciDAC proposals are coming up for renewal early next year. Discussions among collaborators have lead to the using fusion simulation as one of the technical areas where domain-specific development will be proposed. The experience of ORNL CSM staff in the LDRD has increased their ability to gain a stronger position within the collaboration as well as improve the overall competitiveness of the proposal.

## References


Batchelor, D. B. February 2005. "Integrated Simulation of Fusion Plasmas," *Physics Today*, 35–40.

Dahlberg, J. et al. 2001. "Fusion Simulation Project: Integrated Simulation and Optimization of Magnetic Fusion Systems," *J. of Fusion Energy* **20**, 135–195.

Jaeger, E. F., L. A. Berry, E. D'Azevedo, D. B. Batchelor, and M. D. Carter. 2001. "All-Orders Spectral Calculation of Radio-Frequency Heating in Two-Dimensional Plasmas," *Physics of Plasmas* **8**(5), 1573–1583.

# Bringing Statistical Visualization to the Terascale and Beyond: Visual Analysis in Full Context

G. Ostrouchov,[1] D. B. Batchelor,[2] E. F. Jaeger,[2] and A. Mezzacappa[3]
[1]*Computer Science and Mathematics Division*
[2]*Fusion Energy Division*
[3]*Physics Division*

This project focused on the development of dimensionality reduction and clustering techniques that facilitate visualization of massive data sets and provide data decompositions for context in the visualizations. Visual browsing of massive data sets beyond the terascale can take an unreasonably long time when we are limited by human bandwidth to absorb and process visual input. Analysis must assist in the selection of representative views and in limiting redundant information while providing a global context. These methods were developed on a test bed of data from fusion and astrophysics simulations. The project results are mainly in dimension reduction methods that represent a new class of fast and robust algorithms and in clustering methodology that extends to massive data sets. These methods provide essential components for a scalable solution to visualization of large (terascale and beyond) simulation data sets.

## Introduction

While simulation science now routinely produces terascale data sets and will soon produce petascale data sets, browsing only one percent of one petabyte at ten megabytes per second takes 35 work days! As a result, much data is stored with little chance that it is examined in great detail or with great thoroughness. Usually, the data are reduced to a lower resolution movie of the entire simulation with surface or volume rendering or some particular slice or surface at a higher resolution. While these methods are extremely useful and provide insight, they can be considered browsing techniques that require the analyst to select the views or to sit through the entire movie. To avoid human bandwidth overload and to provide more thorough data examination, visualization must be assisted by analysis that selects representative views of interest and provides the global context for the views.

The removal of redundant information can be accomplished through dimension reduction or through clustering. In fact, because massive data sets can represent a wide range of scales and conditions, dimension reduction alone can be dominated by the larger scales and lose information at the smaller scales. Partitioning the data by clustering can reveal components at different scales that can be separately examined with dimension reduction techniques. Ideally, the process of clustering and dimension reduction should be interleaved and supervised by an analyst to direct the separation of information at appropriate scales. Another way to view this is that the analyst must be assisted by and interact with the clustering and dimension reduction software tools to discover data features at relevant scales.

Dimension reduction methods provide projections of the data into a lower-dimensional space that retains most of the data features. Traditional dimension reduction techniques, such as principal components analysis, require the computationally difficult singular value decomposition of the entire data set. Nonlinear methods add another order of magnitude of complexity. Faster methods are needed.

Clustering methods partition the data into groups, possibly of widely different sizes, where visualization of most any element of a group may be sufficient to get a sense of the entire group. At the same time, small groups often represent extreme or rare events in the simulation that may be of most interest. The clustering process allows exclusion of redundant events and highlighting of rare events. Some of the more complex clustering methods can identify clusters of widely different scales and shapes. Unfortunately, these clustering algorithms do not scale well (in terms of time and storage requirements) to the large data sets where they are needed the most. New approaches are needed.

## Technical Approach

Current scientific visualization research strives to provide ever more interactive playback or browsing of a simulation over time or a spatial dimension at various resolutions and crosscuts. The data context is typically narrow along the animated dimension. Because simulation

coverage and resolution continues to increase, browsing or watching the entire simulation becomes increasingly prohibitive even with fast data visualization engines. This project adds a component between the data and the visualization engine to assist with view selection and context generation through an analysis of the variation in the data. The focus is on the statistical methodology needed to assist the analyst in selecting views of the data. The integration of this component, within a specific end-to-end visualization system, is not attempted and is left to follow-on activities.

The vision behind "Visual Analysis in Full Context" is the following: (1) any view of a segment from a massive simulation data set should include some context of the full simulation; (2) this context is a reduction of the entire simulation into a feature space that is interpretable with respect to the application; (3) this feature space is easy to compute from the data; (4) the variability of this feature space is explored by statistical methods to provide guidance of what is interesting, what is redundant, and how can it be classified; and (5) a mapping of the feature space back to the data segments is available to provide fast access to key segments of a terascale or a petascale simulation data set.

To provide the view selection and context generation components of "Visual Analysis in Full Context," this project proceeded on four fronts: (1) fusion simulation and astrophysics simulation specific visualization—this involves bridging knowledge in fusion and astrophysics simulation with dimension reduction and clustering statistical methodology; (2) fast dimension reduction methods for feature extraction from data segments, feature visualization, and clustering workload reduction; (3) clustering methodologies for grouping data segments enabling multiscale selection of representative views and identification of rare or extreme events; and (4) leveraging the public license R statistical computing environment (R 2004), and GGobi high-dimensional data visualization tools (Symanzik 2003) as well as their connection through the Rggobi package.

## Results and Discussion

Several large data sets from fusion simulations were assimilated and made available via the R statistical computing environment. These included a wave energy conversion data set, a particle tracing data set, and a velocity stream data set in frequency domain. Some data format conversion was necessary to make this possible. For example, a C-code was written to convert frequency domain data into the time domain, providing arbitrary resolution data in two of four dimensions on two variables. Although our initial intention was to include data sets from astrophysics simulation, during the project, a decision was made to continue deeper into the fusion application with the available funding (reduced by 30% from the requested amount) without the added benefit of astrophysics simulation data. However, the general nature of the astrophysics data was considered in the design of the new methods.

A promising fast dimension reduction method from the machine learning literature, FastMap, was thoroughly examined from the point of view of statistics and its relationship to principal components analysis. We showed that this method operates on the surface of the convex hull envelope of the data and that this provides a bridge to robust methods in statistics (Ostrouchov 2005a). This result opened the way toward RobustMaps, a new class of robust dimension reduction methods that outperform principal components analysis both in speed and robustness (Ostrouchov 2004). Further work led to a matrix computation view of the method and an implementation with standard Basic Linear Algebra Subroutines (BLAS) software (Ostrouchov 2005b). The BLAS connection taps into machine specific speedups on advanced computer architectures through the BLAS infrastructure. A particularly effective variant of RobustMap that identifies outlying clusters and can take advantage of the BLAS connection was developed near the end of the project (Ostrouchov 2006).

Dimension reduction in the context of fusion simulation and astrophysics simulation data that represent the time evolution of a two- or three-dimensional system takes the form of empirical orthogonal functions (EOF). This is a variant of principal components analysis that is already popular in climate simulation and has yet to be applied in most other simulation domains. Both the RobustMap and FastMap algorithms provide a new approach to EOF-like analysis. Typically, EOF analysis is applied to the data, and then interpretation of the individual components is sought. The new algorithms developed in this project allow the opposite approach of computing components with a specific a priori interpretation. This approach has the potential to revolutionize EOF analysis as more application experience is gained with it.

To develop a clustering methodology for massive data sets, a subset of the fusion simulation data was selected. It describes radio frequency heating of Tokamak plasma and consists of four quasi-linear diffusion coefficients, b, c, e, and f, with units of velocity squared per second. Coefficient values are obtained by averaging around tubes of radius $\rho$ for a given perpendicular velocity and parallel velocity. Imagine doughnut-shaped shells of tube radius $\rho$ and binned according to perpendicular and parallel plasma velocities.We cluster the four diffusion coefficients by pooling data over the radius and the velocity pair values ($32\times65\times129$) for a total of 268,320 observations. The spatial velocity dimensions can be used to map the resulting clusters and interpret the mapped

results. This data set was chosen because it represents a particularly difficult situation for an automated clustering algorithm while providing visually stunning clusters. It is a difficult data set not only because it is large but also because cluster sizes range across several scales and are of different shapes.

Because classification is much faster than clustering, an algorithm was developed that begins by clustering a sample from the data and then attempts to classify the rest of the data into the identified clusters. The remaining data are again sampled and clustered, followed by more classification. Because random sampling most likely selects from the largest clusters, the classification step very quickly reduces the remaining data, leaving a small percentage for subsequent clustering steps and reveals clusters at smaller scales. Because this process can introduce spurious clusters, steering of the iteration was introduced via GGobi (Symanzik 2003). GGobi allows the exploration of high dimensional data with brushing and subsetting capability. Rggobi is a package that connects GGobi to the R statistical analysis environment that provides many data analysis functions, including several sophisticated clustering algorithms and a capability to use the classification functions developed in this project. Through subsetting and brushing, we introduce the ability to select data regions that can be linked back to the spatial velocity domain in the fusion application and displayed either with R or potentially outside R with fast visualization rendering software. This methodology is described in by Bensmail et al. (2006).

Our initial intent to strongly leverage our collaboration with the Scientific Data Management Integrated Infrastructure Software Center project through its parallel-R implementation and ASPECT infrastructure proceeded at a slow pace in response to our budget reduction and also to allow ASPECT and parallel-R to grow more mature under the SDM SciDAC. This collaboration will become more important in follow-on activities.

## Benefits

DOE is the premier agency for simulation science research in its energy-related missions, where visualization of the resulting data from such simulations drives scientific discovery and progress. So far, statistics has seen very little use in simulation science. This project was initiated to bring the tools of statistics, the science that is centered on methods for dealing with variability, to simulation science data and to establish ORNL as a place for statistics research that is relevant to simulation science. At present, there are no other statistics programs at other DOE laboratories that focus on simulation science.

Statistical analysis–driven visualization is critical for exploration of massive data sets whose size prevents effective browsing with scientific visualization alone. The enabling methodology developed under this project has very broad applicability to domains other than fusion science and astrophysics considered here and will benefit research in other domains across most federal agencies. Although one must consider application goals and specifics in each domain, the enabling visual analysis methodology developed under this project can be a major component of any strategy for exploration of massive data sets. Further development can integrate this methodology within an end-to-end solution to visualization in specific simulation science domains.

## References


Bensmail, H., A. Buddana, and G. Ostrouchov. 2006. "Steering of Iterative Clustering to Uncover Multiscale Structure in Large Data Sets," *Journal of Computational and Graphical Statistics* (in preparation).

Ostrouchov, G. and N. S. Samatova. 2004. "Embedding methods and robust statistics for dimension reduction," Proceedings of COMPSTAT 2004, 16th Symposium of IASC, August 23–27, 2004.

Ostrouchov, G. and N. S. Samatova. August 2005a. "On FastMap and the Convex Hull of Multivariate Data: Toward Fast and Robust Dimension Reduction," *IEEE Transactions on Pattern Analysis and Machine Intelligence* **27**, 1340–1343.

Ostrouchov, G. 2005b. "A matrix computation view of some distance based dimension reduction algorithms," *SIAM Journal on Matrix Analysis* (submitted 2005).

Ostrouchov, G., H. Kettani, and L. Lovett. 2006. "RobustMap-L: Distance Based Robust Dimension Reduction with Outlying Cluster Detection," *Journal of Computational and Graphical Statistics* (in preparation).

R. Development Core Team. 2004. R: A language and environment for statistical computing, R Foundation for Statistical Computing, Vienna, Austria, 2004. http://www.R-project.org

Symanzik, J., D. F. Swayne, D. Temple Lang, and D. Cook. 2003. "Software Integration for Multivariate Exploratory Spatial Data Analysis," Book Chapter (based on earlier proceedings paper), http://www.ggobi.org/publications/software-integration.pdf.

# Nanochemistry: The Bridge from Materials to Biological Sciences

B. G. Sumpter, D. W. Noid, R. Harrison, B. C. Hathorn,
W. A. Shelton, V. Meunier, and R. Toedte
*Computer Science and Mathematics Division*

Chemistry at the nanoscale involves the unique properties associated with assemblies of atoms or molecules on a scale between that of the individual building blocks and the bulk material. At this level, quantum effects are usually significant, and innovative ways of carrying out chemical reactions become possible. In this project, we began the development of a computational chemistry effort to examine the dynamics, chemistry, and chemical physics of molecules confined at the nanoscale level. This project has provided new fundamental insight into chemistry and chemical physics of nano-confined systems that could lead to the development of new materials, advances in biotechnology, and modern computational tools bridging chemical, materials and biological sciences.

A long-standing goal in materials science and engineering has been the understanding, controlling, and designing of mechanical and physical properties of matter at the nanometer scale. However, for the most part, this goal has largely proved elusive, even with the advent of high-resolution force spectroscopy instruments that make it routinely possible to measure the physical properties of materials at the molecular level. The complexity of real materials with their intriguing interplay between chemical composition, atomic arrangements, microstructures, and macroscopic behavior makes computational modeling and materials design extremely difficult. Even with the fundamental laws of quantum mechanics and statistical physics, the availability of high-performance computers, and with the growing range of sophisticated software accessible to an increasing number of scientists and engineers, the goal of designing novel materials from first principles continues to elude most attempts. On the other hand, computational experiments have lead to increased understanding at the atomistic level of molecular structure and dynamics. In particular, quantum chemistry, molecular dynamics and mechanics studies have yielded a great deal of knowledge on the fundamental structural and dynamical behavior of various molecular-based materials as a function of temperature, pressure, composition, etc. With the availability of high-resolution local probe microscopy and spectroscopy techniques and advanced structural characterization facilities such as the Spallation Neutron Source (SNS) and Advanced Photon Source (APS) combined with advanced computer facilities and with modern chemical synthetic control of volume fractions of components involved in self-organized micro and nanophase-separated morphologies, such as block copolymers, self-assembled monolayers, and nano-particles, renewed excitement in the pursuit of controlling physical properties has emerged.

ORNL is uniquely positioned to play a key role in making breakthrough advances in nano and biotechnology R&D by integrating advanced computing with physical, chemical, materials, and biological sciences. It is critical that the recent and forthcoming dramatic boosts in supercomputing power be matched by corresponding increases in the capabilities of scientific modeling and simulation codes. We are well positioned to address the rigorous multidisciplinary effort of designing, building, tuning, integrating, and using computer codes to accelerate the solution of emerging or existing complex scientific problems. This LDRD leverages this situation toward developing major breakthroughs in applying and developing computer simulation and modeling methods for examining the complex and unknown chemistry and chemical physics of molecules confined at the nanoscale. The subject proposal, by its very nature of examining the forces of molecular recognition that are critical to self-organization processes as well protein structure, DNA, host-guest complexes, and crystal packing, addresses multiple ORNL thrust areas: advanced materials, biological, chemical, terascale computing, and nanoscale sciences.

## Objectives

We propose the development of a computational chemistry effort to examine the dynamics, chemistry, and chemical physics of molecules confined at the nanoscale level, such as inside carbon nanotubes, ordered nano-pores, or nano-particles. By addressing these fundamentally important processes, enormous benefits in terms of development of new methods for producing desired materials products and the production/optimization of novel computer simulation and modeling tools are expected.

## Technical Approach

The proposed/on-going project has stimulated not only novel scientific discoveries but also breakthroughs in modern simulation codes for examining dynamics and chemistry of materials at the nanoscale. The computers in the National Leadership Computing Facility (NLCF) were crucially important for enabling realistic simulation of many physical processes that, for example, require long-time simulations using either classical or ab initio dynamics. In order to develop a fundamental understanding of how nano-confinement influences chemistry, we performed a number of advanced computational experiments. Major developments in the fundamental understanding of how confinement at the nanoscale alters chemical reactions and dynamics was founded on our expertise in simulation of soft-matter nanoparticles and carbon nanotubes, as well as the fluid flow within the nanotube structures. These particular systems are extremely attractive since nanotubes can be synthesized with variable length, diameter, helicity, and with multi-terminals, and polymeric nanoparticles can be easily produced with controllable size and composition. Of particular interest is examination of where non-classical effects of confinement occur and how this can be used to optimize the properties or induce novel chemistry. This can be studied by simply changing the diameter of the carbon nanotube. A number of possible effects can occur ranging from the mechanical restriction (a classical property) to more complex quantum phenomena as the diameter gets smaller. Understanding the influence of variables such as the nanotube diameter, coupling to phonon nanotube modes, and effects of helicity of the carbon nanotube on chemical reactions will be critical for developing new concepts for nano-chemical materials synthesis.

In this project, we have examined several different nano-confined environments: (1) simple carbon nanotubes; (2) carbon nanotube reaction chambers; (3) nano-holes/pores in the surfaces of various materials; (4) nano-particles. Chemical reaction dynamics and energetics (barrier heights and reaction pathways) of relatively simple molecular species, such as bond dissociation and/or isomerization of small alkanes and phenyl compounds, will be examined in these environments. Comparisons to the analog reactions in the gas or solution phase without nano-confinement can be made to elucidate experimentally observable effects.

## Results

We have successfully shown how the transition state of a chemical reaction can be strongly altered by confinement in a carbon nanotube (Fig. 1). Two processes were studied: (1) thermal pyrolysis of hydroxy substituted para-phenylethyl ether, a model of lignin pyrolysis that is important in optimization of renewable resources conversion into higher value products and (2) internal isomerization of hydrogen peroxide. From extensive first-principles calculations on the model lignin compounds, we have found clear evidence for an intramolecular hydrogen-

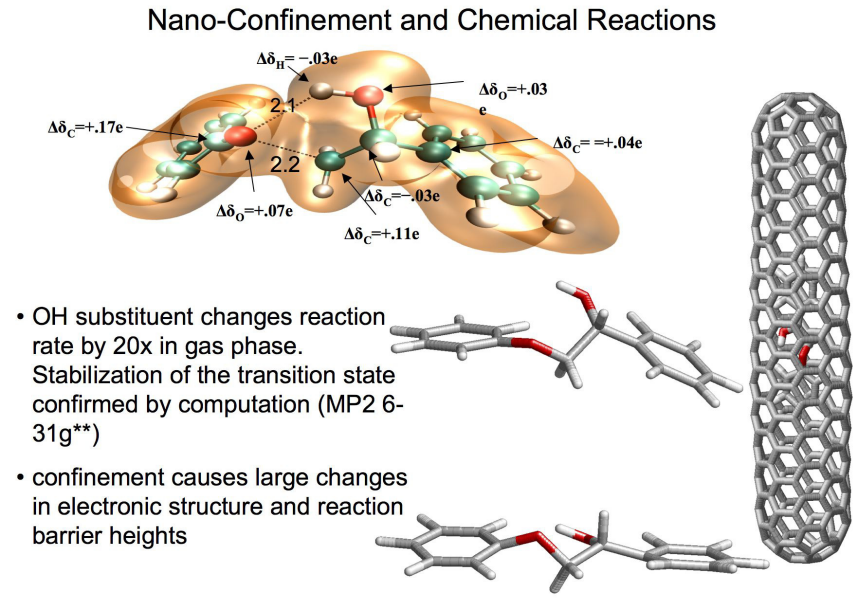


*Fig. 1. Total charge density isosurface (top center) of the transition state determined from multi-reference electronic structure calculations. The change in effective charge from the equilibrium geometry is shown for each atom. The effects on the barrier to the reaction transition state and on its geometry are also shown.*

bonded mediation of the reaction transition state, which lowers the activation energy for thermal pyrolysis 3 kcal/mol, and thereby enhances the rate of reaction by an order of magnitude over that without an intramolecular hydrogen bond. This effect is also noted under nano-confinement provided by a carbon nanotube, but an additional enhancement from electronic confinement is found to occur. These results are in good agreement with recent experimental results at ORNL for reactions in nano-porous silicates (Britt et al, Chem. Comm. 2004). The following conclusions have been obtained which may have numerous ramifications for tailoring the rates of chemical reactions as well as enhancing the efficiency of some types of chemical separations:

- Intramolecular hydrogen bonding leads to a significant modification of the thermally induced chemical reaction rate.
- Nano-confinement tends to reduce the activation energy of the transition state for these types of molecular systems.

In addition to these accomplishments, we have been able to perform large-scale ab initio quantum calculations for the effects of encapsulating different organic molecules inside carbon nanotubes (Fig. 2). In order to investigate and optimize the electronic transport processes in carbon nanotubes doped with organic molecules, the large-scale quantum electronic structure calculations were coupled with a Green's function formulation for determining the quantum conductance. This approach is based on an original scheme where quantum chemistry calculations on finite systems are recast to infinite, non-periodic (i.e., open) systems, therefore mimicking actual working devices. Results from these calculations clearly suggest that the electronic structure of a carbon nanotube can be easily manipulated by encapsulating appropriate organic molecules. Charge transfer processes induced by encapsulated organic molecules lead to efficient n- and p-type doping of the carbon nanotube. Even though a molecule can induce p- and n-doping, it is shown to have a minor effect on the transport properties of the nanotube as compared to a pristine tube. This type of doping therefore preserves the intrinsic properties of the pristine tube as a ballistic conductor. In addition, the efficient process of charge transfer between the organic molecules and the nanotube is shown to substantially reduce the susceptibility of the π-electrons of the nanotube to modification by oxygen while maintaining stable doping (i.e., no de-doping) at room temperature. These results show, for the first time, clear capability for using organic molecules to achieve n- and p-type doping and complement some very recent experimental measurements. The following conclusions and new capabilities were obtained:

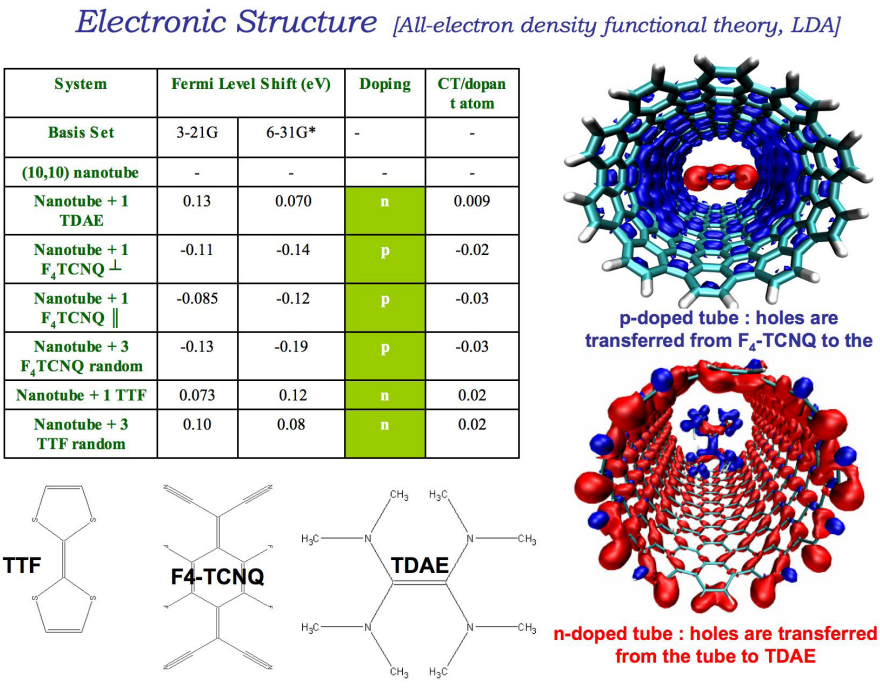


*Fig. 2. Summary of the effects of amphoteric doping on the electronic structure of carbon nanotubes.*

- We have been able, for the first time, to perform very large-scale calculations of the electronic structure and quantum transport properties of doped carbon nanotubes by using quantum chemistry calculations on finite systems that are recast to infinite, non-periodic systems.
- Electronic structure of a carbon nanotube can be manipulated by encapsulating organic molecules, which can be optimized using these new computational methods.
- Charge transfer processes induced by encapsulated organic molecules can lead to efficient n- and p-type doping of a single-walled carbon nanotube.

We have also obtained far-reaching results on how confinement of molecules to nano-sized particles can influence the geometric and electronic structure and subsequent excited state properties (Fig. 3). Extensive computational simulations were used to investigate the dynamics and resulting structures of a number para-phenylenevinylene (PPV)-based polymers and oligomers [PPV, 2-methoxy-5-(2'-ethyl-hexyloxy)-p-phenylenevinylene → MEH-PPV, and 2,5,2',5'-tetrahexyloxy-7,8'-dicyano-p-phenylenevinylene → CN-PPV]. The results show how the morphology and structure is controlled to a large extent by the nature of the solute-solvent interactions in the initial solution phase preparation. A good solvent such as dichloromethane generates non-compact structures with more of a defect-extended chain like morphology, while a bad solvent such as toluene leads to compact organized and folded structures with rod-like morphologies. Secondary structural organization is induced by using the solution-phase structures to generate solvent-free single-molecule nanoparticles. These nanoparticles are very compact and rod shaped, consisting of near-cofacial ordering of the conjugated PPV chain backbones between folds at tetrahedral defects ($sp^3$ C-C bonds). Supporting experimental evidence was provided based on both Fluorescence Correlation Spectroscopy in solution (FCS) and high-resolution fluorescence imaging of individual nanoparticles combined with atomic force microscopy and polarization modulation studies. Some of this work has been highlighted in the 2005 PITAC (President's Information Technology Advisory Committee) June 2005. The following conclusions have been obtained:

- Modified photophysical properties of single-polymer chains can be obtained by using the appropriate solvent and ink-jet printing techniques.
- The photostability and spectral bandwidth are superior to inorganic quantum dots under ambient conditions!
- First definitive evidence of single-site emission in a conjugated polymer system.
- Provided evidence for distance-tunable long-range interactions between individual particles.

## Benefits

This LDRD project is highly relevant to DOE's programs in basic energy sciences, advanced computing, biology, materials and chemical sciences, and energy resources. It addresses fundamental processes that must be understood in order to bridge materials, chemical, and biological sciences. Chemical physics at the nanoscale is crucial to numerous processes involved in energy production and storage, materials properties, environmental toxicity/fate, catalysis, and chem-bio sensors.

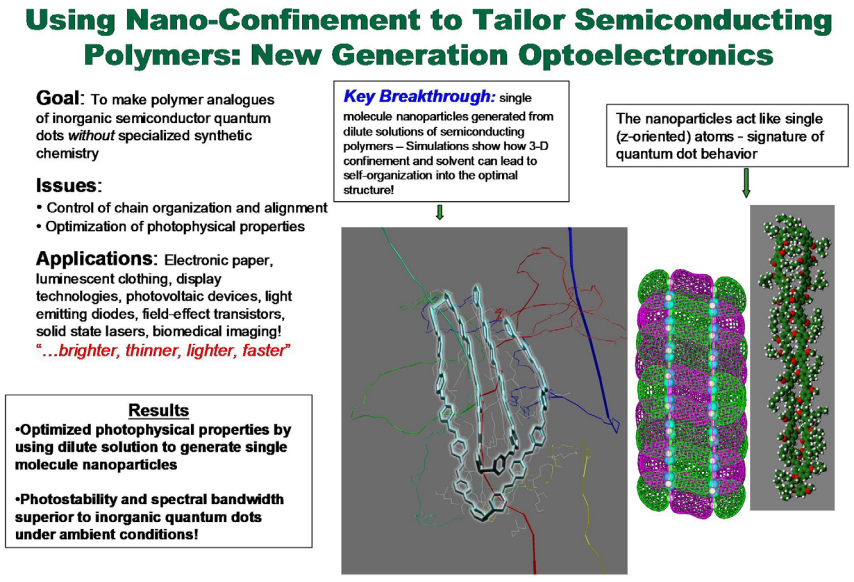


*Fig. 3. Summary of the results and new discoveries found from single-molecule semiconducting polymer particles.*

# Exploratory Computational Biology for Genomes to Life Facility II

E. C. Uberbacher,[1] F. W. Larimer,[1] P. F. LoCascio,[1] D. Tabb,[1] Y. Razumovskaya,[1] Y. Xu,[1]
M. B. Shah,[1] S. Passovets,[1] A. A. Gorin,[2] H. S. Choi,[2] T. Fridman,[2] and R. M. Day[2]
[1]*Life Sciences Division*
[2]*Computer Science and Mathematics Division*

The purpose of this project was to develop key computational technologies necessary to support the proposed Genomes to Life Facility II, "Characterization and Imaging of Molecular Machines." These include (1) computational methods for identifying and predicting the domain structure of membrane proteins; (2) next-generation mass spectrometry data analysis tools for examining protein complexes; and (3) computational methods for constrained protein docking and protein complex geometry modeling using constraints derived from experimental measurements.

## Introduction

ORNL has identified as a major strategic goal the establishment of large-scale facilities to understand molecular machines as part of the Genomics:GTL program. Genomics:GTL Facility II is focused on the "Characterization and Imaging of Molecular Machines" and is ideally suited to ORNL's core strengths in mass spectrometry, structural biology, computational biology, and computing. It will leverage the high-performance computing capabilities of the Laboratory, the Spallation Neutron Source (SNS), and the Center for Structural and Molecular Biology. This project developed specific technological capabilities which have been identified as necessary for such a facility. Understanding the organization, function, dynamics, localization, and role of the many thousands of macromolecular complexes in microbial cells requires a combination of many different types of technologies, such as mass spectrometry and imaging, with complementary views of events and interactions. To make mass spectrometry effective, new algorithms were needed that provided quantitation, post-translational modifications, cross-linking, and peptide identification. Computational methods are needed to interpret confocal image streams and to track and classify events. An additional challenge was to develop methods that incorporate experimental constraints to assist protein docking and molecular machine modeling.

## Technical Approach

Understanding the organization, function, dynamics, localization, and role of the many thousands of macromolecular complexes in microbial cells will require a combination of many different types of technologies with complementary views of events and interactions. Quantitative mass spectrometry can provide data about when and under what conditions proteins are expressed and at what level. This type of information provides clues to proteins that are co-expressed and may interact together in a protein complex, or through less stable more transient interactions. Mass spectrometry can also be used to directly observe protein associations in more stable isolated complexes. Techniques such as chemical cross-linking may stabilize such interactions and provide evidence for structurally adjacent residues in such complexes and interprotein distance constraints. To make mass spectrometry effective, new algorithms are needed that deal with quantitation, post-translational modifications, cross-linking, and peptide identification.

As a complement, confocal microscopy is planned as a component of Facility II because it allows direct visualization and tracking of individual molecules (with fluorescent labels) in a cell. It has the potential advantage of being able to recognize very transient interactions in living cells and also potentially locating where in the cell interactions occur. Confocal microscopy can also be used to track the migration or trafficking of proteins, RNAs, or complexes within the cell. It does not, however, provide much interaction detail and is currently a largely manual and labor-intensive method. Software and algorithms to track movement, migration and trafficking, and automatically recognize, count, and time protein interactions are needed to show a path forward toward the high throughput capability needed in Facility II. More detailed structural techniques, such as cryo-electron microscopy or crystallography, can show the atomic details which form the basis for protein interactions, assembly, and functional dynamics. Cryo-EM will become a very valuable tool for examining the relative orientations of macromolecules within complexes and provide important constraints when building structural models of macromolecular complexes. Since docking methods are often not effective, even with detailed protein structure data, an important challenge is to develop methods that

incorporate experimental constraints to assist protein docking calculations by greatly reducing the search space for docking and limiting possible interaction orientation and geometry. Docking and multiple protein modeling software that utilizes and combines various types of constraints about orientation and interacting residues into models of complexes need to be developed.

Even with this battery of techniques, complexes involving RNA, as well as membrane proteins, will require additional or alternative methods. Computational approaches can be used to at least begin to understand these as well. In the case of membrane proteins, for example, structural hypotheses can be developed from protein sequence which can be evaluated or validated by atomic force microscopes that are capable of probing the specific parts of a molecule at the membrane surface. The recent sequencing of approximately 300 bacterial genomes provides a massive dataset of membrane proteins, presumably containing numerous examples of the many types of internal and external loops that interact with other molecules. It should be possible to derive the basic elements of the interaction language represented in this dataset. Likewise, the data now exists to survey the presence on several types of small RNAs in the combined set of bacterial genomes.

## Results and Discussion

The project focused on three goals:

Task 1 Computational methods for identifying and predicting the domain structure of membrane proteins, was pursued with a modest effort.

Task 2 Next-generation mass spectrometry data analysis tools for examining protein complexes.

Task 3 Computational methods for constrained protein docking and protein complex geometry modeling, were given the majority of resources.

In Task 1, computational methods for predicting the domain structure of membrane proteins, a proof-of-concept exercise was done to catalog functional loops in a major microbial protein family—the ABC transporters. Based on extensive phylogenetic tree generation, analysis, and manual functional annotation of the ABC transporter protein family, each loop type correlated to the specific function of the transporter from which it was derived. Clusters of loop types were then generated using a minimum spanning tree approach. This catalog was then evaluated for its ability to identify the function ABC transporters in a test set using a statistical approach. Specific functions could be identified in test proteins even when the overall protein was not very similar to functional relatives. Resources limited extension of this analysis to other large membrane protein families represented in the body of microbial genomes.

In Task 2, next-generation mass spectrometry data analysis tools, new mathematics, statistics, and algorithms have been developed which increase the computational discrimination of individual peptides in very complex mixtures. This was accomplished using several different approaches to parts of the peptide identification problem including (1) improved scoring functions for statistically rigorous match of experimental and theoretical spectra; (2) de novo identification of ion types in experimental spectra; (3) improved methods for theoretical fragmentation models; (4) methods for combining individual peptide hits to estimate significance of a protein hit in a database; and (5) framework codes that incorporate the above functionalities. These developments are described briefly as follows.

### *Statistically Rigorous Scoring Functions*

Two scoring systems have been developed that significantly improve the state of the art for peptide identification. These include the Hypergeometric Luck Algorithm (HyLA) and the Multinomial MASPIC function. These algorithms are about 100 times faster than the scoring function used in SEQUEST (Yates 1996) and have significantly greater accuracy and lower false positive rate when tested on standard protein mixtures from several sources. The MASPIC algorithm shows an improvement of 20% in accuracy for both the trypsin and complete digest cases and has also implemented a capability to utilize theoretical intensity information from theoretical fragmentation models. It has been published in *Analytical Chemistry* (Narasimhan et al. 2005) and has received significant press coverage (MASPIC 2005).

### *Probability Profiles Method (PPM)*

In the long term, we expect to use a hybrid set of methods that combine de novo and database search approaches to more accurately recognize peptides and proteins in experimental spectra for complex mixtures. PPM represents a partial de novo method that achieves reliable identification of the main fragmentation peaks and efficiently separation of them from other ions and chemical background. The method utilizes patterns recognition in the main peak spectral neighborhoods, which are formed by the satellite peaks corresponding to the loss of various chemical groups, and provides a range of new algorithmic capabilities, including the construction of de novo tag sequences connecting high probability b-ions peaks (PPM-Chain). Preliminary results indicate that a large majority (~70%) of the useful peaks in MS/MS spectra could be identified with a surprising level of confidence, providing the strong foundation for a range of new algorithmic capabilities in MS/MS data analysis.

***Parent Charge Determination***

A neural network systems has been developed that accurately (98%) determines the parent charge of a mass spec ion by combining peak neighborhood information from PPM and global information about peak differences in the spectrum. This identification eliminates experimental spectrum searches against the peptide database using the incorrect charge, thus improving computational efficiency and reducing the false positive hit to about one-third of that in SEQUEST. This becomes very important when very complex mixtures of proteins are examined such as from whole proteomes or microbial communities.

***Improved Theoretical Fragmentation Model***

A decision tree system has been developed to incorporate sequence-dependent fragmentation phenomena into prediction of theoretical intensities. Rules were derived and generated from a very large body of experimental spectra. This system improves the accuracy of experimental-theoretical spectrum matches compared to naïve models and is compatible with the MASPIC scoring system.

***Protein Statistical Scoring from Peptide Matches***

A neural network system has been developed that utilizes peptide hit lists and combines peptide hits to produce a statistical estimate for the proteins with multiple peptide hits. The system is based on the individual peptide scores, possible alternative matches for the same peptide spectrum, and the level of coverage and redundancy of peptides in the protein. The system was trained and tested on a number of standard protein mixtures for different sources.

***The DBdigger Framework Code***

A modular framework code has been developed that flexibly incorporates a number of the above technologies and is structure for high-throughput analysis of tandem mass spec data. It is specially designed to improve the efficiency of the large database search problem and is being used in the ORNL pilot project. It has been published in Analytical Chemistry (Tabb 2005).

***The MASPIC Framework Code***

A modular framework code incorporating MASPIC and a new type of database search strategy has been constructed and deployed. In Task 5, constrained modeling of protein complexes, several methods have been developed to improve initial structure models and incorporate constraints to achieve accurately docked models, and a high-performance protein docking pipeline has been constructed using these technologies.

***Protein Docking Pipeline***

The pipeline integrates multiple codes and implements three principal stages of the protein assembly investigation: (1) initial refinement of the docking components; (2) calculations of the potential energy grid and generation of the decoys; and (3) scoring and filtering of the decoys based on synthetic experimental distance constraints.

***Protein Model Improvement***

To improve protein structures generated by homology, we developed an implementation of new conformational space sampling algorithms based on genetic algorithms and which utilize protein family information to guide the search. This has improved the accuracy of such structure models by about 0.4A for threaded protein structure models.

***Experimental Constraints in Docking Codes***

Several methods were developed to integrate experimentally derived constraint filtering into docking results and into the Fourier space potential for docking. These methods were built into the PALES docking code (Zweckstetter 2000). These included the application of distance constraints and geometry or orientation constraints generated by residual dipolar coupling data. An example of docking using distance constraints is shown in Fig. 1. A version of the code was adapted for the Eagle computer at the ORNL Center for Computational Sciences.

## Benefits

This LDRD effort focused on designing and implementing key technologies for Genomics:GTL and systems biology in general. These technologies are needed to understand complex biosystems in environmental or pathogenic microbes, in environmental systems involving microbes and plants, and in human disease. A number of agencies including the Department of Energy (DOE), National Institutes of Health (NIH), National Science Foundation (NSF), and the Department of Homeland Security (DHS), have initiatives for which this technology is highly relevant.

## References

Yates III, J. R., A. L. McCormack, and J. Eng. 1996. "Mining Genomes with MS," *Anal. Chem*. **68**, 534A–540A..

Narasimhan, C., D. L. Tabb, N. C. Verberkmoes, M. R. Thompson, R. L. Hettich, and E. C. Uberbacher, E. C. 2005. "MASPIC: intensity-based tandem mass spectrometry scoring scheme that improves peptide identification at high confidence," *Anal. Chem.* **77**, 7581–7593.

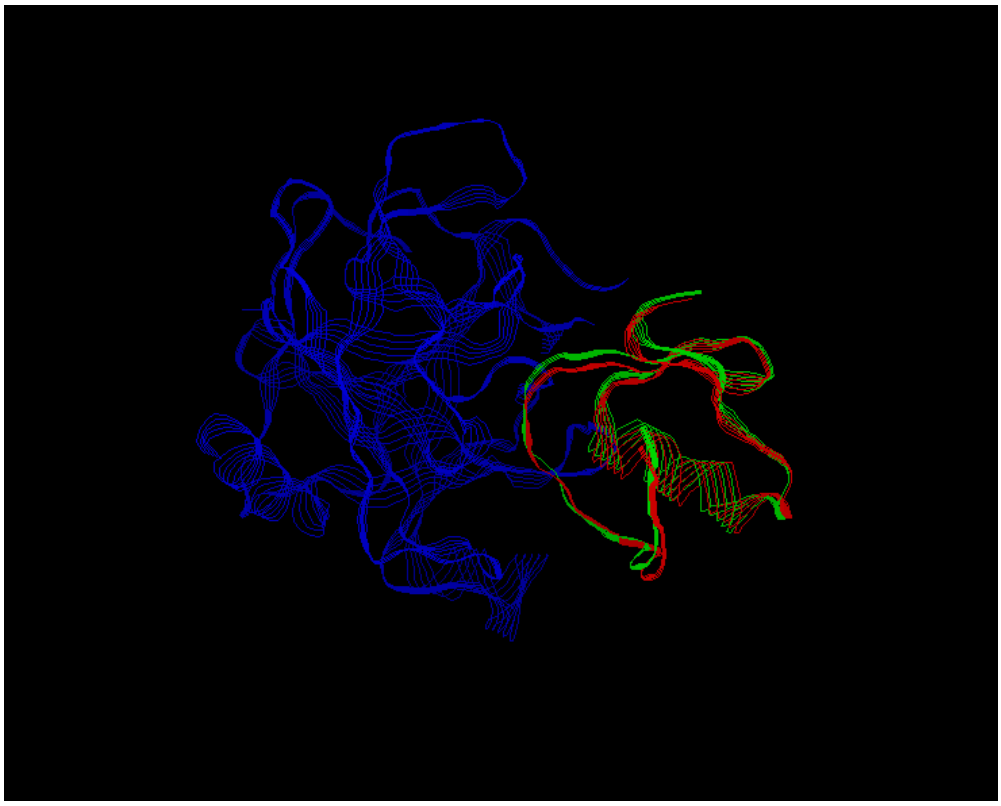

*Fig. 1. An example of constrained docking obtained using "Pales" and docking systems and software built in the project. The two chains E & I of the 1cho protein from PDB. This is an example of a complex of mid-sized proteins, where the whole complex fits into the cubic grid with 128A side. For such system docking procedure, simulated residual dipolar coupling data was used and the search was done in a few minutes using 8 processors of the IBM RS/6000 SP (the Eagle computer at the ORNL Center for Computational Sciences). The results of the docking procedure (red) are compared to the crystal structure (green).*

MASPIC press coverage: http://www.separationsnow.com/coi/cda/detail.cda?id=11405&type=Feature&chId=8&page=1; http://pubs.acs.org/subscribe/journals/jprobs/4/i06/html/i06toolbox.pdf?sessid=6006l3

Tabb, D. L., C. Narasimhan, M. B. Strader, and R. L. Hettich. 2005. "DBDigger: reorganized proteomic database identification that improves flexibility and speed," *Anal. Chem.* **77**, 2464–2474.

Zweckstetter, M. and A. Bax. 2000. "Prediction of sterically induced alignment in a dilute liquid crystalline phase: aid to protein structure determination by NMR," *J. Am. Chem. Soc.* **122**, 3791–3792.

# Information Analysis and Fusion for Threat-Vulnerability Analysis

R. M. Patton,[1] T. E. Potok,[1] T. F. Gee,[2] and K. W. Tobin[2]
[1]*Computational Sciences and Engineering Division*
[2]*Engineering Science and Technology Division*

Vast amounts of textual, image, video, and signal information are being produced that are critical for the security of the United States. The U. S. Department of Homeland Security Technical Intelligence and Information Analysis portfolio lists as a goal to create "New analytical methods and tools for sensor fusion and the synthesis/analysis of text, imagery, sensor measurements, and other information [that] are presented in a scenario-based, analyst-driven computational environment." We propose to demonstrate an information analysis and fusion system for a port security application. This system will allow us to meet the challenge of organizing, analyzing, and fusing vast volumes of information of different formats from different sources to synthesize effectively the critical information required to support homeland security needs. The overall goal is to develop an innovative multi-agent system that can (1) autonomously search through distributed information sources and retrieve new and updated information, (2) verify the information for temporal currency and structural consistency to maintain a dynamic data archive, (3) determine the value of a particular piece of information as it relates to other pieces of information, and (4) analyze and fuse the information from different sources and formats to provide for discovery of relationships among facts and the discovery of relationships between facts and potential threat scenarios. The system will be able to find, analyze, and fuse information of interest for applications such as assessment of potential terrorist threat scenarios, support and optimization of distributed ballistic target tracking, and a variety of other intelligence, security, and monitoring purposes. Our objective is to provide a threat-vulnerability analysis system that can automatically retrieve information about worldwide shipping traffic, correlate this information, detect anomalies, and then present this information to an analyst to view or to query.

The critical challenge in providing adequate security is to have the right information at the right time, such that it becomes actionable intelligence. Unfortunately, a humanly insurmountable volume of intelligence information becomes available every day. This information is produced from different sources, and consequently, different formats as well. In addition, the information is periodically updated or removed, which adds to the challenge of evaluating the information and incorporating it into decision-making or analysis processes in real-time. Another challenge is how to quickly analyze and fuse information of interest from thousands of sources. This is an impossible task at present because information is typically catalogued by content or format type and not necessarily by the facts contained in them. In some cases, the information may not even be catalogued, but simply left in its raw form. Actionable intelligence is critical for threat-vulnerability analysis and for assessing potential terrorist threat scenarios. However, the lack of an automated information discovery and analysis system that allows fast and effective retrieval, analysis, and fusion of information severely weakens the effectiveness and efficiency of using all available information for decision-making and threat analysis. Currently, experienced analysts must perform fusion of such information. As a result, much of the staggering collection of information is not utilized or significantly underutilized.

## Technical Approach

The proposed system will consist of intelligent agents that will retrieve, analyze, and fuse maritime information from across the Internet. These agents would gather new information on a regular basis, perhaps hourly or any other period chosen. They would send this information to a collection point where a merging agent would integrate the gathered information about given vessels. This merged information would then be sent to a route agent who would determine the likely route that a ship will take to get to its new location. The route agent would also determine from observation data if the ship were off course, possibly using published routes from the shipping companies. A database will be the underlying storage for information collected by these agents. The agents will record the time and date of any observation made.

This system will integrate various information sources and formats in a scenario-based, analyst-driven computational environment. Upon evaluation, the agents would then work to determine relationships between the various pieces of information and then determine how the information relates to potential terrorist threat scenarios. The result would be provided to the analyst for evaluation and validation. This system would provide the analyst with a scalable and flexible approach to information management, knowledge discovery, and synthesis and analysis of text, imagery, and other information.

There are two critical challenges to be addressed during the development of the proposed system:

- Intelligent fusion of information sources.
- Processing of images from video.

For the first challenge, there are several sources of unclassified shipping information available. Examples of these sources include the following:

- Weather reports from the ships that contain ship call sign, location, date and time. This information can be retrieved from the Web site of NOAA's National Data Buoy Center: http://ndbc.noaa.gov/data/realtime/ship_obs.txt
- Detailed ship information that includes the type of ship, ship name, ship call sign, ship owner, contact information for the ship owner, and ship tonnage. This information can be retrieved from the web site of International Telecommunication Union: http://www.itu.int/cgi-bin/htsh/mars/ship_search.sh
- Ports or newspapers that publish port traffic information. An example Web site for this information is the Port of New York, Howland Hook Container Terminal: http://www.hhook.com
- Shipping company Web sites that provide detailed ship information. An example Web site for this information is "K" Line America, Inc: http://www.kline.com/
- Imagery and video sources

The proposed system will utilize intelligent agents that collect information from specific sources. Weather reports would be recorded by a set of weather agents. These agents would extract ship locations from weather reports. Information from these sources includes vessel call sign, latitude, longitude, the date, and time. A set of port agents would be used to gather information from a collection of port Internet sites from across the world, such as Houston, London, etc. Port agents monitoring these sites would gather information about ships within a given port. This information may include the vessel name and number, port name, berth, shipping agent, country of origin, cargo, arrival date, and last port of call. Next, a set of shipping agents would gather information about shipping lines from individual corporate Internet sites, such as COSCO, K-Line America, etc. This information may include the vessel name and number, the voyage number, and the departure and arrival dates at given ports. Next, a set of image processing agents would gather images of ships in port or at sea. Finally, additional agents could be marshaled to incorporate additional information from other sources.

The computer vision task will require the interpretation of imagery supplied from satellite and/or earth-mounted cameras. This task will explore methods for detecting and categorizing vessels. By using knowledge from text data of ship schedules, we can know to look for vessels of a particular size at a particular time. The research will make use of recent advances in machine learning and statistical machine vision to create a trainable system for learning features of sea-going vessels.

## Results and Discussion

We are pleased to report the successful achievement of several key milestones identified in the original LDRD proposal. We have focused our efforts on collecting information concerning the Port of San Diego. While our efforts have been specific to this port, the techniques and approach we have used can be generalized to a variety of ports, such as Charleston. Our accomplishments include the following:

- Automated fusion of text and video information
- Development of user interface and databases
- Improved image analysis to include ship tracking

For automated fusion, we have successfully completed the initial fusing of the different information sources together using an agent-based framework. This agent-based fusion allows for the distribution of the data across multiple machines providing both flexibility and speed. The end result of this fusion is a ship profile that describes the various pieces of information from the different sources about a particular ship. With the initial fusion of the information completed, our future work in this area is the development of advanced, automated analysis techniques on these ship profiles that will be needed for threat vulnerability analysis. These techniques include efforts to assess the uncertainty of the data and potential threat, analysis of the temporal aspects (i.e., two ships arriving at the same time), and potential collision detection.

In addition to the automated fusion, we have also successfully completed an initial prototype of the user interface and associated databases. This interface displays information contained within the ship profile (created via the fusion process). This information consists of output images from the image analysis software, mapping of the ship coordinates to a global map, and information about the characteristics of the ship such as the call sign, dimensions, and type of ship. Future work in this area will include the addition of information from the automated analysis techniques to be developed, and refinement of the interface for ease of use.

Finally, for image analysis, our previous work on background subtraction has been utilized to perform tracking on multiple moving objects on the ocean (i.e., ships). This tracking uses rules based on movement, area, and other features to maintain the centroid coordinates of the moving object. Features that are obtained from the

object enable ships nearby each other to be discriminated. In addition, the view of the ocean has bean divided into zones, and the video processing outputs the current zone for each object. By utilizing this zone information, the software can more easily detect the behavior of a ship (i.e., entering or exiting the port). In addition, by calibrating to satellite information, the tracking coordinates have been registered to the ocean surface to enable a real-world understanding of each ship's position. Finally, preliminary development has been performed on fast object detection algorithms that use coarse Haar-like wavelet features. This would be a means to add robustness to the background subtraction approach and improve tracking in noisy conditions.

## Benefits

The draft DHS program literature clearly states that a significant future challenge will be the development for this type of information analysis and fusion. The investment in this program is substantial. If we expand our strengths in information analysis and fusion to include various media types, we will have a capability that is unrivalled within the DHS science and technology community. In addition, we have been asked to develop this type of capability by a number of intelligence organizations, TSWG, and this is of great interest to the Army's Future Combat System program, which has been extensively briefed on our capabilities. Furthermore, the proposed system would position the Laboratory to successfully support the U.S. Department of Transportation's Marine Transportation System vision in the year 2020 (MTS Vision 2020). This vision identifies the need for an intelligent transportation system that "is a collection of electronic communication and information systems and networks that provides the means for collecting, storing, retrieving, analyzing, and disseminating up-to-date information required by all MTS stakeholders and users." The proposed work would be of interest to the U.S. Coast Guard since a strategic objective of the USCG is the protection of maritime infrastructure and the protection of the U.S. Marine Transportation System.

# A Neutron Science Portal Infrastructure to Facilitate Remote Access to Spallation Neutron Source Data and Computation

S. S. Vazhkudai and G. A. Geist
*Computer Science and Mathematics Division*

The goal of this project was to develop an architectural framework for a generic portal infrastructure for the SNS user community that can easily evolve over time to include changing user/facility requirements/capabilities. Further, such a portal could eventually mature as a single gateway where SNS users point to for their neutron science needs. These user needs might include running experiments on SNS instruments using the beam time, analyzing the data generated using tools at the central SNS repository, locating datasets of interest, visualizing results of the analysis operations, collaborating with other users, running the analysis on the facility's high-end computational resources or the Grid. We have designed and deployed a prototype neutron science portal at SNS that shows proof-of-concept for all the above features. It has been demonstrated to the SNS instrument scientists and the international neutron community.

## Introduction

The Spallation Neutron Source (SNS) at ORNL is intended to mature into a facility wherein the neutron user community can run their experiments, generate massive datasets, locate datasets of interest, perform analysis and data reduction operations on this data, render and visualize them, collaborate with other users in the community, and run the analysis on the facility's high-end computational resources or the Grid. These are complex sets of operations, each with their own graphical user interface (GUI) components, associated interfaces, and internal functionality and could be potentially developed by diverse groups. Our design brings all of this functionality under one umbrella, which acts as a single gateway where neutron scientists can go to for their needs. In our proposal, we had put forth the development of an object-oriented generic portal framework that provides a template for the aforementioned service composition and development.

In this report, we document our technical approaches and results in this regard. First, we developed a service-oriented framework for the portal comprising of several individual components. Second, we developed individual component services themselves that encapsulate the inner workings of several features and addresses specific SNS user requirements such as analysis, data management, etc. Finally, we developed a presentation instance of our portal pilot as a Web interface, which has been successfully deployed for use by SNS user community.

## Technical Approach

The intent of our project was to develop an architectural framework for a generic portal infrastructure for the SNS user community. A generic portal infrastructure can easily evolve over time to include changing user/facility requirements/capabilities. Further, such a portal could eventually mature as a single gateway where SNS users point to for their neutron science needs. These user needs might include running experiments on SNS instruments using the beam time, analyzing the data generated using tools at the central SNS repository, locating datasets of interest, visualizing results of the analysis operations, collaborating with other users, running the analysis on the facility's high-end computational resources or the Grid, etc. As can be seen, these are diverse sets of operations, each replete with its own user interfaces, complex internal functionality, etc. There are several benefits in bringing together these services into one fold. First, this would let SNS control the data generated. Second, datasets and operations on them can be annotated with metadata and can thus be made available for future researchers. Third, by way of users coming to SNS for their analyses needs, high-quality, validated software can be provided to the community. Finally, SNS can make available several commercial/legacy software and to the community at large that an individual user cannot afford in isolation. Thus, there is the need to bring all of this functionality under one umbrella, which acts as a single gateway where neutron scientists can go to for their needs.

Our technical approach to this end has been to develop a service-oriented architecture, encapsulating SNS operations such as data management, analysis, visualization, etc., as services talking to each other through well-defined interfaces. This service-oriented framework is exposed to the users using a presentation layer such as a Web portal or Web services. Figure 1 illustrates this notion.

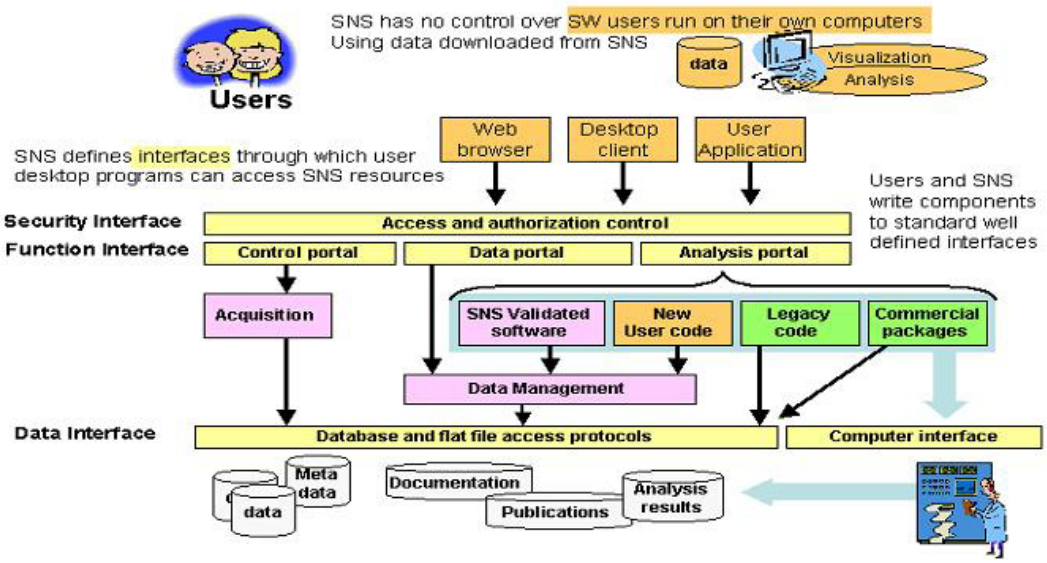


*Fig. 1. Depicts the portal's service-oriented architecture. Web browser, desktop client and user applications denote the presentation layer, Tier 1. Interface layers represent Tier 2. Services such as data management, analysis, acquisition denote Tier 3.*

We have built a three-tired Web portal architecture (Fig. 1) to facilitate remote access to SNS data and computation. Tier 1 represents the user desktop workstation with browsers and other client utilities through which users might access the SNS portal. No special provisioning is necessary in the case of browser-based accesses, in which case requests are encapsulated as HTTP messages by the browsers themselves. Accessing portal services through user desktop tools warrant special massaging of requests as Web services.Tool-based accesses to remote services are proliferating lately due to the ubiquity of Internet which has warranted building "connectivity" into tools themselves as opposed to relying only on browsers for Internet access. Thus, this implies that in addition to providing a graphical portal, a well- defined external interface to SNS services—in terms of APIs—also needs to be supported.

Tier 2 in our architecture is the generic portal framework that exports interfaces to several SNS services. The portal framework is an interface to a collection of services implementing operations such as data access, cataloging, analysis/reduction, instrument and experiment interfaces, etc., and relationships between those services. Thus the portal framework is a series of component objects/services and their entity relationships (say, "uses," "is-a," "has-a," etc.). The interface framework, defines generic guidelines a service should implement so it can be easily plugged into the framework. These interfaces provide access points to the service's GUI, internal functions, etc.

Tier 3 is the service implementation layer. These services include data management, analysis, visualization, acquisition, etc. Separation of the portal framework and the constituent components provides a clean abstraction and also several developmental advantages. In a large software initiative such as the one for SNS, it is likely that different services will be developed by different groups. The service architecture is well suited for such division of labor and creation of polymorphic service implementations.

## Results and Discussion

The prototype portal is implemented as a JAVA applet (Tier 1, presentation level) tying together backend SNS services such as data/metadata management, visualization/ simulation capabilities, and application management. The portal server is built atop the JAVA-based Tomcat server engine, version 5, and the Jetspeed portal framework, version 1.1.3. Jetspeed portal framework is primarily used for servlet/jsp executions, user customizations, and state management. Web services support is implemented through the use of Apache Axis and JAX-RPC. A neutron scientist is only required to have a JAVA Runtime Environment (JRE)–enabled browser to access the portal and its services. The prototype portal brings with it several sophisticated features such as the following:

- Ability to construct and launch simple pipelines of analysis tools for batch processing
- Ability to upload custom analysis scripts
- Integration of legacy/commercial applications such as a DAVE, ISAW, into the Web portal
- Browsing and downloading of datasets
- Launching of simple visualizations and graphs such as histograms
- Access to electronic project notebooks to annotate analyses
- Searching and updating metadata tables through database queries

At the backend, the portal runs on a Linux cluster with access to data held in NFS file systems, metadata in an ORACLE database with JDBC support and several neutron science specific pre-installed binaries and software packages.

The framework (Tier 2) level handles how the portal components interact with each other, concurrency, session management, etc. In our initial design and development, we have cast the various components (Data, metadata, analysis, communication, execution environments, etc.) as simple objects with their interrelationships (aggregations, uses, inheritance, etc). However, they can extended to Web services eventually, if need be. The internal portal design allows for concurrent sessions and accesses by several users and maintains state information in a scalable fashion.

We now elaborate on our Tier 3 service results.

- *Metadata:* While metadata about SNS datasets and analysis tools are still evolving, we needed some basic structure and mechanisms to access them in place. For this purpose, we have developed simple definitions of metadata concerning SNS datasets, analysis tools, experiments, etc. We have developed and installed these metadata schemas into databases and developed metadata services, so this information can be queried through the portal. Several user operations on analysis/data/viz portal interfaces will need to be qualified with metadata, and such metadata is obtained through our conduit servers from the database. In addition, we have developed mechanisms to perform simple searches and updates of metadata stored in databases through the portal interface.
- *Analysis/Simulation/Viz:* SNS will support two kinds of analysis/treatment functionality: those that will be custom developed at SNS users and those legacy/commercial packages that scientists currently use. All of these will reside at software repositories at SNS with metadata concerning them maintained in databases. We have developed execution environments, so both these options can be accommodated. Using our execution environments, tools residing at SNS can be invoked through the portal and executed at the server side. In addition, users can construct sequential pipelines of analysis tools passing outputs of one analysis into another. Finally, users can upload and drop their local tools into this pipeline adding to personalization of the experience.

  These tools are currently treated as cgi-style applications. However, such assumptions cannot be made about commercial or legacy applications which will almost always be interactive with some GUI interface of their own. For this purpose, we have developed mechanisms (using an applet-based X emulation) so that these applications, executing at SNS, can appear on portal users screens. A similar approach is adopted for launching instrument simulations and visualization tools.

  Further, we put forth a simple file I/O interface for these analysis tools so data can be easily passed around between them. We have demonstrated all of the above functionality including execution environments, file I/O interfaces, and pipelining.
- *Data Operations:* We have developed mechanisms so that a portal user can view, download, and upload rawdata, intermediate data, scientific data, and simulation data. In addition, users can also perform similar operations on proposals, publications, and software tools. To support these operations, we have developed a directory/file service which when installed at the SNS server side will serve portal users with their data requests.
- *Authorization:* All of the aforementioned functionality is also limited and authorized on a per user basis. For instance, users can only view datasets they are allowed to access; perform metadata operations on allowed entries; or view their uploaded or shared tools at SNS.

## Benefits

The Spallation Neutron Source facility being built at ORNL is a partnership between six DOE national laboratories (Oak Ridge, Argonne, Brookhaven, Jefferson, Lawrence Berkeley and Los Alamos) in the design and construction of world's most powerful neutron scattering infrastructure. This facility is intended for use by civilians across the world to conduct their neutron experiments, generate terabytes of data and perform computational analyses on these datasets to derive insights into science. One of the key requirements for the realization of these goals is a sophisticated software/data management solution which users can use to perform their analyses. Our portal effort is a step in that direction and attempts to abstract out software/data management services behind a well-defined user interface.

Our project has built an "application-specific portal" for SNS. SNS users will come from all across the USA and especially from academia. We have demonstrated the prototype portal and its features to the SNS instrument scientists and at two international neutron science software workshops (NeSSI 2 and NeSSI 3).

The benefit of the portal is it will make it much easier to access data, compile metadata, and to do analysis on experimental neutron data than has been possible in the past. It also makes it possible to do science in ways that have never been possible in the past by allowing analysis of data from all the experiments ever done at SNS, and by allowing publication results to be tied back to the analysis and raw data.

# Multiscale Mathematics on Massively Parallel Computers: New Tools for Computational End Stations on the Cray X1E, Red-Storm, and the IBM Blue Gene

G. Fann, W. Shelton, B. Sumpter, S. Pannala, S. Simunovic, and A. Khamayseh
*Computer Science and Mathematics Division*

We are (1) deriving and developing multiscale mathematics and fast computational algorithms that will benefit chemical physics, climate dynamics, fusion, computational materials and computational nano-biology and (2) developing general and cross-cutting mathematics and their associated algorithms for multiscale decomposition, fast summation, and associated sampling theory with emphasis on accurate assessment of multiscale multi-particle interactions (e.g., Green function) and numerical models with particle and continuum interactions. These tools will form the basis of a general multiscale tool set. We will apply these techniques to fast sampling techniques to combine a classical density functional theory/Brownian Dynamics method and a combined Kinetic Monte-Carlo/Lattice Boltzmann method and compare both approaches by simulating and validating the results with a well-studied problem of a protein in solution.

Our project is a collaboration of computational scientists, mathematicians, and computer scientists in developing new methods for massively parallel computers. In this progress report, we summarize the developments of separate tasks that will be unified during the second year of the project and applied it to testing and validating classical density functional theory/Brownian Dynamics method and a combined Kinetic Monte-Carlo/Lattice Boltzmann method.

*Task 1: Mathematical Techniques:* We have derived a sampling technique for accurate interpolation of multivariable functions involving discrete models and continuum models related by partial differential equations. This will be used in year two to integrate the Brownian Dynamics (BD)/classical density functional code through a secondary auxiliary equation.

Accurate conservative multi-resolution remapping in field simulation requires the periodic remapping of conserved quantities such as mass, momentum, and energy from an existing mesh to some other arbitrarily defined mesh. This procedure is a type of interpolation, which is usually constrained to be conservative and monotone. We have developed an integral form of this method in mapping the earth's surface orography field from initial logical mesh resolution to an arbitrary hybrid mesh resolution in two and three dimensions. Examples of this approach are shown below. This technique can be applied to climate dynamics and multi-physics based simulations, computational chemistry, computational biology, computational materials, fusion and environmental sciences.

*Task 2: Multiscale DFT:* We have implemented a fully parallel BD code based on the approach of Liu et al. (2004) on several high- performance architectures located at Oak Ridge National Laboratory for simulating polymers in solution. Using traditional approaches,

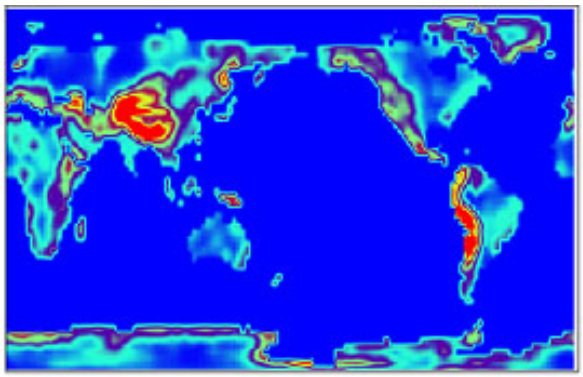

*Unstructured adapted planar mesh based on orographic field data.*

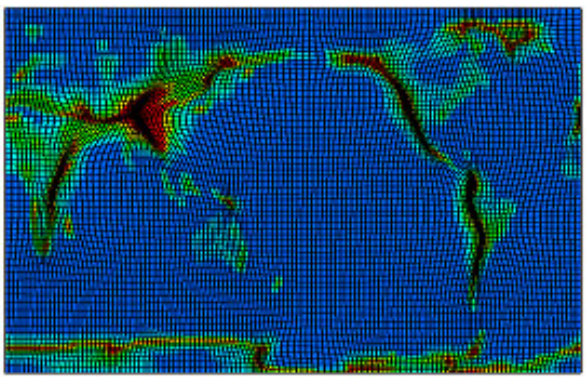

*Hybrid adapted planar mesh based on orographic field data.*

it is often very difficult to simulate the solvent along with the polymer to the appropriate time scale needed to obtain equilibrium quantities (gyration radius, etc.); however, by using BD, one can accelerate the dynamics by approximating the interaction of the solvent by a stochastic forcing term. The mathematical formulation of this dynamic process produces the well-known Langevin equation. The following lists of features incorporated in this code include flexible and semi-flexible polymers, Lenard-Jones interaction, Debye-Huckel interaction, and Ewald summation for treating long range interactions. In addition, hard-wall, Lenard-Jones wall and spheres can be included, and a variety of boundary conditions have been incorporated. We are currently validating this code by performing several simulations of polymer and bio-systems. To date, the bio-system simulation agrees well with published data (Stevens 2001). The polymer study is ongoing.

*Task 3: Lattice-Boltzmann Methods:* A prototype Lattice-Boltzmann code was implemented and validated. During year two, we will apply the sampling techniques developed to facilitate the integration of a kinetic Monte Carlo code with the Lattice-Boltzmann code. This new hybrid software will be validated and compared with the results generated from Task 2.

## References

Liu, S., B. Ashok, and M. Muthukumar. 2004. *Polymer* **45**, 1383.

Stevens, M. J. 2001. *BioPhys. J.* **80**, 130.

# Exploring Alternative Technologies for Next-Generation Leadership-Class Computing

J. S. Vetter,[1] J. Barhen,[1] N. Imam,[1] K. Roche,[1] M. C. Smith,[2] and M. Vose[3]
[1]*Computer Science and Mathematics*
[2]*Engineering Science and Technology*
[3]*University of Tennessee*

This proposal aims to investigate potential disruptive and alternative core technologies for next-generation computer architectures. In this effort, we propose to explore two prototype core technologies that address fundamental limitations of existing high-end computing systems, namely, reconfigurable computing and optical processors. Specifically, we propose to evaluate these two new technologies in the context of ORNL workloads with the goal of developing new algorithms for these architectures and providing empirical evidence to both ORNL and partner vendors about fruitful avenues for next-generation architectures. Ultimately, the purpose of this effort will be to pave the way toward petascale computing and beyond for selected scientific applications.

Our approach is to engage in a thorough assessment of two new technologies against three important ORNL application areas: computational biology, computational nanoscience, and climate simulation. ORNL will evaluate these technologies, using low-level, kernel, and application evaluations to determine their best possible performance. During this analysis, we will develop new algorithm implementations to exploit the full potential of these architectures and reconsider basic algorithm designs when appropriate. Finally, we will use actual applications codes to predict the expected sustained performance on large-scale applications.

At the highest level, the project will perform the following tasks: (1) explore the computational opportunities for each of the two emerging technologies; (2) develop algorithms for these new technologies for select applications; (3) assess the performance of each technology in terms of speed, accuracy, efficiency, and robustness on selected applications and evaluate its potential for future development; and (4) based on this assessment, develop pathways to petascale architectures.

*Reconfigurable Computing:* We have successfully implemented several FP-MAC algorithms on the SRC-6E reconfigurable computing platform. The first implementations are optimized for small matrices. Later implementations comply with BLAS function formats for SGEMV, DGEMV, SGEMM, and DGEMM. Additionally, we have begun investigation of additional areas. These include bioinformatics, climate modeling, molecular dynamics, and iterative solvers.

In molecular dynamics (MD), for example, we are currently working on the implementation of two MD applications: AMBER and LAMMPS. The goal is to sample over long continuous molecular dynamics trajectories where we can only accelerate the algorithm at the time-step level which comprises the fundamental unit of divisible work. We have ported time-consuming subroutines in Amber that lend themselves for vector operations and have interfaced it with the MAP FPGA-side of the SRC reconfigurable computer. An early publication summarizes some of our initial efforts in this area.

*Optical Processing:* We continue to develop algorithms for the Lenslet Optical Signal Processor: EnLight64. These targeted areas include signal processing, bioinformatics, and material science. In signal processing, we are building an algorithm infrastructure for computing time differences of arrival for underwater source localization using the EnLight optical core processor. Various matrix loading schemes have been developed for optimum utilization of the matrix/vector multiplier and reduction of I/O time. Lenslet is in the process of testing ORNL-developed cross-correlation and DFT algorithms. In bioinformatics, gene clustering is a useful technique to gain insight on what genes are co-regulated in an organism. The cluster center/gene scalar products are computed by a series of matrix/vector multiplications. Since the genes remain invariant throughout the algorithm, our *EnLight*$^{TM}$256 clustering implementation creates matrices whose rows are the gene vectors and carries out matrix/vector multiplications in which the "gene matrix" successively multiplies each cluster center. The Enlight algorithm always yielded a result within 10 percent of a "full precision" algorithm and sometimes performed better than its full precision counter part. Finally, in material science, we demonstrated a widely used phenomenological model of friction, in which the driven controlled dynamics of a one-dimensional particle array of $N$ identical particles moving on a surface is described by a system of $N$ coupled nonlinear equations. Through the use of successive matrix/vector decomposition and recombination techniques, it was possible to obtain results that were essentially equal to "full precision" computations, that is, computations performed outside the EnLight using double precision floating-point representations.

# A Chemistry End-Station for the Large-Scale Computing Facility (Chemical Catalysis at the Nanoscale)

R. J. Harrison,[1] W. A. Shelton,[1] B. C. Hathorn,[1] D. E. Bernholdt,[1] E. Valeev[1,2]
A. C. Buchanan III,[3] P. Britt,[2] and S. Overbury[2]
[1]*Computer Science and Mathematics Division*
[2]*Georgia Institute of Technology*
[3]*Chemical Sciences Division*

We are developing a chemistry end station (ChemES) with initial focus on chemical catalysis at the nano-scale. The eventual end station will comprise a nationwide community of developers and end users, and an integrated software suite optimized for execution of capability-class simulations on the computers planned for the National Large-scale Computing Facility (NLCF), notably the Cray X1/2 and Red Storm/Ranier. Activities include research into scalable parallel-vector algorithms and S/W architecture, prototyping of end station infrastructure, selecting, porting, and optimizing existing packages (e.g., NWChem) to the Cray-X1, applying this capability to provide early scientific results and to guide future activities, development of a national user/developer community, and establishment of requirements for end station design and functionality. The selection of nano-scale catalysis as the initial focus area reflects its strategic importance to chemistry within ORNL and DOE as a whole, its economic value to the nation, and that the resulting tools will be broadly applicable including to hydrogen storage, fuel-cell technologies, nano-bio molecular models, combustion and environmental chemistry.

Preliminary results, discussed below, led us to focus our efforts upon specific codes and kernels, providing a broad chemical capability by porting selected codes, growing in-house expertise, and to push hard at the Cray-XT3 in anticipation of this ultimately being the most effective NLCF resource for chemistry. We have considered practical design options for the ultimate endstation and engaged a wide community in these discussions. To provide a virtual center for the project, we have established a blade in the ORNL research enclave and are installing a plone server which will provide a continuously updated (by the community) source of information about high-performance chemistry. In August 2005, we held the second NLCF computational chemistry workshop. The first workshop focused upon the developer community. This second workshop expanded to include researchers interested in using applications to perform chemistry, and even touched a few experimental groups with a strong interest in theory and computation. Program development funds were provided by ORNL to organize the workshop. We have begun porting and tuning several important cross-cutting application codes to all NLCF architectures including first-principles electronic structure and classical molecular dynamic codes. These include VASP, ABINIT, PWSCF, CPMD, FLAIR and octopus, Airebo, DL_POLY, and LAMMPS. Contrary to results presented at the X1 evaluation workshop, VASP has achieved good performance on the NLCF and other resources located at ORNL and shows improved performance in going from the IBM-SP4 (Cheetah) to SGI-Altix (RAM), to Cray X1 (Phoenix) and Cray XT3 (Jaguar) architectures with very little performance tuning. The classical molecular dynamics codes presently require additional tuning on the Cray X1.

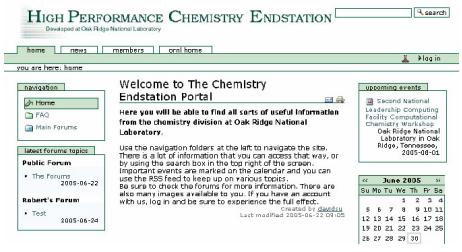


Valeev has substantially revised his automatic code generation for integrals (currently part of MPQC and PSI3) to generate vectorizable code for the Cray X1. This is initially targeting SSP mode, and he is presently evaluating strategies which vary in loop complexity (fat vs. thin loops) and assessing how well the compiler handles large register spill, etc. Among notable achievements are high efficiency (>70%) of scalar code on Intel Itanium2 and high efficiency (>70%) of vectorized code on Cray X1. Preliminary discussions of the software architecture for a chemistry end station have identified some key principles around which the design must be based as well as technology options. Discussion with collaborators and CCA developers has seemingly led to a consensus that CCA is the appropriate technology, though it remains to present these ideas to a wider chemistry audience.

# Computational Mechanics End Station: Parallel Implementation of Finite-Element Software on Ultrascale Computers and Its Application on Modeling of Human Joints

P. K. Nukala,[1] S. Simunovic,[1] R. D. Komistek,[2] M. R. Mahfouz,[2] and M. Puso[3]
[1]*Computer Science and Mathematics Division*
[2]*Computational Sciences and Engineering Division*
[3]*Lawrence Livermore National Laboratory*

General-purpose finite-element software is widely used in many engineering and industrial applications. Large-scale simulations of many of these applications are often limited by the available computational resources. We propose to develop a high-performance, implicit-finite-element (FE) computational toolkit using both finite-element tearing and interconnecting dual-primal (FETI-DP)-style iterative algorithms and a domain-wise multi-frontal sparse direct solver approach suitable for national leadership–class computer architectures. The application base of the proposed work spans materials science, engineering, and industrial applications. The basic idea is to divide the FE domain into a number of non-overlapping subdomains using the FETI-DP algorithm. Subsequently, the proposed study develops parallel iterative solvers based on FETI-DP-type domain decomposition and also investigates the scalability of parallel domain-wise sparse direct solvers (such as MUMPS and PWSMP) within the context of implicit FE calculations.

Since the inception of high-performance computing initiatives such as ASCI, SciDAC, and ASC programs, there have been significant efforts to develop high-performance, parallel finite-element codes at DOE laboratories. Currently, using ParaDyn, explicit finite-element simulations of up to ten million degrees-of-freedom are routinely performed on the ASCI-White computer (12.3 TFlops) at LLNL. However, large-scale implicit finite-element simulations are still limited only to a few million degrees-of-freedom due to the memory constraints imposed by the fill-in during factorization using sparse direct solvers and the necessity of solving large systems of linear equations during each nonlinear iteration. The majority of the computational effort in an implicit code is in solving the linearized system of equations, and the overall performance of an implicit code is significantly influenced by the performance of the equation solver.

The impetus for developing parallel implicit finite-element codes comes from two breakthroughs: (1) the advent of ultra-scale computers that possess thousands of processors and hierarchical memory architectures, and, more importantly, (2) recent developments on the numerical/algorithmic scalability of the computational kernels used in an implicit finite-element code.

The FETI-DP algorithm that we use partitions the global domain into a set of $N_s$, non-overlapping sub-domains $\Omega^s$. The variables that belong to the interior of the sub-domain are called the *local variables*, and those that interface with the adjacent sub-domains are called *interface variables*. For each sub-domain, a set of corner points are chosen such that all zero energy modes are suppressed if Dirichlet boundary conditions are applied to this set of corner points. Points where three or more sub-domains intersect are labeled as corner points C, and these are the primal variables of the problem.

Algorithmically, the FETI-DP procedure decomposes the solution of global system of equations for the entire domain $\Omega$ into three stages: (1) local solves corresponding to each of the sub-domains $\Omega^s$, which can be performed simultaneously; (2) a system of equations corresponding to the interface problem in terms of the Lagrange multipliers, which satisfies the inter-sub-domain compatibility of displacements; and (3) a global solve with at most $6N_s$ degrees-of-freedom for the coarse problem that eliminates the zero energy modes associated with each of the individual sub-domains. Since each of these smaller systems of equations is associated with symmetric positive-definite matrices, FETI-DP uses a domain-wise sparse direct solver for each of the local solves, a sparse direct solve for the coarse problem, and a preconditioned conjugate gradient to obtain the solution of the interface problem. For nonlinear problems, however, a parallel direct solve for the interface problem may also exhibit robust scalable performance since the interface degrees-of-freedom are relatively small compared with the total number of degrees-of-freedom.

In FY 2005, we have completed two essential tasks, namely, (1) porting, performance tuning/optimizing, and benchmarking the NIKE3D code on the Cray-X1, and (2) implement and interface vectorized sparse direct solvers with NIKE3D suitable for use on the Cray-X1. In

terms of benchmarking, we tested a variety of nonlinear benchmarking problems, and a large Boussinesq problem of a million degrees-of-freedom. We accomplished vector processing and multi-streaming (performance tuning) by using pat_build and loopmark listings. Performance comparison of sparse solvers (SSPOTRF/SSPOTRS) of Cray-X1 SciLib, SuperLU, MUMPS, and Vectorized Sparse Solver (VSS) has been completed. Using the VSS (which is the best on the Cray-X1 even in comparison with Cray-X1 SciLib Sparse solvers) on the Cray-X1, the NIKE3D code currently runs at 5 GFlops per MSP (out of 12.8 GFlops) and at 2.5 GFlops per SSP in SSP mode (out of 3.2 GFlops) at an impressive 3.79 Floating Point operations per load, and at an average vector length of 62. The total number of TLB misses are at an impressively low rate of 20/sec.

During FY 2006, we propose to develop FETI-DP domain decomposition algorithm for decomposing the finite-element domain so as to reduce the original large set of system of equations to a smaller set of equations expressed only in terms of the interface degrees-of-freedom. Subsequently, the smaller set (still of the order of a few million degrees-of-freedom) of linear system of equations is solved using either a parallel preconditioned iterative solver or an efficient parallel vectorized sparse direct solver that is best suitable for the ultra-scale architecture.

The proposed work develops a high-performance, implicit-finite-element computational toolkit that would enhance the existing capability to simulate large-scale, finite-element problems. The project is relevant to DOE's MICS program. In addition, the project is relevant to DOE's BES and EERE programs in terms of its use in simulating large-scale materials science and thermomechanical/structural applications. The developed high-performance implicit-FE toolkit is applicable to many scientific areas involving biomedical/biomechanics simulations, materials science, and thermomechanical/structural simulations.

# Advanced Network Capabilities for Terascale Computations on Leadership-Class Computers

N. S. Rao,[1] W. R. Wing,[1] S. M. Carter,[1] Q. Wu,[2] A. Mezzacappa,[3] and J. Blondin[4]
[1]*Environmental Sciences Division*
[2]*Joint Institute of Computational Sciences*
[3]*Physics Division*
[4]*North Carolina State University*

As the scale of computations enabled by the leading-edge supercomputers continues to increase, so will the need for network capabilities that can match their computational speeds and data rates. The ability to strategically and remotely steer large-scale computations and data movements to and from supercomputers is vital to their effective utilization. This project develops the technologies to achieve: (i) efficient realization of data paths between the internal nodes and edges of supercomputers, (ii) effective interconnections between the supercomputer and external networks, (iii) protocols to sustain high-performance data and control streams, and (iv) end-to-end optimization of multiple data and control flows.

Our overall objective of this project is to develop the technologies and expertise needed to provide dedicated network connections between the applications running on Cray X-class supercomputers and remote users. Due to the multi-faceted nature of this project, this task has been divided into a number of component areas: (a) system architecture design and optimization; (b) design, analysis, and testing of data path hardware and transport protocols; (c) application and transport module installation and experimentation; and (d) coordination and collaboration with Cray Inc.

Significant progress was made in a number of the component tasks: (i) We performed a detailed analysis of internal data paths of the Cray X1 to identify methods to improve the performance of network transport to remote client; (ii) We optimized the existing bbcp protocol to achieve 250–400Mbps from Cray X1 to North Carolina State University (NCSU). This protocol is currently being used in production mode by Terascale Supernova Initiative (TSI) investigators at NCSU. The default transport method achieved about 50 Mbps for this connection; (iii) We also developed a new protocol called Hurricane to achieve stable 400Mbps using a single stream between Cray X1 and NCSU; this protocol is specifically optimized to reach Gbps stable throughputs over dedicated channels provided by DOE UltraScienceNet and NSF CHEETAH networks. These throughput levels are the highest achieved between Cray X1 and a remote site located several hundred miles away. We designed an interconnect by utilizing a linux host called UltraScienceNet Cray Network Subsystem (UCNS) that performs media conversion. We tested a configuration of UCNS connected to the Cray X1 via four 2Gbps FC connections. UCNS is in turn connected to another linux host via 1 and 10 GigE connections. We were able to achieve 2Gbps file transfer rate using multiple bbcp streams between the Cray X1 and the host located at ORNL. We also achieved 1.4Gbps using single flow and the Hurricane protocol for the same configuration. To our knowledge, these are the highest file transfer rates achieved over Ethernet connections from a supercomputer to an external, albeit local, host for both multiple and single streams. Our results were presented at three conferences and were accepted for a journal paper.

This project provides networking technologies and expertise for making facilities, such as DOE's Office of Science's National Leadership Computing Facility, available to scientists at national laboratories and universities. There has been a surge in the procurement of supercomputers by federal agencies, including National Science Foundation (NSF), Department of Defense (DOD), and National Aeronautics and Space Administration (NASA). Providing suitable network access to such machines is vital to their effective utilization. Particularly for open research projects envisioned on NSF and NASA supercomputers, the users are distributed across the country at various institutions and universities. Our project can contribute technologies and expertise in providing the high-performance network capabilities to these supercomputers to make them accessible to users and also achieve their effective utilization. For DOD supercomputers, our methods can provide an additional level of security by isolating these flows from other network flows.

# Computational Modeling of Alloy Deformation Based on a Novel Statistical Mechanics Approach

G. B. Sarma,[1] M. N. Shabrov,[1] B. Radhakrishnan,[1] B. C. Larson,[2] J. M. Vitek,[3]
A. El-Azab,[4] and H. Weiland[5]
[1]*Computer Science and Mathematics Division*
[2]*Condensed Matter Sciences Division*
[3]*Metals and Ceramics Division*
[4]*Florida State University*
[5]*Alcoa Technical Center*

This project seeks to develop a next-generation computational capability to simulate deformation processes in structural alloys at the microstructural length scale. The new capability is based on a statistical mechanics theory of dislocations that captures both the basic dislocation mechanisms and their collective behavior during large plastic deformations. Progress during the first year includes parallel implementation of a finite-element formulation for mesoscale deformation simulations using an elastoviscoplastic crystal plasticity model and development of numerical schemes for solving the evolution equations for the dislocation densities. Implementation of these numerical schemes in a parallel code is under way, and the results will be tested and validated using data extracted from submicron resolution 3-D X-ray microscopy measurements.

Deformation of structural alloys, such as that incurred during thermomechanical processing or stress-induced failure, is characterized by complex dislocation structures that depend strongly on the crystal structure and alloy chemistry. Recent advances in parallel computing capabilities have led to much progress in the development of advanced models for structure evolution. However, current mesoscale models (microstructural length scale) based on crystal plasticity rely on empirical constitutive laws that lack sufficient rigor, while models at the scale of individual dislocations (discrete dislocation simulations) are limited to small strains and dislocation densities. The main objective of this project is to develop a computational capability to predict the evolution of complex dislocation densities and other mesoscale structures in alloys at large plastic strains by combining a statistical mechanics theory of dislocations with the crystal plasticity models.

In the statistical mechanics formalism, the plastically deforming crystal is treated as an elastic body with moving dislocations, whose motion is governed by their interactions and by the driving force arising due to internal stress in the crystal. Dislocation density is described by distributions in phase space, one per slip system, that depend on the spatial coordinates, velocity, and line orientation. A set of nonlinearly coupled kinetic equations are developed for these density functions, which, along with the conventional finite deformation kinematics and stress equilibrium equations, give rise to a closed set of equations describing the microstructure evolution. The kinetic equations are subject to a set of gauge conditions that ensures the continuity of the dislocation lines along the tangential direction. The stress field, part of which is due to dislocations, drives further evolution of the dislocation density, which gives rise to further crystal distortion and modification of the internal stress. The numerical solution scheme must solve for all these fields simultaneously.

Accomplishments during the first year include: (i) completion of the theoretical development of expressions for the source terms in the kinetic equations, (ii) development of a numerical scheme to solve the evolution equations for the dislocation densities, and (iii) parallel implementation of a finite-element formulation based on an elasto-viscoplastic crystal plasticity model to compute the deformation and elastic stress field in the material. The source terms for the dislocation model include contributions from cross slip and from short-range interactions, such as annihilation, sessile junction formation, and Burgers vector reactions. The numerical scheme to solve the evolution equations for the dislocation densities is currently being implemented in a parallel code. The solution of the kinetic equations will provide the shear rates on various slip systems for the elasto-viscoplastic constitutive model, while the elastic stress field from the finite-element formulation will drive further evolution of the dislocation densities.

The proposed computational capability will form the basis for generating entirely new levels of materials investigations through the use of unique computational capabilities at ORNL. Many DOE programs, such as Basic Energy Sciences–Materials Division, Industrial Technologies Program, etc., would benefit from such a capability, which would enable not only detailed and fundamental studies on the evolution of dislocation structures during thermomechanical processing but would also provide an advanced tool for alloy design.

# Toward Systematic Computational Instrumentation for Nanoscale, Condensed Matter, and Materials Science

T. Schulthess,[1] P. Cummings,[2] M. Stocks,[3] M. Summers,[4] P. Kent,[5]
D. Nicholson,[1] M. Fahey,[6] and T. Swain[7]
[1]*Computer Science and Mathematics Division*
[2]*Chemical Sciences Division*
[3]*Metals and Ceramics Division*
[4]*Computational Sciences and Engineering Division*
[5]*Joint Institute of Computational Sciences*
[6]*Center for Computational Sciences*
[7]*University of Tennessee*

With the National Leadership Computing Facility (NLCF), the Nanomaterials Theory Institutes of the Center of Nanophase Materials Sciences (NTI/CNMS), and the clearly stated intent to support advanced data analysis for neutron sciences at the Spallation Neutron Sources (SNS), ORNL is becoming the focal point in computational nano-, condensed matter, and materials sciences. For these three facilities to function coherently from a computational sciences point of view, there is an urgent need to systematize the computational instrumentation in the field. This project starts this process with the development of a developer-community software repository for computational nanoscience.

A software repository supporting the synthesis of the computational tools used in the NLCF and the NTI/CMS must be developed to meet two main objectives. It must first provide the means for the community's computational tools to interoperate, and second it must provide for the community's developers to collaboratively develop software and software libraries of the requisite integrity. Tool interoperability is addressed through the development of common I/O systems and data representations which are used to loosely coupled NLCF-optimized tools. Community tool development is addressed through the implementation of a collaboration server and the implementation of multi-developer configuration management systems and quality control processes. The quality control processes enable the joint development of rigorous tools whose quality is certified by standardized testing.

The technical approach to the development of a common IO subsystem involves the community development of common data representations, which are expressed using XML Schema and software libraries that can be linked into Fortran codes, permitting them to read XML input files and validate these inputs against the schemas. The reuse of the Gforge system as a basis of the collaboration server was considered and rejected because it would have been too difficult to modify Gforge to meet Laboratory security standards. Instead a similar capability was developed through the integration of an LDAP server, Subversion, Zope/Plone, and Track, a bug/feature tracking system.

To date the project has (1) launched the collaboration server SciCompForge.org; (2) developed a prototype XML I/O subsystem that is currently being incorporated into two electronic structure Fortran codes; (3) ported and optimized a version of the VASP code to the Cray X1 for which the acquired expertise is presently being encapsulated into a wave function module that will be usable in other plane wave pseudo potential-based electronic structure packages; and (4) implemented quality control procedures, including an automated documentation system for generic toolkits (see http://psimag.org).

DOE is already benefiting from the initial products of this project. The prototype XML IO subsystem is being integrated into existing codes, the collaboration server is currently in active use by many DOE projects including C3, MOLAR, Ψ-Mag, LSMS, MADNESS, and MAD++ (the latter two being SciDAC projects), and the development of the Ψ-Mag tool kit is being supported by quality control procedures, including an automated documentation system developed under this project.

# Reliability, Availability, and Serviceability for Terascale Computing

S. L. Scott,[1] A. S. Bland,[2] C. Engelmann,[1] X. Ma[1,3] and S. Vazhkudai[1]
[1]*Computer Science and Mathematics Division*
[2]*National Center for Computational Sciences*
[3]*North Carolina State University*

It can no longer be acceptable to the high-end computing community to have the world's most powerful computers sit idle (or mostly idle) at times due to unplanned downtime because of hardware failure or software interrupt. Furthermore, the availability of these systems should be minimally impacted as a result of planned downtime (maintenance). Therefore, it is the intent of this work to provide a general solution framework to enable a high level of reliability, availability, and serviceability (RAS) for terascale high-end computing (HEC) resources. Our goal is to produce a proof-of-concept implementation that will enable the removal of the numerous single-points of failure in the large HEC systems while improving scalability and access to systems and data.

High-availability (HA) computing has for a long time played a critical role in mission critical applications. Likewise, HEC has played a significant role for the scientific research community as an enabling technology for scientific discovery. Thus, it is anticipated that a successful combination of HA technology with HEC will positively impact the rate of computational scientific discovery in both academia and industry. To this end, this LDRD will produce a general solution framework that will enable a high level of RAS for terascale HEC resources. Furthermore, we will produce a proof-of-concept framework implementation that will eliminate many of the numerous single-points of failure in large computing systems while improving scalability and access to both systems and their data.

The technical approach is to first leverage our former research of distributed control algorithms in order to increase the reliability of HEC control systems in an active/active high availability framework. Common HEC services, such as the scheduler/queue systems, will then be able to take advantage of this technology, resulting in active/active model support too. This work will then be used to extend research in the area of aggregated commodity storage solutions capable of supporting terascale computing resources in a scalable, secure, and cost-effective manner.

To provide high availability of terascale computing resources, we have developed a flexible, modular, pluggable component framework that allows adaptation to system properties, like network technology and system scale, and application needs, such as programming model and consistency requirements. The developed framework is a configurable substrate that offers high availability to critical terascale system services, such as job and resource management, high-performance communication, and parallel file system. Terascale computing demands large data sets. To provide a high availability solution for terascale data, we are actively developing FreeLoader, a scalable, layered, parallel I/O environment layered across a network of workstations providing a distributed commodity storage infrastructure that may be used in conjunction with high-end storage. FreeLoader offers novel striping strategies that delivers high aggregate throughput comparable to traditional storage systems. To address the commodity nature of workstations, we also developed a soft-state registration mechanism from which benefactor machines (those sharing data storage space) register/deregister with a manager. Furthermore, we have developed mechanisms to control the impact that FreeLoader may have on the cooperating benefactors. There have been seven publications including one master's thesis as a result of this work.

Success in this LDRD will further DOE's long-term objectives and contribute to their expected outcomes as follows: (1) lead DOE and the nation in revitalizing U.S. leadership in high-end computing and computational sciences and (2) enhance the accessibility of high-performance computing power. The expected outcomes will be accomplished through the action of supporting terascale computing through the delivery and deployment of leadership-class computers, storage, networking, and visualization. All federal agencies and commercial entities interested in high-end computing will benefit from this research. Specific programs to note include DARPA's Information Processing Technology Office and NSF's Directorate for Computer and Information Science and Engineering programs of (1) Software and Tools for High-End Computing and (2) National Middleware Initiative.

# Terascale Computations of Multiscale Magnetohydrodynamics for Fusion Plasmas

D. A. Spong,[1] E. A. D'Azevedo,[2] D. B. Batchelor,[1] D. del-Castillo-Negrete,[1] M. Fahey,[3] S. P. Hirshman,[1] R. T. Mills,[3] S. Jardin,[4] W. Park,[4] J. Breslau,[4] G. Y. Fu,[4] and J. Chen[4]

[1]*Fusion Energy Division*
[2]*Computer Sciences and Mathematics Division*
[3]*National Center for Computational Sciences*
[4]*Princeton University Plasma Physics Laboratory*

Magnetic island growth can be amplified in high temperature toroidal plasmas through a feedback loop involving localized pressure profile flattening and suppression of self-driven plasma bootstrap currents. Magnetic islands redirect the rapid plasma transport parallel to the confining magnetic field to an outward direction across the confining field. This can limit the fusion power performance of future devices, such as the International Thermonuclear Experimental Reactor (ITER). Control of island growth requires simulations that operate in realistic regimes and that couple magneto-hydrodynamics (MHD) physics with low collisionality transport effects within the island.

Production of a self-sustained burning fusion plasma in future devices such as the ITER project will require a high level of external control in order to maintain a stable, stationary plasma with good confinement properties. A key ingredient for both designing such controls and understanding the plasma behavior is an integrated plasma simulation capability. An efficient extended MHD model is required to simulate magnetic island growth from toroidal plasma instabilities and will be a critical component for an integrated plasma simulation code.

Extended MHD is a term that is used to describe a truncated moments hierarchy of macroscopic fluid equations that has been augmented with closure relations in order to incorporate either kinetic or shorter scale length phenomena. The particular type of MHD closure that is the goal of this project is a neoclassical closure that provides plasma flows and currents within magnetic island regions. Such closures are important for the simulation magnetic island growth in high-temperature plasmas. An equally important goal is the improvement in efficiency of the nonlinear MHD evolution code on the new vector and superscalar architectures such as the Cray X1E and XT3. Our LDRD project has addressed both of these goals.

Neoclassical closure relations have been developed using a Monte Carlo particle code DELTA5D, which can follow a large number of particles in parallel in the presence of the Coulomb collisions and the perturbed magnetic and electric fields generated in the MHD simulation. We have ported this code to both the Cray X1E and XT3 systems and improved its vectorization on the Cray X1E. Performance on the X1E is about a factor of 5 faster than available super-scalar systems. A new delta-f algorithm has been implemented that self-consistently calculates of the plasma viscous stress tensor as required for MHD closure relations. In order to smooth the magnetic/electric field data of the MHD code and to compress its representation in a form that will be efficient for the particle code, a new method based on principal orthogonal decomposition has been developed and tested.

The efficiency of the M3D extended MHD code has been improved by addressing a primary bottleneck, that of achieving good vectorization on sparse matrix operations. Progress has been made on several levels. First, at the most basic level, a new algorithm was developed that reorders operations in matrix vector multiplies to accomplish better vectorization. This has resulted in a factor of 10 improvement over previous methods for a variety of test problems. Next, at a higher level, new linear system solvers, which can benefit to a greater extent from this improved matrix-vector multiply routine, are being tested. Also, the M3D mesh and finite-element generation routines were rewritten to use co array Fortran, allowing different direct and iterative parallel linear solvers to be readily tested.

During 2006 further work will be done on improving the efficiency of the M3D and DELTA5D codes on both the Cray X1E vector and XT3 super-scalar architectures. The particle-based closure relations will be coupled with the M3D model. This project will benefit DOE programs in the Office of Fusion Energy by providing a more realistic and efficient extended MHD model, as will be needed for integrated plasma simulation of future devices such as ITER.

# Petascale Computation in Condensed Matter Physics

E. Dagotto,[1] R. Fishman,[1] A. Moreo,[1] T. Maier,[2] T. Schulthess,[2] and R. Toedte[2]
[1]*Condensed Matter Sciences Division*
[2]*Computer Science and Mathematics Division*

The study of complex systems, such as high-temperature superconductors, diluted magnetic semiconductors, fermionic quantum gases, and colossal magnetoresistive manganites, is among the most important areas of investigations in science, both from the technological and scientific points of view. Since they embody physics at different energy scales and contain competing degrees of freedom, complex systems require new paradigms and methods that can be solved only with the aid of high-end computation. This project addresses the development of the new computational techniques required to understand the self-organizing and multifaceted properties of complex systems.

## Fermionic Quantum Gases

In contrast to electronic systems, the interaction and scattering length of fermions in atomic gases is tunable in a wide range near a Feshbach resonance. The experiments allow the whole range of attractive interactions, from weak (BCS) to strong (Bose-Einstein-condensate, BEC) interaction, to be investigated, as detailed in the original proposal. On the theory side, the three-dimensional attractive Hubbard model provides an ideal system to study the whole range of scattering lengths and, thus, the evolution between BCS and BEC type physics. This model describes the hopping of fermionic atoms between sites with an amplitude of $t$ and their mutual on-site attraction with magnitude $U$. During the first year of LDRD support, we have implemented complementary, highly parallelized DCA/QMC and diagrammatic determinental QMC (DDMC) codes to solve this model with unprecedented accuracy on the Cray X1. The DCA/QMC code for this model is a 3D extension of the 2D code used in previous studies and hence runs on the X1 with the same efficiency. When completed, this work will provide the first systematic and virtually exact solution of the 3D attractive Hubbard model. See P. R. C. Kent, M. Jarrell, Th. A. Maier, and Th. Pruschke, "Efficient calculation of the antiferromagnetic phase diagram of the 3D Hubbard model," submitted to *Phys. Rev. B*, Rapid Communications, preprint cond-mat/0506337 (2005).

## Colossal Magnetoresistance

The study of manganites, the materials with the colossal magnetoresistance (CMR) effect, is among the most popular areas of research in condensed matter physics. Understanding the CMR is important, both from the conceptual point of view and for future applications in read sensors. Currently, the main ideas in this context involve the presence of quenched disorder and its influence near a first-order transition, producing a so-called clustered state. The key bottleneck preventing a solution to the CMR puzzle is that standard numerical techniques for the study of realistic manganites models can be applied to finite clusters with only about 150 sites. The physics of percolation is important in this context, and it is well known that percolation can be studied only with large systems. It is, thus, important to be able to increase by at least an order of magnitude the number of sites that can be studied computationally using realistic models. Fortunately, recent algorithm developments, as well as the use of the CSMD computational facilities, will allow us in the very near future to achieve this goal. The algorithm that we have implemented already is the Truncated Polynomial Expansion Method. This technique has allowed us to break existing records in the literature regarding lattice sizes. We have implemented a computer program that uses a grid of processors, 50 to 100 for the polynomial expansion and 10 to 20 for the different disorder configurations. Therefore, we expect to be able to use efficiently 500–2000 processors in a single run to study CMR manganites with chemical disorder and diluted magnetic semiconductors with positional disorder. These considerations make the new Cray XT3 computer at ORNL an ideal candidate for the computer system on where to run the simulations. See C. Sen, G. Alvarez, Y. Motome, N. Furukawa, I. Sergienko, T. Schulthess, and E. Dagotto, "Study of the One- and Two-Band Models for Colossal Magnetoresistive Manganites Using the Truncated Polynomial Expansion Method," cond-mat/0509418, *Phys. Rev. B*, to be published.

The proposal also included work in diluted magnetic semiconductors that is not here described in detail for lack of space. The reader can consult "Dynamics of Impurity and Valence Bands in Ga_{1-x}Mn_{x}As within the Dynamical Mean Field Approximation," M. A. Majidi, J. Moreno, M. Jarrell, and R. S. Fishman, submitted to *Phys. Rev. B*, and references therein, for details.

# *Computer and Computational Sciences*

# *Seed Money Fund*

# Modeling and Computational Platform for Architecture Design of Phase-Locked High-Power Semiconductor Laser Arrays

Y. Liu,[1] Y. Braiman,[1] J. Barhen,[1] and A. Fijany[2]
[1]*Computer Science and Mathematics Division*
[2]*Jet Propulsion Laboratory, Pasadena, California*

The objective of this project is to develop a computational platform for high-power laser array architecture design. The computational tool is based on our recent novel modeling for the phase-locked high-power semiconductor laser arrays. The modeling has included, for the first time, both laser structure (stripe width, optical-mode confinement factor) and spatial coupling configuration (coupling type and strength) features of the high-power laser array. In this project, a parallel computational algorithm will be implemented and will be running on a high-performance computing facility available at ORNL to include large numbers (~103) of laser emitters. Such a platform would allow for a continuous parameter adjustment for phase-locking performance optimization.

Recent years have witnessed a number of breakthroughs in the semiconductor laser fabrication field. In 2004, laser diodes have achieved a record power conversion efficiency (PCE) of more than 70%, which is an order of magnitude higher than most other lasers. These achievements have prompted great interest in novel architecture designs of high-power semiconductor laser systems that are able to produce a comparable power level (i.e., >1-KW continuous-wave power operation in a diffraction-limited beam) of solid-state or gas lasers. The eventual goal is to provide up to a 100-KW reliable power with 80% PCE for directed energy and industry applications. Such extraordinary energy-efficient devices can be used for a wide variety of applications.

Due to the output power limitation from a single semiconductor laser, laser diode arrays are currently considered to be the sole semiconductor device able to generate high-power, coherent light. However, the large number of coupled laser diodes not only increases the output power but also leads to complex spatial laser interactions and to the formation of multiple spatial modes. In order to make the array operate in phase so as to produce a single narrow beam, the analysis of the influence of the array architecture (individual laser structure and spatial coupling scheme) on the quality of the combined beam is thus of crucial importance. Such an analysis is not currently available, and most of experimental work relies on simplistic modeling where neither laser structure nor spatial coupling factors has been addressed.

The computational platform to be developed in this proposal is based on our recent novel modeling of coupled high-power semiconductor lasers with the purpose of designing feasible architectures of phase-locked laser arrays. Our modeling, for the first time includes both laser lateral structure (rather than viewing the laser as a single transverse mode oscillator) and laser coupling and, therefore, will be able to provide a comprehensive description of the dynamics in the coupled high-power laser arrays.

Significant progress on broad-area laser modeling and preliminary results on algorithm and numerical simulations have been achieved in the past 6 months. A theoretical modeling for broad-area lasers based on partial differential equations (PDEs) has been built up and parameter ranges have been set by utilizing experimental results/previous measurement. A beam propagation method (BPM), shooting method, and transmission matrix method have been chosen to solve laser field evolution inside laser cavity, carrier diffusion equation, and laser beam transmission in external cavity, respectively. Computer codes (C++) have been implemented for all the three algorithms. Reasonable results for laser field/carrier distributions have been obtained for a single laser. Program testing on supercomputers in the Center for Computational Sciences (CCS) Leadership Computing Facility (LCF) at ORNL has been started.

The eventual objective of this project is to implement a computational platform for architecture design of a phase-locked laser array that consists of a large number of broad-area semiconductor laser emitters. To this end, a parallel algorithm of the program is critical in order to carry out calculations for a large number of PDEs/diffusion equations. The task for FY 2006 will be to implement such an algorithm to allow parallel calculations of up to 1000 PDEs. The program will be running on high-performance computers available at LCF/ORNL. A computational platform, including computer codes and final parameter ranges, will be delivered at the end of this project. The numerical results are expected to be used to develop a novel experimental design for coherent beam combination from large laser arrays (experiments will be conducted with the support from Office of Naval Research).

# Multivariate Dependence in Climate Extremes

A. R. Ganguly,[1] R. Katz,[2] D. J. Erickson III,[3] G. Ostrouchov,[3] T. Hsing,[4] and V. T. D'Urso[5]
[1]*Computational Sciences and Engineering Division*
[2]*National Center for Atmospheric Research (NCAR), Colorado, Boulder*
[3]*Computer Science and Mathematics Division*
[4]*Department of Statistics, Ohio State University*
[5]*Environmental Sciences Division*

New solutions are being developed to enable a better understanding and prediction of climate extremes including extremal teleconnections and abrupt change. Recent advances in statistics are being further developed and implemented, and new theory is being developed to quantify time-lagged extremal associations. This is achieved by utilizing cutting-edge developments in extremal statistics over the last few years, as well as by developing new statistical methodologies for multivariate extremal dependence. The latter includes the use of physically based covariates to improve extreme-value analysis and joint distribution among extremes. The broad focus on multivariate dependence is relevant for high-priority applications in multiple domains.

The secretary of the United Nations weather body WMO Michel Jarrud recently said that "global warming was clearly tied to the increasing incidence of heat waves, and the spread of deserts in areas short of rain." (Quote from Yahoo! News article dated December 15th, 2005). Recent papers in Science and Nature on heat waves (Meehl and Tebaldi 2004) and sea level rise appear to bolster the case. In addition to regional climate extremes caused by global warming, there have been dire warnings on the possibility of abrupt global climate change and/or regional extremes caused by climate "teleconnections." However, the science is not well understood. Just as one example, when asked whether global warming was responsible for generating North Atlantic hurricanes, Jarrud said the following: "The honest answer is: we don't know ...." One of the primary issues for the lack of certainty in climate extremes is the limited use of extreme value theory (EVT) in studies of climate extremes (Coles 2001), often caused by gaps in EVT like the inability to adequately measure and describe extremal dependence among multiple variables, which may be lagged in time and space (NRC 2002). The purpose of this study is to address this gap by utilizing EVT in the study of climate extremes, with a particular focus on utilizing or developing novel approaches for multivariate extremal dependence.

The scope of the project and a short description of the technical approaches used are provided below:

A. New insights on climate change and climate extremes based on the application of extreme value theory to past (observed) and future (simulated) climate variables.
B. Development of new approaches for multivariate extremal dependence for climate, specifically focusing on (a) the use of physically based covariates (Gilleland et al. 2005; Katz et al. 2005) and (b) joint distribution of extremes (Hsing et al. 2005).
C. Initiate development of a complete solution for multivariate dependence, complete with linear and nonlinear dependence among "regular" and unusual values with particular emphasis on temporal and spatial dependence.
D. Once developed, the methodologies in B–C above will be utilized in multiple domains.

We have obtained novel insights on the properties of extremes for temperature and precipitation in selected regions of the world based on detailed analysis of (paleo) climate reconstructions and observed data from public domain sources, as well as high-resolution IPCC runs for the near past and recent future (1870 to 2100) from the CCSM3 climate model runs available at ORNL. Preliminary results have been presented by the PI (Ganguly 2005); detailed results will be presented and published upon completion of the project.

Once developed, the tools for multivariate dependence will be invaluable to decision and policy makers in the United States and worldwide, with significant impacts on energy production/usage, irrigation/ griculture, structural design/insurance rates. The methods for multivariate extremes will be useful for multiple domains ranging from sensor networks and national or homeland security to the management of natural disasters and energy assurance. We have already witnessed evidence of strong interest from sponsors and researchers in areas as diverse as climate change and distributed sensor networks.

## References

Coles S. 2001. An Introduction to Statistical Modeling of Extreme Values, Springer-Verlag.

Ganguly, A. R., T. Hsing, R. Katz, D. Erickson, G. Ostrouchov, T. Wilbanks, and N. Cressie. 2005. *Multivariate dependence among extremes, abrupt change and anomalies in space and*

*time for climate applications, Report of the Workshop on Data Mining for Anomaly Detection*, The Eleventh ACM SIGKDD International Conference on Knowledge Discovery and Data Mining, Chicago, IL, August 2005.

Gilleland, E., R. Katz, and G. Young. 2004. *Extremes toolkit (extRemes): weather and climate applications of extreme value statistics*, National Center for Atmospheric Research.

Hsing, T., C. Kluppelberg, and G. Kuhn. 2005. "Dependence estimation and visualization in multivariate extremes with applications to financial data," to appear in *Extremes* **7**, 99–121.

Katz, R. W., G. S. Brush, and M. B. Parlange. 2005. "Statistics of extremes: Modeling ecological disturbances," *Ecology* **86**, 1124–1134.

Meehl, G. A., and C. Tebaldi. 2004. "More intense, more frequent, & longer lasting heat waves in the 21st century," *Science* **305**, 994–7.

NRC. 2002. *Abrupt Climate Change: Inevitable Surprises*, Committee on Abrupt Climate Change, National Research Council, Washington, D.C., USA, 230 pp.

# *Neutron Sciences*

# *Director's R&D Fund*

# Complex Oxides with Frustrated Orbital Ordering

T. Egami,[1] G. M. Stocks,[1] D. G. Mandrus,[2] V. Keppens,[3] and D. I. Khomskii[4]
[1]*Metals and Ceramics Division*
[2]*Condensed Matter Sciences Division*
[3]*University of Tennessee, Knoxville*
[4]*Universität zu Köln, Germany*

The focus of this project was the understanding of competing interactions including frustrated orbital ordering in complex oxides. The concomitant goal for neutron science was to develop new neutron scattering techniques to study the mesoscopic structural modifications that result from such competition. We studied three oxide systems with frustrated orbital and atomic order, $LiNiO_2$, $Na_{0.3}CoO_2$-$1.4D_2O$ and $Pb(Mg_{1/3}Nb_{2/3})O_3$ (PMN). For $LiNiO_2$, we have used the new capability of the high-resolution pulsed neutron pair-density function (PDF) method out to 20 nm for the first time and studied the temperature dependence of the PDF. We discovered that nano-scale domains are formed below the transition temperature and explained their origin in terms of orbital frustration. The same approach was used on $Na_{0.3}CoO_2$-$1.4D_2O$. We found that the water molecules have anomalous dynamics, which could be related to the superconductivity of this material. We also developed a novel technique of dynamic PDF using inelastic neutron scattering, and applied it to the study of dynamic local ferroelectric polarization in PMN. This study solved the long-standing mystery about the atomistic origin of the relaxor behavior of PMN. In addition we developed the formalism to correct for the inelastic effects in the neutron PDF method. The two new techniques we developed will be powerful tools for the SNS and are expected to be used widely.

## Introduction

Many of the materials of interest for science and technology today are complex because of competing interactions. Such competition usually results in local and/or mesoscopic structural modifications of the long-range average structure. Conventional diffraction techniques are ill suited to study such local and mesoscopic variations, since conventional approaches focus on the Bragg peaks, which contain only the information on the long-range order. The information on local deviations is contained in the diffuse scattering. An alternative technique to determine the local structure is the atomic pair-density function (PDF) method (Egami 2003). In this technique both the Bragg peaks and diffuse scattering (total scattering) are measured over large $Q$ space ($Q$: momentum transfer of scattering) and Fourier-transformed to obtain the atom-atom PDF. This technique has been used for a long time for the study of liquids and glasses (Warren 1969), but its application to crystalline materials became feasible by the advent of synchrotron radiation and pulsed neutron sources that provide high energy probes and allows the total scattering to be determined over a wide range of $Q$.

However, there are two drawbacks in this method, and overcoming these drawbacks is the technical focus of the present LDRD project in neutron science. The first is that the method has been applied mostly for the analysis of the local structure within 1 nm or less, while it has a potential of analyzing the mesoscopic structure. The second is that the total scattering intensity contains both dynamic and static information and thus cannot differentiate dynamic local distortion from static local distortion. The first problem was addressed by using the pulsed neutron diffractometer NPDF of the Lujan Center of Los Alamos National Laboratory, which we recently upgraded with funding from the NSF and DOE. This diffractometer has high $Q$ resolution ($\Delta Q/Q = 0.0015$) and can determine the PDF up to 20–30 nm. The second problem was solved by developing the novel technique of the dynamic PDF method and also by improving the inelastic correction known as the Placzek correction.

The scientific focus of this project is to understand the physics of complex materials with competing interactions. We selected three complex oxide systems as our target; $LiNiO_2$, $Na_{0.3}CoO_2$-$1.4D_2O$ and $Pb(Mg_{1/3}Nb_{2/3})O_3$ (PMN). All of them are controversial in some ways, and the knowledge of the local structure and dynamics will facilitate resolving the mysteries about these compounds.

### *$LiNiO_2$*

$LiNiO_2$ is a layered compound with a triangular arrangement of $Ni^{3+}$ (S = ½) ions in the plane. It is well known that the system of anti-ferromagnetically

interacting S = ½ spins on a triangular lattice is frustrated; that is, the local order (antiparallel spin configuration) is not compatible with the global order. P. W. Anderson proposed the resonating-valence-bond (RVB) state as the ground state of such a system (Anderson 1973). $LiNiO_2$ was proposed as the model system for the RVB state (Hirakawa 1990), but the real nature of the magnetic ground state of this system is still controversial. At the same time, since $Ni^{3+}$ ($t_{2g}^{\ 6} - e_g^{\ 1}$) is a Jahn-Teller active ion, it is possible that the orbital state is also frustrated (Reynaud 2001).

### *$Na_{0.3}CoO_2$-1.4$D_2O$*

$NaCoO_2$ is isostructural to $LiNiO_2$, becomes metallic with hole doping by removing Na, and then becomes superconducting when $H_2O$ is intercalated (Takada 2003). In this work we used $D_2O$, since H is highly incoherent and absorbing to neutrons. Initially the role of $H_2O$ was considered to be merely a separator to enhance the two-dimensional nature of the $CoO_2$ layers, but a more active role for water is conceivable.

### *$Pb(Mg_{1/3}Nb_{2/3})O_3$ (PMN)*

PMN is a prototypical relaxor ferroelectric, which is a highly disordered ferroelectric solid that has diffuse ferroelectric transition and high dielectric response over a wide range of temperature. They are more useful than the regular ferroelectric solids which show strongly temperature-dependent response. However, the atomic origin of the relaxor behavior is not well understood. It is now known that the radio-frequency (up to MHz) response is due to polar nano-regions (PNRs) that are formed at low temperatures (in the case of PMN below room temperature), but the mechanism of formation of PNRs is controversial. The key to this problem is the local lattice dynamics at much higher frequencies, which can be addressed by inelastic neutron scattering.

## Technical Approach

For a long time, the accuracy of the PDF method suffered from the limitation in the $Q$ space accessible by measurement, which produces unphysical oscillations known as termination errors. Since $Q_{max} < 4\pi/\lambda$, where $\lambda$ is the wavelength of the probe, the limitation in the energy of radiation from the X-ray source in the laboratory or a reactor neutron source posed a challenge. While this problem was overcome by the use of synchrotron-based radiation sources that provide high energy probes, the resolution in $Q$ still limited the real space range. Using the upgraded pulsed neutron powder diffractometer (NPDF) of the Lujan Center for Neutron Scattering of the Los Alamos National Laboratory ($\Delta Q/Q$ = 0.0015), we can now determine the PDF up to 20–30 nm. The powder of $LiNiO_2$ that we produced was one of the first samples studied with this upgraded diffractometer, and the PDF was determined up to 20 nm as shown in Fig. 1 (Chung 2005). It is difficult to produce stoichiometric sample of $LiNiO_2$, since Li tends to evaporate, and Li and Ni tend to switch position. Through a careful low-temperature processing, we limited the density of Li/Ni site switching defects to about 3%. Producing $Na_{0.3}CoO_2$-1.4$D_2O$ was even more difficult, since $D_2O$ easily evaporated. Also, it was found that the process of removing Na from $NaCoO_2$ by aqueous nitric iodine introduced $H_2O$, and our first attempt of neutron scattering was not fully successful. We used heavy water solution for the reduction to eliminate $H_2O$. In order to understand the effect of spin polarization, we carried out a first-principles calculation using the local density approximation (LDA).

Now, because the PDF became free of many sources of error that used to limit its accuracy, the accuracy of the conventional correction for inelastic scattering, known as the Placzek correction, became an issue. We discovered that the procedure by Placzek seriously overcorrected the error and introduced artifacts. We have formulated the exact theory of inelastic correction. A more fundamental approach to deal with the local lattice dynamics is to determine the dynamic PDF by Fourier-transforming the dynamic structure factor, $S(Q, \omega)$, along $Q$. While the idea of dynamic PDF has been known, it was never implemented because of technical difficulties and weakness of the neutron source intensity. As explained below we introduced a missing-link in the concept to make the interpretation of the dynamic PDF easier, and using the PHAROS spectrometer of the Lujan Center, we succeeded in obtaining the dynamic PDF for the first time. This method was applied to the relaxor ferroelectric $Pb(Mg_{1/3}Nb_{2/3})O_3$ (PMN) to determine the atomistic origin of the relaxor behavior. In order to obtain an accurate dynamic structure factor, we followed the procedure routinely used in the static PDF method, such as the absorption correction, correction for the sample holder by actual measurement, correction for multiple scattering, and normalization to the source spectrum using a vanadium rod as a standard sample. The measurement at one temperature took 2 days to obtain the data with sufficient statistics. We carried out the measurement at seven temperatures; thus, including the time for measurement of the background and the sample holder, a total of 2.5 weeks was needed to complete the experiment.

## Results and Discussion

Figure 1 shows the PDF of $LiNiO_2$ determined at $T$ = 10 and 585 K (Chung 2005). As the expanded figures show, at short distances the PDF height is reduced with

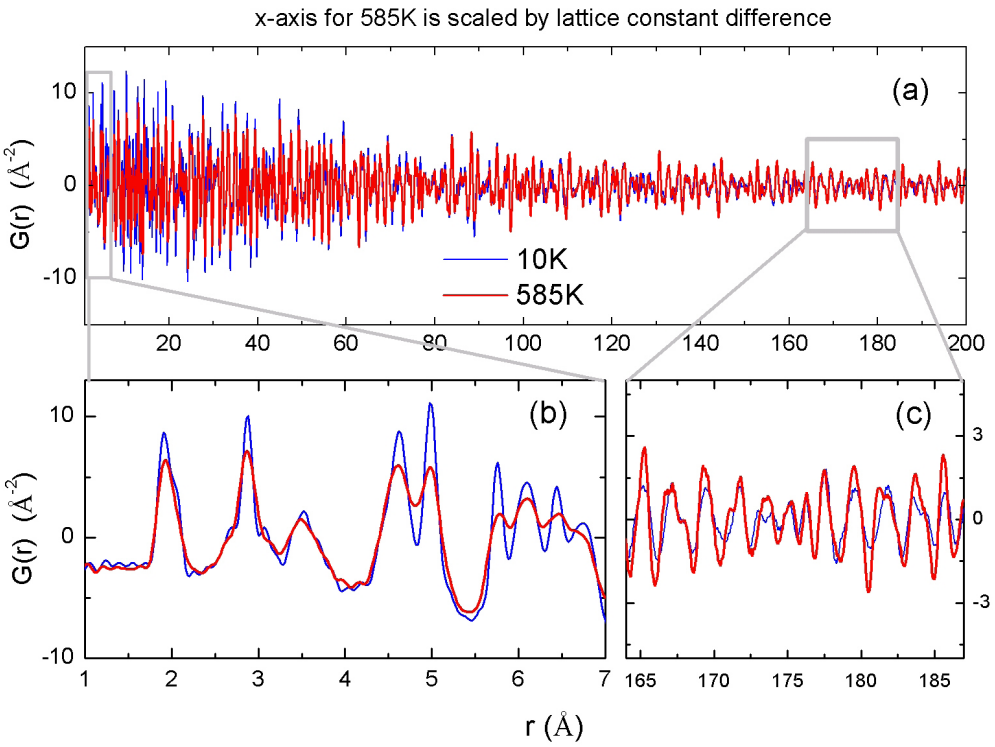


*Fig. 1. Pulsed neutron PDF of $LiNiO_2$ determined with NPDF of Los Alamos National Lab at T = 10 K (blue) and 585 K (red). Below are expansions at short distances (left) and long distances (right). Note that the PDF amplitude decreases with temperature at short distances but increases at long distances (Chung 2005).*

increasing temperature because of increased atomic vibration due to phonons. But, remarkably, at large distances the PDF at 585 K is higher in amplitude than that at 10 K. The crossover occurs around 8.7 nm for one sample and 10.7 nm for the second sample. The temperature dependence of the PDF height at large distances indicates that the decrease starts at 375 K. We interpret this anomalous behavior in terms of domain formation. If domains of about 10 nm are formed at temperatures below 375 K, the inter-domain correlation will be weaker than the intra-domain correlation. The origin of the domain formation was explained as the following. The PDF at the nearest neighbor (Fig. 1, below left) clearly shows that the local environment of $Ni^{3+}$ ion is Jahn-Teller (JT) distorted. However, the crystal structure has no indication of collective JT effect. This dilemma was resolved by successful explanation of the PDF with the model involving three sublattices with the direction of the JT orbital axis along *x*, *y* and *z* directions in each sublattice. The distortion due to JT effect, however, does not quite cancel because of the loss of inversion symmetry, and results in a small curvature in the $NiO_2$ plane. Consequently the JT ordering cannot extend to long-range order, and nano-scale domains are formed. Thus the orbital frustration associated with the JT orbital order can be lifted by the formation of three sublattices, but frustration at a mesoscopic length-scale still remains, resulting in domain formation. Our band structure calculation of $LiNiO_2$ showed that, while the LDA without spin polarization resulted in a metal, spin-polarized LDA (SDA) produced an insulator even without orbital ordering. Orbital ordering will increase the band gap and further stabilize the structure. The consequence of Li/Ni site exchange was found to result in strong exchange interaction along the *c*-axis and may explain the unusual magnetic properties of this compound.

The PDF of $Na_{0.3}CoO_2$-$1.4D_2O$ indicated that the PDF peak corresponding to the D-D correlation in this compound is much weaker than that observed for $D_2O$. This implies (heavy) water in this compound may be modified. It is possible that the hydrogen bond is asymmetric, and $D_2O$ is dynamically ionized as $DO^- + D^+$. This observation of proton dynamics has an implication for the origin of superconductivity in this compound. Even though $T_C$ is low (4.5K), it is much higher than expected for this class of materials. It is possible that the high dielectric response due to proton motion is enhancing the electron-phonon coupling. The effect of inelastic intensity (Placzek) correction is very severe for H or D, since their weight is comparable with that of a neutron. We found that the Placzek correction produces significant distortion in the data by overcorrection. We are in the process of

applying our exact procedure to this data set.

The Fourier-transform of the dynamic structure factor by $Q$ and $t$ (time) was discussed by van Hove (1954), but he stopped short of discussing the physical meaning of the partial transform, only by $Q$ but not by $t$, which actually is not obvious. We found that it corresponds to the phase-averaged dynamic PDF of atoms vibrating at that frequency. Armed with this discovery, we were able to interpret the dynamic PDF of PMN and its temperature dependence to explain the origin of the relaxor phenomena. The dynamic PDF clearly showed that while the low-frequency ferroelectric polarization (up to MHz) exists only up to room temperature, high-frequency (THz) local polarization remains up to 600 K, the so-called Burns temperature (Burns 1983), below which optical response suggests local polarization. This result, for the first time, clearly shows that local dynamic polarization of Pb ions is formed at the Burns temperature, becomes more spatially extended and slows down with lowering temperature, and freezes into the glassy state at the freezing temperature. Pb polarization formed at Burns temperature remains local because of the disorder in the local environment of Pb with $Mg^{2+}$ and $Nb^{5+}$ ions.

## Benefits

The dynamic PDF method we developed has a potential of extremely wide application in detecting the local dynamics of lattice and spin. We expect a significant part of the work carried out at the ARCS spectrometer of the SNS (a wide angle inelastic chopper spectrometer due in operation in 2007) will be the dynamic PDF measurement. We will definitely be the leader in this field. It will also be an effective method to study the local dynamics of hydrogen (deuterium) in the study of catalytic materials for fuel cells and other chemical reactors. While the density of state (DOS) study is easier to carry out, it provides information only on the frequency and not the local mode. The dynamic PDF will tell right away the bond length and amplitude of the mode as a function of frequency. It opens up a totally new avenue of study.

The method of dynamic PDF still needs more development, particularly with respect to the software to make it more user friendly. We have submitted a white paper to DOE/BES (Dr. Helen Kirch) and were encouraged to submit a full proposal, which is being prepared. In the proposed project we plan to apply the dynamic PDF method to the study of local lattice dynamics in the colossal magnetoresistive (CMR) manganites and superconducting cuprates. Such studies will shed light on the role of the local phonons on the mechanism of CMR (polaron formation) and high-temperature superconductivity. We are collaborating with the catalyst group (S. Overbury and S. Dai) to jump start a project on the use of static as well as dynamic PDF on the study of catalytic nano-particles. This project could grow into a full project in the Chemical Sciences Division.

## References


Anderson, P. W. 1973. "Resonating valence bonds: A new kind of insulator?" *Materials Research Bulletin*. **8**, 153.

Burns, G. and F. H. Dacol. 1983. "Glassy polarization behavior in ferroelectric compounds $Pb(Mg_{1/3}Nb_{2/3})O_3$ and $Pb(Zn_{1/3}Nb_{2/3})O_3$." *Solid State Communication* **48**, 853.

Chung, J.-H., Th. Proffen, S.-I. Shamoto, A. M. Ghorayeb, L. Croguennec, W. Tian, C. Sales, R. Jin, D. Mandrus, and T. Egami. 2005. "Local structure of LiNiO2 studied by neutron diffraction." *Physical Review B* **71**, 064410.

Egami, T. and S. J. L. Billinge. 2003. *Underneath the Bragg peaks: Structural analysis of complex materials*. Pergamon Materials Series Vol. 7, ed. Robert W. Cahn, Pergamon Press, Elsevier Ltd., Oxford.

Raynaud, F., D. Mertz, F. Celestini, J-M. Debierre, A. M. Ghorayeb, P. Simon, A. Stepanov, J. Voiron and C. Delmas. 2001. "Orbital frustration at the origin of the magnetic behavior in $LiNiO_2$." *Physical Review Letters* **86**, 3638.

Takada, K, H. Sakurai, E. Takayama-Muromachi, F. Izumi, R. A. Dilanian and T. Sasaki. 2003. "Superconductivity in two-dimensional $CoO_2$ layers." *Nature* **422**, 53.

Van Hove, L. 1954. "Correlations in space and time and Born approximation scattering in systems of interacting particles." *Physical Review* **95**, 249.

Warren, E. B. 1969. *X-ray diffraction*. Addison-Wesley, Reading; Dover Publications, New York, 1990.

# Development of In-Situ Neutron Diffraction Capabilities for Studies of Deformation and Fracture Behavior under Hydrogen-Rich Environments

C. R. Hubbard,[1] H. Choo,[1,2] J. W. Pang,[1] G. Sarma,[3] S. Pawel,[1] and P. Nash[4]
[1]*Metals and Ceramics Division*
[2]*University of Tennessee*
[3]*Computer Science and Mathematics Division*
[4]*Illinois Institute of Technology*

The goal was to develop new in situ neutron-scattering capabilities that would enable experimental determination of constitutive mechanical properties as a function of stress, strain, strain rate, and, for the first time, corrosive environments. This proposal advocated use of the latest improvements in instruments at the High Flux Isotope Reactor (HFIR) as tools for the investigation of micro-mechanical aspects of deformation and environmental effects in structural materials under hydrogen-rich environments. Specific R&D objectives were to (1) develop a load frame for in situ studies, (2) develop an electrochemical environmental cell that can be used with the load frame or standalone, (3) combine mechanical- and chemical-metallurgy research with the neutron facility at Oak Ridge National Laboratory (ORNL), (4) advance the fundamental understanding of deformation and fracture in response to applied stress under "hydrogen-rich" environments, and (5) advance computational deformation models that include environmental effects. This integrated approach combined the programmatic efforts in diffraction, instrumentation, mechanical testing, corrosion science, and computational modeling to (1) develop unique and valuable materials-research capabilities at ORNL (i.e., world's first in situ loading system) equipped with an environmental cell for mechanical studies with neutron diffraction, (2) establish ORNL's leadership in the field of neutron-scattering materials science and technology, (3) establish neutron-scattering studies relevant to the hydrogen technology, and (4) utilize the unique supercomputing capabilities at ORNL.

## Introduction

Sub-critical flaw growth phenomena involving a cooperative interaction between a static stress and the environment are referred to collectively as environment-assisted cracking. For example, corrosion fatigue, a combined environmental and mechanical damage mechanism, is one of the most abundant damage processes in structural materials. Recent thrust towards the "hydrogen economy" could significantly expand the attention to this problem (Birnbaum 2003). The premise of this project is that data from in situ neutron diffraction (ND) characterization techniques can lead to a better understanding of the hydrogen embrittlement (HE) mechanisms and to development of advanced computational simulations that reliably predict the deformation and fracture behavior of advanced structural materials under "hydrogen-rich" environments.

This project focused on the investigation of HE in structural materials with the following specific R&D objectives: (1) develop a load frame and electrochemical environmental cell for in situ neutron-scattering studies; (2) using neutron scattering, advance the fundamental understanding of deformation and fracture in response to applied stress under hydrogen-rich environments; (3) initiate computational modeling of environmental effects through mesoscale deformation modeling to investigate interactions between plasticity, fracture, and environment; and (4) expand user research opportunities at HFIR and SNS.

## Technical Approach

The project consisted of three R&D tasks: (1) instrumentation, (2) in situ neutron diffraction, and (3) computational modeling.

### *Task 1—Instrumentation*

The objective of this task was to design and develop load frames and an electrochemical cell for the NRSF2, the new second-generation Neutron Residual Stress mapping Facility at HFIR. The addition of an environmental cell to the NRSF2 will provide an accessory that does not exist at other neutron strain mapping facilities. The new capabilities provide a unique, high-impact research tool for the corrosion/mechanical-behavior/modeling communities at ORNL. Furthermore, once demonstrated, the enhanced capabilities will attract new and exciting user projects and will generate new opportunities for research and program development such as in "hydrogen technology infrastructure."

***Task 2—In Situ Neutron Diffraction***

This objective aims to experimentally test key hypotheses that have been raised by a number of classic and also recent HE theories. However, defining a general theory of HE is certainly beyond the scope of this project. For the ND studies, we mainly used the new NRSF2 instrument at HFIR. Important features include: 1-$mm^3$ sampling volumes (for spatially resolved strain and texture profiles), and >10 times improvement in counting rate over the first-generation NRSF. For example, strain gradients around a crack tip can be mapped with higher spatial resolution than at any other neutron facilities (Sun 2005). Qualitative and quantitative phase measurements were conducted on Zircaloy-4 round bars subject to hydrogen gas charging at an elevated temperature. In order to determine the relative amount of hydrogen in the Zircaloy-4 samples, the increase of the incoherent scattering with the hydrogen content was calibrated using standard samples for which the hydrogen content was known.

***Task 3—Computational Modeling***

This task is to advance computational modeling of the deformation behavior of metals in the presence of environmental effects at the mesoscopic level using the unique supercomputing capabilities at ORNL.

## Results and Discussion

***Instrument Development***

A dedicated load frame for the NRSF2 was designed and constructed. The load frame can apply uniaxial load for in situ deformation studies (tensile, compressive, and potentially low-cycle fatigue). Key features include a 5000-lbf actuator, load cell with a signal conditioner, frames, grips, extensometer, and dedicated control computer. The system operation is fully computerized with a comprehensive data acquisition/analysis package developed using LabVIEW software (An 2005). The system can apply sufficiently large uniaxial load for in situ deformation studies, which covers the elastic, plastic, and fracture regimes of most structural materials of interest. On NRSF2 we demonstrated that data collection for an aluminum alloy rod of 6-mm diameter can be completed in under 1 hour per diffraction peak using the load and hold approach (widely used for neutron scattering due to need for long count times) or under 30 min using the more standard continuous load and data collection every 0.1 min. A low-cost, small load frame, with ability to hold a compact-tension (CT) specimen under a constant applied load (constant crack opening displacement, COD), was developed as well. The size of the frame is ~30 cm × 40 cm, and the load is applied by tightening the screws at the ends of the load train while monitoring a COD gauge. This frame was used at NRSF2 for mapping of strains and phases as a function of applied load. In addition, a dedicated environmental cell was developed to be used in combination with the load frame at NRSF2 for hydrogen charging, cathodic protection, and corrosion research using ND measurements at HFIR.

***Neutron Scattering Investigations***

A zirconium alloy (Zircaloy-4; 1.4 Sn, 0.2 Fe, 0.1 Cr in weight % and balance Zr) was used in this study because (1) it interacts with hydrogen and forms hydrides, (2) it is a good scattering material well suited for neutron-scattering experiments, and (3) it is technologically important as a nuclear-reactor material. First, qualitative and quantitative phase analyses were conducted on Zircaloy-4 round bars using neutron scattering techniques. The specimens were charged using a 12.5 vol.% hydrogen in an argon mixture in a tube furnace at 430°C under 13.8 kPa for 0.5, 1, and 1.5 hours, respectively. The neutron diffraction phase mapping through the thickness of the specimens showed the presence of the face-centered-cubic delta zirconium hydride ($\delta$-$ZrH_2$) phase on the surface. An assessment of the background due to the incoherent scattering principally from the hydrogen atoms was carried out by performing inelastic scans (energy scans) around the zero energy transfer at the HB-1A at HFIR. To determine the relative amount of hydrogen in the Zircaloy-4 samples, the increase of the incoherent scattering with the hydrogen content was calibrated using polypropylene films for which the hydrogen content was known. Moreover, "incoherent scans" were taken at a fixed two-theta value ($2\theta = 62$ deg) from an angular range with flat background such that no coherent scattering was present (Garlea 2005). Figure 1 shows that incoherent scattering increases with the hydrogen content in the Zircaloy-4 specimens hydrogen charged at 430°C for different amount of time. The estimated total hydrogen contents are 1600, 2800, and 5200 ppm for the samples charged for 30 min, 1 hour, and 1.5 hours, respectively. Further, mapping of the background scattering through the thickness of the specimens was performed on NRSF2. Results qualitatively demonstrated the potential; however, to quantitatively map the hydrogen content within the round bar, the beam room background level would need to be reduced. Changes to NRSF2 detector shielding have been proposed that should enable quantitative measurement.

Second, the evolution of intergranular strains in the hexagonal-close-packed Zircaloy-4 was investigated in situ, using neutron diffraction, to understand the deformation behavior on the microscopic length scale. A series of uniaxial tensile loads was applied to round-bar tensile specimens up to 500 MPa, and the intergranular (hkl-specific) strains, parallel and perpendicular to the loading direction, were studied. The results provide a

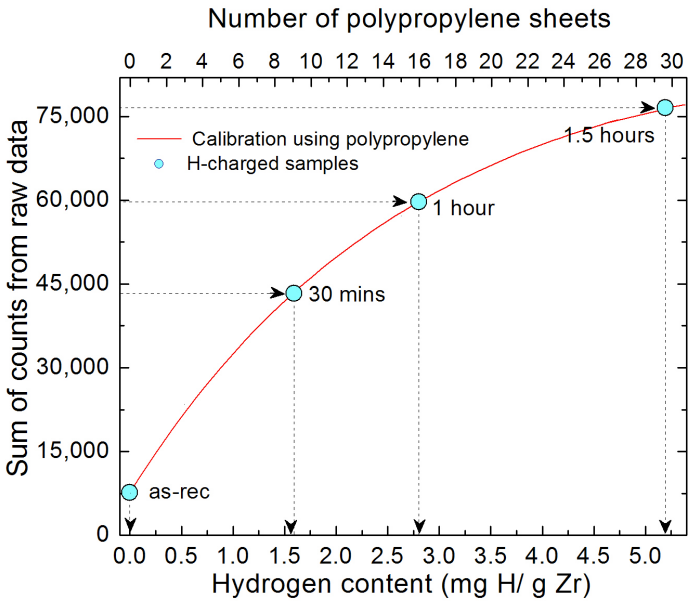


*Fig. 1. Estimation of the hydrogen content for the samples charged with hydrogen. The incoherent scattering increases with the hydrogen content in the Zircaloy-4 specimens hydrogen-charged at 430°C for different amount of time. The estimated hydrogen contents are 1600, 2800, and 5200 ppm for the samples charged for 30 min., 1 hour, and 1.5 hours, respectively.*

fundamental understanding of the anisotropic elastic-plastic deformation of the zirconium alloy under applied stresses (Garlea 2005).

### *Computational Modeling*

A finite element model (FEM) was developed to investigate the interplay between the applied stress and lattice strain in the Zircaloy-4 at the continuum scale. The results show a good agreement with the neutron diffraction data. Furthermore, a polycrystal FEM, for deformation at the mesoscopic length scale, has been developed to investigate the inhomogeneous deformations of individual grains in a polycrystalline zirconium alloy. In this simulation, the finite element discretization is applied directly to the individual grains of the microstructure containing many grains, and plastic deformation by slip is modeled using constitutive laws based on crystal plasticity. The microstructural state of the material was characterized by the orientation of the crystal lattice associated with each element relative to a fixed reference, and by the critical resolved shear stress parameter (strength) of the slip systems. This approach has the benefit of explicitly including the anisotropy due to grain orientation on the deformation behavior. It was shown that the grain-to-grain variations can lead to local values of stress and strain which are much higher or lower than the averaged continuum values.

## Benefits

Development of experimental facilities, measurement and modeling expertise, and advances in fundamental understanding of science issues regarding hydrogen embrittlement problem will benefit energy industry (heat exchangers and piping systems), civil infrastructure industry (steel bridges, reinforcements, water/gas/oil piping systems), nuclear reactor industry (piping, pressure vessels), and the aircraft industry (fuselage, wing).

In transportation, fossil and nuclear energy, and aerospace, a vast interest exists in the area of life prediction of components operating at elevated temperatures and in corrosive environments. Industries related to power-generation and aircraft-engine systems today and in hydrogen storage and transmission in the future involve welding applications, which are particularly sensitive to HE. These nationally important energy and transportation research sectors will benefit from the developing research facility and expertise.

For FY 2006, funding to complete the construction of VULCAN at SNS is being pursued within DOE EERE-FreedomCAR and Vehicle Technologies (FCVT), and this request is being considered by Congress. A milestone within the FCVT program for FY 2007 calls for preparing for successful application of VULCAN (an engineering neutron diffractometer at SNS) to improve materials and materials life prediction. The facilities and expertise developed within this LDRD project allows us to fully utilize the HFIR facilities and support the future SNS opportunities.

The new opportunities for research developed in this project have helped set the stage to pursue programs within DOE-BES neutron and materials sciences and within DOE-EERE Fuel Cell and Hydrogen Technologies programs. Additionally, both DOE and industries involved with nuclear reactor technology are keenly interested in development and validation of models to accurately predict life of components such as critical piping, heat exchangers and welds. Demonstration of measurement methods and computational models developed in this LDRD project will enable us to compete for such funding opportunities.

The use and publication of the results from this work will lead to an expanded number of academic and industrial users coming to ORNL. Toward the end of this work, three HTML User Projects were approved and

measurements completed using the load frame on NRSF2. One involved the load distribution between phases in an aluminum-silicon carbide metal matrix composite; another studied the strains in compression of a granular powder; the third examined ex situ the residual stresses following torsional deformation and showed that the residual strains for two different hkl were substantially different from those for an identical sample subjected to uniaxial tension deformation.

In addition, the project for development of the load frame at NRSF2 helped win two NSF grants that benefit both the universities and ORNL. The University of Tennessee/ORNL research team (P. Liaw, H. Choo, R. Buchanan, X.-L. Wang, and C. R. Hubbard), including two PIs of the current LDRD project, was awarded an NSF Major Research Instrumentation (MRI) grant (4 years, $2M with the UT matching funds) for "Development of an In-Situ Neutron-Scattering Facility for Research and Education in the Mechanical Behavior of Materials." The objective is to build a world-class in situ mechanical loading and environmental capabilities at the VULCAN (the engineering neutron diffractometer) at the Spallation Neutron Source (SNS). The establishment of this LDRD in FY 2004 helped to address a specific concern expressed in the first submission of the NSF-MRI proposal. The rewrite of the proposal to NSF specifically built on the expertise being built via the LDRD. A proposal led by Tennessee Technical University also was awarded, providing fund for research on cement and concrete under applied loads. This award provided funds to develop an attachment to the NRSF2 load frame that converts uniaxial tension to a very accurately aligned compressive load. This was an essential capability that has never been available on a neutron strain mapping facility. The attachment has been built and will be tested under the User Program.

## References


An, K., M. C. Wright, and C. R. Hubbard. 2005. "User Manual for the NRSF2 Load Frame," in preparation.

Birnbaum, H. K. 2003. "Hydrogen Effects on Deformation and Fracture: Science and Sociology." MRS Bulletin, July, 479.

Garlea, E. 2005. "Effect of Hydrogen on Mechanical Behavior of a Zircaloy-4 Alloy." M.S. dissertation, The University of Tennessee, Knoxville, Tennessee.

Sun, Y. et al. 2005. "Changes in Lattice Strain Profiles around a Fatigue Crack through the Retardation Period after Overloading." *Physica B*, accepted for publication.

# Research and Development for Neutron Structural Biology and Soft Matter Science

D. A. A. Myles
*Chemical Science Division*

We conducted research and development work that aimed to build and demonstrate strategic capabilities, competencies, and strength at ORNL in neutron scattering applications for the characterization and analysis of proteins in solution and in single crystals. This work included demonstration of neutron structure analysis to locate functionally important hydrogen atom positions in the catalytic sites of two enzymes, human Aldose reductase and human Carbonic Anhydrase, and demonstration of the potential for low-sample-volume, high-throughput characterization of multi-molecular complexes using small-angle scattering techniques.

We conducted research and development work on the characterization and analysis of proteins in solution and in single crystals. We determined and analyzed the X-ray structure of a fully perdeuterated human carbonic anhydrase and determined both the X-ray and neutron structures of a second perdeuterated protein, human aldose reductase. This work demonstrates the power of neutron diffraction to locate functionally important hydrogen atom positions in enzymes.

Human carbonic anhydrase II (HCA II) is a zinc metalloenzyme that catalyzes the reversible hydration and dehydration of carbon dioxide and bicarbonate, respectively. The rate-limiting step in catalysis is the intramolecular transfer of a proton between the zinc-bound solvent ($H_2O/OH^-$) and the proton-shuttling residue His64. This distance (7.5 Å) is spanned by a well-defined active-site solvent network stabilized by amino-acid side chains (Tyr7, Asn62, Asn67, Thr199 and Thr200). Despite the availability of high-resolution (1.0 Å) X-ray crystal structures of HCA II, there is currently no definitive information available on the positions and orientations of the H atoms of the solvent network or active-site amino acids and their ionization states. In preparation for neutron diffraction studies to elucidate this hydrogen-bonding network, perdeuterated HCA II has been expressed, purified, and crystallized and its X-ray structure determined to 1.5 Å resolution. The refined structure is highly isomorphous with hydrogenated HCA II, especially with regard to the activesite architecture and solvent network.

Human aldose reductase (h-AR; MW = 36 kDa) belongs to the aldo–keto reductase family and is implicated in diabetic complications. Its ternary complexes (h-AR–coenzyme NADPH–selected inhibitor) provide a good model to study both the enzymatic mechanism and inhibition. Neutron diffraction data have been collected to 2.2 Å resolution from a small (0.15-$mm^3$) crystal of perdeuterated in order to help to determine the protonation state of the enzyme h-AR. We have successfully produced fully deuterated human aldose reductase [h-AR(D)], crystallized the ternary complex h-AR(D)–NADPH–IDD594 and collected neutron Laue data to 2 Å resolution at the LADI instrument at ILL using a crystal volume of just 0.15 $mm^3$. This is the first fully deuterated enzyme of this size (36 kDa) to be solved by neutron diffraction and represents a milestone in the field, as the crystal volume is at least one order of magnitude smaller than those usually required for other high-resolution neutron structures determined to date. This illustrates the significant increase in the signal-to-noise ratio of data collected from perdeuterated crystals and demonstrates that good-quality neutron data can now be collected from more typical protein crystal volumes (Fig. 1).

In order to support our work to develop low-sample-volume, high-throughput scattering techniques for characterization of multi-molecular complexes, we have established light scattering and X-ray facilities that will be used for the analysis of proteins and protein complexes in solution. The techniques and methods developed will allow us to extract meaningful spatial and dynamic information on the structure, function, and often transient interactions of protein systems across the multiple levels of functional organization in the cell. The information derived by neutron and X-ray scattering on the structure/morphology and kinetics of complex formation and interactions in solution are of critical interest in molecular biology and are difficult or impossible to obtain by other techniques.

## Benefits

Our work represents proof of principle that perdeuterated and hydrogenated protein structures are extremely similar and validates the use of perdeuterated proteins for neutron crystallography in order to obtain detailed information on the organization and structure at

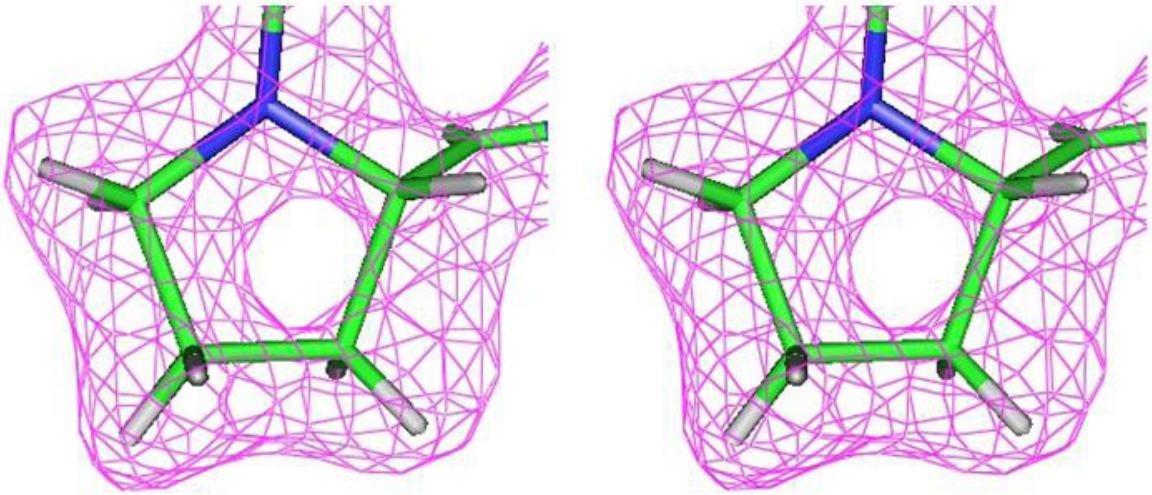

*Fig. 1. Full deuteration of human aldose reductase (MW=36kDa) significantly improved the signal/noise ratio of neutron diffraction data and enabled data to be collected to 2.2 Å resolution from a crystal of volume 0.15 mm³—radically smaller than usual for neutron diffraction studies. Deuterium atoms are clearly visible in neutron scattering density maps at 2.2 Å resolution (see Proline 13, 2Fo-Fc map, 1.5 rms contour).*

the active site of enzymes. The work on deuterated aldose reductase shows that the neutron structures can be directly correlated with X-ray structures for functional annotation and direct visualization of H/D atoms. Moreover, the work on the neutron structure of deuterated human aldose reductase is a groundbreaking achievement and represents a milestone in the field, as the crystal volume is at least one order of magnitude smaller than those usually required for other high-resolution neutron structures determined to date. This example promises to help open up the whole field of neutron protein crystallography. This project helped underpin the successful development of the proposal to build a Macromolecular Neutron Diffractometer at the Spallation Neutron Source.

The tests done on small-volume, high-throughput data collection regimes for X-ray small-angle scattering charaterization of proteins in solution have demonstrated the potential of further development and optimization of these approaches as a potentially powerful tool for parametric characterization of the assembly and disassembly of protein complexes in solution. Such tools and capabilities would be of use and interest to individual researchers and to the programs of NIH, NSF, and other agencies that address structural and kinetic analysis of protein complexes.

# Neutron Reflectometry Studies of the Structure of Polyelectrolyte Thin Films Subject to Shear

G. S. Smith,[1] J. Mays,[2,3] W. A. Hamilton,[1] and T. L. Kuhl[4]
[1]*Center for Neutron Scattering*
[2]*Chemical Sciences Division*
[3]*University of Tennessee, Knoxville*
[4]*University of California, Davis*

This work focuses on measuring the molecular structure of charged polymer chains in selective solvent as a function of graft density, charged group, and ionic strength. When opposing polymer "brushes" are brought into contact, two processes may occur simultaneously: interpenetration and compression. These processes determine the lubrication and adhesive properties of the interfaces. We investigate both the static and sheared structures formed by polyelectrolyte brushes using neutron and X-ray scattering techniques. Using state-of-the-art techniques in polymerization and selective deuteration, we are building controlled model architectures to elucidate the structure of these complex systems at interfaces under confinement and dynamic shear.

Knowledge of the conformations that adsorbed or terminally anchored chain molecules adopt when subjected to confinement and shear flow is essential for predicting the interaction forces, and tribological and rheological properties in thin-films. When densely packed polymers attached to a substrate are placed in a good solvent (for the unbound end of the polymer), the polymer free energy consists of a competition between the osmotic forces which want the chains to dissolve in solution and the energy cost of stretching the coiled chain. The resulting carpet-like molecular structure is referred to as a polymer brush. We are, for the first time, directly measuring the structure of charged polymer brushes under confinement and shear using neutron scattering techniques.

To make the measurements, we have developed a shear/confinement cell capable of sliding two parallel surfaces past each other with a controlled velocity to yield a constant shear rate. The gap between plates is controlled and adjusted in a reproducible way over a range of a few hundred Angstroms. The substrate materials are transparent to neutrons; thus, using this cell on a neutron reflectometer, we can measure the structure of two monolayers of attached polymer brushes as they are being confined and sheared. In order to measure the effectiveness of the shear cell, we first studied uncharged diblock copolymers.

Another aspect of this proposal is to chemically control the architecture of polyelectrolyte block copolymers consisting of sodium poly(styrene sulfonate) (PSS), the charged segment, and poly(tert-butyl styrene) (PTBS), the uncharged adsorbing block. These materials will be used in the neutron scattering experiments. Four different diblocks were synthesized with protonated components. The polymers were synthesized and then sulfonated to provide the ionizable (charged) sulfonated moieties. Currently, we are synthesizing the analogs to these materials with the poly(styrene) block deuterated to provide contrast in the neutron reflection experiments.

We performed the first-ever shear experiments to demonstrate that the technique works for a neutral polymer. We found that the surface relaxation time for sheared polymer-coated substrates is on the order of weeks. More work is needed to learn how to prepare the polyelectrolytes confined in a gap small enough to clearly promote the interactions between the polymers on the two substrates. While developing this sample preparation, we are gaining information about the structure of a single brush at the water substrate interface. Further analysis is being performed on the scattering data to guide upcoming experiments.

Several benefits are expected upon the successful completion of this project. We will be developing new techniques for studying materials in confinement, which will benefit both neutron scattering and nanoscience throughout the DOE complex. The confinement/shear apparatus, once fully developed, will be available for users at the Spallation Neutron Source and the HFIR Center fro Neutron Scattering which will strengthen the user programs at both facilities. This work will not only have applicability in polymer science but will be relevant to molecular biology and nanoscience given that biomaterals such as proteins are charged polymers.

# Small-Angle Neutron Scattering Investigation of the Mechanism and Kinetics of Membrane Protein Crystallization in Self-Assembled Surfactant Mesophases

W. A. Hamilton,[1] G. W. Lynn,[2] D. Singh,[3] W. T. Heller,[2] D. A. A. Myles,[2] L. Porcar,[4,5] U. Perez-Salas,[6] and P. D. Butler[4]

[1]*Center for Neutron Scattering, Condensed Matter Sciences Division*
[2]*Chemical and Analytical Science Division/CSMB*
[3]*Ph.D. Candidate, Johns Hopkins University/ORISE Higher Education Research Experience Program*
[4]*Center for Neutron Research, National Institute of Standards and Technology*
[5]*University of Maryland*
[6]*University of California, Irvine/NIST-CNBT*

Membrane proteins play critical roles in signaling and chemical transport across cell walls and are coded by a substantial fraction of the genome. However, very few of the ~26,000 known protein structures are of membrane proteins because these are difficult to dissolve and crystallize in the quality required for high-resolution X-ray and neutron diffraction studies. Membrane mesophase "in meso" templating of crystallization has had some success, but the mechanism remains conjectural, which makes improving the process difficult. We are using neutron scattering contrast techniques to reveal the exact structural evolution of proteins in these mesophases to determine the parameters governing crystallization.

Our project concentrates on the behavior of membrane proteins under crystallization in templates comprising membranes similar to those of living cells. Whereas previous studies, primarily using X rays, have only tracked the template structure, the use of neutron scattering will allow the determination of the as yet unknown pre-crystalline and crystalline nucleus protein morphologies, as the mesophase signal is reduced by matching out membrane and solvent neutron contrasts. An important task of the second year will be synthesis of the required deuterated lipids, which are often not commercially available.

In the first year of this project, we have made small-angle neutron scattering measurements on structures and triggered phase behavior in three self-assembled membrane lipidic phases. Two of these, the cubic phase of the lipid monoolein (MO) and mixed lipid bicelle (discoid) phase, have already been used as membrane protein crystallography reactor phases, while a third new lamellar gel phase was obtained as a by-product of our first attempt to create a lipidic sponge phase.

For the MO system, test measurements to determine a protein distribution were made using the relatively cheap protein Gramicidin, rather than the more expensive and larger Bacteria Rhodosopsin (BR), which being the canonical demonstration membrane for both cubic and discoid phase crystallization is the main object of our investigation. Despite being performed with this smaller protein, thus giving an inherently lower signal, and in hydrogenated lipid, with a high background and little contrast between the protein and solvent, these measurements clearly indicated that Gramicidin remains well dispersed in the membrane even at high concentrations. These promising first measurements give us the expectation that with deuterated lipid a detailed understanding of BR protein distribution within the membrane prior to and during crystallization will be achievable.

Our interest in bicelle crystallization is driven by two objectives. As a membrane phase crystallization process, it is of direct interest, but as a discrete phase, it is also a test of common explanations of the cubic phase crystallization method that invoke its bicontinuous nature. With respect to the latter question, we found that that the purported pure bicelle crystallization phase is in fact a complicated mixed phase system and that mixed surfactant theory is required in order to explain its thermodynamics.

In addition, our first year also saw preliminary neutron reflectometry experiments in a solid-solution cell made on the MO cubic system, which showed a high degree of temperature-dependent surface ordering. This was our first step in exploring the possibility of a hybrid crystallization technique combining the microscopic bulk ordering of the "in meso" method with the macroscopic alignments of surface precipitation—an effort which will continue to be informed by our small-angle scattering investigations of "in meso" phase templating.

A basic understanding of the mechanisms of "in meso" protein crystallization and their dependence on process variables will allow faster more efficient production of

the crystals essential for atomic-scale-resolution X-ray or neutron diffraction studies. The structures so derived will contribute initially to our understanding the operation of proteins as machines in life processes and ultimately to the engineering of protein functionality in technological applications ranging from bioweapon detection and defense (DOD and Homeland Security) and hazardous waste cleanup (DOD, DOE) to healthcare therapies and bio-sensors (NIH).

# In-Situ, Time-Resolved Neutron Diffraction Study of Materials Behavior under Severe Thermomechanical Deformation

Z. Feng,[1] W. Woo,[2] X. L. Wang[1,3] C. R. Hubbard,[1] S. A. David,[1] B. Radhakrishnan,[4] G. Sarma,[4] and H. Choo[2]
[1]*Metals and Ceramics Division*
[2]*University of Tennessee*
[3]*Spallation Neutron Source*
[4]*Computer Science and Mathematics Division*

The microstructure evolution of materials under rapid and severe thermomechanical deformation is one of the most important yet least understood areas in materials science and engineering. A major contributing factor has been the lack of direct, in situ observation and determination of the temperature, stress, and microstructure changes as they evolve rapidly under the complex thermomechanical synthesis environment. This project aims at addressing this challenge by developing novel neutron scattering measurement and data analysis techniques that would enable unique in situ, time-resolved measurement of material behavior under severe thermomechanical loading conditions, a completely new territory for neutron scattering applications in materials science and engineering.

The deep penetration capability of neutrons into most metallic materials makes neutron diffraction a unique and powerful tool in understanding their structures and properties. Until now, the majority of neutron diffraction research (in the context of stress and microstructure phase evolution) has been limited to the so-called "static" behavior of materials—behavior that does not change or changes very slowly with time (in hours or days), primarily because of the inadequate neutron fluxes from existing facilities. In this project, we proposed to develop innovative neutron scattering measurement techniques that would enable in situ, time-resolved studies of transient material behavior (temperature, stress and phase transformation) under severe thermomechanical deformation conditions.

The proposed approach utilizes the so-called quasi-steady state phenomenon existing in many thermomechanical material synthesis processes. This makes it possible to perform neutron scattering measurements in the Eulerian reference frame in which the neutron collection time is independent of the rate of changes in material behavior and is selected purely based on neutron flux and sampling volume requirements of a test. Major tasks of the program include (1) a novel in-situ data collection technique to drastically improve the temporal resolution of neutron scattering; (2) a cost-effective portable system for controlled thermomechanical conditioning of materials; (3) new data processing and interpretation methodologies to decode the temperature, stress, deformation, and microstructure information from neutron scattering data; and (4) in-situ measurement of recrystallization, precipitation, and deformation processes in Al alloys.

*In-Situ Time-Resolved Neutron Measurement Technique:* We have developed the theoretical basis for the proposed Eulerian measurement technique based on quasi-steady state phenomenon. In addition, we developed the quasi-steady-state measurement procedure to experimentally realize our concept and established the equivalency of the quasi-steady Eulerian measurement to the direct Lagrangian in situ measurement under specially designed experimental conditions in which the direct Lagrangian measurement could be carried out.

*Neutron Diffraction Data Analysis and Synthesis:* We have also made significant progress in decoding the temperature, stress, and microstructure information from the neutron measurement data. A procedure has been developed that enables us to de-convolute the stress and temperature from neutron diffraction data for two-dimensional situations. In addition, the calculated temperature has been validated by the experimental thermocouple measurements.

The significant progress in FY 2005 provides a solid foundation to carry out the planned research in FY 2006. With the delivery of the portable thermomechanical processing system at the beginning of FY 2006, the in situ neutron experiments will focus on the material behavior caused by severe thermomechanical deformation. In addition to NRSF2 at HFIR, the pulsed neutron source at Los Alamos Neutron Science Center (LANSCE) will also be used to explore the advantages of pulsed neutrons with simultaneous multiple HKL reflection measurement and multiple detector banks.

This program is relevant to DOE-BES efforts in neutron and materials sciences, as it leads to novel use of neutron scattering to understand the fundamentals of

materials behavior. If successful, this project will provide a better understanding of the intricate interplay of stresses, temperature, and microstructures in complex metal processing and synthesis, which would be important to a wide range of advanced structural and functional materials for DOE Energy Efficiency, Fusion Energy, and Fossil Energy programs.

# A Deuteration Facility for In Vivo H-D Isotopic Labeling of Biological Macromolecules for Neutron Structural Biology and Soft Matter Science

D. A. A. Myles[1] and D. Pelletier[2]
[1]*Chemical Sciences Division*
[2]*Life Science Division*

This proposal will establish a pilot-phase bio-deuteration laboratory for in vivo production of hydrogen- and deuterium-labeled bio-macromolecules to support development of the neutron structural biology research and user programs at ORNL's neutron scattering facilities

Neutron scattering provides a unique non-destructive tool able to probe delicate macromolecule complexes and higher order assemblies over a wide range of length and time scales that provides key insights into the structure and dynamics of complex systems. These studies are enhanced by the design and production of specific, random, and uniform H/D-labeled biological macromolecules that permit selected parts of macromolecular structures to be highlighted and analyzed in situ. The development of a bio-deuteration laboratory for the D-labeled macromolecules will have significant strategic impact on neutron scattering at ORNL, provide benefits not just in higher quality and throughput of experiments but in extending the range, scale, and complexity of strategic biological problems that can be addressed.

Objectives of our program are as follows:

- To establish a bio-deuteration laboratory to enable efficient production of H/D-labeled proteins/ nucleic acids and other bio-molecules for the user community.
- To develop and implement robust, reliable, and efficient technologies for the production of deuterium-labeled biomacromolecules.
- To evaluate and exploit these reagents in improved downstream applications, including data collection and interpretation for neutron scattering at HFIR and SNS.
- To train researchers from academia and industry in these powerful techniques, ensuring broader access and innovative use of our neutron scattering facilities.
- To expand our user base at ORNL by providing a critical "point of entry" that will attract and support users from the wider biology community.

Providing access to the methods and tools needed to produce H/D-labeled materials at the Bio-Deuteration Laboratory will ensure broader access and innovative use of ORNL's neutron scattering facilities. The range of materials that can be labeled in vivo extends from individual amino acid residues, to signaling peptides and hormones, and through individual proteins up to multimeric protein complexes and multi-component systems, including protein/protein and protein/RNA/ DNA complexes and functional molecular motors and machines. Work in the pilot project will focus specifically on expression of deuterated recombinant proteins that have been selected for analysis by SANS, reflectometry, or neutron protein crystallography. The technical approach in the pilot phase is to (1) establish protein labeling and production facilities, (2) import and implement baseline technologies and scale-up procedures for over expression of H/D labeled proteins in commonly used microbial (*E.coli*) systems, and (3) demonstrate use of these materials in downstream neutron applications.

As a central training and user facility, the bio-deuteration laboratory will provide a critical "point of entry" and interface that will make neutron scattering visible and accessible to the broader community, DOE, and other government labs, academia, and industry. The ability to tackle complex problems in structural biology will leave ORNL strategically placed to attract project and program funding from agencies such as DOE, NIH, and NSF.

# *Neutron Sciences*

# *Seed Money Fund*

# Development of a Position-Sensitive Neutron Detector for Use at High Flux Source Facilities: SNS and HFIR

V. Cianciolo,[1] D. M. Markoff,[2] C. L. Britton,[3] R. G. Cooper,[4] G. L. Greene,[1,5] and R. J. Warmack[3]
[1]*Physics Division*
[2]*North Carolina Central University—Co-Principal Investigator*
[3]*Engineering Science and Technology Division*
[4]*ORNL Spallation Neutron Source*
[5]*University of Tennessee*

In the August 2003 report to the Nuclear Science Advisory Committee (NSAC), the Subcommittee on Fundamental Physics with Neutrons recommended the construction of the cold beam line at the Spallation Neutron Source (SNS) and the program of measurements in fundamental neutron science that it can support. This Fundamental Neutron Physics Beamline (FNPB) is now under construction at the SNS and will be ready for experiments starting in 2007–2008. In order to take full advantage of the large neutron flux expected at the SNS, high-current neutron detectors must be developed with specifications optimized for the different types of fundamental neutron experiments.We proposed to develop a prototype detector which is position sensitive (~1-cm resolution) and nearly 100% efficient, even at the prodigious SNS fluence (>$5 \times 10^{10}$ neutrons/sec). Such a detector is critical for transmission experiments proposed for the FNPB and may perhaps find use in materials science measurements. The proposed detector concept expands the segmented ionization chamber design that has successfully been used in a preliminary measurement of the neutron spin rotation in a liquid helium target (Penn 2001) and builds upon technology currently being developed at ORNL for low-efficiency beam-transmission monitors for the SNS (Britton 2004; Stephan 2004).

## Introduction

Experiments proposed for the FNPB will allow a variety of precision measurements that will provide insight into the nature of matter and the forces that govern it. One specific example is the measurement of the parity-violating neutron spin rotation in light atomic targets (e.g., hydrogen and helium). In this experiment, a polarized neutron beam is passed through a thick target. The weak nuclear force introduces tiny parity violating differences in the index of refraction for different neutron helicity states, which results in a rotation of the polarization vector through the target by $\Phi_{PV} \sim 1$ microradian. Great care in the experimental design is required to eliminate sensitivity to background sources of spin rotation, $\Phi_{BG}$, in particular rotation due to stray magnetic fields. The beam is split into two; one half with its spin rotated by $\Phi_{BG} + \Phi_{PV}$, the other half by $\Phi_{BG} - \Phi_{PV}$. The split beam is passed through a spin analyzer and the flux difference is proportional to $\Phi_{PV}$. Great statistical precision is required, thus sensitivity must be maintained in the face of very high neutron flux. Measurement of the position dependence is necessary to identify and eliminate systematic variation across the beam profile. No currently existing detector satisfies these requirements.

## Technical Approach

Our detector design combines the features of two existing detector designs; a segmented $^3$He/Ar ionization chamber and a neutron MicroMegas detector. A segmented ionization chamber, with coarse position and energy resolution, was used for a preliminary measurement of the neutron spin rotation in a liquid helium target. Neutrons are detected via the reaction

$$n + {}^3He \rightarrow {}^3H + {}^1H .$$

The reaction products ionize the fill gas, producing a signal proportional to the neutron flux. MicroMegas detectors were originally developed at CERN for charged particle detection and subsequently modified for fast neutron detection (Andriamonje 2002). They are specially designed to accept high rates with little dead time. A version suitable for slow neutrons was developed by ORNL and BNL. In that device, a solid neutron converter material (e.g., boron) is placed on the aluminum drift electrode. Neutrons convert in the boron, producing alpha particles which ionize gas in the drift volume. The produced electrons are accelerated to the amplification gap, which consists of a nickel mesh grid and a series of readout electrodes of various geometries. This technology

is limited to low efficiencies (desirable for a transmission monitor) because the converter material is passive and very thin layers will absorb the alpha particle signature of the neutron conversion. We replaced the solid converter material with $^3$He, thus making an active converter that is not self-limiting.

## Results and Discussion

The detector that was developed is shown in Fig. 1. The detector is shown mounted on one flange of the pressure vessel used to contain the process gas and to provide electrical shielding. The detector consists of two back-to-back drift/conversion gaps, with the conversion gaps in the center of the two drift regions. The drift regions are read out with strips at a 1-mm pitch. Six

*Fig. 1. Photograph of neutron detector developed for this project (a Neutron Micromegas detector using $^3$He as the converter and process gas).*

strips are ganged together into a single readout channel. The strips for each drift region are oriented in orthogonal directions, each perpendicular to the incoming neutron beam. The expected rate at the SNS will be too high to allow identification of individual pulses. Therefore the readout electronics are designed to operate in current-mode so that the total output current is proportional to the flux of neutrons that converted in the corresponding detector element. We used a modified version of the standard readout electronics developed for a variety of SNS instruments. Neutron conversion to slow charged particles in $^3$He is well understood. Therefore we carried out detector tests with an α-source which mimicked the neutron conversion products. This simplified the tests and avoided the use of costly $^3$He. The initial results were promising, and as a result we are developing a proposal to DOE for a full-scale detector. In order to achieve 100% efficiency a full-scale detector will need to be rather thick (>10 cm). If constructed as a single drift/conversion gap, a detector this thick would have unacceptably poor position resolution. This suggests a design with multiple drift/conversion gaps in series. Such a design would have an added advantage for experiments at high flux polychromatic sources (such as HFIR): crude energy resolution. The velocity-dependent cross section in $^3$He would result in a different average neutron energy sampled by each segment.

## Benefits

The SNS will soon be providing the world's most intense flux of pulsed neutrons for materials science and basic research. The FNPB at the SNS will be home to a wide variety of basic science experiments which can use the large neutron intensity and which can use knowledge of incident neutron energy to reduce systematic errors. Research at this facility is expected to form a key component of the Physics Division research portfolio for years to come. At the first FNPB Proposal Review and Advisory Committee meeting, held in September 2005, an experiment to measure the parity violating neutron spin rotation in a helium target was approved (an acknowledgement that the SNS intends to include the experiment in its scientific program, not a guarantee of funding). The detector developed in this proposal is an enabling technology for this experiment. This detector will also likely find use in other experiments that wish to run at the FNPB and may perhaps find use in materials science measurements.

## References


Penn, S. D. et al. 2001. "Development of a Low-noise 3He Ionization Chamber for Measuring the Energy Spectrum of a Cold Neutron Beam," *Nuclear Instruments and Methods* **A457**, 332.

Britton, C. L. et al. 2004. "A Detector for Neutron Imaging," *IEEE Transactions on Nuclear Science* **51**, 1016.

Stephan, A. C. et al. 2004. "Monte Carlo Studies of a Micromegas Neutron Beam Monitor," *Nuclear Instruments and Methods* **A521**, 441.

Andriamonje, S. et al. 2002. "Experimental Studies of a Micromegas Neutron Detector," *Nuclear Instruments and Methods* **A481**, 120.

# Lead-Free Electromechanical Transducer Materials

D. J. Singh[1] and T. Egami[2]
[1]*Condensed Matter Sciences Division*
[2]*Metals and Ceramics Division*

We are using a combination of neutron scattering and first-principles calculations to study the lattice instabilities and local structural distortions in novel ferroelectrics, especially materials related to the perovskite oxide solid solutions. The immediate goals of the work are to do proof-of-principle studies related to our frustration model and more generally to refine our understanding of these materials in chemical terms, and thereby guide the search for practical lead-free materials that can be used for electromechanical transduction in automotive, medical, and other applications. This project will enable us to establish a strong research program into the atomic-scale origins of piezoelectricity in lead-free materials.

Understanding the interplay of the *A*-site and *B*-site cation off-centerings in perovskites is a key point in engineering morphotropic phase boundary systems. We analyzed the results of density functional calculations for the trends in the lattice instabilities of the perovskites, $BaTiO_3$, $PbTiO_3$, $BaZrO_3$, and $PbZrO_3$ with volume. A simple scheme for classifying perovskites in terms of *A*-site and *B*-site activities was found in relation to competition between rhombohedral and tetragonal ground states. The results can be summarized in four trends, which may be regarded as "design rules" for chemically modifying properties of $t < 1$ ferroelectric perovskites. These are as follows:

1. As is well known, ferroelectricity can be stabilized at the expense of octahedral rotations by hybridization between the unoccupied states of the *A*-site cation and the oxygen *p*-states. This is the role of the Pb lone pair.
2. Alloying on the *A*-site with small cations, such as Cd or Bi can increase the tetragonality, *c/a*, of the tetragonal ferroelectric phase.
3. In materials with stiff octahedra, as characterized by large pressure dependence of the rotational instability and/or strong dispersion of the zone boundary phonons associated with tilt instability, a mixture of large and small *A*-site ions may be used to favor ferroelectricity over tilted structures. This may provide an alternative to the Pb lone pair for obtaining new MPB systems, and in addition may be useful for raising the Curie temperatures of existing systems. One way to exploit this would be to split the *A*-site ion; for example, $\mathrm{Na} \rightarrow x\mathrm{Li} + (1 - x)\mathrm{K}$.
4. The balance between rhombohedral and tetragonal ferroelectric ground states can be controlled via the polarizability of the *B* site. For example, since Nb and Ta are the same size, but Nb has greater covalency with O in perovskites, substitution of Nb for Ta, besides generally favoring ferroelectricity, would also favor a rhombohedral over a tetragonal ground state; that is, it would shift the MPB position.

While these trends are qualitative, they may be useful in modifying perovskites to find new compositions that are useful as electroactive materials. We are presently doing structural studies of lead-free $(K,Li)NbO_3$ supercells and do find that with high-Li-fraction (~50%) ferroelectricity is favored, even though there is no lone pair *A*-site atom, and the average perovskite tolerance factor is less than unity. Neutron scattering experiments are being done studying relaxor ferroelectricity in mixed-cation solid solutions. The results show very interesting changes in the dynamic pair distribution function over a specific energy range at the Burn's temperature. This offers a window into the long-standing central questions in relaxor ferroelectricity—specifically what happens at the Burn's temperature and what are the polar nano-regions that develop at this temperature.

# *Biological Sciences and Technology*

# *Director's R&D Fund*

# Nano/Micro Systems for Advanced Neuronal Interfacing

M. N. Ericson,[1] T. E. McKnight,[1] A.V. Melechko,[2] C. L. Britton, Jr.,[1] J. S. Baba,[1] A. D. McMillan,[3]
S. S. Frank,[1] B. L. Fletcher,[2] M. L. Simpson,[4] G. D. Griffin,[5] M. A. Wilson,[6,7] P. S. Khalsa,[8] and M. Dichter[9]
[1]*Engineering Science and Technology Division*
[2]*The University of Tennessee*
[3]*Office of the Laboratory Director*
[4]*Condensed Matter Sciences Division*
[5]*Life Sciences Division*
[6]*Pittsburgh VA Healthcare System*
[7]*University of Pittsburgh Medical School*
[8]*State University of New York, Biomedical Engineering Department*
[9]*University of Pennsylvania, Department of Neurology*

This research focused on integrating novel nanostructured materials and microelectronics to overcome existing limitations associated with conventional neuronal interfacing techniques. Vertically aligned carbon nanofiber–based electrode architectures were integrated with microscale integrated circuits to provide a base technology enabling the realization of highly integrated and functionally specialized miniature neural interface systems. Our approach takes advantage of inherent properties of nanofibers that provide significant improvements over conventional techniques for nerve interfacing, including the ability to insert directly into neural tissue, the ability to electrically address fibers as independent elements, the improved stability of carbon electrodes in neuronal tissue over time, and the ability to pattern and synthesize very high-resolution stimulus geometries (or pixelation). Full realization of this new technology combining nanoscience, microelectronics, and neuroscience will provide new strategies in neuro-nanomedicine for treatment of individuals struggling with profound neurological impairments.

## Introduction

Conventional strategies for neuronal interfacing employ a variety of probe types that can be generally grouped into two primary categories: surface electrodes (external skin electrodes, epimysial electrodes, epineural electrodes, and cuff electrodes) and penetrating pin type (percutaneous intramuscular electrodes, surgically implanted intramuscular electrodes, and wire and silicon intraneural electrodes) (Heiduschka et al. 2001; Tatic-Lucic et al. 1997; Zeck et al. 2001; Lundqvist et al. 1998; Cunningham et al. 2001; Craighead et al. 2001). Though many variations exist, these approaches are functionally limited by one or more of the following: poor stability due to epithelial cell growth resulting in passivation (all surface electrode types), limited resolution or nerve selectivity (pin- or needle-based topologies), and intrinsic limitation in array size due to perimeter connection to the probes. Consequently these techniques suffer from poor neural interface efficiency, are not well suited for chronic implantation due to instability, and offer limited nerve selectability. With the advent of micro and nano materials, a considerable effort has been under way at a variety of fabrication research facilities to develop micro-needles for improved interfacing to neuronal tissue. Driving this research is the realization that improved contact to neuronal tissue via vertical elements that extend above conventional planar microelectronic substrates and into the neuronal environment results in more efficient neural stimulation and less susceptibility to the fouling and passivating effects of protein and epithelial cell accumulation on electrode interfacial surfaces. However, state-of-the-art arrays fabricated using micromachining techniques still exhibit several characteristics that significantly limit their use, including technology-dependent pitch limitations preventing close cell placement on a large scale, limitations in array size due to perimeter interfacing strategies, and reduced signal integrity due to electronics placement outside the perimeter of the probe array.

This research focused on integrating carbon nanofiber–based probes with pixelated integrated circuits, producing a new technology enabling the realization of highly parallel, programmable, neuronal stimulus, and monitoring systems, an essential component for continued progress in the areas of neuroscience and neuromedicine. As will be detailed in further sections, a number of technical advancements were accomplished during the course of this research, demonstrating the efficacy of this new approach.

## Technical Approach

A number of technology developments were required during the course of this research to enable full realization of the proposed neural interfacing strategy shown in Fig 1(i). Individual fabrication of the nanoprobes and the pixelated integrated circuits was necessary due to temperature incompatibilities in the associated fabrication methods. This necessitated the development of a nanofiber liftoff and attachment method to allow full integration of the probes and pixelated electronics. Research in the use of biocompatible encapsulants and directed application to nanostructured probe surfaces was required to enable long-term bio-compatibility with tissue. Specifics associated with the culturing of neuronal differentiated cell lines and primary cells were investigated including array surface treatments for improved cell adhesion. Low-noise, pixelated preamp circuits were designed and fabricated enabling localized amplification of neuronal action potentials. Finally, techniques for invoking neural exocytosis and monitoring of the associated neurotransmitter release using nanoprobe arrays were developed and used to successfully demonstrate efficacy of interfacing to neuronal cells using vertically aligned carbon nanofiber (VACNF) probe arrays.

### *Pixelated Integrated Circuits*

Two measurement approaches were investigated for monitoring the excitation of neurons: voltage mode and charge sensitive mode. A mode-specific pixelated preamplifier was designed for each mode and two separate integrated circuits were designed, each configured as a 4×4 pixelated array. One of the pixels on each chip was replaced with a stimulus cell allowing external application of a stimulus waveform. The voltage mode approach (preamp_ASIC1) consists of a low-noise preamplifier (30V/V, 10-kHz bandwidth) followed by a variable gain

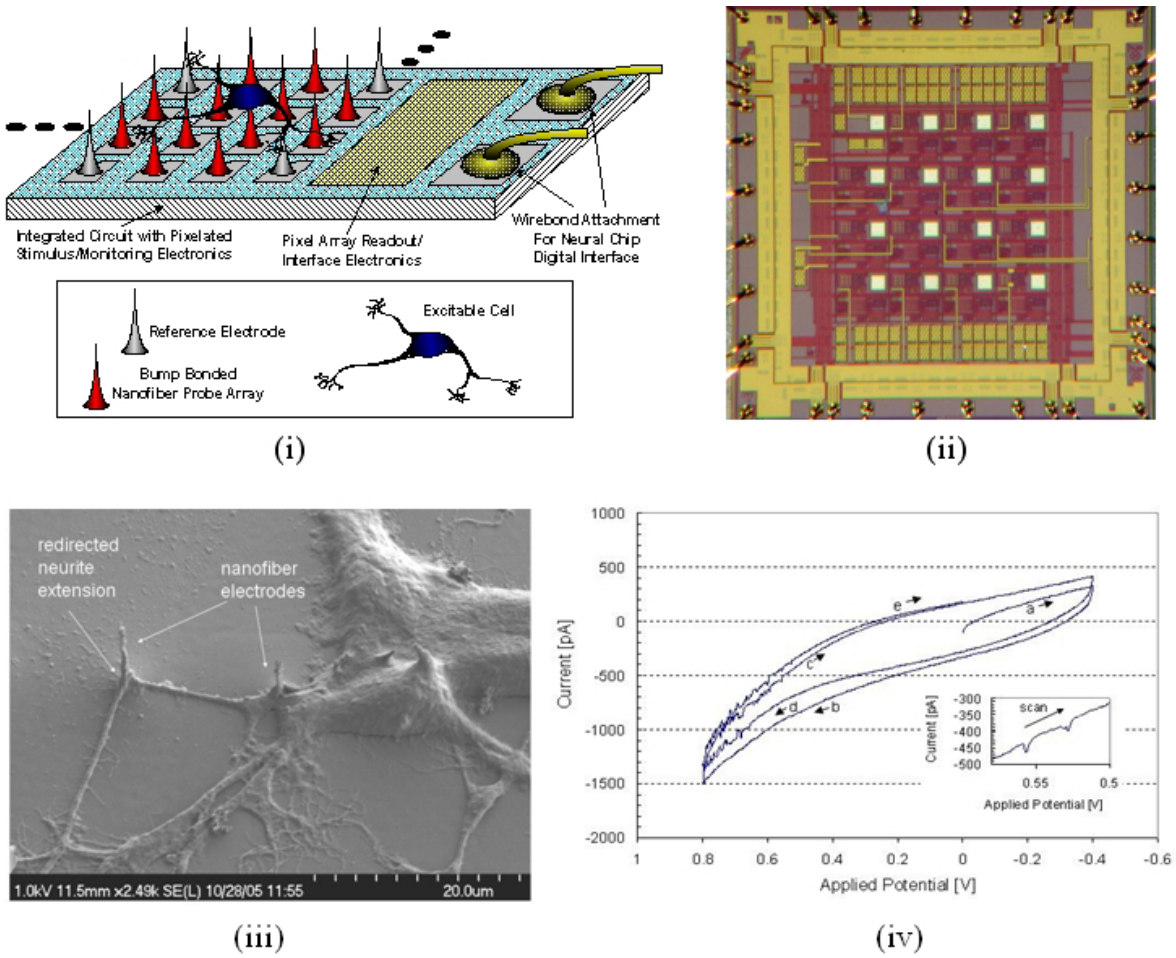


*Fig. 1. (i) Neuronal interfacing strategy using VACNF-based nanoprobe arrays and pixelated integrated circuits; (ii) 4x4 pixelated low-noise preamplifier integrated circuit; (iii) Scanning electron micrograph of differentiated PC-12 cells on a Type II nanofiber array. Prior to imaging, cells were fixed in 2% gluteraldehyde and dehydrated with methanol. The neurite processes of differentiated PC-12 cells can clearly be distinguished as can occasional varicosities at neurite junctions. (iv) Cyclic voltammogram of response of a Type I array following 16-day culture and differentiation of E18 cells (scan rate 1 V/sec, Pt pseudo reference). Oxidative bursts of putative neurotransmitter release can be distinguished as pulses in sweeps c, d, and e of the voltammogram. These spikes only occur at potentials greater than 0.4 V, sufficient for the oxidation of dopamine and norepinephrine.*

amplifier (1, 2, 4, 8 V/V), as shown in Fig. 1(ii). The charge-sensitive mode approach (preamp_ASIC2) uses a low-noise amplifier with a charge gain of 10V/pC. Each chip design was fabricated in a 0.5-µm bulk CMOS process and packaged for testing. The output of each amplifier channel was routed to a perimeter pad for wire bonding/packaging. Pixelated preamp arrays were packaged in a 44-pin J-lead ceramic package for evaluation.

### *VACNF Electrode Array Liftoff Process*

A key component of this research is the integration of nanofiber arrays with pixelated integrated circuits. Since temperatures associated with the nanofiber growth process are incompatible with other materials used in the overall implant system, special techniques were developed to enable separate fabrication, liftoff, and attachment of nanofiber arrays to the chip containing the pixelated integrated circuits. Typically, high-quality carbon nanofibers are grown at temperatures between 600 and 700ºC, a range not compatible with standard CMOS integrated circuits. In the newly developed technique, VACNFs were grown on a sacrificial high-temperature substrate and transferred to the CMOS chip using one of two methods: bump bonding at 100ºC or using conductive epoxy patterned on the integrated circuit using a micro fabricated polymer stencil. This process allows attachment of a nanofiber array to an integrated circuit or other substrate having properly patterned conduction layers.

### *Preparation of VACNF Electrode Arrays*

Two styles of ORNL nanofiber probe arrays were employed in this research: a 5-µm square array having 10 groups of 4 individually addressed nanofibers at an inter-group spacing of ~400 µm (Type I), and a 15-µm-square die having a linear array of 40 individually addressed nanofibers at a 15-µm pitch (Type II). These devices were used for cell culture studies without pixelated electronics. Type I devices were previously designed and reported in literature (McKnight et al. 2003; McKnight et al. 2004). The Type II array was developed specifically for neuronal experiments. Both array types were fabricated with an SU-8 passivation layer (a negative tone photoresist, Microposit) that was surface modified using an oxygen-based inductively coupled plasma etch to increase the hydrophilicity and roughness of the SU-8 surface. This procedure promotes subsequent cellular adhesion or optional functionalization with extra cellular matrix materials to further promote cell attachment. These devices were packaged to enable individual electrical connectivity to the nanofiber probes, potted to encapsulate the peripheral wire bonds using a medical grade epoxy (FDA2T, Tracon, MA), and configured with an attached cell culture dish (25-mm Nunc Delta, or 15-mm-OD glass cylinder), also attached using medical grade epoxy. Fully assembled nanofiber arrays were characterized using cyclic voltammetry by measuring the steady-state reduction current of ruthenium hexamine trichloride at various concentrations (McKnight et al. 2004).

### *Cell Culture*

A multitude of cell culture experiments were performed throughout the course of this project for evaluation and optimization of both the biocompatibility and electrical probing characteristics of the fabricated arrays. Commercially available rat hippocampal cells (E18, BrainBits, LLC) were disassociated and seeded onto the nanofiber array chips. Rat pheochromocytoma cells (PC-12) were maintained in non-differentiated culture and then seeded onto the nanofiber array chips. Differentiation media was applied using standard published techniques. Both cell culture types were monitored via optical microscopy to observe attachment and outgrowth of neural processes.

### *Neural Activity Recording*

Cultured VACNF arrays were monitored for activity using cyclic voltammetry having a typical scan between -0.8 V and 0.8 V vs Pt (pseudo) at scan rates from 500 mV/sec to 10 V/sec. Constant potential amperometry was also conducted by applying potentials sufficient to oxidize dopamine and norepinephrine (0.85 V vs Pt pseudo) at the nanofiber electrode and monitoring oxidation current over a typical period of 30 seconds to several minutes. In many experiments, the applied potential to the working electrode was sufficient to induce excitable activity in the neighboring cell matrix. Cell stimulation was also applied in some experiments either by application of potential to neighboring nanofiber electrodes within the array, or by application of a secretogogue, $K^+$, to the solution via pipette or pulled capillary.

## Results and Discussion

Two integrated circuit designs were fabricated using a 0.5-µm bulk CMOS process. Each chip incorporated a high-gain, low-noise preamplifier for neuronal action potential monitoring configured as a 4×4 array of preamplifier pixels at a pitch of 320 µm. Preamp_ASIC1 employed a variable input impedance amplifier (> 5MΩ) with measured selectable voltage gains of 30, 60, 120 and 240 V/V. This amplifier provided a very low input-referred noise measured as ~4 µVrms (10-kHz bandwidth). A microphotograph of the Preamp_ASIC1 chip is shown in Fig. 1(ii). Preamp_ASIC2 incorporated a charge-sensitive amplifier with a measured charge gain of 10V/pC. Both designs clearly demonstrated the feasibility of realizing high-density, pixelated preamplifier arrays with either full analog waveform readout or time-resolved spike detection

at each pixel. The use of small feature size fabrication processes, advanced analog design techniques, and increased focus on pixel miniaturization will enable the realization of fully programmable, high-density arrays (≥512 pixels) having both programmable stimulation and monitoring capability with pixel pitch of 100–200 μm.

Type I and Type II nanofiber array types were successfully grown by DC-plasma-enhanced CVD from lithographic definition of a nickel catalyst film. Type I nanofibers typically measured 100-nm diameter and approximately 10 microns in length. Projection lithography definition of the interconnect pattern provided individually addressable nanofibers as close as 2 microns apart. For the Type II arrays, the nickel catalyst was defined using contact lithography, producing catalyst dots of 1–2 microns in diameter. These typically broke up during nanofiber growth, producing a small group of fibers with one dominant fiber near the center of each grouping. The interconnect pattern provided by contact lithography allowed individual addressability of these groups at a 15-micron pitch. Following SEM examination, devices were packaged and a culture volume defined using culture dishes or glass tubes, and medical-grade epoxy.

Methods for seeding and growth/differentiation of PC-12 and E18 on packaged and operable nanofiber array chips were developed and optimized, including evaluation of surface preparation techniques, sterilization methods, passage and feeding schedules, and a variety of handling techniques to promote adhesion and proliferation. The attachment of the derived Rat pheochromocytoma cell line (PC-12) and the primary rat hippocampal neurons (E18) were both enhanced following oxygen plasma etching of the SU-8 interface. This process increases the surface roughness and hydrophilicity of the substrate, making it more suitable for cell attachment. Figure 1(iii) shows a scanning electron micrograph of differentiated PC-12 cells on a Type II nanofiber array. Prior to imaging, cells were fixed in 2% gluteraldehyde and dehydrated with methanol. The neurite processes of differentiated PC-12 cells can clearly be distinguished as can occasional varicosities at neurite junctions.

Following typically at least 7 days of differentiation in culture on nanofiber arrays, PC-12 and E18 cells were electrophysiologically evaluated via the nanofiber electrode substrate. Figure 1(iv) presents the response of E18 after 16 days in vitro (DIV) during cyclic voltammetry at an individual nanofiber electrode of the Type I device. In this cyclic voltammogram, oxidative bursts can be discriminated after the first set of sweeps (a and b) at potentials greater than 0.4 V on each of the subsequent three sweeps (c, d, and e). These spikes are putatively indicative of exocytosis and oxidation upon the nanofiber electrode of easily oxidized catecholamines, such as dopamine or norepinephrine. Integration of the CV under each spike provides a measurement of the associated oxidized charge, and calculated values are consistent with other studies of E18 vesicular quanta.

This study has established that arrays of non-planar, high-aspect-ratio nanofiber electrodes may be employed for relatively long-term studies of neuronal cell differentiation and communication. Nanofibers are electrochemically active structures that may be integrated into parallel arrays using the conventional tools and approaches of micro fabrication. Similar to planar electrode arrays, nanofiber electrodes may be employed in a resident interfacing mode, where neuronal cells are cultured, differentiated, and electrophysiologically evaluated directly on the electrode array. In contrast to conventional planar arrays, however, nanofibers provide a novel, non-planar, high-aspect-ratio structure that may provide unique opportunities for probing intercellular phenomena. As part of this study, we have demonstrated electroanalytical application of the nanofiber electrodes for observing chemical forms of communication between cells, and specifically the exocytotic release of easily oxidized neurotransmitters from differentiated cultures of primary rat hippocampal neurons and rat pheochromocytoma. We anticipate that future efforts with patterning neuronal differentiation upon nanofiber arrays and temporal electrophysiological probing of the differentiation cultures will provide unique insights into neurogenesis, neuro-pharmacological response, and the fundamental mechanisms and subtleties of cell-to-cell signaling.

These research accomplishments provide a solid foundation for future efforts directed towards full realization of a high-density, integrated neuronal stimulus/monitoring array. Advancements were made in fabrication and transfer methods, allowing the integration of nanofiber arrays with lower-temperature structures, including CMOS integrated circuits. Measurement results from fabricated custom integrated low-noise preamplifiers indicate comparable or improved performance over less integrated published circuits for action potential monitoring. Furthermore, experimental results demonstrating successful electrophysiological responses and post-culture SEM inspection of devices support the premise of healthy cell/nanofiber interaction over culture durations of several weeks.

## Benefits

The base technology advances resulting from this research have great potential for wide application in neuroscience and neuromedicine, including brain-machine interfacing, advanced prosthetics interfacing, functional neuromuscular stimulation, retina and auditory nerve stimulation, spinal cord stimulation for treatment of chronic pain, and genomics and pharmacological research.

Specifically, we anticipate interest from DOE OBER, DARPA, NIH, and the commercial sector. Efforts are under way to establish new programs with NIH (NINDs and NIBIB) and with DARPA (advanced prosthetics interfacing). In addition, it is expected that significant commercial interest will develop, resulting in new licensing and funding opportunities.

## References


Craighead, H. G., C. D. James, and A. M. P. Turner. 2001. "Chemical and topographical patterning for directed cell attachment." *Current Opinion in Solid State & Materials Science* **5**(2–3), 177–184.

Cunningham, W., K. Mathieson, F. A. McEwan, A. Blue, R. McGeachy, J. A. McLeod, C. Morris-Ellis, V. O'Shea, K. M. Smith, A. Litke, and M. Rahman. 2001. "Fabrication of microelectrode arrays for neural measurements from retinal tissue." *J. Phys. D: Appl. Phys*. **34**, 2804-2809.

Heiduschka, P., I. Romann, T. Stieglitz, and S. Thanos. 2001. "Perforated Microelectrode Arrays Implanted in the Regenerating Adult Central Nervous System." *Experimental Neurology* **171**, 1–10.

Lundqvist, J. A., F. Sahlin, M. A. I. Aberg, A. Stromberg, P. S. Ericsson, and O. Orwar. 1998. "Altering the biochemical state of individual cultured cells and organelles with ultrmicroelectrodes." *Proc. Natl. Acad. Sci.* **95**, 10356–10360.

McKnight T. E., A. V. Melechko, G. D. Griffin, M. A. Guillorn, V. I. Merkulov, F. Serna, D. K. Hensley, M. J. Doktycz, D. H. Lowndes, and M. L. Simpson. 2003. "Intracellular integration of synthetic nanostructures with viable cells for controlled biochemical manipulation," *Nanotechnology* **14**(5), 551–556.

McKnight T. E., A. V. Melechko, D. K. Hensley, G. D. Griffin, D. Mann and M. L. Simpson. 2004. "Tracking Gene Expression after DNA Delivery Using Spatially Indexed Nanofiber Arrays," *NanoLetters* **4**(7), 1213–1219.

Tatic-Lucic, S., J. A. Wright, Y. C. Tai, and J. Pine. 1997. "Silicon cultured-neuron prosthetic devices for in vivo and in vitro studies." *Sensors and Actuators B* **43**, 105–109.

Zeck, G., and P. Fromherz. 2001. "Noninvasive neuroelectronic interfacing with synaptically connected snail neurons immobilized on a semiconductor chip." *Proc. Natl. Acad. Sci.* **98**(18), 10457–10462.

# Characterizing the Complex Metaproteomes of Microbial Communities

B. H. Davison,[1] N. C. VerBerkmoes,[2] G. B. Hurst,[2] A. P. Borole,[1] M. Shah,[1]
B. Raman,[1] F. W. Larimer,[1] and R. L. Hettich[2]
[1]*Life Sciences Division*
[2]*Chemical Sciences Division*

This project demonstrated metaproteome analysis techniques for mixed cultures, establishing the basis for "whole community proteomics." We have obtained preliminary data demonstrating that the analytical dynamic range of liquid chromatography-mass spectrometry and bioinformatic tools are capable of identifying individual proteins from specific microbes while in a mixed culture. We focused on analysis of complex proteomes by 2D-LC techniques coupled with quadrupole ion traps for peptide sequencing by tandem mass spectrometry. Results to date using "constructed" mixed cultures of known microbes indicate that we can detect the presence of a sequenced microbe, *Rhodopseudomonas palustris*, below 1% of the total population and that key marker proteins of metabolic state (i.e., phototrophic) are identified even when present at less than 0.2% of the total population. Our primary goal was to establish the dynamic range and "deep" proteome coverage of mass spectrometry (MS) analysis for mixed cultures, both for simple identification of the presence of a minor community member and for the far more difficult goal for telling the state of the microorganism while in the community. We also examined the bioinformatics challenge using the impact of the number of different microbes in the proteome database on the ability to identify unique peptides.

## Introduction

Recently, there have been strong efforts to develop techniques for genomic sequencing and annotation of microbial communities (metagenomics). With the potential of partial or near-complete microbial genomes obtained from environmental samples, along with the rapid proliferation of isolated microbial genomes, systems biology in microbial communities by combining genomic, transcriptomic, proteomic and metabolic studies may be possible in the near future. Our exploratory project sought to develop and demonstrate metaproteome analysis techniques for mixed cultures, establishing the basis for "whole community proteomics." Our major focus was to use controlled, simple microbial mixtures of four species (*E. coli*, *S. cerevisiae*, *R. palustris*, and *S. oneidensis*) to develop MS-based proteomics methods, as well as the proteome bioinformatics tools for detailed analysis of sequenced microbial communities. These experiments grew from preliminary data on the growth of mixed cultures, "shallow" peptide MS analysis to identify microbes in mixtures, and "deep" proteome analysis ongoing for single microorganisms. Our goal was to provide an experimental and computational platform for "deep" and "wide" proteome measurements of complex microbial mixtures.

When mass spectrometry–based systems are extended to mixed cultures, several critical questions arise:

1. the power to find a protein in the "cloud" of interference from other proteins and other microbial proteomes;
2. the evaluation of the "state" of a community when most (or all) members are unknown (e.g., unsequenced) microorganisms; and
3. the ability to quantitate the proteins' amounts. We focused on the first two questions. The goal of this study was to assess and improve MS-based "shotgun" proteomics technology for analyzing simple known microbial mixtures. The purpose was to evaluate the limit of current LC-MS/MS technologies and then improve upon current techniques and develop analytical procedures for analyzing highly complex communities and environmental samples.

There are multiple considerations for proteome analysis of microbial communities. These include genomic information on the level of DNA sequence availability and quality of annotation for species in that community, total biomass available, the number and dynamic range of species present, and inter- and intra-species relationship at the amino acid level.

## Technical Approach

We originally proposed three aims to demonstrate state-of-the-art mass spectrometry for "deep" proteomic characterization of microbial communities. We focused on analysis of complex proteomes by automated liquid-based chromatography techniques coupled with ion traps for peptide sequencing by MS/MS. Because of its wide metabolic diversity, *R. palustris* was our target for these first sentinel studies. This project was funded in FY 2004 with $150K and in FY 2005 with $170K, requiring the

project to be rescoped to focus primarily on Aim 1, while deleting Aim 2 and reducing Aim 3.

### *Specific Aim #1. Improved "deep" proteome characterization in the presence of other microorganisms*

The objective of this specific task was to develop and demonstrate advanced mass spectrometric technology and bioinformatic data mining for mixtures of microorganisms. Emphasis was placed on evaluation of the depth of proteome characterization of a target microbe at different proportions in the mixture, as well as the dynamic range of protein measurement until the metabolic information is lost in the background.

We grew separate single microbial cultures under defined conditions and then mixed these biomass samples together in defined ratios prior to protein digestion via trypsin and MS analysis. We used *E. coli*, *Saccharomyces cerevisiae*, *R. palustris*, and *Shewanella oneidensis* as model organisms. We cultivated batch aerobic heterotrophic biomass samples of each grown on a common media that we developed. To provide sufficient biomass for uniform analysis, large samples were frozen for later use. For the MS-based proteomics, we verified the four proteomes individually. Mixed samples were run with equal portions of each (25 wt % each); then only the *R. palustris* fraction was decreased to 5%, 1%, 0.2% and 0% of the total, while the other organisms were held constant. *R. palustris* was produced under anaerobic photoheterotrophic (on succinate and on benzoate), photoautotrophic, and nitrogen fixation conditions. These samples were mixed with the other bacteria to determine if we could distinguish the active metabolism of the *R. palustris* cells in the presence of other bacteria. Comparisons were then made between nitrogen fixation vs. photoheterotrophic and chemoheterotrophic vs. photoheterotrophic. Mixed cell pellets were washed twice with Tris buffer and sonicated. A crude and membrane fraction were separated by ultracentrifugation at 100,000g for 1 hour. Protein fractions were quantified and digested with sequencing grade trypsin. The digested mixed proteomes were desalted via solid-phase extraction and concentrated to ~10µg/µL and frozen at -80ºC until analysis. Experimental artifacts can be caused by differential lyses of different microbes, as shown by the yeast protein proportion due to the resistance of yeast to sonication.

The tryptic digestions of the crude and membrane fractions from all mixtures were analyzed via 24-hour two-dimensional LC-MS/MS with a split-phase MudPIT column. The LC-MS system was composed of an Ultimate HPLC (LC Packings) and an LCQ-DECA XP ion trap mass spectrometer (Thermo Finnigan) or an LTQ linear trapping quadrupole (Thermo Finnigan). Each analysis required ~500µg of starting protein material from either the crude or membrane fraction. The resultant MS/MS spectra from the mixed proteomes were searched with SEQUEST (Thermo Finnigan) against the four databases highlighted below. The resultant files were filtered and sorted with DTASelect, and unique and non-unique peptide identifications were extracted with in-house perl scripts. Reverse database searches were employed to test false positive levels.

### *Specific Aim #2. Proteome differentiation and bioinformatic analysis of mixed microbial cultures*

The goal here was intended to replace the constructed mixtures of different bacteria with a mixed culture cultivated together. After successful preliminary co-cultivation and analysis of the mixture, this was eliminated in favor of analyzing more growth states above and moving to exploratory tests in Aim 3.

### *Specific Aim #3. "Sentinel organism" proteome monitoring in microbial communities*

A challenge to the application of current genomic or proteomic techniques in natural microbial communities is that the vast majority of microorganisms have not been sequenced, and the bioinformatic use of the genome sequence is the Rosetta stone on which the MS protein identification rests. One conceivable approach within current bioinformatic limits is to study these microbial communities using a characterized "sentinel" organism. A sequenced, characterized microbe would be added to a mixed microbial culture or environmental community, and the response of its proteome to the microbial community and environment could be followed – allowing prediction of community state, interactions, upsets, shocks, excreted proteins, quorum sensing, etc. We are completing proteome analysis of natural pond water that was spiked with *R. palustris*. This challenges using proteomics in an uncharacterized unsequenced mixed cultures. The critical question: can we characterize *R. palustris* proteome deeply enough to establish its state in a real uncharacterized unsequenced messy mixed culture, similar to the natural environment from which it was isolated?

## Results and Discussion

With 24-hour 2D-LC-MS/MS analysis on LCQ, *R. palustris* was easily identified at 25%, 5% and 1%, although the latter condition was somewhat difficult to measure (Fig. 1). However, the 70 unique proteins identified at the 1% level were distributed across all of the functional groups, indicting that some functional state information could be determined. A few unique proteins could be detected confidently at the 0.2% level. Specifically, a marker of phototrophic growth, *puhA*,

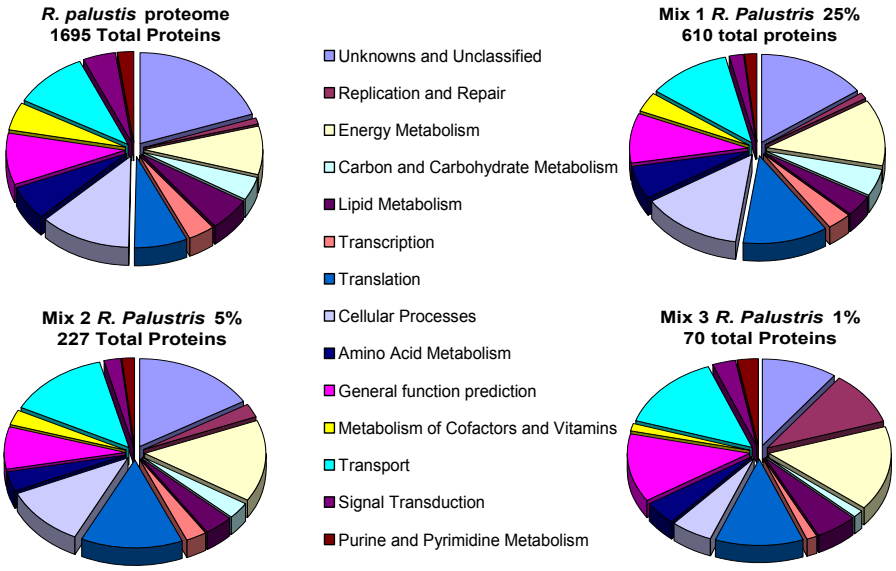


*Fig. 1.* R. palustris *functional categories at decreasing wt fractions.*

was clearly identified by a unique diagnostic peptide at the 0.2% level. While these results were promising, it was clear that improvements were needed to obtain deep enough proteome coverage at less than 5% to clearly classify metabolic state information.

One fundamental challenge of community proteomics is that the statistics of one sequenced microbe favor each protein to have several unique peptides. But when a full diversity of multiple species is included in the peptide database, the statistics falter. We created three proteome databases (of 4, 13, and 260 species) to test the effect of database size. Larger databases diminish identification of unique peptides for any given species, but species such as *E. coli* with many close relatives in the database are affected disproportionately. Even so, *R. palustris* was still distinguishable. However, the number of false positives increases with database size and began to approach the level of *R. palustrsis* at 1%. The false positive rate found using the reverse database was relatively low for the identified peptides and proteins at the 2-peptide level. Proteins identified at the 1-peptide level had a comparatively higher false positive rate, indicating the conservative 2-peptide filter was more accurate. The effects of database size on unique peptide identification were examined. Databases should be limited to the community genome plus a small number of distracters.

We have identified clear metabolic functional protein markers for different functional metabolisms of *R. palustris* (aerobic chemoheterotrophic, anaerobic photoheterotrophic, nitrogen fixing) in pure culture samples using 2D-LC-MS/MS. These were compared in the presence of the three other microbes (all at 25%). 3D-LC-MS/MS methods were tested with LCQ technology but supplanted by the more powerful LTQ MS instrument to obtain deep proteome analysis of the same *R. palustris* fraction samples with 2D-LC techniques.

Table 1 shows differential expression of some nitrogen fixation proteins from the nitrogen fixation vs. photoheterotrophic metabolic states at the 25% mixture. The strongest differences are highlighted in red and blue, highlighting represents known nitrogen fixation proteins. This indicates the ability to measure metabolic state. These experiments have been extended to the 5% and 1% mixture on the LTQ with the nitrogen fixation state. Results clearly indicate that the nitrogen fixation metabolic state can be directly characterized with 2D-LC-MS/MS on LTQ ion traps.

In this project, we have developed methods for deep metaproteome characterization and have tested the limits of these methods in microbial communities.

## Benefits

The success of this project should position ORNL for high probability funding from DOE Biological and Environmental Research Genomics:GTL (GTL) program in understanding microbial communities. Microbial communities are a central part of Goal 3 of the GTL program. We have preliminary evidence on our development and demonstration of advanced technology for complex proteome measurements (primarily focused on MS) and bioinformatics of mixed cultures. This should establish ORNL's capabilities in microbial community proteomics and in proteomics as future tools to understand the state and function of communities of DOE interest. Dr.

**Table 1. Nitrogen Fixation vs. Photoheterotrophic Activated Genes in Rpal at 25%**

| | Anaerobic Heterotroph | | | Nitrogen fixing conditions | | | |
|---|---|---|---|---|---|---|---|
| Run | LCQ1 | LCQ2 | LTQ1 | N2_LCQ1 | N2_LCQ2 | N2_LTQ1 | |
| Gene | % Coverage | | | % Coverage | | | Function |
| **RPA0274** | 0 | 0 | 0 | 38.4 | 38.4 | 71.4 | glnK2 GlnK, nitrogen regulatory protein P-II |
| RPA1927 | 0 | 0 | 0 | 32 | 32 | 57.7 | hypothetical protein |
| RPA1928 | 0 | 0 | 0 | 20.5 | 20.5 | 61.6 | ferredoxin-like protein [2Fe-2S] |
| RPA2125 | 0 | 0 | 26.4 | 31.8 | 31.8 | 68.2 | conserved unknown protein |
| RPA2903 | 0 | 0 | 9.1 | 0 | 0 | 45.5 | lexA SOS response transcriptional repressor |
| RPA3011 | 0 | 0 | 9.9 | 0 | 0 | 58.5 | unknown protein |
| RPA3669 | 0 | 0 | 0 | 28.6 | 28.6 | 45.2 | putative urea short-chain amide or branched-chain amino acid uptake ABC |
| **RPA4209** | 0 | 0 | 0 | 12.5 | 12.5 | 27.5 | glnA II glutamine synthetase II |
| **RPA4602** | 0 | 0 | 0 | 19.4 | 19.4 | 11.2 | fixX ferredoxin like protein |
| **RPA4603** | 0 | 0 | 0 | 23.4 | 23.4 | 52 | fixC nitrogen fixation protein |
| **RPA4604** | 0 | 0 | 0 | 13.6 | 13.6 | 25.5 | fixB electron transfer flavoprotein alpha chain protein |
| **RPA4605** | 0 | 0 | 0 | 13.9 | 13.9 | 59.8 | fixA electron transfer flavoprotein beta chain |
| **RPA4608** | 0 | 0 | 0 | 0 | 0 | 11.2 | nifS2 nitrogenase cofactor synthesis protein |
| **RPA4614** | 0 | 0 | 0 | 14.9 | 14.9 | 49.4 | DUF269 |
| **RPA4615** | 0 | 0 | 5.3 | 0 | 0 | 33.3 | nifX nitrogenase Mo-Fe protein |
| **RPA4618** | 0 | 0 | 0 | 45.9 | 45.9 | 65.1 | nifK nitrogenase MO-Fe protein beta chain |
| **RPA4619** | 0 | 0 | 0 | 37 | 37 | 63.2 | nifD nitrogenase Mo-Fe protein alpha chain |
| **RPA4620** | 0 | 0 | 0 | 49.3 | 49.3 | 60.7 | nifH4 nitrogenase iron protein |
| RPA4621 | 0 | 0 | 0 | 12.7 | 12.7 | 22.3 | conserved hypothetical protein |
| **RPA4623** | 0 | 0 | 0 | 68.2 | 68.2 | 69.7 | fixU, nifT conserved hypothetical protein |
| RPA4624 | 0 | 0 | 0 | 28.6 | 28.6 | 28.6 | hypothetical protein |
| RPA4631 | 0 | 0 | 0 | 14.1 | 14.1 | 15.6 | fer1 ferredoxin 2[4Fe-4S], fdxN |
| **RPA4632** | 0 | 0 | 0 | 1.4 | 1.4 | 6.5 | nifA Mo/Fe nitrogenase specific transcriptional regulator |

Davison discussed this with Dr. Drell and Dr. Thomassen of the Office of Biological and Environmental Research (OBER), who agreed that this is of interest. Dr. Drell has encouraged submission of a white paper.

The analysis improvement and techniques will also aid in other GTL goals, such as Goal 4 to "develop computational capabilities … to model complex biological systems." The techniques for "deep" proteomics in mixed cultures will be directly applicable to more rapid and "deeper" protein identification in pure cultures with smaller samples and would assist the identification of protein machines (GTL Goal 1) Also certain important protein complexes may be more easily produced in mixed culture cultivation techniques.

The several project directions were described in more detail in the original proposal and are still valid.

1. The "sentinel" organism concept and its extension to the use of naturally present close relatives of sequenced organisms to probe microbial communities, states, and functions in realistic scenarios. While not fully proven here, this would access unobtainable knowledge in the natural environment without the addition for "foreign" organisms and without direct genome sequencing. This approach in the environment could track functionally the metabolically versatile *R. palustris* or *S. oneidensis* where its metal reduction abilities are needed. This could drive another research area into bioinformatics to relax the guidelines to search for homolog proteins while maintaining critical activities and informative knowledge.
2. A proposed complete characterization of an entire specific microbial community by linking with ORNL's techniques and efforts in metabolomics and community genomics; this would directly feed into the environmental systems initiative and could utilize the Field Research Center.
3. Mixed culture proteomic studies of a specific mixed microbial culture. These tools are already being applied in other projects. This has been successful with an extremophile acid-mine-drainage community that has a limited diversity of about five populations (Tyson et al. 2004). This LDRD positioned ORNL

to receive some OBER funds to support Banfield's work in FY 2005 at University of California-Berkeley with descriptive MS proteome analysis resulting in a Science paper (Ram et al. 2005). It also positions ORNL to be part of a new GTL project in this area. These projects do not address the technology development or broad questions on communities. Microbial communities also are critical in biological methane production, in soil carbon cycles, and in bioremediation and stabilization of pollution. This could also impact studies of pathogens in their environment and in ecosystems research. Microbial-plant communities are important for agricultural and biomass growth—especially in the uptake of nutrients and high productivity.

## References

Ram, R. J., N. C. Verberkmoes, M. P. Thelen, G. W. Tyson, B. J. Baker, R. C. Blake II, M. Shah, R. L. Hettich, and J. F. Banfield. 2005. "Community proteomics of a natural microbial biofilm," *Science* **308**, 1915–20.

Tyson, G. W., J. Chapman, P. Hugenholtz, E. E. Allen, R. J. Ram, P. M. Richardson, V. V. Solovyev, E. M. Rubin, D. S. Rokhsar, and J. F. Banfield. 2004. "Community structure and metabolism through reconstruction of microbial genomes from the environment," *Nature* **428**, 37-43.

# Exploring New Methodologies in Detecting Low-Abundance Protein Complexes

Y. Wang,[1] Y. Liu,[1] and G. Hurst[2]
[1]*Life Sciences Division*
[2]*Chemical Sciences Division*

While mass spectrometry coupled with liquid chromatography (LC-MS) has been successfully used to identify abundant protein complexes for DOE's Genomics:GTL program in ORNL, a more effective method is needed to improve affinity purification and identification of low abundant protein complexes that are of greater biological relevance. For this purpose, we have engineered nine novel tandem affinity tag (TAP) vectors with a Tev cleavage site flanked by high-affinity short tags at N- or C-terminals driven by constitutive and regulatable promoters. An in-frame fused tetra-cysteine motif has enabled us to detect tagged proteins in live cells and gels without the need of antibody application prior to MS analysis. In comparison with the single tag, we demonstrated that the TAP system allowed more efficient and accurate isolation of low abundant telomere-associated proteins, verified by co-immunoprecipitation experiments. We optimized the expression, tandem-affinity purification, protease cleavage and elution conditions and pushed the limit down to $1 \times 10^7$ cells as starting materials for MS identification. Due to the efficiency of sequence coverage, we were able to map putative and known phosphorylation sites of a telomere-associated-protein TRF2 by LC-MS. This work will benefit our current efforts in identification and characterization of microbial protein complexes for Genomics: GTL project.

## Introduction

The study of complex proteomes is an important research area emerging from the Genome Projects. Currently at ORNL, single protein tagging coupled with "shotgun" mass spectrometric approach has been applied to high-throughput identification of protein complexes in the anoxygenic photobacterium *Rhodopseudomonas palustris*. Although the "shotgun" approach is high throughput (Link et al. 1999) and has great potential for the Genomics:GTL program, it often results in less robust protein identification even by the standard of the most sensitive quantitative LC-MS approach. This would dramatically compromise the accuracy in protein complex identification. The tandem affinity purification (TAP) method allows multiple harsh purification procedure. The original TAP tag consists of two IgG binding domains of *Staphylococcus aureus* (ProA) and a calmodulin binding peptide separated by a Tev protease cleavage site (Rigaut et al. 1999). Due to the high versatility of the TAP, we have vigorously engineered nine novel TAP vectors. The focus of this project is to establish a high affinity protein tagging and pull-down system, which, in combination with the advanced high-throughput MS technology, will greatly facilitate the identification of specific-interacting proteins and reduce unspecific contaminants that hinder the identification of authentic sub-stoichiometric components of low abundant protein complexes. The newly engineered vectors utilize the Gateway system (Invitrogen), which will allow for a simple one-step transfer of our original source clones into expression "destination" vectors of multiple species. This tandem-affinity purification system has enabled us to monitor the tagged proteins throughout the purification steps using an easy detection of tetra-cysteine motif, and LC-MS identification of low abundant telomerase-associated proteins and post-translational phosphorylations with "push-to-limit" starting materials. Our study suggests that the TAP system we have developed can be used to purify and identify low abundant protein complexes in combination with "shotgun" LC-MS efficiently.

## Technical Approach

In this study, various peptide tag combinations have been developed to increase our ability to address difficulties that may arise from using a single tag or a single vector for the protein complex pull-down studies. These include those that could affect complex formation or stoichiometry, such as steric interference or structural perturbations due to the incorporation of the tags. Since many of these problems can be avoided by altering either position of the tag (C- or N-terminal), type of tag, level of expression, or protein purification procedure, we design to create and explore new TAP vectors that include various short high-affinity peptide tags, a Tev protease recognition site in between the two tags, a tetra-cysteine motif, and a regulatable promoter. The high affinity of the tags in combination with the site-specific protease cleavage-purification can tolerate multiple stringent purification

procedures (Rigaut et al. 1999) and will allow us to perform a more robust and rapid two-step protein purification of complexes from a relatively small amount of cells. This can be accomplished even without prior knowledge of the complex composition, activity, or function. The incorporation of the tetra-cysteine motif and a regulatable promoter will facilitate easy detection of the tagged protein throughout the purification steps and modulation of tagged protein expression at will, respectively. For this purpose, we have created the following TAP vectors (Fig. 1A, a simplified vector map):

(1) tetracycline regulatable N-terminal tagging vector I: His-tev-strep-4Cys
(2) tetracycline regulatable N-terminal tagging vector II: His-strep-4Cys
(3) tetracycline regulatable N-terminal tagging vector III: ProA-tev-strep-4Cys
(4) C-terminal tagging vector I: 4Cys-strep-tev-His
(5) C-terminal tagging vector II; 4Cys-strep-His
(6) C-terminal tagging vector III: 4Cys-strep-tev-ProA
(7) C-terminal tagging vector IV: strep-4Cys-tev-ProA
(8) C-terminal tagging vector V: His-tev-HA
(9) C-terminal tagging vector VI: HA-tev-ProA.

All the vectors are engineered in the Invitrogen Gateway system, which allows for rapid high-throughput cloning of target genes and are compatible with the Gateway entry clones of *R. palustris* genes; that is, with one-step modification, our vectors can be readily used for the Genomics:GTL project.

To demonstrate the "proof-of-principle," we first cloned two mammalian proteins, TRF-2 and Cdc-14 into these vectors. We chose TRF-2 and Cdc-14 as a test model system because they are low-abundant, telomere and cell cycle–related proteins (Gomez in press; Cho et al. 2005), and some of the protein components in the complex are known. We first examined the usefulness of the in-frame tetra-cysteine motif. Membrane-permeant biarsenical dyes such as FlAsH and ReAsH fluoresce upon binding to genetically encoded tetracysteine motifs expressed in living cell (Martin et al. 2005). We found that in the presence of this embedded motif, the tagged proteins can be visualized in living cells and correctly targeted to their authentic subcellular locations in the presence of biarsenic compound. For example, we detected the tagged TRF2 and Cdc14B in telomeres, mitotic chromatins and nucleus, respectively (Fig. 1C, middle panel). In addition, instead of the time-consuming and labor-intensive western blot, we can easily detect the fusion proteins in SDS-PAGE gel using a commercial-available Lumio-compound (Fig. 1C, bottom panel). This has significantly shortened the time one usually has to spend for the confirmation of the quality of the tagged proteins using conventional antibody-based western blot approach. We also demonstrated that the level of the expressed tag protein can be modulated close to physiological level through the tetracycline-inducible promoter [Fig. 1B, lane 3: comparison between the upper band (exogenous TRF2) and lower band (endogenous TRF2)]. This later

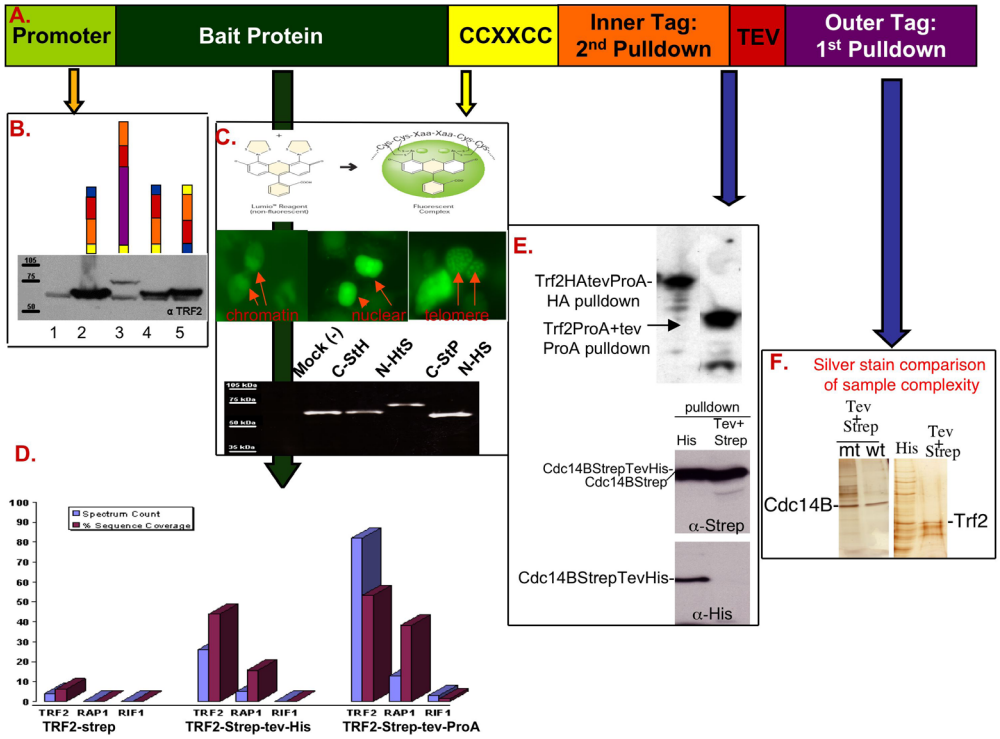


*Fig. 1. Schematic and summary of the tandem-affinity purification system developed in this study.*

helped us to significantly reduce the non-specific bound proteins due to the notorious overexpression scheme most of the protein labs usually implemented in their protein complex pulldown studies.We compared both N- and C-terminal tagged TRF2 and Cdc14B for the fidelity of complex identifications by LC-MS and found that there is no general rules on which terminal tagging is better than the other. Individual protein has to be tested and treated differently perhaps due to conformation or structure of a particular protein. Seven out of nine TAP vectors were engineered with a site-specific Tev protease cleavage site flanking by two high-affinity short peptide tags. This provided us the opportunity to explore and optimize the tandem affinity binding, Tev protease cleavage and elution conditions for the fusion proteins. We compared both batch and column purifications with buffers of different stringency. We found that in general the column purification provided cleaner materials for the subsequent LC-MS analysis. In comparison with the single tagging strategy, we found that the TAP tag system usually can tolerate more stringent high salt washing conditions and reduce many non-specific bound proteins (Fig.1F). We tried up to 400 mM NaCl in washing steps before and after Tev cleavage and were still able to pulldown specific interacting proteins of TRF2 with a sequence coverage (spectrum count) of 44.0% (26) and 53.2% (82) for the TRF2 and 15.8 (5) -38.3% (13) for a TRF2 interacting protein RAP1 (Fig.1 D). With the same washing condition for TRF2 single tag, the sequence coverage was down to 6.2% (spectrum count of 4). We optimized the buffer compositions for Tev cleavage and protein complex elution, which are often encountered as the most troublesome in obtaining sub-stoichiometric components of low abundant protein complexes because improper buffer change can usually cause protein aggregation during Tev cleavage and protein elution. We found that commercial Tev cleavage buffer was the worst, whereas our modified 300 mM NaCl containing buffer resulted in more than 90% recovery of the cleaved tagged proteins (Fig.1 E). We verified the efficiency and applicability of our new tagging system by LC-MS identification of several known TRF2 and Cdc14B interacting proteins, such as PARP2, RAP1, RIF1 and B23, which were in turn confirmed by co-immunoprecipitation with specific antibodies. We also identified several potential novel TRF2 and Cdc14B interacting proteins which are currently under investigation. With this approach, we were able to obtain sufficient sequence coverage and spectrum count of the tagged TRF2 and specific interacting protein RAP1 (see above) from as low as $1 \times 10^7$ cells. The significant sequence coverage and spectrum counts of TRF2 enabled us to search the masses of TRF2 peptides for possible post-translational modification, such as phosphorylation by DBDigger, a search engine developed in house by ORNL team (Tabb et al. 2005). We identified 24 potential phosphorylation sites in TRF2, two of which have been biochemically characterized previously and thirteen of which were predicted by the NetPhos 2.0 with a score of >0.500, a neutral-network I in silico-based approach for predicting sites of phosphorylation.

## Results and Discussion

We engineered nine novel TAP tagging vectors for affinity purification of low abundant protein complex. As noted above, the advantage of the TAP system include the following:

1. easy detection throughout the affinity purification steps,
2. variety of choices on the length and property of tags, N- vs C-terminal fusions,
3. controllable expression to near physiological levels,
4. more tolerance to harsh washing conditions, and
5. less starting materials (cells) needed.

We have also demonstrated the advantage of TAP vectors in two-step protein purification over single-step purification. This was both in the quality of the purified protein complex and its suitability for downstream mass spectrometry analysis. Our success has been demonstrated using the low abundant telomere-binding and cell cycle–regulated proteins as baits, and we have identified novel telomere-associated and cell cycle–specific proteins using a shotgun-base mass spectrometry approach. More importantly, the quality and the quantity of sequence coverage was good enough for protein post-translation modification studies. Data obtain from this study has been summarized in a manuscript for publication(Giannone et al. in preparation).We envision that the applicability of the newly developed TAP system will be enormous. All our TAP tags are constructed in the Invitrogen Gateway system. Invitrogen Gateway system utilizes λ phage-based att homologous recombination strategy to catalyze plasmid ligation with unprecedented efficiency. A gene, once introduced into pDONR vectors of the Gateway System, can be easily transferred into our TAP Gateway destination vectors and any other Gateway destination (expression) vectors of a variety of species using a single directional, non-restriction enzyme-based cloning step. Since the *R. palustris* genes for the Genomics:GTL project in ORNL have been constructed in the Gateway system, a single step modification by PCR will convert our TAP tag vectors to Genomics:GTL–compatible TAP expression vectors. We believe that application of our TAP tag system for Genomics:GTL project will benefit current efforts of the high-throughput protein complex studies. However, we do not want to imply that our TAP tags will work for all the proteins. A potential problem intrinsic to the all tagging system is the possibility that some tags might not be sufficiently exposed to allow binding of

the bait protein to affinity beads. Also the fusion of an affinity tag might affect the protein conformation in such a way as to eliminate certain protein-protein interactions. Moreover, ectopic overexpression of tagged proteins may lead to the assembly of non-physiological complexes, thus yielding false positive interactions. These problems can be minimized by leveraging a variety of TAP vectors with different combinations of tags (type of tags, size of the tags, C- or N-terminal position) and controlled via a tetracycline-inducible promoter. Furthermore, using different TAP vectors with the same bait protein will serve as excellent internal controls for each other and allow a more accurate assessment of background binding proteins.

## Benefits

Pursuing this research program has not only permitted us to solve important biological questions, such as identifying protein complexes important for cellular functions, but also brought a new avenue of research to ORNL. Demonstration of the improved sensitivity and selectivity in our complete pipeline for protein tagging, expression, purification, identification, and verification of protein complexes will greatly strengthen ORNL's position to secure funding for the proposed Genomics: GTL program for the Characterization and Imaging of Molecular Machines, and will benefit to the entire proteomics research community. This study has also resulted in one NIH grant application currently under review.

## References


Cho, H., Y. Liu, M. Gomez, J. Dunlap, M. Tyers, Y. Wang. 2005. "The dual specificity phosphatase Cdc14B bundles and stabilizes microtubules." *Mol. Cell. Biol*. **25**, 4541–4551.

Giannone, J. R., H. McDonald, G. Hurst, Y. Liu, and Y. Wang. In Preparation. "Development of novel protein tagging vectors to identify protein-protein interactions in mammalian cells using mass spectrometer."

Gomez, M., V. Schreiber. J. Dunlap. G. de Murcia, Y. Wang, Y. Liu. In Press. "PARP1 is a TRF2-associated poly(ADP-ribose) polymerase and protects eroded telomeres." *Molecular Biology of the Cell*.

Link, A. J., J. Eng, J., D. M. Schieltz, E. Carmack, G. J. Mize, D. R. Morris, B. M. Garvik, and J. R. Yates III. 1999. "Direct analysis of protein complexes using mass spectrometry." *Nature Biotechnology* **17**, 676–682.

Martin, B. R., B. Giepmans, S. Adams, and R. Tsien. 2005. "Mammalian cell-based optimization of the biarsenical-binding tetracysteine motif for improved fluorescence and affinity." *Nature Biotechnology* **23**, 1308–1314.

Rigaut, G., A. Shevchenko, B. Rutz, M. Wilm, M. Mann, B. Seraphin. 1999. "A generic protein purification method for protein complex characterization and proteome exploration." *Nature Biotechnology* **17**, 1030–1032.

Tabb, D. L., C. Narasimhan, M. B. Strader, and R. L. Hettich. 2005. "DBDigger: Reorganized Proteomic Database Identification That Improves Flexibility and Speed," *Analytical Chemistry* **77**(8), 2464.

# Genetic Variability in Host Responses to Bioterror Agents

D. K. Johnson,[1] C. T. Culiat,[1] E. J. Michaud,[1] G. Gupta[2]
[1]*Life Sciences Division, ORNL*
[2]*Los Alamos National Laboratory*

Human susceptibility/resistance to infection can be recapitulated in mice by generating mutations in genes known to influence host responses to a specific pathogen. A collaboration with Los Alamos National Laboratory (LANL) scientists who have been studying host-pathogen interactions using anthrax and other bioagents was established to generate such mutant mice and use them to understand how genetic variation in the host animal influences the ability of a pathogen to cause disease. We began by focusing on anthrax because of materials in hand at LANL but also included a more global approach by manipulating a mouse gene central to cellular pathways commonly co-opted by many pathogens. Understanding disease mechanism(s) in terms of gene or protein networks will significantly strengthen the Homeland Security effort to protect individuals from attack. Our results may reveal new molecular targets for therapeutics and also lead to the identification of individuals whose genetic makeup makes them especially vulnerable to attack.

## Introduction

The health threat to people who are exposed to sublethal doses of bioterror agents is uneven both because of the presence in the population of genetic variants that affect susceptibility to illness and also because of differences in age, gender, and general health status. In order to understand the differential vulnerabilities of individuals within an exposed population, we must (a) analyze the functions of genes that control response and (b) determine how environmental factors impact gene function. Our approach is to introduce mutations into the mouse homologs of genes that are known players in response to infection to see how mutation changes the infection outcome by changing the efficiency of the response pathway. We can then use the mice to investigate the roles of age, gender, and health status.

We want to understand genes, proteins, and disease mechanisms on a molecular level, so that pharmacological countermeasures may be designed to attack and/or inhibit the pathogen infection and disease-producing process before it starts. In addition, this knowledge can help classify individuals as susceptible or resistant to a particular bioagent, such that one can know a priori which countermeasures to take in the event of an attack or exposure.

These same mice can be used to investigate the molecular bases of variability in vaccine side effects, a related, but different, human susceptibility/variability problem in the arena of biothreat management. Pre-screening of populations that will be vaccinated would give us the opportunity to offer special medical surveillance to people likely to react to a vaccine.

Our goal in this LDRD project was to provide our microbiology colleagues who have Biosafety Level 3 facilities at Los Alamos National Laboratory (LANL) with immune-system cells from mice with mutations that might affect susceptibility as measured by dose required to initiate infection, time to onset of infection, quantitative and qualitative measurements of response molecules, and morbidity/mortality resulting from infection. This goal was met insofar as was possible given the safety-related stand-down at LANL and has spawned a number of continuing activities.

## Technical Approach

The laboratory of Dr. Goutam Gupta at LANL specializes in the study of genetic pathways that respond to pathogen infection in mammalian cells. Dr. Gupta designated two mouse genes critically involved in the infection process for which mutant mice would be invaluable, and we undertook to target mutations to these two genes. One gene is *Myd88*, a small adaptor protein that connects a generic cell-surface receptor used by many pathogens with intracellular proteins that direct immune-system response. The second is the anthrax receptor, *Atrx1*, a cell-surface protein used by the toxin from anthrax as a route of entry into immune-system scavenger cells in the lung. Because the kinds of mutations required for these two genes are unlike, two different mutagenesis approaches were used.

***Myd88***

The required mutation for *Myd88* was a minor one that compromises, but does not ablate, the function of the protein; a null mutation in this gene simply takes the entire pathway out of action and is not useful for understanding pathway function. This mutation was generated by scanning our Cryopreserved Mutant Mouse Bank (CMMB), which contains single-base mutations for every gene in the genome, for mutations in the part of the *Myd88* protein that interacts with the generic cell-surface receptor. From a functional standpoint, a small change in this part of the protein would likely cause a difference in the strength or quality of the protein-protein interaction that governs the response pathway. Importantly, it is this kind of small mutation that characterizes human-to-human differences in genetic makeup that control susceptibility/resistance to exposure.

***Atrx1***

Protein-binding studies at LANL as part of this project determined the specific peptide in the *Atrx1* protein that binds the toxin ligand at the cell surface. Dr. Michaud undertook to alter this protein, using homologous recombination technology, in two ways. First, he would change certain amino acids in the specific *Atrx1* peptide to increase the avidity of binding for the toxin ligand. Second, he would change the receptor itself so that the specific *Atrx1* peptide, normally integral to the extracellular portion of the receptor, would now be a free protein secreted into the extracellular space. The result would be an avid extracellular peptide scavenger of toxin molecules competing with the normal cell-surface *Atrx1* receptor and a resulting decrease in the number of toxin molecules getting into cells.

## Results and Discussion

*Myd88*

We have made mice that are homozygous (and viable) for a new mutation at base-pair 899; this changes the DNA sequence from ATA to AAA, and the amino acid at position 273 in exon 5 from isoleucine (neutral and hydrophobic) to lysine (basic). Live spleen cells and macrophages have been supplied to the Gupta laboratory and are being tested for changes in pathway dynamics when a bacterial substance binds to the cell-surface receptor.

***Atrx1***

Because the biology program at LANL was shut down for nearly 9 months in the midst of this project (3 months actual closure, 3 months re-opening and certification of laboratory operations, 3 months recovery of frozen or discarded reagents), the *Atrx1* project has not been re-started. Michaud will resume making the *Atrx1* mutant mice if/when the Gupta laboratory can use them.

***The CMMB***

When this LDRD project began, the CMMB was in use but not yet operating in standardized mode at high-throughput. Thanks to funding from this LDRD and the drive to obtain mutants for LANL, the CMMB now operates a very high efficiency and has recovered 39 mutations in genes of interest to DOE and to collaborators. This progress led to a publication highlighting the CMMB (Michaud et al., "Efficient gene-driven germ-line point mutagenesis in C57BL/6 mice," *BMC Genomics*, 2005).

## Benefits

We and our collaborators at LANL have been invited by the Army Research Office to submit a proposal entitled, "Directed targeting of adaptor molecules shared by interleukin-1 and toll-like receptor immune response pathways for broad spectrum therapeutic intervention against infection and sepsis." The invitation for this proposal arose from a white paper (BAA W911NF-05-R-0011) that included our joint work on the effects of mutation of the *Myd88* gene on immune-system response to infection. Preparation of this proposal, due January 6, 2006, is under way at both national laboratories. In addition, the greatly increased efficiency of CMMB scanning has led to its inclusion in several NIH grants; only one of those grants, led by the University of Alabama–Birmingham, has been reviewed as of this date, and that grant has been funded. Michaud will receive $75,000 per year for 4 years from this collaboration.

Program development activities by Johnson continue; to date, she has given the following invited presentations:

1. Edgewood Chemical and Biological Center, Aberdeen Proving Grounds, MD, May 25, 2005. This visit resulted in a collaboration with Army biochemist, Jennifer Sekowski, who is investigating the use of hair-follicle proteins as biomarkers of chemical exposure.
2. "Genetics of Exposure Response", Scientific Interaction Subcommittee, Ft. Detrick, MD, July 18, 2005. This presentation was attended by representatives from the Army, Air Force, DHS, EPA, NIH (NIAID), and USAMERIID.
3. "Using Mice to Understand Genetic Variants in Susceptibility," USAMERIID, September 22, 2005. This invitation resulted from the presentation at Ft. Detrick.
4. "Genetic Variation in Host Response to Bioterror Agents," Caroline Purdy of DHS, October 12, 2005.

# High-Throughput Biological Data Analysis and Modeling Tools for Genomes to Life Facilities

N. F. Samatova,[1] A. Gorin,[1] R. L. Hettich,[2] B.-H. Park,[1] B. Zhang,[1] C. Pan,[1,3] G. Kora,[1] N. C. VerBerkmoes,[2] W. H. McDonald,[2] G. B. Hurst,[2] D. A. Pelletier,[4] M. Langston,[5] and D. L. Tabb[3]

[1]*Computer Science and Mathematics Division*
[2]*Chemical Sciences Division*
[3]*UT-ORNL Graduate School of Genome Science and Technology*
[4]*Life Sciences Division*
[5]*Computer Science Department, University of Tennessee, Knoxville*

This report summarizes a fresh stream of computational technologies capable of discovering strong functional "clues" into molecular machines from complex and noisy microbial data. This work is motivated by the DOE Genomics:GTL Molecular Machines Facility's needs for gaining biological insights into function of molecular machines ranging from placing proteins on a metabolic pathway to detailed identification of the residues involved into the formation of recognition interfaces (both in real time and on a genome scale). We describe novel computational methods for (1) discovery of post-translational modifications from proteomics data; (2) robust relative quantification of mass spectrometric data obtained from both stable-isotope-labeled and unlabeled bacterial proteome samples; (3) identification of protein-protein interaction interfaces from sequence and structural information; and (4) recognition of protein functional "spots" (e.g., active, regulatory, and enzyme-substrate specificity determining sites) critical for biomolecular interactions. We have developed software tools in each of those areas, released these tools to a biological community at large, and applied them to characterize some molecular machines in DOE-important microbial organism, *Rhodopseudomonas palustris*.

## Introduction

Ultrascale computing and high-throughput technologies, such as genomics, transcriptomics, proteomics, and metabolomics, will revolutionize the way systems biology is conducted. For the first time there is a unique opportunity to build models of molecular interaction networks including physical, chemical, and biological processes at necessary level of detail, and to use ultrascale computation for predictive simulation of their dynamics. With this promise, however, comes the challenge of interpreting and integrating, in a biologically meaningful way, the avalanche of complex and noisy data so produced. Unlike simulations from "first principles" in other disciplines, systems biology will require these data to guide model building as well as to make simulations computationally tractable by constraining the space of feasible models.

The existing computational tools for systems biology have contributed a lot to our understanding of biological systems. However, there remains an inability to characterize, model, simulate, and, eventually, control molecular-scale biological processes. The difficulty lies in the growing gap between the high-throughput biological data and the mathematical models, along with computational and analytical tools that have the capacity to derive from the data all the working elements and to annotate them within functional systems context. At the same time, to experimentally define the functional role of these working elements, the experimentalists must know what functional aspect should be tested and how to set up the experiments to examine their functions. As a result, the number of hypothetical genes across all the genomes is on the Moore's Law trajectory of growing at an exponential rate; most of the metabolic pathways are incomplete; and pieces of regulatory pathway models are obtained only for a handful of organisms.

The DOE Genomics:GTL workshops called for urgent pioneering data science programs to enable a quantum leap in systems biology through high-throughput data production and data intensive computing. Our goal is to provide a fresh stream of computational technologies capable of discovering strong functional "clues" from complex and noisy data, and then integrating those clues to enable systems-level annotation of molecular interactions. As a result, this project aimed to deliver a capability that would allow researchers to determine a protein function and put it in both a macro context of interaction networks and a micro context of particular residues involved into functions.

## Technical Approach

This project started with an intention to provide a new suite of computational technologies capable of discovering strong functional clues from complex and noisy data and then integrating them to enable systems-level annotation of molecular interactions. Our general strategy is to "mine" high-throughput and complex biological data in order to "learn" the mathematical relationships among the known data about those functional clues. These "learned rules" will then be used for predicting functional clues for unknown protein machines in microbial genomes.

We focused on the following four tasks: (1) discovery of post-translational modifications from proteomics data; (2) robust relative quantification of mass spectrometric data obtained from both stable-isotope-labeled (2.a) and unlabeled (2.b) bacterial proteome samples; (3) identification of protein-protein interaction interfaces from sequence and structural information; and (4) recognition of protein functional "spots" (e.g., active, regulatory, and enzyme-substrate specificity determining sites) critical for biomolecular interactions. Below, we describe the accomplishments for each task and more details about our technical approach.

## Results and Accomplishments

### *(1) Discovery of Post-Translational Modifications*

Post-translational modifications constitute one of the most important types of the protein active sites: signaling and regulatory activities in the cell are often conducted through post-translational modifications. Knowledge of PTMs is crucial because they may alter physio-chemical properties, folding, and activity, and, thus, extend the range of protein functions. The current methods to find PTM in the experimental data are very laborious, inefficient and often fail when they are faced with unexpected PTMs or heavily modified protein segment (containing several PTM). We have prototyped a novel technology, called "de novo PTM," for mining PTMs in experimental proteomics data. It utilizes our de novo peptide tag construction (Probability Profile Method, PPM) from tandem MS data (Day et al. 2004). The two basic situations are handled: PTMs are located inside or outside the de novo tag. About 80% of PTMs were reproduced when tested on the benchmark set of 54 ribosomal proteins in *R. palustris* generated by a very laborious process. The work is under way to understand the cases where benchmark PTMs were not found and then tune up the technology.

### *(2.a) Relative Quantification of Mixed Stable-Isotope-Labeled Proteomes*

To improve both quantification accuracy and quantification confidence, we systematically optimized the core analysis steps for robust quantification: chromatographic peaks detection, peptide relative abundance estimation, and protein relative abundance estimation. Our novel parallel paired covariance algorithm has largely enhanced the signal-to-noise ratio of the two isotopologues' chromatograms and, as a result, has enabled much more accurate peak detection. Principal component analysis (PCA) was employed to estimate peptide abundance ratios and demonstrated superior estimation accuracy than the traditional methods based on peak height and peak area. It was observed that the relative quantification of the standard proteome mixtures is of highly variable accuracy for peptides and consequently for proteins. To estimate quantification error, we proposed a novel signal-to-noise measure derived from principal component analysis and showed a linear correlation of this measure with the peptide ratio estimation in the standard mixtures. Finally, maximum likelihood estimation (MLE) was used for protein relative quantification from the PCA-estimated abundance ratios of its proteolytic peptides. MLE not only showed more accurate protein quantification and better coverage than the widely used RelEx program but also a more robust estimate of a confidence interval for each differential protein expression ratio. For an automated data processing and streamlined data visualization, these algorithms were integrated into a computer program, called ProRata (Fig. 1). ProRata has been evaluated on the metabolically labeled *R. palustris* mixed proteome samples performed on two platforms (ThermoFinnigan LCQ and LTQ) using multidimensional protein identification technology ("MudPIT") with an average of >16,000 peptide identifications and ~2000 protein identifications per LTQ experiment.

Dr. Dale Pelletier's lab performed metabolic labeling of *R. palustris* strain CGA010 with stable isotopes of nitrogen, $^{14}N$ and $^{15}N$, under photoheterotrophic conditions, and Dr. Hayes McDonald implemented MudPIT at ORNL. A number of refereed publications are in preparation to report this work (Pan et al. 2006.a).

### *(2.b) Detection of Differential and Correlated Protein Expression in Label-Free Shotgun Proteomics*

We used two published LC-MS/MS label-free shotgun proteomic data sets from the eukaryotic *Saccharomyces cerevisae* and prokaryotic *Rhodopseudomonas palustris* to explore the methodologies for detecting differential and correlated protein expression in this study. We compared the technical reproducibility of three sampling statistics and found that spectral count and peptide count were highly reproducible, while sequence coverage was relatively nonreproducible. Thus, we focused on the application of spectral count in quantitative proteomics in this study. We have evaluated different statistical tests for pair-wise comparison using the yeast data set with

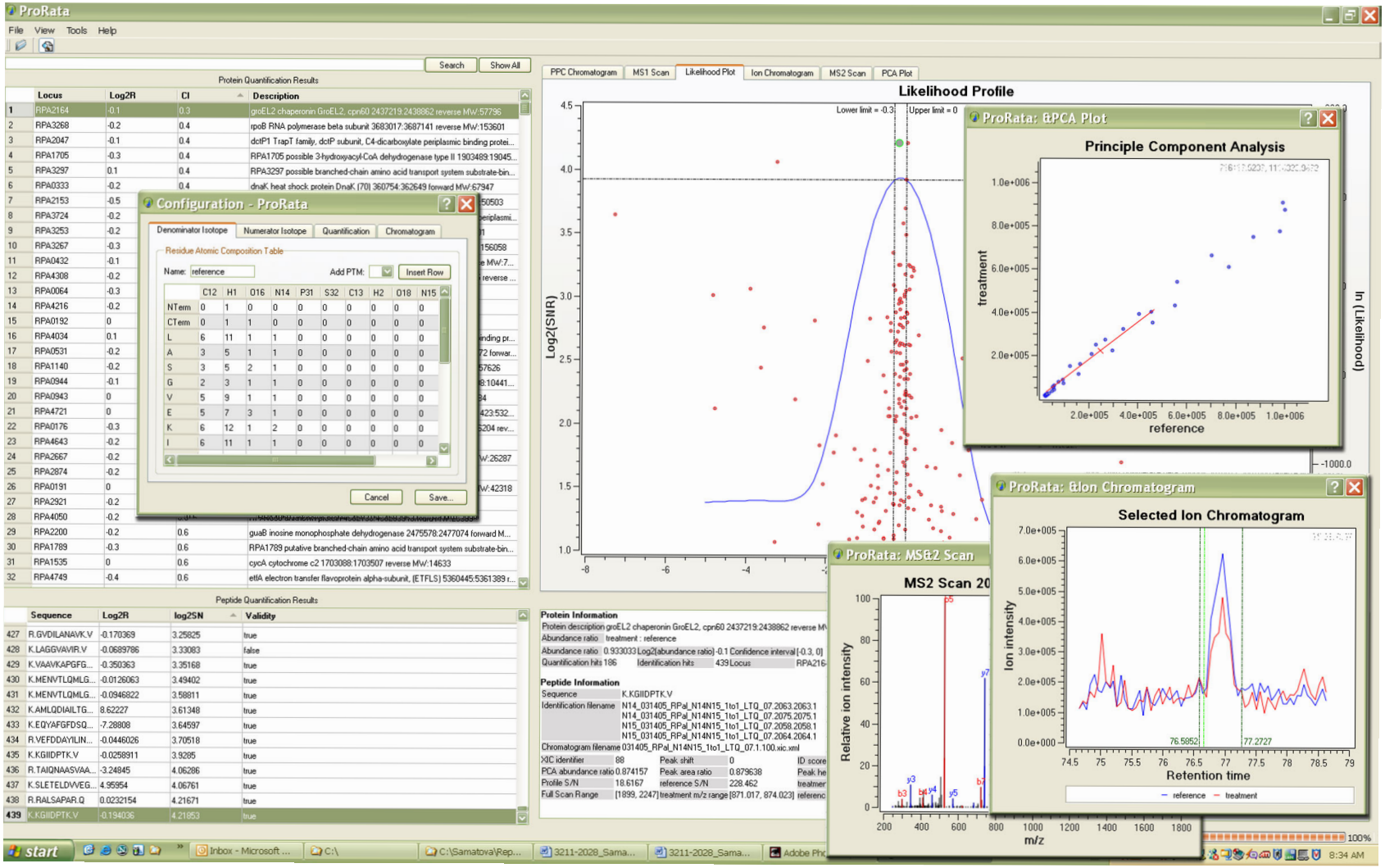


*Fig. 1. The display of ProRata analysis results for $^{14}N$:$^{15}N$-labeled* R. palustris *proteome. The ProRata graphical user interface consists of four parts: protein table (top left), peptide table (bottom left), graph pane (top right), and text pane (bottom right). The graph pane contains seven graphs: Likelihood Plot, Sequence Coverage Plot, Ion Chromatogram, PPC Chromatogram, PCA Plot, MS1 Scan, and MS2 Scan. All graphs can be detached from the graph pane.*

spike proteins. Fisher's exact test, G test, and AC test performed similarly. They were able to identify a 10-fold change with FDRs (False Discovery Rate) less than 0.4%, and a 5-fold change with FDRs less than 0.7%, even with only one replicate. For a 2-fold change, the FDRs could be greater than 10% with one replicate, while less than 5% or 3% with two or three replicates, respectively. T-test performed best when there are three replicates. We have generalized the G test for detecting differential expression in multi-condition comparisons and identified 1,119 *R. palustris* proteins that were differentially expressed under the six growth conditions studied in the data set. Among the 625,521 protein pairs between the 1,119 differentially expressed proteins, we found that operon pairs were strongly co-expressed relative to the non-operon pairs. Combining clustering analysis with protein set based functional interpretation, we have revealed six protein clusters with biological significance (Zhang et al. 2006).

***(3) Identification of Protein-Protein Interfaces***

Biomolecular interactions are fundamental to cellular processes, such as DNA transcription, regulation of metabolic pathway, and signal transduction. They are rendered by a number of contacting residues. Knowledge of such residues is important for understanding biological processes at the molecular level. Their identification can guide/validate MS experiments to identify protein complexes. It can also boost the performance of multi-protein docking by suggesting potential contacting regions between proteins. We developed mathematical models and a computational framework for predicting protein-protein recognition interfaces. The problem was addressed at two resolution levels: (1) given a protein sequence, which residues are interface, surface, or core ones and (2) given two protein sequences that are known to interact, which residue pairs are in direct physical contact.

For the former, we quantified that a high-dimensional space of residue feature points contains multiple non-coinciding subspaces that makes it difficult, or even impossible, to build a single monolithic binary classifier. This partially explained why traditional methods achieved low prediction accuracy of 53–60%. Based on this discovery, we devised a statistical model that incorporates Boosting weight distribution to derive robust confidence for interface or surface residue assignment from a committee of classifiers (Park et al. 2004). The cross-validation for >30,000 residues from 303 protein complexes shows the prediction accuracy of 75% with >70% confidence.

For the latter, we created a Markov model to quantitatively describe co-evolution of contacting residue pairs and to derive a 400 × 400 residue-pairing propensities table. The table is similar to a 20 × 20 amino-acid substitution BLOSSUM table but is used for detecting correlated mutations that happen during co-evolution. Our Markov model answers the question: given multiple sequence alignments of two proteins, what is the probability of interaction between residues in position *i* and position *j* from the first and second alignments, respectively? Each pair is assigned a correlated mutation score obtained from the table that represents the degree of likelihood compared to what is expected at random. Two residues are predicted to be in contact, if the score is above a given threshold. The results on 6000 SCOP domain-domain interactions show higher sensitivity to putative interactions and less sensitivity to false interactions. We are in process of publishing this paper in a peer-reviewed journal (Pan et al. 2006.b).

***(4) Discovery of Functional Spots***

As an initial effort to recognize protein functional spots, we focused on identification and characterization of residues that are responsible for enzyme-substrate recognition. Enzyme-substrate binding is a subset of the protein interactions that is of key importance in metabolic, signaling, and regulatory pathways. One of the most remarkable properties of this binding is high substrate specificity among highly homologous enzymes. We believe that there must be clusters of amino acids whose structural, dynamic, and physicochemical properties directly or indirectly affect enzyme-substrate interactions. Identification of these residues is essential for elucidating the order and control principles of substrate recognition and would have immediate implications for drug design, protein engineering, and molecular pathway elucidations.

Unlike most existing approaches that are limited to identifying a single residue only, we developed surface patch ranking method, called SPR, that finds putative specificity-determining residue clusters (Yu et al. 2004; Yu et al. 2005.a). The SPR, our combinatorial method, ranks clusters of residues based on their discriminating power measured by the classification accuracy of Support Vector Machine. We applied the SPR to multiple families of enzymes that are homologous but with different functional subtypes. We showed a considerable agreement with site-directed mutagenesis experiments. Single-residue clusters are directly involved in enzyme-substrate interactions. Most multi-residue clusters are vital for domain-domain and regulator-enzyme interactions, playing a complementary role in specificity determination. The latter are usually weakly conserved and are not recognized by existing computational methods.

We also applied our SPR method to extract a set of $CO_2/O_2$ specificity-determining residue clusters and study when and how the residues mutate during the RuBisCo evolution to accommodate significant changes in $CO_2/O_2$ specificity and affinity among the three RuBisCo groups

—marine non-green algae, plans, and cyanobacteria (Yu et al. 2005.b). We extended SPR with our evolutionary scheme to prioritize predicted residues and suggest their substitutions for site-directed mutagenesis.

Based on our methodology, we have developed a software package and are in the process of releasing it to a broader community. We have been contacted by a number of drug discovery companies about software availability and collaboration.

## References


Day, R. M., A. Borziak, and A. Gorin. 2004. "PPM-Chain: new capabilities in de novo peptide identification by tandem MS," Proceedings of the Computational Systems Bioinformatics Conference (CSB2004).

Pan, C., G. Kora, D. L. Tabb, W. H. McDonald, D. Pelletier, G. Hurst, N. F. Samatova, and R. L. Hettich. 2006a. "Novel algorithms for quantitative shotgun proteomics that improve the estimation of protein abundance ratios" (in preparation).

Pan, C., B.-H. Park, P. Chandramohan, and N. F. Samatova. 2006b. "A Markov model approach to co-evolution of interacting residues" (in preparation).

Yu, G.-X., B.-H. Park, P. Chandramohan, A. Geist, and N. F. Samatova. 2004. "In-silico prediction of surface residue clusters for enzyme-substrate specificity," Proceedings of the IEEE Computational Systems Bioinformatics Conference (CSB2004), Stanford, California, August 16–19, 2004.

Yu, G.-X., B.-H.Park, B.-H., Chandramohan, P., Munavalli, R., Geist, A., and N. F. Samatova. 2005.a, "In-silico discovery of enzyme-substrate specificity-determining residue clusters," *Journal of Molecular Biology* **52**(5):1105–17.

Yu, G.-X., B.-H. Park, P. Chandramohan, A. Geist, and N. F. Samatova. 2005.b. "Evolutionary-based characterization of $CO_2/O_2$ specificity-determining factors for RuBisCo protein complex," *Protein Engineering Design and Selection* (in press).

Zhang, B., N. C. VerBerkmoes, M. A. Langston, R. L. Hettich, and N. F. Samatova. 2006. "Detecting differential and correlated protein expression in label-free shotgun proteomics" (in preparation).

# Advanced Plasmonic Sensor Array for Homeland Security

T. Vo-Dinh,[1] G. Griffin,[1] A. Vass,[1] A. Wintenberg,[2] F. Yan,[1] and M. Wabuyele[1]
[1]*Life Sciences Division*
[2]*Engineering Science and Technology Division*

We propose to develop a novel sensing technology based on the Advanced Plasmonic Sensor Array (APSA) concept for rapid and sensitive detection of spectral signatures for both chemical and biological warfare (CBW) agents. Specific innovations of the integrated system include (1) an advanced sensing concept based on plasmonics and (2) an array of sensors using nanotechnology-based probes. We envision that the APSA device developed during this project could form an important component of the generation-after-next sensor program, as the proposed sensor would "significantly change the detection paradigm."

## Objective

Our proposed novel sensor technology based on the Advanced Plasmonic Sensor Array (APSA) concept is designed to be the next generation of sensor technology for sensitive detection of spectral signatures for CBW agents. This project will support the following application scenarios for detection in both indoor and outdoor environments: first responder operations, intelligence, CBW threat assessment, early warning, deterrence, and military operation.

## Technical Approach

In this project, we propose the use of "enhanced spectral signatures" for CBW detection as an additional approach to detection, because of the tremendous diagnostic power of spectral techniques such as Raman and fluorescence. The novel features of the APSA technology include the following:

(1) advanced sensing concept based on plasmonics (enhanced electromagnetic fields)
(2) array of sensors using nanotechnology-based probes
(3) combination of bioreceptor recognition and enhanced spectral signatures for detection

We will develop a novel sensor array system based on nanostructured probes capable of producing highly enhanced electromagnetic fields (plasmonics). With the novel selective plasmonics enhancement (SPE) approach, the molecular interactions between the adsorption layer molecules and the plasmonics substrate depend on the chemical nature of the analyte molecules and the adsorption layers. The APSA technology is based on the selective-enhancement of the plasmonics effect in metallic nanostructures.

## Results and Discussion

### *Task 1: Development of a Plasmonic Arrays*

In this task, we planned to investigate methods to produce nanostructures that will permit enhanced field detection (Raman, fluorescence) of model compounds of interest to CBW detection. These methods include the following: (i) deposition of metal-island films on smooth surfaces, and (ii) deposition of metal on nanoparticle arrays. During FY 2005, we optimized our approaches to preparing plasmon-active substrates which could be produced by evaporating a thin silver layer (~100-nm thickness or less) directly onto a solid base support. Under the optimal conditions, the silver layer develops into a uniform plasmonic array on the support in the form of isolated metal islands, and we have successfully demonstrated their application to the detection of various CBW simulants.

### *Task 2: Waveguide for Plasmonic Probe Array*

In this task, we planned to develop sampling platforms based on optical waveguides for the plasmonic sensor array. These sensor arrays would be based on polymer-coated APSA sensors and data processing using pattern recognition and chemometric techniques. During FY 2005, we developed a waveguide-based multi-spectral imaging system to record the entire 2-D image of the plasmonic probe array. Our experiments demonstrate the potential of the plasmonics array for multi-analyte detection capability. In an actual application, perhaps different polymeric matrices could be used as a part of the plasmonics array to provide specific surfaces which would absorb different CBW agents. Following laser excitation and imaging, the location of specific SERS peaks on the image could be correlated to a specific agent, based upon the absorptive properties of the polymer. Alternatively, different plasmonic-active receptors could be spotted

at different sites on the plasmonics array, and following selective reaction with individual CBW agents, the alterations in spectral properties of the various receptors could be correlated with the presence of specific threat agents.

***Task 3: Development and Evaluation of the Integrated APSA Sensor***

In this task we planned to develop and evaluate the integrated APSA sensor using CW simulants and biomarkers of pathogenic agents. In this period, we have successfully demonstrated that both surface-enhanced Raman scattering and surface-enhanced fluorescence, which are two complementary plasmonic detection modalities, could be combined into a single platform for sensing of Raman-active dye-labeled biomolecules. The introduction of a thicker $SiO_2$ spacer, along with layering of other linking compounds, gave rise to an enhancement factor between 2 and 8 in our study. By properly adjusting the thickness of the $SiO_2$ overlayers, it is possible to retain the SER signals to a greater extent, while achieving a maximal SEF enhancement. This property could be very useful in applications which require better Raman fingerprints than only fluorescence dyes. Our preliminary study suggested that the surface density of the underlying silver islands, and the sampling procedures for CW simulants and biomarkers of pathogenic agents, as well as the experimental configurations, etc., could be the main factors for both better SEF and SERS enhancement.

## Benefits

The results of the proposed research will provide critical preliminary results and should benefit such agencies as DHS, DOE, DOD, DTRA, DARPA, DOJ, NIH, and NSF.

# A Systems Biology Framework for Post-Genomic Microbiology

E. C. Uberbacher,[1] F. W. Larimer,[1] A. A. Gorin,[2] N. F. Samatova,[2] L. J. Hauser,[1] B. H. Park,[2] B. Zhang,[2] Y. Tian,[2] D. D. Schmoyer,[1] D. A. Pelletier,[1] M. A. Langston,[3] J. R. Snoddy[1,3] and W. H. McDonald[4]

[1]*Life Sciences Division*
[2]*Computer Science and Mathematics Division*
[3]*University of Tennessee*
[4]*Chemical Sciences Division*

We propose to develop a systems biology framework for post-genomic microbiology, using *Rhodopseudomonas palustris* as a model, with the following specific goals: (1) create a comprehensive annotated map of protein-protein interactions in *R. palustris* using the whole set of available predictive algorithms, public databases, and data mining tools; (2) devise a feedback loop between this map and ongoing pull-down and whole proteome experiments so that experiments could be guided toward key targets and their results could be validated; (3) integrate results from mining the expression arrays; and (4) build the capability for integration of regulatory and metabolic information, with a potential to conduct metabolic flux balance analysis and other large-scale modeling of the constructed system.

The objective of the project is to develop computational methods for inferencing about potential molecular interactions and interaction networks from a variety of types of data. These include data from structure databases, pathway databases, experiments, to statistically score observations and inferences and combine knowledge about interactions, and to build these combined observations into mathematical representations of molecular systems for key organisms. The project is focused on technologies needed for Genomics:GTL Facility II, Characterization and Imaging of Molecular Machines.

The project is using computational and bioinformatics approaches to devise methods that can predict interactions by homology, integrate information about interactions, statistically weight and combine information, and synthesize well-structured machine and network knowledge. This includes the developing methods to mine and compare protein interactions in remotely related structures, combining experiments with interaction inferences from homology, scoring the reliability of various observations using statistical approaches, developing relational and Web-based systems for capturing and visualizing interaction knowledge, and applying methods of computational network modeling and simulation to microbial systems.

In the first year, new mathematics, statistics, and algorithms have been developed which can inference about potential interactions in a new genome from seven different information sources including databases of protein structure databases, pathway data, database of interaction data, and built methods to apply these inferences to *Rhodopseudomonas palustris* genome. Machine learning methods have been applied to develop a statistically reliable score for predicted and observed interactions based on a naïve Bayesian approach. A knowledge base has been built which combines interaction data from multiple sources and provides ways for users to visualize complex networks of interactions.

This LDRD is implementing key technologies for DOE Genomics:GTL and also relevant to environmental or pathogenic microbes, in environmental systems involving microbes and plants and in human disease. NIH, NSF, and DHS have initiatives for which this technology is highly relevant.

# Molecular and Cellular Imaging

J. L. Morrell-Falvey,[1] M. J. Doktycz,[1] and D. C. Joy[2]
[1]*Life Sciences Division*
[2]*The University of Tennessee and Metals and Ceramics Division*

Imaging technologies that complement DNA sequencing, gene expression, and proteomics studies are needed to provide a comprehensive description of molecular function at the cellular level. These imaging techniques need to validate bioinformatic predictions as well as illustrate how genomic instructions are executed across spatial and temporal dimensions. The objective of this project is to develop the molecular resources and expertise needed to extract functional information from bacterial systems, particularly carbohydrate metabolism in *Escherichia coli*, using a combination of confocal laser scanning microscopy, atomic force microscopy, electron microscopy, and automated image analysis.

No single imaging method can address every experimental question, but different techniques possess particular strengths and, in combination, can provide a comprehensive "picture" of biological systems. This proposal seeks to integrate data from confocal laser scanning microscopy, atomic force microscopy, electron microscopy, and image analysis to unravel complex molecular interactions and deduce the function of biomolecules in live cells. Currently, these reagents and techniques are being applied to understanding the interrelationship between the genes and gene products involved in carbohydrate metabolism in *E. coli*.

*Confocal Laser Scanning Microscopy:* To test protein localization in live bacterial cells, we constructed a number of plasmids for expressing proteins in bacteria fused to Green Fluorescent Protein (GFP) or its spectral derivatives, CFP (cyan fluorescent protein) or YFP (yellow fluorescent protein) based on the broad range host plasmid pBBR1MCS (Kovach 1995), which propagates in multiple bacterial species, including *E. coli, Shewanella oneidensis*, and *Rhodopseudomonas palustris*. In addition, we have also developed reagents for labeling proteins with fluorescent markers by chromosomal insertions. To date, two *E. coli* proteins involved in glucose metabolism, the glucose receptor IICBGlc (encoded by ptsG) and its transcriptional regulator Mlc, have been labeled with GFP by chromosomal insertion. Strains expressing GFP-IICBGlc or GFP-Mlc are being evaluated microscopically under various physiological conditions to investigate the dynamic spatial and temporal protein distributions in real time in live cells.

*Cathodo-Luminescence:* As a complement to optical microscopy, improved spatial resolution can be achieved using the technique of cathodo-luminescence (CL), which is based on the observation that any fluorescent center that can be excited by photons can also be excited by energetic electrons. We have performed preliminary experiments to image bacterial cells, and other entities, in a liquid environment inside a scanning electron microscope (SEM) using sealed Quantomix capsules. In initial experiments, fluorescent polystyrene beads or *E. coli* cells labeled with Quantum dots were immersed in water or gelatin and imaged in cathode-luminescence mode. These experiments confirm that labeled cells can be imaged with sub-micron spatial resolution using an electron beam with an energy in the range 10–30 keV for depths upwards of 10 micrometers in water, and rather less successfully in gelatin. This result implies that complementary imaging using SEM CL mode, and confocal scanning optical microscopy, would be possible, substantially extending the useful range of optical imaging.

*Automated Image Characterization:* Automated image analysis techniques allow for a quantitative description of images, facilitate standardization, and enable searching and retrieving of images from databases. We have focused on extracting quantitative features such as area, volume, and height from AFM images of *E. coli*. We have used a simple but effective technique that employs morphological operators, based on MATLAB functions, to estimate and subtract the background and then label and mark the objects of interest in the image.

This research aims to connect gene expression studies, proteomic analyses, and metabolic flux information with dynamic imaging studies in the live cell. Integration of these data will allow functional interpretation of biological systems. Although we have focused on the well-characterized model of glucose metabolism in *E. coli* to demonstrate the feasibility and utility of these techniques, these methods should be widely applicable to other biological systems.

## Reference

Kovach, M. E., et al. 1995. "Four new derivatives of the broad-host-range cloning vector pBBR1MCS, carrying different antibiotic-resistance cassettes." *Gene* **166**, 175.

# *Biological Sciences and Technology*

# *Seed Money Fund*

# Advanced Diagnostics Algorithm for Cancer Detection Using Hyperspectral Fluorescence Imaging

T. Vo-Dinh,[1] M. Martin,[1] S. G. Kong,[2] and Z. Du[2]
[1]*Life Sciences Division*
[2]*The University of Tennessee*

The objective of this research is to develop a novel advanced computing algorithm (ACA) for real-time, non-invasive diagnosis of cancer using a hyperspectral imaging (HSI) system. To accomplish this, we developed a non-invasive system for the detection of tumors on mouse skin based on the analysis of hyperspectral fluorescence images. Hyperspectral imaging reveals spectral information useful for the classification of tumorous tissue. The hyperspectral images used are fluorescence images consisting of 21 spectral bands in the visible spectrum of the wavelengths from 440 nm to 640 nm. An acousto-optic tunable filter is used to obtain hyperspectral images from mouse skin. Each spectral band image is spatially registered to compensate for the offset caused during the image capture procedure. A subset of spectral bands was selected in terms of maximum class separability for feature dimensionality reduction. A support vector machine (SVM) classifies the spectral signatures of a small number of selected bands to detect the skin tumor pixels. Once the systems have been optimized, studies will be performed on human patients for potential cancer diagnosis. This approach could lead to significant advances in effective and rapid detection of tumors over large areas of organs and in the understanding of cancer in general.

## Introduction

Exposure to carcinogenic compounds (e.g, polycyclic aromatic compounds) related to energy technologies (petroleum, synfuel industries) could lead to skin cancer. Current diagnostic methods for skin cancers rely on physical examination of the lesion in conjunction with skin biopsy that involves the removal of tissue samples from the body for examination. Biopsy of large lesions often requires substantial tissue removal. Though this protocol for skin lesion diagnosis has been accepted as the gold standard, it is subjective, invasive, and time consuming. Since suspicious areas are identified by visual inspection alone, there are a significant number of false positives that undergo biopsy. Conversely, many malignant lesions can also be overlooked. There is an urgent need for objective criteria that would aid the clinician in evaluating whether biopsy is required.

Optical techniques such as laser-induced fluorescence spectroscopy have been suggested as an effective tool in medical diagnostics. Spectroscopy offers an instant, non-invasive diagnostic method to detect cancer based on the spectral properties of tissue. A three-dimensional volume of data in spatial and spectral space characterizes a hyperspectral image. A hyperspectral image contains spatial (x,y) information measured at a sequence of individual wavelength across a sufficiently broad spectral (z) range. Hyperspectral imaging sensors provide continuous spectral signatures obtained from dozens or hundreds of narrow spectral channels. This feature enables hyperspectral imaging to reveal more useful information for material identification than conventional imaging techniques (Shaw et al. 2002; Landgrebe 2002). Different tissues exhibit unique spectral characteristics at particular bandwidths (Chang et al. 1999). With high resolution and multiple bandwidths, subtle differences in the signature characteristics of tissues can be identified (Kong et al. 2004).

This project involves collaboration between Dr. T. Vo-Dinh from the Life Sciences Division of ORNL and his coworker Dr. S. Kong of the Electrical and Computer Engineering Department at the University of Tennessee to pursue the integrated approach toward the development and application of this ACA-HSI system. Dr. Vo-Dinh designs the instrumental system and performs experiments on in vivo sample tissues for data acquisition of hyperspectral fluorescence images. Dr. Kong collaborates with Dr. Vo-Dinh to develop an advanced computing algorithm for the real-time classification of tumors from hyperspectral signatures.

## Technical Approach

We develop a cancer detection technique based on hyperspectral fluorescence imaging and an optimal classifier with a subset of spectral bands selected to ensure maximum class separability. Fluorescence imaging techniques are generally regarded as sensitive optical tools and have proven to be useful in a number of scientific areas. The Advanced Biomedical Science and Technology

(ABST) Group at ORNL has been developing advanced instrumentation for hyperspectral imaging for a wide variety of applications including environmental sensing (Moreau et al. 1996a; Moreau et al. 1996b) and medical diagnostics (Vo-Dinh et al. 2004; Martin et al. 2005). Fluorescence is a phenomenon where light is absorbed at a given wavelength and then is normally followed by the emission of light at a longer wavelength. Fluorescence imaging involves excitation of fluorophores within a tissue medium by an external ultraviolet light source. The ultraviolet light excitation results in the emission of fluorescence. There are a number of compounds that emit fluorescence in the visible spectral range when excited with ultraviolet radiation. The altered biochemical and morphological state of the neoplastic tissue is reflected in the spectral characteristics of the measured fluorescence. All the spectral band images are spatially co-registered to obtain exact pixel-to-pixel correspondence by eliminating the offset caused during the image capturing procedure. Then a spectral band selection technique identifies a subset of spectral bands that achieves detection accuracies comparable to the case when all the bands are employed for tumor detection. Hyperspectral image data typically contains dozens or hundreds of contiguous spectral channels. As a result, each hyperspectral sample has an enormous amount of data. Support vector machine (SVM) classifiers are developed to reduce the data and detect cancer from the original image. Classification results for a mouse sample demonstrate the potential of the proposed method in detecting cancer.

## Results and Discussion

The ABST Group has developed a hyperspectral imaging system capable of reflectance and fluorescence imaging. Figure 1 (top figure) shows a schematic diagram of hardware components of the ORNL hyperspectral imaging system used to obtain hyperspectral images. This system consists of fiber probes for image signal collection, an endoscope, an acousto-optic tunable filter (AOTF) for wavelength selection, a laser excitation source an endoscopic illuminator (model Olympus CLV-10) equipped with a 300-watt CW Xe arc lamp source, a charge-coupled device (CCD) color camera (model Sony CCD-Iris) for reflection detection, an intensified charge-coupled device (ICCD) camera (model IMAX-512-T-18 Gen. II) for fluorescence imaging, and a spectrometer for single point spectroscopic measurements.

Both fluorescence and reflected lights are collected through the endoscope into the AOTF device via collimating lenses. A mirror placed in front of the AOTF projects acquires images onto the ICCD camera for fluorescence imaging and onto the CCD camera for reflection measurement. Excitation for the reflectance images is accomplished using an endoscopic illuminator. The reflection source is coupled to an endoscope (Olympus T120) equipped with an imaging bundle. Excitation for the fluorescence spectra and images is accomplished using a LSI pulsed nitrogen laser (model VSL-337) with a maximum repetition rate of 20 Hz.

The fluorescent light emitted by the tissues is diffracted by the AOTF (Brimrose TEAF10-0.4-0.65-S) at a 6º angle from the undiffracted (zero-order) beam, thus separating the reflected image from the fluorescent image. Individual wavelengths diffracted by the AOTF are thus sent to the ICCD. A Brimrose AOTF controller (model VFI-160-80-DDS-A-C2) controls the AOTF. The controller sends an RF signal to the AOTF based on input provided by the Brimrose software. Wavelength selection takes place in microseconds, enabling ultra-fast modulation of wavelength output to the ICCD. Wavelength-specific images are taken between 440–640 nm every 10 nanometers.

Fluorescence images were acquired by gating the intensified ICCD camera. A timing generator incorporated into the ICCD camera's controller (ST-133) allowed the ICCD to operate in the pulsed mode with a wide range of programmable functions. A 500-ns delay between the laser trigger and the detector activation was programmed to synchronize the laser and the detector. The intensifier was gated for 500 ns during which a 5-ns laser pulse was delivered to the tissues. An image was captured 20 times per second, integrated by internal software, and output to a screen once per second. This method allowed real-time fluorescence detection.

Single point spectroscopic measurements were taken to validate the experimental results. These measurements were taken at corresponding locations to the fluorescence imaging data. To accomplish this function, an Ocean Optics (USB2000) spectrometer was used as the wavelength selection device rather than the AOTF.

The hyperspectral image data used in this experiment were laser-induced fluorescence images taken of a mouse at ORNL. An adult mouse was injected subcutaneously with 100 μL of Fischer rat 344 rat tracheal carcinoma cells (IC-12) to induce tumor formation. A nude mouse was used to allow the implanted cancer cells to be able to grow due to the lack of an immune system in the animal. The lack of hair on the mouse enabled imaging directly without the need for depilation. The subdermal injection was done as close to the skin surface as possible to allow tumor formation close to the skin surface. This also allowed experiments to be performed in vivo rather than after tissue extraction. After injection, the nude mouse was incubated for a period of four days to allow tumor formation to occur. Once a tumor was observed of approximately 1 cm, the mouse was anesthetized for approximately 30 minutes to permit data collection.

The measured hyperspectral fluorescence images consist of 165 × 172 pixels with 21 spectral bands from the wavelength $\lambda_1$ (440 nm) to $\lambda_{21}$ (640 nm) with 10-nm spectral resolutions in the spectral region. Such a fine spectral resolution provides sufficient information for precise study of tumor detection. The fluorescence images are enhanced by a gamma correction with the parameter $\gamma = 0.8$. The mapping is weighted toward higher (brighter) output values. Figure 1 (bottom figure) (a) shows a reflectance image of a skin tumor region taken from a mouse sample. Figure 1(b) is a fluorescence image of the sixth band (490 nm) of the same spot. Lower part of the fluorescence image (a bright U-shaped area) corresponds to normal tissue, and the dark part above the normal tissue is a tumor region.

The AOTF is an optical bandpass filter whose passband can be electronically tunable using the acousto-optic interaction inside an optical medium whose refractive index is changed by an acoustic wave. The acoustic wave produces a wavelength-selective single-tone grating in the AOTF transducer that can be varied by simply changing the acoustic frequency. Radio-frequency (RF) signals are used to generate the acoustic waves. The RF amplitude level applied to the transducer controls the filtered light intensity level. The AOTF has a dynamic range of 400–650 nm with a 10 × 10 mm aperture and a spectral resolution of 1–2 nm. The AOTF shows a fast response time (in μs), is accurate and exhibits a high extinction ratio.

The AOTF produces the offset between neighboring spectral band images. The result shows the amount of offsets at different wavelengths that the AOTF generates during the image capturing procedure. The offsets are estimated by maximizing the mutual information between the given band images and the reference band image. The spectral band of the wavelength 490 nm was selected as a reference band with zero offset. A positive (negative) offset value indicates that the band image is shifted to the left (right) by the amount of pixels with respect to the reference band. All the spectral band images are spatially co-registered with the reference band image at 490 nm to obtain exact pixel-to-pixel correspondence by eliminating the offsets before extracting spectral signatures.

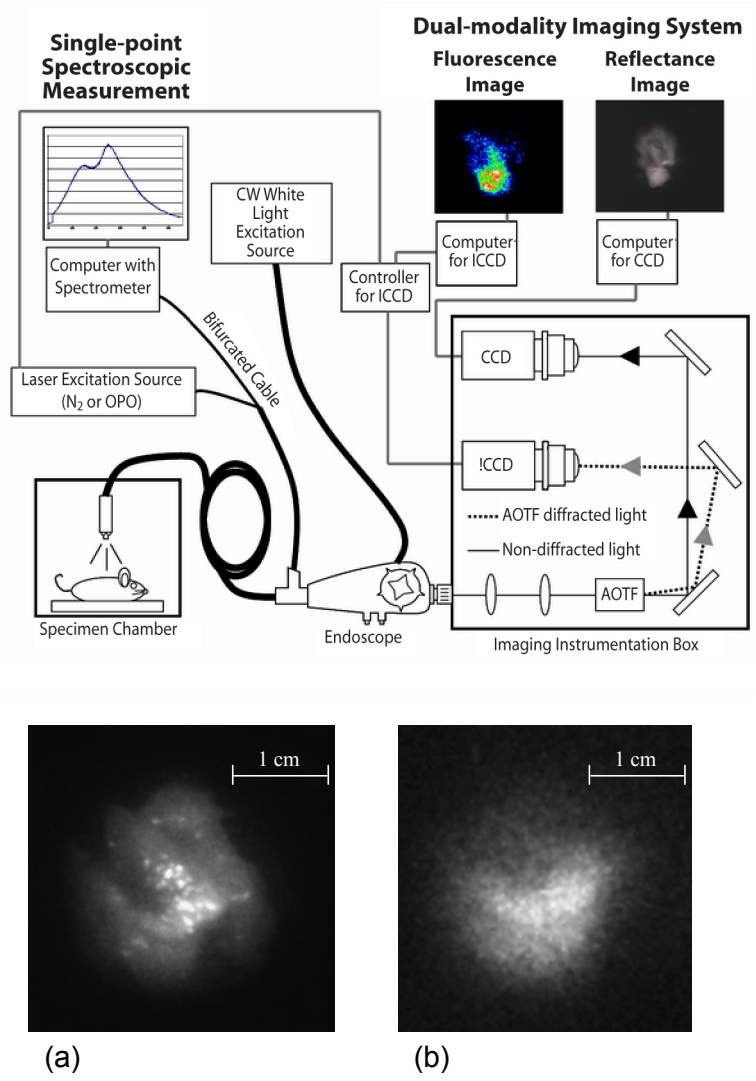


*Fig. 1. Top: Hardware component of Hyperspectral Image System. Bottom: Skin tumor region of a mouse skin sample. (a) Reflectance image, (b) Fluorescence image at wavelength 490 nm.*

The experiment with a mouse sample having a tumor region provides an illustration of the potential of the proposed hyperspectral fluorescence imaging technique for in vivo skin cancer diagnosis. Optical imaging of reflectance demonstrates nearly uniform responses to both normal tissue and skin tumor areas, which makes visual classification of malignant tumors difficult based on reflectance images. A mouse tumor expert verified the tumor location on mouse skin. Fluorescence shows better discrimination for skin tumor region. The fluorescence component shows stronger response to normal tissue in comparison to the tumor region. Normal tissue corresponds to the bright U-shaped area with stronger fluorescence intensity. The relatively darker area in fluorescence intensity marked by a circle above normal tissue indicates a malignant tumor region.

The hyperspectral image data can be represented by a three-dimensional (3-D) cube of data $I(m, n, \lambda_i)$, where $(m, n)$ denotes

the spatial coordinates of a pixel location in the image and $\lambda_i$ denotes a spectral band ($i$ = 1, 2, . . . , $L$), where $L$ is the number of spectral bands ($L$ = 21). Each pixel in the hyperspectral image can be represented as a spectral signature $x = (x_1, \ldots, x_L)$ vector, where $x_i$ denotes an $i$th spectral component. For hyperspectral fluorescence measurements, the choice of the laser excitation wavelength is important. In this study, $N_2$-pumped laser at wavelength 337 nm was used as an excitation source of the fluorescence signal. A nitrogen laser provides the lowest excitation wavelength of 337 nm that corresponds to highest energy. Longer wavelengths can be selected for excitation by using the tunable dye laser system. However, the use of shorter wavelengths tends to excite more components in tissues. This wavelength produces fluorescence spectra of spectral signatures useful to discriminate normal and malignant tissues.

The measurements involve fluorescence spectra taken from a mouse sample in terms of two categories of interest: normal tissue and malignant tumor. The spectral signatures show a peak response near the wavelength 490 nm while the fluorescence intensity of malignant tumor is weaker than that of the normal tissue. The higher fluorescence intensities in the normal tissue can be attributed to several factors, depending on what collection wavelength region is being described. In the wavelength region of 450 nm to 510 nm, the higher fluorescence intensity seen in the normal tissues is due primarily to a decrease in collagen and elastin from normal to malignant tissues and a decrease in nicotinamide adenine dinucleotide (NADH) levels in the malignant tissues. The decreases in fluorescence seen in the images in the wavelength region between 500 nm and 600 nm can be attributed to whole blood absorption in this region. An increase in blood volume in the malignant tissues causes more of the fluorescence from fluorophores such as lipo-pigments and flavins to be absorbed.

## Benefits

The development of the Advanced Diagnostics Algorithm for cancer detection using hyperspectral fluorescence imaging, described in the final report, will provide benefits to DOE's and NIH's biomedical imaging initiatives. This technique is also of value to DOE as it may provide diagnostic capability to detect early diseases due to exposure to energy-producing processes and substances and thereby allow more effective therapeutic intervention.

## Conclusion

This report presents a hyperspectral fluorescence imaging technique for non-invasive detection of malignant tumors on mouse skin. Hyperspectral images have proved useful in providing information for detecting tumors. The fluorescence information captured by the hyperspectral imaging system contains a higher level of contrast and thus provides greater possibility of detecting tumors. The classification result shows that the method proposed in this report can efficiently detect tumor and normal tissues. This system has obvious applications as a medical diagnostic tool. The next step for this project is to conduct human clinical trials. The modality of imaging combined with spectroscopic data will prove useful in the detection of tumors as well as in the assessment of tissue response to therapy.

## References


Chang, C., Q. Du, T. Sun, and M. Althouse. 1999. "A joint band prioritization and band-decorrelation approach to band selection for hyperspectral image classification," *IEEE Transactions on Geoscience and Remote Sensing* **37**(6), 2631–2641.

Kong, S. G., Y. R. Chen, I. Kim, and M. S. Kim. 2004. "Analysis of Hyperspectral Fluorescence Images for Poultry Skin Tumor Inspection," *Applied Optics* **43**(4), 824–833.

Landgrebe, D. 2002. "Hyperspectral Image Data Analysis as a High Dimensional Signal Processing Problem," *IEEE Signal Processing Magazine* **19**(1), 17–28.

Martin, M., M. Wabuyele, M. Panjehpour, B. F. Overholt, R. Denovo, S. Kennel, G. Cunningham, and T. Vo-Dinh. 2005. "An AOTF-Based Dual-modality Hyperspectral Imaging System Capable of Simultaneous Fluorescence and Reflectance Imaging," *Medical Engineering Physics* (in press).

Moreau, F., S. Moreau, D. M. Hueber, and T. Vo-Dinh. 1996a. "Fiberoptic Remote Multisensor System Based on AOTF," *Applied Spectroscopy* **50**(1295).

Moreau, F., S. M. Moreau, D. M. Hueber, and T. Vo-Dinh. 1996b. "Fiber-Optic Remote Multisensor System Based on an Acousto-Optic Tunable Filter (AOTF)," *Applied Spectroscopy* **50**(10).

Shaw G. and D. Manolakis. 2002. "Signal processing for hyperspectral image exploitation," *IEEE Signal Processing Magazine* **19**(1), 12–16.

Vo-Dinh, T., D. L. Stokes, M. Wabuyele, M. E. Martin, J. M. Song, R. Jagannathan, E. Michaud, R. J. Lee, and X. Pan. 2004. "Hyperspectral Imaging System for In Vivo Optical Diagnostics," *IEEE Engineering in Medicine and Biology* **23**, 40–59.

# A Shortcut to Making Mouse Models for Stressor Resistance for Application to Longevity (Aging) and Other Exposure-Biology Research

Y. You,[1] W. Chick,[2] and S. Mentzer[1]
[1]*Life Sciences Division*
[2]*University of Colorado Health Sciences Center*

A body of evidence indicates that one of the factors associated with longevity is the ability to deal effectively with reactive oxygen species (ROS): even cells derived from long-lived animals exhibit higher ROS resistance. This project mutagenized mouse embryonic stem (ES) cells by N-ethyl-N-nitrosourea (ENU) followed by selection for the mutant ES cells with ROS resistance in cell culture. ENU causes single-gene mutations, and ROS is generated by paraquat (1,1'dimethyl-4,4'-bipyridylium dichloride, or PQ for simplicity). ES cells that survived ENU treatment and PQ selection were characterized, and their germline competency was evaluated. We concluded that mutagenized ES cells could be screened by PQ-containing cell culture media for ROS resistance; however, the surviving ES cells lost germline competency, therefore, could not be used to create mice. ROS may have an adverse effect on ES cells germline competency.

## Introduction

Reactive oxygen species (ROS), generated as a by-product of aerobic respiratory chain, are harmful and lead to accelerated aging and ultimately to death. Studies of long-lived mutants have shown increased resistance to oxidative stress; on the other hand, short-lived mutants are often sensitive to such stress. Thus increased resistance to oxidative stress is a biological marker for longevity in many species. About a dozen or so long-lived mouse mutants have been identified in the last decade, and recent evidence suggests that these are also associated with increased resistance to several stressors. In this project we intend to identify ROS-resistant mutants in the mouse and to see if these mutants show extended longevity. The mouse is an attractive model for studying many biological systems in humans due to the similarity of many physiologic systems between them and their genetic similarity. However, most of the mutants so far identified in the mouse have been found serendipitously in preexisting mutants. To accelerate the recovery of long-live mouse mutants, we propose to use mouse ES cells in our mutagenesis scheme. ES cells are mutagenized by N-ethyl-N-nitrosourea (ENU) followed by selection for resistance to a ROS generator such as paraquat (PQ) or withdraw of β-mercaptoethanol (β-ME) from the cell culture media. Those ROS-resistant ES cell clones will then be converted to mice with the rationale that oxidative resistant is a major trait conferring extended life span. Mutagenesis in ES cells is an efficient approach for recovering mutants that show an altered cellular phenotype. Since most of the experimental manipulation will be performed in cell culture, the throughput of mutant recovery is considered greatly increased, compared to the mutagenesis in living mice for longevity mutants.

## Technical Approach

1. ENU mutagenesis in mouse embryonic stem (ES) cells: The experimental procedure for ENU mutagenesis in ES cells is based on the reported method of Chen et al. (2000). Germline-competent F1 hybrid ES cells derived from C57BL/6 x 129X1Sv/J (EC7.1) (Chick et al. 2005) were used for ENU mutagenesis. Briefly, EC7.1 ES cells were treated with ENU at various concentrations for 2 h at 37°C with constant rocking. The survival rate was evaluated after growing the ENU-treated ES cells on plates.

2. Isolation of oxidative resistant ES cell clones: there are two ways to achieve this. A: ENU-mutagenized ES cells in culture were trypsinized into single-cell suspension and plated onto culture dishes. The reducing agent β-ME was removed from the cell culture media to select the oxidative resistant ENU-mutagenized ES cells. B: ENU-mutagenized ES cells that were screened under different concentrations of PQ to identify ROS-resistant mutant cells.

3. Loss of heterozygosity (LOH) in ROS-resistant ES cells: ES cells selected for ROS resistance (i.e., survived β-ME withdrawal and further verified by PQ incubation) were analyzed for loss of heterozygosity across the genome. Two polymorphic (between C57BL/6 and 129X1/SvJ) microsatellite markers per chromosome, mapped proximally and distally, were used to genotype each PQ-resistant clone to scan for LOH. LOH is required since most of mutant traits can be detected only when the

mutation is in homozygosity, which has to be generated by LOH in this project.

4. Germline transmission of oxidative stress-resistant ES cells: Selected ENU-mutagenized, PQ-resistant ES cells were aggregated with 16-cell stage mouse embryos or injected into the 3.5-day embryos (caleedblastocysts) to test for germline competence.

## Results and Discussion

1. We observed that higher concentration of ENU led to increased rate of cell death, as ENU is both mutagenic and cytotoxic. Freshly prepared ENU at concentrations of 0.6 mg/ml killed 85% of EC7.1 ES cells. It appears that our ENU concentrations were higher than those reported in order to achieve the same cell death rate; it may be that due to our hybrid EC7.1 ES cells are more vigorous than the ES cells used by others, although plating techniques among other aspects of these procedures were different from those seen on previous studies. Another possibility is the way to plate the ENU-treated ES cells. We intentionally plated more ES cells that were treated at higher concentration of ENU to compensate for the cell loss, by ENU toxicity, so that about same number of surviving colonies over the range of ENU concentrations would be obtained in the culture. It may be a more accurate method compared to plate fix number of ES cells at different ENU concentration since plating efficiency is known to be affected by viable cell number of cells plated. The unstable nature of the ENU solution was evident in our results: ENU stock solution stored at –20°C for 10 days showed reduced potency such that about 6–10% less ES cells were killed over the concentration of 0.2–0.6 mg/ml.

2. We found that feeder cells interfered with the PQ-mediated cell death. With the presence of feeders, ES cells seemed to be partially saved from killing by PQ treatment and tended to have significant differentiation, which will have adverse effect on the germline transmission of the ES cells. On the contrary, ES cells without the ENU treatment selected for the PQ-resistant in the absence of feeders were either killed completely or survived with much less differentiation. Thus, we routinely selected ROS-resistant clones on non-feeder plates. The recovery rate of ROS-resistant clones by withdrawal of β-ME was 75 clones (PQ0 clones) out of $5 \times 10^6$ ES cells seeded. Selection using 40 mM PQ yielded 54 clones (PQ40 clones) out of 5 × 106 ES cells. We have picked 12 PQ0 clones and 23 PQ40 clones, and they were expanded and frozen. Genomic DNA of the respective clones was isolated from the confluent 35-mm plates using the Qiagen DNeasy tissue kit.

3. All ROS-resistant, ENU-mutagenized ES cell clones were subject of genome scanning by PCR. We found one PQ0 clone and three PQ40 clones to show LOH in the distal part of chromosome 9 (Fig. 1). Whether this was mediated by a chromosomal deletion or mitotic recombination was not yet determined. No LOH has been found in other chromosomes to date. We reasoned that if the ENU-induced mutation conferring the ROS-resistant phenotype is recessive, mitotic recombination occurring in that genomic region is required to reveal this phenotype. Thus, it is desirable to significantly increase mitotic recombination events for screening recessive mutations in the future.

Eight different ROS-resistant ES cell clones have been injected into the blastocysts at least twice per clone, but no chimera mice were produced. Similar results were also obtained by others (personal communication, Tomas Johnson, consultant of this project). It appears that the PQ clones may have lost their capability to colonize the germline. We concluded that the oxidative stress imposed on the ES cells during selection causes them to lose their germline transmission capability.

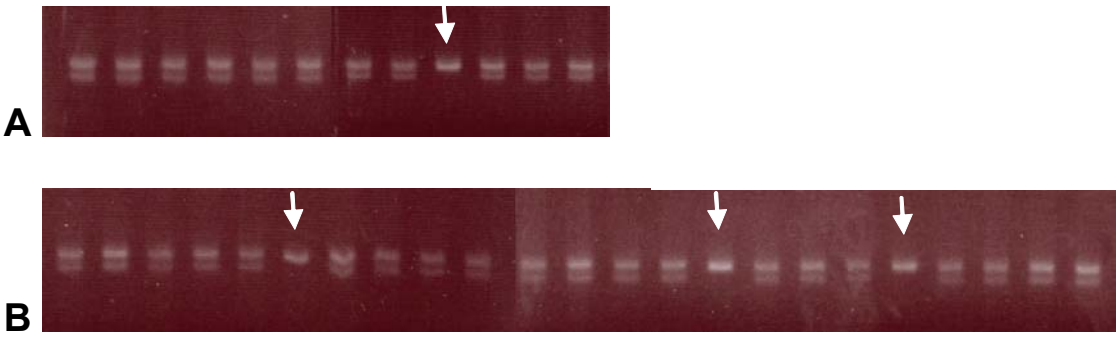


*Fig. 1. Molecular typing of (A) PQ0 clones and (B) PQ40 clones with the microsatellite marker, D9Mit279. One PQ0 clone and three PQ40 clones showed LOH at which 129X1/SvJ allele of D9Mit279 was lost.*

This study confirmed that ENU-mutagenized ES cells can survive both withdraw of β-ME from the cell culture media or addition of PQ in the culture media. However, the fact that ROS-resistant ES cells failed to go germline implies that our mutagenesis-selection strategy have to be modified in order to mutagenize the ES cells, select for ROS-resistant ES cells, and generate longevity mice from the ENU-mutagenized ROS-resistant ES cells.

## Benefits

As discussed in the introduction, so far, mouse mutants with extended life-span were identified serendipitously in the previously existing mutants. Screening mutagenized ES cells with ROS-resistant is a novel approach to identify genes affecting the mammalian life-span. This project established ENU and PQ concentrations in ES cell culture to generate and screen for the ROS-resistant ES cells. However, there are two major obstacles have to be overcome before the ES cell-based approaches can be employed to generate longevity mice efficiently: mutation homozygosity after the ES cell mutagenesis and germline transmission of the ROS-resistant ES cells. Mutation homozygosity has to be generated by LOH in ES cells. This is a long sought-after objective in the mouse genetic community so that recessive traits can be selected directly in ES cell culture. No ideal solution has been found at this point, and many ideas are being tested. Loss of germline transmission in the ROS-resistant ES cells was unexpected since our EC7.1 ES cells were very robust. Even after exposure to 400 rad of X rays, which killed more than 80% of ES cells, the surviving ES cells can still go germline (Chick et al. 2005). New experimental approaches have to be explored to solve these two problems, which is beyond the scope of this seed money project. However, former post-doctoral fellow Wallace Chick, who worked on this project and is now at University of Colorado Health Sciences Center, is applying for funding to continue this project. Dr. Thomas Johnson, who is the consultant on this project, will be co-PI, and Yun You, PI of this project, will be consultant in the new proposal.

## References

Chen, Y., D. Yee, K. Dains, A. Chatterjee, J. Cavalcoli, E. Schneider, J. Om, R. P. Woychik, R. P., and T. Magnuson. 2000. "Genotype-based screen for ENU-induced mutations in mouse embryonic stem cells," *Nat. Genet.* **24**, 314–317.

Chick, W. S., S. E. Mentzer, D. A. Carpenter, E. M. Rinchik, D. Johnson, and Y. You. 2005. "X-ray-induced deletion complexes in embryonic stem cells on mouse chromosome 15," *Mamm. Genome* **16**, 661–671.

# Development of a Multi-Mode and Multi-Spectral Automated Mueller Matrix Polarization Imaging System for Non-Invasive Skin Cancer Detection and Diagnosis

J. S. Baba,[1] M. N. Ericson,[1] P. R. Boudreaux,[2] S. Y. Chon,[3] and M. Duvic[3]
[1]*Engineering Science & Technology Division*
[2]*Oak Ridge Associated Universities (ORAU)*
[3]*The University of Texas, M. D. Anderson Cancer Center*

Melanoma, the deadliest form of skin cancer, will account for approximately 7600 U.S. deaths this year. Present techniques employed for early detection involve cost-intensive physical examinations and frequently unnecessary tissue biopsies. In an effort to improve patient outcome and reduce cost, researchers at ORNL are developing a non-invasive, non-contact, multi-mode, and multi-spectral automated Mueller matrix polarization imaging instrument to enable rapid and efficient early detection of melanoma. This instrument was used to image nine consenting patients at M. D. Anderson Cancer Center (Houston, Texas) to ascertain its sensitivity for non-invasive discrimination of human cancerous and non-cancerous lesions, in vivo. The preliminary data collected will serve as the basis for a NIH proposal for further instrumentation development and miniaturization to enable the reduction of the device to a size more suitable for clinical practice.

## Introduction

With the aging of the baby boomer generation en masse, the health care system is being tasked with an increasingly larger number of patients. The continued shortage of qualified medical care personal and the rising costs of medical insurance are all indicative of the strain on healthcare resources, and they forebode what lies ahead. Hence, there is urgent need to develop more reliable instruments for medical diagnostics and treatment that will enable the early detection and treatment of potentially fatal diseases, such as melanoma, while reducing the associated necessary medical resource burden.

## Technical Approach

Our technique, based on imaging suspect skin lesions with different colors of light (multi-spectral imaging), provides many significant improvements over current research and clinical methods. For one, by incorporating the use of polarized light, it provides increased structural contrast and detail to improve structural visualization and segmentation. Secondly, by utilizing multi-spectral images to enhance metabolic contrast of suspect lesions, it improves discrimination based on the increased cellular activity of active tumors. Thirdly, by employing image processing techniques that fuse the multi-mode data, it will facilitate accurate and automated detection and diagnosis.

## Accomplishments and Outstanding Work

Since the project was initiated in March 2004, we successfully obtained IRB approval to clinically demonstrate our instrument on volunteer human patients, completed system design, and purchased and ordered the necessary system components, of which several were custom optical components. Construction of the instrument in conjunction with system integration and calibration was completed prior to going to the clinic to collect patient data. At the end of FY 2005, we were able to collect data on nine pigmented lesions prior to biopsy for possible melanoma and are still awaiting histology results for correlation with our optical measurements.

## Benefits

This project, when completed, will provide a measurable improvement in the discrimination of cancerous and benign skin lesions using a new non-invasive multi-mode alternative to biopsy. The direct consequence will be improved patient outcome, reduced patient discomfort, and a reduction in the costs associated with skin cancer diagnosis and treatment. The indirect consequence will be the advancement of non-medical fields such as atmospheric science research where a high resolution multi-mode and multi-spectral imaging system would be a useful tool for dynamic studies. Based on our recent clinical experience, we have determined that in order to realize our clinical objective, we will need further instrumentation development and miniaturization to make the tool more effective for clinical studies that will be conducted to establish its efficacy. To this end we are targeting National Institutes of Health National Institute of Biomedical Imaging and Bioengineering (NIH-NIBIB) for follow on funding.

This project fits in with the DOE Office of Science's general mission to advance research that improves the quality of life for all Americans and, more explicitly, pursues the goal of DOE Office of Science Medical Science Division (MSD) to develop innovative diagnostic and treatment solutions to critical problems in human health. The success of this research will ultimately lead to the development of a medical instrument that can be transferred to the NIH for clinical testing or to industry for further development; a stated major objective of the DOE Advanced Biomedical Technology (ABT) Research initiative. Currently, this research directly addresses two NIH-National Cancer Institute funding areas: (1) Novel Technologies for Noninvasive Detection, Diagnosis, and Treatment of Cancer, and (2) Industry–Academic Partnerships for Development of Biomedical Imaging Systems and Methods That Are Cancer Specific (R21), and also targets NIH-NIBIB objectives. Additionally, this project leverages ORNL's new expertise in the field of biomedical engineering and optics to develop a high-impact instrument with significant clinical application while advancing its initiative to increase collaborations with world class institutions.

In summary, the successful completion of this research will result in improved patient outcome, reduced patient discomfort, and a reduction in costs associated with unnecessary biopsy procedures. Combining the synergy and expertise of groups within ORNL with a world-class clinical center will favorably position the Laboratory for new funding opportunities with NIH and the commercial sector.

*Figure 1: System installed in the procedure room of the Cancer Prevention Dermatology Clinic, at The University of Texas M. D. Anderson Cancer Center, for preliminary patient data collection.*

# An Image-Based Method for Screening and Diagnosis of Blinding Eye Disease

K. W. Tobin,[1] E. Chaum,[2] V. P. Govindasamy,[1] T. P. Karnowski[1]
[1]*Engineering Science and Technology Division*
[2]*University of Tennessee Health Science Center, Memphis, Tennessee*

The World Health Organization estimates that 135 million people have diabetes mellitus worldwide, and that the number of people with diabetes will increase to 300 million by the year 2025 (Amos et al. 1997). Diabetic retinopathy (DR) is the leading cause of new blindness in working-age adults in the industrialized world (Centers 2003). The objective of this project was to research and test a unique image-based retinal screening and diagnostic method that leverages ORNL's previous research in content-based image retrieval (CBIR) technology. In collaboration with the University of Tennessee Health Science Center (UTHSC) Department of Ophthalmology, we used digital retinal photography to automatically quantify specific disease-based changes in the human retina. Through this research, we developed an extensive image database of retinal disease states for CBIR analysis, and completed research to develop methods for characterizing important retinal structures, culminating in the award of a 3-year, $1.62 million R-01 Grant from the National Eye Institute of the National Institutes of Health (NIH). Through this NIH research, we will take our preliminary results through clinical trials.

## Introduction

Early detection and treatment of prevalent blinding eye diseases related to diabetic retinopathy (DR) and age-related macular degeneration (AMD) can have a significant impact on reducing vision loss and blindness worldwide. The primary objective of this proof-of-principle project was to develop and test a unique image-based retinal screening and diagnostic method that leveraged content-based image retrieval (CBIR) technology originally developed by ORNL for industrial and geo-spatial image data analysis (Tobin et al. 2002; Bingham et al. 2004; Tobin et al. 2005). In collaboration with the University of Tennessee Health Science Center (UTHSC) Department of Ophthalmology, we used digital retinal photography to image and quantify specific disease-based changes in the retina. We developed an extensive image database of retinal disease states for CBIR analysis. Using this image database, new image analysis and management methods have been developed that have the potential to improve the sensitivity and specificity of ocular diagnosis, and to monitor therapeutic responses to treatment in a robust, objective, and deterministic manner.

## Technical Approach

The use of digital retinal imagery to analyze DR has been reported in numerous studies (Stellingwerf et al. 2003; Larsen et al. 2003; Lin et al. 2002). Image analysis algorithms have demonstrated the ability to detect features of DR such as exudates and microaneurysms using color and monochromatic retinal images. These small pilot studies have shown that between 75–85% sensitivity and specificity for certain features of DR can be achieved. Studies by these groups and established retinal reading centers (e.g., Joslin Vision Network, Boston, MA; Inoveon Corp., Oklahoma City, OK; and the Vanderbilt Ophthalmic Imaging Center, Nashville, TN) have shown that digital photography is an excellent tool for identifying DR when performed by experienced, certified readers (Cavallerano et al. 2003; Fransen et al. 2002).

Moving beyond the current requirements of a certified human reader is a requisite for achieving broad-based, high-throughput, and low-cost screening. To achieve increased levels of automation in the digital analysis of retinal disease, it is required that the important structures of the eye be systematically and reliably located. Key elements of this process include the ability to normalize a large population of images to accommodate acceptable variations in illumination and contrast from fundus cameras used for data acquisition (Foracchia et al. 2005). Detection and segmentation of the vascular structure (Martin-Perez et al. 1999; Lin and Zheng 2002; Qing 2004) is just as critical due to the spatial relationship that exists between the vasculature and the position of the optic nerve in the retina (Foracchia et al. 2004; Hoover and Goldbaaum 2003). Achieving this retinal characterization became the primary focus of this research effort due to the fundamental underpinning that this capability provides for continued future research in this area.

## Results and Discussion

This Seed Money project was initiated in May 2004 and was concluded in the summer of 2005. Due to the nature of the human data that was being evaluated for this project, it was required that IRB approval or exemption be obtained. An exemption from the ORAU IRB (ORNL

EX04-10) was received in June 2004 and allowed ORNL to receive anonymized, diagnosed human data from UTHSC. We then worked with Dr. Ed Chaum to assemble a database of approximately 1000 digital fundus images representing 331 patients. This dataset comprises our initial image repository and patient context for developing our image and feature analysis methods. Once the dataset was initially established, we visited the Ophthalmology Department at UTHSC to interview Dr. Chaum and his staff to document the visual attributes of digital fundus imagery that are used to diagnose the various pathologies that this data represent. Subsequent to this visit, we defined and implemented a database architecture. This database architecture is extensible and allows us to append the data at later dates and to incorporate our descriptive feature data for performing image-based queries and diagnostics.

Through this research we contributed two novel methods for localizing retinal structure. First, we developed a probabilistic approach using a Bayes decision rule for the binary problem of classifying an image pixel as optic nerve or not optic nerve. This was achieved by using statistical features of the vasculature with a multivariate normal density function (e.g., the vascular density, thickness, and orientation for every image pixel). The second is a method for locating the approximate macula center based on empirical geometric relationships between the structure of the vascular arcade and the location of the optic nerve. Both of these methods work together to automatically place a coordinate system on the retina that is used to describe the relationship between retinal lesions, edema, and hemorrhages, relative to the optic nerve and macula positions.

Figure 1 shows two examples of a red-free fundus image representing a human retina. In (a) we have manually annotated a variety of lesion types that are key indicators of retinal disease. In (b) we show a composite result of a retina characterized through our automated process. This includes the location of the optic nerve by the statistical Bayes method that uses knowledge obtained from the segmented vascular tree (both shown). The vascular tree is also used to fit a simple parabolic model that orients the macula-center axis between the optic nerve and the fovea. Also shown are the results of the detection of a number of drusen, a lesion type typically associated with AMD.

Based on these results, we developed the preliminary data required to apply for a grant from NIH. The NIH National Eye Institute (NEI), at its June 9th Council meeting, fully funded our collaborative R-01 grant application entitled "Automated Screening for Diabetic Retinopathy by Content" (1 R01 EY017065-01). The NEI award leverages the original seed money investment to provide a 3-year, $1.62 million NIH research program and a long-term collaboration between ORNL and the University of Tennessee Health Science Center (UTHSC), including the UT Center for Health Innovation and Community Outreach.

The results of our research to date are being prepared for publication and presentation in several different venues. Our paper, entitled "Characterization of the Optic Disc in Retinal Imagery using a Probabilistic Approach," was accepted for presentation at the SPIE Medical Imaging Conference, San Diego, CA, in February 2005. We have also had two additional papers accepted for presentation at the 11th Annual Meeting of the American

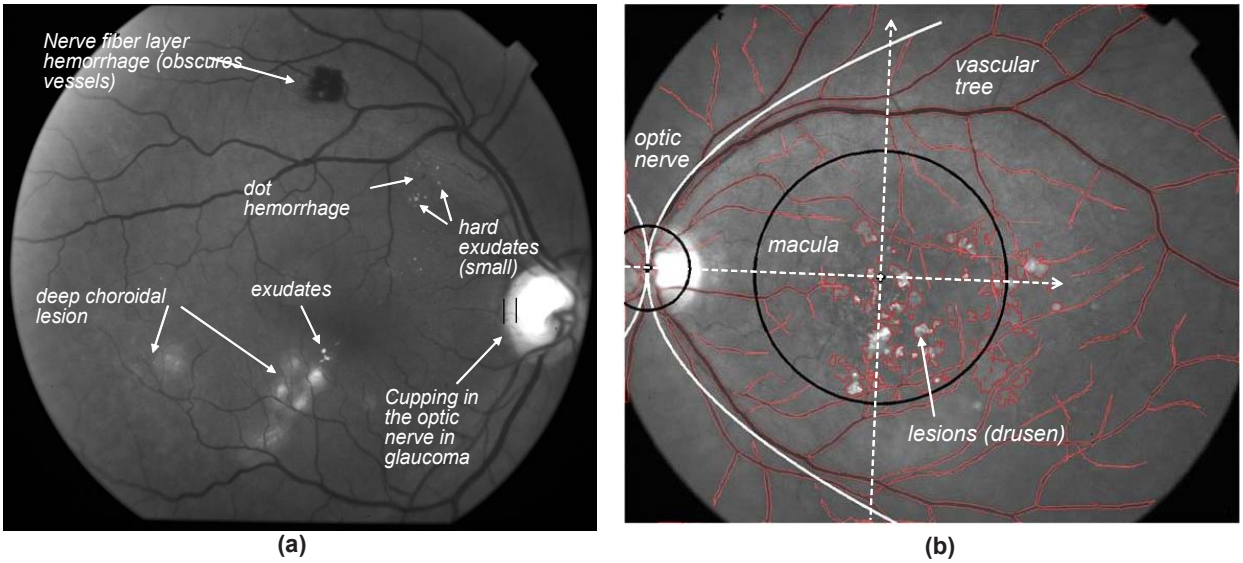


*Fig. 1. (a) Example of a digital red-free fundus image showing the variety of visible lesions indicating the state of retinal disease. (b) Example of the detected retinal structures (e.g., optic nerve, vascular structure, and lesions) and macula-centered coordinate system imposed by the ORNL analysis method developed through this Seed Money project.*

Telemedicine Association, entitled "Automatically Diagnosing Retinopathy using Digital Fundus Imagery" and "Automated Image Analysis to Characterize Prevalent Structures in Digital Retinal Imagery," San Diego, CA, in May 2006. Finally, we are preparing a peer-reviewed journal article entitled "Detection of Critical Structures in Human Retinal Imagery" for submission to IEEE Transactions on Medical Imaging, in December 2005.

## Benefits

This research in biomedical image analysis supports the DOE Office of Science and the area of Biological and Environmental Research. The underlying technology that is being leveraged for this project was developed at ORNL through research supporting the Office of Energy Efficiency and Renewable Energy and the Industrial Technologies Program. This original work was performed in the area of industrial automation and waste mitigation through image-based quality control and is now being applied to the automated diagnosis of blinding eye disease.

It is estimated that as much as $167 million dollars and 71,000–85,000 sight-years can be saved annually in the United States alone with improved retinal screening methods (Larsen et al. 2003). Current diagnosis of diabetic retinopathy is performed by ophthalmologists and reading centers. Reading centers have recently begun to adopt high-speed data transmission of digital images instead of using older photographic film technology (shipped by commercial carriers). This type of diagnosis is slow and labor intensive compared with our CBIR approach. There are also limits in the number of reading centers and the number of trained personnel at each center. Our technology will seek to replace this manual screening activity with a low-cost, high-throughput, reliable, and repeatable computer-aided diagnosis system.

## References


Amos, A. F., D. J. McCarty, and P. Zimmet. 1997. "The rising global burden of diabetes and its complications: estimates and projections to the year 2010," *Diabetic Med*. **14**, S57–85.

Bingham, P. R., J. R. Price, K. W. Tobin, and T. P. Karnowski. July 2004. "Semiconductor Sidewall Shape Estimation," *SPIE Journal of Electronic Imaging* 13(3).

Cavallerano, A. A., J. D. Cavallerano, P. Katalinic, A. M. Tolson, L. P. Aiello, and L. M. Aiello, Joslin Vision Network Clinical Team. 2003. "Use of Joslin Vision Network digital-video nonmydriatic retinal imaging to assess diabetic retinopathy in a clinical program," *Retina* **23**(2), 215–23.

Centers for Disease Control and Prevention. 2003. National Diabetes Fact Sheet (http://www.cdc.gov).

Foracchia, M., E. Grisan, and A. Ruggeri. Oct. 2004. "Detection of the optic disc in retinal images by means of a geometrical model of vessel structure," *IEEE Trans. on Medical Imaging* **23**(10), 1189–1195.

Foracchia, M., E. Grisan, and A. Ruggeri. June 2005. "Luminosity and contrast normalization in retinal images," *Medical Image Analysis* **9**, Issue 3, pp. 179–190.

Fransen, S. R., T. C. Leonard-Martin, W. J. Feuer, P. L. Hildebrand, Inoveon Health Research Group. 2002. "Clinical evaluation of patients with diabetic retinopathy: accuracy of the Inoveon diabetic retinopathy-3DT system," *Ophthalmology* **109**(3), 595–601.

Hoover, A. and M. Goldbaum. Aug. 2003. "Locating the optic nerve in a retinal image using the fuzzy convergence of the blood vessels," *IEEE Tran. on Medical Imaging* **22**(8), 951–958.

Larsen, M., J. Godt, and M. Grunkin. 2003. "Automated detection of diabetic retinopathy in a fundus photographic screening population," *Invest. Ophthal. Vis. Sci.* **44**, 767–71.

Lin, D. Y., M. S. Blumenkranz, R. J. Brothers, and D. M. Grosvenor. 2002. "The sensitivity and specificity of single-field nonmydriatic monochromatic digital fundus photography with remote image interpretation for diabetic retinopathy screening: a comparison with ophthalmoscopy and standardized mydriatic color photography," *Am. J. Ophthalmol*. 134(2):204–13.

Lin, T. and Y. Zheng. Sept. 2002. "Adaptive image enhancement for retinal blood vessel segmentation," *Electronic Letters* **38**, Issue 19, pp. 1090–1091.

Martin-Perez, M. E., A. D. Hughes, A. V. Staanton, S. A. Thom, A. A. Bharath, and K. H. Parker. 1999. "Segmentation of retinal blood vessels based on the second directional derivative and region growing," pp. 173-176 in *IEEE International Conference on Image Processing*, Vol. 2.

Qing, Z. H. 2004. "Segmentation of blood vessels in retinal images using 2-D entropies of gray level-gradient co-occurrence matrix," pp. 509–512 in *IEEE International Conference on Acoustics, Speech, and Signal Processing*.

Stellingwerf, C., P. Hardus, and J. Hooymans. 2001. "Two-field photography can identify patients with vision-threatening diabetic retinopathy: a screening approach in the primary care setting," *Diabetes Care* **24**, 2086–90.

Tobin, K. W., T. P. Karnowski, L. F. Arrowood, R. K. Ferrell, J. S. Goddard, F. Lakhani. 2002. "Content-based Image Retrieval for Semiconductor Process Characterization," *EURASIP Journal on Applied Signal Processing* **2002**(7).

Tobin, K.W., B. L. Bhaduri, E. A. Bright, A. Cheriyadat, T. P. Karnowski, P. J. Palathingal, T. E. Potok, and J. R. Price. 2005. "Large-Scale Geospatial Indexing for Image-Based Retrieval and Analysis," ISVC 2005, LNCS 3804, Springer-Verlag, Berlin, pp. 543–552.

# A New Forensics Tool: Development of an Advanced Sensor for Detecting Clandestine Graves

A. A. Vass,[1] C. Thompson,[2] R. Smith,[2] and W. H. Andrews, Jr.[3]
[1]*Life Sciences Division*
[2]*Chemical Sciences Division*
[3]*Engineering Sciences and Technology Division*

Locating clandestine graves, identification of victims (development of biological profiles from unidentified persons), and odor recognition (in locating and identifying individuals) are still very difficult, costly, and time-consuming tasks which impact law enforcement, intelligence, and military operations around the world. The Federal Bureau of Investigation recognizes these deficiencies and has funded studies to develop databases comprised of odor signatures of human decomposition, canine scenting, and canine tracking abilities. The database comprising the odor liberation from human cadavers was developed at ORNL in conjunction with the University of Tennessee's Decay Research Facility and continues being developed for long-term burials. In this proposal, we utilized this very specific and unique database of human decompositional odor to modify existing technology to develop a sensor package capable of locating clandestine graves. This detector, based on specific chemical compounds found relevant to human decomposition, is the next step forward in clandestine grave detection and will take the guesswork out of current methods using canines and ground-penetrating radar, which have historically been unreliable.

## Introduction

There are three primary means of locating clandestine graves today: manual probing, canines, and ground penetrating radar (GPR). Manual probing is very inexpensive and is used to locate disturbed soil regions but cannot confirm the presence of a corpse and can only be used in small areas. GPR is usually expensive and also locates areas of disturbed soil. Under ideal conditions, and if the grave is very fresh, GPR can sometimes indicate the presence of a corpse but can be easily fooled by objects in the environment (e.g., roots, stumps, rocks, debris, man-made objects, etc.) and requires a significant amount of training to interpret the signals indicative of clandestine graves. Canines that detect human remains, commonly referred to as cadaver dogs, have been minimally represented in the law enforcement canine population across the United States. For a variety of reasons, this canine detector specialty has not been given the attention that is afforded both explosive and narcotic specialties. The current concern facing cadaver dog units is that training is inadequate since it is unknown to what odor signals the dogs respond to when alerting, and the alerting may not completely be in response to odor. This jeopardizes search and seizure as well as probable cause rules currently established for search warrants and chain of custody. Many agencies usually employ a combination of these methods when searching for clandestine graves, mass graves, or missing persons, which also results in an increased cost, significant utilization of man-hours and logistic and time concerns.

For the past 3 years, the Federal Bureau of Investigation has funded a study at ORNL seeking to determine the chemical markers associated with odor of human decomposition, primarily aimed at legitimizing the training efforts of cadaver locating dogs. This study has focused on human remains in graves of various depths and of various ages (fresh–15 years old) under a variety of environmental conditions. The results of this study to date has been a collection of over 400 different chemical compounds liberated from human decomposition in burial situations, of which only about 40 make it to the surface in a reproducible fashion regardless of the depth of burial and age of the grave.

The modified detector built for this project keyed in on hydrocarbon and halogenated compounds identified in the aforementioned odor study with successful trial runs both in the laboratory and in the field.

## Technical Approach

The technology, which is to be modified for this purpose, is a hand-held leak detector called the "Informant 2" dual purpose refrigerant and combustible gas leak detector. This is currently under evaluation at ORNL as a detector for identifying locations which produce illegal methamphetamines. It is designed to detect all halogens and combustible hydrocarbons using two different interchangeable sensor tips. The combustible sensor is a semiconductor-type sensor and has a sensitivity of 50 ppm methane at a minimum. The refrigerant sensor is a heated diode with a sensitivity of 14 g/yr of R-134a.

Preliminary testing of these two sensors at the University of Tennessee's Decay Research Facility over graves gave weak responses. The weak responses (for both sensors) are due to the fact that of the 40 specific chemicals under study, several of these are fluorinated halogens and hydrocarbons to which the detector is designed to respond to in a non-specific fashion (e.g., dichlorodifluoromethane; 1,2, dimethyl benzene).

This study looked at the current sensors in the "Informant 2" and determined how to increase the sensitivity and specificity of the instrument to create a grave detector. The pathway to success lay in an orthogonal approach—coupling the two different detectors (creating a dual simultaneous response) for increased selectivity as well as increasing the active area [and collection efficiency—e.g., using microthermally desorbed sorbents (already available at ORNL)] of the detector for increased sensitivity. Once completed, the detector was tested under a variety of field conditions at the University of Tennessee's Decay Research Facility to determine the level of sensitivity and selectivity which has been achieved. This included surface decomposition as well as burials and included a variety of depths, ages, environmental conditions and possible interferents such as decaying leaf/plant material. These test plots were already established at the decay facility, and no additional preparation was necessary.

In developing the grave sensor, we coupled two sensors typically used independently into one device where they are used simultaneously to provide greater selectivity in chemical detection. A sorbent cartridge was added to the modified device to permit collection and concentration of the very volatile chemicals of interest, followed by thermal desorption of the sorbent bed (Carbosieve SIII) and subsequent analysis by both the sensors. A sample pump was also added to the device, replacing a small fan used on the original device which wasn't capable of providing the sample flows necessary through the sorbent bed.

The grave sniffer electronics are based on sensors and electronics from the commercially available Informant leak detector instruments. The electronics boards were removed from their original instrument cases are mounted in a common plastic enclosure along with a pump for drawing air through the sensors. One sensor is mounted in its original flexible snorkel, and the other is mounted in an extension of the snorkel. The desorber is mounted on yet another extension at the fore end of the snorkel so that air is drawn through the filter media before it reaches the two sensors. The distance between the desorber and the sensors was minimized to reduce sensor response time. No modifications were made to the circuitry on the electronics boards. The indicator lights on the boards are visible through the clear lid on the plastic enclosure, and the two pushbutton controls on each board are accessible through small holes in the lid. Alarm tones were clearly audible through the enclosure (Fig. 1).

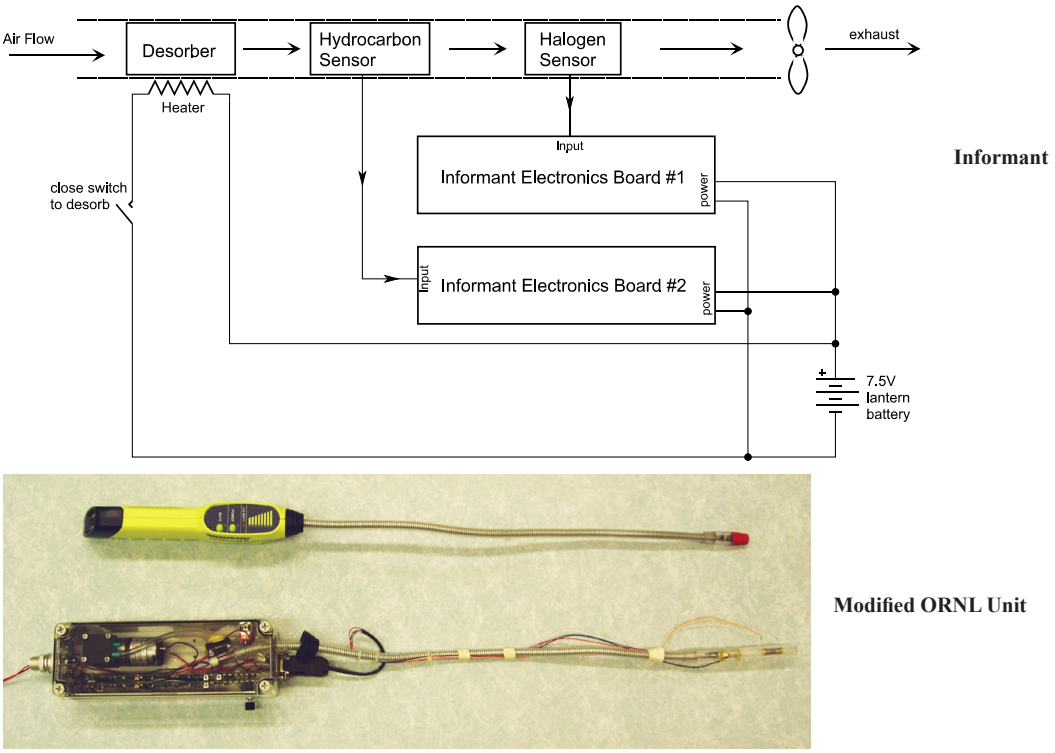


*Fig. 1. Modification of the Informant which resulted in greater sensitivity and specificity.*

## Results and Discussion

The new device has been tested with various concentrations of trichloroethylene, a halogenated hydrocarbon, which elicited a response from both sensors on the modified device at levels of 100 ppb.

While the redesign of the Informant to achieve greater sensitivity and selectivity was successful, we did encounter several issues which will require additional modification before complete success can be claimed. One feature of the Informant is an auto zero feature which zeros the instrument every 15 seconds. We have to disable that continuous auto-zero action in the Informant electronics by building a "basic" circuit that gives an output circuit proportional to the sensor response. We could carry a source of clean air (or nitrogen, etc.) to use for setting the zero manually for our proof-of-principle prototype. This additional modification is necessary since the desorbtion feature of the modified unit takes greater than 15 seconds. The sensors are also probably very sensitive to environmental conditions, so the electronics would need to allow for their variations with temperature and humidity. One additional modification that also requires another modification is that a separate battery is needed for the desorber heater. It appears to be interfering with the operation of the other circuitry.

Field testing of the unit at the decay facility met with limited success. It appeared to outperform the original Informant unit, but testing was hampered by the inability to defeat the auto-zero circuitry, making interpretation of some of the "hits" difficult.

## Benefits

Continued success in this project (CRADA development) will provide immediate benefits to local and federal law enforcement agencies (for individual graves) as well as military troops overseas attempting to locate mass graves. Agencies that would be responsive to extending this work for a variety of applications could include DoD (locating very old mass graves in Iraq and Iran and C.I.L.H.I.—ongoing M.I.A. missions to Vietnam and Korea), DTRA, NSF, FBI, NIJ, U.S. SS (Secret Service), and/or DoJ.

## Reference

Vass, A. A., R. R. Smith, C. V. Thompson, M. N. Burnett, D. A. Wolf, J. A. Synstelien, B. A. Eckenrode, and N. Dulgerian. 2004. "Decompositional Odor Analysis Database – PHASE I," *J. Forensic Sciences* **49**(4), 760–769 (July 2004).

# Creation of Photosystem II Designer Alga for Hydrogen Production

J. W. Lee, B. Zhao, and B. Evans
*Chemical Sciences Division*

This project will provide the proof of principle to create a photosystem II (PSII) designer alga for efficient and robust production of hydrogen with temporal separation of oxygen production. By creating such a PSII designer alga, we will be able to simultaneously solve the three associated oxygen problems in the field of photosynthetic hydrogen production: (1) drainage of electrons by oxygen, (2) poisoning of hydrogenase by oxygen, and (3) mixed hydrogen and oxygen gas-product separation and safety issues. During this reporting period (FY 2005), significant progress has been made. Briefly, two synthetic genes have now been designed, physically synthesized, and successfully delivered into the algal host organism *Chlamydomonas reinhardtii* to encode for an interference iRNA that could suppress the expression of a photosystem II gene OEE1.

This proof-of-principle project will lead to the creation of our envisioned photosystem II (PSII) designer alga for production of pure hydrogen without the oxygen production so that all of the three oxygen-related problems will be eliminated under hydrogen-producing conditions. It is expected that this study will significantly advance the basic science and produce a preliminary PSII designer alga for enhanced clean hydrogen production. Successful development of such a PSII designer alga will have a significant impact (a 10-fold improvement) on technology development in the field of renewable hydrogen research. Therefore, this project has direct relevancy to DOE's national (energy) security mission by creating a clean and renewable algal hydrogen energy resource. It supports President Bush's Hydrogen Initiative and is in line with the goal of the DOE EERE and BES Hydrogen Programs.

During this reporting period (FY 2005), significant progress has been made. Briefly, two synthetic genes have now been designed, physically synthesized, and successfully delivered into the algal host organism *Chlamydomonas reinhardtii* to encode for an interference iRNA that could suppress the expression of a photosystem II gene OEE1. The gene synthesis of the two designer genes was accomplished in collaboration with an outside biotechnology company. The delivery of the designer genes into the alga was accomplished using the technique of electroporation gene transformation in our laboratory. We have now verified the transformation of the designer genes into algal nuclear genome by DNA PCR experiments. The transformants have now been characterized by mRNA assays in our laboratory as well. During the mRNA assays, we discovered that the promoter of the two genes seemed not to be working. Now we have a much better promoter DNA sequence, and a new set of synthetic genes has now been re-designed using the new promoter. Currently, we are working with the biotechnology company to synthesize this new set of designer genes. The gene synthesis by the company usually takes about 2–3 months. We expect to fully harvest the fruits of the seed project at the beginning of FY 2006.

# Three-Dimensional Imaging of Multiple Fluorophores

J. R. Price[1] and J. P. Biggerstaff [2]
[1]*Engineering, Science, and Technology Division*
[2]*University of Tennessee, Knoxville*

Current three-dimensional (3D) fluorescence microscopy techniques are limited in the number of fluorescent probe colors that can be analyzed at one time. Some leading-edge systems can be configured to resolve up to 10 probes, but with substantial loss of sensitivity. Improvement in this area is especially important in sciences studying complex distributions and interactions between organisms such as environmental microbiology. The objective of this project is to develop microscopy techniques that enable the resolution of 20–30 fluorescent probes in 3D by combining the methods of 3D deconvolution and 2D interferometric microscopy.

Three-dimensional (3D) microscopic techniques, such as wide-field deconvolution and various confocal microscopies, are particularly useful for the study of many biological phenomena, ranging from the visualization and characterization of sub-cellular structures to the analysis of multi-species microbial communities. Current techniques, however, are limited in the number of parameters (e.g., fluorescent probe colors) that can be analyzed at one time. Although there exist some technologies that can resolve up to 10 probes, these technologies suffer sensitivity and photo-bleaching issues and can be prohibitively expensive for many laboratories. The goal of this project is to develop new microscopy techniques that will enable the resolution of many (20–30) fluorescent probes in 3D using conventional deconvolution microscopy in conjunction with a commercially available 2D intereferometric microscope (Applied Spectral Imaging). An additional goal is to develop preliminary computational methods to characterize the structure and organization of the observed 3D multi-probe data in order to provide biologists with quantitative representations of the experimental data.

To illustrate the potential for probe resolution using spectral information, two probes (propidium iodide and Texas Red) with significantly overlapping spectra and peaks no more than 5nm apart were considered. Spectral data was acquired from *E. coli* preparations labeled with these two probes. A spectral unmixing technique was developed that employed principal components analysis and linear discriminant analysis. The results clearly demonstrate that these probes can be readily distinguished from one another, despite their almost identical spectra. This opens the door for the simultaneous use of many probes that have not traditionally been used together because of coincident, or nearly coincident, spectral peaks. In continuing work, this technique is being expanded to resolve larger numbers of probes.

The acquisition of 3D spectral information has been demonstrated using 1-μm fluorescent beads that emit in red, green, and blue wavelengths (TetraSpeck™ Fluorescent Microspheres, Invitrogen Molecular Probes). Spectral information was acquired at 29 focus planes spaced at 0.11μm. Individual spectral channels were subjected to 3D image deconvolution, resulting in a 3D image stack for each sampled spectral wavelength comprising 66 spectral channels over a wavelength range of 350 nm to 816 nm. This dense spectral sampling in three spatial dimensions is significantly better than what is achievable on other currently available systems.

Ongoing efforts will be focused on employing the techniques described above to increase the number of resolved probes and on improving the results of the 3D image deconvolution. Preliminary computational tools to quantify structure and organization of the multi-probe data sets will also be developed.

Continued success in this project will result in microscopy and imaging tools that will enable the study of significantly more complex systems than can be studied under existing protocols. Some example applications include the study of microbial communities in bio-remediation, drinking water distribution, as well as human bowel disease. Specific DOE programs that may benefit include the Genomes to Life program and the Natural and Accelerated Bioremediation Research program. Improved tools for microbial community study will also be beneficial to the National Institutes of Health and the Environmental Protection Agency.

# Alzheimer's Disease Detection via Nonlinear Analysis of EEG

N. B. Munro,[1] L. M. Hively,[2] D. R. Wekstein,[3] and W. R. Markesbery[3]
[1]*Life Sciences Division*
[2]*Computational Sciences and Engineering Division*
[3]*Sanders-Brown Center on Aging, University of Kentucky, Chandler College of Medicine, Lexington*

Early detection of progressive brain disorders will provide clues about the origin of those diseases and would enable pre-symptomatic diagnosis and early treatment. Alzheimer's disease (AD) is the most common of a number of dementias that exact high medical and societal costs and are expected to involve an increasing number of sufferers with the graying of the U.S. population. EEG analysis offers a much more cost-effective approach to diagnosis than current functional imaging modalities.

The goal of this proposal is to show proof of concept for early detection of Alzheimer's disease and possibly even the pre-Alzheimer's changes evidenced in mildly cognitively impaired (MCI) patients by means of innovative analysis of electroencephalogram (EEG) data. Early detection by such a cost-effective means would enable earlier initiation of treatment and extention of ability to function at home, with concomitant improvement in quality of life and significant medical cost savings.

This project involves innovative analysis of human scalp EEG data, including (1) a carefully chosen subset of the available EEG channels in (2) a multi-channel extension of ORNL's patented approach for phase-space dissimilarity measures (PSDM). A third innovation uses PSDM across the patient population, rather than comparison of data segments from the same patient. A fourth innovation takes advantage of the network that is formed by the dynamical linkages among the discrete brainwave states from (2), for which statistical measures of the network properties reveal distinctive features. Indeed, the objective is determination of unique signatures to distinguish among the following four groups of aged patients: (i) normal; (ii) MCI; (iii) early AD; and (iv) dementia with Lewy Body Disease (DLB). Collaborators at the University of Kentucky (UK) will acquire EEG data from 80 patients under standard clinical protocols, with 20 patients in each of the four groups. Half of the data (ten datasets from of each group) will be analyzed to train the methodology. ORNL will be blinded to the characterizations of the other half, which we will analyze as a validation test of the methodology.

ORNL submitted an IRB application and received IRB approval for the study. A subcontract was initiated and put in place with UK. Test data EEG sets were obtained from the UK Neurosciences clinical EEG lab. Data quality analysis was performed by ORNL, and data quality issues were addressed. At about the time the contract was finalized, the UK Neurosciences EEG lab lost a technician and determined that they could not perform EEG studies to support this project. Our UK collaborators identified a researcher in another department with EEG capability. Use of a different EEG acquisition system required a new round of data quality analysis on a new test data set that verified the high quality of the data. We have received data for the first two subjects in the study and have determined that the data quality is adequate for analysis.

While waiting for the subcontract to be put in place, subjects recruited, and the second EEG lab to be identified and adequacy of their EEG data verified, work was initiated using surrogate EEG data to develop methods for sensitively distinguishing among the various groups. Analysis of the data from the first two subjects is imminent; the various analysis approaches will be compared and extended as necessary.

Success in this proposed Seed Money project will open up lines of related research on neurodegenerative diseases, other dynamical brain disorders, and a variety of additional biomedical diagnostic applications (e.g., brain biometric and voice signature analyses). Other potential application areas include orthopedic injury from joint sounds, EEG data to quantify fatigue, and for deception detection.

# Nano/Microelectromechanical Systems Tools for Retinal Surgery

C. L. Britton,[1] Jr., R. J. Warmack,[1] M. N. Ericson,[1] J. S. Baba,[1] J. Simpson,[1] B. D'Urso,[1] and E. Chaum[2]
[1]*Engineering Science and Technology Division*
[2]*The University of Tennessee Health Science Center*

The ability to design and fabricate mechanical structures in both MEMS (micro-electro-mechanical systems) and NEMS (nano-electro-mechanical systems) processes creates the possibility of very small, surgery-specific tools that will enable the physician to perform faster, safer, and more effective surgical procedures. The obvious generic tools, forceps and needles, have already been fabricated in MEMS processes but have not enjoyed wide use primarily because they are simply extensions of the obvious—make smaller versions of existing tools. This brings little if any new capability to the physician. In this project, we propose to begin considering new approaches that are not simply miniaturized versions of existing tools.

We propose to begin considering new approaches that are not simply extensions of existing tools but new structures that have not been built before and will facilitate great improvements in surgical care.

The purpose of this research is to build a prototype instrument that can be used to successfully perform ERM surgery. Our approach is proprietary since the patent application has not been filed.

Extensive work was performed to select appropriate materials and determine methods for fabricating test MEMS structures. We have fabricated and tested several of the instruments. Though any conclusions at this point are preliminary, it appears that we are still on the right track. Variations in results were observed that are likely due to a number of confounding factors associated with proper fixturing of the probes. Furthermore, variations in the membrane shape, fibrous content and orientation, and surface wetness also affect measurement repeatability. Future experiments will be conducted once we have devised a standard system calibration sample and a more planar and rigid probe testing membrane substrate. Collagen-based gels are being investigated for this purpose. In addition, a number of experiments will be repeated using larger probes (at least ~1 cm × 1 cm) to eliminate frictional forces associated with the probe edges. This will require significant changes to the fixture used to hold the membrane but should produce more repeatable experimental results. In addition, structures are being prepared for testing by Ed Chaum.

The demonstration of an improved method of retinal surgery will increase speed, efficacy, and success rates of the procedure.

# Orientational Imaging in Biological Systems by Electromechanical Scanning Probe Microscopy: Galvani Experiment on the Nanoscale

S. V. Kalinin[1] and T. Thundat[2]
[1]*Condensed Matter Sciences Division*
[2]*Life Sciences Division*

Mechanical, electromechanical, and chemomechanical interactions on the level of molecules, cells, and tissues are the basis of functionality in biological systems. These properties are ultimately related to the relative ordering and orientation of relatively small number of biopolymers, such as collagen. The objective of this project is the development of the Scanning Probe Microscopy (SPM) approach for the molecular orientation imaging in biological systems based on the detection of local electromechanical response of the surface.

Unique mechanical properties of the biological systems such as calcified and connective tissues are ultimately controlled by ordering and orientation of relatively small number of biopolymers, such as collagen. To date, a number of approaches for measuring local molecular orientation based on electron and optical microscopy or diffraction methods have been developed; however, in most cases the spatial resolution as determined by signal generation volume has been extremely limited. We have formulated the requirements for quantitative orientation imaging using Scanning Probe Microscopy–based techniques, which include (a) high spatial resolution, (b) insensitivity to tip geometry, and (c) signal that should contain information sufficient to recover orientation vector.

From the analysis of existing SPM techniques, only those sensitive to properties described by a third-rank tensor, such as piezoelectricity, electrooptical properties, and second harmonic generation, satisfy aforementioned conditions. The previous work by the PI in collaboration with the Tufts group (Mark Kachanov and Edgar Karapetian) has demonstrated that piezoelectric signal is independent of tip geometry. Thus, Piezoresponse Force Microscopy, based on the detection of bias-induced surface displacement, provides a natural approach for high-resolution molecular orientation imaging. In this proposal, we addressed three issues: (a) whether the piezoelectricity in biological systems can be detected locally, (b) whether high spatial resolution can be achieved, and (c) whether the complete electromechanical response vector can be measured and local molecular orientation can be reconstructed.

To date, we have successfully demonstrated electromechanical imaging of biological systems with sub-10-nm resolution using Piezoresponse Force Microscopy [*Appl. Phys. Lett*. **87**, 053901 (2005)]. These measurements have been compared with elastic imaging by Atomic Force Acoustic Microscopy, and it has been shown that PFM allows imaging free of topographic cross-talk, in agreement with theoretical predicitions [*J. Vac. Sci. Technol. B* **23**, 2102 (2005)]. To verify the contact mechanical model employed, collaboration has been established with G. Pharr group, and the newly developed method of piezoelectric nanoindentation has demonstrated the quantitativeness of the proposed approach [*J. Mat. Res.* accepted]. In addition, a detailed analysis of frequency-dependent signal formation mechanism in PFM, a prerequisite for quantitative measurements, has been performed *[Nanotechnology*, submitted].

Further work is in progress to calibrate the in-plane components of electromechnical response vector and relate the measured electromechnical response to local composition using artificial and natural samples with controlled surface chemical functionality. A number of collaborations with groups at NCSU (T. Wright), NIH (M. Young), and UPenn (C. Gibson) have been established to link the measured physical properties to biological functionality in these systems.

# *Environmental Science and Technology*

# *Director's R&D Fund*

# An Integrated Experimental and Modeling Approach for the Study of Microbial Biofilm Communities

A. V. Palumbo,[1] C. C. Brandt,[1] S. D. Brown,[1] M. Doktycz,[2] and J. Morrell-Falvey[2]
[1]*Environmental Sciences Division*
[2]*Life Sciences Division*

The development of new molecular and imaging techniques has enabled examination of the interactions among members of microbial communities, and this type of research is of interest in several DOE programs and federal agencies. Biofilm communities offer a spatially structured community in which we are applying techniques such as imaging and microarrays to obtain data on the spatial structure of communities and on expression of unique genes (e.g., those expressed in response to the presence of other bacteria or to growth in a biofilm). The objective of the research is to develop a foundation for examination of microbial communities building on ORNL strengths in imaging and measurement of gene expression.

Understanding the genetic basis of microbial community functional stability and adaptation is a critical goal in systems biology and is a principal aim of the DOE GTL program. Biofilm communities are important in several areas relevant to DOE and are the focus of this study.

We are developing and integrating molecular methods, imaging technology, and modeling into a systems-based examination of the biotic and abiotic factors that affect the structure and function of simple microbial biofilm communities. We planned to use three bacteria species (*Shewanella, Desulfovibrio* and *Rhodopseudomonas*). However, based on feedback from the review committee after the first year of the project, we have decided to minimize efforts on *Rhodopseudomonas*. Ongoing laboratory experiments are yielding data on community structure and gene expression that will be used to parameterize a spatially explicit simulation model. The model predictions will then be tested with additional laboratory experiments.

During FY 2005, we have focused on technique development and obtained data and experience to set the stage for completion of the project in FY 2006. We have evaluated several systems for biofilm growth and have designed and successfully tested a novel hybrid system consisting of a flow though chamber with a slide that is used for confocal microscopy and an extension consisting of silicon tubing for growth of sufficient biomass for gene expression studies. We have obtained confocal microscopy images of *Shewanella* with and without green fluorescent protein (GFP) using this system. We have obtained and used image analysis software to generate metrics related to the structure of the growing *Shewanella* biofilm. We have obtained modeling software that will be used to generate data that will be calibrated to the metrics measured on the biofilms. We have also designed and tested FISH probes for *Shewanella* and *Desulfovibrio* so that we can make measurements on the structure of mixed species biofilms. We have developed common media that will support growth of all strains. We have obtained growth curves for anaerobic growth of *Shewanella* and *Desulfovibrio* and will grow them together and evaluate gene expression. The results of our microarray studies indicate that there were few cross hybridization reactions between DNA from *Desulfovibrio* and *Rhodopseudomonas* with microarrays for *Shewanella*. Similarly there were very few cross reactions of *Shewanella* DNA with the *Desulfovibrio* microarray. Thus, the microarrays will be able to be used for measurement of gene expression with co-cultures of these bacteria. We have also obtained log and stationary phase gene expression data for *Shewanella* which we will compare to gene expression in a biofilm. We are exploring spatially explicit, individual-based models to integrate the experimental data and make predictions about the structure of biofilm communities.

This research is relevant to DOE's interests in bioremediation, carbon sequestration, energy production, and bioproduct manufacturing. The methods being developed in this project will be applicable to DOE and several National Science Foundation and National Institutes of Health (NIH) programs. For example, within NIH, this project is pertinent to "Research on Microbial Biofilms and Quantitative Approaches to the Analysis of Complex Biological Systems."

# Inhalation Exposure to Processed Nanoparticles: Exploring Nanotechnology and Biological Links

M.-D. Cheng,[1] D. L. Thompson,[1] S. D. Brown,[1] D. K. Johnson,[2] and D. B. Geohegan[3]
[1]*Environmental Sciences Division*
[2]*Life Sciences Division*
[3]*Condensed Matter Sciences Division*

It is unclear how defense mechanisms of animals and cells would respond when they are exposed to nanomaterials. The major difficulty moving the science forward is the lack of a methodology for high-precision experiment of material toxicology. We devoted a significant amount of effort in the first year exploring precision methods suitable for this research and getting the team ready for focusing on inhalation toxicology during the second year. In addition, the team has been moving forward in putting together a center proposal for studying the toxicology of nanomaterials.

Nanoscale materials and nanoscale structure may be directly accessible by human bodies and ecological species, and even stealth to common biological defense mechanisms such as macrophages. Little is known about the biological responses, absorption, distribution, metabolism, and exclusion (ADME) to the nanomaterials. This research project explores/develops methodologies for inhalation toxicology research and investigates toxic effects of selected nanomaterials in cell lines and in-breed mice of selected genes.

A number of technologies were explored for studying the toxicology of nanomaterials in its original state and alien environments in FY 2005. Cells used include human cell (ATCC A549) and mice cell C10 lines. Nanomaterials were introduced to the cells by either through a liquid route or an air route in exposure experiments. The air exposure was performed using an ORNL-developed air-cell exposure device, while the liquid route introduced nanoparticles to cells while they are submerged in medium. Aluminum particles of nominal sizes 20 μm, 82 nm, and 51 nm were used as the target agent in separate experiments. The original batches of particles were very non-uniform in size, and several aerosol size-selection techniques had to be employed for producing monodisperse particles. One of them is a multi-channel ultrasonicating/tandem differential mobility analysis technique. Wet-SEM technique was explored to imaging and visualizing nanoparticles on cells in their liquid state. Raman spectroscopy was also used to detect and chemical profiling of aluminum on cells. Feasibility of microarray for toxicological responses measurement was tested in limited number of trails.

We learned substantial efforts are needed to purify and process nanomaterials before a repeatable high-precision exposure experiment could be conducted. This is due to the challenge in maintaining the integrity of the nanoscale materials in its original state for a high-precision biochemical experiment. We also learned once nano-aluminum particles aggregated, the toxicological properties of the nanomaterials changed to a great extent; the nanoparticles become much less toxic to A549, C10, and even microbial (*Shewanella oneidensis* strain MR-1) cells; however, in their original nanoscale state, they were much toxic than their micrometer-sized counterparts. The aggregation came from the interaction with surrounding species, water, proteins, amino acids, etc. Thus, the results further enforce our previous notes that exposure procedure needs to be defined properly; detailed characterization of the materials become critical for nanotoxicology.

The results, although preliminary, are important for DOE to consider for worker safety and potentially for ecological health. There are just too many unknowns at this point, but limited data do point to the enhanced toxicity of nanoscale materials toward cell lines. The methodologies we explored in FY 2005 would pave the road for a much smoother research investigation in FY 2006 when our focus will be on inhalation exposure. The research will also be of benefit to other federal agencies involved in the National Nanotechnology Initiative and application of nanomaterials such as NIH, NIEHS, USDA, DOD, NASA, and EPA.

# Genome-Enabled Detection of Differential Mortality in a Northern Temperate Forest Ecosystem

G. A. Tuskan, S. P. DiFazio, and T. M. Yin
*Environmental Sciences Division*

Genomes of any form are integrators of evolutionary history, simultaneously reflecting the environmental past and guiding future potential responses. Ecosystems comprised of intact wild populations contain information that could be used to predict responses to fluctuating global climatic change, that is, a molecular signature of adaptation. Furthermore, keystone organisms that have a disproportionate influence on the composition and function of ecosystems, and the genetic composition of these organisms, condition their ecosystem effects. Therefore, the molecular characterization of keystone species can provide insights into system responses at higher scales of organization, including the community and ecosystem. In 2005, we collected nearly 2500 leaf samples from 499 aspen (*Populus tremuloides*) trees in Rocky Mountain National Park (RMNP). DNA was extracted and the degree and scope of linkage disequilibrium in the sampled population was determined. By utilizing natural populations and surveying the genetic information contained within the genomes of such organisms, it will be possible to determine the degree of inherent response that may be present in a species and thus predict its stability and adaptability over a range of climatic conditions.

Genomes are integrators of evolutionary history, simultaneously reflecting the environmental past and guiding future potential responses of the host organism. By employing population-level systems biology approaches, we are exploring the possibility that variation at the DNA level is associated with natural variation in intact wild populations of *Populus*. We are attempting to reconstruct the process of adaptation by examining the genome over time and space. If successful, we will use this molecular signal of adaptation to ultimately build a predictive model of ecosystem level changes as affected by global climate change. The two hypotheses that we are investigating are as follows: (1) genomes are reflective of adaptive potential and vary in a predictable fashion along environmental gradients, and (2) uncovering molecular signatures of adaptation will lead to mechanistic understanding and prediction of higher-order processes, including species response to environmental perturbations.

Evolutionary biologists and applied plant and animal breeders have long been interested in the study of the genetic basis of adaptation. A rich array of analytical techniques for quantifying genetic variation has been developed. Early attempts at quantifying the effects of natural selection focused on spatial and temporal changes in phenotypes and, later, on changes in gene frequencies in response to environmental gradients or stimuli. Preliminary studies in our laboratory have confirmed this expectation: LD is generally low and deteriorates in *Populus* over short distances. We will use both an anonymous survey of the whole *Populus* genome along with directed examination of candidate genes suggested by genomic regions containing polymorphisms associated with environmental gradients in order to identify genomic segments specifically associated with adaptation.

In 2005 we accomplished three important objectives for this project:

a. Tissue was collected from 499 trees in our study site.
b. DNA was extracted and quantified from nearly 2500 tissue samples.
c. Over 800 molecular markers were designed and screened in these samples to select robust, highly polymorphic markers covering the entire genome.

A total of 840 primers were selected from the first round of screening. In the second round of screening, we amplified eight samples from different stands using the 840 primers screened from the first round screening. The primers were ranked according to the number of alleles revealed and quality of the signal. Fifty primer pairs were selected based on the objectives of this project, which will survey the samples at 50 different loci.

The screening results showed that those primers designed using random sequences had a successful amplification rate in aspen of 43.4%, whereas the rate for those primers with Exon priming sites had a 58.7% success rate. Therefore, exon-derived primers had a significantly higher success rate ($\chi^2 = 37.1$, $p < 0.0001$).

We are currently genotyping the full set of samples using 10 primers. The aim for these preliminary analyses is to determine the genetic structure of aspen populations, which will help delineate distribution of clones on the

*Fig. 1. Research geneticist samples leaves from aspen trees in Rocky Mountain National Park.*

landscape. This information is essential for the design of our subsequent experiments and for exploring linkage disequilibrium between candidate genes and the differential mortality of the genotypes adapted to these ecosystems.

We have compiled a library of putative candidate genes by identifying gene models from other organisms. These candidates represent genes known to be involved in cold tolerance, moisture response, and/or phenology, all factors expected to influence survival in the Yellowstone ecosystem (Table 1). Moisture availability and temperature are believed to be the two most important environmental factors determining growth and survival of aspen in the subalpine forests of YNP. We are in the process of designing PCR primers for each candidate gene. Multiple priming sites within each locus will be identified and tested for amplification efficiency and SNP abundance. The selected PCR primers will be tested on the plant materials collected in RMNP in August 2005. Those polymorphisms that occur within expressed regions and result in non-synonymous substitutions will be chosen as targets for SNP genotyping for the broad population assay.

During FY 2006 we will perform the following tasks:

1. Use the MicroCat to analyze increment cores and estimate tree ages.
2. Collect 1500 new samples from Yellowstone National Park.
3. Compare 300 samples collected after the 1988 fires in Yellowstone to the newly collected samples using SSR and SNP markers.
4. Conduct a preliminary study on the association between candidate genes and the differentially mortality of the survival during the 20 years following the fires.
5. Use our preliminary data to support a proposal to NSF's Population and Evolutionary Processes panel and to a new DOE program on constraints to plant migration during rapid climatic change.

**Table 1. A list of putative candidate genes that will be targeted for SNP analysis**

| Gene/gene family | Functions |
|---|---|
| Aquaporins | Water transport across membranes |
| Dehydrins | Protein stabilization in response to moisture and heat stress |
| Osmotin | Fungal defense and desiccation resistance |
| CBF1 | Transcription factor for cold response genes |
| Trehalose-6-phosphate synthase | Trehalose synthesis; dehydration and cold tolerance |

# *Environmental Science and Technology*

# *Seed Money Fund*

# Sounds of Rapids as an Attractant for Migratory Fish

C. C. Coutant,[1] M. S. Bevelhimer,[1] A. M. Fortner,[2] and G. R. Wetherington, Jr.[3]
[1]*Environmental Sciences Division*
[2]*Department of Energy, Student Undergraduate Laboratory Internship*
[3]*Engineering Science and Technology Division*

This project tested whether stream fish are attracted to natural underwater sounds of flowing water, particularly rapids, which might be used to guide fish away from damaging water intakes. Unnatural sound has been used to repel fish, but we hypothesized that fish may be attracted to natural sounds that we recorded in the field. We conducted preference-avoidance experiments in a U-shaped laboratory tank in which recorded sound (natural rapids, flowing water, or sounds of dams) was played from an underwater speaker at the end of one arm. Rainbow trout were placed individually at the base of the "U," so that the fish had a choice of arms. A digital video system observed and recorded the location and behavior of fish after release, and the average position and average activity level of the fish were calculated. In 173 trials with 32 fish, there was a large individual variation in responses such that fish did not show statistically significant attraction to natural sounds or repulsion from sounds of dams. A second study conducted to test the ability to condition trout to sounds during feeding was inconclusive. The experience has led to additional funded research at ORNL on behavioral technologies.

## Introduction

This project tested the hypothesis that stream fish can be attracted to natural underwater sounds of flowing water, particularly rapids, which may guide their migration. Hydropower dams can prevent migratory fish from traveling downstream to the sea after hatching. Many dams provide upstream passage opportunities for adult fish via fish ladders, but downstream passage around dams for juveniles is still yet to be perfected. Fish can be killed or injured when passing through a turbine and even though up to 90% of juveniles may survive passage through any given hydropower project, there are multiple dams on many rivers, thus multiplying the number of fish that do not survive. The hydropower industry is seeking ways to guide fish to downstream bypasses at dams.

Many methods have been developed to direct fish away from hydropower turbine intake areas, including the use of infrasound, strobe lights, bubble curtains, electric fields, and others (Coutant 2001a). Unfortunately, if exposed to these repulsive methods for a long time, fish can become accustomed to them and no longer frightened away. Use of attraction cues or attraction and repulsion combined (multisensory techniques) might produce better results than the use of a single technology alone (Coutant 2001b). Little research has been done on sound attraction, however.

Waters directly above hydropower projects usually become reservoirs and lose the environmental characteristics of the streams and rivers, which are the natural environment of juvenile salmonids. This causes the fish to become disoriented when approaching a dam, not only because of lost navigational cues for guidance but also because of the many unnatural stimuli around dams. We hypothesized that the natural sound environment could be an orientation cue and that sounds of natural stream features such as rapids might be an attractant of use for guiding fish to dam bypasses. Many studies have documented the hearing ranges, awareness reactions, and avoidance responses to certain sounds in fish (Knudsen et al. 1992; Popper 2003). Sound has been used to control fish behavior (Popper and Carlson 1998). Studies of coral reef fishes demonstrated that reef fish larvae are apparently attracted to sounds produced on coral reefs (Tolimieri et al. 2000).

## Technical Approach

We developed a "sound library" from a variety of field locations. A portable hydrophone was connected to a laptop computer containing a sound recording and analysis program (Spectrogram v.8). The sound of flowing water was recorded in the unimpounded Clinch River near Clinton, Tennessee, the Clinch River above and below Melton Hill Dam, the unimpounded St. Joseph River, Michigan, the creek behind the Aquatic Ecology Laboratory, and several other locations.

The attraction or repulsion effects of recorded sounds were investigated in the laboratory using a series of preference-avoidance trials with rainbow trout, *Onchorhynchus mykiss* (Salmonidae). For a first set of experiments, sounds recorded from field locations, either in natural streams or near dams, were played in a laboratory preference tank. A second study was conducted to determine if trout could be conditioned to a sound presented at feeding and subsequently be attracted to it.

All experiments were conducted in the Aquatic Ecology facilities of the Environmental Sciences

Division at Oak Ridge National Laboratory in Oak Ridge, Tennessee. An initial group of 32 rainbow trout (mean length 25 cm at end of experiments) was obtained from the Tennessee Wildlife Resources Agency's Buffalo Springs Fish Hatchery in Blaine, Tennessee. Fish were held in round, 235-gal flow-through tanks and were returned to a different tank after being used for an experiment. Tanks used for the preference-avoidance experiments were U-shaped so that the fish could make a choice, as in classic "Y-maze" experiments, with arms approximately 9 m long and an approximately 0.3-m-square wetted cross section. The tanks were marked in numbered 1-m increments, and movements of fish were recorded by overhead digital video cameras; when video was reviewed, the numbered meter in which the fish was positioned every 30 seconds was recorded onto a data sheet and then entered into a spreadsheet using Microsoft Excel software.

For the initial preference-avoidance experiment, the recorded sound was playing through an underwater speaker at one end of the U as the fish was placed into the tank. The fish had only a few seconds to acclimate to its surroundings (so that the initial response of the fish was observed); then it was allowed to explore the tank for 30 min. The sounds that were used for experiments included sounds of rapids recorded in the field, sounds of running water recorded in the lab, and sounds recorded near dams. These sounds were played at various volume levels and combinations, and the tank arm containing the speaker was alternated. From the data collected, we calculated average position of the fish during the entire 30-min period, the average position for both the first and last half of the 30-min period, the number of times the fish was within 4 m of either end of the tank (i.e., nearest and furthest distance from the sound), and average activity level of the fish during the 30-min experiment and for each half of the experiment.

For conditioning experiments, 107 rainbow trout were obtained from Buffalo Springs Hatchery. We attempted to condition fish to the stimulus of gentle tapping on the side of the round, 235-gal flow-through holding tank at feeding time (twice per day, for 25 to 39 days, depending on trial). The response experiments were conducted in the same "U-shaped" tanks described above, but the speaker was placed at the bottom of the U, and two fish could be tested simultaneously, one in each arm. The sound played for these experiments was a recording of the gentle tapping as presented in the conditioning tanks.

## Results and Discussion

We successfully recorded underwater sounds consisting of a wide range of frequencies. Running water in streams has a "sound environment" different from impounded waters, as suspected. Dams generate a large amount of sound that is qualitatively different from natural rivers and is detectable for nearly a kilometer upstream and downstream. Our speculation that the sound environment for a downstream migrating fish would change markedly as the fish entered an impoundment and approached a dam was verified.

Results from the initial set of sound experiments showed no statistically significant differences between average position, activity level, or amount of time spent at opposite ends of the tank for each sound presented to fish (one-way repeated measures analysis of variance; ANOVA). Data showing average position data for the 173 trials conducted are shown in Fig. 1.

Data from conditioning experiments did not exhibit any obvious trends and were not statistically significant. Results did not change with amount of time fish were exposed to stimulus; that is, the last experiments at day 39 of conditioning were not different from those conducted at day 25.

There could be many reasons to explain why the experiments did not yield attraction or repulsion, as hypothesized. First could be our use of hatchery fish. McLean et al. (2004) describe ways in which fish raised in hatcheries are different from wild fish, including fecundity, reproductive timing, and adult behavior. Hatchery fish have shown domestication effects; genetic adaptations to hatchery environments; altered morphology, migration and feeding behavior; and are overall maladapted to the

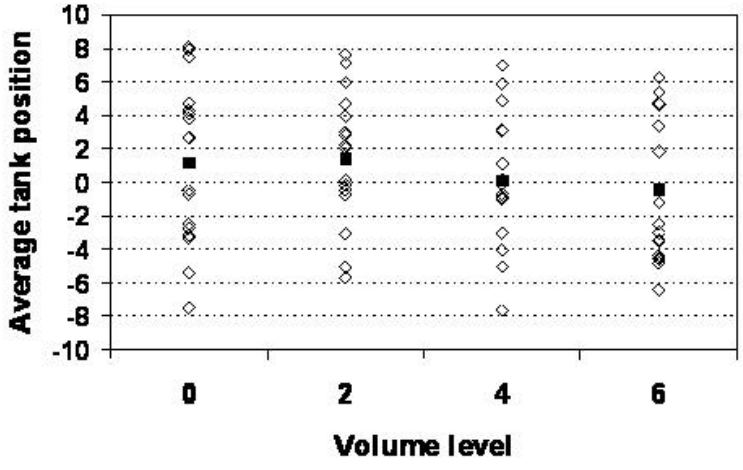


*Fig. 1. Average position of fish during sound attraction experiments using control (no sound), and sounds of rapids at volume levels 2, 4, and 6. Light-colored diamonds represent individual fish and dark squares represent mean position for individuals in that treatment. Zero is at the bend of the U; positive numbers are in the arm toward the sound; negative numbers are away from the sound.*

wild. Since the fish we used were obtained from a hatchery, they may be different from those that would be found in the wild, and may not respond in the same ways.

Second, the fish may not have responded as predicted because the fiberglass experimental tanks used were inappropriate by virtue of transmitting sound waves in all directions. If so, the fish may not have detected sound direction and therefore could not follow the sound. We explored this possibility after the preference experiments were concluded by mapping sound intensity through the tank. We discovered that there was, indeed, a sound gradient from tank walls to the centerline, suggesting sound transmission from the tank and not just through the water along the centerline from the speaker (although that longitudinal gradient was also identified). Further research will require a different tank without sound transmission through the walls.

Finally, there is always the possibility that fish do not respond to natural sounds as hypothesized and would not use sounds as navigational cues in the wild. If experimental problems can be remedied and wild fish tested, further research could be important to determining if natural cues are an important factor in fish orientation.

## Benefits

These experiments, while not markedly successful, benefit the search for behavioral technologies for fish protection. Behavioral technologies for fish guidance offer important opportunities for electricity-generating industries to reduce detrimental environmental impacts at modest cost. Both hydropower and thermal-electric generation pass large amounts of water in which fish can be entrained and damaged. Successful application of the underwater "sound environment" to fish guidance may be important for the energy industry. This project has helped define the underwater sound environment and it has identified some of the pitfalls for testing behavioral responses of fish to sound, if any, in the laboratory.

The interest and experience of ORNL staff in behavioral technologies has led the Electric Power Research Institute (EPRI) to fund further research in this area. ORNL currently is funded by EPRI to conduct a test of the effectiveness of strobe lights in repelling fish from the intakes of TVA's Widows Creek Fossil Plant near Stevenson, Alabama, in 2006.

## References


Coutant, C. C. 2001a. "Behavioral technologies for fish guidance." American Fisheries Society Syposium 26, Bethesda, Maryland.

Coutant, C. C. 2001b. Integrated, multisensory, behavioral guidance systems for fish diversions. American Fisheries Society Symposium 26,105–113.

Knudsen, F. R., P. S. Enger, and O. Sand. 1992. "Awareness reactions and avoidance responses to sound in juvenile Atlantic salmon, Salmo salar L.," *Journal of Fish Biology* **40**, 523–534.

McLean, J. E., P. Bentzen, and T. P. Quinn. 2004. "Differential reproductive success of sympatric, naturally spawning hatchery and wild steelhead, Oncorhynchus mykiss," *Environmental Biology of Fishes* **69**, 359–369.

Popper, A. N. 2003. "Effects of Anthropogenic Sounds on Fishes," *Fisheries* **28**, 24–31.

Popper, A. N., and T.J. Carlson. 1998. "Application of Sound and Other Stimuli to Control Fish Behavior," *Transactions of the American Fisheries Society* **127**, 673–707.

Tolimieri, N. A., A. Jeffs, and J. C. Montgomery. 2000. "Ambient sound as a cue for navigation by the pelagic larvae of reef fishes," *Marine Ecology Progress Series* **207**, 219–224.

# Development of A Novel Method for Extracting Cellular Materials in the Air

M.-D. Cheng and M. W. Fields
*Environmental Sciences Division*

The ability to rapidly extract material from a cell can open new frontiers and opportunities for biosynthesis and manufacturing of new medicine and food. The same ability can also provide high-quality nucleic signatures enabling positive genetic identification of biological species in real time. Current practice for quality extraction of nucleic materials from a cell takes time, and subsequent purification of the materials requires elaborate treatment. Through the tedious extraction and purification, one anticipates obtaining high-quality cellular fragments for genetic analysis and reduction/elimination of false positives. The proposed technique utilizing laser-induced shock wave, aerodynamic and differential mobility separations will significantly increase the speed of extraction and improve the purity of extracted materials. The generic nature of the technique will enable it to be applied, modified, and adapted to a wide range of fields from fundamental research to industrial applications. The proposed technology is also the front-end module of a wide-range microarray-based biodetection/bioanalysis system concept we are pursuing for a larger bioaerosol research program.

## Introduction

Several methods exist for breaking cells and releasing intracellular materials. An ultrasonic wave creates rapid formation of microbubbles, which grow and coalesce until they reach their resonant size, vibrate violently, and eventually collapse, thereby disrupting the bacterial and fungal cells. Ultrasound methods, however, generate heat that can destroy organelles and alter the configuration of biological molecules. Shock-wave disruption has been applied to microbial cells in anaerobic sludge digestion (Onyeche et al. 2002), to *E. coli* DNA fragments extraction (Teshima et al. 1995), and to bladder cancer cells analysis (Endl et al. 1996) and used as a new gene transfer method (Lauer et al., 1997). Mulholland et al. (1999) applied laser-generated stress waves to human red blood cells. They found that a high-stress gradient of the stress wave was required for the permeabilization of the plasma membrane leading to rapid drug uptake. Andriyano and Smirno (1999) found that by applying a combined pulse electrical field and acoustic shock-wave field, all ovary carcinoma cells disintegrated. Sonden et al. (2000) employed laser-induced shock wave on endothelial cell monolayer and found that the waves caused immediate cell injury. Lin et al. (2001) demonstrated the feasibility of performing laser-disruption of single cells and multiple cells for measurements on subcellular compartments using capillary electrophoresis technique. The previous efforts cited above demonstrate the possibility of developing a rapid technique based on shock waves to extract intracellular components for genetic analysis. At present, one has to collect the airborne cells into liquid and analyze the cells using traditional methods. The technique developed in this project would enable a quick identification of cell types by analyzing the breakdown structure/pattern of the cellular fragments.

## Technical Approach

Biological cells were nebulized into the air in an enclosed chamber of the volume of 10 L. Shock waves produced by a laser-induced breakdown in the air were shaped through a wave guide to the bioaerosol particles focused to the focal point of the waveguide. This prevents the biological particles from being directly exposed to the laser beam and eliminates photodecomposition of cellular fragments. The subcellular fragments have different shape, size, and surface charge properties from that of the disrupted cell membranes. The differences or the distribution of these parameters are used for subsequent on-line separation. Once the separation in the air process is successfully completed and the nucleic acids have been separated from the cellular milieu, the purity of extracted materials will be assessed with conventional methods. The size and quality of the nucleic acids are determined (spectroscopy), and the feasibility of molecular manipulation will be tested with conventional molecular techniques (i.e., PCR and cloning).

## Results and Discussion

(1) Source of shock wave: The cell lysing technique depends primarily on the shock wave produced by laser-induced breakdown caused by the deposition of hundreds of mJ of 1064 nm energy train in a small confined volume. The variation of laser energy as a result of different rep. rate is on the order of ± 1–2%. We characterized the shock

wave under room pressure and temperature conditions as a function of pulse energy from the laser. In either case, we found the traveling velocity of the shock wave decreases by about 45% within some 20 microseconds after it was initiated, which translates into a decrease in Mach number from 7 to 5. The pressure at the shock wave front was estimated to be about 31 atm. The pressure propagation appears to be isotropic as we could not detect differences at several angles on the same plane. The pressure front has a thickness about 4 mm under this condition, creating a sharp force embedded in the wave propagation.

(2) Modification of original cell disruption configuration: We initially planned to use a co-axial design where the laser beam direction is parallel to the flow of bioaerosol particles. Through trail and error, we learned that it is extremely difficult to align the bioparticles so they would not be ablated by pulsed laser plasma. We want the breakage of cell structure to be done by the shock wave, not by laser ablation. The solution was a batch operation strategy using a pulsed and delayed introduction of bioparticles by coupling an aerosol beam focusing technique that we developed in an earlier project.

(3) Disruption of cell structure in the air: *Shewanella oneidensis MR-1* cells available from a colleague in the Environmental Sciences Division were selected as the test agent out of convenience. The microbial cells were suspended in a medium solution overnight before use. We used a 6-jet pneumatic nebulizer operated at low volumetric rate and pressure drop to minimize any possible damages or stresses to cells. Also, the operating condition we used minimized foam formation. The aerosolized droplets went through a condenser followed by diffusion dryer to remove water that is loosely associated with the microbial cells. The size distribution of the conditioned particles then was measured by a time-of-flight aerodynamic particle sizer (APS). The peak size showed 2.1–2.4 μm, which is consistent with the microscopic measurements. Effect of dehydration on cell viability was not significant, as verified by using Trypn Blue.

After lysing, the size spectra of fragmented cells, measured by both scanning mobility particle sizer (SMPS) and APS and using the original cell sample, showed interesting differences. Figure 1a shows that the original cell distribution peaked at 2.21 μm. Distribution of fragments in the supermicrometer region, which is basically nonexistent, indicates a very clean disruption of the cells. The APS measurement was done every 1 second; thus, the post-disruption spectrum shown in Fig. 1a is very clean. The nanometer-size distributions were measured by SMPS and shown in Fig. 1b. The black distribution basically reflected what's in the APS distribution of the pre-disruption population. The small peak at about 20–30 nm region is likely from water clusters on residues in the air. From Fig. 1b of the post-disruption distribution, one can see a very complicated size pattern emerged; many peaks are identified in the SMPS detection region from 10 to 640 nm. Most of the small peaks in this figure could not be repeated in repeated experiments, which is now understandable considering the random nature of the shock-wave disruption. However, the peak in 300–400 nm range appears to be always the largest in repeated experiments with different laser energy and rep. rate. The results appear to indicate the pattern might be unique and reproducible for the MR-1 species under a specified laser operation and fragment size classification; however, to be able to explore this finger printing capability of the technique, more cell types will have to be tested, which was not attempted in this project.

(4) Separation and characterization of breakup fragments: The original research plan called for the corroboration of the breakup fragments with DNA genetic analysis. With the departure of my co-investigator, I did not pursue this line of inquiry. Instead, we devoted ourselves to focusing on the separation techniques for the breakup fragments after the lysing technique was shown to provide unique fragment signature to MR-1 [see the description in (3) above]. The fragments appear to be negatively charged, most likely having functional groups such as –COOH, -OH, and –OOH undetached and embedded during the cell breakup. These functional groups were detected by FTIR analysis on the collected fragments downstream. In-line laser-induced plasma spectroscopy indicated some fragments carry Mg, Ca, P, and Cr elements. The former three are most likely part of the cellular structures and/or from the MR-1 LB medium ingredients. The presence of Cr was unclear since this is a heavy element and serves no biological purpose for the microbial species. The fragments could be easily isolated or extracted by using the differential mobility technique.

## Benefits

A year ago this project was conceived to develop a rapid cell lysis technique for follow-on genetic analysis. Preliminary investigation demonstrates the shock wave disruptive mechanism can actually provide a fingerprint to a particular cell type based on the breakdown pattern of fragments as registered in the differential mobility analyzer. Although verification of the genetic content of each fragment has its virtue, the unexpected result indicates the technique can actually be further developed into an effective detector suitable for biological particle characterization. Furthermore, the differential mobility analysis is flexible in collecting fragments of any desirable mobility sizes on a convenient substrate for subsequent laboratory analysis. Advances in the development of multistage differential mobility analysis for particle characterization and further verification of the genetic

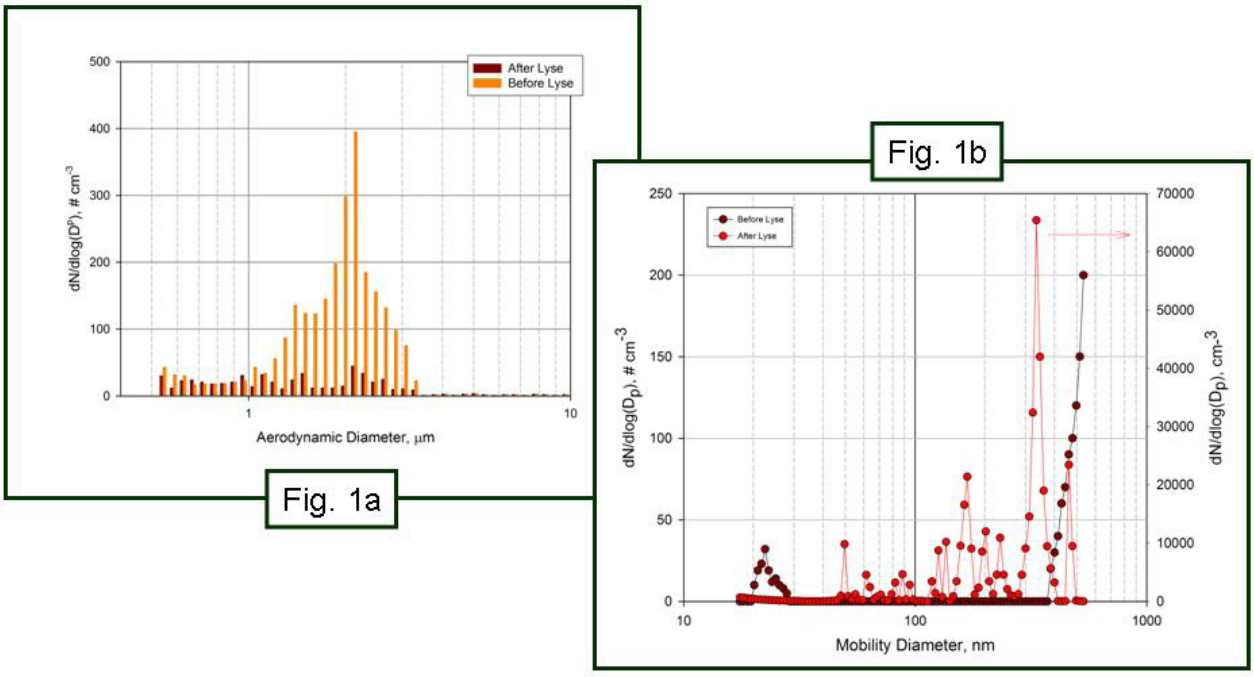


*Fig. 1. Contrast of size distributions between original cells and lysed fragments.*

content of the fragments would benefit applications for which this research project was initially considered. Nevertheless, current results indicate the technique might be of great interest to homeland security, forensic, and environmental applications where characterization of biological particles has been tedious and inexact. Department of Defense, Homeland Security, Justice, and Environmental Protection Agency will be the logical funding sources for follow-on research.

## References


Andriyano, Y. V. and V. P. Smirnov. 1999. "Increased lethality of cells in suspension under simultaneous effects of pulse electrical and shock-wave acoustic fields," I*zvestiya Akademii Nauk Seriya Biologicheskaya* **4**: 390–395.

Endl, E., P. Steinbach, J. Scharfe, S. Fickweiler, K. Worle, and F. Hofstadter. 1996. "Cell-type-specific response to shock waves of suspended or pelleted cells as analyzed by flow cytometry or electrical cell volume determination," *Ultrasound in Med. and Bio.* **22**(4): 515–525.

Lauer, U., E. Burgelt, Z. Squire, K. Messmer, P.H. Hofschneider, M. Gregor, and M. Delius. 1997. "Shock wave permeabilization as a new gene transfer method," *Gene Therapy* **4**(7): 710–715.

Lin, H. N., C. E. Sims, H. Y. Wu, and N. L. Albritton, 2001."Spatial control of cellular measurements with the laser micropipette," *Anal. Chem.* **73**(19): 4625–4631.

Mulholland, S. E., S. Lee, D. J. McAuliffe, and A. G. Doukas. 1999. "Cell loading with laser-generated stress waves: the role of the stress gradient," *Parma. Res.* **16**(4): 514–518.

Onyeche, T. I., O. Schlafer, H. Bormann, C. Schroeder, and M. Sievers. 2002. "Ultrasonic cell disruption of stablilised sludge with subsequent anaerobic digestion," *Ultrasonics* **40**(1–8): 31–35.

Sonden, A., B. Svensson, N. Roman, H. Ostmark, B. Brismar, J. Palmblad, and B. T. Kjellstrom. 2000. "Laser-induced shock wave endothelial cell injury," *Laser in Surgery and Med.* **26**, 364–375.

Teshima, K., T. Oeshima, S. Tanaka, and T. Nagai. 1995. "Biomechanical effects of shock wave on Escherichia-Coli and Lambda-Phage DNA, Shock Waves," **4**(6): 293–297.

# Environmental Isotope Forensics of Perchlorate Contamination

J. Horita,[1] B. Gu,[2] G. M. Brown,[1] N. C. Sturchio,[3] and J.-K. Böhlke[4]
[1]*Chemical Sciences Division*
[2]*Environmental Sciences Division*
[3]*University of Illinois at Chicago*
[4]*U.S. Geological Survey, Reston*

Perchlorate has been detected recently in a variety of soils, waters, plants, and food products at levels that may be detrimental to human health. These discoveries have generated considerable interest in perchlorate source identification. In this study, comprehensive stable isotope analyses ($^{37}Cl$:$^{35}Cl$ and $^{18}O$:$^{17}O$:$^{16}O$) of perchlorate from known synthetic and natural sources reveal systematic differences in isotopic characteristics that are related to the formation mechanisms. In addition, isotopic analyses of perchlorate extracted from groundwater and surface water demonstrate the feasibility of identifying perchlorate sources in contaminated environments based on this technique. Both natural and synthetic sources of perchlorate have been identified in water samples from some well-known perchlorate occurrences in the United States by the isotopic method.

## Introduction

Perchlorate ($ClO^{4-}$) has been detected recently in groundwater, surface water, soils, plants, and food products at concentrations exceeding µg/L levels in many areas of the United States (Urbansky 2002). Because of the potential for small concentrations of perchlorate to affect thyroid function by interfering with iodide uptake, its widespread distribution in the environment has generated considerable interest in techniques to distinguish natural and artificial perchlorate sources. The manufacture, use, or disposal of artificial products (explosives, rocket propellants, roadside flares, fireworks, matches, automobile airbags, etc.) is thought to be responsible for many local occurrences of perchlorate contamination in the environment. However, perchlorate also has been detected in precipitation at sub-µg/L levels (Dasgupta 2005), it has been reported in some natural potassium-rich salt deposits, and it is a well-known natural constituent of the nitrate-rich salt deposits in the Atacama Desert of Chile (Orris et al. 2003; Ericksen 1981). Imported Chilean nitrate (mainly $NaNO_3$) was used extensively as nitrogen fertilizer for agriculture during the early 1900s, and it is still imported to the United States for use on cotton, tobacco, citrus, and some vegetable crops.

Based on these observations, perchlorate may be present in the environment from various combinations of (a) artificial production and artificial distribution (e.g., military and commercial uses), (b) natural production and artificial distribution (e.g., application of imported Chilean nitrate fertilizer), or (c) natural production and natural distribution (e.g., local atmospheric deposition concentrated by evapotranspiration). Understanding the relative importance and distribution of these different sources is important for evaluating exposure risks, determining liability, and optimizing perchlorate remediation efforts. We demonstrate the application of the technology for environmental perchlorate isotope forensics in representative water samples with different perchlorate sources.

## Technical Approach

Purified $ClO^{4-}$ salts of Na, K, Rb, and Cs were prepared for isotopic analysis by conversion to CO, $O_2$, and $CH_3Cl$, as described below. The $ClO^{4-}$ was extracted from mixed salt solutions in the laboratory and in the field by using highly selective bi-functional anion-exchange resin columns (Gu et al. 2000). Groundwater samples were collected from existing wells using submersible pumps. The water was passed through glass columns containing ion exchange resin (Purolite A530E) at flow rates ranging from 0.3 to 0.9 L per minute until at least 10 mg of $ClO^{4-}$ was collected. Columns from the field were placed on ice and shipped to the laboratory for extraction and purification of the $ClO^{4-}$. The $ClO^{4-}$ was eluted from ion exchange columns with a solution of $FeCl_3$ and HCl, then precipitated by addition of KCl, RbCl, or CsCl to form $KClO_4$, $RbClO_4$, or $CsClO_4$, which was purified by gentle rinsing with $H_2O$ (Bao et al. 2004). The purity of the salts was verified by micro-Raman spectroscopy or by ion chromatography (> 99 % $ClO^{4-}$). Tests of the ion exchange extraction and purification procedures using reagents with known isotopic compositions indicated that no measurable

isotope fractionation was associated with the procedures used to produce the $ClO^{4-}$ salts. These tests included isotopic analyses of $ClO^{4-}$ reagent before and after being dissolved, extracted, precipitated, and purified.

For $\delta^{18}O$ determinations, $ClO^{4-}$ salts were reacted with glassy C at 1325°C to produce CO, which was transferred in a He carrier to an isotope-ratio mass spectrometer and analyzed by monitoring peaks at m/z 28 and 30 (Böhlke et al. 2003). Yields of O (as CO) from the $ClO^{4-}$ and $NO^{3-}$ reagents and samples typically were within ±2 %. Average reproducibilities of normalized $\delta^{18}O$ values were approximately ±0.2‰ (1σ). For $\Delta^{17}O$ determinations, $ClO^{4-}$ salts were decomposed at 650°C in evacuated quartz glass tubes to produce $O_2$, which was admitted to an isotope-ratio mass spectrometer and analyzed by measurements at m/z 32, 33, and 34. Yields of O (as $O_2$) from $ClO^{4-}$ reagents and samples typically were within ± 5 percent. Average reproducibilities of normalized $\Delta^{17}O$ values were approximately ± 0.1 ‰ (1σ). For $\delta^{37}Cl$ determinations, $ClO^{4-}$ salts were decomposed at 650°C in evacuated borosilicate glass tubes to produce $Cl^-$ salts, which were dissolved, converted to AgCl, and reacted with $CH_3I$ to produce $CH_3Cl$ (Sturchio et al. 2003). The $CH_3Cl$ was purified and then admitted to an isotope-ratio mass spectrometer and analyzed by measurements at m/z 50 and 52. Average reproducibilities of $\delta^{37}Cl$ values were approximately ±0.3 ‰ (1σ).

## Results and Discussion

### *Synthetic Perchlorate*

Synthetic perchlorate is produced by a series of electrolytic oxidation reactions beginning with aqueous chloride. The measured $\delta^{37}Cl$ values of synthetic perchlorates range from -3.1 ‰ to +1.6 ‰ with an average of +0.6 ± 1.2 (n=13), similar to typical Cl source values (0 ± 2 ‰). The $\delta^{18}O$ values of synthetic perchlorates range from -25 ‰ to -15 ‰ and are about 0–20 ‰ lower than expected values in water supplies near manufacturing plants. In one specific case, the $\delta^{18}O$ value of synthetic perchlorate was approximately 7 ‰ lower than that of the local water supply. These data indicate moderate amounts of O-isotopic fractionation during synthesis and are qualitatively consistent with the incomplete electrolytic conversion and incorporation of the water O. There is no measurable variation in the $\Delta^{17}O$ values of the synthetic perchlorates ($\Delta^{17}O = 0.00 \pm 0.06$, n=16).

### *Natural Perchlorate*

Nitrate and perchlorate in Atacama Desert deposits have positive $\Delta^{17}O$ values, indicating that they were produced largely by photochemical reactions involving atmospheric ozone and accumulated in the desert soils from atmospheric deposition over long periods of time (Michalski et al. 2004; Bao et al. 2004). The $\delta^{37}Cl$ values of perchlorate extracted from Atacama nitrate ore and from Chilean nitrate fertilizer products range from -14.5 to -11.8‰. These are the lowest $\delta^{37}Cl$ values reported for any common substance on Earth and indicate large Cl isotope fractionations associated with perchlorate formation in the atmosphere. The $\delta^{18}O$ values of the Atacama perchlorates analyzed in this study range from -9.3 to -2.2 ‰, and the $\Delta^{17}O$ values range from +7.9 to +10.5‰. Although the isotopic characteristics of the Atacama perchlorate are thought to reflect atmospheric processes in its formation, it is not known if these characteristics are representative of atmospheric perchlorate in general.

### *Perchlorate Extracted from Environmental Water Samples*

Having established distinctive isotopic signatures for some of the major perchlorate sources, we tested the environmental forensic application of these data by analyzing perchlorate extracted from representative water samples. Perchlorate in groundwater beneath a rocket-fuel disposal location in the North Base site at Edwards Air Force Base, California (site E, with $ClO_4$ ~400 µg/L) and from two wells at another southern California site involved in rocket testing (sites C1 and C2, with $ClO^{4-}$ ~65 and 100 µg/L, respectively) have isotopic signatures similar to those of synthetic sources (Fig. 1). These data are consistent with the interpretation that the groundwaters in these areas were contaminated with electrochemically manufactured perchlorate. Similar results were obtained for groundwater collected near former perchlorate production facilities at Henderson, NV (site H, with $ClO^{4-}$ ~20,000 µg/L) and for surface water from Las Vegas Wash (site L, with $ClO^{4-}$ ~200 µg/L), a stream draining

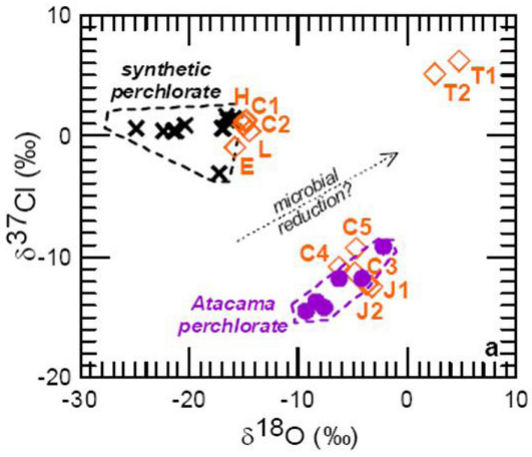


*Fig. 1. Cl and O isotope data for perchlorate. Labeled data points (diamonds) indicate a surface-water sample from Las Vegas Wash, Nevada (L), and groundwater samples from Edwards Air Force Base, California (E), Henderson, Nevada (H), southern California (C1-C5), northern New Jersey (J1, J2), and west Texas (T1, T2).*

the area near the Henderson site. These data are consistent with the interpretation that the groundwater and stream water were contaminated by the same or similar synthetic perchlorate sources.

In contrast to the above sites, where local synthetic sources of perchlorate can be identified, there also are numerous occurrences of perchlorate in groundwater that cannot be explained readily as a result of local introduction of synthetic material. Near the contaminated rocket-testing site represented by C1 and C2 in southern California, three other groundwater samples (sites C3, C4, and C5, with $ClO^{4-}$ ~12, 10, and 5 µg/L, respectively) have relatively low values of $\delta^{37}Cl$ (-11.3, -10.9, -9.3‰), relatively high values of $\delta^{18}O$ (-4.8, -6.3, -4.7 ‰), and large positive values of $\Delta^{17}O$ (+8.3, +7.3, +7.5 ‰) (Fig. 1). These isotopic characteristics are similar to those of the natural Atacama perchlorates. The isotopic signature of these samples could be consistent with at least two hypotheses for the origin of the perchlorate in the groundwater: (1) the perchlorate is from Chilean nitrate fertilizers that were used in the recharge areas of the samples, or (2) the perchlorate is from natural atmospheric perchlorate deposition, isotopically similar to that of the Atacama Desert, that was concentrated locally by evapotranspiration. Similar isotopic results were obtained for two groundwater samples from northern New Jersey (sites J1, J2, with $ClO^{4-}$ ~25, 90 µg/L), where concentration of perchlorate from atmospheric deposition is considered less likely owing to the humid climate and a Chilean nitrate source from fertilizer use therefore is suspected.

A major perchlorate occurrence of unknown origin has been reported in groundwater from the southern High Plains in west Texas (Jackson et al. 2005). Beneath an area of at least 155,000 $km^2$, perchlorate is almost ubiquitous in groundwater, with concentrations ranging from <0.1 to 50 µg/L. Atmospheric deposition has been proposed as a likely source of this perchlorate, although contributions from other sources such as Chilean fertilizer and chlorate defoliants used in agriculture, or explosives used in seismic exploration for hydrocarbons, also may be present. Perchlorate in two samples from this region (sites T1 and T2, with $ClO^{4-}$ ~140 and 17 µg/L, respectively) has small positive $\Delta^{17}O$ values (+0.4 and +0.5 ‰), indicating that a minor atmospheric component may be present; however, positive values of $\delta^{18}O$ (+4.7 and +2.5‰) and $\delta^{37}Cl$ (+6.2 and +5.1 ‰) indicate that the samples either are dominated by a source that has not been isolated elsewhere, or have been isotopically fractionated (Fig. 1). Given limited information about perchlorate isotopic fractionation during microbial reduction, the $\delta^{37}Cl$, $\delta^{18}O$, and $\Delta^{17}O$ values of the Texas samples could be consistent with a mixture dominated by synthetic perchlorate (>90%), possibly with a minor fraction of atmospheric perchlorate (<10%), that was reduced by about one-third of its original amount. Alternatively, the data may indicate another (non-atmospheric?) source of perchlorate with O-isotopic characteristics similar to those of biogenic nitrate, which contains O atoms derived from $H_2O$ and $O_2$.

## Benefits

This study demonstrates that comprehensive analyses of Cl and O isotopes can be used to distinguish between some of the major natural and synthetic sources of perchlorate. Our innovative techniques for perchlorate extraction, purification, and isotope mass spectrometry have great potentials in perchlorate isotope forensics to real environmental samples of groundwater and surface water. Stakeholders in these contamination cases include federal agencies (Department of Defense, Environmental Protection Agency), private sectors (perchlorate manufacturers and users, agricultural industry), and the public.

In response to a call for proposal in the area of perchlorate remediation from the DOD Environmental Science and Technology Compliance Program (ESTCP), a multi-institutional team (ORNL, U.S. Geological Survey, Univ. of Illinois at Chicago, and Shaw Group) submitted a collaborative proposal to identify and characterize the sources of perchlorate in several high-profile cases in the United States. We are awarded a 2-year project and have already started a full-scale environmental forensics study.

## References


Bao, H., and B. Gu. 2004. "Natural Perchlorate Has a Unique Oxygen Isotope Signature," *Environmental Science and Technology* **38**, 5073.

Böhlke, J. K., S. J. Mroczkowski, and T. B. Coplen. 2003. "Oxygen isotopes in nitrate: new reference materials for 18O:17O:16O measurements and observations on nitrate-water equilibration," *Rapid Communications in Mass Spectrometry* **17**, 1835.

Dasgupta, P. K., P. K. Martinelango, W. A. Jackson, T. A. Anderson, K. Tian, R. W. Tock, and S. Rajagopalan. 2005. "The origin of naturally occurring perchlorate," *Environmental Science and Technology* **39**, 1569.

Ericksen, G. E. 1981. "Geology and origin of the Chilean nitrate deposits," U.S. Geological Survey Professional Paper 1188.

Gu, B., G. M. Brown, S. D. Alexandratos, R. Ober, J. A. Dale, and S. Plant. 2000. Pages 165–176 in *Perchlorate and the Environment*, E. T. Urbansky, ed., Kluwer Academic, New York.

Jackson, W. A., S. K. Anandam, T. Anderson, T. M. Lehman, K. Rainwater, S. Rajagopalan, M. Ridley, and R. Tock. 2005. "Perchlorate occurrence in the Texas Southern High Plains Aquifer System," *Ground Water Monitoring and Remediation* **25**, 137.

Michalski, G., J. K. Böhlke, and M. H. Thiemens. 2004. "Long term atmospheric deposition as the source of nitrate and other salts in the Atacama Desert, Chile: New evidence from mass-independent oxygen isotopic compositions," *Geochimica et Cosmochimica Acta.* **68**, 4023.

Orris, G. J., G. J. Harvey, D. T. Tsui, and J. E. Eldridge. 2003. *Preliminary analyses for perchlorate in selected natural materials and their derivative products*, U.S. Geological Survey Open-File Report 03-314.

Sturchio, N. C., P. B. Hatzinger, P. B., M. D. Arkins, C. Suh, and L. J. Heraty. 2003. "Chlorine isotope fractionation during microbial reduction of perchlorate," *Environmental Science and Technology* **37**, 3859.

Urbansky, E. T. 2002. "Perchlorate as an environmental contaminant," *Environmental Science and Pollution Research* **9**, 187.

# Using Live Cell Imaging Technologies to Probe Molecular Interactions between Bacterial Cells and Heavy Metals

D. K. Thompson,[1] M. Doktycz,[2] S. D. Brown,[1] and J. Morrell-Falvey[2]
[1]*Environmental Sciences Division*
[2]*Life Sciences Division*

High-resolution imaging of cell surface structure and molecular interactions in real time and under physiological conditions will be essential for solving structure-function questions in the post-genomics era. The overall objective of this project was to investigate the feasibility/utility of live cell imaging techniques in exploring microbial cell surface structure and morphology under heavy metal stress conditions and dissecting the molecular interactions involved in metal uptake and/or resistance. The research initially centered around three main tasks: (i) the use of atomic force microscopy (AFM) to characterize the morphology and cell surface structure of *Shewanella oneidensis* cells in the presence of heavy metals (Task 1), (ii) the use of fluorescence microscopy to investigate in vivo protein localization and expression dynamics (Task 2), and (iii) the development of an assay for examining cell surface receptor-siderophore binding (Task 3). This study directly addressed the need to identify and characterize cellular interactions with metals at the cell-surface level and underlying localization dynamics and protein-protein interactions potentially involved in the microbial mechanisms controlling the fate and transport of heavy metals.

## Introduction

To develop effective bioremediation strategies for the cleanup of contaminated DOE sites, fundamental knowledge is needed on microbe-metal interactions and the ability of metal-reducing microorganisms to survive in relevant contaminated environments. Understanding how organisms respond to their environment requires the ability to observe molecular events in live cells in real time. Characterization of the interaction between the metal-reducing bacterium *S. oneidensis* and heavy metals beyond that of a snapshot genomics view will require new, innovative approaches capable of probing single cells at molecular-scale resolution. The technical objectives of this project focused on (i) developing robust cell mounting techniques enabling live cell imaging in *Shewanella*; (ii) developing the capability of producing reporter gene fusions encoding tagged proteins for in vivo visualization; and (iii) validating a novel technique for investigating cell surface receptors. The scientific goals were (i) to determine whether morphological changes occur on the surface of *S. oneidensis* cells in the presence of metals; (ii) to determine temporal and spatial localization patterns for proteins up-regulated in response to metals; and (iii) to demonstrate siderophore-cell surface receptor binding.

The availability of complete genome sequence information for numerous microorganisms and the development of advanced analytical, high-throughput technologies such as DNA microarrays and mass spectrometry have enabled a detailed, global characterization of microbial cellular processes that previously has been unattainable. While transcriptome and proteome analyses provide an important first step toward the goal of understanding microbial-mediated reductive metal transformations on a genomic scale, elucidating the dynamics of the biochemical and regulatory mechanisms underlying such functional phenotypes within the context of complex, multicomponent environments will require other innovative approaches capable of probing single cells at high resolution and under physiologically relevant conditions. This Seed Money project has begun to explore the use of advanced cell imaging methods to determine how relevant environmental parameters and contaminants impact the dynamics of cell surface topography, cellular interfacial interactions with the environment, and biochemical/regulatory pathways underlying metal resistance and reduction in *Shewanella oneidensis* MR-1.

## Technical Approach

This project utilized various imaging techniques. AFM is a relatively new method for biological imaging that produces a high-resolution topographical map of a cell surface using a cantilever-mounted probe tip. Importantly, this method can provide three-dimensional images of the surface ultrastructure with molecular resolution in real time and under physiological conditions (Doktycz et al. 2003; Dufrene 2002). AFM is ideally suited for imaging cell-metal interactions at the cell-surface level in real time and under physiological conditions. Because microbial surfaces are known to serve as templates for nucleation and growth of metal precipitates (Beveridge 1989), AFM will be crucial for examining the interface

between bacterial cells and metals. In this project, cell preparation and mounting protocols were developed for imaging *S. oneidensis* cells using AFM. Fluorescence microscopy was used to investigate protein expression dynamics/localization within live *S. oneidensis* cells. GFP (green fluorescent protein) and/or its spectral derivatives YFP (yellow fluorescent protein) or CFP (cyan fluorescent protein) were used as reporters for protein expression dynamics and localization in *S. oneidensis*. GFP, YFP, and CFP are well characterized and relatively small monomeric proteins (~27–40 kDa) that do not require exogenously added substrate or co-factors for fluorescence, making them ideal fusion proteins for live cell imaging.

## Results and Discussion

### *Task 1*

For Task 1 (the use of AFM to characterize the morphology and cell surface structure of *Shewanella oneidensis* cells in the presence of heavy metals), we have acquired data on the morphological and cell surface structure of *S. oneidensis* MR-1 cells grown in the presence or absence of $SrCl_2$ and $K_2CrO_4$ (potassium chromate). Using light microscopy, we observed that cells grown in the presence of high concentrations of $SrCl_2$ (100–150 mM) were more elongated than cells grown at lower concentrations (0–50 mM). This elongation phenotype was also observed when cells were grown on solid LB medium containing strontium as well as in liquid cultures exposed to 1 mM chromate. In addition, we have imaged MR-1 cells grown in complex medium containing 0 or 50 mM $SrCl_2$ using AFM. In previous growth studies, we observed the formation of a precipitate in cell cultures grown for several days in the presence of 50 mM $SrCl_2$. Cells were prepared for AFM imaging to determine whether this precipitate was associated with the cell surface. Prior to mounting on gelatin-coated mica disks, the cells were pelleted by centrifugation and resuspended in water or a solution of 50 mM $SrCl_2$ to avoid dissolving any precipitate associated with the cells. Unexpectedly, some "bumps" were observed at the ends of cells grown in 50 mM $SrCl_2$ for 24 h, although they appeared to be considerably smaller than those observed after a longer incubation in $SrCl_2$ (6 days; Fig. 1). In addition, higher magnification images of the cells did not reveal any obvious signs of precipitate associated with the surface [Fig. 1(B) and (D)]. We did, however, image what appears to be mixtures of cells and large flocculant precipitate from the culture [Fig. 1(C) and (D)]. Based on these observations, it is tempting to speculate that the cells may be sequestering strontium internally. More research is needed to determine the nature of the internal structures and the conditions that cause their formation; however, with support from this Seed Money Fund project, we have been able to develop important AFM experimental protocols and generate preliminary data for possible future funding in this area.

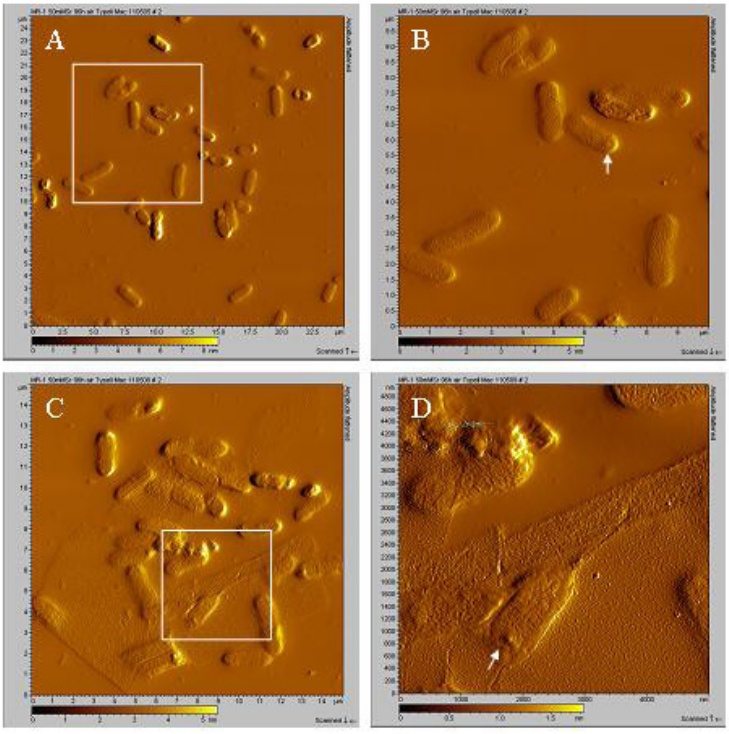


*Fig. 1. Amplitude images of MR-1 cells grown in the presence of 50 mM $SrCl_2$ for 96 h. Cells were pelleted by centrifugation, resuspended in a solution of 50 mM $SrCl_2$, mounted on gelatin-coated mica disks, and imaged in air. (B) shows a higher magnification of the area outlined by the white box in (A). (D) shows a higher magnification of the area outlined by the white box in (C). Cells displaying internal "structures" are indicated by arrows.*

***Task 2***

We have also used fluorescence microscopy methods to investigate protein expression dynamics/localization within live *S. oneidensis* cells (Task 2). Initial studies verified that we could obtain proper expression of GFP and YFP off of a pBBR1 plasmid under the control of a constitutive promoter in *S. oneidensis* MR-1 cells and that MR-1 did not exhibit any inherent background fluorescence. We have also successfully prepared gfp and/or yfp fusions for *S. oneidensis* MR-1 genes encoding two conserved hypothetical proteins, one hypothetical protein predicted to localize to the cellular membrane, the cell division protein FtsQ, and a DNA-binding response regulator implicated in metal stress response pathways. With the exception of ftsQ, the genes encoding these proteins showed up-regulated expression profiles in response to chromate. The fluorescently tagged proteins were expressed in *E. coli* cells and imaged using a Leica scanning confocal microscope. One of these MR-1 genes, which encodes a hypothetical protein of unknown function, was expressed as a GFP fusion protein in *S. oneidensis* cells. This protein, which is predicted to have one transmembrane spanning domain based on hydrophobicity curves, showed weak localization to the cell membrane. Furthermore, we have also expressed SO3585 (a putative azoreductase upregulated under chromate exposure) as a N-terminal GFP fusion in *E. coli* cells. Imaging of these cells showed the formation of inclusion bodies containing GFP, suggesting that the GFP-tagged SO3585 is misfolded or non-functional. We are continuing to attempt to tag the SO3585 protein with GFP at its C-terminus and to test whether this produces a functional protein, because our transcriptome data suggest that this protein plays an important role in the response of *S. oneidensis* MR-1 to toxic chromate levels and will likely have implications in the use of MR-1 for bioremediation.

***Task 3***

Given the time constraints, we were not able to pursue Task 3 (the development of an assay for examining cell surface receptor-siderophore binding), which was less important in terms of the overall project goal of developing protocols and construct resources for the imaging of *S. oneidensis.*

## Benefits

Preliminary data acquired as a result of Seed Money funding was used to develop research ideas for a proposal that was submitted to the DOE Natural and Accelerated Bioremediation Research program last March 2005. Although the proposal was reviewed well, it was not selected for funding. However, it is anticipated that the data generated in this Seed Money Fund project will be included in future publications, which will serve as a basis for requesting follow-on funding from DOE or NSF.

## References

Beveridge, T. J. 1989. "Role of cellular design in bacterial metal accumulation and mineralization," *Annu. Rev. Microbiol.* **43**, 147–171.

Doktycz, M. J., C. J. Sullivan, P. R. Hoyt, D. A. Pelletier, S. Wu, and D. P. Allison. 2003. "AFM imaging of bacterial in liquid media immobilized on gelatin coated mica surfaces," *Ultramicroscopy* **97**, 209–216.

Dufrêne, Y. F. 2002. "Atomic force microscopy, a powerful tool in microbiology," *J. Bacteriol.* **184**, 5205–5213.

# Metabolic Profiling of Phosphorylated and Coenzyme-Bound Metabolites Using Pressure-Assisted Capillary Electrophoresis Mass Spectrometry

T. J. Tschaplinski,[1] G. J. Van Berkel,[2] B. A. Tomkins,[2] and M. Mentinova[3]
[1]*Environmental Sciences Division*
[2]*Chemical Sciences Division*
[3]*Lawrence University, Appleton, Wisconsin*

Metabolic profiling of phosphorylated carbon intermediates of the respiratory pathways, adenylates, nucleotides, and other highly charged metabolites, such as coenzyme-bound metabolites, is critically important, given their involvement in redox balance and energy transduction. These pathways have proved challenging to study directly. A hybrid instrument has been assembled to separate and quantify low concentrations of highly charged metabolites by interfacing a Beckman Coulter pressure-assisted capillary electrophoresis (P/ACE) system in tandem with ion trap (Finnigan/Thermo LCQ DECA) mass spectrometer (MS). The main objective, to optimize the electrophoresis and mass spectrometer settings for nanogram-level detection of charged metabolites, has been achieved.

A hybrid P/ACE-MS system holds tremendous promise for simultaneously detecting and characterizing the many highly charged phosphorylated carbon intermediates, organic acids, and coenzyme-bound metabolites that are currently difficult to quantify directly. Such highly charged metabolites are not being adequately addressed in Genomes-to-Life (GTL) studies that require metabolomic analyses to establish the health and metabolic status of microbial cultures and the metabolic consequences of genetic manipulation. Our goal was to interface a Beckman Coulter P/ACE electrophoresis unit with a Finnigan/Thermo LCQ DECA ion trap mass spectrometer (MS) and to optimize the electrophoresis and MS settings for reproducible nanogram-level detection.

The Beckman Coulter P/ACE system was obtained with Intellectual Property Maturation Funds, initially operated in a stand-alone mode and optimized for the standard separation of two angiotensin isomers. The P/ACE was then interfaced to the MS, configured according to the manufacturer's instructions, and optimized. Electrophoresis parameters that were considered included injection pressure and duration, separation voltage, and pressure "assistance" for the run buffer. MS parameters included the exact positioning of the electrophoresis capillary within the electrospray ionization (ESI) "needle," composition and flow of the ESI sheath liquid and gas, quality of the "spray" produced by the sample and sheath liquid, and ionization voltage. The separation of the angiotensins specified by the manufacturer was achieved, but it was deemed insufficient for project needs. Therefore, the ESI "needle" was modified to produce a finer and more consistent spray than that achieved using the standard "needle." This modification, with subsequent minor adjustments in other parameters, permitted a separation of the test compounds that exceeded the manufacturer's specifications and was therefore more appropriate for project needs. Our most recent experiments employ benzenesulfonic acid, a negatively charged species, as a marker for the targeted phosphorylated sugar analytes. Detection of this model compound was achieved by configuring the LCQ DECA in the "negative ion" mode. Initial results demonstrated that 2 ng (12 pmole) of benzenesulfonic acid could be easily observed. Similar operating conditions will permit the separation and detection of selected metabolomes.

The novel hybrid mass spectrometer will have broad utility for the separation of highly charged metabolites. Given that such metabolites are involved in the energy transduction pathways, their accurate quantification can be used to assess cellular homeostasis in GTL studies and will additionally be of interest to NIH to determine how cellular homeostasis is perturbed by disease or xenobiotic agents. Additionally, the sequencing of the numerous microbial and plant genomes by a number of agencies, including NSF's Plant Genomics Research Program, will benefit from metabolite profiling as a tool for gene discovery. Profiling will be able to include the essential classes of charged metabolites targeted in this project.

# Integrating Hydrologic and Economic Data for Water-Energy Nexus Assessment

G. A. Oladosu,[1] S.W Hadley,[2] D. P. Vogt,[1] and T. J. Wilbanks[1]
[1]*Environmental Sciences Division*
[2]*Engineering Science and Technology Division*

From drought conditions that worsened the California energy crisis of 2000–2001 to moratoriums on energy development in several states, water stresses are beginning to have visible effects on energy production and use in the United States. A crucial research need is the development of tools for assessing the costs and benefits of technologies and modeling water supply and use balance. This project is aimed at developing a prototype tool for this purpose. The objectives of the project are to provide quantitative validation of the hypothesis that water constraints would have significant negative energy security impacts and demonstrate an integrated approach for water-energy nexus assessment.

The hypothesis underlying much of the discussion on the water-energy nexus is that water stresses will have significant impacts on energy security in the United States. Despite the abundance of qualitative evidence, there is a dearth of quantitative estimates needed to both validate this hypothesis and to serve as the basis for addressing the important issues that it generates. An objective of this project is to attempt a quantitative validation of this hypothesis. Furthermore, the regulatory, technological, spatial, and policy issues associated with the water-energy nexus are complex. An adequate assessment of these issues requires an integration of research techniques spanning different disciplinary frameworks. Therefore, an additional objective of the project is to demonstrate, as a proof-of-concept, an integrated approach for water-energy nexus assessment.

The above objectives call for three main steps: (1) estimation of water supply characteristics at the county level; (2) modeling of state-level economic activities, with particular attention to energy; and (3) linkage of county-level water supply measures to state-level economic activities. Steps 1 and 2 are nearing completion, and work has begun on Step 3.

In the first step, models to interpolate precipitation data and estimate stream network flow throughout the four state region of the analysis have been produced. The precipitation model integrates historical monthly precipitation measurements and hydrologic landscape regions data produced by the United States Geological Service (USGS) to derive precipitation estimates in the region. Historical monthly stream gauge measurements, precipitation, and other hydrologic parameters are used to estimate a statistical stream flow model, which is then applied to estimate stream flow at each node of a stream network derived for the region. In the second step, a monthly electricity model that determines plant-level shares in total state generation for each of the four states included in this project has been constructed. This model incorporates fuel prices, prime-mover type, fuel type, plant capacity, and water use data for 1996. These data were derived from several EIA databases. In addition, prototype computable general equilibrium economic models for each of the four states have also been constructed. Two databases are being put together (a Hydrologic database and an Economic database) to document data inputs and outputs of the various project components.

Parameter estimates from the monthly electricity generation model have provided some quantitative evidence that water constraints would have negative effects on electricity generation. First, these estimates show a positive correlation between water withdrawals and distribution of electricity generation among power plants in a state. Although available water use data was in average annual withdrawal terms, estimation results show that its effects on monthly electricity generation vary considerably over the year. The lowest effects are found for January and March–July.

In FY 2006 we plan to link the models developed in steps 1 and 2 into an integrated framework with calibrated to year 2002 data. We would then perform an evaluation of a few water availability scenarios relevant to water-energy nexus issues in the southeastern United States.

# Exploring New Pathways in the Impact of Aerosols on Terrestrial Carbon and Hydrological Cycles

L. Gu,[1] M. Cheng,[1] M. Post,[1] Q. Liu,[1] R. A. Pielke, Sr.,[2] and D. Niyogi[3]
[1]*Environmental Sciences Division*
[2]*Duke University and Colorado State University*
[3]*Purdue University*

Aerosols are a critical component of the atmosphere. Through their influences on atmospheric radiative transfer, formation and properties of clouds, and precipitation processes, aerosols play a fundamental role in the dynamics of the climate system. Prediction of climatic responses to increasing atmospheric greenhouse gas concentrations requires concerted understanding of the roles of atmospheric aerosols, terrestrial carbon, and water cycles in our earth climate system. The objective of this project is to develop an integrated model to interactively simulate effects of aerosols, carbon, and water cycles and to use these simulations to identify crucial processes that must be represented in the next generation of coupled climate-carbon models.

Aerosols, carbon cycle, and water cycle are in the core of U.S. climate research programs. The U.S. Climate Change Research Initiative (CCRI) identifies three key areas for climate science: (1) developing reliable representations of the climate forcing resulting from atmospheric aerosols, (2) improving understanding of the global carbon cycle (sources and sinks), and (3) increasing knowledge of climate feedback processes. In order to make significant progresses in these key areas, an integrated research approach on aerosols, carbon, and water cycles is needed. We will couple, through a flux coupler, the Regional Atmospheric Modeling System (RAMS) developed at Colorado State University with the terrestrial Fluxes and Pools Integrated Simulator (FAPIS) developed at ORNL. We will use the coupled model to explore the dynamic relationships between aerosol loading and terrestrial carbon dioxide and water vapor exchanges with the atmosphere at regional scales.

The RAMS model has been installed at ORNL, and successful runs have been conducted. Effects of aerosols on land surface albedo have been simulated. We found that aerosols significantly influence surface albedo over vegetation, and the effects depend on leaf area index and solar elevation angles. These results have been communicated to the chief scientist of DOE atmospheric science program, which has a focus on atmospheric aerosols and climate. Offline runs using FAPIS have revealed that vegetation biomass heat storage is an important component of surface energy budget and influences surface water vapor and sensible heat fluxes. We will investigate how crucial accurate representation of this component is for prediction of cloud formation. The Flux Coupler and spatial datasets for the coupled RMAS-FAPIS simulation are under development. The interface of the FAPIS model has been redesigned for better communication with the Flux Coupler. In addition, we have provided inputs to the Science Plan of DOE ARM Cloud Land Surface Interaction Campaign (CLASIC). Our contributions are explicitly acknowledged in the CLASIC Science Plan.

As part of this project and based on a proposal submitted by the PI, American Geophysical Union (AGU) will have a special session in the coming AGU Fall meeting in San Francisco to discuss effects of aerosols and clouds on terrestrial carbon and water cycles. The PI will serve as the convener and chair of this special session. Many prominent scientists in areas of atmospheric aerosols, carbon, energy, and water cycles have submitted to the session and will give speeches.

Early June of this year (2005), our university collaborators (Prof. Roger Pielke, Duke / Colorado State University and Prof. Dev Niyogi, Purdue University) visited ORNL. During their visit, we discussed RAMS-FAPIS coupling and simulation issues. They also gave two informative seminars to ORNL researchers.

# *Chemical Sciences and Technology*

# *Director's R&D Fund*

# Advanced Ion Trap Mass Spectrometry for the Rapid and Confident Identification of Biological Agents

M. B. Wise,[1] K. J. Hart,[1] D. E. Goeringer,[1] L. J. Hauser,[2] I. F. Robbins,[3] and D. A. Clayton[4]
[1]*Chemical Sciences Division*
[2]*Life Sciences Division*
[3]*Computational Sciences and Engineering Division*
[4]*Engineering Science and Technology Division*

Biological weapons are a significant potential threat to national security and our armed forces. This project has focused on the development of instrumentation and methods to provide rapid detection and confident identification of biological agents including bacteria, toxins, and viruses. The primary objective has been to develop and demonstrate novel methodologies and instrumentation to enable rapid detection and identification of biological agents using protein markers that are characteristic and exclusive to targeted biological agents. The prototype instrument and methods investigated in this project are intended to permit characteristic protein markers to be identified based on their molecular weights and peptide sequence. The approach is based on a novel mass spectrometer configuration that includes an electrospray (ES) source for production of protein ions and a hybrid mass analyzer for ion storage, molecular weight separation, and analysis of peptide sequence.

## Introduction

The looming threat of terrorism has created a need for rapid detection and identification of biological threat agents in complex samples. Bio-agents can be detected and identified based on unique biomarkers from at least one of the major classes of macromolecules: DNA/RNA, lipids, and proteins. The detection of viruses and bacteria can be based on either DNA/RNA or protein biomarkers, whereas toxin detection is limited to proteins. Because of significant protein variability between species type, analysis of unique proteins will likely provide the most specificity for bio-threat detection. Protein-based identification, however, is a tremendous analytical challenge, especially in complex mixtures.

Mass spectrometry (MS) offers speed, sensitivity, and versatility that is virtually unmatched by other analytical techniques for the analysis of protein markers. In addition to measuring the masses of proteins, mass spectrometers can also produce information from fragmentation patterns that usually occur along peptide backbone bonds, creating a pair of fragment ions. Identification algorithms use this property to deduce peptide sequence information. This process is tandem MS (or MS/MS), which includes the following steps: isolation of precursor ions at a particular mass-to-charge (m/z) ratio, dissociation of these ions, and mass analysis of the resulting fragment ions. By using the m/z of the precursor peptide and its corresponding peptide fragmentation pattern, a biological molecule can be identified.

Quadrupole ion trap (QIT-MS) instruments are often used for MS/MS; however, acquisition of a complete fragment ion mass spectrum can be time-consuming because the mass analyzer must scan through many m/z values. Thus, during the fragment ion mass analysis time, ions produced by the ion source may be wasted, resulting in a low duty cycle and reduced sensitivity. To overcome such limitations, hybrid ion trap/time-of-flight (QIT-TOF) instruments have been developed. Precursor ion selection by m/z and dissociation occur in the QIT, but the fragment ions are pulsed into the TOF for mass analysis. The advantage of the TOF-MS is that it can record 10,000 or more complete mass spectra per second. This speed advantage is somewhat negated, however, because the QIT is only capable of selecting and dissociating precursor ions at less than 50 times per second.

There are currently two main MS methodologies for protein characterization: the top-down and bottom-up methods. The top-down method involves measuring the mass of intact proteins, while the bottom-up, or shotgun, method entails proteolytic digestion that cuts the proteins into shorter amino acid stretches (peptides) with one or more proteases, followed by mass analysis of these peptides. Before proteins are analyzed by MS, they are separated into smaller fractions, generally via liquid chromatography (LC). Either of these methods can be coupled with MS/MS. The advantages of top-down analysis are the potential speed of measurement (i.e., no protein digestion) and reduced complexity in the identification process. The disadvantages involve difficulty in deconvoluting the intact protein spectra and in dissociating intact proteins. In contrast, the bottom-up method generally results in nearly complete peptide fragmentation. However, the total analysis time is longer due to the time spent performing proteolytic digestion.

The identification complexity is also increased since each protein typically yields multiple peptides. Nevertheless, the overall speed, sensitivity, and dynamic range of current shotgun proteomics techniques cannot currently be matched by other methods.

Database searches are the methods used to deduce sequence information and identify proteins from mass spectrometric data. Database search algorithms use a comparison between theoretical fragmentation patterns of peptides in a database and the experimental peptide fragmentation pattern. The theoretical fragmentation patterns are scored against the experimental tandem spectrum, and the theoretical peptide with the highest similarity to the experimental measurements is accepted. All MS/MS data in this study were processed by the SEQUEST algorithm, a well-established database search program. From the collection of detected peptides, those unique to an organism (see below) were subsequently identified with the DTASelect algorithm.

## Technical Approach

Experimentally, the detection and identification of a target organism within a mixture of other organisms was assessed with experimental shotgun proteomics simulations based on ES ionization, peptide separation via LC, dissociation of the mass-selected biomarker ions, and mass analysis of the diagnostic fragment ions using QIT-MS. The *E. coli* K-12 strain served as the target. Background organisms (*S. cerevisiae, R. palustrisS. oneidensis, A. thaliana*) were selected to mimic common biological species found in typical environmental samples. All corresponding genomes have been sequenced and are publicly available (Table 1).

Two different situations were simulated in the first part of the study. The first situation, termed the "instrumental analysis time test," evaluated one-dimensional (1D) LC-MS/MS under conditions that demanded rapid, reliable identification. The target, at a high concentration, was mixed with equal amounts of the background species. Identification reliability was assessed as a function of analysis time. Four separate time points were tested: 60-, 120-, 180-, and 240-min total experiment time.

In the second situation, termed the "target concentration level test," the biothreat agent was assumed to be present at a much lower concentration relative to the background. Identification was not as time sensitive, although a high degree of reliability was required. This scenario involved varying the target concentration (the background species were mixed as above) while fixing the analysis time to determine the low concentration limit for target identification. The first experimental set was run exactly as for the 240-min 1D LC-MS/MS experiment, except the target species concentration varied from 20, 6, 0.6, and 0.06% total protein quantity. The second experimental set involved a two-dimensional (2D) LC-MS/MS analysis of the 20, 0.6, and 0.3% concentration samples. The 2D analysis involved nine salt steps (ammonium acetate) each taking 3 h for a total analysis time of 30 h.

To evaluate false positive peptide identifications for *E. coli*, another sample was prepared with no target specie and four background species at 25% each and analyzed with the 240-min 1D LC-MS/MS method. The number of false positive peptides for *E. coli* was determined as detailed below.

The second part of this study focused on the effects of database size on positive identification of unique peptides. Unique peptides can be defined as those found in a proteomic measurement that are specific to a given species in the relevant database. If a specific peptide is present in multiple species, it cannot be used for identification. As the size of the database increases (especially if that database contains many related species with many conserved proteins), the number of unique peptides for any given species in that database decreases. This becomes a serious concern when the concentration of the target species decreases since not all of the unique peptides will be reliably detected. Another problem is the positive matching to unique peptides from species in the database which are not present in the test mixtures as target or background species (i.e., false positives). This does not define the false positive identification of a species in a mixture but rather the random matching to peptides in the database. These effects were investigated by taking the dataset from the (1D LC-MS/MS) target concentration level test and searching against a very large microbial and

**Table 1. Composition of representative sample for experimental simulations**

| Organism | Description |
|---|---|
| *Escherichia coli* K-12 | target species<br>frequently found in mammalian intestines |
| *Saccaromacis cereviciae* | eukaryotic yeast species<br>widely utilized in food production industry |
| *Rhodoseudomonas palustris* | gram negative prokaryote<br>commonly found in sediment |
| *Shewanella oneidensis* | gram negative prokaryote<br>found in water and soil |
| *Arabidopsis thaliana* | model plant species |

plant database. This database was generated from public and DOE/JG-ORNL sources and contained 2 plant species (Oryza sativa and A. thaliana) and 259 microbial species.

## Results and Discussion

### *Control Analysis*

For this analysis, three, two, and zero unique *E. coli* peptides were identified in each of three runs. This random level of false positive peptide identifications, ranging from zero to five unique peptides per species, was observed for all experiments in this study as well, validating the quality of this analysis.

### *Instrumental Analysis Time Test*

This dataset was searched against the small database. The number of unique peptides identified from the target using 1D LC-MS/MS was reproducible: time point 240 (283.7 average peptide IDs, standard deviation 9.0), time point 180 (236.0 average peptide IDs, standard deviation 7.8), time point 120 (154.3 average peptide IDs, standard deviation 12.9), and time point 60 (44.0 average peptide IDs, standard deviation 3.6). The false positive peptide identifications showed a similar consistency but with much lower average values. Clearly this particular common and simple shotgun proteomics technique was capable of correctly identifying the target species, at relatively the same concentration as four other background species, against a database containing seven additional background species.

### *Target Concentration Level Test*

These data were searched against the small database. The resultant number of unique peptide identifications from the target using 1D LC-MS/MS was very reproducible: concentration point 20% (270.3 average peptide IDs, SD 15.3), concentration point 6% (83.3 average peptide IDs, SD 0.6), concentration point 0.6% (4.3 average peptide IDs, SD 2.08), and concentration point 0.06% (1.7 average peptide IDs, SD 0.5). False peptide identifications showed a similar consistency. For this experiment and database size, the data for average peptide identifications and the corresponding standard deviations suggest positive target identification is attainable at the 20% and 6% concentrations. However, the data imply that positive target identification is not achievable at the 0.6% or the 0.06% concentration levels given the current false peptide identification rate.

Detection of unique peptides from the other species in the mixtures was also observed. The microbial background species were all identified with a consistent rise in peptide identifications from each as the *E. coli* concentration decreased. Reproducibility similar to that with *E. coli* was found for these species. However, the *A. thaliana* species was not clearly detected above the background in any experiment, even though its concentration was equal to that of *R. palustris*, *S. cerevisiae*, and *S. oneidensis*. It is unclear why *A. thaliana* was consistently difficult to detect in the presence of the other species.

Although 2D LC-MS/MS methods typically require longer analysis times, they generally improve the dynamic range, separation ability, and sensitivity. Thus, searching against the 13-species database, the target was again easily identified at the 20% concentration level and the number of peptides identified was much greater than in the 1D analysis. Unfortunately, the data for the 0.6 and 0.06% concentrations implied that positive target identification is still not achievable at those levels even with the 2D methodology.

### *Database Size*

The number of false positive peptide identifications significantly increased with database size. For all concentrations, an average of 8.5 false positive peptides were identified with the 13-species database and an average of 71 false positive peptides were identified with the 261-species database. The resultant losses for the *E. coli* target were so drastic that positive identification could not be made at any concentration. The effect on the identification of unique peptides from *R. palustris*, *S. cerevisiae*, and *S. oneidensis* was not as dramatic for the larger database. For any of these three species, the loss was only 30–50 unique peptides on average going from the small to the large database. This is likely due to the fact that *E. coli* is a γ-proteobacterium, and a large number of species in this family were included in this database. In contrast, few genomes of species related to *R. palustris*, *S. cerevisiae*, and *S. oneidensis* have been sequenced.

## Conclusions

Current 1D or 2D LC-MS/MS systems, based on available mass spectrometry techniques, will not easily be able to detect and identify target species if they are at less than 1% in the background matrix. However, this study gives a good starting point for possible alternative separation techniques and MS methodologies. Such advances may extend the dynamic range of proteome measurements, allowing positive identification of target species below 1% in a background matrix. That level of dynamic range is important for shotgun proteomics techniques to be applicable to the identification of low-level species in complex matrices. Issues with database size must also be addressed to determine the efficiency of this technique for a wide range of biothreat agents.

This project has also resulted in a conceptual design for a prototype instrument and the filing of a patent

application. The resulting novel mass spectrometer and associated operational method is expected to be well suited for rapid and sensitive analysis of protein biomarkers. Shown in Fig. 1, it is comprised of: a three-dimensional quadrupole ion trap, a linear quadrupole (q), and a time-of-flight mass spectrometer (QITqTOF). The operational mode is as follows:

1. A heterogenous population of (precursor) ions from the ES source is collected in the QIT
2. A mass-selected packet of precursor ions is ejected from the QIT into the q
3. The packet of precursor ions undergoes dissociation during transit through the q
4. TOF operation is synchronized with arrival of the fragment ion packet in the acceleration region
5. Fragment ion mass analysis occurs in the TOF
6. Repeating steps 2–5 enables MS/MS analysis of all precursor ions initially stored in the QIT without reloading

This instrument will allow generation of MS/MS spectra on multiple packets of parent ions selected arbitrarily from a heterogeneous ion population collected in a single accumulation event. Because of the high speed of the TOF-MS, a significant enhancement in the overall throughput for MS/MS is expected.

## Benefits

There is tremendous need for rapid detection and positive identification of biological threat agents directly from complex environmental samples. Additionally, our military needs a reliable biological agent detector for all type of threats. The mass spectrometry-based instrumentation and techniques investigated in this research are a potential solution. The combination of ES ionization with the proposed hybrid mass analyzer configuration has potential for rapidly generating large volumes of data needed to identify specific markers in unknown samples without extensive sample preparation and time-consuming chromatography.

The instrumentation and methodology should be capable of detecting a wider range of biological agents than any other current technique. It is expected that variations of this instrument will be of interest to agencies involved in national defense and homeland security. Additionally such instrumentation should have applications in the medical profession and environmental analysis.

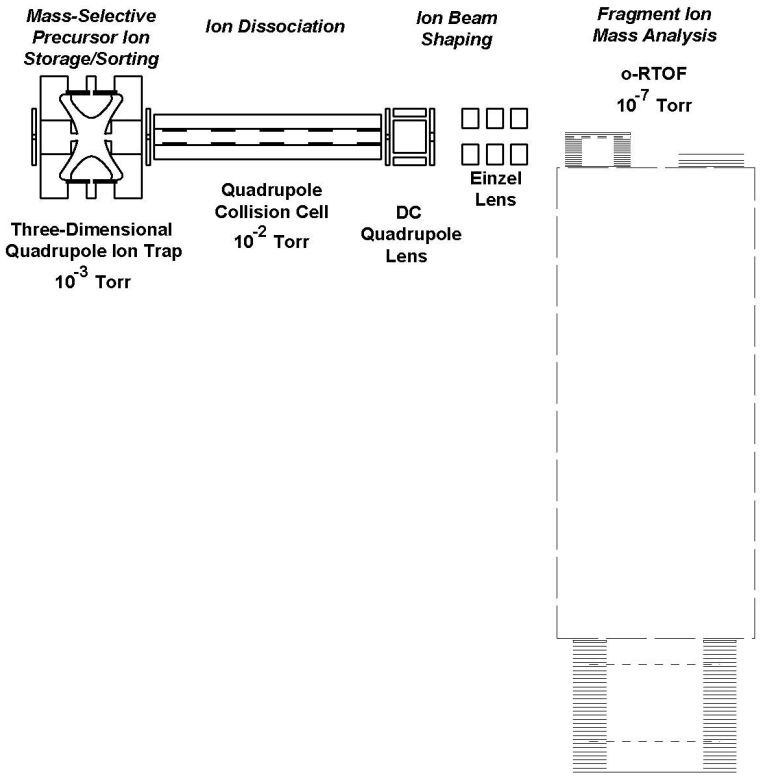


*Figure 1. Hybrid mass spectrometer design for rapid bio-marker analysis*

# Comprehensive Analysis of Microbial Proteomes Using Signature Peptides

R. S. Foote,[1] G. B. Hurst,[1] S. J. Kennel,[2] R. S. Ramsey,[3] and J. M. Ramsey[3]
[1]*Chemical Sciences Division*
[2]*Life Sciences Division*
[3]*University of North Carolina–Chapel Hill*

This project addressed the need for improved high-throughput methods for microbial proteome analysis in support of the DOE Genomes to Life (GTL) program. Quantitative proteomics data are important to this program to (1) confirm the presence in cells of proteins indicated by the analysis of isolated protein complexes, (2) establish cellular levels of proteins required for complex formation, (3) provide a quantitative database for modeling protein-protein interactions, and (4) allow predictions of the presence of complexes in new organisms based on their protein complements. We have developed methods that will greatly simplify the "bottom-up" approach to proteome analysis, in which trypsin digests of whole protein extracts are analyzed by mass spectrometry to identify proteins based on peptide sequences. Our methods involve isolating terminal peptides from each protein in the extract, which can be used as signature molecules to identify and quantify the parent proteins. These methods will reduce the complexity of microbial protein digests by a factor of ~30 and improve the efficiency and throughput of analysis. The methods are applicable to a variety of biological and biomedical problems, including analysis of altered cellular proteomes in human disease, and would be of interest to a number of funding agencies, including DOE and NIH.

## Introduction

High-throughput mass spectrometry (MS) methods for proteome analysis include both "top-down" and "bottom-up" approaches. The top-down approach involves MS of intact proteins. This method provides information on the total masses of the proteins and can also reveal some structural features by using isotopic labeling techniques. It is less useful for protein sequencing and is limited in the mass range of the proteins that can be analyzed. The bottom-up method involves enzymatic digestion of whole protein extracts followed by liquid chromatography (LC) coupled with MS for analysis of the peptides. The peptides can be sequenced by MS/MS techniques, and this information compared with protein databases for identification of the parent protein. However, due to the high complexity of the peptide mixtures, most of the individual peptides are not resolved by LC and only a fraction of the total number can be subjected to MS/MS sequencing during an analytical run. Many proteins may therefore not be detected during the analysis. The complexity of the mixtures may be simplified by isolating specific types of peptides for use as signature molecules for the parent proteins. Previous methods include the affinity isolation of peptides containing specific amino acids (e.g., cysteine) or post-translational modifications (e.g., glycosyl groups). However, these methods are not comprehensive, as proteins lacking an affinity target are not represented in the isolated peptide mixture. For example, many microbial proteins do not contain cysteine, which is commonly used in the ICAT (Isotope-Containing Affinity Tag) method to tag and isolate peptides for MS analysis of relative protein concentrations in different extracts. Furthermore, the peptide complexity may remain relatively high due to multiple affinity targets in other proteins. Neither the top-down or bottom-up approach provides data for absolute protein quantification using mass spectrometry alone.

The principal objective of this project was to develop methods for isolating single signature peptides from all proteins in a cell extract, in order to simplify and facilitate the LC-MS of peptides for comprehensive microbial proteome analysis. These signature peptides could also be tagged with fluorescent groups or other types of quantifiable labels to allow quantitative analysis of the parent proteins.

## Technical Approach

The approach explored in this project was to isolate peptides from the protein C- and/or N-terminus for use as signature molecules for proteome analysis. The approach has the following advantages:

1. The number of peptides is approximately 30-fold less than the number in a normal tryptic digest, greatly reducing the complexity of mixtures for separation and analysis.
2. Each parent protein is represented by a single peptide that, when unique, can be used for its identification and quantification.

3. The defined position of the signature peptide at the C- or N-terminus allows constrained database searching, resulting in fewer ambiguous sequence matches than in methods requiring unconstrained searches.
4. The reduced peptide sample mass allows the use of capillary or microfabricated separation devices with improved detection sensitivity and throughput.

### Terminal peptide isolation

Our proposed method for isolating N-terminal peptides is shown schematically in Fig. 1 and consists of the following steps: (1) blocking all protein amine groups on lysine and at the N-terminus by an amine-reactive acylating agent (e.g., succinic anhydride), (2) cleaving the modified protein at unblocked arginine residues with trypsin or Arg-C endoproteinase, (3) reacting all newly formed amine termini with an affinity reagent (e.g., biotin), and (4) removing all tagged peptides by affinity chromatography (e.g., on streptavidin-agarose). The blocked N-terminal peptide is nonreactive with the affinity reagent and is therefore eluted in the passthrough from the affinity column. Blocking the lysyl ε-amines in Step 1 prevents affinity tagging of N-terminal peptides containing lysine and also increases the average length and uniqueness of the signature peptides. This method was demonstrated in a preliminary experiment using lysozyme as a model protein. The protein was first treated by standard methods to reduce disulfide groups and to block sulfhydryl groups with iodoacetamide (Allen 1989). Steps 1–4 were then carried out using succinic anhydride to block the primary amines (Step 1) and sulfosuccinimidobiotin to biotinylate peptide amine termini (Step 3). After removing the biotinylated peptides by streptavidin-agarose chromatography (Step 4), a single peptide was isolated from the original digest in approximately 90% yield, based on HPLC analysis. Its mass corresponded to that of the expected derivative of the lysozyme N-terminal peptide, KVFGR, in which both the α- and ε-amines of lysine (K) are blocked with succinyl groups (total monoisotopic MW = 805.39).

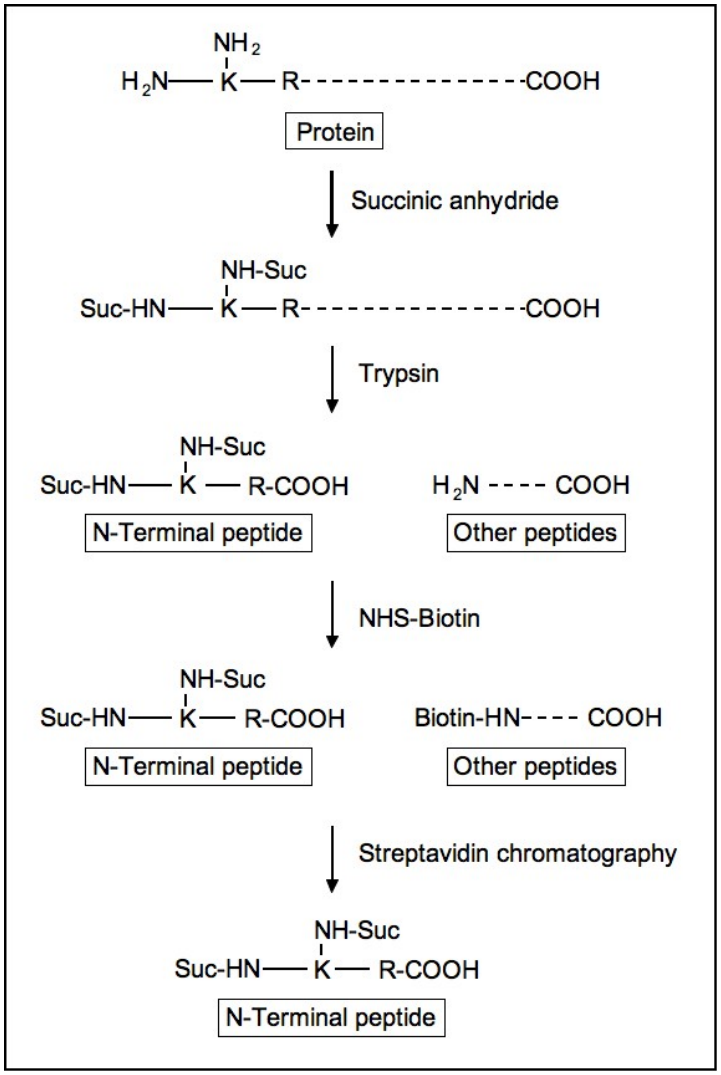


*Fig. 1. Schematic showing method for isolation of N-terminal peptides. Only arginine (R) and lysine (K) residues nearest the N-terminus are shown.*

A similar approach could potentially be used for the isolation of C-terminal peptides: (1) blocking all reactive protein carboxyl groups by esterification or amidation, (2) digesting with Arg-C endoproteinase or other specific protease, (3) tagging newly formed carboxyl termini with a carboxy-reactive affinity reagent, and (4) removing tagged peptides by affinity chromatography. Alternatively, the C-terminal peptides may be isolated from an aliquot of the same digest used for the isolation the N-terminal peptides, by using anhydrotrypsin affinity chromatography. Anhydrotrypsin binds to peptides having arginine or lysine at the carboxy terminus and can be used to isolate C-terminal peptides from trypsin digests of proteins that do not bear either of these amino acids at the C-terminus (Kumazaki 1986). The C-terminal peptides prepared by this method would have a single unblocked amino group that could be reacted with fluorescent reagents for quantitative analysis. Cation-exchange chromatography has been used as an alternative to anhydrotrypsin (Mann 1990) based on the presence of strongly basic arginine or lysine residues in all but the C-terminal peptide (unless present at the C-terminus of the parent protein). C-terminal peptides containing a succinyl-blocked lysine residue would not bind to the affinity or cation exchange columns. However, approximately 8.7% of *E. coli* proteins terminate in arginine, and their C-terminal

peptides would therefore bind to the column and would not be isolated by this procedure. Nevertheless, the probability of obtaining a unique signature peptide in at least one of the two isolation mixtures (N- and C-terminal peptides) obtained by this alternative method would be >95%.

These basic isolation methods yield the terminal peptides regardless of whether or not the protein termini are naturally modified by aminoacylation, carboxyamidation, or other reactions. Although missed enzymatic cleavages or post-translational modifications could result in multiple peptides being isolated from a single protein, these variations would not decrease the specificity of their signatures (a longer peptide resulting from a missed cleavage would actually have a greater probability of being unique).

## Computer Analysis

To evaluate the potential of the approach, computer analysis was performed on the translated *E. coli* K12 genome (NCBI, 4279 protein sequences). This analysis indicated that approximately 83% of the N-terminal peptides and 93% of the C-terminal peptides produced by cleavage at arginine residues would have a unique amino acid sequence and could therefore provide an unambiguous signature of the parent protein. Both terminal peptides were unique for 78% of the proteins and at least one was unique for 98%. In addition, the calculated masses of 76% of the N-terminal peptides and 84% of the C-terminal peptides varied by more than 1 ppm from their nearest neighbors and could potentially be used as accurate mass tags for their parent proteins. Both peptides met this criterion for 64% of the proteins and at least one met the criterion for 95%. Average lengths for the N- and C–terminal peptides were approximately 20 and 18 amino acids, respectively, compared to the average protein length of 318 amino acids. The average number of peptides produced by cleavage at both arginine and lysine was 29 per protein. The isolation of signature peptides by the methods described in this proposal would therefore reduce the complexity (number of peptides) of normal tryptic digests by an average of 29-fold and would reduce the total sample mass by ~17-fold. (The reduction in mass is less than the reduction in complexity because peptides resulting from cleavage only at arginine are longer, on average, than those resulting from normal tryptic cleavage at both arginine and lysine).

The N-terminus of microbial proteins is frequently modified by post-translational cleavage of one or more amino acids. Analysis of an available database of 852 N-verified *E. coli* protein sequences (http://bmb.med.miami.edu/EcoGene/EcoWeb/CESSPages/VerifiedProts.htm) showed that the N-terminal methionine residue alone is removed from approximately 40% of the proteins, while multiple amino acids (14–58) are removed from an additional 16%. Approximately 91% of the Arg-C-cleaved N-terminal peptides and 98% of the C-terminal peptides were unique in this database of mature proteins. (The increases in specificity are due in part to the smaller size of the database, since each sequence has a lower probability of redundancy when compared with a smaller number of other sequences.) In any case, separate analysis of both N- and C-terminal peptides should provide a high probability (≥98%) of observing at least one unique signature for each member of the *E. coli* proteome. Searching procedures using gene-translation databases need to allow for the possibility of post-translational processing of the N-terminus (the C-terminus is much more rarely modified).

## Results and Discussion

The N-terminal peptide isolation procedure was initially tested on a mixture of model proteins in order to identify and address technical problems. Potential problems included incomplete protein modification and cleavage (steps 1–2) and incomplete peptide tagging and removal (steps 3–4). These problems were addressed by using a large excess (10- to 100-fold) of blocking and tagging reagents and removing excess reagent after each step. Trypsin cleavage was carried out overnight using a high ratio of enzyme to protein (>40 units/mg) to ensure complete digestion. Two affinity tagging and chromatography methods were examined for removing the non-terminal peptides: the biotin-streptavidin biochemical system, as described above, and the recently described fluorous chemical system (Brittain 2005). The latter system employs perfluorinated alkyl tags that bind strongly to similar groups immobilized on silica supports. Preliminary experiments indicated that the biochemical system can remove the affinity-tagged peptides more completely, although it is significantly more expensive and requires pre-removal of excess biotin reagent to avoid overloading the streptavidin column. Further optimization of the chemical system may avoid these disadvantages. A method of rapidly removing excess biotin reagent from tagged peptides was developed, using solid-phase extraction. HPLC analysis of the peptides isolated from a mixture of seven proteins showed a maximum of 8–10 peptides, compared to 82 predicted peptides in the initial digest of the modified proteins (cleaved only at arginine) and >260 predicted peptides in the trypsin digest of the unmodified proteins (cleaved at both arginine and lysine). MS analysis will be performed to identify the isolated peptides.

In a variation of the N-terminal peptide isolation procedure, an amine-reactive fluorescent reagent (5-carboxytetramethylrhodamine succinimidyl ester, 5-TAMRA-SE) was used in step 1 to both block and fluorescently tag primary amines in the model protein

mixture. The isolated N-terminal peptides were separated by micellar electrokinetic chromatography (MEKC) on a microfluidic chip and detected by laser-induced fluorescence. The relative fluorescent peak sizes in this analysis were consistent with the initial protein concentrations. However, some terminal peptides tagged by this method will contain multiple labels, due to the presence of multiple lysines, whereas peptides isolated from naturally N-acylated proteins may contain no fluorescent tag. A method of fluorescently labeling the single arginine residue contained in each N-terminal peptide was therefore proposed for accurate fluorescence-based quantification. The terminal peptides from more complex protein mixtures may not be completely resolved by one- or even two-dimensional chromatographic separations. However, computer modeling was used to show that correlated fluorescence and MS analysis data could be used to deconvolute and quantify unresolved peaks in a peptide separation. This would allow quantitative analysis of complex signature peptide mixtures by chromatographic or electrophoretic separations coupled with both fluorescence detection and mass spectrometry.

N-terminal peptide isolations were also performed on whole protein extracts of *Rhodopseudomonas palustris*. This microorganism plays an important role in environmental carbon management and recycling and is currently the focus of efforts in ORNL's Genomes-to-Life program to characterize microbial protein-protein interactions. Analysis of the isolated peptides by LC-MS/MS in a preliminary experiment indicated significant enrichment of peptides with start positions at or near the predicted N-terminus: ~30% within 15 amino acids of the terminus. (Start positions within this range or even greater could be due to post-translational processing of the N-terminus, as noted above.) Peptides at longer start positions may also have been due to incomplete removal of the non-terminal peptides. Because of the non-quantitative nature of MS analysis, the relative masses of the putative terminal, and non-terminal peptides could not be estimated, and it is therefore not clear whether the latter peptides were present in significant amounts or were minor contaminants detected by the high sensitivity of MS. Experiments with model protein mixtures have indicated that incomplete non-terminal peptide removal is most likely to be due to saturation of the affinity (streptavidin) column in step 4. A subsequent isolation from *R. palustris* proteins was performed using ~10-fold larger affinity columns for this step. The MS analysis of this isolate will be compared with that of a normal tryptic digest of the proteins to determine their relative complexities and coverages of the *R. palustris* proteome. (These analyses were still in progress at the time of this report.) A preliminary isolation of the C-terminal peptides from *R. palustris* proteins was also performed using cation-exchange chromatography, as described above. Although these samples have not yet been analyzed by MS, the isolation procedure resulted in an expected mass reduction (~20-fold) in peptide mass, based on HPLC comparison with the initial tryptic digest.

## Benefits

These studies have provided a firm theoretical and experimental basis for the proposed signature peptide approach. This approach can significantly enhance proteome research at ORNL by increasing the throughput of MS analysis and by allowing quantitative protein analyses based on fluorescent signature peptides. In addition to benefits to the ORNL Genomes-to-Life program described in the abstract, these methods could be used to determine the stoichiometries of protein complexes that cannot be determined by MS alone. Signature peptide samples can be analyzed by microfluidic techniques developed at ORNL (Lazar 1999; Ramsey 2003) and will therefore enhance their potential use for proteome analysis. These methods will be applicable to a variety of other biological and biomedical problems, including the analysis of altered cellular proteomes in human disease, and would benefit research sponsored by NIH as well as DOE.

## References


Allen, G. 1989. *Laboratory Techniques in Biochemistry and Molecular Biology*. Vol. 9, 2nd ed., R. H. Burdon and P. H. van Knippenberg, Eds., New York, Elsevier.

Brittain, S. M., S. B. Ficarro, A. Brock, and E. C. Peters. 2005. "Enrichment and analysis of peptide subsets using fluorous affinity tags and mass spectrometry," *Nature Biotechnology* **23**, 463–468.

Kumazaki, T., T. Nakako, F. Arisaka, and S. Ishii. 1986. "A novel method for selective isolation of C-terminal peptides from tryptic digests of proteins by immobilized anhydrotrypsin: application to structural analyses of the tail sheath and tube proteins from bacteriophage T4," *Proteins: Structure, Function and Genetics* **1**, 100–107.

Lazar, I. M., R. S. Ramsey, S. Sundberg, and J. M. Ramsey. 1999. "Subattomole-sensitivity microchip nanoelectrospray source with time-of-flight mass spectrometry detection." *Anal. Chem.* **71**, 3627–3631.

Mann, K., R. Jander, E. Korsching, K. Kühn, and J. Rauterberg. 1990. "The primary structure of a triple-helical domain of collagen type VIII from bovine Descemet's membrane," *FEBS Lett.* **273**, 168–172.

Ramsey, J. D., S. C. Jacobson, C. T. Culbertson, and J. M. Ramsey. 2003. "High efficiency, two-dimensional separations of protein digests on microfluidic devices," *Anal. Chem.* **75**, 3758–3764.

# Development of New Capabilities for Genome-Scale Quantitative Measurements of Protein Complexes

G. B. Hurst,[1] D. A. Pelletier,[2] F. W. Larimer,[2] R. L. Hettich,[1] W. H. McDonald,[1] N. F. Samatova,[3] D. L. Tabb,[2] I. I. Harruna,[4] K. G. Asano,[1] T.-Y. Lu,[2] T. K. Lankford,[2] A. Savidor,[5] and C. Pan[5]

[1]*Chemical Sciences Division*
[2]*Life Sciences Division*
[3]*Computer Science and Mathematics Division*
[4]*Clark Atlanta University*
[5]*Graduate School of Genome Science and Technology*

This report summarizes a focused program to advance the state of the art for quantitative mass spectrometry–based measurement of protein complexes. The motivation for this work was to develop capabilities at ORNL that will be critical components of the U.S. Department of Energy Genomics: GTL Molecular Machines Facility. The specific mission of this facility for which the work described in this report has particular relevance is to "isolate and analyze molecular machines from microbial cells." Information critical to gaining biological insight into function of any such molecular machine lies in its concentration in the cell, and its subunit composition. We describe progress toward (1) a new approach to protein complex stoichiometry determination based on chemical tagging reagents for proteins and (2) the development of an optimum strategy for quantitative analysis of protein complexes based on state-of-the-art mass spectrometry–based methods for proteins. We have identified commercially available fluorous reagents as promising candidates for tags to facilitate measurement of relative amounts of subunits in protein complexes. We have developed a computer program, ProRata, for robust quantitative analysis of mass spectrometric data obtained from stable-isotope-labeled bacterial proteome samples.

## Introduction

Systems biology requires new tools for high-throughput, quantitative measurements of proteins and protein complexes. Considerable qualitative information concerning the identities of proteins in a proteome can be obtained using present MS technology. However, accurate measurement of protein amounts is much more difficult yet absolutely critical to an understanding of biological function. As recognized by DOE's Genomics: GTL program, the next step beyond quantitative protein measurements is the quantitative measurement of protein complexes, or, to use the terminology of Genomics: GTL Goal 1, the "machines of life" (http://www.doegenomestolife.org). The mission of the Genomics: GTL Molecular Machines Facility will be to identify and characterize "all" the machines of life (protein complexes) in selected microbial species. Major defining characteristics of any such complex will include its concentration and its subunit composition. There are currently no robust, high-throughput MS-based methods for measuring amounts or stoichiometry of protein complexes. Our project combined an original approach to protein complex stoichiometry determination (Aim 1) with the development of a more general optimum strategy for quantitative proteomics, based on state-of-the-art quantitative mass spectrometry-based methods (Aim 2).

### *Aim 1*

Traditional methods for determining stoichiometries of protein complexes (Cantor et al. 1980) typically involve a combination of isolation and characterization of the intact complex, and denaturation to disrupt the complex into its subunits. The intact complex can be characterized using techniques such as X-ray crystallography, electron microscopy, and electrophoretic or hydrodynamic methods. On denaturing, the molecular masses of the subunits of the complex can be determined using similar methods. Weight fractions of the various subunits are estimated using spectroscopic, radioisotopic, or immunoassay techniques which often require labeling, staining, or derivatization steps. These data must all be integrated to develop a stoichiometric description of the complex; this procedure depends heavily on the nature of the complex being studied.

In this Aim, we sought improved methods for determining relative amounts of subunits of a protein complex, using mass spectrometry. The major hurdle to developing such methods is the fact that the magnitude of the mass spectrometric response to identical amounts of any two peptides or proteins of different amino acid sequences will generally be different. However, based on encouraging literature reports (Thompson et al. 2003), we explored the possibility that chemical derivatizing reagents could be used to provide a more sequence-

independent response from different peptides, in addition to imparting other useful characteristics.

***Aim 2***

The current state-of-the-art for quantitative measurements in proteomics involves measurement of differential expression of each protein in two samples representing, for example, a "normal" cell line versus a "diseased" cell line. The purpose of this Aim was to implement this capability at ORNL, with emphasis on bacterial proteomes of interest to the Department of Energy.

Current mass spectrometry–based techniques for quantitative protein measurement rely on ratioing signals from peptides that are chemically identical but bear distinctive "heavy" and "light" stable isotope signatures (Lill 2003). This class of measurements circumvents the large variation in magnitude of mass spectrometric response among peptides with different amino acid sequences. Labeling methods fall into two broad groups—in vivo and in vitro. In vivo labeling is performed during growth of the bacteria, with two separate cultures (growth states, strains, etc.) grown in media that differ in isotopic composition (e.g., $^{14}N$ vs. $^{15}N$) (Washburn et al. 2002) or with isotopically distinct versions of an amino acid (Jiang and English 2002). The bacteria incorporate the isotope label as they synthesize proteins during growth. In vitro labeling involves differential derivatization of proteins from two different cultures during the isolation or digestion of the protein content of the bacteria. The "light" isotopic form of the derivatization reagent is reacted with the proteome of one culture, while the "heavy" form is reacted with the other culture. In vitro labeling techniques include reaction with of proteins with isotopomers of amino-acid-specific derivatizing reagents, such as isotope-coded affinity tags, or "ICAT" (Gygi et al. 1999). For either in vivo or in vitro labeling, the ratio measurement between a pair of labeled peptides is obtained by combining in known proportion the samples containing the heavy and light labels prior to mass spectrometry. A relative measurement is obtained, providing an estimate of the difference in protein expression level between the two growth conditions.

## Technical Approach

***Aim 1***

We developed a chemical labeling strategy to attach a multi-purpose chemical "tag" to each protein subunit of a protein complex using well-known chemistries, such as those based on N-hydroxysuccinimide (NHS) esters, that are reactive towards lysine residues. On enzymatic digestion, the tag should remain attached to one or more proteolytic peptides from each subunit of the complex. The collection of tagged peptides will be subjected to liquid chromatography–mass spectrometry (LC-MS) for measurement of peptide masses and fragmentation patterns. The ideal tag would have several characteristics. It should contain a moiety to allow enrichment of tagged peptides using affinity chromatography. The ideal tag would increase uniformity of ionization efficiency for all tagged peptides, reducing the dependence of MS response on amino acid composition of peptides. The ideal tag would dissociate under collisional activation in the mass spectrometer to produce a characteristic fragment ion marker that is of identical mass for every tagged peptide. This characteristic marker ion could not only flag the presence of a "tagged" peptide, but its peak area in the mass chromatogram could provide the basis for a quantitative measurement of the peptide. This strategy would yield information on the amount of each peptide, in the form of a peak area for the characteristic marker ion, and the identity of each protein in the complex, based on fragmentation of the attached peptide. This information, along with the size of the intact complex, should provide a basis from which the stoichiometry of the complex can be determined.

We investigated a phosphate-containing compound that can be attached to lysine residues via reaction with N-hydroxysuccinimide. A variety of phosphate-bearing compounds that also contain carboxylic acid moieties are available, such as phosphocreatine and 3-phosphoglycerate. Activation of the carboxylic acid group in these compounds with EDC (1-ethyl-3-[3-dimethylaminopropyl]carbodiimide hydrochloride) and NHS will yield reagents that are selective for the primary amines on lysine side chains and the N-terminal amine of proteins. The phosphate group potentially performs multiple functions. It can serve as the affinity isolation group, using immobilized-metal affinity chromatography (IMAC). Phosphate ions are often observed as fragments in tandem mass spectra of phosphopeptides, thus providing the low-mass marker ion.

Fluorous tags were also investigated as chemical labeling reagents. These reagents have been applied to proteomics (Brittain et al. 2005). A major practical advantage of fluorous tags is their commercial availability as NHS esters and other peptide- or protein-reactive forms.

***Aim 2***

In Aim 2, we applied existing MS capabilities for relative quantitative measurements between *R. palustris* proteomes resulting from growth in $^{15}N$ vs. $^{14}N$ labeled media. We combined these cultures in varying ratios (1:1, 1:5, 5:1, 1:10, 10:1), digested with trypsin, and performed LC-MS-MS experiments using two types of mass spectrometers. Initial experiments were performed

on a ThermoFinnigan LCQ quadrupole ion trap mass spectrometer, while later measurements were performed using a newer ThermoFinnigan LTQ mass spectrometer.

The large quantities of data produced in these measurements, along with deficiencies in existing software, prompted us to develop a new computer program for determining relative amounts of $^{14}N$- and $^{15}N$-labeled peptides (and their corresponding proteins) from the raw data.

## Results and Discussion

### *Aim 1*

Prof. I. Harruna from Clark Atlanta University participated in this project as a visiting faculty member during the summers of 2004 and 2005. During his time at ORNL, Prof. Harruna made significant progress in synthesizing two types of reactive tags and evaluating a commercially available class of reactive tags, for quantitative mass spectrometric measurements of proteins.

The first synthesized reagent was the NHS ester of phosphoglyceric acid. This reagent should react with primary amines on lysine residues and N-termini of proteins. The phosphate group on these reagents will contribute a fixed negative charge site, as well as a labile group that should yield a low-mass marker fragment in negative-ion tandem mass spectra. $^{1}H$ NMR analysis suggests that the desired products were synthesized, although other species are also present. The second type of chemical tag, prepared for positive-ion mass spectrometry, is an NHS ester of N-benzyl glycine. This reagent, also selectively reactive towards lysines and N-termini, should, under collision-induced dissociation, yield a characteristic benzyl marker ion in the tandem mass spectrum of a labeled peptide. While synthesis of these reagents was successful, attempts to react them with peptide model systems did not yield definitive results.

During the course of this project, a new commercially available class of amine-reactive reagents came to our attention for use in MS analyses of proteins and proteomes (Brittain et al. 2005). These reagents are based on "fluorous" chemistries, which involve addition of perfluorinated moieties to peptides or proteins to allow subsequent purification using specialized fluorous chromatography or solid-phase extraction. This characteristic should allow enrichment of fluorous-reagent-tagged peptides, an important component of our general strategy. We further investigated the possibility that the perfluorinated portion of these reagents could perform other functions of protein-tagging reagents for quantitation, including imparting more uniform ionization, and providing a marker fragment ion in the tandem mass spectrum. We initially chose two fluorous reagents, N-succinimidyl-3-perfluorohexylpropionate ("hexyl" tag) and N-[4-(1H,1H,2H,2H-perfluorodecyl)benzyloxycarbonyloxy]succinimide ("BOC" tag). The hexyl and BOC tags were reacted with a variety of peptides of varying isoelectric point and hydrophobicity. Products of the reactions were characterized using matrix-assisted laser desorption time-of-flight mass spectrometry (MALDI-TOF-MS), and results are summarized in Table 1. In general, successful reaction of one or both types of tag was obtained with all the peptides.

Untagged and fluorous-tagged pairs of peptides of the same sequence were mixed and analyzed using reversed-phase high-performance liquid chromatography (HPLC) with absorbance-based detection in-line with an electrospray source on a mass spectrometer. This measurement obtained, from the identical sample, both a tagged peptide:untagged peptide molar ratio from the

**Table 1: Peptides reacted with fluorous tags**

| Peptide | Sequence | Number of tags reacted with peptide* | |
|---|---|---|---|
| | | Hexyl tag | BOC tag |
| Neurotensin | pELYENKPRRPYIL | 1-2 | 1 |
| Bovine insulin a chain** | GIVEQ$C_{ox}$$C_{ox}$ASV$C_{ox}$SLYQLENY$C_{ox}$N | 0 | 0-1 |
| - | GDVKAAWGR | 2 | 0-2 |
| - | FSNGMKHLDDLR | 1 | 0 |
| - | LHVDPENFKLLGNVLVVVLAR | 2 | 0 |
| Myelin basic protein fragment 4-14 | QKRPSQRSKYL | 2-4 | - |
| [Ser25]-protein kinase C fragment 19-31 | biotinyl-KRFARKGSLRQKNV | 3-4 | - |
| Amyloid beta protein fragment 17-40 | LVFFAEDVGSNKGAIIGLMVGGVV | 2 | - |

* measured by MALDI-TOF-MS. "-" indicates no reaction was performed.
**all cysteines oxidized to cysteic acids

absorbance measurement and a relative MS response. Although final data analysis is in progress, in general the ratio of tagged:untagged MS response was greater than the tagged:untagged absorbance response, suggesting that the fluorous tag increased the MS response of a peptide over its untagged counterpart.

Tandem mass spectrometry of fluorous-tag-derivatized peptides from bovine hemoglobin showed preliminary evidence for a characteristic immonium ion derived from cleavage of the derivatized amino acid. This evidence, which must be confirmed by further experiments, suggests that the fluorous reagents could also be useful for providing a characteristic marker ion in MS measurements.

***Aim 2***

Dr. Dale Pelletier's lab performed metabolic labeling of *R. palustris* strain CGA010 with stable isotopes of nitrogen, $^{14}N$ and $^{15}N$, under photoheterotrophic conditions. Cells were harvested, lysed, and centrifuged to provide crude soluble protein and membrane protein fractions. Mixtures of the labeled proteins were prepared at $^{14}N$:$^{15}N$ protein ratios of 1:10, 1:5, 1:1, 1:0, 0:1, 5:1, and 10:1. Each mixture was digested with trypsin, divided into aliquots, and archived at -80ºC.

Mass spectrometric characterization of the metabolically labeled *R. palustris* mixed proteome samples was performed on two platforms (ThermoFinnigan LCQ and LTQ) using multidimensional protein identification technology ("MudPIT") (Wolters et al. 2001), recently implemented at ORNL by Dr. Hayes McDonald. For the LTQ experiments, an average of >16,000 peptide identifications and ~2000 protein identifications were obtained per measurement.

Because of the lack of suitable software tools to extract relative peptide and protein amounts from mass spectrometric measurement of mixed stable-isotope-labeled proteomes, we developed a computer program for this purpose called ProRata. The data processing procedure was systematically optimized in the following three steps: chromatographic peak detection, peptide relative quantification, and protein relative quantification. A parallel paired covariance algorithm was developed that greatly enhanced the signal-to-noise ratio of the chromatograms for peak detection. It was observed in the standard proteome mixtures that the relative quantification is of highly variable accuracy for peptides and consequently for proteins. This necessitates estimating the quantification confidence for each quantified peptide and protein as a predictive measure of the quantification error. The principal component analysis was applied to peptides' mass spectral data for peptide quantification. Maximum likelihood estimation was employed for protein quantification, which uses peptide quantification confidence to improve the protein quantification accuracy and to calculate the confidence interval for the protein abundance ratio estimate. Figure 1 compares performance of ProRata with RelEx (MacCoss et al. 2003), a widely used program for this purpose. ProRata provides a larger number of ratios that are closer to the "known" ratio for the two standards evaluated for this figure. Additionally, ProRata provides a more robust estimate of a confidence interval for each differential protein expression ratio. A manuscript describing ProRata is currently in preparation.

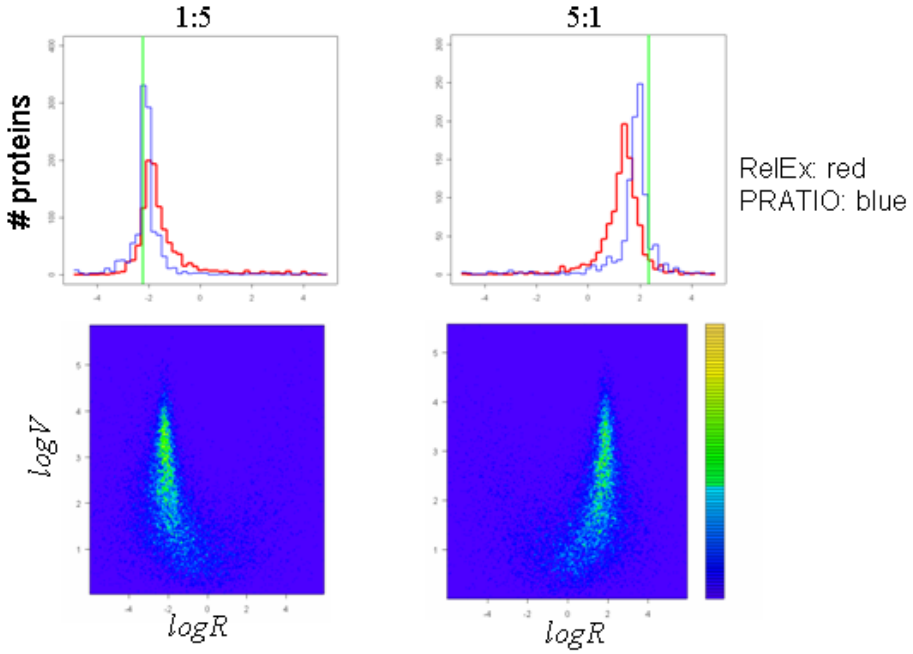


*Fig. 1. Results of ProRata analysis of 1:5 (left) and 5:1 (right) $^{14}N$:$^{15}N$-labeled* R. palustris *proteomes. The top two panels plot the number of identified proteins versus the base-2 logarithm of the measured ratio. The "correct" ratio for this sample is represented by the vertical green lines. The red curve shows results obtained from RelEx, while the blue curve shows results from ProRata. The narrower distribution and closer proximity to the expected ratio indicates superior performance of ProRata. The bottom two panels are two-dimensional histograms showing the distribution of peptides by signal-to-noise estimate (logV) and measured ratio (logR). Peptides with higher estimated signal-to-noise (higher on the plots) tend also to lie closer to the "correct" ratio on the x-axis.*

## Benefits

Our primary programmatic goal has been to demonstrate specific capabilities in quantitative protein mass spectrometry that will strengthen ORNL's planned proposal to DOE for the $275M Genomics:GTL Molecular Machines Facility. Additionally, a genome-scale capability for protein complex analysis should be attractive to funding agencies in a number of biological and medical areas other than microbiology. One such potential future funding opportunity is the "Building Blocks, Biological Pathways, and Networks" pathway of the NIH Roadmap (http://nihroadmap.nih.gov/buildingblocks/index.asp).

## References


Brittain, S. M., S. B. Ficarro, A. Brock, and E. C. Peters. 2005. "Enrichment and analysis of peptide subsets using fluorous affinity tags and mass spectrometry." *Nature Biotechnology* **23**, 463–468.

Cantor, C.R. and P. R. Schimmel. 1980. *Biophysical Chemistry. Part I: The conformation of biological macromolecules*. W. H. Freeman, San Francisco, pp. 135–137.

Gygi, S. P., B. Rist, S. A. Gerber, F. Turecek, M. H. Gelb, and R. Aebersold. 1999. "Quantitative analysis of complex protein mixtures using isotope-coded affinity tags." *Nature Biotech.* **17**, 994–999.

Jiang, H. and A. M. English. 2002. "Quantitative analysis of the yeast proteome by incorporation of isotopically labeled leucine." *J. Proteome Res.* **1**, 345–350.

Lill, J. 2003. "Proteomic tools for quantitation by mass spectrometry." *Mass Spectrom. Rev.* **22**, 182–194.

MacCoss, M. J., C. C. Wu, H. B. Liu, R. Sadygov, and J. R. Yates. 2003. "A correlation algorithm for the automated quantitative analysis of shotgun proteomics data." *Analytical Chemistry* **75**, 6912–6921.

Washburn, M. P., R. Ulaszek, C. Deciu, D. M. Schieltz, and J. R. Yates. 2002. "Analysis of quantitative proteomic data generated via multidimensional protein identification technology." *Anal. Chem.* **74**, 1650–1657.

Yao, X. D., A. Freas, J. Ramirez, P. A. Demirev, C. Fenselau. 2001. "Proteolytic O-18 labeling for comparative proteomics: Model studies with two serotypes of adenovirus." *Anal. Chem.* **73**, 2836–2842.

Wolters, D. A., M. P. Washburn, and J. R. Yates III 2001. "An automated multidimensional protein identification technology for shotgun proteomics." *Analytical Chemistry* **73**, 5683–5690.

# Redefining ORNL's Suite of Protein Analysis Technologies by Adding Flexibility, Analytical Capacity, and Biological Utility

W. H. McDonald,[1] G. B. Hurst,[1] D. A. Pelletier,[2] D. L. Tabb,[2] T. K. Lankford,[2]
M. R. Thompson,[3] G. Khalsa-Moyers,[3] and N. C. VerBerkmoes[1]
[1]*Chemical Sciences Division*
[2]*Life Sciences Division*
[3]*Graduate School of Genome Science and Technology*

This report focuses on our efforts to enhance ORNL's capabilities for the analysis of complex mixtures of proteins—from protein complexes to proteomes. We were motivated by the need to provide in-depth and consistent data and to enable us to expand our analysis into even more complex types of samples. To aid us in reaching these goals, we have instituted well-vetted sets of protein and peptide standards that provide for rapid and controlled evaluation of new technologies and instrumentation QA/QC. The standards have proven useful for the optimization of instrumentation parameters for data acquisition on our various mass spectrometers including our recently acquired linear ion trap (LTQ). These standards have also proved useful for supporting computational and information system development as they provide quality "known" data for algorithmic optimizations. Institution and refinement of multidimensional peptide separation protocols such as MudPIT (multidimensional protein identification technology) have impacted not only the depth with which we were able to characterize protein complexes but also our ability to perform more involved proteomic analyses.

## Introduction

The robust analysis of proteins in complex mixtures is a key capability for any biological mass spectrometry group. To remain at the cutting edge, it is essential that we continue to expand both the depth and breadth of our analysis. For relatively simple protein mixtures, such as protein complexes, the key metrics are absolute sensitivity, dynamic range, and analysis of modified peptides. These enable one to analyze protein complexes from much lower amounts of starting material, to detect low-stoichiometry or low-affinity binding partners, and to analyze post-translational modifications. For more complex mixtures, total sensitivity is also an issue, but the total number of proteins one is able to characterize becomes much more important. Flexibility and reproducibility are also essential to enhance the confidence with which these tools can be applied to biological questions. Work performed under this funding has enhanced ORNL's mass spectrometry–related capabilities to aid in answering biological questions.

Several tasks have come together to aid in this enhancement. One, we have developed a protocol to bring new affinity purification "tags" developed in Yie Liu's and Yisong Wang's laboratories (Life Sciences Division) into vectors that could be of use in bacteria. This same strategy could be used to move other tag combinations into the existing vector system used in the DOE Genomics: GTL Center for Molecular and Cellular Systems (CMCS). The next was establishing a series of controls that could be used in both instrument optimization and quality assurance/quality control (QA/QC). These have proven helpful not only in our day-to-day tuning and upkeep of instruments but also were incredibly useful in evaluation of new instrumentation. Finally we have implemented and optimized the use of MudPIT (multidimensional protein identification technology). This and other chromatographic optimizations have allowed us to analyze samples under conditions that were previously either impossible or were so problematic as to not be routine.

## Technical Approach

### *Task 1*

Affinity purification of proteins engineered to express tags that allow for their capture has proven to be a powerful technique for the analysis of proteins and protein complexes. More recently, dual affinity purification tags are being used because they allow for two sequential rounds of affinity purification. As in the case of the original tandem affinity purification (TAP) tag (Rigaut 1999), the elution from the first step of affinity purification must be performed under conditions that do not disrupt associated proteins. Subsequent capture by the second affinity tag allows for incredibly "clean" purifications, even for low copy-number proteins.

The current CMCS endogenous pipeline primarily uses a dual affinity tag that includes the V5 epitope recognized by a commercially available monoclonal antibody and a 6-His tag that allows for purification on an immobilized metal affinity purification column (IMAC). This affinity purification tag has proven quite robust and has to date been used for the affinity isolation of >200 individual protein targets in *Rhodopseudomonas palustris*. However, it does have some limitations. One is that the affinity of 6-His tag for the IMAC can be too low for efficient isolation of low abundance proteins. Second, the nature of the tag requires that the final elution step be performed under denaturing conditions. While this is not a problem for identifying binding partners, it does preclude further work to characterize the complex itself. These include any structural or biophysical characterizations.

To address these issues, we have designed a cloning strategy to move two tags developed in Drs. Liu and Wang's lab into bacterial plasmids. The two tags chosen for this were the carboxy-terminal tags that encode (1) tetra-cysteine motif (recognized by FlAsHTM reagents from Invitrogen), two strepII tags (recognized by avidin), two tobacco etch virus protease (TEV) sites (allowing for cleavage-based elution from the distal tag), and the 6-His tag (recognized by Ni-IMAC), and (2) two copies of the HA epitope (recognized by commercially available monoclonal antibodies), two TEV sites, and two copies of the IgG binding domain of protein-A (allowing for purification via antibody coupled beads). The cloning strategy involves the PCR-based amplification of these tags using primers with the needed restriction enzyme sites to allow for replacement in the vector backbone of the currently used V5/6-His tag. Further, the introduced XbaI site will allow for movement of the entire tag/gateway destination portion to a completely different vector backbone (e.g., one that allows for targeted single crossover integration into the bacterial chromosome). Unfortunately, the initial steps of PCR amplification and subcloning have proven problematic, and we have not been able to generate these desired constructs. Work on these will likely segue into the CMCS where they will be most immediately useful.

***Task 2***

Having a set of appropriate and consistent controls for our protein analysis workflows is an invaluable resource. For this goal we have instituted peptide, protein, and digested protein standards. Our peptide standard consists of a series of peptides mixed together over three orders of magnitude of concentration in a solution suitable for direct infusion electrospray (50% MetOH, 0.1% acetic acid). The peptides include angiotensin I [1 pmol/µl], ATCH [100 fmol/µl], Bradykinin [10 fmol/µl], and Angiotensin II [1 fmol/µl]. This mixture is of use for both tuning and quality assurance of mass spectrometer performance. Appropriate injection times, full scan signal to noise, and MS/MS sensitivity, along with more qualitative characterizations of spectral quality, all go into making certain that our mass spectrometers are operating at peak performance. These same standards also proved to be incredibly valuable during our recent evaluation of the ThermoElectron LTQ-Orbitrap. While our current instrumentation allows for detection of the low abundance peptides by MS/MS, the Orbitrap performed the amazing full scan detection feat of measuring these lowest abundant peptides in the background of the higher concentration peptides (Fig. 1).

Our group now commonly uses two sets of protein standards, the "protein standard mix" (PSM) and the "extended protein standard mix" (EPSM). Both consist of sets of known proteins that have been mixed together at approximately equimolar concentrations. The PSM is made up of 6 proteins, and the EPSM is made up of 20 proteins, although there are small amounts of contaminating proteins present in both samples. While the protein mixtures themselves have proven useful for our protein analysis steps (e.g. proteolytic digestion), they are most often used after the mixtures themselves have been digested with trypsin. These produce even more complex mixtures of peptides and are useful for both chromatographic and data acquisition QA/QC. In fact, a digested PSM is run at the beginning of each week of the CMCS pipeline. Another application of these standards is in the development of algorithms for the analysis of peptide MS/MS spectra. By having known proteins, it is possible to establish false positive and false negative rates. Because the analysis of peptide MS/MS spectra is a multi-step process, it is also necessary to use standards in optimizing the entire analysis workflow.

***Task 3***

The coupling of chromatographic separations to mass spectrometry is one of the key enabling technologies for the analysis of proteins and peptides. In the past, our group has used both single and multidimensional chromatography strategies. However, the use of disposable, self-packed multidimensional columns was not employed until more recently. These MudPIT (multidimensional protein identification technology) columns as they are known were developed in the Yates lab (Link 1999, McDonald 2002, Washburn 2001, Wolters 2001) and have proven useful for a variety of shotgun or bottom-up proteomic analyses. While MudPIT has proven to be exceptionally useful in the group, especially for the analysis of challenging samples, many of our analyses do not require that degree of separative capacity. In these instances, a single reverse-phase separation is all that is needed. We have attempted to improve efficiency, duty cycle, and robustness of

these single-dimensional separations as well. Work in this area has focused on utilization of self-packed direct spray columns and exploration of various new plumbing mechanisms for the "trapping" columns that allow for fast sample loading.

## Results and Discussion

The impact of work performed under this project has had broad application to improving our capabilities to analyze both protein complexes and even proteome-scale mixtures of proteins. To round out our suite of tools for the analysis of bacterial protein complexes, we have designed and begun the cloning process to bring two of the new tandem affinity purification tags developed in the Liu and Wang laboratories into bacterial vector backbones. Subsequent cloning into non-replicating plasmids will provide us with the ability to tag the endogenous copy of the protein and thus avoid any artifacts associated with episomal expression of the tagged protein.

Development and implementation of protein standards has also been an important contribution of this effort. The peptide standard contains peptides at known concentrations spanning three orders of magnitude. It has been incorporated into our regular QA/QC workflows to

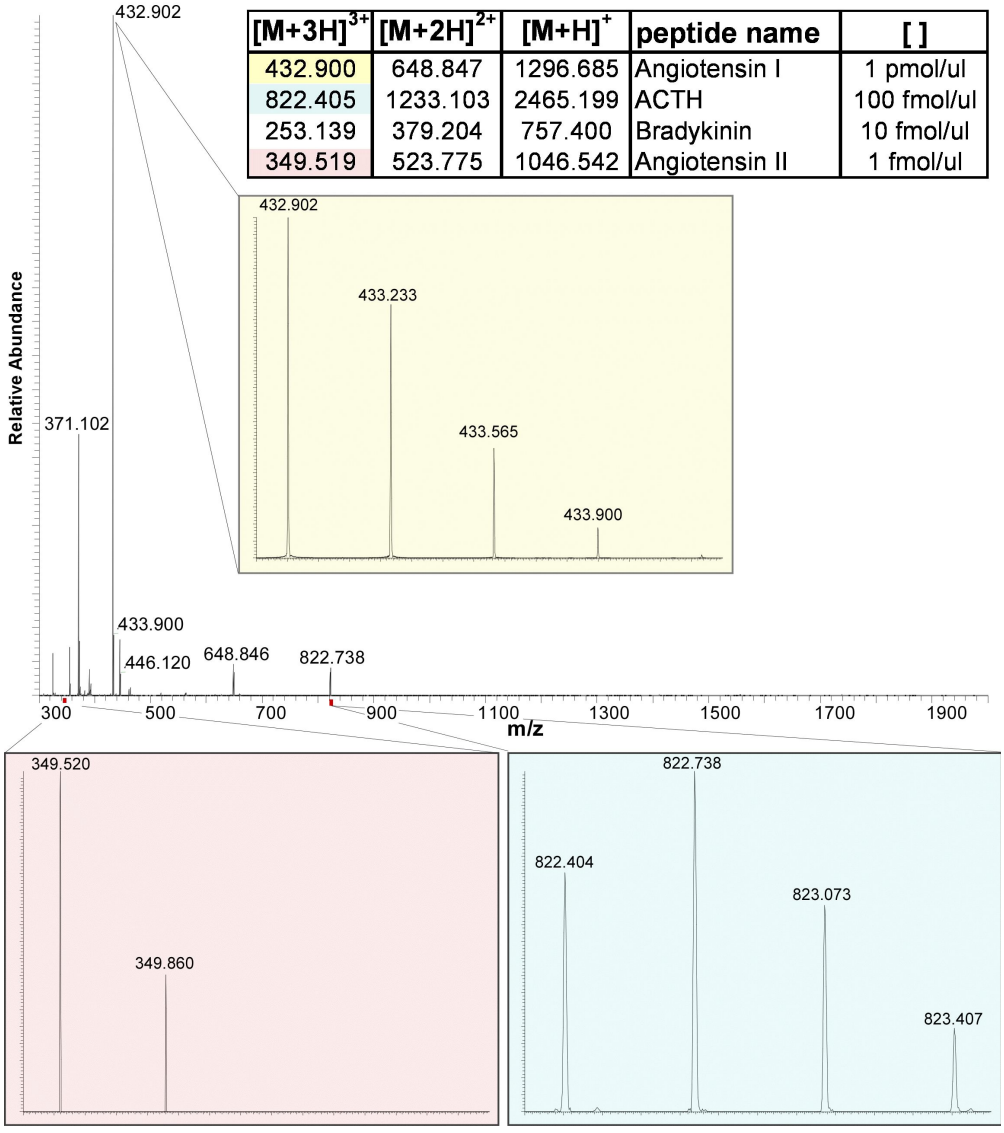


*Fig. 1. Use of peptide mixture to assay the intra-scan dynamic range of the ThermoElectron LTQ-orbitrap. Our 4 peptide mixture (see text for description) was infused and full-scan data collected in profile mode. The table shows the 4 peptide constituents, their concentrations, and the predicted m/z of their various charge states (+1, +2, and +3). Colored boxes are blow-ups from various regions of the spectrum. Yellow is the most intense ion species from angiotensin I (scaled at 1.2 * 107). Blue is the most intense ion species from ATCH (scaled at 5.5 * 105). Red highlights the lowest abundance peptide, angiotensin II (scaled at 5.9 * 103)*

ensure that the mass spectrometers used in the laboratory are performing optimally. It also provides a test mixture to help differentiate relative performance across various mass spectrometry platforms not only within the group but also any new mass spectrometers that the group is considering purchasing. An excellent example of this application arose during our "demo" of the recently introduced LTQ-orbitrap from ThermoElectron. While we were able to run numerous other samples to test other aspects of instrument performance, one of the most impressive demonstrations of this new instrument's capabilities was the ability to detect the lowest concentration peptide in the mixture in full-scan mode (Fig. 1). This was in the presence of peptides in the mixture at 10, 100, and 1,000 times its concentration. By contrast our current workhorse instruments (LCQ and LTQ) are only routinely able to detect the two most abundant peptides in the mixture.

The protein mixtures (PSM and EPSM) have also proven valuable resources for QA/QC of additional steps in our protein analysis workflows including enzymatic digestion protocols, HPLC separation and optimization, and data acquisition settings for the mass spectrometer. These have the additional benefit of defining sets of "known" proteins for the optimization and calibration of various algorithms used in the analysis of peptide MS/MS spectra. Development of the following programs (among others in development) benefited by having access to such data: DBDigger (Tabb 2005a), MASPIC (Narasimhan 2005), and MS2Grouper (Tabb 2005b).

Consistent efforts at optimizing separation strategies for the upstream separation of peptides prior to ionization are absolutely essential to remain at the forefront of protein and peptide analysis. Not only must these strategies have high analytical capacity, but they must also be flexible enough to deal with a variety of sample types. One optimization that was added to the CMCS pipeline analysis was the use of a "packed tip" column from which the peptides are directly ionized via nanoelectrospray. Our current column has been running pipeline samples now for several months in a row. We have also implemented MudPIT within the group. This has not only provided greater dynamic range and sensitivity for the analysis of protein complexes but also has had dramatic impacts on our bacterial proteomic projects. While it has proven useful for several project, its most dramatic success was its use for the proteomic analysis of the acid mine drainage communities (Ram 2005). The added flexibility to vary stationary phases, load amounts, and pre-run cleanup has allowed us to deal with samples that would have previously proved much more challenging if not impossible (e.g., membrane samples with high detergent concentrations).

## Benefits

Our primary programmatic goal has been to expand our specific capabilities in protein mass spectrometry that will benefit DOE's proposed Genomics:GTL Molecular Machines Facility. It has also benefited our bacterial and community proteomics capabilities. The additional flexibility and robustness of MudPIT has allowed us to progress on existing projects and aided in securing a new Genomics:GTL grant led by Jill Banfield to study acid mine drainage communities.

## References


Link, A. J., J. Eng, D. M. Schieltz, E. Carmack, G. J. Mize, D. R. Morris, B. M. Garvik, and J. R. Yates III. 1999. "Direct analysis of protein complexes using mass spectrometry," *Nat Biotechnol.* **17**, 676–82.

McDonald, W. H., R. Ohi, D. Miyamoto, T. J. Mitchison, and J. R. I. Yates. 2002. "Comparison of three directly coupled HPLC MS/MS strategies for identification of proteins from complex mixtures: single-dimensional LC-MS/MS, 2-phase MudPIT, and 3-phase MudPIT," *Int J Mass Spectrometry* **219**, 245–251.

Narasimhan, C., D. L. Tabb, N. C. VerBerkmoes, M. R. Thompson, R. L. Hettich, and E. C. Uberbacher. 2005. "MASPIC: Intensity-Based Tandem Mass Spectrometry Scoring Scheme That Improves Peptide Identification at High Confidence," *Analytical Chemistry* **10**.

Ram, R. J., N. C. Verberkmoes, M. P. Thelen, G. W. Tyson, B. J. Baker, R. C. Blake II, M. Shah, R. L. Hettich, and J. F. Banfield. 2005. "Community proteomics of a natural microbial biofilm," *Science* **308**, 1915–20.

Rigaut, G., A. Shevchenko, B. Rutz, M. Wilm, M. Mann, and B. Seraphin. 1999. "A generic protein purification method for protein complex characterization and proteome exploration," *Nat Biotechnol.* **17**, 1030–2.

Tabb, D. L., C. Narasimhan, M. B. Strader, and R. L. Hettich. 2005a. "DBDigger: Reorganized Proteomic Database Identification That Improves Flexibility and Speed," *Anal. Chem.* **77**, 2464–2474.

Tabb, D. L., M. R. Thompson, G. Khalsa-Moyers, N. C. VerBerkmoes, and W. H. McDonald. 2005b. "MS2Grouper: group assessment and synthetic replacement of duplicate proteomic tandem mass spectra," *J Am Soc Mass Spectrom*. **16**, 1250–61.

Washburn, M. P., D. Wolters, and J. R. Yates III. 2001. "Large-scale analysis of the yeast proteome by multidimensional protein identification technology," *Nat Biotechnol.* **19**, 242–7.

Wolters, D. A., M. P. Washburn, and J. R. Yates, 3rd. 2001. "An automated multidimensional protein identification technology for shotgun proteomics," *Anal Chem.* **73**, 5683–90.

# Radioimmunotherapy Using Oxide Nanoparticles: Radionuclide Containment and Mitigation of Normal Tissue Toxicity

A. J. Rondinone,[1] S. Dai,[1] S. Mirzadeh,[2] and S. J. Kennel[3]
[1]*Chemical Sciences Division*
[2]*Nuclear Medicine Group*
[3]*UT-Medical Center, Knoxville*

Radionuclides with specific emission properties can be incorporated into metal-chalcogenide and metal-oxide nanoparticles. Coupled to antibodies, these conjugates could be injected into the bloodstream to target and destroy non-solid tumors or target organs for radioimaging. In the first year of this project, two types of radioactive nanoparticles, CdTe:$^{125m}$Te and $Y_2O_3$:$^{170}$Tm, were synthesized and coupled to antibodies specific to murine epithelial lung tissue. The nanoparticles successfully target the lung tissue in vivo. Some leaching of the radioisotope was observed. The coming year will explore other types of nanoparticles (other crystal chemistries) in order to minimize leaching.

Nanoparticles have been shown to couple to proteins, and the resulting conjugates may find applications as targeted drug delivery systems or medical imaging diagnostic tools (Tiefenauer et al. 1993; Frey 1999; Akerman et al. 2002; Wang et al. 2002; Gao et al. 2004). These conjugates could be injected into the bloodstream to target and destroy non-solid tumors or target organs for single photon emission computed tomography (SPECT) and positron emission tomography (PET) imaging [for a review of small molecule analogs (Goldenberg 2002)]. The nanoparticle-based drugs may also mitigate unintentional radiotoxic effects by effectively sequestering and retaining the radionuclides and daughter products.

CdTe nanoparticles were selected for the first experiments because the techniques for synthesizing CdTe nanoparticles are well developed and the surfaces can be easily modified to allow for protein coupling. The CdTe nanoparticles can be doped with small quantities of the radioisotope $^{125m}$Te ($t_{1/2}$ = 58 days), which emits low-energy 35.5-keV γ-rays with no complicating beta or alpha emission, thus allowing for verification of antibody performance and nanoparticle fate within the test mice.

Cadmium telluride nanoparticles doped with $^{125m}$Te were prepared based on the Peng method (Peng et al. 2001) in which CdO reacts with $^{125m}$Te metal within trioctylphosphine micelles at 250ºC. A reaction time of 5 min affords homogeneous and unaggregated 5-nm-diam nanoparticles. The CdTe nanoparticle surfaces were derivatized by mercaptoacetic acid (Wuister et al. 2003).

The surface-derivatized CdTe nanoparticles were reacted with the targeting antibodies (murine lung mouse antibodies, mAB 201B) using traditional protein coupling chemistry (Wang 2002). The CdTe-antibody conjugates were then purified by gel filtration and column chromatography. A typical radiography gel was employed to determine the fractions of crosslinked antibody, heavy antibody-nanoparticle conjugates, and other impurities. The 200 kD fraction (one antibody plus one nanoparticle) was selected from the gel and injected into Balb/c female mice for in vivo testing. The mice were sacrificed after 2 hours. Biodistribution analysis was performed by vivisection and $^{125m}$Te counting of organs. Radioactivity in the skin, muscle, liver, spleen, kidney, intestines, heart, lung, and blood was determined. For CdTe, approximately 60% of the injected dose targets the correct organ. For $Y_2O_3$, around 25% of the injected dose reached the target organ. Leaching was observed for some longer experiments (5 days post injection); however, that was not unexpected for these nanoparticle as they were selected for surface chemistry, not solubility.

FY 2006 will focus on the mitigation of leaching through the selection of less soluble nanoparticles. Candidate materials include CdTe/ZnS, $ZrO_2$, and $Al_2O_3$.

This project will benefit both DOE and the National Institutes of Health. The techniques developed here will have direct application to SPECT and PET imaging by providing a new delivery medium for radionuclides. The nanoparticle-based delivery approach may also have specific application in lymphoma treatment, by allowing heavier and more toxic alpha-emitting metals to be delivered safely within a patient.

## References

Akerman, M. E. et al. 2002. "Nanocrystal targeting in vivo." *Proceedings of the National Academy of Sciences of the United States of America* **99**(20): 12617–12621.

Frey, A. et al. 1999. "Immunization of mice with peptomers covalently coupled to aluminum oxide nanoparticles." *Vaccine* **17**(23–24), 3007–3019.

Gao, X. H. et al. 2004. "In vivo cancer targeting and imaging with semiconductor quantum dots." *Nature Biotechnology* **22**(8), 969–976.

Goldenberg, D. M. 2002. "Targeted therapy of cancer with radiolabeled antibodies." *Journal of Nuclear Medicine* **43**(5), 693–713.

Peng, Z. A. et al. 2001. "Formation of high-quality CdTe, CdSe, and CdS nanocrystals using CdO as precursor." *Journal of the American Chemical Society* **123**(1), 183–184.

Tiefenauer, L. X. 1993. "Antibody Magnetite Nanoparticles - in-Vitro Characterization of a Potential Tumor-Specific Contrast Agent for Magnetic-Resonance-Imaging." *Bioconjugate Chemistry* **4**(5), 347–352.

Wang, S. P. et al. 2002. "Antigen/antibody immunocomplex from CdTe nanoparticle bioconjugates." *Nano Letters* **2**(8), 817–822.

Wuister, S. F. et al. 2003. "Highly luminescent water-soluble CdTe quantum dots." *Nano Letters* **3**(4), 503–507.

# Imaging Molecules, Active Sites, and Reactions on Nanocatalysts

S. H. Overbury,[1] A. P. Baddorf,[2] S. V. Kalinin,[2] V. Meunier,[3] D. R. Mullins,[1] J. Zhou[1]
[1]*Chemical Sciences Division,*
[2]*Condensed Matter Sciences Division,*
[3]*Computer Science and Mathematics Division*

The promise of nanoscale materials science is universally recognized in the realm of catalysis, a trillion dollar industry. With rapid improvements in imaging capabilities and computational power, we now have the potential to observe and model individual molecules on single clusters of a supported catalyst. In this project we are taking advantage of the sensitivity of scanning tunneling microscopy to study individual molecules and electronic orbitals, interpreted with the aid of high-performance computation. The goal is a picture of the active sites, reaction pathways, and energetics of catalytic processes of metal particles on oxide supports.

The objective is to demonstrate and develop at ORNL the technique of scanning microscopy for imaging molecular processes at surfaces. This technique promises the ability to directly image the elementary steps that occur on a heterogeneous catalyst surface: adsorption, migration, bonding, and reaction.

Adsorption and reaction of selected molecules on a $TiO_2$(110) surface and on metal clusters supported on the $TiO_2$ are being directly imaged in controlled ultrahigh-vacuum environment by scanning tunneling microscopy (STM) using a new Omicron variable temperature microscope in the CMSD. Computational modeling for interpretation is performed in the CSMD using first-principles density functional theory implemented at ORNL's supercomputing center. High-resolution atomic images of $TiO_2$ have been obtained. Oxygen vacancies are observed, along with extended defect structures. A new model is proposed for certain defects which is based upon $Ti_2O$ clusters bonded between surface anion rows and is confirmed by computation. Theoretical estimates of the defect energy and its dependence upon structural details were obtained. Vapor deposition of Au and Pd particles was examined. Control of the metal cluster deposition is crucial, since the catalytic activity may be highly dependent on cluster size and morphology. Factors controlling Pd particle size during deposition and thermal processing were explored and found to exhibit self-limiting growth. Several catalytically interesting molecules on $TiO_2$ including $O_2$, CO, benzene, and phenol have been examined. $O_2$ is highly mobile at 300 K and clusters at surface oxygen vacancies but does not readily dissociate to fill the vacancies. Benzene adsorption has been studied at temperatures between room temperature and 25 K. Even at the lowest temperature, the benzene is apparently mobile along rows but does not readily cross anion rows. Computation supports a relatively strong adsorption energy of 64 kJ/mole, and a diffusion barrier of about 10 kJ/mole. The computed most stable bonding configuration shows benzene interacting with the surface through its $\pi$ system and adsorbed between anion rows. The computed barrier for the benzene to rotate about its $C_6$ axis is substantial but does not preclude rapid rotating moving about the axis, even at low temperature. This suggests that the atoms of the molecules could not be resolved and the molecule should appear torroidal rather than hexagonal. Adsorption of phenol is expected to differ considerably from benzene. The presence of the –OH functionality should enhance interactions with the surface, alter mobility, and enhance dissociative adsorption via a phenoxy adsorbate. Initial experimental support these expectations.

The approach and goals of this project are well matched to those of a recent Chemical Sciences call for proposals in "Chemical Imaging." It fits well with goals of the ORNL's Center for Nanoscale Materials Science. We are meeting the challenge of the DOE Workshop Report on Opportunities for Catalysis in the 21st Century in May 2003, "To establish, using the latest in characterization diagnostics, firm relationships between catalyst structure, rates, and selectivity of elementary reactions steps."

# Mass Spectrometry Beyond 100 Kilodaltons: A New Generation of Mass Spectrometers to Solve a New Generation of Problems

P. T. A. Reilly, W. B. Whitten, and R. S. Foote
*Chemical Sciences Division*

Mass spectral measurements beyond 100 kilodaltons have been made previously; however, resolution and sensitivity are poor. Two fundamental problems set this limit—the tremendous kinetic energy imparted to the high mass species during expansion into vacuum and large ion detection. We have developed a reverse jet–based inlet to reduce the expansion-induced kinetic energy and a detector that thermally vaporizes and fragments the massive charged species and subsequently ionizes the fragments for on-the-fly detection. These technological advances are now being integrated with a frequency-variable digital ion trap to create a mass spectrometer with an essentially unlimited mass range capable of $MS^n$.

The objective of this project is to produce a mass spectrometer capable of high-resolution mass measurement between 1 and $10^{14}$ daltons (Da). This instrument will be able to isolate a particular mass-to-charge ratio from a background of large ions, dissociate it, and measure the mass spectrum of the fragment ions to yield an identifiable signature of the analyte.

Our approach is to aerodynamically create a well-collimated beam of charged particles in vacuum. We then pass that particle beam through a reverse jet to slow it down using the same forces that accelerated it. The slowed charged species are recollimated and further slowed in a gas-filled digitally operated quadrupole ion guide. The thermalized large ions are then injected into a digitally operated ion trap whose potential frequency can be set to trap any ions in the proscribed mass range. The potential frequency can be swept and manipulated to measure the mass-to-charge ratio of the ions in the trap or isolate specific ions. The isolated ions can then be fragmented by a variety of techniques, whereupon the mass spectrum of the fragment ions can be measured to yield an identifiable mass spectrum. The large ions ejected from the trap are impacted into a filament-heated cup for vaporization. The vapors then expand into an electron impact ionization source to produce small positive ions that are extracted and detected by an electron multiplier. Charged species are detected in real time as they are ejected from the mass spectrometer.

To date, we have designed, built, and demonstrated both the kinetic energy reducing inlet for introducing kinetically thermalized massive ions into a mass spectrometer and the large ion detector capable of detecting individual ions above 100 KDa. The digital ion trap has been developed elsewhere. We are now integrating the inlet, digital ion trap, and detector to produce the previously described mass spectrometer. Once completed, the mass spectrometer will be demonstrated using known analytes.

The benefits of this technology are enormous and difficult to define with foresight because of the large number of areas where it will have an impact. For example, this instrument should be able to identify, characterize, and quantify biological species such as viruses in complex media such as blood fractions. If successful, it will markedly increase the rate of antiviral production. Whole bacteria could be studied. Proteomes could be completely characterized and quantified as a function of environmental factors. The full impact of this technology is hinted at by comparison with the development of electrospray and MALDI ionization. That technology extended the range of mass spectrometry from $10^3$ to $10^5$ Da and enable detailed study of biochemistry. It was one of the key reasons for the tremendous medical advances in the past 20 years. Our technology extends the mass range much further to $10^{14}$ Da. It will enable the detailed study of biology. Its impact has yet to be defined; however, it is certain that it will greatly benefit many of the programs sponsored by DOE, DOD, NIH, and DHS.

# Fog Vortices with Electrospray Mass Spectrometry for Detection of Chemical and Biological Agents

P. J. Todd, K. J. Hart, and M. B. Wise
*Chemical Sciences Division*

Rapid, reliable, and sensitive biological agent detection remains a high priority for the Departments of Defense and Homeland Security. This project focuses on development of a sampling system ideally suited for use with operational and emerging mass spectral analytical methods. The primary objective of the first part of this proposal—an aerosol collection system based on artificial fog—displays significant improvement in sample collection time and bioagent detection sensitivity. Fog as a collection medium decreases the cost, complexity, weight, and power requirements of biogent collection, while delivering the collected agent in fluid form for on-line workup and analysis. The second task involves evaluation and integration of a single-station liquid sample cleanup and handling systems to marry the output of fog collection with liquid-based electrospray spectrometric and MS/MS methods.

In simple terms, the goals of this project have been (a) to evaluate and optimize fog as a collection medium for biological and chemical warfare agents, and (b) to integrate the fog collection system with an electrospray mass spectrometer detector system. Evaluation of fog consists of determining the value of appropriate sampling air speed, fog density and particle size, mixing time, collection efficiency and power consumption.

It is tempting to think there is one optimal set of parameters, but in fact, the various parameters are not orthogonal; a fog collection system must be optimized for the particular environment. For example, with a mobile sampling system, the figures of merit are minimized weight, power, and water consumption. For a standing system, such as at a transportation portal, the figures of merit are sampling rate and efficiency. The approach we have taken has been to construct a prototype fog collection system, and then, using surrogates, measure the relative effect of different parameters on the efficiency of the system.

The prototype system consists of a standard fog sampling system, as used for cloud measurement, but modified for using fog as a collection medium. In simple terms, this is a 6-in.-diam plastic pipe 2 m long with a variable speed fan at the exhaust and a fog intake at the opposite end of the pipe. Air is sucked into the system via a Venturi eductor. Sets of 12.5-mm- and 1-mm-diam polytetrafluoroethylene (PTFE) rods act as large and small fog droplet collectors. This system can sample air at speeds up to 4 $m^3$/min, with a power consumption of about 100 W; this sampling rate is about 4× greater than the DoD specification of 1 $m^3$/min at a power consumption about 10% of existing systems. Under these conditions, and with a mixing time of about 100 ms, about 20% of an albumen sample is collected. By slowing the air sampling rate, and thus increasing the mixing time, this efficiency can be increased to nearly 100%. Mixing time can also be increased by increasing the length of pipe, as well as by modifications of the Venturi educter system.

Inexpensive and efficient sampling is needed to take full advantage of the sensitivity and specificity of mass spectral methods. Fog-based mass spectrometry looks to be at least one cornerstone of a broad program of chemical surveillance necessary for homeland security. The system may also have broad applications to environmental monitoring in the workplace, particularly in DOE fabrications sites, such as Y-12, mainly because of fog's affinity for dust and the very toxic materials employed at these sites.

# *Chemical Sciences and Technology*

# *Seed Money Fund*

# Metallic Nanofuels for Vehicles

B. G. Sumpter,[1] S. D. Labinov,[2] D. W. Noid,[1] D. B. Beach[3]
[1]*Computer Science and Mathematics Division*
[2]*Engineering Science and Technology Division*
[3]*Chemical Sciences Division*

This proposal addressed the concept of novel, renewable, high-energy-density, non-emission fuels for vehicles based on clusters of metallic nanoparticles and the experimental proof-of-principles of the outstanding characteristics of the combustion of these fuels. Our results clearly show that due to the high surface-to-volume ratio typical of nanoparticles, complete and fast oxidation, ~500-ms combustion time, occurs at temperatures of 1000–1200 K, completely in the condensed phase. The combustion process leads to near-complete retention of the combustion products on a substrate (estimated at 93% complete) and effectively avoids pollution of the air by nitrogen oxides. The combusted products can be effectively reduced back to iron with conservation of the nanostructure using flowing hydrogen at T = 400°C. We have been successful in developing this new direction by employing the joint efforts of specialists in chemistry, solid-state physics, energy, transportation, computation, and mathematics.

The problem addressed by this proposal is that of an alternative energy supply system for vehicles that is renewable and nonpolluting and has a high energy density. Limited reserves of liquid fossil fuel, security issues due to foreign oil dependence, and the air pollution caused by the burning of fossil fuels are the major drivers in the search for alternative fuels for transportation. We propose the use of engineered clusters of metallic nanoparticles as a fuel for vehicles. When compared to conventional liquids, this metallic fuel features greater energy capacity per volumetric unit, lower flammability, is virtually explosion-proof, and does not require any special storage conditions. The combustion products of the metals are solid oxides that can easily be stored and transported to reduction facilities or directly reduced/recycled as part of the engine utilizing the energy produced. Metallic fuel, in spite of all the advantages just mentioned, has not been used in vehicles with the exception for solid-propellant rocket boosters. Certain unique aspects of metal combustion account for this fact. The process of metal oxidation with gaseous oxygen (air) is accompanied by the formation on the metal surface of an oxide film that prevents oxygen molecules from entering into the zone of reaction. The passivating action of the film is increased with increasing film thickness. To avoid this phenomenon, the temperature of reaction has to be above the temperature for oxide film evaporation, about 2500–3000 K for the majority of metals. At this temperature, metal evaporation takes place on the surface and the oxidation reaction progresses in the gas phase. Outside the high-temperature zone of combustion, the metal oxide is condensed and solidifies, forming particles of solid ash which are carried-over by the air flow and deposited on the walls of a combustion chamber and other parts of an engine. Obviously, such a fuel is unfit for any conventional engine. The high temperature of metal combustion contributes to intensive formation of nitrogen oxides in the heated air, thus adding to atmospheric pollution. Also, there are few structural materials that can stand the high temperature of metal combustion. In summary, the following problems have not yet been solved: (a) the control of the metallic fuel combustion process; (b) the quick decrease or increase of released heat quantity depending on engine load; and (c) systems providing for fuel delivery to a combustion chamber and for ash removal.

## Objective

Our proposed solution to the problems detailed in the body of the report is to use an engineered metallic fuel cluster composed of individual nanoparticles. The underlying basis for this approach is that experimental evidence suggests that the ignition and combustion temperature of metallic particles decreases rapidly with decreasing particle size, while the speed of combustion and intensity of heat release are increased. These desired effects are primarily due to the fact that as the particle size decreases, the surface-to-volume ratio rapidly increases. A cluster of nanoparticles should thus be capable of providing the desired combustion properties of intensive and rapid heat release but occur at temperatures below 1600 K in the solid state without significant production of volatile species. The goal of this project was to experimentally verify and test this fundamental hypothesis.

## Technical Approach

An experimental apparatus for examining the peak combustion temperature of an engineered cluster of metallic iron nanoparticles was designed (Fig. 1). Following combustion of the metal cluster, the cluster can be removed and examined via microscopy or X-ray diffraction to determine if the combustion produced significant amounts of volatile products instead of occurring mainly in the solid/condensed phase. The approximate fuel cluster size and shape to achieve the necessary heat flow was determined from computation and modeling, and a method for experimentally producing this thin disk-shaped pellet composed of iron nano-particles was designed. The experimental method employed was relatively simple, using commercial-grade iron nanoparticles (a TEM of the iron nanoparticles is shown in Fig. 1; diameters of the particles are ~50 nm), which were sintered on a glass substrate using magnetic forces. These iron clusters consisted of ~15 mg/pellet, giving a disk ~1 mm in height and 2 cm in diameter. The glass slide containing the iron cluster can be mounted in the device (Fig. 1) and placed into an infrared temperature sensor based on heterodyne or radiometric measurements to determine the combustion temperature. The infrared temperature sensor was constructed to specifically monitor time-dependent temperature changes on a sample. This sensor performed two different forms of temperature measurement; one was from a heterodyne measurement of power over a narrow wavelength band (at 10.6 microns) and the other from a radiometric measurement over a broad wavelength band (from 1 to 14 microns). The sensor involves the mixing of infrared radiation from either the blackbody source or a sample and a $CO_2$ laser tuned to the 10.6-micron wavelength. Because the blackbody source operates at a set temperature, the detector's response can be calibrated for absolute temperature measurements. The focusing optics was aligned through the 2-millimeter aperture that was replaced with a sample for performing measurements. The high-speed response of the Mercury-Cadmium-Telluride (MCT) detector and the integration nature of heterodyne detection allowed measurements to be performed at speeds up to 1 millisecond. By simply turning off the laser, the device can be used as a radiometric temperature sensor. Again the blackbody source was used for performing absolute temperature measurements but required integration over the systems wavelength sensitivity. This was primarily the detector's sensitivity as supplied by the manufacturer.

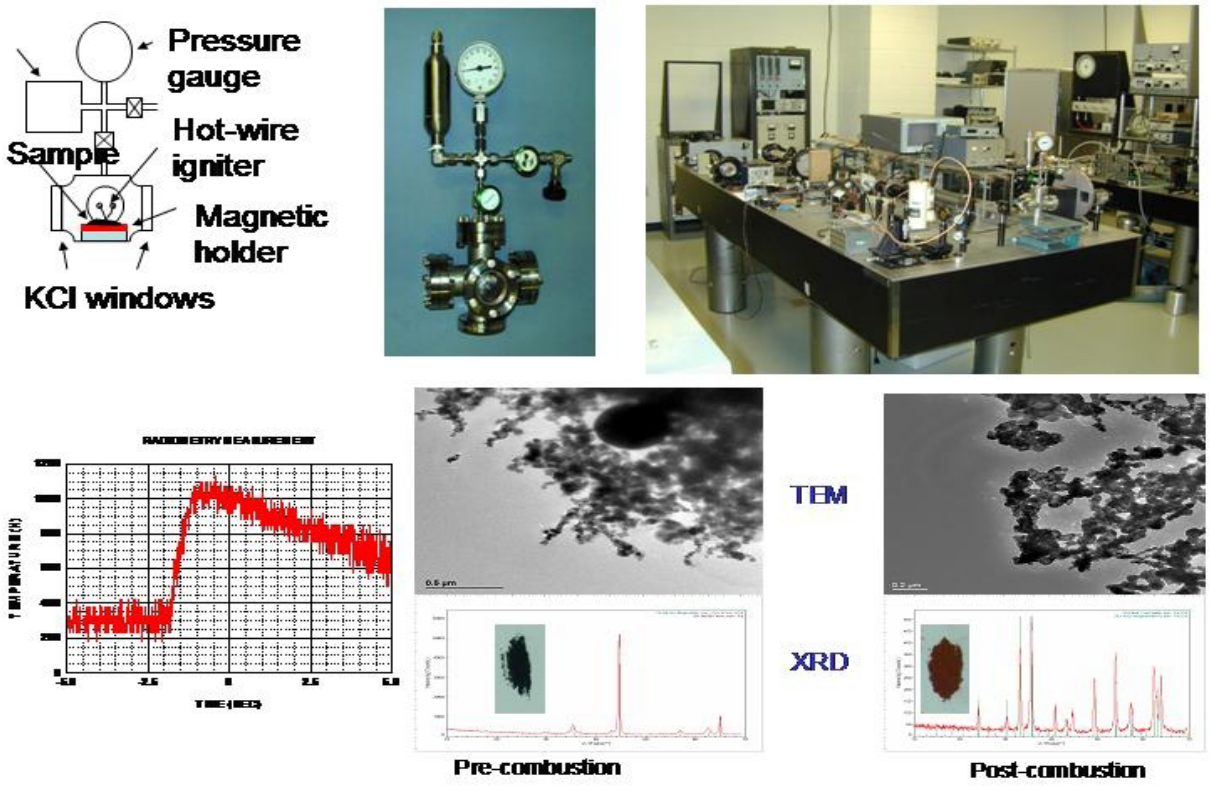


*Fig. 1. Experimental apparatus and results for combustion of iron nanoparticle–based clusters: Top panel shows a schematic and photograph of the apparatus designed to perform combustion and reduction and the laser-based heterodyne device for measuring the temperature of combustion. Bottom panel shows the results obtained from the temperature measurements in radiometry mode (left) and TEM of the iron nanoparticles revealing particles ~50 nm in diameter and after combustion. The X-ray diffraction patterns obtained for the iron nanoparticle cluster before and after combustion are also shown in this panel.*

## Results

Multiple samples were tested, and in all cases, combustion proceeded rapidly (~500 milliseconds), generating peak temperatures between 1000 and 1200 K, without the observable production of volatile products. The reproducibility of the process is very good, and since the temperature is well below that required to form NOx, it is reasonable to assume there is virtually none formed from the combustion process. Visual observations of the combustion process were quite dramatic as one can clearly follow the wave front of combustion through the cluster by noting the change in color which goes from black to red. (Figure 1 shows a before-and-after picture of the iron particles that were part of the cluster.) As mentioned, there was no observable smoke produced from this process, as opposed to the combustion of magnesium or steel wool, which indicates very little production of volatile species. Additional and more substantial evidence for solid-state combustion was obtained from X-ray diffraction of the iron cluster before and after combustion (Fig. 1) combined with analytical mass determination. These results clearly show that the combustion process oxidizes 93% of the iron into primarily hematite ($Fe_2O_3$) and maghemite, only leaving ~7% of the iron in its original state (seen in the X-ray diffraction patterns, peaks at green and blue and supported by analytical mass determination). Chemical reduction of the combusted metallic cluster was successful by using flowing hydrogen gas in a chamber at 400ºC as schematically shown in Fig. 2. This reduction also preserved the original nanostructure, and the reduced material could be used again in a combustion process, yielding similar results to the first combustion cycle. This result demonstrates the possibility for efficient regeneration of the nanostructured metallic fuel.

## Summary and Proposed Future Work

Clearly, proof-of-principles for the solid-state combustion of a cluster of iron on a reasonable time scale and with the production of an intense source of heat now has been demonstrated. We have also demonstrated the solid state reduction of the oxidized iron nanoparticle–based cluster back to its original nanostructured state, thereby allowing the potential for fuel recycling (a regenerable energy carrier). Theoretic and mathematic modeling has been successful for optimizing the size and shape of the metallic nanocluster and has proven to agree with the experimental results. The following has been successfully demonstrated:

- Demonstrated solid-state combustion of a cluster composed of 50-nm Fe particles
- Peak temperature below 1400 K
- Nearly complete combustion >95%
- ~0.5-sec combustion time for 15-mg pellets
- Combustion time variable from milliseconds to seconds by cluster formation
- Theoretical/mathematical model for optimizing the size and shape of the metallic cluster
- Combusted particles reduced with $H_2$ and passivated with a thin oxide coating

Still a number of crucial experiments and calculations remain:

1. Examination of the combustion process at elevated temperatures and pressures common in combustion chambers as well as determination of how many cycles of oxidation-reduction can be carried out on the same nanostructure metallic sample
2. Investigation of other metals and alloys with the consideration of task I above. For this task, we will need to implement advanced computational first-principles approaches to efficiently study the behavior of elements such as aluminum and boron as these particular elements offer considerable potential in terms of higher energy density, but experimentally it may be more difficult to chemically reduce and/or nanostructure them
3. Design of a simple external combustion chamber

Ongoing work via a different funding vehicle is currently addressing some of these issues.

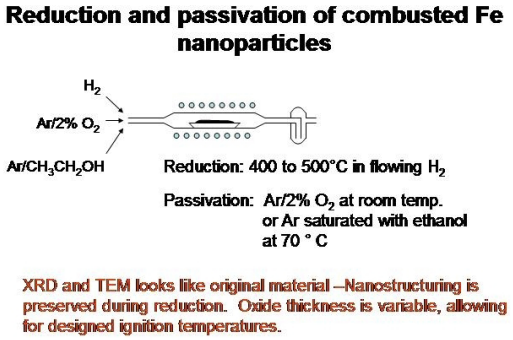


*Fig. 2. Schematic illustrating the method used to reduce the oxidized iron nanoparticle–based fuel cluster back to its near-original state.*

# Hydrogen Production From Naturally Occurring Iron Silicates

D. J. Wesolowski,[1] J. G. Blencoe,[1] L. M. Anovitz,[1] E. M. Ripley,[2] and J. S. Beard[3]
[1]*Chemical Sciences Division*
[2]*Indiana University, Bloomington*
[3]*Virginia Museum of Natural History, Martinsville, Virginia*

This project focused on the evaluation of a variety of naturally occurring rocks and minerals as potential sources of hydrogen, via the reaction of water with Fe(II) contained in iron-silicate minerals. Rocks rich in reduced iron make up the bulk of the Earth's crust beneath the major oceans, as well as in localized terrestrial deposits such as ultramafic (very high Mg+Fe) igneous intrusions and sedimentary iron formations. Samples of Fe(II)-rich rocks from the Duluth Complex, an intrusion exposed for hundreds of miles along the shores of Lake Superior, and from the Biwabik Iron Formation, the principal source of iron ores in the Mesabi Iron Range of northern Minnesota, as well as selected high-Fe(II) minerals (olivine, siderite), were reacted with water at 200–350ºC in a specially designed pressure vessel containing a hydrogen-permeable membrane. The rate of hydrygen gas evolution was continuously monitored for periods of days to weeks. All materials tested produced measurable hydrogen, though the rates were low. Greenalite and siderite, Fe(II)-rich minerals in sedimentary iron formations, as well as Fe(II)-rich olivine, abundant in certain ultramafic igneous rocks, proved to be the most reactive phases, producing significant quantities of hydrogen at moderate temperatures. This research will help spark discussion among industry and the scientific community as to whether hydrogen might be considered a "fuel" (like oil, gas, coal and uranium) rather than simply an "energy-carrier" and that a truly enormous amount of hydrogen might be produced from naturally occurring rocks under ideal conditions.

## Introduction

Natural emanations of $H_2$-rich gas have been recorded from a number of terrestrial sites worldwide (Neal and Stanger 1983; Abrajano et al. 1988; Fritz et al. 1992; Peretti et al. 1992; Kiyosu and Okamoto 1998). In nearly all cases, the $H_2$ has been shown to result from the reaction at temperatures of 60–160ºC of groundwater with "ultramafic" rocks containing abundant Fe(II)-bearing silicate minerals. In recent years, the discovery of high concentrations of dissolved hydrogen (up to 0.02 moles per kilogram of water) and methane (up to 0.001 moles per kilogram of water) in seafloor hydrothermal vent fluids (Ding et al. 2001; Holm and Charlou 2001; Kelley et al. 1999; Charlou et al. 2002) have established abiogenic releases of $H_2$ and $CH_4$ to the atmosphere and hydrosphere as a major factor in global elemental cycling. Kelley and Früh-Green (1999) have estimated that seafloor hydrothermal systems, with vent $H_2$+$CH_4$–rich fluids at temperatures of 300–400ºC and pressures of several hundred atmospheres, represent an immense reservoir (approximately 1019 g) of abiogenic methane. Geological relationships, isotopic and chemical characteristics of the produced methane, and direct water-rock experimental studies (Janecky and Seyfried 1986; Berndt et al. 1996; Horita and Berndt 1999) suggest that the bulk of methane in both terrestrial and seafloor vents results from reduction of dissolved carbonate by molecular hydrogen produced from the reaction of water with Fe(II)-bearing silicates. Curiously, the excitement over abiogenic hydrocarbon production (Gold and Soter, 1982) via inorganic processes appears to have overshadowed the recognition of water-rock interaction as a source of enormous quantities of hydrogen. For example, if the fluids venting from the Rainbow seafloor hydrothermal field along the Mid-Atlantic Ridge (365ºC, 0.016 molal $H_2$, Charlou et al. 2002) were cooled to room temperature, the temperature-dependent solubility of this gas would result in an $H_{2,g}$ overpressure of over 20 atmospheres (ca. 300 psi). Theoretical calculations (Wetzel and Shock 2000) indicate that at low water/rock ratios, alteration of ocean peridotites at 350–400ºC could produce fluids containing ten times as much dissolved hydrogen as found in the Rainbow fluids. Therefore, it is not unreasonable to speculate that direct extraction of hydrogen from subseafloor circulation systems, either natural or engineered, might be feasible in the future. In either case, basic understanding the detailed reaction rates and mechanisms for various minerals and rock types will become a critical need. An exciting new discovery by Kelley et al. (2001) indicates that fluids interacting with a subocean peridotite in the mid-Atlantic at only 40–75ºC are producing hydrogen concentrations up to 0.00045 molal, and these might represent minimum values, due to rapid metabolism of free hydrogen by microbial consortia.

To our knowledge, only one research group (Goebel et al. 1984; Angino et al. 1984; Coveney et al. 1987), investigating $H_2/N_2$-rich gas seepages along the subsurface extension of the North American Mid-Continent Rift System in Kansas, has urged oil and gas companies to consider exploratory drilling and hydrofracturing to identify natural accumulations of $H_{2,g}$ as a potential energy source. Though these authors demonstrate that many methane-dominated natural gas accumulations contain abundant free hydrogen, most likely derived abiogenically and independently of the organically derived hydrocarbons, it is likely that natural accumulations of pure hydrogen gas will be rare, due to the high reactivity of this gas and its extremely high diffusion rates, even through unfractured and highly impermeable rocks. Rather than advocating the search for natural accumulations of exploitable hydrogen gas, we suggest that well-established processes such as hydrofracturing and water/steam injection into subsurface formations, as well as mining and above-ground ore processing of high Fe-silicate rocks, might prove economical at some future date. Using such techniques, nearly carbon-free $H_{2,g}$ could be produced, or alternatively, $CO_2$ could be recycled into burnable $CH_4 + H_2$ fuel by reacting the rocks with hot flue gases in the presence of a suitable $H_2 + CO_2 \rightarrow CH_4$ catalyst (Horita and Berndt 1999), similar to the process that is obviously active in seafloor hydrothermal systems.

## Technical Approach

It is clear from the literature cited above that hydrogen is readily produced in various geologic settings via reaction of water with Fe(II)-silicates from near-surface conditions to temperatures and pressures in excess of 400ºC and 500 atmospheres. The most abundant Fe(II)-bearing silicates in oceanic peridotites as well as in continental ultramafic rocks are Fe-Mg solid solutions of olivine {fayalite-forsterite — $(Fe,Mg)_2SiO_4$} and orthopyroxene {ferrosilite-enstatite — $(Fe,Mg)SiO_3$}, with typical Fe/(Fe + Mg) ratios in the range of about 0.15 or less. McCollom and Seewald (2001) demonstrated that reaction of 15.6 g of olivine [Fe/(Fe + Mg) ratio of 0.12] with 38.6 g of water at 300ºC and 350 atmospheres generated a solution containing 0.08 moles of dissolved $H_2$ per kilogram of water after 600 h, via the reaction

$$Fe_{.24}Mg_{1.76}SiO_{4,olivine} + 1.34H_2O \leftrightarrow$$
$$0.25Mg_6Si_4O_{10}(OH)_{8,serpentine} + 0.26Mg(OH)_{2,brucite} +$$
$$0.08Fe_3O_{4,magnetite} + 0.08H_2 \quad . \qquad (1)$$

This represents conversion of about 6% of the available Fe(II) to Fe(III) in the form of the mineral magnetite — Fe(II)Fe(III)2O4, with the concomitant reduction of water to hydrogen. "Serpentinization" via such reactions is the typical mode of alteration of Mg-rich olivine-pyroxene rocks (peridotite, dunite, ophiolite, etc.), which form the bulk of the deep oceanic crust and which are abundant in many near-surface geological environments, both on the continents and near the seafloor. There have been very few experimental studies of the rate of production of hydrogen from such reactions, and it is not known how temperature, pressure, particle size, or seeding with reaction products will affect such rates or the absolute quantities of hydrogen that can be produced. Large quantities of ultramafic rocks in shallow terrestrial environments exhibit much higher Fe/(Fe+Mg) ratios. A typical example is the Duluth Complex, which outcrops along a 160- by 30-mile portion of the north shore of Lake Superior in the Mid-Continent Rift System in northern Minnesota. Olivines in this complex average 30–50 mole % Fe(II), and pyroxenes 15–30% (Snyder 1959). Extremely large, high-iron ultramafic rock complexes occur throughout the world, such as the Stillwater Complex in Montana, the Muskox and Sudbury Complexes in Canada, the Bushveld Complex in South Africa, the Great Dike in Zimbabwe, and many large bodies in Russia, India, Europe, Asia and Australia.

Hydrogen-producing reactions of the pure Fe(II) end member olivine and orthopyroxene are

$$3Fe_2SiO_{4,fayalite} + 2H_2O \leftrightarrow 2Fe_3O_{4,magnetite} +$$
$$3SiO_{2,quartz} + 2H_{2,g} \qquad (2)$$

and

$$3FeSiO_{3,ferrosilite} + H_2O \leftrightarrow Fe_3O_{4,magnetite} + 3SiO_{2,quartz}$$
$$+ H_{2,g}. \qquad (3)$$

In addition to these igneous and metamorphic rocks which contain abundant anhydrous Fe(II)-silicates, the enormous sediment-hosted iron formations that formed as a result of seafloor venting of high Fe-Si fluids during the Archean period (ca. 2.2 billion years ago) contain many primary minerals that have the potential for hydrogen production. Space does not permit a detailed description of these deposits, which constitute the largest ore bodies in the world (Appel 1974; Klein 1974; Floran and Papike 1975, 1978; Gole 1981; Miyano 1982; Webb et al. 2003). Coincidentally, the Mesabi Iron Range, outcropping just north of the Duluth Complex in northern Minnesota, is one of the largest and best studied of these supergiant iron ore deposits. These stratiform orebodies, which can be hundreds of feet thick and outcrop over hundreds of miles, exhibit a range of mineralogies, only some of which constitute economic iron ores. The emerging consensus is that these deposits were originally laid down in the form of

amorphous or poorly crystalline silica and Fe(II)-silicates, which gradually crystallized to chert (microcrystalline quartz) and the Fe(II) minerals greenalite and minnesotaite. Unmetamorphosed iron formation typically contains 20–40 wt % Fe(II). Progressive metamorphism leads to the conversion of these phases to other Fe(II) silicates, including grunerite and more complex hydrous silicates. With further metamorphism, these rocks are driven to nearly pure quartz-magnetite rocks, via natural processes of hydrogen production such as

$$Fe_3Si_2O_5(OH)_{4,greenalite} \leftrightarrow H_2O + Fe_3O_{4,magnetite} + 2SiO_{2,quartz} + H_{2,g} \quad (4)$$

$$Fe_3Si_4O_{10}(OH)_{2,minnesotaite} \leftrightarrow Fe_3O_{4,magnetite} + 4SiO_{2,quartz} + H_{2,g} \quad (5)$$

$$3Fe_7Si_8O_{22}(OH)_{2,grunerite} + 4H_2O \leftrightarrow 7Fe_3O_{4,magnetite} + 24SiO_{2,quartz} + 7H_{2,g} \quad (6)$$

In order to assess the feasibility of hydrogen production from naturallyoccurring rocks and minerals, we conducted scoping studies using olivine concentrates from high-Fe(II) olivine-pyroxene rocks of the Duluth Complex and greenalite-minnesotaite-rich rocks from the Mesabi Iron Range. A pure mineral specimen of high Fe(II) olivine was also tested, as well a sample of pure Fe(II) carbonate (siderite), since this phase was found to react quickly when iron formation rocks were heated to temperatures in excess of 200ºC. Experiments were conducted in a pressure vessel fitted with a hydrogen-permeable $Pd_{75}Ag_{25}$ membrane connected to a manifold containing pressure tranducers enabling the precise and continous monitoring of the partial pressure of hydrogen within the reaction vessel as a function of time and temperature. The rocks and minerals, along with a known quantitity of liquid water, were placed in a Teflon or fused-silica cup (for experiments below and above 300ºC, respectively) and sealed in the pressure vessel prior to heating.

## Results and Discussion

Table 1summarizes all experimental results. Three powdered rock samples from the Biwabik iron formation were tested, as well as olivine-rich concentrates from two samples of peridotite (olivine-pyroxene rock) from the Duluth Complex. A hand-picked olivine concentrate containing 93 mole % $Fe_2SiO_4$ was also tested. The mineral lizardite, a polymorph of the "serpentine" product shown in reaction 1, was observed in the final run products from all tests of the olivine concentrates. In the iron formation samples, the most reactive minerals proved to be greenalite (reaction 4 above) and siderite, the latter mineral an Fe(II) carbonate that is commonly found in iron formations. Because of this, we also tested an artificial mixture of powdered siderite and low-iron olivine. As can be seen in Table 1, hydrogen was produced in all of the experiments, with the rate of production increasing with increasing temperature. Surprisingly, the pure olivine containing 93% $Fe_2SiO_4$ exhibited the lowest hydrogen production rates, with no hydrogen detected at temperatures below 273ºC. The highest production rates were observed for the mixture of siderite with low-iron olivine, and from one of the Duluth Complex olivine concentrates. The iron formation samples produced hydrogen at the lowest temperatures, but the production rate did not increase with increasing temperature as much as was the case for the olivine concentrates. In all experiments 1–10% of the total Fe(II) was converted to Fe(III), as determined from the cumulative hydrogen produced during the experiment. Magnetite was not detected as a run product, but the brown-yellow-red color of many of the run products and traces of FeOOH detected by XRD indicate that pure Fe(III) oxides were formed.

## Benefits

This study demonstrates that all Fe(II)-bearing rocks and minerals studied reacted with water to produce Fe(III) and hydrogen gas, at temperatures of 200–345ºC. Such temperatures are typical of seafloor hydrothermal vents and are also common in terrestrial rocks at depths of 10–30 thousand feet, depending on the local geothermal gradient. Such temperatures can be achieved at much shallower depths in areas of high heat flow and/or active terrestrial volcanism. Therefore, we have successfully demonstrated that hydrogen can be produced by the interaction of water with a variety of commonly occurring and abundant rock types. Because such rocks are extremely abundant worldwide, this represents a significant source of hydrogen. Total world energy consumption amounts to approximately 1018 BTU per year. The energy equivalent of the hydrogen that would be produced if just 2% of the Fe(II) contained in shallow terrestrial ultramafic igneous rocks that are readily accessible to mining and drilling were converted to hydrogen exceeds 1019 BTU. The world's known iron formations contain considerably less total Fe(II) content, but hydrogen can be extracted from them at lower temperatures, and the highest-grade Fe(II) silicate portions of these deposits have already been identified. The total Fe(II) contained in the shallow oceanic crust represents an essentially limitless supply of hydrogen, if practical methods of extracting this hydrogen can be developed. Localized regions of much-higher-than-average Fe(II) also occur in the oceanic crust, and these regions typically coincide with very high local geothermal gradients as well as seafloor hydrothermal

**Table 1. Summary of experimental results obtained in this study**

| Sample | Starting Composition (%) | Temperature (°C) | $H_2$ generation rate (psi/hour) | Duration | Comments |
|---|---|---|---|---|---|
| DDH 54-22<br>Interval 288-298<br>Biwabik Iron formation<br>50.01 grams solid,<br>28.0 grams $H_2O$<br>Ground to fine powder | Magnetite (8.7), hematite (1.6), quartz (31.4), minnesotaite (22.0), greenalite (17.8), stilpnomelane (1.1), ankerite (3.6), siderite (9.9), calcite (3.6) | 200<br>266<br>293 | Slight increase<br>0.005<br>0.0092 | Overnight<br>3 days<br>2 days | XRD analysis of starting material and run product indicates all siderite consumed, minnesotaite reduced 75% and greenalite reduced 25%. Starting material green, run product rust red. |
| DDH 189<br>Interval 1403<br>Olivine/pyroxene concentrate from Duluth Gabbro<br>20.08 grams solid,<br>40.2 grams $H_2O$<br>Ground to fine powder | Olivine is 35% fayalite, 65% forsterite. | 201<br>265<br>295<br>295 | None detected<br>0.11<br>0.143<br>0.039 | Overnight<br>3 days<br>4 days<br>4 days | Run product was black, emitting strong odor of $H_2S$. XRD analysis shows that a large amount of serpentine (lizardite, magnesium silicate hydroxide) formed during reaction. |
| DDH 86-19<br>Interval 434-444<br>Biwabik Iron Formation<br>20.12 grams solid<br>18.49 grams $H_2O$ | Magnetite (0.4), hematite (1.2), quartz (25.9), minnesotaite (13.3), stilpnomelane (19.3), chamosite (0.4), greenalite (12.0), talc (0.4), ankerite (2.5), siderite (20.4) | 264<br>264<br>296 | 0.0024<br>0.0015<br>0.0022 | 1 day<br>2 days<br>8 days | XRD analysis of starting material and run product indicates that a significant amount of the minnesotaite and nearly all of the siderite were consumed during the experiment, and significant ferric oxide formed. |
| DDH 7UL10<br>Interval 117-124.5<br>Biwabik Iron Formation<br>23.40 grams solid<br>25.70 grams $H_2O$ | Magnetite (20.1), quartz (21.6), minnesotaite (43.2), stilpnomelane (6.9), greenalite (2.1), talc (2.6), ankerite (0.3), siderite (3.6) | 200 | 0.0045 | 4 days | Run product includes a significant amount of very fine grained red powder. XRD analysis indicates that the red powder is mainly quartz and amorphous ferric oxides. |
| DDH 7UL10<br>Interval 117-124.5<br>Biwabik Iron Formation<br>19.90 grams solid<br>20.40 grams $H_2O$ | Same as above | 263<br>294 | 0.0026<br>0.0035 | 4 days<br>11 days | Same as above. Red, fine grained material contains detectable amounts of clays and zeolites |
| Hand-picked olivine grains from subseafloor peridotite<br>19.50 grams solid<br>19.66 grams $H_2O$<br>Coarsely ground | Fayalite 93%, Forsterite 7% solid solution | 202<br>249.4<br>314.6<br>344.7 | None detected<br>None detected<br>0.0011<br>0.0014 | Overnight<br>Overnight<br>1 day<br>5 days | Not analyzed |

vents, since the ultimate origin of the highest Fe(II) oceanic crust is the lower crust and upper mantle, exposed in areas of suboceanic volcanism and magma intrusion. Since hydrogen utilization is of current interest to the Department of Energy, this research suggests an important new line of investigation and a paradigm shift in the potential of this energy source.

## References


Abrajano, T. A., N. C. Struchio, J. K. Bohlke, G. L. Lyon, R. J. Poreda, and C. M. Stevens. 1988. "Methane-hydrogen gas seeps, Zambales ophiolite, Philippines: Deep or shallow origin?" *Chem. Geol.* **71**, 211–222.

Angino, E. E., R. M. Coveney, Jr., E. D. Goebel, E. J. Zeller, and G. Dreschhoff. 1984. "Hydrogen and nitrogen—origin, distribution and abundance, a followup," *Oil & Gas J.* Dec 3, 142–146.

Appel, P. U. 1974. "On an unmetamorphosed iron-formation in the early Precambrian of south-west Greenland," *Mineral. Deposita* **9**, 75–82.

Berndt, M. E., D. E. Allen, and W. E. Seyfried, Jr. 1996. "Reduction of $CO_2$ during serpentinization of olivine at 300ºC and 500 bar," *Geology* **24**, 351–354.

Charlou, J. L., J. P. Donval, Y. Fouguet, P. Jean-Baptiste, and N. Holm. 2002. "Geochemistry of high $H_2$ and $CH_4$ vent fluids issuing from ultramafic rocks at the Rainbow hydrothermal field (36º14'N, MAR)," *Chem. Geol.* **191**, 345–359.

Coveney, R. M., Jr., E. D. Goebel, E. J. Zeller, G. A. M. Dreschhoff, and E. E. Angino. 1987. "Serpentinization and the origin of hydrogen gas in Kansas," *AAPG Bull.* **71**, 39–48.

Ding, K., W. E. Seyfried, Jr., M. K. Tivey, and A. M. Bradley. 2001. "In situ measurement of dissolved $H_2$ and $H_2S$ in high-temperature hydrothermal vent fluids at the Main Endeavor Field, Juan de Fuca Ridge," *Earth Planet. Sci. Let.* **186**, 417–425.

Floran, R. J. and J. J. Papike. 1975. "Petrology of the low-grade rocks of the Gunflint Iron-Formation, Ontaria-Minnesota," *Geol. Soc. Am. Bull.* **86**, 1169–1190.

Floran, R. J. and J. J. Papike. 1978. "Mineralogy and petrology of the Gunflint iron formation, Minnesota-Ontario: Correlation of compositional and assemblage variations at low to moderate grade," *J. Petrol.* **19**, Part 2, 215–288.

Fritz, P., I. D. Clark, J-C. Fontes, M. J. Whiticar, and E. Faber. 1992. "Deuterium and $^{13}C$ evidence for low temperature production of hydrogen and methane in a highly alkaline groundwater environment in Oman," in *Water-Rock Interaction,* Y. K. Kharaka and A. S. Maest, eds., Proc. 7th Int. Symp. Water-Rock Int., A. A. Balkema, Rotterdam, volume 1, 793–796.

Goebel, E. D., R. M. Coveney, Jr., E. E. Angino, E. J. Zeller, and G. A. M. Dreschhoff. 1984. "Geology, composition, isotopes of naturally occurring $H_2/N_2$ rich gas from wells near Junction City, Kans," *Oil & Gas J.*, May 7, 215–222.

Gold, T. and S. Soter. 1982. "Abiogenic methane and the origin of petroleum," *Energy Explo. Exploit.* **1**, 89–104.

Gole, M. J. 1981. "Archean banded iron-formations, Yilgarn Block, Western Australia," *Econ. Geol.* **76**, 1954–1974.

Holm, N. G. and J. L. Charlou. 2001. "Initial indications of abiotic formation of hydrocarbons in the Rainbow ultramafic hydrothermal system, Mid-Atlantic Ridge," *Earth Planet. Sci. Let.* **191**, 1–8.

Horita, J. and M. E. Berndt. 1999. "Abiogenic methane formation and isotopic fractionation under hydrothermal conditions," *Science* **285**, 1055–1057.

Janecky, D. R. and W. E. Seyfried, Jr. 1986. "Hydrothermal serpentinization of peridotite within the oceanic crust: Experimental investigations of mineralogy and major element chemistry," *Geochim. Cosmochim. Acta* **50**, 1357–1378.

Kelley, D. S. and G. L. Früh-Green. 1999. "Abiogenic methane in deep-seated mid-ocean ridge environments: Insights from stable isotope analyses," *J. Geophys. Res*. **104** B5, 10439–10460.

Kelley, D. S., J. A. Karson, D. K. Blackman, G. L. Früh-Green, D. A. Butterfield, M. D. Lilley, E. J. Olson, M. O. Schrenk, K. K. Roe, G. T. Lebon, P. Rivizzigno, and the AT3-60 Shipboard Party. 2001. "An off-axis hydrothermal vent field near the Mid-Atlantic Ridge at 30ºN," *Nature* **412**, 145–149.

Kiyosu, Y. and Y. Okamoto. 1998. "Variation in fumarolic $H_2$ gas and volcanic activity at Nasudake in Japan," *J. Volcanology and Geotherm. Res.* **80**, 27–37.

Klein, C., Jr. 1974. "Greenalite, stilpnomelane, minnesotaite, crocidolite and carbonates in a very low-grade metamorphic Precambrian iron-formation," *Canadian Mineralogist* **12**, 475–498.

McCollom, T. M. and J. S. Seewald. 2001. "A reassessment of the potential for reduction of dissolved $CO_2$ to hydrocarbons during serpentinization of olivine," *Geochim. Cosmochim. Acta* **65**, 3769–3778.

Miyano, T. 1982. "Stilpnomelane, iron-rich mica, K-feldspar and hornblende in banded iron formation assemblages of the Dales Gorge member, Hamersley Group, Western Australia," *Canadian Mineralogist* **20**, 189–202.

Neal, C. and G. Stanger. 1983. "Hydrogen generation from mantle source rocks in Oman," *Earth Planet. Sci. Let.* **66**, 315–320.

Peretti, A., J. Dubessey, J. Mullis, B. R. Frost, and V. Trommsdorff. 1992. "Highly reducing conditions during Alpine metamorphism of the Malenco peridotite (Sondrio, northern Italy) indicated by mineral paragenesis and $H_2$ in fluid inclusions," *Contrib. Mineral. Petrol*. **112**, 329–340.

Snyder, J. L. 1959. "Distribution of certain elements in the Duluth complex," *Geochim. Cosmochim. Acta* **16**, 243–277.

Webb, A. D., G. R. Dickens, and N. H. S. Oliver. 2003. "From banded iron-formation to iron ore: geochemical and mineralogical constraints from across the Hamersley Province, Western Australia," *Chem. Geol.* **197**, 215–251.

Wetzel, L. R. and E. I. Shock. 2000. "Distinguishing ultramafic- from basalt-hosted submarine hydrothermal systems by comparing calculated vent fluid compositions," *Journal of Geophysical Research (Solid Earth)* **105**, issue B4, 8319–8340.

# Cyclopentadienyl Iron Clusters as Nanoscale Building Blocks for Multi-Electron Electrocatalysis

G. M. Brown, P. V. Bonnesen, and D. R. Mullins
*Chemical Sciences Division*

The goal of this research project is to gain an increased understanding of multielectron electrochemical reactions involving coupled electron transfer and atom transfer processes. A fundamental problem in electrochemistry is the design of electrodes to efficiently carry out processes in which atom transfer accompanies electron transfer, examples of which are the 4e reduction of oxygen to water in fuel cells or the 4e oxidation of water to oxygen in water electrolysis. Our approach to electrocatalysis involves the attachment of molecules that are selective for the reaction of interest in homogeneous solution to a conducting support. Redox active electron donors or acceptors that provide the multiple electron oxidizing or reducing equivalents at the required potential for near-thermodynamic reversibility are attached to the active catalyst site as well. This is a new approach to the design of electrocatalysis involving multielectron electrochemical reactions. The objective of this project was to apply this approach to the proof-of-principle design of a catalyst for the four-electron reduction of oxygen to water. We laid the groundwork for the synthesis of a catalyst based on a cobalt porphyrin coordination site for oxygen and four iron clusters as electron donors. Tetranuclear iron clusters based on the cyclopentadienylironcarbonyl tetramer, $[(\eta^5\text{-}C_5H_5)Fe(\mu_3\text{-}CO)]_4$, were attached or sorbed to the surface of carbon electrodes, and experiments were conducted to determine the oxidation state of the Fe during electrochemical experiments by in situ X-ray synchrotron spectroscopy methods.

## Introduction

A fundamental problem with fuel cells using oxygen as an oxidant is that the $O_2$ electrode is voltage limited. The cell voltage decreases rapidly from the theoretical value of 1.23 V as the current density increases. In all cases, the overpotential (voltage in excess of the thermodynamic potential) for the reduction of oxygen at operating currents is too high. This overpotential is caused by the slow electrochemical kinetics of oxygen reduction, due to the build-up of intermediate oxygen reduction products, and this overpotential represents an additional driving force needed to obtain significant currents in the cell. The result is a decrease in cell voltage, with a corresponding loss in efficiency. To carry out the oxygen reduction reaction at a significant current density somewhere near the reversible potential will require an electrocatalyst that can carry out multi-electron redox processes involving atom transfer as well as electron transfer.

The potential for the 4e reduction of $O_2$ is +1.23 V.

$$O_2 + 4e^- + 4H^+ \rightarrow 2H_2O \qquad E° = +1.23\ V$$

$$O_2 + 2e^- + 2H^+ \rightarrow H_2O_2 \qquad E° = +0.67\ V$$

$$O_2 + e^- + H^+ \rightarrow HO_2 \qquad E° = +0.12\ V$$

If reduction of oxygen occurs by a 2e reduction pathway to $H_2O_2$, which occurs at a much lower potential (0.67 V) than the 4e pathway, then the intermediate must be stabilized by coordination or otherwise bonding to the electrode or catalyst if the potential is going to be anywhere near the reversible value of 1.23 V. Electron transfer at "inert electrodes" will tend to occur in single electron steps. If we are going to get $O_2$ to react in a 4e step, then we must design an electrode with a binding site for $O_2$ and include provisions for the transfer of multiple electrons as well as provisions for the stabilization of the two "oxides" formed by breaking the oxygen-oxygen bond. The over-arching goal is to develop a research program to address the grand challenge of understanding multi-electron redox processes involving atom transfer as well as electron transfer, targeted at the problem of reducing the overpotential for oxygen reduction.

## Technical Approach

An attractive approach to the design of electrocatalysts is the attachment of molecules that are selective for the reaction of interest in homogeneous solution to conducting supports. A further elaboration of this approach is the attachment of redox active electron donors or acceptors that provide the multiple electron oxidizing or reducing equivalents at the required potential for near thermodynamic reversibility to the active site. This approach to the design of "molecular electrodes," capable of carrying out multi-electron electrochemical reactions involving atom transfer, will result in a more energy efficient process. Fundamental scientific research is needed to understand both the reactivity of supramolecular

or nanoscale assemblies that are capable of effecting selective chemical transformations driven by electrical energy, and the methodology to construct these assemblies on a conducting support at the required density. It is our aim to develop a fundamental research program that will provide an increased understanding of multielectron redox processes involving coupled electron transfer and atom transfer reactions.

In a series of elegant studies, Anson and coworkers (Anson 1997) were able to show that a cobalt porphyrin complex could also be used for effecting the 4e reduction of oxygen to water, avoiding the intermediate hydrogen peroxide. The Co porphyrin used by Anson was tetra-4-pyridylporphyrin, and a pentaammineruthenium group was bound to each of the pyridine groups. The function of the pentaammineruthenium(II) groups was to act as electron donors for the reduction of oxygen. This compound was applied to a graphite disk electrode in a rotating ring-disk arrangement with a platinum ring electrode. The potential of the modified disk was varied with the ring electrode held at a potential where the reduction of the hydrogen peroxide intermediate, if present, could be observed. In the absence of the four Ru complexes, hydrogen peroxide was observed as an intermediate. In the presence of the four Ru groups, hydrogen peroxide was absent, indicating the reduction of oxygen had taken place by a 4e process. The back bonding of the Ru d-electrons to the pyridine ligand of the porphyrin was theorized to have made it possible to have electron transfer fast enough to be competitive with the disassociation of the peroxy intermediate (Udit 2004).

The potential at which oxygen is reduced is a critical elements in the design of an oxygen electrode that operates at near the reversible potential. Our approach is that the attachment of reduced redox couples to the binding site for oxygen will allow greater control over the potential of the electrode. It is well known from corrosion phenomena and other electrochemical processes in which mixed reactions are influencing the potential of an electrode that the redox couple with the highest exchange current density (fastest kinetics) will control the potential at which a process is occurring. Our hypothesis is that the active site for the 4e reduction of oxygen can be coupled to nanostructured supramolecular assemblies designed to supply or take up electrons at near the thermodynamically reversible potential. These electron transfer reagents will function as "electron antennas" with the conducting support. These nanoscale assemblies of electron donors or acceptors and catalytically active site can be attached to conducting carbon supports for an efficient electrode. We designed, synthesized, and characterized novel nanoparticles based on the stable, multinuclear metallic cluster cyclopentadienyl iron carbonyl tetramer ($[(\eta^5\text{-}C_5H_5)Fe(\mu_3\text{-}CO)]_4$ (structure shown in Fig. 1) that can function as the charge carrier in catalytic electrochemical reactions. The iron tetramer was chosen as a prototype because it exists in four stable oxidation states, interconnected by the gain or loss of one electron, as shown below where $Fe_4$ is $[(\eta^5\text{-}C_5H_5)Fe(\mu_3\text{-}CO)]_4$,

$$Fe_4^{2+} \rightarrow Fe_4^{+} \rightarrow Fe_4 0 \rightarrow Fe_4^{-1} ,$$

and because the synthetic chemistry can be developed to allow the redox properties to be systematically varied.

## Results and Discussion

The proposed research involved three tasks. (1) The synthesis of model electrocatalytic species incorporating the tetrameric iron clusters, (2) attachment of the nanoclusters to substrate binding sites and electrode surfaces and determination of electrocatalytic properties, and (3) an in situ study of the catalyzed reactions by X-ray spectroscopy methods. Good progress was made toward each of these goals.

We synthesized the cyclopentadienylironcarbonyl tetramer, $(C_5H_5)_4Fe_4(CO)_4$, where $C_5H_5$ is Cp, along with $Cp_3Fe_4(CO)_4CpCO_2H$, $Cp_3Fe_4(CO)_4CpCO_2Ph$, and $Cp_3Fe_4(CO)_4Cp\text{-}C_6H_5$. The electrochemistry of these materials was examined in acetonitrile solution. Ferrocene compounds with these substituents have a fairly large variation in the potential for oxidation of Fe(II) to Fe(III). The potential for the $[(C_5H_5)_4Fe_4(CO)_4]^{+/0}$ couple varied with substituent, but the effect is far less than observed for ferrocene. A trivial explanation is that the inductive effect of a substituent is spread over four iron atoms rather than a single iron in the tetramer. The chemistry for attachment of $Cp_3Fe_4(CO)_4CpCO_2H$ and ferrocenecarboxylic acid to high-surface-area carbon electrodes was investigated. In the course of these electrochemical investigations, we observed that this method of attachment to the electrode was not as stable as desired. The proposed attachment of iron tetramers to porphyrins by an ester linkage was abandoned in favor of direct carbon-carbon bonding.

The ferrocene and iron tetramer acids were converted to the acid chlorides, the surface of the carbon electrode was oxidized to create more phenol-like functionalities, and the two were reacted to chemically bond the iron compound to the surface of the carbon. An electrochemical cell in which the oxidation state of the Fe compound attached to the electrode could be changed while the X-ray near-edge absorption spectroscopy (XANES) is simultaneously measured was designed and tested. Electrochemical-XANES experiments were conducted at the National Synchrotron Light Source (NSLS) at Brookhaven National Laboratory. We can clearly see the near-edge peak of the Fe compounds, either adsorbed or chemically bound to the carbon electrode, while the electrode is under potentiostatic control using the detection of Fe X-ray emission. However the spectrum of the

$Cp_4Fe_4(CO)_4^+$ oxidation product compared to the neutral tetramer does not show a clear shift in peak energy with oxidation state. The experimental work at NSLS revealed some shortcomings in our electrochemistry-XANES cell, and the cell was redesigned to correct these problems.

We observed that the intensity of the near-edge peak in the XANES was a factor of ten more intense than observed for normal octrahedrally coordinated iron complexes, and this phenomenon of CpFe complexes will be examined in more detail as time permits. We intend to examine the XANES of a series of CpFe complexes to understand this intensity enhancement and the concept of oxidation state in these compounds with follow-on funding. We observed that the pre-edge adsorption feature of CpFe compounds was more intense for "locally unsymmetrical" cyclopentadienyl iron compounds than we had anticipated based on results with other Fe compounds (Westre 1997). The pre-edge feature of the iron tetramer and the analogous iron dimer $[(\eta^5\text{-}C_5H_5)Fe(CO)_2]_2$ are an order of magnitude larger than the pre-edge feature of the symmetrical compound ferrocene and octahedrally coordinated Fe(II) compounds such as ferrous ammonium sulfate and $Fe(bipyridine)_3(ClO_4)_2$, presumably due to hybridization of the Fe 3d orbitals with the 3p orbitals.

We have prepared the porphyrin precursor needed to prepare the cobalt porphyrin adducts with the cyclopentadienylironcarbonyl tetramer. The synthetic scheme devised to accomplish this is shown in Fig. 1. The cobalt porphyrin-iron tetramer complex will be tested for kinetic activity in the reduction of oxygen supported by follow-on funding.

## Benefits

This work was directly applicable to the DOE, Office of Science, Basic Energy Science call for propoals for the Hydrogen Fuel Initiative which appeared while this work was in progress. The ideas developed while conducting this work, and the preliminary experimental result gathered during this project were instrumental in allowing us to write a strong proposal for this funding initiative. Based on a preproposal, we were invited to submit a full proposal which reviewed well enough to be awarded funding of $300K/year for three years. ORNL management believes we will get additional funding past three years, and there is a possibility for an increase in annual funding in FY 2007.

## References


Anson, F. C., C. Chunnian, and B. Steiger. 1997. "Novel multinuclear catalysts for the electroreduction of dioxygen directly to water," *Accounts Chem. Res.* **30**, 437.

Udit, A.K., M. G. Hill, V. G. Bittner, F. H. Arnold, and H. B. Gray. 2004. "Reduction of Dioxygen Catalyzed by Pyrene-Wired Heme Domain Cytochrome P450 BM3 Electrodes," *J. Am. Chem. Soc*. **126**, 10218.

Westre, E., P. Kennepohl, J. G. DeWitt, B. Hedman, K. O. Hodgson, and E. I. Solomon. 1997. "A multiplet analysis of Fe K-Edge 1s-3d pre-edge features of iron complexes," *J. Am. Chem. Soc*. **119**, 6297.


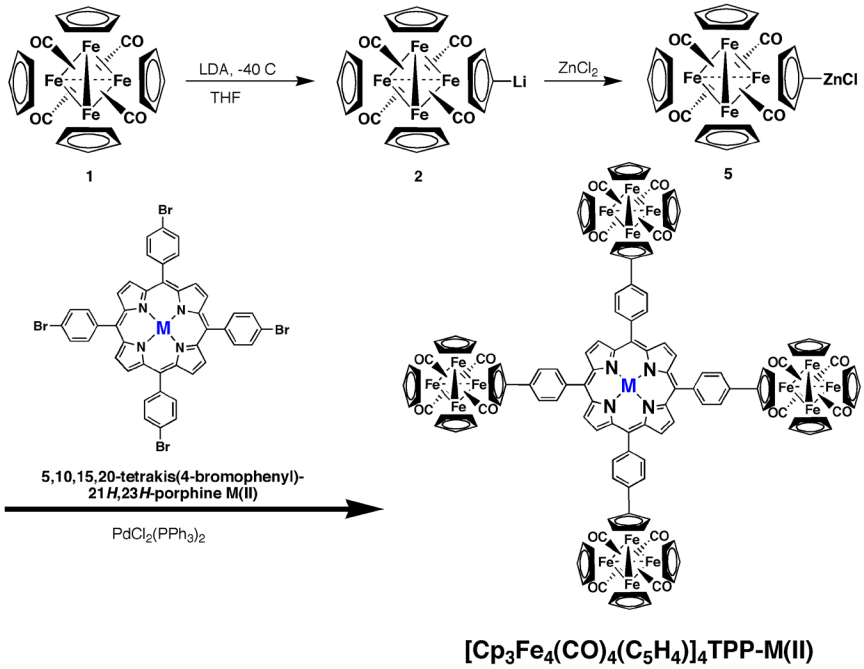


*Fig 1. Synthetic procedure for attaching the iron tetramer units to the four phenyl groups of a tetraphenyl porphyrin. LDA is lithium diisopropylamide and M is Co(II). The structure of the $[(\eta^5\text{-}C_5H_5)Fe(CO)]_4$ tetramer is a tetrahedron of iron atoms with cyclopentadienyl groups bound to each iron and CO groups bound to three Fe atoms in the face of the tetrahedron.*

# Novel Technologies for Wide-Scale Production of Magnesium and Hydrogen

J. G. Blencoe,[1] S. L. Marshall,[2] and J. Caja[2]
[1]*Chemical Sciences Division*
[2]*Electrochemical Systems, Inc., Oak Ridge, Tennessee*

Laboratory experiments were conducted to investigate the possibility that magnesium chloride, magnesium oxide, and/or magnesium carbonate can be electrolyzed at 1 atm, T ≤300°C, to form solid magnesium metal at the cathode and effervescing gas at the anode. Temperature and electrolyte composition were the principal variables in the tests. Results for magnesium oxide and magnesium carbonate were generally negative, due partly to the low solubilities of these compounds in ionic liquids and organic solvents that have electrochemical stabilities suitable for magnesium production. In contrast, promising results were obtained for magnesium chloride, which was found to mix with N-methyl-N-butylpyrrolidinium chloride to form stable magnesium chloride–rich liquids at temperatures as low as 120°C.

## Introduction

Reactions of interest in manufacturing magnesium (Mg) from three Mg-rich feedstocks—magnesium chloride ($MgCl_2$), magnesium oxide (MgO) and magnesium carbonate ($MgCO_3$)—are as follows:

$$MgCl_2 \rightarrow Mg + Cl_2 , \quad (1)$$

$$MgO \rightarrow Mg + \tfrac{1}{2}O_2 , \quad (2)$$

and

$$MgCO_3 \rightarrow Mg + CO_2 + \tfrac{1}{2}O_2 . \quad (3)$$

Current industrial production of magnesium metal by Reaction 1 involves electrolysis of molten $MgCl_2$, producing liquid Mg at the cathode and chlorine gas ($Cl_2$) at the anode. Reaction 2 is induced commercially in two ways: by chemical reduction at high temperatures (>1000°C) using a strong reducing agent (usually silicon or ferrosilicon) and by direct electrolytic decomposition of MgO to Mg and $O_2$ using an oxide–ion conducting ceramic electrolyte. Reaction 3 is a novel, and as yet untested, means for electrowinning magnesium that relies on the use of one or more ionic liquids (± an organic solvent) to solubilize and electrolyze the magnesium feedstock (crystalline $MgCO_3$). Since current practices of magnesium electrowinning are very energy intensive and environmentally damaging (by production of various airborne pollutants, along with copious amounts of $CO_2$), and because the efficacy of Reaction 3 is, to date, undemonstrated, there is considerable economic and scientific incentive to identify new pathways for magnesium production that are more cost-effective and environmentally sound.

Production of magnesium by electrolysis of a hypothetical solution of magnesite (Reaction 3) is of particular interest because it offers substantial energetic advantages. Assuming that production of Mg + $CO_2$ + $\tfrac{1}{2}O_2$ can be made to occur at 298.15 K, the minimum electrical energy required can be estimated from the standard Gibbs energies of formation for solid magnesite (-1029.5 kJ•mol$^{-1}$) and $CO_2$ (-394.4 kJ•mol$^{-1}$) (Robie and Hemingway 1995). Thus, the standard Gibbs energy change for Reaction 3 is

$$1029.5 - 394.4 = 635.1 \text{ kJ•mol}^{-1} .$$

If the gaseous products are ideal, the mole fractions of $CO_2$ and oxygen (at 1 bar) are 2/3 and 1/3, respectively. Assuming that the activity of the $MgCO_3$ in the ionic liquid is 0.01, this contributes additional energies of

$$RT \ln (2/9) = (8.31431 \times 298.15 \text{ J/mol}) \times \ln(2/9) = -3.728 \text{ kJ•mol}^{-1} \text{ and}$$
$$RT \ln a = (2.479 \text{ kJ•mol}^{-1}) \times \ln(0.01) = -11.416 \text{ kJ•mol}^{-1},$$

respectively. Consequently, the Gibbs energy change is

$$635.105 + 11.416 - 3.728 = 642.793 \text{ kJ•mol}^{-1} \text{ or } 7.346 \text{ kWh/kg}.$$

Although this corresponds to a rather large decomposition potential of 3.331 V, the minimum energy requirement is less than half that of the conventional fused-chloride electrolysis (Reaction 1), and the need for high temperatures (and for use of an inert cover gas) is avoided.

## Technical Approach

The electrochemical experiments of this project involved the use of a potentiostat/galvanostat—a device that can control either the potential across an electrochemical cell, or the current that flows through it. The potential of the working electrode is measured with respect to a reference (or quasi-reference) electrode, and current flows between the working electrode and a third (counter) electrode. In addition to its simplest possible use as a constant-current power supply to an electrochemical cell, a potentiostat can be used to measure the transient currents resulting from imposition of a time-dependent potential, or the transient potential resulting from driving a time-dependent current through the cell.

We used our electrochemical cells primarily to conduct cyclic voltammetry, which measures the transient current resulting from an applied potential that varies linearly with time between specified limits. Results of our experiments indicated the current-potential characteristics of the anodic and cathodic reactions, which are used to estimate the cell voltage corresponding to the specified current.

## Results and Discussion

The most significant results obtained in this project are summarized below.

- A recent journal article reported the extraordinary solvent properties of the deep eutectic mixtures formed between choline chloride (CC) and amides, such as urea, and mono-, di-, tri-, and tetramethyl urea. The fact that the CC-urea eutectic liquid (formed at 12°C) can dissolve silver chloride to 0.66 $mol \cdot dm^{-3}$ suggested to us that it might be possible to dissolve a similar amount of $MgCO_3$ in that liquid (magnesium carbonate has a solubility product in water that is comparable to that of silver chloride). Thus, we prepared the liquid in an inert-atmosphere dry box, and observed no obvious reaction with magnesium metal. However, cyclic voltammetry of this mixture in an electrolytic cell with a glassy-carbon working electrode, a silver quasi-reference electrode, and a platinum wire counter-electrode showed that reduction of urea occurs at a lower (less negative) potential than that at which $Mg^{2+}$ reduction occurs. In other words, reduction of magnesium ions occurs outside the electrochemical stability window of urea.
- We investigated the possible use of liquid choline hydroxide (COH) as a room-temperature electrolyte. This material is commercially available as a 45% w/w solution in methanol. Unfortunately, it proved impossible to remove the methanol by vacuum distillation. Moreover, COH is far less stable than CC (as evidenced by a strong smell of trimethylamine) and is more reactive towards oxygen (as shown by rapid discoloration). For these reasons, no further work with this material was attempted.
- Experiments were performed to investigate the possibility that solid magnesium could be electrodeposited from solutions of magnesium chloride in dimethyl formamide (DMF). We prepared an ~1 $mol \cdot kg^{-1}$ solution of magnesium chloride in DMF and carried out cyclic voltammetry. The large discrepancy between the anodic and cathodic current transients indicated that the dominant process is the reduction of the solvent rather than reduction of the solute.
- Phase-equilibrium and electrochemical experiments on mixtures of $MgCl_2$ and N-methyl-N-butylpyrrolidinium chloride (MBPyrCl) containing 6.0, 10.5, 13.9, 16.2, 21.2 33.3 and 40.0 mole percent $MgCl_2$ were conducted to investigate the possibility that solid magnesium could be electrodeposited on platinum and/or tungsten electrodes at hypersolidus temperatures. Results of the phase-equilibrium tests, summarized in Table 1, indicate complex melting relations involving at least two eutectics. The very low liquidus temperature observed for sample #5 suggests that one of these eutectics occurs near 20 mole percent $MgCl_2$ at ~120ºC. This circumstance being potentially favorable for electrodeposition of magnesium, cyclic voltammograms were obtained for the 21.2 mole percent $MgCl_2$ composition at 135ºC. Results indicate a wide electrochemical window for

**Table 1. Results of melting experiments on binary mixtures of $MgCl_2$ and N-methyl-N-butylpyrrolidinium chloride (MBPyrCl)**

| Sample # | Mole % $MgCl_2$ | Physical state at 175°C | Melting behavior |
|---|---|---|---|
| 1 | 6.0 | Solid | - |
| 2 | 10.5 | Solid + liquid | - |
| 3 | 13.9 | Solid + liquid (more liquid than in sample #2) | - |
| 4 | 16.2 | Liquid | Partial melting at 150°C; additional liquid present at 170°C |
| 5 | 21.2 | Liquid | Solid softens at 120°C; all liquid at 130°C |
| 6 | 33.3 | Solid | - |
| 7 | 40.0 | Solid + liquid (60 to 70 vol % liquid) | Partial melting at 110°C; additional liquid present at 145°C |

the liquid, -3.2V to +2.5V, which was determined using a silver, quasi-reference electrode. Although the reduction potential of this mixture is much more negative than that of magnesium (approximately -2.6 V vs. a silver, quasi-reference electrode), magnesium electrodeposition was not observed. This negative finding is tentatively ascribed to the formation of one or more magnesium complexes in the liquid. Electrodeposition of magnesium during cyclic voltammetry would be expected if $MgCl_2$ dissolved in MBPyrCl by the reaction

$$MgCl_2 \rightarrow Mg^{2+} + 2Cl^-.$$

Such deposition would not be expected, however, if magnesium formed strong complexes with chloride ion and/or MBPyrCl. (Note: For numerous $MgCl^{2-}$ alkali chloride systems it has been shown that magnesium forms strong complexes with chloride ion by the reaction $Mg^{2+} + 4Cl^- \rightarrow MgCl_4^{2-}$). Thus, it is evident that additional research is required to determine whether MBPyrCl is potentially useful in electrodepositing solid magnesium at low temperatures. A logical line of follow-on inquiry would make use of a third component—e.g., an organic solvent, or another type of ionic liquid—to solvate $Mg^{2+}$, thereby preventing its complexation with other species.

The foregoing observations, and a critical evaluation of related work reported in the published literature, suggest that organic solvents may be essential for future commercial electrowinning of magnesium from low-temperature ionic solutions. Ethereal solvents such diethyl ether, tetrahydrofuran (THF), and polyethers of the "glyme" family are often used as solvents for the preparation of Grignard reagents in synthetic organic chemistry, since these solvents are resistant to reduction or deprotonation. For example, the successful use by Rieke et al. (1988) of bis(2-methoxyethyl) ether (diglyme) as a solvent for the reduction of magnesium chloride by metallic potassium not only indicates that this solvent is unreactive towards magnesium metal but also suggests that it can dissolve appreciable concentrations of magnesium chloride. In connection with work on the development of rechargeable magnesium batteries, Aurbach et al. (2000) showed that magnesium can be reversibly electrodeposited from electrolytes consisting of Grignard reagents or magnesium organochloroaluminates in THF. These authors postulated that the organic ligand of the Grignard reagent provides a means of stabilizing the magnesium in the nonaqueous solvent, thereby preventing it from precipitating on the magnesium surface as a passivating film of inorganic salt.

Another attractive possibility is an organic solvent that has a substantial capacity for dissolving magnesium compounds—for example, one that contains a "crown ether." Crown ethers are structurally similar to the conventional ether solvents in consisting of oxygen atoms separated by alkyl groups, but differ from them in being connected end-to-end to form a cyclic structure. These compounds are freely soluble in nonpolar solvents but also have the ability to form strong complexes with metal cations of different sizes, which facilitates a wide range of chemical processes that would otherwise be difficult or impossible. A seminal paper by Pedersen (1967) noted that these compounds also promote the dissolution of inorganic salts in organic solvents in which such salts normally have negligible solubility. For the smaller crown ethers, the most stable complexes are formed when there is a close match between the crystallographic diameter of the metal ion and the internal diameter of the ring. Thus, the crown ethers "12-crown-4" (1,4,7,10 tetraoxacyclododecane), "15-crown-5" (1,4,7,10,13-pentaoxacyclopentadecane), and "18-crown-6" (1,4,7,10,13,16-hexaoxacyclooctadecane) form especially strong complexes with $Li^+$, $Na^+$, and $K^+$, respectively. (The simplest possible compound in this class would be THF, which could also be called "6-crown-2.") Addition of the related compound "dibenzo 18-crown-6" (in which two of the carbon-carbon bonds forming the macrocycle are sides of benzene rings) was found by Pedersen (1967) to increase the methanol solubility of hydrated magnesium chloride from 0.025 to 0.068 $mol \cdot dm^{-3}$. Stable complexes of magnesium salts with 15-crown-5 and 18-crown-6 have been prepared, but since lithium and magnesium ions are of similar diameters (120 and 130 pm, respectively), 12-crown-4 would appear to offer the best prospects for use as an agent for solubilization of magnesium salts in aprotic liquids. Magnesium-selective electrodes containing PVC membranes that incorporate 12-crown-4 as an ionophore have been described by Gupta et al. (2002). The electrolysis of nonaqeous solutions of magnesium salts produced in this way does not appear to have been studied. Since 12-crown-4 is composed entirely of single bonds that numerous experiments with non-cyclic ethers have shown to be resistant to attack by strong reducing agents, use of a solvent containing 12-crown-4 or some similar compound may provide sufficiently high concentrations of (otherwise insoluble) magnesium salts to allow useful rates of electrodeposition of magnesium from a nonaqueous solvent.

## Benefits

The results presented in this report are potentially useful to researchers and technologists in the Department of Energy (particularly the Offices of Fossil Energy, Energy Efficiency and Renewable Energy, and Basic Energy Sciences), the Defense Advanced Research Projects Agency, the Environmental Protection Agency, and the National Science Foundation.

## References


Aurbach, D., Z. Lu, A. Schechter, Y. Gofer, H. Gizbar, R. Turgeman, Y. Cohen, M. Moshkovich, and E. Levi. 2000. "Prototype systems for rechargeable magnesium batteries," *Nature* **407**, 724–727.

Gupta,V. K., S. Chandra, and R. Mangla. 2002. "Magnesium-selective electrodes," *Sensors and Actuators B-Chemical* **86**(2–3), 235–243.

Pedersen, C. J. 1967. "Cyclic polyethers and their complexes with metal salts," *Jour. Amer. Chem. Soc.* **89**, 7017–7036.

Rieke, R. D., S. E. Bales, P. M. Hudnall, T. P. Burns, and G. S. Poindexter. 1988. "Highly reactive magnesium for the preparation of Grignard reagents: 1 norbornanecarboxylic acid," *Organ. Syn., Coll.* **6**, 845–850.

Robie, R. A., and B. S. Hemingway. 1995. "Thermodynamic properties of minerals and related substances at 298.15 K and 1 bar (105 pascals) pressure and at higher temperatures," *U. S. Geol. Surv. Bull. 2131*, U. S. Government Printing Office, Washington, D.C.

# Light-Activated Decontamination of Chemical Agents Using the ORNL Plasma Arc Lamp

W. H. Griest,[1] G. M. Brown,[1] T. J. Huxford,[2] R. R. Smith,[1] P. G. Engleman,[2] and R. H. Ilgner[1]
[1]*Chemical Sciences Division*
[2]*Metals and Ceramics Division*

The objective of this work was to provide a proof-of-principle demonstration showing the practicality of using a Plasma Arc Lamp (PAL) for the decontamination of chemical warfare agents on surfaces. Two experiments were performed, using both a 1-kW Xe arc lamp and a multi-100 kW PAL in the Infrared Processing Center (IPC) at Oak Ridge National Laboratory (ORNL). The latter experiments were designed to emulate the photon flux of a field deployable lamp system that could stand off 17 m from a 12-$m^2$ target area and uniformly expose the surface at 1360 W/$m^2$. The chemical decontamination was carried out by irradiating the chemical warfare agent simulant diisopropyl methyl phosphonate (DIMP) on a glass surface in the presence of the photosensitive catalyst, titanium dioxide ($TiO_2$). Analysis of the recovered $TiO_2$ showed the disappearance of the DIMP, but the de-esterified products expected from published studies of UV irradiations carried out in water slurries of $TiO_2$ and DIMP were not observed. A second test trapping and analyzing gaseous decomposition products of DIMP was conducted to test the hypothesis that the photochemical decomposition was more extensive than expected. The DIMP was again almost fully decomposed, and products showing de-esterification and further decomposition of the ester groups were observed, including propane/propene, isopropyl alcohol, and acetone. These results, plus earlier experiments showing rapid killing of a biological warfare agent simulant, *Bacillus subtilis* var. Niger (commonly known as "BG"), demonstrate the feasibility of a rapid chemical and biological warfare agent decontamination that does not require toxic or corrosive reagents or generate hazardous wastes.

## Introduction

The *Chemical and Biological Defense Program 2002 Annual Report* (Deputy Assistant to the Secretary of Defense for Chemical and Biological Defense, April 2002) explicitly states that "existing [decontamination system] capabilities currently rely upon the physical application and rinse down of decontaminants on contaminated surfaces. Existing systems are effective against a wide variety of threat agents, yet are slow and labor intensive and present logistical, environmental, material and safety burdens. In addition, existing systems are inadequate for electronic equipment decontamination, deficient for large areas, ports, and airfields and rely upon Decontamination Solution 2 (DS2) and water." Consequently, there is an immediate need for incorporating the Plasma Arc Lamp, as an existing technology, into the arsenal of countermeasures against chemical, biological, radiological, nuclear, and explosive threats and weapons of mass destruction.

The PAL is a unique, established facility within the Infrared Processing Center (IPC) at ORNL capable of producing a very powerful source of incoherent light that is approximately equivalent to the solar spectrum. Within this facility there exist two multi-configurationally plasma arc lamps with powers of 300 kW and 500 kW. Existing technologies that could easily be incorporated into this system include wide-angle reflectors capable of producing an irradiance of 0.14 W/$cm^2$ at 200-kW input power over an area of 3 m × 4 m (at a standoff distance of 17 m) or a radiance of 1.66 W/$cm^2$ at 200-kW input power over an area of 1 m × 1 m. Addition of pulse technology could increase the irradiance by up to a factor of 10. This results in 6-decade kill times of a biological warfare agent simulant, BG spores, between 1 and 7 seconds (normalized to a wavelength of 2137Å). Furthermore, the nature of this unique facility is to promote usability by minimizing the effort required to adjust the equipment between experiments and by minimizing the effort required to make amendments during an experiment.

## Technical Approach

### *UV Irradiation*

The first photochemical experiments were conducted using a 1-kW xenon arc lamp as the irradiation source. This lamp has good output between 300 and 400 nm, and it has an output of roughly 1 W $m^{-2}$ $min^{-1}$ which was focused to an area of 0.03 $m^2$. The treated Petri dishes were held horizontally in this area and were irradiated for about 15 min. The samples were removed from in front of the lamp and analyzed for DIMP and DIMP degradation products as indicated as follows.

Due to changes and upgrading of the Plasma Arc Lamp system, a different configuration was used for the chemical decontamination testing versus previous

work with BG spores. The significant changes included a change to a 750-kW power supply and the addition of a uniform irradiance reflector capable of producing a uniform flux density (+/-2%) over a 15-cm × 20-cm area. Each experiment was performed by placing a DIMP-inoculated plate in the processing chamber (in this case a water-cooled aluminum box covered with a quartz plate) and passing either argon or air through the chamber. The effective temperature was monitored using a thermocouple attached to an aluminum plate inoculated with the decontamination media. The lamp standoff distance and power were regulated to produce a flux equivalent to approximately twice that of the solar flux outside of the earth's atmosphere. The lamp was then started and the experimental apparatus was moved underneath the lamp for the 300-second exposure time. A part of the atmosphere exiting the box was sampled in a Triple Sorbent Trap (TST) for analysis.

### *$TiO_2$ Application*

Petri dishes (100 mm in diameter) were prepared with a thin layer of titanium dioxide coating by spraying on successive coats of $TiO_2$ in isopropanol using an air brush while the dish was rotated horizontally at approximately 100 rpm. A heat lamp was used to expedite solvent evaporation between coats. $TiO_2$ loadings were in the range of 100–200 mg per plate.

### *DIMP Application*

Solutions of DIMP in methanol were sprayed onto the coated Petri dishes. DIMP loadings ranged from 5 mg to 100 mg per plate. The addition rate was adjusted such that the maximum coverage was obtained when balanced against the evaporation rate and the physics of the spinning plate. DIMP addition was conducted within approximately 30 min of lamp exposures.

### *$TiO_2$ Extraction and Analysis*

After the first set of irradiation experiments, the $TiO_2$, DIMP, and photochemical products on the plates were extracted 3 times by adding 1 mL of methanol and scraping with a spatula, filtering the particles, and concentrating the volume to 1 mL. A 1-µL aliquot of the extract was coinjected with a tetramethyl ammonium hydroxide reagent into an HP 5890 GC-MS equipped with an HP 5972 mass selective detector operated in electron impact mode. Identifications were made by comparison of chromatographic retention times and mass spectra with authentic standards.

### *Vapor-Phase Sample Analysis*

After irradiation experiments, the TSTs were analyzed by thermal desorption GC-MS. The HP 5890 gas chromatograph was equipped with a modified injection port consisting of a coil heater through which a TST could be inserted and connected to the GC injector. An HP 5972 mass selective detector was coupled to the GC for column eluent identification. This was operated in electron impact mode. Identifications were made by comparison with spectra in the instrument library.

## Results and Discussion

A greater-than-expected effort was required to develop the analytical method for the products expected from irradiations conducted in a water slurry (O'Shea et al. 1997). These compounds are isopropylmethylphosphonic acid, phosphonic acid, and phosphate.They would be observed as their methyated products, isopropylmethylmethylphosphonate, dimethylmethylphosphonate, and trimethylphosphate, respectively, from the methylation reaction in the sample injection. In the first photochemical test, plates coated with $TiO_2$ and inoculated with DIMP were irradiated for 5 and 15 min. Extraction of the plates and $TiO_2$ layer, reaction of the extract with the methylation reagent, and GC-MS analysis showed the disappearance of the DIMP. However, the expected decomposition products were not detected in any of the samples.

A more extensive photochemical decomposition was hypothesized, and an experiment was conducted on the PAL to detect and identify gaseous photochemical decomposition products of DIMP. In these tests, the gaseous products from the plate irradiations were collected in TST sorbent tubes which were thermally desorbed into the GC-MS for analysis. Figure 1 shows the GC-MS total ion current chromatograms from two tests using 300 seconds of irradiation and argon (lower chromatogram) and air (upper chromatogram) chamber atmospheres. The experiment with an atmosphere of argon tested for a dark (non-photochemical) reaction, and DIMP was identified from its retention time (ca. 19.5 min) and mass spectrum (not shown). No decomposition products were detected. The peaks at 12.7 (octane) and 3.8 (diethyl ether) minutes were from the background of the experimental apparatus. The experiment with an air atmosphere clearly demonstrated the disappearance of DIMP and the appearance of three decomposition products derived from the isopropyl ester groups in DIMP. These products are propane and propene (at ca. 3.9-min retention time), which are not resolved and are difficult to distinguish under the chromatographic and mass spectral conditions used, acetone (at ca. 5-min retention time) and isopropanol (at ca. 5.6-min retention time). These expected products resulted from the further oxidation by hydroxyl radicals of the isopropyl ester group from the DIMP. The degradation of organic compounds by $TiO_2$-catalyzed photo-oxidation has been extensively studied as reported by Fox and Dulay (1993). The anticipated

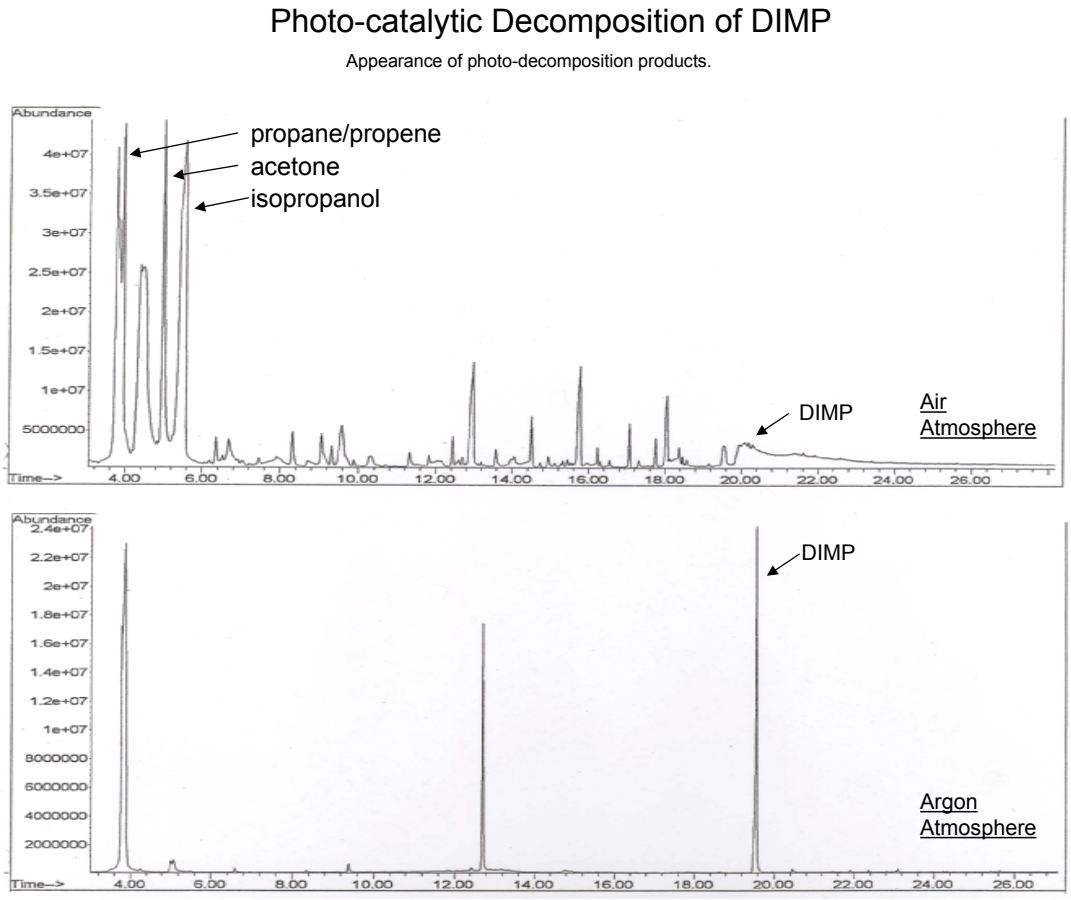


*Fig. 1. Gas chromatography–mass spectrometry total ion current chromatograms of DIMP irradiation in air (upper chromatogram) and in argon (lower chromatogram) atmospheres.*

reaction of a surface hydroxyl radical with DIMP sorbed on a surface produces isopropanol and, in addition, will give the hydrogen abstraction products, acetone and propene.

## Benefits

These results are important because they demonstrate that the PAL, coupled with a $TiO_2$ photosensitizer, can decompose DIMP on surfaces, and they indicate that the PAL has the potential for the photochemical decomposition of chemical warfare agents. Toxic and corrosive reagents are not used and hazardous by-products are not generated in the process. Earlier tests demonstrated the ability of the PAL to very quickly kill a biological warfare agent simulant, BG spores. Optimization of the parameters of this technology for actual chemical and biological warfare agents on the specific surfaces of importance (e.g., vehicles, building materials) will greatly benefit the military and the civilian sectors by permitting both chemical and biological warfare agent decontamination to be conducted more easily and less expensively and without generating toxic wastes that themselves are a disposal problem with current decontamination methods.

## References

Deputy Assistant to the Secretary of Defense for Chemical and Biological Defense. April 2002. *Department of Defense Chemical and Biological Defense Program. Vol. 1: Annual Report to Congress*, section 2.5.2, "Decontamination Modernization Strategy," available at http://www.acq.osd.mil/cp.

Fox, M. A. and M. T. Dulay. 1993. "Heterogeneous Photocatalysis," *Chem. Rev.* **93**, 341.

O'Shea, K. E., S. Beightol, I. Garcia, M. Aguilar, D. V. Kalen, and W. J. Cooper. 1997. "Photocatalytic decomposition of organophosphonates in irradiated TiO2 suspensions," *J. Photochem Photobio.* **A:107**, 221–226.

# Ionic Liquids as Novel Lubricants

J. Qu,[1] J. J. Truhan,[2] H. Luo,[3] S. Dai,[4] and P. J. Blau[1]
[1]*Metals and Ceramics Division*
[2]*University of Tennessee*
[3]*Nuclear Science and Technology Division*
[4]*Chemical Sciences Division*

The physical and lubricating properties of two categories of ionic liquids have been studied. A large range of viscosities were observed for the selected ionic liquids that correlated to their molecular structures. Tests have been conducted on selected ionic liquids in lubricating steel-aluminum contacts. The ammonium-based ionic liquids significantly outperformed the imidazolium-based ones, though the latter category was successful in lubricating steels and ceramics. The two most attractive candidates have shown both better lubricating performance and higher thermal stability than fully formulated hydrocarbon oil–based lubricants. Both aluminum and steel alloys exhibited active-passive behavior in ionic liquids, implying the formation of stable surface boundary films, which explains their unique lubricating mechanisms.

Friction and wear are estimated to cost 6% of the U.S. gross national product, or around $700 billion annually. A new class of more effective lubricants could lead to huge energy savings. Limited recent literature has suggested great potential for using ionic liquids as lubricants; however, only a few (out of thousands) have been evaluated, and there is a lack of fundamental understanding of their lubricating mechanisms. The objective of this project is to conduct proof-of-principle studies to investigate the physical and lubricating properties of ionic liquids with various molecular structures and gain a mechanistic understanding of how they lubricate difficult-to-lubricate metals like aluminum.

Nineteen different ionic liquids from two categories, imidazolium and ammonium based, have been synthesized. Viscosities have been measured at room temperature (23ºC), 40ºC, and 100ºC and show strong correlation to the molecular structure. Reciprocating sliding friction tests have been conducted on 14 candidate ionic liquids and compared with 3 conventional oil-based lubricants (mineral oil and two premium diesel engine oils) in lubricating steel-aluminum contact at room temperature. Although the literature has demonstrated the ability of using imidazolium-based ionic liquids to lubricate steels and ceramics, our experiments have shown very limited success for aluminum alloys using this category of ionic liquids. The ammonium-based ionic liquids, however, have produced more promising results in our study. Particularly, the two fluids with bis(trifluoromethylsulf onyl)-imide anions have proper viscosities and showed the best lubricating performance. Using unidirectional sliding with various sliding speeds, Stribeck curves have been constructed for these two best candidate ionic liquids and baseline oil lubricants. Compared to the oils, these two ionic liquids transitioned from elasto-hydrodynamic to boundary lubrication at more harsh conditions and produced 20–50% lower friction at each lubrication regime. In addition, thermo-gravimetric analysis has shown much higher thermal stability of these two ionic liquids (decomposition temperature ~360ºC) than oils (decomposition temperature ~250ºC). The main hypothesis in the proposal of reducing friction and wear using ionic liquids is the formation of protective boundary films on metal surfaces due to their inherent polarized molecules. Electrochemical measurements have shown active-passive behavior of both aluminum and steel alloys in ionic liquids, indicating the formation of surface films. Results to date are quite encouraging. Research will continue in FY 2006 and focus on lubricating behavior at elevated temperatures, wear mechanisms, and surface boundary film analyses.

The success of this study will provide the scientific basis for developing a new class of friction-reducing ionic liquid-based lubricants. The substantial friction and wear reductions using ionic liquids could lead to huge energy savings and performance improvement, and their ultra-low vapor pressure will potentially reduce air emissions. The potential for excellent lubricating properties, along with negligible volatility and high thermal stability, make ionic liquids highly attractive for aerospace and military applications too.

# *Engineering Science and Technology*

# *Director's R&D Fund*

# Flameless Combustion Engines in the Transition to Hydrogen

R. L. Graves,[1] C. S. Daw,[1] K. Chakravarthy,[2] R. M. Wagner,[1] J. B. Tassitano,[1] and J. C. Conklin[1]
[1]*Engineering Science and Technology Division*
[2]*Computer Science and Mathematics Division*

The overall objective of this LDRD was to help refocus ORNL's transportation engine R&D in response to changes in DOE priorities toward increased emphasis on fuel efficiency and non-petroleum fuels. We specifically sought to identify technical challenges and opportunities in the use of hydrogen fueling and flameless combustion for engines.

Our approach included thermodynamic second law analysis of the fundamental efficiency limits of engine combustion, analysis of experimental engine data for both conventional and flameless combustion modes, direct collaborations with experts from universities, other national labs, and industry, and implementation of hydrogen fueling capabilities in the NTRC experimental engine facility. Our analyses confirmed that combustion irreversibility is the single largest contributor to the inefficiency of current engines. We further demonstrated that opportunities for directly minimizing combustion irreversibility are limited to a relatively small number of possibilities. Hydrogen and other small-molecule fuels offer an irreversibility advantage over conventional fuels such gasoline and diesel, but these advantages may be offset by fuel production penalties. Gas-phase (homogeneous) flameless combustion does not appear to be inherently more reversible than conventional combustion, but it may offer incremental efficiency advantages because of reduced wall heat losses. The development of techniques for measuring and exploiting this heat transfer effect may be an important new research opportunity for ORNL.

It is now clear that large engine efficiency improvements will only be possible through substantial design changes. Opportunities for near-term incremental efficiency improvements include development of high-compression-ratio engines, more effective utilization of recirculated exhaust gas heat, and introduction of multiple work extraction stages (i.e., cycle compounding). In the longer term, more radical modifications are needed to restructure the combustion process. One promising candidate approach is a heterogeneous flameless combustion concept referred to as Staged Combustion with Oxygen Transfer (SCOT).

The results of this LDRD have substantially improved ORNL's analytical and experimental capabilities in engine efficiency analysis and hydrogen combustion. ORNL is now more optimally positioned to be a strong contributor in achieving DOE and industry goals for engine efficiency. ORNL's expertise in this area is also more widely recognized by DOE and the engine research community.

## Introduction

Over the past 2 years, the programmatic emphasis of ORNL's primary DOE engine research sponsor in the Office of Freedom Car and Vehicle Technologies (OFCVT) has shifted away from control of pollutant emissions and toward increased fuel efficiency and utilization of non-petroleum fuels. This shift in emphasis has occurred because of the growing strategic need to reduce U.S. dependence on imported oil and the significant benefits now emerging from the intense emissions control investment over the last 15 years. In response to this shift, ORNL and other national labs are re-evaluating their programmatic roles and investigating new opportunities for aligning their engine R&D to OFCVT's mission. This LDRD has been a key component of ORNL's re-evaluation process.

## Technical Approach

The technical focus of this LDRD was to investigate new opportunities for increasing the fuel efficiency of internal combustion engines and utilizing hydrogen as a primary fuel. Of particular interest was the role of so-called "flameless" combustion modes (such as homogeneous charge compression ignition or HCCI). These are a relatively new type of gas-phase combustion in which there is little or no flame. These combustion modes have been of growing interest to the engine community because of their potential for reducing emissions of nitrogen oxides and particulates from both gasoline and diesel engines. The potential value of these advanced combustion modes for increasing fuel efficiency and the use of hydrogen has only recently begun to be considered.

Key elements of the project scope included the following: thermodynamic availability analyses for

existing and theoretical engines, analysis of the efficiency potential for hydrogen as a primary engine fuel, analysis of the efficiency potential of flameless combustion in engines, identification of "out-of-the-box" types of flameless engine combustion, development of stronger collaborations with internationally recognized engine efficiency experts, and enhancement of our in-house experimental capabilities for running engines with hydrogen fueling. Although previous research in the 1970s and 1980s identified various components of conventional engine inefficiency, this work has not been updated to reflect the significant changes in engine design, the availability of new fuels, and the existence of flameless combustion that have recently occurred. The analytical part of the work scope was designed to update this previous theoretical work on engine efficiency and connect it with the fundamental understanding about the thermodynamic limits of combustion that has emerged in recent years. To do this, we developed a new set of in-house computational tools that can be applied to any type of combustion process as well as engines. A particularly important feature of these tools is that they account for both first and second law aspects of engine and combustion processes; that is, they consider both overall energy conservation and the reduction in work potential caused by the generation of entropy. Since the ultimate objective of engines is to convert fuel chemical energy to motive work, both of these thermodynamic constraints are critical in understanding fuel efficiency. In addition, a license was also acquired for the Ricardo WAVE engine simulation software that can be used in conjunction with the in-house tools to simulate the physical and thermodynamic details of both conventional and flameless combustion modes.

We were aided in our analyses by direct collaborations with internationally recognized engine research groups at the University of Wisconsin and Texas A&M University, and also by consultations with a panel of experts assembled specifically for the LDRD. Key members of this panel were Jerry Caton (Texas A&M University), Dave Foster (University of Wisconsin), John Clarke (Caterpillar, retired), Roy Primus (General Electric), and Dennis Siebers (Sandia National Laboratory). On recommendations from the panel, we also had in-depth discussions with Noam Lior from the University of Pennsylvania, another highly recognized expert in combustion thermodynamics and the application of second law analysis. Beyond the analytical studies described above, the LDRD team defined appropriate strategies for measuring and quantifying thermodynamic availability balances for experimental engines. This process utilized both the computational tools described above as well as experimental data from the NTRC engines operating in both conventional and flameless modes. Again, collaborations and consultations with the panel members proved to be very beneficial in this process.

Extensive equipment modifications were implemented in one of the NTRC engine test cells to accommodate utilization of hydrogen fuel. The experimental engine involved was a modified 0.52-L single-cylinder Hatz Diesel engine. The compression ratio of the engine was lowered to permit operation in both SI and HCCI modes under similar conditions. Other modifications included an electric air preheater and a specialized hydrogen flow delivery and measurement system. Our experimental set up was based on previous hydrogen engine facilities described by (Natkin 2002) and (Stenlaas 2004). Numerous shakedown experiments were performed to improve our understanding of the stable operating range of hydrogen HCCI combustion and its differences with hydrogen spark-ignition (SI) combustion.

## Results and Discussion

Our analyses confirmed assertions by previous investigators that internal combustion engines (ICE's) are theoretically no less efficient than fuel cells (Lutz et al. 2002). However for current homogeneous (gas-phase) combustion ICE's, approximately 20% of the usable fuel energy is transformed by the thermodynamic irreversibility (entropy generation) of the combustion process. Once transformed, this energy becomes "unavailable" to do useful work and can only be expelled to the surrounding environment (i.e., no amount of effort can recover it for generating propulsive power). Combustion irreversibility is the largest component of engine inefficiency, but it has received relatively little research attention, with few solutions identified. Unless combustion irreversibility can be significantly reduced, a large fraction of ICE efficiency potential will remain untapped. If combustion irreversibility can be reduced by as much as half and combined with modest improvements in heat transfer losses, it is reasonable to expect that engine fuel efficiencies of over 60% could be obtained. Such efficiencies would be equal to or greater than that anticipated for practical fuel cells (Agrawal 2005).

Previous investigators have shown that the most important contributing factor for irreversibility in all types of combustion is the so-called internal heat transfer process. This process involves the exchange of thermal energy between reactant and product molecules as the combustion reactions proceed, and its net effect is to lower the final temperature and thermodynamic availability of the exhaust gas. As a part of this LDRD, we have been able to demonstrate that it is theoretically possible to overcome most of this availability destruction if the reaction and heat transfer steps are carried out in a very controlled manner (Daw et al. in press). However, while such an idealized

heat transfer and reaction process could theoretically be applied to ICE's, the increased availability of the resulting hot exhaust gas can only be effectively utilized if it can be extracted as work by the piston. Our analyses have also revealed a previously unrecognized constraint that limits the extractability of the increased exhaust availability. Specifically, for a single-stage expansion, it is not possible to extract most of the additional energy made available by improving the combustion. Instead, it is necessary to utilize compound cycles for extracting the increased availability. The analysis of such compound engine cycles goes beyond the scope of this project but clearly offers opportunities for future study.

For single-stage engines utilizing homogeneous (gas-phase) combustion and piston-expansion work extraction, the opportunities for directly reducing combustion irreversibility are relatively limited and include hydrogen fueling, higher compression ratio, and more effective utilization of heat from recirculated exhaust gas. Hydrogen and other small-molecule fuels offer an irreversibility advantage over conventional fuels such as gasoline and diesel because the destruction of these small molecules during combustion produces less entropy. However these advantages of small-molecule fuels may be offset by the entropy of their original production, especially from petroleum or coal sources.

Because high engine compression ratio increases the effective fuel and air preheating, it also reduces combustion irreversibility from internal heat transfer. In addition, the higher final pressure allows a greater fraction of the exhaust gas availability to be extracted as work, reducing the need for cycle compounding. R&D opportunities associated with higher compression ratios include the development of improved piston sealing systems and materials, high pressure lubricants, and the measurement and modeling of the impact of such pressures on the combustion kinetics and chemistry.

Exhaust gas recirculation (EGR) is a key feature of modern engines that is needed for both emissions control and for inducing flameless combustion. In simple terms, EGR involves recycling a fraction of the exhaust gases back into the engine air intake. Currently, these recirculated gases are exposed to large temperature gradients as they mix with the incoming air, further increasing the irreversibility of the combustion process. It appears that there may be an opportunity for at least incrementally improving efficiency in the development of advanced heat exchangers for more optimally transferring the exhaust gas heat back to the inlet air. By reducing the temperature gradient between these streams, the irreversibility could be reduced as much as a few percent. Such development efforts are likely to require consideration of materials of construction, modeling of complex fluid mechanics and heat transfer, and possibly catalytic combustion of unburned hydrocarbons and particulates before or in conjunction with the heat exchange process. These engineering issues align well with staff capabilities in the ESTD, M&C, and CS&M divisions.

Two additional key findings from our analytical studies are that neither homogeneous flameless combustion nor matching of the rates of combustion and work extraction (such that they occur simultaneously and isothermally) inherently reduces combustion irreversibility. In spite of its spatial uniformity and lack of global gradients, homogeneous flameless combustion involves essentially the same level of irreversibility as conventional combustion because internal heat transfer still occurs over large gradients at molecular scales.This is also true of isothermal combustion with matched reaction and work scales. These observations imply that R&D for implementing and controlling flameless combustion modes or for creating isothermal combustion is not likely to have a major impact on increasing engine efficiency. On the other hand, there appear to be modest efficiency advantages associated with reductions in wall heat loss associated with flameless combustion. The development of techniques for measuring and exploiting this heat transfer effect may be an important new research opportunity for ORNL.

Our very limited theoretical studies of alternative combustion processes indicate that, in the long term, combustion with some type of mediated chemistry is likely to be a fruitful direction for achieving the greatest reductions in combustion irreversibility. One particular promising approach is to utilize staged, heterogeneous reactions (reactions on a solid surface) to moderate entropy generation. A specific concept for implementing this type of combustion in engines, referred to as Staged Combustion with Oxygen Transfer (SCOT), was developed under the LDRD and filed as an invention disclosure (Daw et al. 2004).

The hydrogen engine shakedown experiments were successful in demonstrating our ability to achieve hydrogen-fueled HCCI and conventional spark-ignition (SI) combustion in the laboratory. The heat release rates for the two combustion modes at nearly identical power-output levels are shown in Fig. 1. The exhaust nitrogen oxide concentrations for the HCCI experiments were in the single ppm range, which is, as expected, considerably less than observed for the SI experiments. The experience acquired during this activity will provide a solid basis for future experimental efforts in hydrogen-fueled HCCI.

## Benefits

Through our continuing dialogue with the DOE OFCVT, the results of this project have already helped them refocus their research portfolio toward more effective efficiency-oriented activities. The analytical

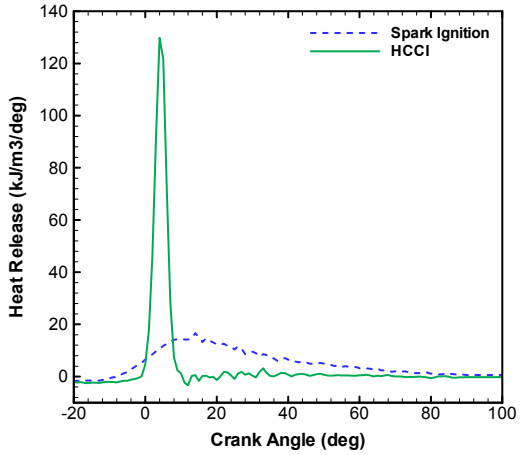


*Fig. 1. Heat release rates for the single-cylinder hydrogen fueled engine at ORNL, comparing HCCI vs spark-induced flame propagation. Engine power was approximately the same for both modes. The observed heat release rate for HCCI "volumetric combustion" is characteristically much higher.*

results have been used to call attention to the remaining potential for improving combustion engines, and these ideas were incorporated into OFCVT technical roadmaps and multiyear plans. The engine modeling tools that were acquired and developed are already being used in newly funded research efforts. ORNL has been awarded a lead role to achieve and demonstrate the engine efficiency goals for the Freedom CAR partnership. DOE funding to ORNL is being increased for FY 2006 in a related project on stretching combustion engine efficiency. The enhanced collaborations among ORNL, Texas A&M, and the University of Wisconsin are expected to lead to continued undergraduate and post-graduate activities at ORNL and joint proposals to DOE.

## References

Agrawal, R. 2005. "Energy Supply Challenges and Opportunities," 57th AIChE Institute Lecture, American Institute of Chemical Engineers Annual Meeting, Cincinnati, October 30–November 4, 2005.

Caton, J. A. 2000. *A review of investigations using the second law of thermodynamics to study internal-combustion engines*. Society of Automotive Engineers. SAE 2000-01-1081.

Daw, C. S., K. Chakravarthy, J. C. Conklin, and R. L. Graves. In Press. "Minimizing destruction of thermodynamic availability in hydrogen combustion," *International Journal of Hydrogen Energy* (corrected proof available online from 18 August 2005).

Daw, C. S., R. L. Graves, K. Chakravarthy, and J. C. Conklin. October 2004. "Staged Combustion with Oxygen Transfer (SCOT) for Automotive Propulsion," ORNL ID No. 1479.

Lutz, A. E., R. S. Larson, and J. O. Keller. 2002. "Thermodynamic comparison of fuel cells to the Carnot cycle," *Int. J. Hydrogen Energy* **27**, 1103–1111 (2002).

Natkin, R. J., X. Tang, K. M. Whipple, D. M. Kabat, W. F. Stockhausen. 2002. "Ford Hydrogen Engine Laboratory Testing Facility," SAE paper 2002-01-0241.

Stenlaas, O., M. Christensen, R. Egnell, and B. Johansson. 2004. "Hydrogen as Homogeneous Charge Compression Ignition Engine fuel," SAE paper 2004-01-1976, 2004.

# Advanced Processes for Nuclear Fuel Microspheres

D. F. Williams,[1] G. D. Del Cul,[1] R. D. Hunt,[1] T. L. White,[2] F. C. Montgomery,[3] and T. N. Tiegs[3]
[1]*Nuclear Science and Technology Division*
[2]*Fusion Energy Division*
[3]*Metals and Ceramics Division*

This project focused on the application of microwave technology to the heating of liquid drops to reaction temperatures necessary to produce uniform microspheres. These microspheres are used in a number of advanced reactors that require particulate fuel. Previous gel-precipitation processes have required the use of toxic solvents as the heat-transfer media to make fueled microspheres. These conventional gel-precipitation methods required extensive solvent cleanup, and many additional waste streams were generated. Proposals have been made for a microwave-driven process that couples directly to the droplet in air. This new approach has not yet been optimized, and the models necessary to understand and expand its application have not yet been developed. Microwave heating of droplets is extremely uniform and rapid, and the gel-microstructure will be much more uniform than for conventional processes. The internal-gelation chemistry can be applied to make inorganic materials that span nearly the entire periodic chart. This process has the potential for many applications, both nuclear and non-nuclear. The goal of this project was to develop a "solvent-free" microwave process for making microparticle fuel by a combination of mathematical modeling of the process and experimental testing, with non-radioactive simulants selected as the model system for initial investigation.

## Introduction

ORNL possesses extensive experience and capability in the synthesis of microparticle fuels by conventional means, so the primary focus of this project was on the application of new microwave technology to the heating of spherical droplets. This approach was recommended because of the desirability of a simple solvent-free heating step for making uniform microspheres. However, both the German proposals (Ledergerber 1982) and the Japanese work (Yamagishi 1998) in this area did not answer key technical questions associated with this approach. A more intensive study was needed, and this project undertook the study to understand and assess this new method for microparticle synthesis.

## Technical Approach

The application of microwave methods to heating small drops and fine particles is a relatively new area. The benefit of this type of heating is the speed and uniformity that can be achieved, most especially for small drops or particles. However there is also a degree of complexity in microwave heating that requires we understand, measure, and model the transitions in dielectric susceptibility that occur as the material is transformed by processing, because these transitions effect the degree of microwave heating and thus the end product. This basic information on dielectric response is needed to specify the microwave heating regime, and to optimize the process. The methods that were developed to measure and model these changes permit control of the heating process and the properties of the microparticles that are formed. The dielectric response is the key piece of information necessary to develop models that will enable accurate heat transfer modeling and support use of this technology in an industrial setting.

In the first phase of the project, the measurement of the relevant dielectric properties of the actual solutions to be processed by microwave heating was conducted. This information was used to design an optimized cavity for heating droplets by using a microwave heating model. Heating water droplets tested the effectiveness of this new cavity. The predicted and experimentally determined microwave heating were in close agreement. Conventional internal gelation tests were also done to define the proper post-microwave processing (washing, calcining, sintering) needed to attain high-quality dense microspheres.

In the second phase of the project, an optimized microwave apparatus was used to explore the processing regimes most suitable for making uniform microspheres with appropriate microstructure. The actual microwave heating of drops is preceded by the breakup of a capillary jet into uniform droplets, much like the process used in ink-jet printing; however, the ink-jet drops are much smaller than fuel particles. The jet break-up process is complex, and therefore it is important to learn about how this process is most effectively coupled to a microwave heating apparatus. The various modes of coupling were explored in the last phase of the project.

## Results and Discussion

The key factors and necessary design features of microwave systems for heating small drops were defined. Some of these factors and requirements were apparent at the beginning of the project, and others were discovered as the R&D was under way.

Modeling of a spherical droplet heated in a cylindrical microwave cavity was conducted. The effective dielectric susceptibility was found to be

$$\varepsilon''_{eff} = 9\varepsilon''/[(\varepsilon' + 2)^2 + (\varepsilon'')^2]$$

where ε' is the real component of the relative dielectric constant, and ε" is the imaginary component of the relative dielectric susceptibility. Both components are dimensionless.

This parameter, $\varepsilon''_{eff}$, was measured for the both uranium and surrogate (Zr, Hf) solutions used to form microparticles. The parameter was measured over a range of microwave frequencies (1–10 GHz) and the relevant temperature range (5–70°C) and was found to vary between 0.05 and 0.15, which are characteristic of low-loss microwave absorbers. The droplet heating is proportional to $\varepsilon''_{eff}$ times the external electric field squared, so the external cavity electric field needed to be very high to heat the spherical droplets to the desired temperature. Further modeling using these results showed that only a small portion (<1%) of the microwave power would be effective in heating perfectly spherical shapes due to low-loss properties of the droplets but that a considerable fraction of the cavity energy could be deposited in non-spherical shapes, such as a co-axial capillary jet, or non-spherical modes in the breakup of a capillary jet. Thus our system design included provisions for allowing the cavity to pre-heat the capillary jet before it was dispersed into droplets.

Based upon the dielectric measurements and microwave heating calculations, an optimized microwave heating systems was designed and built. It was concluded that a simple low-frequency (2.4-GHz) cavity would be adequate to test the microwave heating modes. Several unique features were developed to optimize the system for droplet heating. The cavity matching circuit uses a unique microwave phase detection technique to measure the amount of frequency tuning needed to maintain optimum microwave heating of the falling droplets. A method for measuring the mass of each drop was also developed based on a microwave cavity perturbation technique successfully used by the ORNL fusion program to measure high-speed deuterium pellets. A means to minimize the effect of off-specification "satellite" droplets (that occur during startup) on the operation of the cavity was also designed into the system. The unique features of this system were included in an invention disclosure (White 2005).

During the period of microwave cavity development, conventional microsphere tests identified the necessary washing, drying, and sintering conditions to produce acceptable microspheres containing Zr an Hf. Optimized conditions were found that produced materials superior in quality to those recently reported in the scientific literature (Idemitsu 2003; Arima 2005). The key step involved using a more suitable solution to wash out the soluble reaction product from the rather small pores in the hydrous zirconia/hafnia gel.

Early experiments with the new microwave heating system showed that the system was effective in heating single water droplets to the prescribed temperatures (~70°C) and that the amount of heating was close to that predicted by the microwave-heating model. More extensive experiments with actual solutions of high dielectric constant revealed somewhat different behavior that was dominated by effects of "satellite" drops on the cavity and of effects related to exceeding the breakdown voltage of the cavity. These effects are most clearly revealed by discussion of the operation of the microwave cavity in three distinct modes.

At low flow through a vertical capillary, a large pendant drop will be formed that falls through the cavity nearly free of any peripheral "satellite" droplets (associated with jet-breakup or droplet detachment). These large drops require high microwave power (1500 watts for this apparatus) and are heated with low efficiency. Only about 0.2% of the microwave energy is deposited as heat inside the drop—the balance of the power heats the cavity wall due to the low coupling efficiency to the spherical droplet shape. This pendant drop mode is capable of heating drops up to 70ºC above ambient temperature. The cavity electric fields are so high that the cavity occasionally breaks down the air to form a steady-state plasma arc discharge that terminates on the top wall of the cylindrical cavity near the axial central hole. The pendant drop mode is not suitable for the efficient production of microspheres because the drops are too large and the drop rate is too slow compared to the capillary jet mode used in the conventional process. In addition, brief transient arcing was observed—forming on the droplets themselves near the region where the drops entered the cavity electric field. The arcing is also manifested by high-frequency noise superimposed on the reflected power waveforms. The arcing was quickly quenched as the drops fell below the entrance region; however, this transient droplet arcing resulted in small satellite particles of liquid coating the cavity walls and the quartz tuning tube that encompasses the entrance to the cavity. The buildup of these particles quickly reduces the cavity droplet heating efficiency, and the system must be shut down and cleaned.

As the flow to the needle is increased beyond the pendant drop mode, irregular drops are formed due to

the transition between various drop detachment and jet-breakup modes. This unstable mode is characterized by many more satellite drops and is unsuitable for making uniform drops. However, as the flow is increased still further, a more stable capillary jet is formed, provided the needle tip is perfectly round and without physical imperfection, and provided the flow is kept below the threshold flow for capillary jet turbulence. Extremely uniform drops were formed by imposition of a flow oscillation at the natural frequency for jet-breakup. Under these conditions, a several-millimeter-long stable cylindrical jet is formed at the end of the capillary. At moderate flow rates, and with imposed resonant flow oscillations, the capillary jet breaks up into a controlled stream of uniform drops directed along the cavity axis with very few "satellite" drops. If droplet stream is in the microwave cavity and the capillary jet is not inside the cavity, the heating mode is denoted as "droplet-stream" mode. The droplet-stream mode is characterized by smaller spherical droplets compared to the pendant drop mode. However in this mode there are more numerous drops inside the cavity, resulting in only a slightly higher volume of heated material compared to the pendant drop mode. This mode still requires the highest available powers from the generator and the highest electric fields in the cavity due to the spherical shape of the drops. This droplet stream mode is also capable of heating drops up to ~70 ºC above ambient temperature. Transient droplet arcing was indicated by the high-frequency noise superimposed on the reflected power waveforms, and prolonged operation in this mode was impossible due to ejected particles coating the cavity walls and tuning tube.

If the capillary jet and the droplet stream are both in the microwave cavity, this heating mode is denoted as the "capillary-jet mode." The capillary-jet mode produces the same drops as the droplet stream mode, but because the capillary jet itself is inside the cavity and the efficiency of heating the cylindrically shaped capillary jet is many times higher compared to heating spherical drops, most of the microwave energy goes into heating the jet, as predicted by the microwave heating model. In theory, the capillary jet mode requires only about a hundred watts of generator power to heat the droplets to 100°C, and the cavity electric fields are much lower as a result. However, the capillary-jet mode suffers from satellite drop buildup on the quartz tuning tune near the capillary jet. This capillary jet mode is capable of effectively heating drops, and great care is required to avoid overheating the drops. No arcing has been observed due to the low electric fields required. The capillary jet mode is therefore the most promising mode of operation for this vertical microwave cavity. However the control of this type of heating is very sensitive to the position of the capillary jet in the cavity, and the rapid residue buildup on the tuning tube, which eventually overheats and terminates the run.

A final trial was conducted to explore the limits of operation in this capillary-jet mode. Only a hundred watts of power were required to heat the drops by 30°C above room temperature. However, after about 5 min of operation the quartz tuning system was coated with very fine particles. It is likely that some of these very fine droplets are actually generated due to high field strengths that are generated at specific surface locations on the jet or droplet. After about 10 min of operation, an increase in power caused an electrical arc, thus terminating the run. The accumulation of micro-drops on the cavity wall and tuning system was observed, and this is the cause of the arcing. All of our experience confirms that a small closed cavity, such as the one we have used, is very sensitive to "rogue" micro-droplets that are inevitability formed, and that a new approach is necessary to ensure uninterrupted heating by microwaves.

An open cavity concept shown in Fig. 1 would avoid the satellite collection problems of the current closed cavity apparatus. Unlike the cylindrical closed cavity used in this project, the open cavity consists of a confocal resonator with a large open space for droplet and satellite formation, heating, and collection. The two identical spherical mirrors are spaced one radius apart, and the microwave beam is fed through the center of one mirror in the HE11 "hybrid electric" mode. The beam diverges, and most of the energy is refocused at the center of the confocal resonator. The beam makes many bounces between the mirrors and the electric fields build up at the focus. The main advantage of this concept is that the cavity is virtually immune to the collection of satellites from the droplet formation process. In addition, the parabolic trajectory of the droplet stream results in a droplet residence time about double that of a simple vertical trajectory used in the cylindrical cavity. The main disadvantage to the confocal resonator approach will be microwave leakage between the mirrors, so any adjustments to the needle may need to done remotely during operation, and a microwave-absorbing shield will need to be built around the mirrors.

## Benefits

The path for application of microwaves to particle processing applications has been defined, and it is expected that open-cavity designs will be explored for applications that derive special benefit from microwave processing of drops. In particular, nuclear applications that require spherical microparticles benefit from an advanced microwave process to make microparticles that do not require solvents, and to eliminate many steps and secondary wastes. Two Department of Energy programs require microparticle nuclear fuel: (a) the Generation-IV Very High Temperature Reactor and (b) the NNSA Gas Turbine Modular Helium Reactor for Pu-disposition. In addition to these ongoing programs, a number of concepts

**Closed Cavity Design**
**Vertical Cylindrical Cavity**

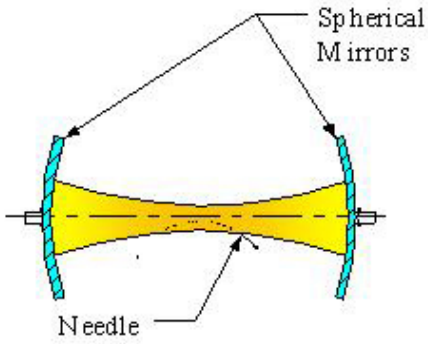


**Open Cavity Design**
**Confocal Geometry (Proposed)**

*Fig. 1. Comparison of current closed-cavity apparatus and proposed open-cavity design.*

for nuclear waste transmutation require microparticulate fuels (Deep-Burn TRISO fuel and sphere-pac fuel for water-cooled and sodium cooled reactors), and are being pursued by the Department of Energy Advanced Fuel Cycle Initiative.

It is also likely that the highly efficient co-axial mode of closed-cavity heating of cylindrical jets or material dispersed in a thin tube will be developed. A large number of high-temperature materials and high-temperature processes can benefit from application of this type of microwave heating technology. Lower temperature applications, which derive benefit from microwave-driven chemistry, are also good candidates for co-axial heating modes.

## References

Arima, T. et al. 2005. "Application of internal gelation to sol-gel synthesis of ceria-doped zirconia microspheres as nuclear fuel analogous materials," *Journal of Alloys and Compounds* **394**(1–2), 271–276.

Idemitsu, K. et al. 2003. "Manufacturing of zirconia microspheres doped with erbia, yttria and ceria by internal gelation process as a part of a cermet fuel," *Journal of Nuclear Materials* **319**, 31–36 (2003).

Ledegerber, G. 1982. "Improvements in the Internal Gelation Process," *Trans. of the Am. Nuclear. Soc*. **40**, 55–56.

White, T. L. 2005. *Microwave System to Rapidly Heat Falling Droplets and Capillary Jets*, invention disclosure report, Rev. 1, Department Of Energy,*/S-105,172/*, May 25, 2005.

Yamagishi, S. 1998. "A new internal gelation process for fuel microsphere preparation without cooling initial solutions," *Journal of Nuclear Materials* **254**(1), 14–21.

# Real-Time, Interconnection-Wide, Power System Analysis and Visualization

J. Stovall,[1] B. Kirby,[1] B. Bhaduri,[2] A. Sorokine,[2] P. Nukala,[3] S. Simunovic,[3]
J. Nutaro,[2] R. Toedte,[2] T. Overby,[4] and R. Jeffers[5]
[1]*Engineering Science and Technology Division*
[2]*Computational Sciences & Engineering Division*
[3]*Computer Science and Mathematics Division*
[4]*University of Illinois*
[5]*Virginia Polytechnic Institute and State University*

A wide-area analysis and visualization environment (WAVE) is being defined and developed to monitor power systems larger in size than today's present regional transmission operators (RTO) with the goal of improving overall system reliability, situational awareness, and avoidance of widespread cascading outages.

The objective of this project is to develop the conceptual framework and test the proof of principle for collecting real-time data from all the control centers within the North American interconnections, analyzing that data for topology estimation, state estimation and contingency analysis, and returning the results to the control system operators. It consists of five tasks: (1) scoping analysis, (2) topology estimation, (3) reduced scale analysis, (4) visualization, and (5) interconnection-wide analysis.

**Task 1:** The scoping analysis began in January 5, 2005, with a visit to PJM Interconnection and then a visit to TVA on March 3. A technical paper entitled "Issues Associated with the Development of a Wide-Area Analysis and Visualization Environment" was prepared and submitted for peer review to an IEEE Conference in Jan. 2006. In the renewal year, the scoping analysis would continue to further develop the wide area analysis and visualization environment.

**Task 2:** Initially, this task was to determine requirements to develop a topology estimator that could resolve connectivity based upon the aggregate of the measured data. An alternate approach has been selected to develop a method of combining state estimator's outputs from two or more RTO's. This task will be completed in collaboration with TVA and Virginia Tech (an ORNL Core University) including test and verification of the method.

**Task 3:** The task will demonstrate a reduced-scale version of the solution strategy developed in Task 1. The approach is using an existing method and source code of analyzing the failure of discrete lattice model, quasi-brittle materials under stress developed at ORNL. At the conclusion of this task, ORNL will have a load flow and contingency model capable of handing wide-area power system networks and execution on the ORNL supercomputers as necessary.

The initial analysis method depended upon developing a state estimator for a large network but is no longer necessary at the wide-area level. Nonetheless, the importance of the state estimator at the RTO level is still a key to the overall methodology. Therefore, the state estimator will continue to be examined for improvements in its solution algorithm and execution in parallel computing environments.

**Task 4:** ORNL visualization experts will analyze the power system operations center requirements for visualization and will explore ways to address them. As a starting point, the state-of-the-art software for power system visualization, PowerWorld Simulator, has been acquired and is being installed on the EVEREST for evaluation. The ORNL visualization expertise will be focused on displaying a 24-hour time series of data, representing the power system condition in a geographically oriented manner.

**Task 5:** This task will use the previous task results and apply them to a portion of an interconnected power system. This will still be at the proof-of-principle level. Establishing a robust production environment is well beyond the scope of this LDRD. Results should be sufficient to demonstrate the potential to system operators, NERC, and FERC in order to obtain support for continued development and deployment.

# *Engineering Science and Technology*

# *Seed Money Fund*

# Development of a High-Throughput, Laser-Based Technique for Quantifying the Elemental Composition of Wood: Applications in the Forest Products Industry

M. Z. Martin,[1] S. D. Wullschleger,[1] and T. G. Rials[2]
[1]*Environmental Sciences Division*
[2]*University of Tennessee*

In this project we have successfully designed and evaluated a laser-induced breakdown spectroscopy (LIBS) system capable of rapid, accurate, and simultaneous elemental analysis in wood. A laser beam, focused onto the surface of the sample, evaporates small amounts of the material and simultaneously excites a plasma discharge. The analysis of the emitted element–specific spectral lines permits the direct determination of the atomic composition of substances. A high-energy Nd:YAG laser and precision Echelle spectrograph (200–780 nm) will permit multi-element analysis of wood and wood products with a high degree of specificity. A comparison between elemental analysis using LIBS and AES was undertaken and from these data calibration curves for up to 20 elements were generated using multivariate analysis. Our efforts have focused not only on demonstrating the application of LIBS as a tool for use in the forest products industry but also on addressing sampling errors, limits of detection, reproducibility, and accuracy of measurements as they relate to multi-elemental analysis in wood and engineered wood composites.

## Introduction

The forest products industry, which encompasses the production of wood, pulp, paper, and engineered wood products, is increasingly using spectroscopic-based techniques to assess product quality and to facilitate on-line process monitoring and control. Various techniques have been used to assess the structural behavior of wood and engineered wood products, and several high-throughput spectroscopic techniques have shown promise in providing information on the chemical, physical, and mechanical properties of paper, wood, and wood products (Rials 2002; Häkkänen 2001; Kelly 2004). Hybl et. al. (2003) used LIBS as a method for detecting airborne biological agents. Principal component analysis was applied to the spectra to discriminate bioaerosols from interferences.

This report describes the design and evaluation of a LIBS system capable of rapid, accurate, and simultaneous analysis of multiple inorganic constituents in wood. The system is used to identify elements of interest in CCA-, ACQ- and ACZA-treated wood from two forest tree species; Eastern Hemlock and Douglas Fir. In addition to characterizing the inorganic composition of preservative-treated wood, quantitative relationships between LIBS and elements of interest using principal component analysis and latent structure models are established (Madhavi 2005). This approach extends the value of LIBS and provides a powerful tool for analyzing the inorganic composition of wood and related lignocellulosic materials. This capability also adds a valuable new analytical method to the suite of rapid assessment tools for wood and biomass.

## Technical Approach

The experimental setup employs a Big Sky™ laser, model Ultra 532. This Q-switched Nd:YAG laser has a fundamental wavelength of 1064 nm and is frequency doubled to 532 nm which is used as the excitation wavelength. The maximum beam energy at this wavelength is 50 mJ per pulse. The laser pulse width is 5 ns, and the repetition rate is variable from 1 to 20 Hz. When operated at a repetition rate of 2 Hz, all the processes such as plasma formation, optical emission, gated detection, and data collection and analysis are completed within 500 milliseconds before the next pulse arrives at the sample.

A pellet for each of the samples from the four different chemically treated woods was formed under pressure using approximately 300 mg of the powder.

A pulsed laser beam was focused onto these pellets, creating a plasma spark with light emission in all directions. The light emitted by the plasma was collected by a second lens array situated perpendicular to the direction of both the sample and the laser input and delivered to a broad band (200–950 nm) Catalina Scientific spectrometer (SE200A) via a carbon-core fiber-optic cable bundle. The spectral resolution for the broad band spectrum is 0.04 nm. The time-resolved spectrum was detected by

an intensified charge coupled device (ICCD) built by Andor Technology, which was delayed and gated by a delay generator that is integrated onto the detector head. The intensity and signal-to-background ratio for these emitted wavelengths are used to determine the presence of the specific element of interest. The emitted wavelengths are fingerprints for the different elements present in the wood matrix that was sampled. The first step in LIBS is plasma initiation. Plasma can be formed when a laser beam of sufficient energy is focused onto a small volume of material (~ 14 x $10^{-9}$ $cm^3$), creating a power density inside the volume exceeding tens of gigawatts per square centimeter. All species in the sample matrix are instantly released into their elemental constituents. A computer software data acquisition program written by the Catalina Scientific Corp., KestrelSpec® is used to acquire the spectra, identify the peaks, calculate the full width at half maximum (FWHM) of the peaks of interest, and also to calculate the area under the peak which can be used in the semi-quantification of elements from a similar matrix.

## Multivariate Analysis

The LIBS spectra data sets are large, complex representations of the samples. Each spectrum provides more than 7500 data points. The challenge is to isolate the spectral variables (wavelength) that can be correlated with chemical differences between the samples. PCA removes the redundancy (inter-correlation) in a data set, transforming it into a few loadings, which contain most of the valuable spectral information while retaining most of the original information content.

Partial least squares (PLS) is a second multivariate analysis technique that provides a model for the relationship between a set of predictor variables *X* (*n* objects, *m* variables) and a set of response variables *Y* (*n* objects, *p* response). In this case *m* variables are the LIBS wavelengths and *p* responses are properties such as the inorganic content. The *p* response has to be independently measured for each sample. If the spectral data contain information about the properties of interest, a reliable calibration model can be constructed. In this study, PLS-2 is performed on the sets: ACZA/Douglas fir, CCA/Eastern Hemlock, and CCA/Hemlock-Fir because the several *Y* responses (Cu, As, Zn or Cr content) are intercorrelated with each other; that is, if the loading of one *Y* response increases, the other one increases too, since they are from the same treated solution. PLS-1 is performed for ACQ/Hemlock-Fir set where only one *Y* response (Cu) is present.

The wavelength range for the LIBS spectra collection was 200–800 nm. Three LIBS spectra were collected for each sample. The LIBS data were first averaged to one spectrum per sample and reduced to 0.08 nm wavelength spacing. Multiplicative scattering correction (MSC) was applied to all the data prior to analysis. MSC is a transformation method used to compensate for additive and/or multiplicative effects in the spectra (Martens 1991). PCA was used to observe any clustering and/or separation in the samples sets. For partial least-squares analysis, two-thirds of each sample set was used for calibration (calibration set) to create the model and the rest used to validate the model (validation set). The number of principal components (PC) used for the models was selected by observing the response of the residual *Y* variance to added factors as described earlier (Martens 1991). Models were generated using full cross validation, in which one sample is systematically removed from the data set, a model is created from the remaining samples, and this model is used to predict a value for the extracted sample. This process is subsequently repeated for all remaining samples. This fully cross-validated model was then used to predict the response of the validation set that contains about one-third of the samples that were not included in the original model. This conservative approach ensures that the predictive capabilities of the model are reliable.

## Results and Discussion

Figure 1 shows a typical spectrum for each of the sample sets. Visual comparison of the averaged LIBS spectra of the treated wood reveals clear differences between the different treatments, particularly between samples treated by CCA and ACZA.

In the ACQ/Hemlock-Fir spectrum, one can assign clearly the emission lines of copper at 324.74, 327.38, 510.30 and 521.78 nm. Two emission lines at 588.98 and 589.54 nm are also observed in all the spectra with different intensity. These signals are due to the presence of sodium in the samples. The two sets (Hemlock-Fir and Eastern Hemlock) treated by CCA give similar spectra. However, an emission line at 266.90 nm is present only in the CCA Eastern Hemlock set. An emission line characteristic of zinc (472.26 nm) is observed only in the Douglas Fir samples treated by ACZA. Although chemical differences are obvious by direct visual evaluation of the spectra, complexity of the LIBS spectra and sample mixtures suggest that interpretation may benefit from the application of multivariate statistical techniques.

Principal component analysis (PCA) was performed on different combinations of sample sets. Figure 2 shows the two largest variations in magnitude within the data, PC2 versus PC1. This scores plot results from the complete sample set. This result shows that PCA can distinguish the treatment, and the species, even when the samples have received the same preservative treatment. Another attribute of PCA is the loadings. Loadings describe the data structure in terms of variable correlations. Each variable has a loading on each PC. It

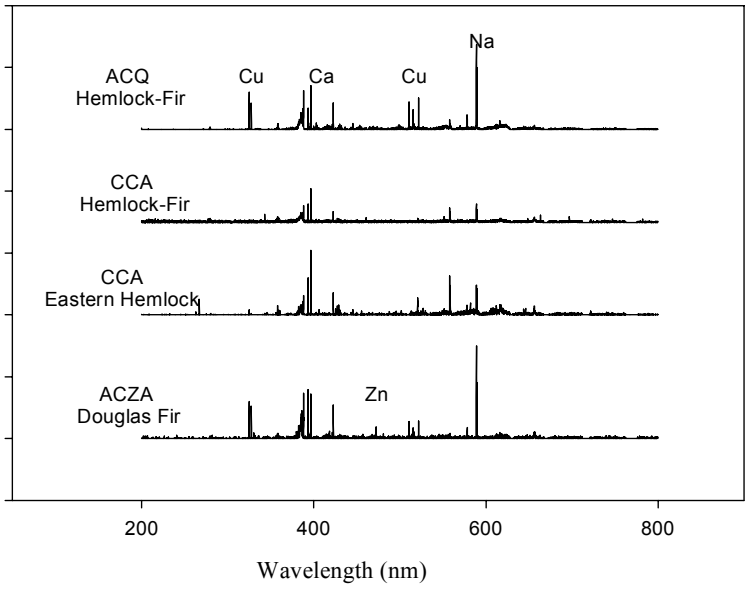


*Fig. 1. Comparison of LIBS spectra collected from the different treated samples.*

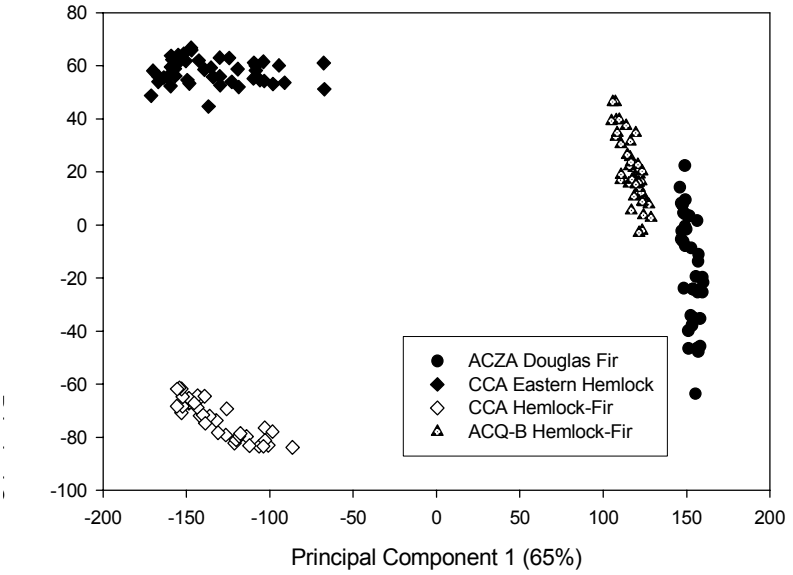


*Fig. 2. Principal component analysis from LIBS spectra collected for all sample sets.*

reflects both how much the variable contribute to that PC, and how well that PC takes into account the variation of that variable over the data points. The loadings plot provides information on the chemical features that are responsible for grouping the samples along the different principal components. Interestingly, several lines for Ca (393.38, 393.82, 422.66, 428.90, 430.26, and 558.26 nm) are found to be responsible for the grouping. This observation clearly points to a contribution from the wood substrate, presumably resulting from variable growth conditions; As, Cu and Cr also contribute to the clustering, probably due to their interaction with the different substrate. The sensitivity of LIBS data to chemical composition of treated wood samples highlights the potential of this approach to evolve as a means to classify chemically treated wood at the end of its lifecycle.

To further examine the effects of the treatments, PLS models were constructed to investigate the correlations between the LIBS spectral features and the concentration of elements. The PLS models were constructed by using the elemental composition information determined by atomic absorption and the LIBS spectra collected on the surface of the pellets of the treated wood samples. All the results presented here are based on PLS-2 models that predict all three wood-treated elements, for example, copper, zinc, and arsenic for samples treated by ACZA and copper, chromium, and arsenic for samples treated by CCA. A PLS-1 model was built for the ACQ/Hemlock-Fir set where only copper was predicted.

A strong correlation is obtained between the measured and the predicted Cu, As, Zn concentration. The 27 samples in the calibration set were used to construct the PLS-2 models for all three (Cu, Zn, As) of the treated wood elements. These PLS-2 models were then used to predict the elemental composition of samples in the validation set, which had not been included in the original data used to construct the models. Testing the model with samples that were not contained in the original model is an example of how these models might be used to predict the composition of a large number of unknown samples.

For all the treated wood sets, very strong correlations are obtained for the calibration set. PLS regression coefficients provide some insight into the chemical features in the LIBS spectra that are important in predicting preservative content. Large absolute values indicate large importance (significance), and small values (close to 0) indicate an unimportant variable.

## Benefits

Two years ago, an effort was initiated to establish an ORNL R&D Forest product analysis program based on a number of technologies (e.g., LIBS, NIR, midIR, Raman, statistical quantification methodologies, and

multivariate approaches) for energy savings applications. The logical entry was to establish a basic research program on chemical and mechanical properties for the next generation of engineered and natural wood identification, as there were existing programs at other DOE laboratories that focus on environmental samples such as soils, plants, and biomaterials but not specifically wood. Thus, this LDRD project chose to focus on advanced wood materials by taking advantage of the expertise in the different spectroscopy techniques mentioned here.

The advanced concepts for total analysis of natural and engineered wood materials developed in the project will have a major impact on fossil energy, sensor and separation programs, and forest products consortium. Advances in the development of new technologies, along with quantification and identification of the wood materials, would benefit applications being considered by the Department of Defense (e.g., Department of Homeland Security for Navy and Marine Corps and the Defense Advanced Research Projects Agency's Defense Sciences Office).

## References


Häkkänen, H., J. Houni, S. Kaski, and J. E. I. Korppi-Tommola. 2001. "Analysis of paper by laser-induced plasma spectroscopy," *Spectrochimica Acta Part B* **56**, 737–742.

Hybl, J. D., G. A. Lithgow, and S. G. Buckley. 2003. "Laser-induced breakdown spectroscopy detection and classification of biological aerosols," *Applied Spectroscopy* **57**, 1207–1215.

Kelley, S. S., T. G. Rials, R. Snell, L. H. Groom, and A. Sluter. 2004. "Use of Near Infrared Spectroscopy to Measure the Chemical and Mechanical Properties of Solid Wood," *Wood Science and Technology* **38**, 257–276.

Martens, H. and T. Naes. 1991. *Multivariate Calibration*, John Wiley & Sons, N.Y.

Martin, M. Z., N. Labbe, T. G. Rials, and S. D. Wullschleger, 2005. "Analysis of preservative-treated wood by multivariate analysis of LIBS spectra," *Spectra Chimica Acta B*. **60**(7–8), 1179–1185.

Rials, T. G., S. S. Kelley, and C-L. So, "Use of advanced spectroscopic techniques for predicting the mechanical properties of wood composites," *Wood and Fiber Science* **34**, 398–407 (2002).

# Optically Manipulated Microelectronics Artificial Retina

Z. Hu,[1] T. Thundat,[1] and E. Greenbaum[2]
[1]*Life Sciences Division*
[2]*Chemical Sciences Division*

Retinitis pigmentosa (RP) and age-related macular degeneration (AMD) are two common retinal degenerative diseases that have caused blindness for millions of people worldwide. The objective of this project to study the possibility and feasibility of building a novel optoelectrical artificial retinal (AR) prosthetic device that integrates an optical sensor, electrical circuitry, and a stimulation electrode into one unit, forming a high-resolution (>10,000 pixels) imaging device for vision improvement. This complete system-on-chip approach reveals a design of a thin (~25 μm thick) disc-like (~ 4-mm-diam.) device that is suitable for either epiretinal or subretinal implantation in vision-deficient patients.

## Introduction

In order to address the great need of retinal prosthesis, DOE launched a research project (DOE Lab 01-14) in 2000 to develop an artificial retina. ORNL is the leading DOE laboratory and is teamed with the University of Southern California (USC), University of California Santa Cruz (UCSC), North Carolina State University (NCSU), Second Sight, LLC, and four other DOE laboratories—Argonne National Laboratory (ANL), Lawrence Livermore National Laboratory (LLNL), Los Alamos National Laboratory (LANL), and Sandi National Laboratories (SNL).The team had proposed and worked on on a retinal prosthesis device based on a "one-pixel-one-electrode" design in which every electrode needs one wire from outside the eye. The key drawback of this approach is the extreme difficulty of packing a high-density electrode array into a small area (~ 5-mm diam.). Currently the largest arrays contain 60 electrodes in which the size of an electrode and its connection wire is less than 200 μm. Given the very restrictive eye structure and physical size of the electrodes, it is very unlikely that a much higher number of electrodes (>100 electrodes) could be packed into the eye without introducing other significant problems such as loss of flexibility and space.

To achieve high-quality and high-resolution visual stimulation, we proposed a semiconductor-based thin and flexible chip that could contain a large array of photodiodes (>10,000), field effect transistors (FET), and other microelectronic circuits powered by one pair of DC/AC biases between the chip and human body. The key advantage of our design is that each stimulation pixel is self-contained, and there is no need to have a large number of wires from outside the patient's eye (only two wires are needed). In order to learn if this new approach would work, two questions needed to be answered: (1) if the circuitry could be fabricated and perform as needed and (2) if a Si chip could still function properly after being thinned down to ~25 μm.

## Technical Approach

After reviewing the benefits and shortcomings of current approaches, we proposed a complete system-on-chip approach to address the needs and requirements of an artificial retinal prosthesis device. We designed a semiconductor-based microelectric device that contains an array of photodiodes, metal oxide semiconductor field-effect transistors (MOSFETs), stimulation electrodes, and other circuitry elements. Photodiodes capture light and convert optical energy to a DC/AC voltage that controls the gate voltage of a DC/AC-biased complementary metal oxide semiconductor (CMOS)-FET. By doing so, the electrical current passes from the FET source (connected common DC/AC bias) to drain (connected to retina) and is controlled and manipulated by the photo diode–generated DC/AC voltage and current. In other words, the light intensity captured by the array of photodiodes changes the retina stimulation current and voltage. Present CMOS fabrication technology allows us to make both photodiodes and FETs as small as only a few micrometers on silicon or other semiconductor substrate. The photodiode and FET pair circuits are arranged in a large array that is repeated through entire chip. A common bus connects all bias leads of the photodiode FET pair circuit, while a doped conductive semiconductor substrate serves as a common ground that is connected to patient's body. Metalized FET drain exposes and is in direct contact with the retina neural cells above each drain lead. The electrical circuit is completed by connection to a fixed or variable DC/AC power source (such as a battery) between the common bias bus line and the patient's body, which connects to the backside of chip. Depending on the particular power source that is selected, this part of the circuit could be inside or outside of patient's body. As a result, only a single DC/AC power lead is needed to connect from the implanted chip, which greatly simplifies the system and reduces the difficulty of implantation. With a suitable circuit design, this device should be able to generate a

high-resolution image onto the patient's retina neural network and create a visual impression. If a variable DC/AC power source is used, the neural stimulation intensity could be changed with the DC/AC bias voltage, which implies that a patient could see images at different light intensity levels, just like adjusting the volume control of hearing add device.

Figure 1 shows the concept design of implantable optical manipulated FET artificial retina array. An array of photodiodes and FETs, interconnected with each other, is built on a very thin silicon or another semiconductor substrate. In order to fit better to the contour of eye and avoid damaging the retina, the proposed device is a thin, flexible, round disc that has a thickness less than 30 μm and is a few millimeters in diameter. As the bottom of the chip is conductive and touches the outer layer of retina that conducts electrical current through patient body, DC/AC bias voltage is applied between the power lead and patient's body (preferably close to eye). In this way a close-loop circuit is formed. The drain lead of the FET of the individual photodiode/FET pair is also conductive and touches the inner layer of retina when the device is implanted between the inner and outer layer of the retina. When a photodiode senses incoming light, it converts light power into an electrical voltage potential that acts like a valve changing the electrical current from the FET source to the drain and stimulates the retina nerve cells right above each FET drain conductive pad. The size of each photodiode and FET are in a range from thousands of micrometers to less than 1 μm, depending upon the fabrication process.

In a more sophisticated design, more complex circuitry might be utilized, replacing the single FET to perform other functions, such as signal filtering and amplification, that could help further improve the patient's visual capability.

The photodiodes could be operated under three modes: zero bias, positive bias, and negative bias conditions. Depending upon a particular patient's retina situation, the device could be designed and fabricated to operate under one mode. For a more complex situation, it is possible to have a mixture of all three modes circuits on different areas of a single device for better clinical responses.

Silicon or other semiconductor-based photo diodes have a spectrum response range from 300 to 1100 nm, which is much wider than the human eye spectrum response. This implies that a patient with an implanted artificial retina device could see infrared (IR) and ultraviolet (UV) images that are not visible even to people with perfect vision. It also implies that this device could help people with healthy eyes enhance their visual capabilities. For example, a solider with an implanted device could see clearly at night (IR vision) or see through the cover of an object (UV vision) without the need to carry and wear a heavy night vision device or UV vision

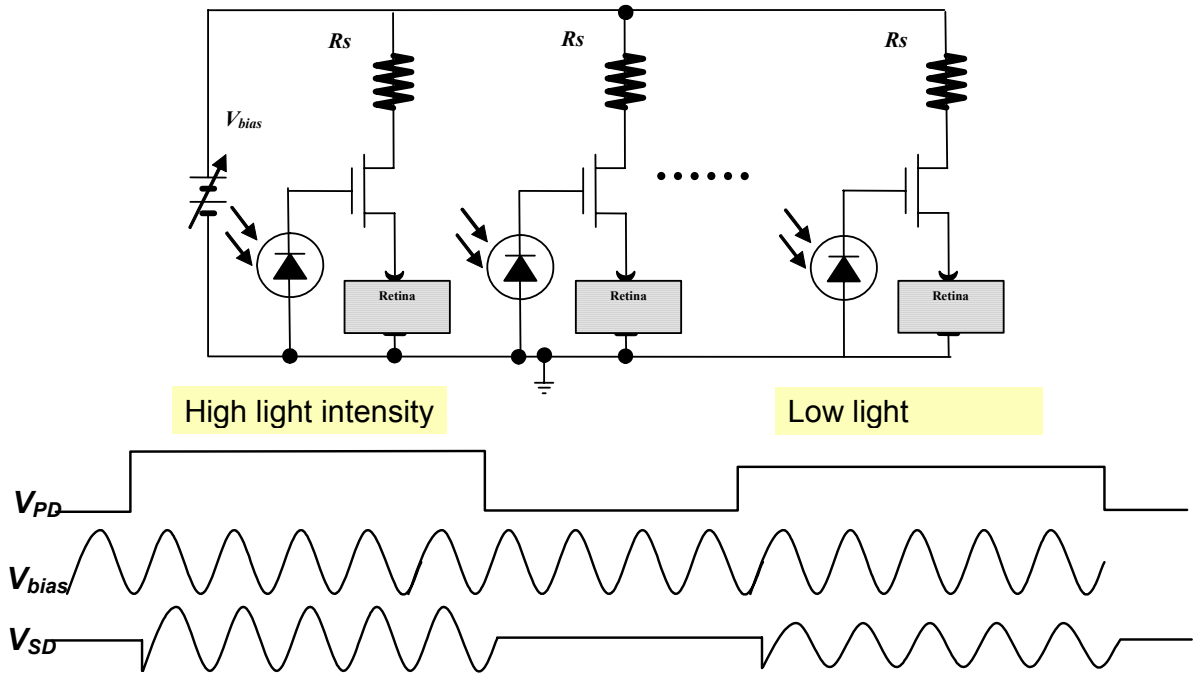


*Fig. 1. Concept design of implantable optical manipulated FET artificial retina array.*

device. A special microelectronics circuit could select and enhance the optical signal in different wavelength ranges as needed.

The output of the photodiode when reverse biased is extremely linear with respect to the illuminance applied to the photodiode junction. This implies that the FET gate voltage and ISD linearly correspond to the intensity of light luminance. A photodiode's capability to convert light energy to electrical energy, expressed as a percentage, is its Quantum Efficiency (Q.E.). The sensitivity of a photodiode may also be expressed in practical units of amps of photodiode current per watt of incident illumination. Q.E. is a wavelength dependence quantity which has a range of 0.161 to 0.887 for a wavelength range from 300 to 1100 nm for silicon-based photo diode.

MOSFET is a voltage-controlled device with three leads: source, gate and drain. A small change in input voltage at the gate lead causes a large change in output current. Depletion and enhancement modes are two basic FET operation modes. MOSFET has very high input resistance (>100 MΩ) and very small gate leakage current (~nA).

As preparation work, we successfully designed and fabricated a photodiode array in an area of 1 mm x 1mm which contains more than 6,000 40-µm × 40-µm photodiodes. Initial experiments demonstrate that the photodiode array responds to the intensity of light under the three operation modes discussed above.

## Results and Discussion

To answer the first question at the end of the Introduction, we first designed and built a 100-pixel array model (4.5 in. × 6 in. × 1 in.) using off-the-shelf parts in which 100 photodiodes are placed on one side of a printed-circuit (PC) board and 100 LEDs with FET amplification circuits are on the other side of the board and powered it with four D-size batteries. When a light pattern was projected on the photodiode side of board, the amplified LEDs reproduced the same light spot pattern and correspondingly mimicked the light intensity on the backside of the PC board. Additionally, we also tested the circuit with one DC power and one AC signal and obtained desirable results. Then the tested circuit was successfully transferred into a chip layout using integrated circuit (IC) design software. Limited by current funding ($75K total), we could not pursue actual fabrication as each run would cost about $30K plus packing costs. Nevertheless, our work thus far has already proved the feasibility of the proposed circuit design concept, thus meeting the original objective of this seed money project.

Additional efforts were devoted to determining whether any commercially fabricated IC chip and silicon wafer could be thinned down to ~25 µm from the original 300 µm. Two thinning methods have been tested: chemical mechanical polishing (CMP) and deep reactive ion etch (DRIE). Both methods demonstrated the possibility of thinning down the IC chips and silicon wafers. We thinned several commercially fabricated simple IC chips down to about 40 µm. At that thickness these samples exhibited a certain degree of flexibility, as shown in Fig. 2(a). Thinned Si chip could be bent around a 42-mm-diam. quartz tube [Fig. 2(b)].

Beginning with 250-µm-thick wafers, our thinning procedures can be summarized as follows:

- Deep reactive ion etching (DRIE)—1~2 mm/min. etching rate; down to ~100 mm
- Chemical mechanical polishing (CMP)—down to ~60 mm

For DRIE, we were able to obtain up to 1-µm/min

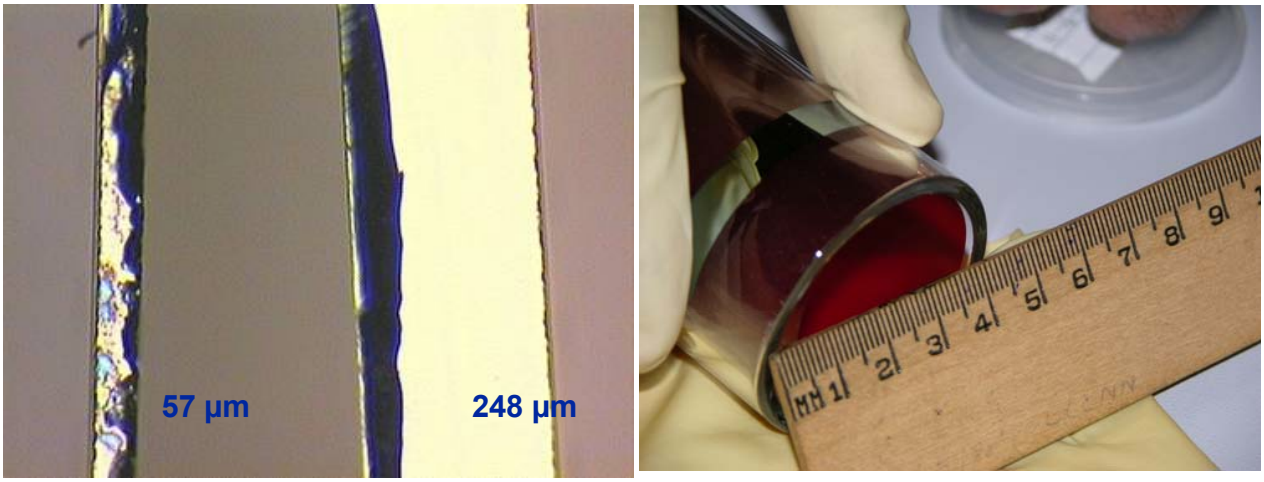


*Fig. 2(a). Side-to-side comparison of the original Si 250 µm chip (right) had been thinned down to 57 µm (left) using a chemical mechanical polishing process. (b) Flexibility of Si sample shown wrapped around a 42-mm-diam quartz tube.*

etching rate, but the etching rate dramatically decreased when the sample chamber became hot, even when we were under a 5-min-etching/5-min-cooling operation pattern. A cooling stage in our DRIE system would overcome this problem and also prevent possible thermal damage caused by the high temperatures experienced during ion etching.

## Benefits

During this project, we filed an invention disclosure entitled "Direct view imaging and displaying electronic system" (ID 1465, S-105,064) to the ORNL intellectual property office. In this disclosure, we described a novel fully integrated imaging and displaying system. The described device borrowed the same concept from our original artificial retina proposal and could be made by the standard CMOS process at rather low costs with ultrahigh anti-dilution display pixel resolution (<100 μm/pixel) with unlimited theoretical display area, high pixel density, low power consumption, and possible full-bandwidth light sensing spectrum (from UV to IR). The device is also lightweight, easy to assemble and integrate to other imaging system (such as a telescope), and very thin (silicon wafer thickness 300–500 μm). The possible applications of this device could be found in many areas for both civilian and military purposes. Besides DOE, this device might be applied in areas of anti-terrorism and defense and scientific research in other federal departments such as DHS, DOD, NASA, NIH NRC, and EPA. We have approached both Army and Navy research program managers for possible funding. They have expressed great interest in our concept in defense-related applications such as active camouflage and concealment. We are still working with those agencies to secure possible future funding.

# Mesoscopic Fluidic-Based Actuators

J. F. Jansen and L. J. Love
*Engineering and Science Technology Division*

Mesoscopic systems (characterized as being in the "sugar-cube to fist size") bridge the gap between the micro-electro-mechanical systems, commonly called MEMS, and the human scaled world. While ubiquitous in nature, there are still fundamental hurdles that must be crossed before the design and control of systems of this scale can become reality. The primary focus in this research effort has been directed at actuation at this scale. Miniaturization of actuation to the mesoscopic scale promises to enable new classes of systems in future medical instruments to future military and aerospace systems. However, existing approaches to miniaturization of actuation technologies (electromagnetic, electrostatic, piezoelectric, magnetostrictive, shape memory, and electro-active polymer material) have limited performance due to fundamental physical limitations based on scaling laws (Jansen 2000). While fluidic devices scale well into the mesoscopic domain (e.g., lab-on-a-chip technology for chemical analysis applications), preliminary studies on mesoscale fluidic actuation suggests the potential for forces and displacements up to several orders of magnitude greater than existing meso-scale actuation technologies are possible. The fundamental challenge to meso-scale fluidics is the control of the fluid. The target pressures (~1000 psi) and the ability to precisely modulate the fluid flow (<< mL/sec to 10s of mL/sec) quickly are far beyond the current state of the art. Based on internal feasibility analysis, it appears that the proposed actuators technologies have the potential of radically improving the performance of a robotic surgical system. Improvements in static stiffness by an order of magnitude, increase in overall packaging by an order of magnitude, improvement in closed-loop bandwidth by almost an order of magnitude, and the potential of tracking the surgeon's tactile signal and removal of tremor all appear feasible.

## Introduction

One of the most advanced robotic assist device on the market is the DaVinci® Surgical System by Intuitive Surgical®. This system has been cleared by the United States Food and Drug Administration to perform surgical procedures including general laparoscopic surgery, thoracoscopic (chest) surgery, laparoscopic radical prostatectomies, and thoracoscopically assisted cardiotomy procedures. The advantage of the DaVinci® and other systems like it (e.g., AESOP® system by Computer Motion, Inc.) is that the recovery time is significantly reduced due to the smaller incisions made on the patient. Other application areas such as hip and knee replacement are just beginning (e.g., ROBODOC® by Integrated Surgical System), with robotic-like-devices being applied utilizing modern-day machine tool techniques to damaged joints and thereby radically improving the success rates and overall durability. While these systems are called robotic assistants, they are really teleoperated systems (i.e., only operate under the guidance of a human operator) similar to the master-slave electromechanical manipulators developed by the nuclear industry.

While the DaVinci® represents the state of the art in robotic surgery, many in the medical community believe that significant improvements will be required before this technology will become pervasive. Specifically, the current system is force reflecting (i.e., the surgeon can feel what the slaves are toughing and can transmit his/her forces back to the slave). However, this important mode of operation is typically disabled due to poor performance resulting from mechanical friction and compliance. Due to the poor mechanical properties of the slave manipulators (e.g., significant mechanical compliance, large friction, hysteresis, etc.), automating or assisting with some of the mundane surgical tasks such as suturing is not possible with the current system. Finally, the overall volume of the slave system is too large; it literally takes up most of the operating room. Multiple arm pairs allowing multiple surgeons to work in unison is currently not feasible. Volume and weight are of critical importance in certain military applications such as portable trauma facility. One of the critical technologies required to overcome these limitations is in the area of actuation.

Based on internal feasibility analysis, robotic surgery needs actuators that have the performance of hydraulics but in the sugar-cube to human-fist size. This size range is in the mesoscopic domain (Dew 1988), and hydraulic actuators in this regime will be called mesoscopic fluidic actuators (MFAs). Actuation through controlled fluid displacement is actually one of the oldest forms of actuation; however, very few researchers (Peirs 2000) have explored the general merit of this form of actuation at the meso-scale. There are many advantages to scaling of fluidic devices (e.g., the lab-on-a-chip) in terms of movement of small amounts of materials (Love 2004).

However, it is our contention that there are likewise many advantages to scaling fluidic systems in terms of actuation.

## Objectives

Some of our concerns when trying to understanding how fluidic systems scale (Drexler 1992; Peirs 2000) into this domain are (1) when laminar flow and capillary forces dominate in the transmission of a fluid, (2) when the basic orifice equation (flow $\alpha\sqrt{}$Pressure) changes from the turbulence assumptions, and (3) when the rubbing friction of seals against the wall dominates over the frictional forces due to fluid pressure in an actuator as well as other physical phenomenon. Our primary scientific challenge will to be to develop the scaling laws and to experimentally verify that fluidic actuators can be controlled at the mesoscopic scale at the required performance levels. Based on the flow requirements, any flow control valve would have to overcome fluid forces of just a few ounces with displacements in the 10- to 100-μm range and would have to fit inside a packaging volume of less than 1/8th to 1/16th of a cubic inch. To verify our results, we designed and fabricated an actuator with a control valve that exceeded the power density of a conventional electric motor system.

## Results and Discussion

The two major accomplishments of this work include (1) understanding and developing the scaling laws associated with the mesoscopic regime and (2) the design, construction, and testing of flow control valve and actuators. Two actuators are shown on the left of Fig. 1. The smaller actuator (0.09 in. in diameter) provides 2.4 lb of force with 0.3 in. of displacement, while the larger actuator (0.38 in. in diameter) provides 19.8 lb of force with 1.0 in. of displacement. Both have a dynamic response exceeding equivalent human muscle actuation. A positional sensor based on a change in the internal magnetic field of the hydraulic piston (not shown) would be integrated into the outer housing. To modulate the fluid flow, a mesoscale servo valve was constructed and is shown to the right of the Fig. 1. The power density of the overall system exceeded the power density of an electric system by a factor of three. The working fluid can be human friendly such as water or saline solution.

## Benefits

While the original motivation for this research was in improving robotic surgical systems, recent efforts are directed at enhanced prosthetic devices supported under DARPA's Revolutionary Prosthetic Program. In terms of prosthetic fingers and thumbs, mesofluidic actuators is one of the most promising new enabling technologies in terms of providing high-performance actuation within the volumetric constraints of the human finger and hand. Furthermore, technologies developed for fingers and hands have the potential to be scaled up to impact larger joints such as ankles, wrists, elbows, shoulders, and knees. While other markets exist (e.g., aerospace to industrial automation), the initial emphasis will be on this biomedical application, including medical robotic applications found in surgery due to the superior aspect ratio achievable with MFAs.

## References


Dew, A. 1988. "Mesoscopic Systems: Bridging from Micromachined Devices to Macroscopic Systems." *Mechatronics*. **8**, 521–534.

Drexler, E. 1992. pp. 28–35 in *Nanosystems: Molecular Machinery, Manufacturing and Computation*, John Wiley & Sons.

Jansen, J., et al. 2000. *Exoskeleton for Soldier Enhancement Systems Feasibility Study*, ORNL/TM-2000/256, Oak Ridge National Laboratory, Oak Ridge, Tennessee.

Love, L., J. Jansen, T. McKnight, Y. Roh, and T. Phelps. 2004. "A Magnetocaloric Pump for Microfluidic Applications," *IEEE Transactions on NanoBioscience* **3**(2), 101–110.

Peirs, J., et al. 2000. "Design of Miniature Manipulators for Integration in a Self-Propelling Endoscope," pp. 603–606 in Proceedings of Actuator 2000, 7th Int. Conf. on New Actuators, Bremen, Germany.


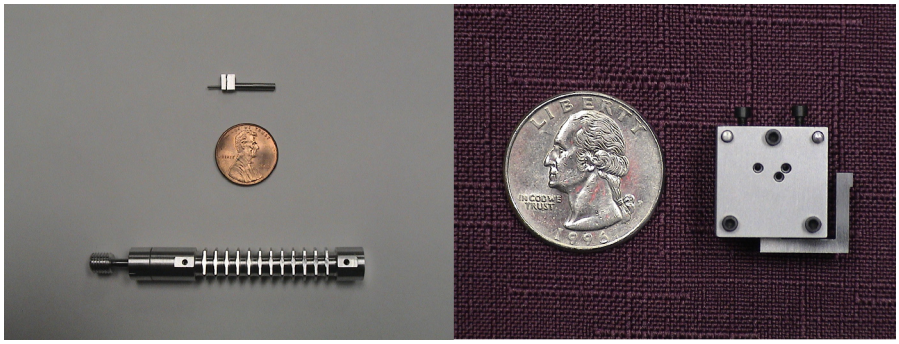


*Fig. 1. ORNL mesofluidic actuators and mesofluidic valve.*

# Development of a Methodology for Using Automotive Knock Sensors to Detect Start-of-Combustion for Diesel Engines Operating in both CIDI and HECC Modes

C. S. Sluder and R. M. Wagner
*Engineering Science and Technology Division*

This project focused on identifying a means of detecting start-of-combustion (SOC) in diesel engines that is sufficiency inexpensive and robust to enable deployment as a production measurement for use in engine control algorithms. Non-traditional combustion regimes for diesel engines (such as modulated kinetics, low-temperature combustion, and high-efficiency combustion) focus on causing conditions of pre-mixed combustion. Thus, it is of important to measure the length of the ignition delay period during which the fuel is mixed with in-cylinder gases. Detection of SOC can enable this measurement and therefore closed-loop feedback control of the engine parameters that are used to manipulate the ignition delay period. Knock sensors have been used for many years in spark-ignited engines to determine the presence of auto-ignition but were not used to determine the precise timing of the auto-ignition events. A suitable knock sensor was selected and deployed on a modern diesel engine. Experiments were carried out to investigate the response of the sensor to varying combustion conditions. An electronic monitoring circuit was conceived based on initial experiments. The circuit allowed monitoring of the knock signal on a crank-angle degree basis by an industry-standard combustion characterization system. Experiments showed that some aspects of the fuel injection events could be monitored in addition to robust detection of SOC under some engine conditions, at least on a cycle-averaged basis. Reliable detection under a broad range of fuel injection conditions and on a cycle-resolved basis remains as an area for future research.

## Introduction

This project was conceived as a means of enhancing the state-of-the-art in combustion control in diesel engines. In the past several years, much research has been conducted in pursuit of diesel combustion processes that do not produce either nitrogen oxides (NOX) or particulate matter (PM) emissions. These methods have mainly focused on producing conditions that result in increased fuel charge combustion in lean, pre-mixed modes. This is generally accomplished through introducing the entirety of the fuel charge prior to the passage of the ignition delay period. Exhaust gas recirculation (EGR) is used in tandem to reduce the thermal production of NOX. The combination of these conditions results in very low engine-out emissions. In some cases this is accomplished while retaining the characteristically high fuel efficiency traditionally associated with diesel engines.

At present, operation in non-polluting combustion modes (such as modulated kinetics, low-temperature, or high-efficiency clean combustion) is limited to low-power operation of the engine. Thus, real-world applications of this technology result in engines that must mode-shift as the demand for output power varies. The transient nature of engine conditions in real-world operation means that an engine must accomplish these mode shifts while the ignition delay period is variant. A robust, economical technology for sensing the start of combustion (SOC) would allow direct estimation of the ignition delay period and thus the opportunity for closed-loop feedback control. This would in turn allow for broader, more stable application of non-traditional combustion regimes, resulting in cleaner, more-efficient vehicles in the fleet. One study has investigated the use of knock sensors with diesels but did not include the effects on non-traditional combustion regimes (Jargenstedt 2000). There does exist a sizeable body of knowledge on the use of knock sensors with spark-ignited engines, with applications in pressure reconstruction (Urlaub 2004), knock detection (Worret 2002; Samimy 1996; Xiaofeng 1993), and heat transfer analysis (Zeng 2004).

The objectives of this project were to investigate whether a knock sensor (traditionally used and already in mass production for spark-ignition engines) could be used to provide the needed SOC measurement in a diesel engine and, if so, to outline a methodology for interpreting the signal. These objectives were achieved under certain engine conditions.

## Technical Approach

This project was approached from an experimental perspective. A knock sensor with a broad frequency response range was identified for use in this project since little knowledge of the characteristic knock frequencies for diesel combustion was available. Two identical sensors

were installed on a Mercedes 1.7 liter, 4-cylinder diesel engine at the Oak Ridge National Laboratory Fuels, Engines, and Emissions Research Center. Both sensors were located near cylinder 1, with one near the top of the cylinder bore and the other near the bottom. The engine was characteristic of a modern, direct-injection diesel engine and was equipped with a PC-based flexible control system. This control system was crucial to this project as it allowed parametric variation of the fueling parameters needed to investigate the knock sensor signal. The engine was also outfitted with high-speed piezo-electric pressure transducers to monitor the in-cylinder pressures. These were coupled with an AVL Indimodul pressure analysis system to characterize the combustion process in each cylinder. An IOTech Wavebook data acquisition system was utilized for high-speed data acquisition.

Early experiments focused on high-speed acquisition of the signals from both knock sensors as fuel injection parameters were varied. These data were utilized to determine the characteristic frequencies associated with combustion and to determine which sensor location offered the least extraneous noise. This was accomplished by examining the short-time Fourier transform (STFT) of the signals. This analysis provided a means of determining the frequency range of interest by examining the energy content of specific frequency ranges in specific time increments as the fuel injection and combustion processes occurred. Once a target frequency range was determined, digital filtering of the data was used to further investigate the relationship of the signal to the combustion process. These analyses allowed continuing data acquisition to focus on specific frequencies of the knock sensor signal response.

An electronic circuit was designed and implemented to allow measurement of the knock signal by the AVL Indimodul. This circuit incorporated a band-pass filter to reject unwanted signal, plus an RMS measurement to condense the highly transient signal to a DC voltage that was representative of the energy envelope of the signal. The AVL Indimodul was then utilized to gather the conditioned knock sensor signal in parallel with combustion and fuel-injection data. Data were recorded for 1000 sequential engine cycles for statistical correlation of the conditioned knock signal with combustion measurements.

## Results and Discussion

Initial experiments showed that the signal from the knock sensor that was located near the top of the cylinder bore contained less extraneous noise for this particular engine installation. Thus, this sensor signal was utilized for the remainder of the reported work. The sensor exhibited the strongest response to events in and around cylinder #1 because of its proximity. Events associated with other cylinders were also detectable to a lesser degree. Experiments were carried out with cylinder #1 firing and also with cylinder #1 deactivated. STFT analyses of both conditions showed that the energy content of the 20- to 30-kHz frequency band increased about 1 millisecond (ms) after the fuel injection event when the cylinder was firing. The non-fired condition did not exhibit the same increase. Therefore, this frequency range was investigated further.

A digital band pass filter was implemented in Matlab™ to reject signal components outside the frequency range of 20–30 kHz. The resulting filtered signal was examined in time-space to investigate its relationship to the fuel injection event. The filtered signal exhibited a sharp change shortly after the fuel injection event, suggesting that it did indeed correspond either to the fuel injection or combustion process. Since analysis of a large number of datasets was needed to examine the statistical correlation between the knock sensor signal and the fuel injection and combustion events was needed, a hardware implementation of the filter was undertaken. This allowed use of the AVL Indimodul and Concerto™ software to analyze the statistics of the combustion process during each engine cycle and the conditioned knock sensor signal simultaneously. The filter circuit selectively rejected portions of the knock response outside the 20- to 30-kHz band of interest and converted the resulting sinusoidal signal to a DC voltage proportional to the root-mean-square (RMS) value of the sinusoid. The time constant for this RMS measurement was selectable and was initially set at 200 μs (microseconds), or just less than 2 CAD at the 1,500 RPM speed at which most experiments were conducted.

Measurements of the 1000-cycle average conditioned knock sensor signal when injector #1 was fired at 100 CAD past top dead center (TDC) showed that a portion of the knock signal was due to the fuel injection process, rather than combustion. 100 CAD was selected as an injection location unlikely to result in combustion at any injection duration, and because the background knock signal was very low in this area. As the injection duration was varied from 100 μs to 160 μs, the knock signal was observed to increase when the AVL system (and engine output power) showed no combustion was taking place. It is very unlikely that the fuel injector opens at the 100-μs duration, and probably only partially opens up to a duration of 160 μs, which is the minimum duration for which this fuel injection system operates correctly. (This is due to the minimum injection duration of 160 μs that fully charges the injector drive circuit for the following injection event. Shorter durations do not fully charge the circuit, resulting in incomplete injector opening.) Once the duration exceeded 160 μs and was increased to 200 μsand then 300 μs, the signal was observed to remain more or

less constant. This suggests that the portion of the knock signal that is attributable to the fuel injection process is probably related to the opening or closure of the injector. Unfortunately, the fuel injectors for this engine were not equipped with a needle-lift sensor to confirm this hypothesis.

Repeating the parametric variation of the injection duration at an injection location of 20 CAD before TDC allowed investigation of the same signal when combustion was present. During these experiments, the lowest duration at which combustion was observed to occur was 225 µs. In this instance, only a very small combustion event was observed. As the duration increased, the amount of heat released by combustion increased. Once again, the 1000-cycle average conditioned knock sensor signal showed a positive response with injector firing, even though no combustion occurred at the shortest durations. The response was approximately the same magnitude as was observed with injections at 100 CAD after TDC. Once the duration reached 225 µs and combustion was observed, the average conditioned knock signal began to exhibit growth of a second peak following the initial response that has been attributed to the injection process. This response to combustion became noticeable in the signal behavior at approximately 225–250 µs duration and was pronounced at 300-µs duration, as shown in Fig. 1.

Examination of the average signal responses showed that under conditions of high EGR or retarded injection timing, the rate-of-heat-release (ROHR) was lower and produced correspondingly lower knock sensor response even at equivalent fuel mass rates, confirming dependence upon the rate of cylinder pressure rise. Variation of the fuel injection rail pressure during these experiments also showed that the sensor response to the fuel injection process did not appear to be significantly impacted by the fuel rail pressure in the range evaluated.

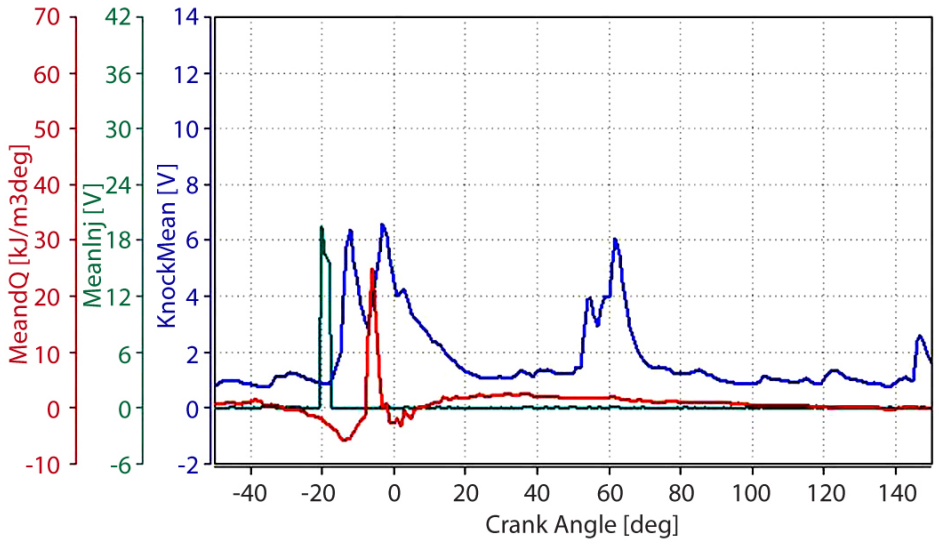


*Fig. 1. Fuel injection trace, averaged heat release, and averaged conditioned knock signal for a fuel injection event of 300-µs duration located at 20 CAD before TDC.*

## Benefits

Identification of a reliable, inexpensive means of measuring the start-of-combustion in diesel engines opens the opportunity to utilize this measurement in closed-loop feedback control system that can directly respond to variations in the ignition delay. Such variations can result from fuel quality issues (fuel cetane index), changes to the combustion process (such as EGR and combustion mode changes), and the normal range of operation of the engine. The ability to adjust engine control parameters to take advantage of opportunities and mitigate problems associated with these variations can allow broader use of non-traditional combustion regimes, resulting in cleaner, more-efficient diesel vehicles. The results of this study will be shared with DOE sponsors and industrial partners in an effort to glean feedback and funding for future studies in this area.

## References


Jargenstedt, M. 2000. "Detecting Start of Combustion Using Knock Sensor Signals," Linkopings University.

Samimy, B. and G. Rizzoni. 1996. "Engine Knock Analysis and Detection Using Time-Frequency Analysis," SAE Paper Number 960618.

Urlaub, M., and J. Bohme. 2004. "Reconstruction of Pressure Signals on Structure-borne Sound for Knock Investigation," SAE Paper Number 2004-01-0521.

Worret, R., S. Bernhardt, F. Schwarz, and U. Spicher. 2002. "Application of Different Cylinder Pressure Based Knock Detection Methods in Spark Ignition Engines," SAE Paper Number 2002-01-1668.

Xiaofeng, G., R. Stone, C. Hudson, and I. Bradbury. 1993. "The Detection and Quantification of Knock in Spark Ignition Engines," SAE Paper Number 932759.

Zeng, P., and D. Assanis. 2004."Cylinder Pressure Reconstruction and its Application to Heat Transfer Analysis," SAE Paper Number 2004-01-0922.

# Integrating High-Surface-Area Electrodes in Microfluidic Manifolds

T. E. McKnight,[1] A. V. Melechko,[2] G. W. Wright,[3] J. Matteo,[4] and M. L. Simpson[2]
[1]*Engineering Science and Technology Division*
[2]*Condensed Matter Sciences Division*
[3]*Nuclear Science and Technology Division*
[4]*Nanotek, LLC*

The feasibility of integrating exceptionally high-surface-area electrodes into microfluidic platforms was investigated. Close packed forests of vertically aligned carbon nanofibers (VACNFs) were synthesized as addressable electrode elements and successfully integrated with custom fabricated microfluidic manifolds. The VACNF electrodes provided approximately 6–10 times greater effective surface area than a planar electrode of equal geometric footprint. Additionally, the nanostructured architecture provided effective scaffolding for the electropolymerization of various films, thereby enabling the potential for even greater surface area in addition to demonstrating feasibility for application of the platform for a variety of processing approaches, including ion exchange and electroactive ion loading and release. Follow-on funding has been secured for further development of these architectures for the extraction and processing of $^{18}F$ from cyclotron-irradiated water for the development of positron emission tomography (PET) radiopharmaceuticals.

## Introduction

Based on technologies developed at ORNL, microfluidic systems have emerged that enable extremely complex chemical processing with very small amounts of reagents, including chemical separations (Gottschlich 2000), biochemical amplifications (Khandurina 2000), and combinatorial synthesis strategies (McKnight, pending J. M. Ramsey submission to *Anal. Chem.*, available on request). To date, a limitation of conventionally produced microfluidic platforms is that they cannot efficiently exploit electrochemical processing techniques, due to limitations in available surface area for integrated electrodes. This limitation has impacted the applicability of microfluidic systems for a variety of low-reagent-volume industrial applications. This proposal seeks to integrate novel, nanostructured high-surface-area ORNL electrode materials into microfluidic platforms to address the electrode-surface area-limitation of electroanalytical processing techniques. Successful demonstration will open new areas of research in microfluidic-based chemical processing and will position the Laboratory as a unique resource for integrating these nanoscale materials into functional fluidic platforms.

As an example application that leverages local industrial resources, we directed our research towards development of a platform that would be of value for radiopharmaceutical production of positron emission tomography (PET) tracers. PET has emerged as the leading-edge clinical tool for high-resolution, diagnostic in-vivo imaging, and specifically for imaging of cancer. In brief, very short half-life radiolabelled ($^{18}F$) deoxyglucose, FDG, is administered to the patient and accumulates in malignant tissue. Positron emission of the FDG within the tissue results in production of two simultaneous gamma rays in opposite directions, which enables high-resolution determination of the location of malignant tissue. The short half-life of FDG and other positron emitting pharmaceuticals mandates that they are quickly prepared and administered. Currently, PET pharmaceutical precursors are prepared in cyclotrons located in close proximity to the point of use. FDG is produced by first generating $^{18}F$ by cyclotron irradiation of $^{18}O$ water and then extracting $^{18}F$ from aqueous phase and performing an organic reaction in dry acetonitrile. Existing methodologies for this extraction and reaction are slow, bulky, consume large amounts of reagents, and may be unreliable, producing variable yield of final product. Improved methods to extract $^{18}F$ from $^{18}O$ water are required that will provide high yield of extracted $^{18}F$ into a minimal volume of dry acetonitrile (50-µL target volume) over a very short extraction period (2 min for 5 mL of $^{18}O$ water). Ideally, this extraction methodology could be compatible with microfluidic systems, which could provide both the extraction and reaction of $^{18}F$ to produce useful radiopharmaceuticals, such as FDG. We anticipate our microfluidic platform will provide newer, faster processing of $^{18}F$ for PET radiopharmaceutical production.

## Technical Approach

A promising electrochemical approach for $^{18}F$ extraction from $^{18}O$ water has been developed by the Institute for Nuclear Chemistry in Julich, Germany (Hamacher 2002). $^{18}F$ is accumulated from $^{18}O$ water

by anodic deposition onto the inner surface of a hollow bore glassy carbon tube. Rinsing and elution into aprotic solvents (i.e., acetonitrile) with or without phase transfer catalysts are then performed by reversing the holding potential on the electrode (vs a Pt pseudo-reference within the hollow bore). In its current format, the Hamacher apparatus provides efficient transfer of $^{18}F$ into aprotic solvents, but the macroscale geometry of the system does not provide the necessary concentration of $^{18}F$. Further, the macroscale geometry of the electrode system results in electrolytic decomposition of water during anodic accumulation, and this results in loss of the valuable $^{18}O$ from the system as evolved oxygen. Microfluidic manifolds to perform this approach are attractive but limited by the available surface area of the microfluidic platform if using traditional electrode approaches.

Using the Hamacher method as a guide, but by exploiting VACNFs as a unique, high-surface-electrode material, we have developed and are characterizing a microfluidic platform for performing the $^{18}F$ extraction from $^{18}O$ water. The originally proposed operational mode of the platform is similar to the Hamacher device (i.e., extraction via electrophoretic migration and anodic accumulation during hydrodynamic flow of aqueous phase $^{18}F$). However, based on preliminary results of the performance of this approach, we are now also incorporating the electropolymerization of a polypyrrole film to better accumulate and retain the fluoride anion. Ultimately, dry MeCN (or another dehydrating solvent) will be passed through the microfluidic platform while the $^{18}F$ is electrostatically retained upon the VACNF electrode. An elution volume of dry acetonitrile will then be loaded into the chip and the holding potential removed or reversed, allowing elution of the $^{18}F$ into a volume of dry acetonitrile equal to that of the fluidic platform (i.e., 50 µL). While operationally similar to the Hamacher apparatus, but with the addition of a fluoride-retaining polypyrrole film, the volume and microscale dimensions of our system will allow much more rapid and efficient concentration of the $^{18}F$ into dry MeCN and will eliminate electrolytic loss of the $^{18}O$ from the aqueous phase.

## Results and Discussion

Microfluidic prototypes have been constructed as outlined in Fig. 1. Four-inch silicon wafers were thermally oxidized to provide a 1-micron-thick insulation layer on their surface (1A). The thermal oxide was then metallized with 100A Ti, 1000A W, 100A Ti, and 100A Si (1B) to provide an underlying conductive layer for interconnection to the VACNF electrode material. Lithography and a liftoff technique were used to pattern nickel catalyst in regions of desired nanofiber growth (1C-1F). Nanofiber synthesis was conducted in a dc-PECVD system dedicated to nanofiber growth (1G). A subsequent lithography step then defined the underlying electrode interconnect for the nanofiber electrode (1H), and a refractory metal etch was used to pattern this electrode interconnect (1G). In parallel, glass microfluidic manifolds were fabricated as outlined in Part 2 of Fig. 1. Fused silica plates were metallized with 500A of chrome (2A) and lithographically patterned to define the regions that were subsequently etched to produce microfluidic channels (2B-2C). A wet chrome etch was used to strip the protective chrome from these regions (2D), and the silica was etched using a buffered oxide etch (2E). The plate was then cleaned with a resist strip/chrome etch (2F) and metallized with a chrome/gold electrode using a photostencil shadow mask and angled deposition in order to provide coverage on the sidewall of the channel (2G). The silica plate was then diced into multiple fluidic manifolds, and each manifold was drilled to provide fluidic access ports into the manifold. The two parts fabricated in part 1 and part 2 were then mated and sealed

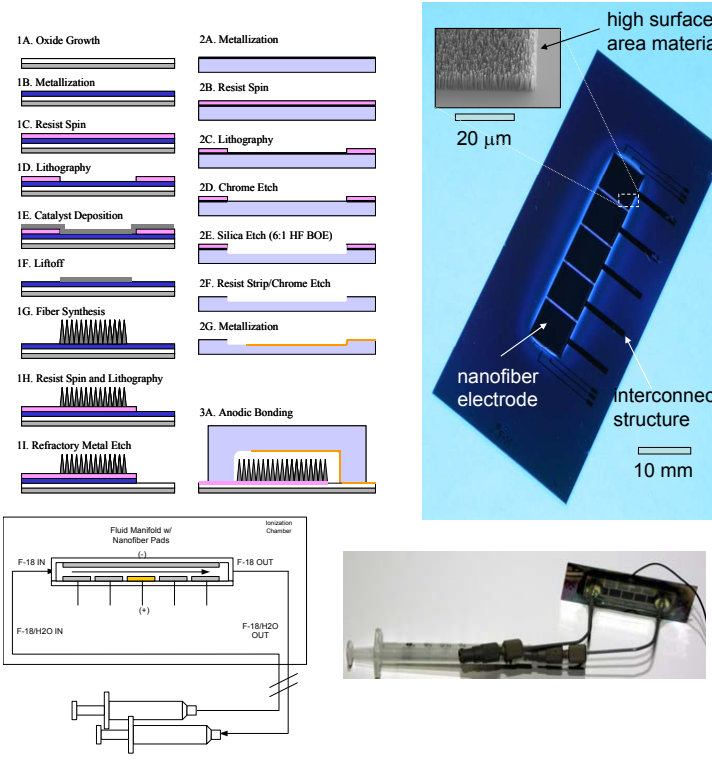


*Fig. 1. (Top Left) Schematic of the fabrication of microfluidic manifolds with integrated VACNF-based high surface area electrodes. (Top Right) A completed multielement nanofiber electrode substrate and scanning electron micrograph of the high-surface-area VACNF electrode material. This substrate is subsequently mated with an etched fused silica microfluidic manifold (bottom right) to complete the fabrication of the device.*

using a commercially available medical grade epoxy. Fluid injection ports were then attached to the entry ports and the prototypes were fluidically driven with syringe pumps. Electrical interconnects to the manifold were provided via silver-loaded epoxy attachment of a wiring harness. The assembled manifold provided five individually addressed VACNF electrodes with 6-mm × 6-mm geometric surface area, and 6 additional microelectrodes with 100-μm × 100-μm footprint.

Electrochemical characterization of nanofiber forest electrodes has been performed and has validated that the nanostructured surface provides a nanofiber-height-dependent increase in the apparent surface area of the electrode (e.g., for 10-micron-tall fibers, there is approximately 6–10 times the amount of surface area vs planar electrodes of identical geometric footprint). Experiments have also been conducted to verify the survival of the nanofiber-based electrode material during $^{18}F$ processing. Nanofiber electrodes remain intact under typical operating parameters (<2V vs Au pseudo reference). At higher potentials, putative generation of low levels of HF appear to attack the electrode interconnect structure and release the fibers from their substrate. However, the nanofiber electrode material itself remains intact. While these operating conditions are beyond those necessary for our immediate application, it is anticipated that substrate passivation layers (UV-crosslinked epoxy) would eliminate this failure mode if higher voltages are required in future efforts (McKnight 2003).

Anodic capture experiments were conducted by placing the microfluidic manifold in an activity counter and measuring the activity and therefore amount of $^{18}F$ accumulated in the manifold during flow and electrostatic capture on the native nanofiber electrode surface. Initial experiments have demonstrated some retention of activity (and therefore fluoride ion) in the device during fluidic capture. However, these experiments are conducted blind due to the necessity of running the manifold within the confines of a hot cell and within the activity counter apparatus. Further, access to the hot cell and cyclotron produced $^{18}F$ was limited. Therefore, we have also investigated cold fluoride capture based upon direct fluoride concentration measurement with an ion selective electrode. These measurements are conducted with a solid state fluoride selective electrode and therefore require relatively large processing volumes (>5 mL) and are inherently less sensitive than activity counting methods. We anticipate that the lack of sensitivity is limiting our ability to observe fluoride accumulation in the system and therefore are developing further improvements in the apparatus to promote more efficient fluoride ion capture. These include the electropolymerization of anionically doped polypyrrole on the nanofiber scaffold. This electronically conductive polymer can be synthesized with specific anionic dopants, and these dopants may be incorporated or expelled from the polymer matrix based upon its oxidation state resulting from applied potentials. Follow-on funding has been secured, allowing the continuation and optimization of fluoride capture and release from the nanofiber electrode. We are currently investigating a variety of anionic dopants to arrive at a polypyrrole film well suited and perhaps even specific for fluoride ion capture and release.

## Benefits

This project has successfully demonstrated the incorporation of VACNFs into microfluidic manifolds for the purpose of providing high surface electrodes using standard, and readily available, microfabrication techniques. For our demonstration system, we have designed and are now optimizing a microfluidic platform for the rapid and efficient concentration and extraction of $^{18}F$ from cyclotron irradiated water. A fluoride ion concentration chip is complementary to both future microfluidic chemistry platforms and to current conventional chemistry platforms for synthesizing PET biomarkers. The perceived value of this specific demonstration platform has successfully generated follow-on funding to continue this research effort.

## Acknowledgments

The authors wish to thank P. H. Fleming and T. Subich for assistance with metal depositions, D. Hensley for nanofiber synthesis, and D. Thomas and R. Kasica for CNMS User Support.

## References

Hamacher, K., H. Coenen, and G. Stocklin. 1986. "Efficient stereospecific synthesis of no-carrier-added 2-[18F]-fluoro-2-deoxy-D-glucose using aminopolyether supported nucleophilic subsitiution," *J. Nucl. Med.* **27**, 235–238.

Hamacher, K., T. Hirschfelder, H. H. Coenen. 2002. "Electrochemical cell for separation of [F-18] fluoride from irradiated O-18 water and subsequent no carrier added nucleophilic fluorination," *Applied Radiation and Isotope* **56**, 519–523.

Gottschlich, N., et al. 2000. "Integrated microchip device for the digestion, separation, and postcolumn labeling of proteins and peptides," *J. of Chromatography B* **754**, 243–249.

Khandurina, J. et al. 2000. "Integrated system for rapid PCR-based DNA analysis in microfluidic devices," *Anal Chem.* **72**, 2995–3000.

McKnight, T. E., et al. 2003. "Effects of microfabrication processing on the electrochemistry of carbon nanofiber electrodes," *J. Phys. Chem B* **107**, 10722–10728.

# Distributed Capacitance Sensor System for Conduit Monitoring Applications

L. C. Maxey and H. D. Haynes
*Engineering Science and Technology Division*

Some of the most sensitive and valuable electronic information today is often transmitted through simple conduits. While much information is encrypted, there remain signals of interest that for various reasons cannot be encrypted at their source. Often visual inspection of the conduit is the only means for detecting potential tampering events. A means for providing real-time tamper monitoring of conduits is of interest for protecting un-encrypted information and for enhancing the security of encrypted information. In the course of this project, a proof-of-principle system has been demonstrated for detecting intrusion into and/or tampering within installed conduits. The system is based on a distributed capacitance sensor (a cable) that is included among the cables within the conduit. The sensor is coupled to a very high gain charge-sensitive amplifier and is capable of detecting motion or contact. Electrical signature analysis (ESA) is applied to the signals from the sensor to distinguish potential tampering events from those arising from foreseeable background noise sources. The results demonstrated that the system could detect the signals that would likely be generated during an attempt to breach the conduit. Moreover, signals from events intended to simulate foreseeable background noise sources were virtually always recognized and differentiated from the simulated tampering events.

## Introduction

Capacitance sensors are among the most sensitive sensors employed for metrological and security applications. A variety of commercial systems exist that use capacitance sensors for security and safeguards applications. Among these are several systems that use distributed capacitance sensors in the form of cables that can be attached to items of interest. These are commonly applied as perimeter fence sensors, where the cables are attached to (typically) chain-link fencing to detect signals that would be produced by cutting, climbing, or otherwise penetrating the perimeter fence. These products are extremely effective and serve their product markets well, reliably detecting intrusion events. However, the task of differentiating environmental noise from actual intrusion events is challenging. Moreover, it varies significantly with each application. The typical means for addressing this challenge is to use band pass filtering (usually only one or two selectable pass bands) as the primary means of signal analysis. Secondary analysis methods may include counting the number or duration of events that exceed a preset threshold to differentiate between situational noise and actual intrusion events. By employing more elaborate means of signal processing, the applications for distributed capacitance sensors may be significantly expanded. Electrical signature analysis (ESA) (Haynes 1995) is a technology that has been applied to a wide variety of challenging measurement scenarios during the last two decades. It provides a means for extracting information from beneath what would conventionally be considered the "noise floor" of the applications to which it is applied. It combines elements of time domain analysis, frequency domain analysis, and pattern recognition to enable important diagnostic information to be extracted from signals as mundane as the current applied to an inductive motor. Through the use of ESA, specific signal characteristics have been used to identify incipient failures (bearings, gears, and pumps etc.), enabling preventive maintenance to forestall potential peril. The sensitivity of capacitance sensors combined with the selectivity of ESA enables the development of enhanced sensor systems capable of recognizing tampering events in the presence of a large variety of background noise events.

## Technical Approach

The conduit monitoring system developed by the authors employs a distributed capacitance sensor cable that is extremely sensitive to motion or contact. Several types of cable transducers were considered, including custom configurations, but the sensitivity of one particular type of twisted, shielded-pair cable provided excellent results. A low bias voltage (6 V) was applied to the shield of the cable, and the motion signal was extracted from one of the two conductors in the twisted pair. A high-gain (A = 1010), charge-sensitive amplifier was used to convert the tiny motion-induced current signal into a voltage signal. The preferred preamplifier configuration was a self-contained unit powered by two lithium batteries. The current consumption of the circuit was so small that the unit operated reliably for many months on a single set of batteries.

A test platform was initially constructed by placing a 1-m length of conduit in a series of clamps to mount it to a benchtop. The conduit was then filled with several un-energized cables to simulate an installed conduit. A distributed capacitance sensor cable was then added into the conduit and connected to an amplifier. A laptop computer incorporating a National Instruments data acquisition card and Labview software enabled the amplifier signals to be acquired and analyzed. After initial experiments and development of preliminary signal analysis routines, a more elaborate bench-scale test apparatus was assembled. This consisted of a test frame approximately 2 m long into which a length of flexible conduit was suspended. This provided the ability to subject the conduit to a variety of vibration scenarios without directly touching the conduit. This apparatus is shown in Fig. 1.

ESA techniques were applied by first gathering a series of signals that were generated under a variety of scenarios. The system was configured so that any signal that exceeded a preset triggering threshold would cause a data sample of 10 s to be acquired for analysis. Tampering scenarios were simulated by manipulating the conduit or the conductors within it in ways that might be anticipated during an attempt to breach the conduit or penetrate a cable. Background signals were generated in a variety of scenarios seen as foreseeable in an industrial environment: electrical noise spikes, vibrations from rotating machinery, even a tool being inadvertently dropped onto a conduit. Signals were also generated by simulating tampering activities while simultaneously introducing background noise. The collected data were then analyzed to observe the characteristics associated with tampering versus background events.

Some of the signature analysis methods were adapted from previous applications of ESA, while others were developed based on the specific nature of the signals observed in the collected data. The signature analysis methods that were used to analyze the acquired data were arrived at empirically through many iterations. Fundamentally, the approach was to use a multi-pass analysis to determine if the data appeared to be characteristic of background sources alone. When any of the analysis methods determined that the signature of the signal was characteristic of a background event, the analysis halted, and the event was identified as background on the user interface. However, any event that did not meet the criteria for a background-only event was identified as tampering on the user interface.

## Results and Discussion

The sensor/amplifier combination was stable at the millivolt level under quiescent conditions yet was extraordinarily sensitive to any contact or motion. Even a light touch with a fingertip produced a signal response of tens of millivolts. The sensor system proved to be sensitive to the kind of bending, probing, and twisting that might be expected during tampering events, as well as single-shock transients and periodic vibrations that might routinely be expected in an industrial environment.

A total of 75 data blocks that represent a variety of simulated tampering and background events were obtained using the prototype system. Several types of background events were created in the lab to simulate what might be expected in normal conduit installations. For example, an unbalanced fan was used to simulate conduit vibrations that might result from nearby rotating equipment. Single mechanical impacts were performed that would simulate something bumping the conduit. The conduit was also placed near an energized motor, which resulted in induced electromagnetic noise. Multiple tampering events were generated by conducting the kind of manipulations that might be required to breach a conduit wall. Other tampering events were generated with the assumption that the conduit wall had been breached. In these cases, the cables themselves were manipulated in a manner

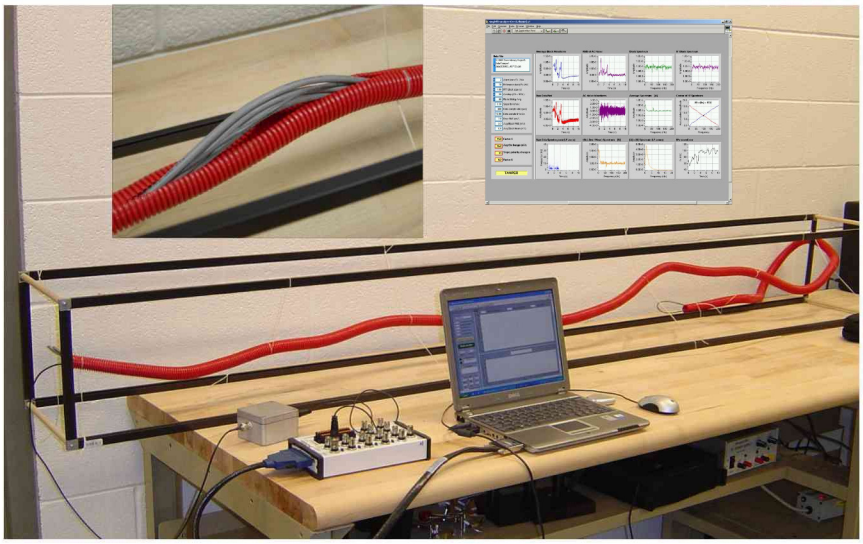

*Fig. 1. Bench-scale conduit monitoring sensor system test and development apparatus.*

consistent with trying to access a particular cable or insert a probe into one of the cables. Several tamper events were simulated while background noise was also present. In these cases, each tamper event was performed by gently pushing, twisting, or bending the conduit. The overall performance of the bench-scale system was impressive: A correct event diagnosis was automatically made by the system software in 74 of the 75 cases (98.7%).

A brief video was created to illustrate the performance of the system. This video shows the system being subjected to major vibrations and impacts, which are recognized as background events. In contrast, the video shows that simply grasping the conduit or manipulating any of the cables within the conduit results in a tampering indication.

## Benefits

The results of this work were presented at the annual meeting of the Institute of Nuclear Materials Management (INMM) (Maxey 2005). Attendees from the International Atomic Energy Agency (IAEA), Department of Energy (DOE), and Department of Homeland Security (DHS) all approached the presenter afterwards to express interest in the technology. In subsequent discussions with the IAEA, they have expressed immediate interest in seeing further development of the technology and have initiated a request to the International Safeguards Project Office (ISPO) to fund that development. This is expected to result in a multi-year-funded effort to produce a sensor system prototype for application in international monitoring scenarios.

A program development effort, supported by funds from the Engineering Science and Technology Division, has been has been initiated to develop additional applications and research related to this technology. It is anticipated that DOE will support additional funding of this sensor technology for applications other than conduits. Similarly, DHS is expected to be interested in the technology as a means for ensuring the security of shipping containers or other items that might represent potential terrorism targets.

While this project draws much of its success from the diagnostic applications of ESA at ORNL, it also promises to contribute additional expertise to the ESA diagnostics portfolio. One of the areas that will be targeted for development through the IAEA funding will be a "learning mode" in which the system will begin to differentiate different types of events using an automated process (neural net, fuzzy logic or other). While primarily intended to facilitate the identification of "tampering" events for monitoring systems, this methodology is expected to be useful in diagnostic applications, for automating the development of markers that are indicative of the state of health of industrial equipment. This will likely lead to additional funded research and development of ESA diagnostic systems.

## References

Haynes, H. D. 1995. "Electrical Signature Analysis (ESA) Developments at the Oak Ridge Diagnostics Applied Research Center," in *Proceedings - COMADEM '95, the 8th International Congress on Condition Monitoring and Diagnostic Engineering Management*, Kingston, Ontario, Canada, June 26–28, 1995. For the interested reader, more information on ESA may be found at http://www.ornl.gov/sci/esa.

Maxey, L. C. and H. D. Haynes. 2005. "Distributed Capacitance Motion Sensor Employing Electrical Signature Analysis," in *Proceedings - INMM Annual Meeting*, July 10–14, 2005, Phoenix, AZ.

# A Device for Gated Gas Sampling of Transient Combustion Exhaust Events

W. P. Partridge, S. A. Lewis, and J. E. Parks
*Engineering Science and Technology Division*

Two gated sampling systems were demonstrated and evaluated based on rigid and deformable containers. The function of the systems is to selectively sample within fast exhaust species-pool transients and allow post-sampling analysis by conventional steady-state instrumentation. Both sampling systems displayed linear response with number of samples and gate width. With a fast direct-lift solenoid switching valve, transient response times as high as ca. >10 Hz can be realized. The two designs have unique strengths and can be tailored to specific application challenges. The unique insights afforded by gated sampling of dynamic exhaust streams was demonstrated by gated sampling of actual diesel-engine-catalyst-system exhaust and post-sampling GCMS analysis.

## Introduction

Dynamic engine-system operation is used to manage diesel-catalyst systems. For example, to regenerate diesel LNT catalysts, a fuel-rich exhaust condition is periodically generated; this might be a 3-s wide fuel-rich event every 60 seconds. The emissions pool during such short fuel-rich events are very different from that under normal operation; that is, different from that for 95% of the 60-s cycle discussed above. Detailed understanding of catalyst chemistry requires analytical techniques capable of selectively sampling the environment during and within the short periodic events.

## Technical Approach

Two methodologies for gated sampling were demonstrated; the first uses a rigid sample container as described in the original proposal, and the second uses a deformable or bag-like sample container.

### *Technical Approach for Gated Sampling with Rigid Sample Container*

The GSS using rigid containers is as described in the original proposal and is the most easily implemented approach. The fundamental limitation of this approach is that it requires at least 2-to-1 dilution of the sample for most analytical techniques. In this approach, the sample is continuously drawn through a critical flow orifice, CFO (0.016-in, 1.235-LPM sample rate) and three-way switching valve (Parker Rmax, pneumatic drive) by a continuous sample pump. Oxygen sensors are used to detect sample transients and provide input to a control program to selectively gate the switching valve. An initially evacuated rigid sampling container is connected to the normally closed outlet of the switching valve; typically the sample container was initially evacuated to 25.5 in. Hg vac. The switching valve allows gated sips into the sample container at specified width and delay relative to the sample transient. To maintain choked flow across the CFO, the downstream pressure must be maintained at less than half an atmosphere (<15 in. Hg vac) for atmospheric sampling regardless of the position of the switching valve. Thus, the number of gated samples is limited by the requirement to maintain choked flow across the orifice. Once the required or limiting number of gated samples has been captured, the sample is diluted with appropriate diluent to atmospheric or the desired pressure. Dilution to atmospheric pressure is typically required because most analytical techniques do not accommodate sampling from vacuum. In fact dilution to greater than atmospheric pressure may be required to fill a bag for subsequent sampling or, for example, an FTIR white cell. One benefit of the rigid sample container approach is that the containers can be heated in ovens during sampling and analysis to mitigate interactions between the sample and the container walls.

This system was assessed for linearity as a function of gate width and number of samples. Sample quantity was quantified gravimetrically and via GCMS analysis of a sample-stream standard.

The rigid-container GSS was used to demonstrate intra-transient sampling of exhaust transients from a diesel engine and downstream oxidation catalyst. Fuel was periodically injected (2-s width) into the exhaust pipe before the oxidation catalyst. A dilution tunnel sampled the exhaust after the oxidation catalyst; the GSS sampled the resulting diluted exhaust. An oxygen sensor, positioned at the dilution tunnel inlet, was used to trigger the switching valve. Because the sampling rate of both the dilution tunnel and GSS are based on CFOs, the sample transit time between the triggering oxygen sensor and switching valve is a constant. A LabView-based control program

allowed the sample gate to be positioned relative to the emissions transient. Gated samples were collected for 12 events using a 2-s-wide gate: (i) centered on the pulse, (ii) off the pulse, (iii) in the first half of the pulse, and (iv) in the last half of the pulse. These gated sampling results were compared to conventional integrated (10 min) bag sampling. Analysis was based on GCMS, using undecane, benzene, and pentene as indicative of fuel, monoaromatics and cracking products, respectively.

### *Technical Approach for Gated Sampling with Deformable Sample Container*

A second GSS based on deformable or bag sample containers was demonstrated. The resulting sample is contained in a deformable bag at ambient pressure, and the full sample can be extracted at ambient pressure. In this design, Fig. 1 inset, the rigid sample container is replaced with a sample bag contained within a vacuum canister. The bag is connected to the normally closed port of the switching valve, and the vacuum canister environment outside the bag is isolated from the sample contained within the bag. The vacuum canister functions to pull sample into the sample bag. For canister vacuum control, a continuous atmospheric leak (0.025 orifice, 2.50 LPM leak rate) and subatmospheric back-pressure regulator and roughing pump are used. For this instrument, a faster switching valve (Parker, direct-lift solenoid) was used, and a needle valve was added after the normally open port of the switching valve; the needle valve was set to approximately equilibrate the CFO downstream pressure during normal and gating sampling. Under normal operation, the bag and vacuum canister were initially evacuated to ca. 25 and 17 in. Hg vac, respectively, via a regulator bypass, and the regulator was set to maintain this target canister pressure; this target pressure is sufficient to conservatively maintain choked flow but also allow maximum sample. Ultimately this design is limited in terms of sample quantity; a full 10-L sample bag inside the vacuum canister will contain only ca. 4.32 L of sample at STP.

The system was assessed for linearity as a function of sample number and gate width. A dry test meter was used for analysis.

The transient response of the GSS with the faster switching valve was assessed using an air stream with 40-ms-wide argon pulses. The SpaciMS instrument was used to characterize the argon transient; for this standard characterization, the SpaciMS was configured with a 1.75-in long, 15-µm ID capillary which provides 105-ms, 9.5-Hz, $T_{10\text{-}90}$ response time. To characterize the GSS transient response, the stream was sampled at different switching-valve delays while the SpaciMS monitored the argon concentration in the sample bag. For species monitoring within the bag, temporal response is unimportant so the SpaciMS was configured with longer sample capillaries (18 in. long, 30-µm ID; 130-ms, 7.7-Hz, $T_{10\text{-}90}$ response time); the SpaciMS sampling rate is ca. 10µL/min, so its extractive sampling methodology is sufficiently noninvasive. To resolve the argon transient, the switching valve gate delay was precessed through the transient in 0.05-s increments. For the measurements, the sample bag was initially evacuated to <17 in Hg vac. Initially ten 0.25-s-wide samples were taken with the gate positioned off the argon pulse to equilibrate the bag and vacuum canister pressures. Subsequently, sufficient (10–30) samples were acquired with a 0.05-s gate width until the SpaciMS-indicated argon concentration in the sample bag was equilibrated. The equilibrated argon concentration was indicative of the argon concentration at the corresponding switching valve delay.

## Results and Discussion

### *Results and Discussion for Gated Sampling with Rigid Sample Container*

The linearity of the rigid-container GSS versus number of samples was characterized based on 5 to 30 500-ms-wide samples using gravimetric and GCMS analysis. The relationship was found to be linear with 0.995 and 0.992 values of the square of the linear correlation coefficient for the gravimetric and GCMS analysis, respectively. This early work established the sufficiency of gravimetric analysis for assessing the instruments performance. The linearity of the system versus gate width was characterized for gate widths from 100 ms to 4s based on gravimetric analysis. The results indicated continuously increasing gate-width error with decreasing command width below 3 s; errors resulted in the gate being too long. Gate-width error were greater than 10% and 20% for command widths less than 1 s and 700 ms, respectively, and increased to 97% for command gates of 100-ms width.

The gated sampling results provided insights not resolved by conventional integrated sampling. Both oxygen sensors resolved transient exhaust signatures not only of the in-pipe fuel pulsing but also of engine intake throttling and EGR changes. The GSS was determined to be greater than 10 times more sensitive than conventional integrated sampling. GCMS results indicated monoaromatics and cracking products to be uniformly distributed between the front and back half of the fuel-rich pulse, while undecane was biased to late-pulse times. The measured on-pulse quantities were approximately equal to the sum of the front and back pulse quantities, and the off-pulse quantities were negligible. Moreover, a unique, possibly diene of C11, compound was formed early in the exhaust pulse. The results suggest a model where the injected fuel initially interacts with a sufficiently high-temperature system to create unique (possibly diene) species; the system rapidly cools below

a temperature sufficient to distill off heavy hydrocarbons but sufficiently high as to distill the fuel light ends; by the second half of the fuel-injection width, the system temperature is sufficient to distill the heavier fuel ends not evolved at early pulse times; during the subsequent cycle and before the next fuel-injection event, the system temperature increases to produce the unique compound at the early times of the subsequent event.

***Results and Discussion for Gated Sampling with Deformable Sample Container***

The linearity of the deformable-container GSS versus gate width was characterized over the range of 4 s to 25 ms. The error in the gate was less than 9% over the gate-width range of 100 ms to 4 s, and increased to ca. 10–14% for 25- to 50-ms gate widths. The linearity versus sample number was assessed based on 600-ms, 800-ms, and 1-s gate widths, and the corresponding values of the square of the linear correlation coefficient were determined to be 0.996, 0.991 and 0.998, respectively. The most significant deviation from linearity appeared to occur at the initial samples; this effect might be due to the various system pressures not being equilibrated and could possibly be eliminated by initial diluent sampling (like initial off-pulse sampling described earlier) to allow equilibration.

The transient argon pulse as resolved by the deformable-container GSS and fast SpaciMS are shown in Fig. 1. The SpaciMS served as a fast analytical standard and indicated a $T_{10\text{-}90}$ of 135 ms, 7.41 Hz, and a FWHM of 220 ms. The GSS is clearly faster than the SpaciMS and indicates a $T_{10\text{-}90}$ of 130 ms, 7.7 Hz, and a FWHM of 168 ms. The difference is particularly notable when the falling edge of the argon transient is considered as with the FWHM figure of merit. Additional work would be required to better quantify the transient response of the GSS, but it appears that the system has a transient response on the order of >10 Hz. This is attributable to the faster direct-lift-solenoid switching valve, and the improved response could be similarly realized with the rigid-container GSS too.

## Benefits

The research is consistent with DOE missions to increase energy efficiency, reduce dependence on foreign oil, and improve environmental quality. This project will help continue to demonstrate and maintain ORNL FEERC's leadership in emissions characterization and control technology in transportation research sponsored by the Department of Energy's Office of Freedom Car Vehicle Technology.

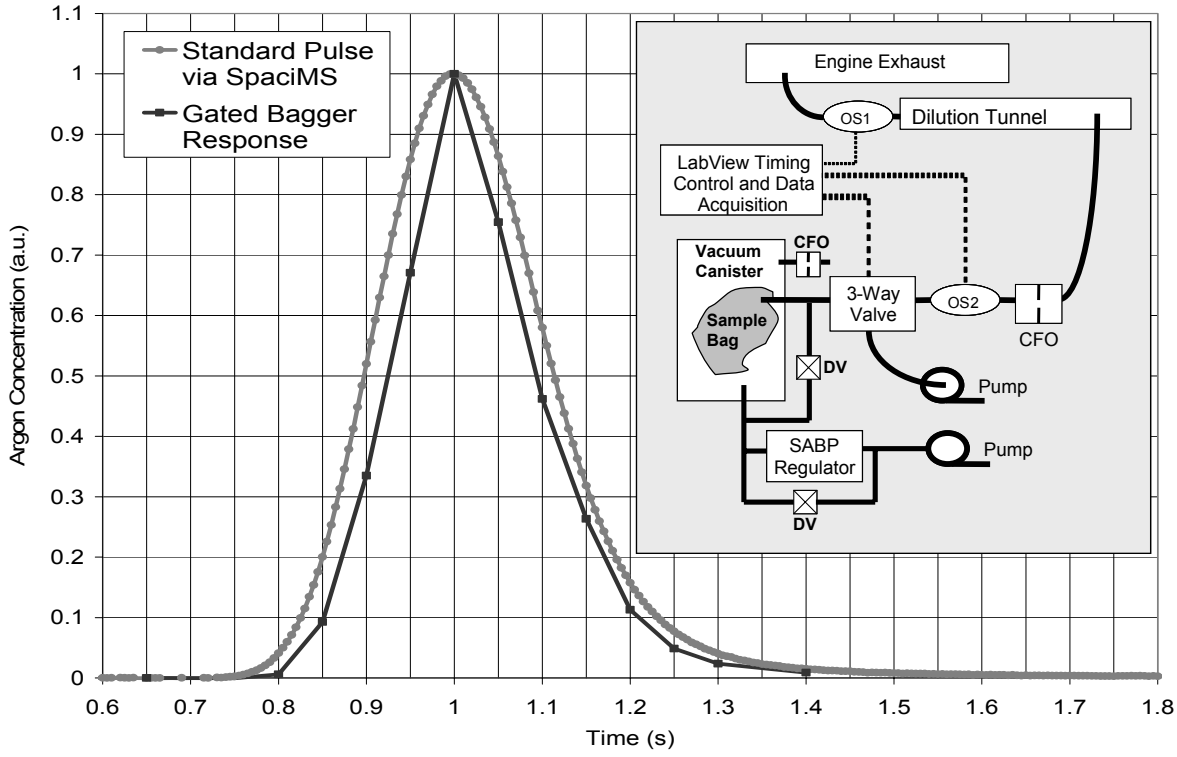


*Fig. 1. Transient response of the GSS relative to the fast SpaciMS. Inset: schematic of the deformable-container GSS; CFO: critical flow orifice; SABP: subatmospheric back pressure; OS: oxygen sensor; DV: diaphragm valve.*

# Evaluation of Urea-Diesel Emulsions to Lower $NO_x$ Emissions

M. D. Kass, S. A. Lewis, C. S. Sluder, and B. H. West
*Engineering Science and Technology Division*

This project investigated the feasibility of reducing $NO_x$ emissions from diesel engines via a direct selective non-catalytic reduction process, whereby urea (and ethanol) were blended to the diesel fuel. The solubility limit for urea in EPA certification diesel fuel was determined to be approximately 0.1% for a blend containing ethanol, biodiesel, and cert fuel. Several fuel compositions were developed and evaluated to determine the influence of urea, ethanol, biodiesel and water on the combustion and resulting emissions from a diesel engine. A 1999 1.7-L Mercedes diesel engine was operated at fixed speed (1500 rpm) and two engine loads (21 and 50 ft-lb). Recirculated exhaust was added at these conditions to ascertain the influence of bulk combustion temperature. The fuel blends did not reduce the $NO_x$ emissions relative to neat biodiesel. However, the smoke meter data indicated that 10% ethanol lowered the particulate emissions by 50%, which is a greater reduction than has been observed for micro-emulsions of ethanol and No. 2 diesel fuel.

## Introduction

Over the last 20 years, efforts have been made to reduce the $NO_x$ emissions of diesel engines to molecular nitrogen through selective reduction using either catalytic- or non-catalytic-based reduction methods. One of the more promising approaches is to apply selective catalytic reduction (SCR) using ammonia as the reducing agent. This method (known as urea-SCR) has demonstrated $NO_x$ conversion efficiencies over 95% within a 300 to 400ºC temperature window. However, the performance of these systems falls dramatically when the catalyst temperature drops below 250ºC for most applications.

$NO_x$ emissions can also be significantly reduced by direct reduction with ammonia (without using a catalyst to facilitate the reaction). This is known as selective non-catalytic reduction (SNCR). In practice, ammonia in its pure form is not used in the starting form as the reductant due to its inherent toxicity and handling problems. Therefore, the preferred reductant in SNCR systems using ammonia as the primary reducing agent is urea, $CO(NH_2)_2$, since it is non-toxic, safe, and commercially available.

At temperatures above 160ºC, urea begins to decompose and hydrolyze to form the $NH_2$ radical and $NH_3$. According to Willand et al. (1998), the predominant SNCR reaction mechanism involves a starting reaction whereby the ammonia is converted to the more reactive amidogen radical $NH_2$ by the reaction of ammonia with the OH. The amidogen radical $NH_2$ then reduces NO to molecular nitrogen and water. This is the desired reaction sequence for effective urea-SNCR. However, Willand et al. (1998) have also shown that for temperatures below 880ºC, the reaction rate coefficient is too low to form sufficient levels of $NH_2$, and for temperatures greater than 1080ºC, the $NH_2$ radical will oxidize rather than undergo the NO reduction reaction. As a result, there exists a narrow temperature window in which urea-SNCR is active. However, it should be noted that the starting reaction ($NH_3 + OH \rightarrow NH_2^- + H_2O$) requires OH radicals to form $NH_2$. If the concentration of available OH radicals is increased, the level of the primary reductant $NH_2$ is increased as well. Therefore, increasing the OH concentration would also accelerate the reduction reaction, thereby expanding the temperature window to around 900 K, depending on the OH concentration.

Willand et al. (1998) showed that urea solution injected into the exhaust or into the cylinder was effective at lowering NO emissions by over 65%, which is significant (especially with no catalyst being present). In our proposed approach, the urea would be introduced to the combustion process along with the diesel fuel; thus we would expect OH radicals to be formed via the much hotter adiabatic flame temperature. The flame temperature would be greater than 900ºC, even at conditions of light load (including idle operation) and can be lowered or raised by increasing or decreasing EGR, respectively, thereby keeping the temperature within the optimum temperature window. Since the flame temperature would drive the reduction, this approach would have the advantage of not being susceptible to low exhaust temperature limitations.

## Technical Approach

Our initial approach was to evaluate the potential of neat biodiesel (B-100) to act as a co-solvent for ethanol, which is insoluble in diesel fuel. Biodiesel is completely miscible in both neat ethanol and cert fuel (No. 2 diesel

fuel) and therefore may enable the dissolution of urea in cert fuel. The advantage is that such a mixture would be more stable than a micro-emulsion and would not contain surfactant compounds which could potentially contribute to increased toxic emissions. We also limited ourselves to blends containing 80% diesel (or biodiesel) since it was felt that higher concentrations of additives would not be economically practical and would also severely lower the heating value of the fuel. Blending studies were performed to establish the solubility limits of (1) urea in neat ethanol, (2) urea and ethanol in biodiesel, and (3) urea-ethanol-biodiesel solutions in cert fuel. Based on information gained through the blending study, we prepared several compositions for evaluation. The compositions were selected to elucidate the contribution of urea, water, and several co-solvents to the exhaust emissions. The original intent of the proposal was to evaluate the influence of micro-emulsion fuels consisting of urea and cert fuel. However, we later felt that biodiesel was a more attractive alternative as a urea-ethanol to cert fuel co-solvent; therefore, emphasis of this project was redirected to focus more closely on this application.

The powertrain used to evaluate these fuel blends was a 1999 Mercedes 1.7-L 4-cylinder common rail diesel engine equipped with a control system to enable manipulation of the exhaust gas recirculation (EGR) valve position. The engine was coupled to a Mid-West inductor dynamometer capable of providing over 100 ft-lb of torque. During the evaluation, the engine was operated at a constant speed of 1500 RPM. The load was controlled at two settings, 21 ft-lb and 50 ft-lb. For each speed-load setting, the EGR was controlled to provide either 0% EGR or 20% (for 21 ft-lb) or 16% (for the 15,000-rpm/50 ft-lb condition. The application of EGR reduces the oxygen content during combustion and is used as a means of lowering $NO_x$ emissions in diesel engines. EGR also influences combustion by increasing the temperature of the intake gases.

The gaseous exhaust emissions were measured using a standard emissions bench containing analyzers to measure CO, $CO_2$, $NO_x$, $O_2$, and HC concentrations in the engine exhaust. The particulate concentration was also determined for each condition using an AVL smoke meter.

## Results and Discussion

A number of solubility studies were performed to determine the solubility limits (1) of urea in ethanol, (2) urea and ethanol in biodiesel, and (3) urea, ethanol, and biodiesel, in cert fuel. We were able to obtain a maximum solubility of 0.1% urea in B-100/Cert fuel blend containing 17.6% ethanol. Based the results from the blending study, we formulated fuels composed of (1) neat biodiesel, (2) 10% ethanol in neat biodiesel, (3) 0.1% urea/17.6% ethanol/82.3% biodiesel, (4) 0.1% urea/21.7% ethanol/43.4% biodiesel/34.7% cert fuel, and (5) 2% water/18% isopropanol/cert fuel. (Note that percentages are based on volume.) The fifth fuel composition listed was developed to evaluate the influence of water on combustion. Since it is well known that water injected into the combustion chamber reduces $NO_x$ emissions, we felt that it merited inclusion into our fuels matrix. These fuels were made in 9-L batches and evaluated in the Mercedes engine described earlier in this report.

The resulting $NO_x$ emissions and accompanying smoke numbers are shown in Fig. 1. As shown in Fig. 1(a), the $NO_x$ emissions were relatively constant for each of the fuels tested and for each engine condition. The fuel blends containing ethanol and urea did show slightly reduced $NO_x$ levels when the engine was run at 50 ft-lb of torque and zero EGR. However, this is not considered especially noteworthy. In contrast, the smoke numbers shown in Fig. 1(b) were approximately 50% lower for the fuel mixtures that contained ethanol for all engine conditions. This result strongly indicates that ethanol substantially lowered engine-out particulate emissions from the engine. This is not surprising since previous studies have shown that ethanol reduces particulate matter up to 15% for micro-emulsion blends of 10% ethanol and cert fuel. The reduction observed for these ethanol and urea fuel blends is more dramatic. A 50% reduction in smoke number for the biodiesel blend containing 10% ethanol is much higher than would be expected (around 15%). The oxygen present in ethanol is believed to react with elemental carbon during combustion to form CO, and in fact, the CO emissions for the ethanol-bearing fuels were quite high compared to neat biodiesel. This finding is important since PM emissions are stringently regulated by the EPA. A 50% reduction in PM with the addition of ethanol would attract attention from engine manufacturers and the DOE.

## Benefits

The fuels program within the Department of Energy is interested in exploring the development and utilization of alternative-renewable fuels such as biodiesels and ethanol. The benefits to our DOE sponsor are an improved understanding of the combustion and emissions generated by biodiesels and biodiesel-blended fuels. This project advances the subject of biodiesels and emission control additives and the results are expected to lay the foundation for continued support in this important area.

## References

Willand J. et al. 1998. *Selective Non-Catalytic $NO_x$-Reduction in Diesel Engines Using Aqueous Urea*. SAE982651.

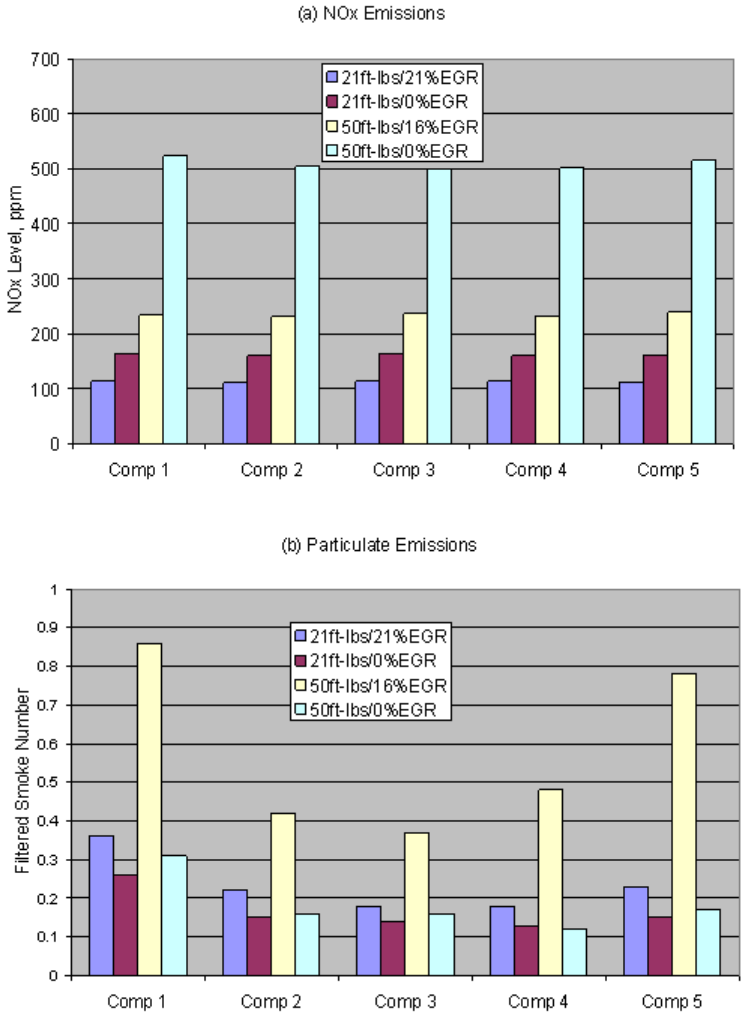


*Fig. 1. Resulting $NO_x$ and particulate emissions for each of the fuels evaluated. For each fuel composition, the $NO_x$ emissions and smoke numbers are indicated for the four engine conditions that were evaluated. The compositions listed above are identified as follows: Comp 1 is neat biodiesel, Comp 2 is 10% ethanol in neat biodiesel, Comp 3 is 0.1% urea/17.6% ethanol/82.3% biodiesel, Comp 4 is 0.1% urea/21.7% ethanol/43.4% biodiesel/34.7% cert fuel, and Comp 5 is 2% water/18% isopropanol/cert fuel.*

# No-Moving-Parts Pump and Preconcentrator

R. J. Warmack,[1] C. L. Britton,[1] J. E. Hardy,[1] P. F. Britt,[2] and T. Thundat[3]
[1]*Engineering Science and Technology Division*
[2]*Chemical Sciences Division*
[3]*Life Sciences Division*

A breakthrough technology is being developed and tested that would enable real-time sampling and pumping of concentrated vapors in a 1-cm$^3$ package and using very low power. The technique uses a microfabricated device that absorbs and pumps selected analytes to a variety of detectors or analyzers. The demonstration of the device should lead to research programs to produce truly compact, low-power, highly selective detectors for trace analysis. Such detectors should be more reliable than those employing traditional pump designs and also have greatly improved chemical selectivity over that of single-stage analyzers, more closely approaching that of laboratory analytical instrumentation.

Our long-term objective is to develop a small, low-power sampling stage that will extend detection limits of existing detectors by a factor 100 to 1000 times, while greatly improving the overall chemical selectivity and real-time response. The specific goal of this proposal is to fabricate a demonstration device to verify concentration and pumping of selected vapors experimentally.

A micro-electro-mechanical systems (MEMS) approach is being used to increase the effective area of a detector by two to three orders-of-magnitude. The proposed concentrator has micromachined surfaces coated with stationary phases in which the analyte vapors can adsorb and be preferentially concentrated. Heating the surfaces allows absorbed material to be periodically desorbed and programmatically eluted, enabling improved selectivity and extended detection limits. Delivery of the desorbed material to a detector is accomplished with a proprietary pumping action that also acts to draw fresh vapor through the device for improved real-time sampling.

Extensive work was performed to select appropriate materials and determine methods for fabricating test MEMS structures. A 14-step microfabrication process was developed that successfully produced a number of preconcentrators in both individual die and 4-in. wafer formats. The completed die was mounted and wire-bonded on a printed circuit platform with a custom circuit to drive and monitor the operation of the preconcentrator. A pulse power of 400 mW over only 10 ms provided a temperature rise of about 250ºC, which should be sufficient to rapidly desorb anticipated analytes. A complete preconcentration cycle should then require less than about 100 mJ. Compared to the energy storage of a typical AA battery (104 J), about 100,000 cycles could be expected. This validates the low power objective of this study.

Next steps include measuring the pumping action with anemometry and coating the surfaces to evaluate preconcentration.

The demonstration of a preconcentrator and pump that has no-moving parts (high reliability) and that has the potential to rival laboratory analytical instrumentation should prove to be very attractive to DOE to allow sensors for environmental, industrial, and personnel monitoring where size, power, and real-time monitoring of low levels of analytes are important. The implications for homeland security and the military are obvious for a toxic-agent monitor that can be reliably produced at low cost in high-volume quantities.

# Preliminary Study of Phosphor-Based Tracer Rounds

M. R. Cates and S. M. Goedeke
*Engineering Science and Technology Division*

The use of phosphors for novel constant-mass, low-field-of-view tracer ammunition requires many preliminary tests to be performed. The materials used for this application are long persistence phosphors that are excited by visible. In this case it is anticipated that burning of the powder in the chamber will produce enough light to charge the phosphor and allow it to glow as it travels downrange. An added advantage of using phosphor is that many of these materials produce light upon impact. This would provide a means to locate where the tracer rounds are hitting and can be used for targeting.

Conventional tracer ammunition consists of a projectile that contains a pyrotechnic composition in a hollow base that is ignited during firing by the combustion of nitrocellulose-based propellants. This pyrotechnic charge gives off light, allowing the operator of a firearm and potentially the target to observe the path of the tracer projectile. The goal of this research is to evaluate possible phosphors for use in tracer ammunition. The main focus of the work will be to evaluate commercially available long persistence phosphors and binder materials. The first major hurtle of this research is to find a phosphor binder combination that will withstand the harsh environment produced by firing a bullet. The next goal would then be to design an experiment that can capture light from the modified round. The final goal is to test the ability of phosphors to produce light from impact.

To determine the survivability of a phosphor binder combination, commercially available ammunition was modified. This modification was initiated by removing bullets from commercially available rounds. The pulled bullets are then coated with phosphor and reinstalled in the casings. As an alternative, 12 ga. shotgun slugs can were purchased and coated. They will be loaded into shells and fired. In each case, the rounds will need to be fired in a darkened environment and some portion of the rounds recovered. This requires either an outdoor range at night or an indoor range with the lights turned out. When the round strikes the target, the impact should be enough to produce light from triboluminescence.

Over the past five months, many of the project goals have been attempted. First, preliminary testing was performed to try and measure impact on a phosphor-coated target. Next, through collaboration with the University of Louisiana at Lafayette, testing has been performed on at least two different rifle calibers. For the first series of tests, 26 rounds .223 bullets were coated with phosphor and loaded. Upon firing, two produced light on impact and one appeared to produce a tracing effect. Attempts were made to collect expended rounds, but the binder survivability results were inconclusive since the bullet shattered on impact. For the next series of round .35 caliber rounds were prepared and fired. Twelve rounds were recovered, and most appeared to have phosphor coating after impact. These rounds were also tested at night, and it appeared that some of them produced light on impact. A third test with .223 rounds was performed with similar results to that of the .35 caliber. The final test to be performed is the use of the 12 ga. shotgun slugs. The slugs have been prepared and the RSS for the test has been approved for testing in Building 5800. It is hoped that the data can be collected early next quarter.

The development of phosphor-based tracers has application in a multitude of military applications. Since these tracers would have a limited field of view, they would provide an extra measure of security for the soldier in the field.

# *Nuclear Science and Technology*

# *Director's R&D Fund*

# Optimization Studies for ISOL-Type High-Powered Targets

T. Gabriel,[1] M. Wendell,[1] I. Remec,[1] G. Bollen,[2] R. Ronningen,[2] and M. Grossbeck[3]
[1]*Oak Ridge National Laboratory*
[2]*Michigan State University*
[3]*University of Tennessee*

With the development of ever more powerful accelerators at spallation neutron sources, muon collider/neutrino facilities, and rare isotope production facilities, the target systems at these facilities must be designed and developed such that they cannot only handle the beam power reliably and safely but also must be optimized to yield maximum performance relative to their design requirements. The purpose of this project is to investigate the development of one of the target systems mentioned above, in particular, the rare isotope production targets (ISOL or Isotope Separation on Line) for the Rare Isotope Accelerator Facility (RIA). With a primary RIA beam power of 100–400 kW, these targets present a major challenge since the damage and heating levels are five times greater than those encountered at the Spallation Neutron Source or at the ISAC Facility at TRIUMF. Detailed neutronic, activation, criticality, damage, and heating calculations have been started to determine how best to handle the anticipated design requirements associated with these targets.

The objective of this research is to develop an optimized high-powered isotope production target which can be built and is based on the best neutronic and thermal hydraulic methods available. The optimization depends on many factors. These include the size of the system, the spallation and fission rates leading to the production of the interested nuclide, the diffusion rate out of the matrix, which can be different for all isotopes, the effusion to the ion gun area, the lifetime of the nuclide of interest, safety issues, and the method of ionization of the nuclei so they can be captured and transported either to another accelerator or to an experimental area. To be the most efficient, targets just about have to be designed specifically for a given isotope, but this is generally not done due to cost and the necessity of providing different isotopes to several experimental areas simultaneously.

Calculations have been carried out on one-step and two-step ISOL targets. The first data presented here is for a two-step target which has mercury as the primary target and uranium carbide as the secondary target. Two of the parameters of the most interest are the number of fissions produced in the secondary target, which determines the rate of production of isotopes, and the total energy deposited in primary target, which determines the cooling requirements and will likely be the factor limiting the beam power for the operation of the target. A flat beam profile with radius of 1 cm was used. The 400-kW beam of 1-GeV protons impinging on a mercury primary target produces $1.84 \times 10^{15}$ fissions per second in the secondary target (UC) and deposits 106 kW of energy in the primary target. Comparison of proton, deuterium, and He-3 beam results indicate that the proton beam gives the best performance based on the fission rate in the secondary target and the energy deposition in the primary target. The next data discussed is for a one-step target composed of uranium carbide. Initial calculations indicate that the maximum power level that can be obtained for this target with a 400-kW proton beam is 100 kW.

The development of ever more powerful target systems or in general systems that can handle more power density is an important area for the Department of Energy and other private and government agencies. If targets cannot reliably, efficiently, and safely operate at higher power levels, the development of additional high-powered accelerators or the upgrade of existing accelerator facilities will be extremely limited.

# *Nuclear Science and Technology*

# *Seed Money Fund*

# Development of a Three-Dimensional Radioisotope Depletion Method Using Monte Carlo Transport

M. D. DeHart, S. M. Bowman, and L. M. Petrie
*Nuclear Science and Technology Division*

Accurate calculation of the depletion of nuclear materials requires careful determination of the neutron flux density and spectrum in the region(s) of interest. Increasing complexity in reactor designs, evolutionary concepts, and non-reactor applications, such as safeguards, securities, and nonproliferation, are beginning to require robust geometrical modeling capabilities to capture neutron transport for complex configurations. Monte Carlo transport methods offer the flexibility needed for such applications, but present other difficulties not encountered in deterministic transport methods. The objective of this project was the development of a prototypic code sequence to perform Monte Carlo-based depletion. As a result of this project, both the KENO V.a and KENO-VI Monte Carlo transport codes have been adapted to work within a depletion code sequence; comparisons with other methods and measured data show excellent agreement.

## Introduction

The NEWT discrete ordinates package developed at ORNL (DeHart 1998, 2004a) has significantly extended the capabilities of discrete ordinates transport calculations due to its completely arbitrary grid discretization approach. A significant application of NEWT in nuclear systems analysis has been as the radiation transport solver in a new two-dimensional (2-D) depletion package named TRITON (DeHart et al. 2003; Dehart 2004b). Under TRITON, NEWT is used to calculate spatial flux distributions and to collapse nuclide cross sections for use in the ORIGEN-S depletion code. TRITON uses a predictor-corrector method iteratively calling NEWT and ORIGEN-S to track changing flux and power distributions with burnup, matching time-dependent power to user-specified operating histories. TRITON uses the geometry flexibility of NEWT to allow analysis of complex fuel lattices. However, despite broad applicability of the 2-D version of TRITON to fuel depletion analysis, there are some domains in which accurate three-dimensional (3-D) depletion capabilities are necessary. This project was proposed to develop a 3-D depletion capability similar in function to the 2-D capabilities currently available in TRITON but based instead on the 3-D Monte Carlo-based KENO codes available in SCALE.

The original proposal sought to develop a depletion sequence based on the 3-D KENO V.a Monte Carlo code. Additionally, research was to include the study of methods for error propagation and to work to reduce uncertainty by using variance reduction techniques. Complete incorporation of error propagation was determined to require more effort than could be justified for this work, although independent work ongoing at ORNL will eventually make this option practical to implement. Variance reduction was implemented to a limited extent. However, the scope of the work was extended to include development of a KENO-VI-based depletion sequence. KENO V.a uses a somewhat limited geometry input paradigm, whereas KENO-VI applies a more robust combinatorial geometry package. Conversely, KENO V.a calculations run significantly faster than KENO-VI (by a factor of 5–10).

## Technical Approach

The SCALE code system is based on a modular concept, where computer codes developed for specialized functions referred to as functional modules, are executed in sequence with data transferred and processed by a control module, a code designed to control one or more automated sequences of calculations in a predetermined manner. Control modules are developed to perform specific classes of analysis with a subset of functional modules. The TRITON control module is used to perform general neutron transport calculations, but its primary application at present is for multidimensional depletion and decay calculations. TRITON coordinates cross-section processing using BONAMI, CENTRM, PMC, and WORKER functional modules; 2-D transport calculations via NEWT; and depletion calculations using COUPLE and ORIGEN-S. TRITON also coordinates iteration in time and space to properly characterize fuel burnup.

In this project, the primary goal was to develop a capability in TRITON similar to that in the existing depletion sequence but based on KENO V.a as the transport solver. The modular nature of the TRITON module made this approach feasible without requiring ground-up development of a new sequence. Although not nearly as simple as just replacing calls to NEWT with calls to KENO V.a, the process was relatively straightforward. However, because NEWT was developed in tandem with

TRITON, certain data needed by TRITON to perform depletion calculations was built into NEWT and made available to TRITON via data files. A standalone KENO V.a post-processing utility, KMART, was already available within SCALE and was simply expanded to prepare data in the form required by TRITON.

The KENO V.a and KMART codes were added to TRITON and validation studies were performed to debug the modified sequence and to assess performance relative to NEWT-based calculations. Once satisfied with the general performance of the new calculational sequence in TRITON, research proceeded in parallel to improve both variance reduction and uncertainty propagation efforts.

With respect to variance reduction, TRITON was updated to use the converged neutron source from the preceding pass as a starting guess for the next KENO calculation. Early iterations in a Monte Carlo simulation are used to determine the proper distribution of source neutron. Generations of neutrons used to converge on a spatial source distribution must be discarded because they contain a bias toward the initial guess for a starting source. By restarting calculations based on the starting source computed in the previous transport simulation, a much-improved estimate is made of the spatial shape of the neutron source, and fewer neutrons need be discarded, thereby reducing the statistical variance. However, variance reduction is best accomplished in Monte Carlo methods by "biasing" neutrons by an importance function. A properly developed importance function could be used to obtain a spatially uniform uncertainty in neutron fluxes, reducing variances in regions in less reactive regions of the fuel. Consideration was given to employing a one-dimensional (1-D) deterministic approximation to calculate an adjoint profile to be used to generate bias factors for KENO, since such an approach would be relatively easy to implement and would run extremely fast. However, while this was felt to be appropriate for most commercial fuel designs, where radial homogenization could be applied with a 1-D axial adjoint solution using SCALE's XSDRNPM module, this approach would not be universally applicable, as it would fail in fuel concepts where significant radial variations would be expected. Nevertheless, ongoing work in other projects within SCALE seek to (1) demonstrate the 1-D approach for commercial LWR-type fuels and (2) develop and apply a 3-D adjoint solver for application in shielding analysis domains. It is anticipated that the results of these projects will influence the direction of future development of biasing methods in KENO-based depletion.

In the course of performing validation calculations, comparing predictions for isotopic concentrations to those obtained using a deterministic NEWT solution and to measured data showed that the isotopic predictions obtained using KENO V.a to generate fluxes were remarkably good, with differences that were very small relative to differences between calculated and measured data. Errors introduced in the depletion calculation itself or in the actual measurements are much larger than those due to flux uncertainties. This does not suggest that uncertainty propagation is unnecessary; however, it has become clear that meaningful application of uncertainty methods must also include uncertainty in measurements and in built-in data used in depletion and decay calculations as well as uncertainty in fluxes and cross sections derived using stochastic methods. The state of the art at ORNL in uncertainty propagation for depletion methods is described in a report by Gauld (2001). This was to serve as a starting point for additional development within TRITON. However, study of issues and the tight coupling of stochastically weighted cross sections, fluxes, and depletion behavior have led the researchers to the conclusion that a full depletion perturbation approach (Williams 1979) will be necessary to properly capture and quantify all uncertainty effects. Such an implementation would be a major development effort and would not be possible within the scope of this project's funding.

Because the implementation of depletion using the KENO V.a functional module was so successful and performance greatly exceeded expectations, it was decided to use the remaining funding to develop a similar sequence based on KENO-VI. This implementation was built upon the experience gained in adapting TRITON to function with KENO V.a and was completed in relatively short order. In fact, sufficient funding remained to support a summer student in performing code-to-code and code-to-measurements with TRITON to further test the performance of the codes and validate their ability to accurately perform depletion calculations.

## Results and Discussion

Depletion calculations have been performed using reactor fuel assembly data provided in validation reports of the 1-D SAS2 depletion sequence in SCALE. Models of the spent fuel assemblies have been developed with both KENO V.a and KENO-VI versions of TRITON. Results have been compared with the measured radiochemical spent fuel assay data and calculated SAS2 and TRITON/NEWT results. Benchmark calculations have been performed for measured data from four reactor designs. Results of analyses of all four assemblies are summarized (Bowman 2005). More detailed validation analysis using TRITON are being prepared in a report by Gill (2006).

The remainder of this discussion will focus on the results of analysis of the San Onofre MOX fuel assembly. Limited measured assay data (primarily actinides) are available from a pellet obtained from pin 079 at an elevation of 49 in. from the bottom of the fuel stack, with a burnup of 20.89 GWd/MTU. At this height, axial leakage effects are negligible, and the pellet's depletion can be accurately characterized by a 2-D (radial) representation.

Comparisons of the calculated results from SAS2, TRITON/NEWT, TRITON/KENO V.a, and TRITON/KENO-VI with the measured data are presented in Table 1. The calculated results are consistent and generally agree well with the measured data. The two nuclides with poor results, $^{234}$U and $^{238}$Pu, have relatively low concentrations and importance. The errors here are consistent, indicating a possible inaccuracy in measurement or in cross-section data. Interestingly, nuclides such as $^{235}$U, and the Pu nuclides, which are sensitive to the neutron spectrum, are in very good agreement among the three sets of TRITON results. As evidence of this, SAS2 results, based on a 1-D radial approximation, cannot accurately capture local spectral effects, and shows less precise predictions.

**Table 1. San Onofre MOX fuel assembly DX51, pin 079 (20.89-GWd/MTU burnup)**

| Nuclide | Measured mass (kg/MTU) | SAS2 % Diff. | TRITON / NEWT % Diff. | TRITON / KENO V.a % Diff. | TRITON6 / KENO-VI % Diff. |
|---|---|---|---|---|---|
| $^{234}$U | 4.66E–02 | –13.1% | –13.4% | –13.7% | –13.5% |
| $^{235}$U | 4.40E+00 | –2.0% | 0.8% | 1.1% | 1.0% |
| $^{236}$U | 4.89E–01 | 6.6% | 2.6% | 2.6% | 2.4% |
| $^{238}$U | 9.43E+02 | 0.0% | 0.0% | 0.0% | 0.0% |
| $^{238}$Pu | 2.82E–01 | –36.3% | –35.4% | –34.8% | –35.1% |
| $^{239}$Pu | 1.65E+01 | 5.2% | 3.0% | 4.0% | 3.8% |
| $^{240}$Pu | 7.68E+00 | –3.3% | 2.6% | 1.9% | 2.3% |
| $^{241}$Pu | 3.66E+00 | 1.5% | 0.1% | 1.6% | 1.1% |
| $^{242}$Pu | 8.97E–01 | 5.9% | 3.6% | 3.2% | 3.4% |

## Benefits

To-date, KENO-based depletion within SCALE has been well received by the technical community. Presentations of the application of KENO-based depletion (Bowman 2005, DeHart 2004c, DeHart et al. 2004d) have sparked interest and general discussion of the capability. The capability has been discussed with international participants in the OECD/NEA Expert Group on Burnup Credit Meeting and at the IAEA Technical Meeting on Burnup Credit, held in London in August 2005. It has been presented as part of the TRITON training courses held in Paris in 2004 and at Brookhaven National Laboratory, ORNL, and NRC Headquarters in 2005. A three-hour tutorial on KENO-based depletion was taught at the American Nuclear Society Nuclear Criticality Safety Division Topical meeting in September 2005. Interest has been such that ORNL is working to release an update to SCALE late in 2005 so that the updated version of TRITON is publicly available.

Additionally, a Windows-based graphical user interface to simplify model development, visualization, and execution has been developed at ORNL this year under separate funding. This capability makes the extremely powerful capabilities of TRITON even easier to apply for new and occasional users. The 3-D analysis capability has already been applied at ORNL in several ongoing projects for NRC and for the Department of Homeland Security. Future work is planned for NRC during FY 2006. This capability will likely generate new work as well as additional funding for future development.

## References


Bowman, S. M., M. D. DeHart, and L. M. Petrie. 2005. "Integrated KENO Monte Carlo Transport for 3-D Depletion with SCALE," usr-stevebowman-1-paper.pdf in Proceedings of the MC2005 Conference, Chattanooga, Tennessee.

DeHart, M. D. 1998. "An Advanced Deterministic Method for Spent-Fuel Criticality Safety Analysis," *Transactions of the American Nuclear Society* **78**, 170–172.

DeHart, M. D., Z. Zhong, and T. J. Downar. 2003. "TRITON: An Advanced Lattice Code for MOX Fuel Calculations," 14-01.pdf in *Proceedings of American Nuclear Society, Advances in Nuclear Fuel Management III*, Hilton Head Island, S.C., October 5–8, 2003.

DeHart, M. D. 2004a. "NEWT: A New Transport Algorithm for Two-Dimensional Discrete Ordinates Analysis in Non-Orthogonal Geometries," Vol. II, Sect. F21 of *SCALE: A Modular Code System for Performing Standardized Computer Analyses for Licensing Evaluation*, ORNL/TM-2005/39, Version 5, Vols. I–III, April 2005. Available from the Radiation Safety Information Computational Center at Oak Ridge National Laboratory as CCC-725.

DeHart, M. D. 2004b. "TRITON – A Multidimensional Depletion Sequence for Characterization of Spent Nuclear Fuel," Vol. I, Sect. T1 of *SCALE: A Modular Code System for Performing Standardized Computer Analyses for Licensing Evaluation*, ORNL/TM-2005/39, Version 5, Vols. I–III, April 2005. Available from the Radiation Safety Information Computational Center at Oak Ridge National Laboratory as CCC-725.

DeHart, M. D., and L. M. Petrie. 2004c. "Integrated KENO V.a Monte Carlo Transport for Multidimensional Depletion Within SCALE," *Transactions of the American Nuclear Society* **91**, 667–669.

DeHart, M. D., and L. M. Petrie. 2004d. "A Radioisotope Depletion Method Using Monte Carlo Transport with Variance Reduction and Error Propagation," *Proceedings of PHYSOR 2004 Topical Meeting*, April 25–29, 2004, Chicago, IL, on CD-ROM.

Gauld, I. C., and C. V. Parks. 2001. *Review of Technical Issues Related to Predicting Isotopic Compositions and Source Terms for High-Burnup LWR Fuel*, NUREG/CR-6701 (ORNL/TM-2000/277), U.S. Nuclear Regulatory Commission, Oak Ridge National Laboratory, January 2001.

Gill, D., and S. M. Bowman. 2006. *Validation of TRITON*, ORNL/TM-2005/170, UT-Battelle, LLC, Oak Ridge National Laboratory, to be published.

Williams, M. L. 1979. "Development of Depletion Perturbation Theory for Coupled Neutron/Nuclide Fields," *Nuclear Science and Engineering* **70**, 20–36.

# Development of a Prototypic Three-Dimensional Deterministic Shielding and Criticality Analysis Capability

S. Goluoglu
*Nuclear Science and Technology Division*

The input and cross-section preparation requirements associated with the use of existing multi-dimensional deterministic radiation transport codes are extremely burdensome in terms of user's effort and costly in terms of user's time. Furthermore, due to the amount of detailed input data required and the multiple steps associated with problem-dependent cross-section preparation, the process is very tedious and error prone. The input data requirements are dictated by the method, which solves the discretized Boltzman transport equation over a detailed space and energy grid along discrete directions and involves numerous parameters related to the solution algorithms and their convergence properties. An attempt has been made to significantly reduce the volume of input data and burdensome input preparation through the development and implementation of a new, innovative input structure and associated algorithms. The developed algorithms automate the generation of the detailed input data and solution parameters (needed by the transport code) based on a more intuitive and significantly reduced input structure (in terms of amount of required data). Primarily due to cost savings associated with user time and reduced input error, the resulting sequence is a significant value to programs in advanced reactor designs, space and terrestrial reactor shielding applications, spent fuel storage and transportation, safeguards, security, and nonproliferation, and related programs.

## Introduction

Shield design, analysis, and optimization require accurate radiation transport calculations to determine detailed information (e.g., energy deposition and dose profiles) throughout shields and critical components. Therefore, deterministic methods, which calculate detailed information throughout the entire modeled problem, are strongly preferred, as compared to Monte Carlo methods, which calculate localized information as requested by the user. Furthermore, for such problems, deterministic methods offer superior computational performance. However, current production-level deterministic radiation transport tools are not user friendly, requiring substantial user time and experience for all but the simplest problems. Preparation of the problem-dependent cross sections that are required by the code also requires considerable effort on users' part. An easy-to-use 3-D deterministic radiation transport code that includes automated preparation of problem-dependent cross sections does not exist. The ORNL-developed 3-D deterministic transport code, TORT, has widely recognized capabilities but a relatively limited user base due to its less-than-friendly user interface, the current disconnect between the code and suitable cross-section libraries needed by the code, and the lack of active development and maintenance.

This project focused on developing a prototypic easy-to-use computational sequence that relies on modern keyword-based input with automatic generation of problem-dependent cross sections. The new sequence was based on TORT to demonstrate feasibility. An innovative approach was employed due to the complexity of problem input parameters and data (e.g., cross sections) inherent in a 3-D deterministic code. The prototypic sequence was developed for the SCALE code package, which is developed and maintained by ORNL to perform criticality safety, radiation shielding, and spent fuel characterization of nuclear fuel facilities and transport/storage package designs.

## Technical Approach

To fulfill the objectives of this project, the following tasks have been completed in the order given:

### *Automation of Problem-Dependent Cross Section Processing by Utilizing SCALE Cross Section Processing Modules*

Since TORT uses multigroup cross sections for calculations, the neutron cross sections must be processed to generate the so-called problem-dependent cross sections that are resonance shielded to treat the energy self-shielding effects. This is accomplished by the BONAMI computer program for the unresolved resonance energy range (i.e., high energy range) and either the NITAWL-III or CENTRM/PMC computer programs for the resolved resonance range. If NITAWL-III is used, the spatial self-shielding effects are accounted for through the incorporation of Dancoff factors since NITAWL-III is based on the collision probability method. Finally,

the problem-dependent cross sections are written in the so-called group-independent format that is used by the TORT code. The SCALE module ICE is used to generate the group-independent cross sections for TORT. Hence, the automated generation of problem-dependent cross sections requires sequential execution of several modules that pass information to each other via either binary or ASCII data files. Algorithms have been developed to automate this complicated process and ensure all interface files are properly created and used.

***Development of a New Input Structure and Related Algorithms to Provide an Easy-to-Use Interface***

A new keyword-based input structure has been developed and implemented. The related algorithms ensure an easy-to-use interface between the user and the code and data, namely TORT and the cross section sets, by employing innovative techniques to overcome the difficulties that arise from complex input parameters, code execution, and interface files related to cross section processing. The new input structure is easy to understand, easy to use, capable, and robust. User friendliness is ensured by making the underlying data exchange transparent to the user. In addition, the amount of information required on the user's part is minimized. An example of an input file with the new input structure that uses keywords and keyword-based data block designators follows:

```
=tortsq
first test case
44groupndf5
read comp
 u          1 den=19.05 1 300 92235 90 92238 10 end
 wtptwater      2  1  2 1001 11.11111 8016 88.88889 1 300 end
end comp
read controls
 sn=6 nsrmx=35 ktype=1 icsprt=1
end controls
read geometry
! fine meshes
   fmesh       kset -9 -8 -7 -6 -5 -4 -3 -2 -1 0 1 2 3 4 5 6 7 8 9  / z direction
               iset  -9 -8 -7 -6 -5 -4 -3 -2 -1 0 1 2 3 4 5 6 7 8 9  / x direction
               jset  -9 -8 -7 -6 -5 -4 -3 -2 -1 0 1 2 3 4 5 6 7 8 9  / y direction
! bodies
   body  -9 9 -9 9 -9 9 1 2  / outer, water region
   body  -7 7 -7 7 -7 7 2 1  / inner, fuel region
end geometry
end
```

This structure allows many of the TORT input parameters to be inferred or calculated by the code internally, which simplifies and minimizes the input considerably. The old style input file for the same problem would contain more than twice the information in the input, was not keyword based, and was very cryptic.

## Results and Discussion

The algorithms and a prototypic sequence have been developed and demonstrated to work. In addition, a robust memory management module has been implemented. This module allows dynamic memory allocation based on the available memory on the specific computational platform that is being utilized. As a result, the total computing time, which is especially a limiting issue for shielding applications, has been reduced. Significant reduction in wall-clock time (~90%) has been observed when executing over a network file server.

The addition of this new sequence will enhance the capabilities of the SCALE code package, making it an even better and more complete code package for shielding applications that need proven technology. With the new sequence, the users will have ready access to the latest evaluations of the cross sections that are available with SCALE instead of having to use decades-old obsolescent cross section evaluations.

## Benefits

Promising sources for additional funding are NRC, DOE, NASA, and DTRA. NRC and DOE are primary SCALE sponsors, providing significant support for enhancements and maintenance of proven capabilities. DOE has a variety of shielding and criticality-related needs across the complex, from shielding analyses for spent nuclear fuel to detector placement studies for criticality accident alarm systems. NASA has needs related to bulk shielding design and safety for space reactors. DTRA and NGIC have needs related to the MASH (Monte Carlo Adjoint Shielding) Code System, which utilizes codes from DOORS and is the NATO reference code for all armored vehicle prompt radiation nuclear vulnerability calculations. NRC has needs related to cask shielding and PWR and BWR fluence analyses. Since the proof-of-principle has been demonstrated, it is expected that some of the above DOE or other federal agencies will benefit from having such a prototypic tool and will provide additional funding for further development of a production sequence.

The establishment of the new prototypic user-friendly sequence in SCALE is anticipated to open the door to significant follow-on funding for development activities such as: (1) automated mesh-generation to further simplify the input; (2) development of sensitivity/uncertainty analysis tools for shielding-related quantities of interest based on the TORT sequence; (3) the expanded coupling of Monte Carlo and discrete ordinates methods for solving difficult problems and accelerating convergence of Monte Carlo calculations; (4) expansion to include time dependence; (5) development of an intelligent, fully automated, problem-dependent cross-section collapsing capability (automated fine-group collapse); (6) advanced solution and solution acceleration algorithmic development, and (7) parallelization for high-performance computing. The current plan is to pursue NRC for incorporation into the SCALE code package as

a production code followed by development of algorithms and capability to perform automated-mesh generation. Automated mesh-generation is a natural next step as it simplifies the input even further and makes it easier to incorporate into other sequences for accelerating Monte Carlo calculations.

Finally, the new user-friendly sequence for discrete ordinates transport analyses will not only reduce the time and effort required to perform shielding analyses for current sponsors, it will give ORNL a distinct advantage in this area that will improve our ability to attract funding for large multiyear shielding design and analysis-related projects (e.g., NRC for cask and cask array shielding, NIH for improved shielding design to protect radiation therapists).

## Reference

Radiation Safety Information Computational Center. April 2005. *SCALE: A Modular Code System for Performing Standardized Computer Analysis for Licensing Evaluations*, ORNL/TM-2005/39, Version 5, Vols. I–III. Available from the Radiation Safety Information Computational Center at Oak Ridge National Laboratory as CCC-725.

# Detecting Concealed Nuclear Materials with Photofission

S. A. Pozzi,[1] E. Padovani,[2] and M. Monville[3]
[1]*Nuclear Science and Technology Division*
[2]*Polytechnic of Milan, Italy*
[3]*Nuclear Science and Technology Division*

Recent efforts have been aimed at investigating active interrogation methods based on the use of photons to interrogate containers for the detection of fissile materials. The present project has the aim of generating a Monte Carlo tool based on the codes MCNP-X and MCNP-PoliMi. The tool is aimed at simulating the neutron and photon field generated by interrogating fissile (and non-fissile) material with a high-energy photon source. Photo-atomic and photo-nuclear collisions are modeled, with particular emphasis on the generation of secondary particles that are emitted as a result of these interactions. The simulations can be used to design and analyze measurements that are performed in a wide variety of scenarios, and an application of the methodology to the interrogation of packages on a luggage belt conveyor has been investigated.

The detection of shielded highly enriched uranium (HEU) is one of the most urgent concerns that are being addressed by homeland security efforts. Recent efforts in the fields of nuclear nonproliferation, national security, and counter-terrorism have been aimed at developing new measurement techniques for the rapid identification of fissile materials that could be concealed in shielded containers. A number of techniques that are currently being proposed rely on the use of photon sources to induce fission in the nuclear material and on the detection of the subsequent gamma rays and neutrons from fission. The design and analysis of such measurements are based, in turn, on the use of Monte Carlo codes to simulate the interaction of neutrons and photons with the nuclear material, the shielding, and the radiation detectors. However, currently available Monte Carlo codes lack the ability to simulate the emission of correlated particles from photofission. The product of this research will provide a tool to address and solve this deficiency. The proposed methodology is based on the use of two existing and well-benchmarked codes, MCNPX and MCNP-PoliMi.

The currently released version of MCNP-PoliMi includes the description of neutron-induced fission, other neutron interactions, and photo-atomic interactions. The code provides a description of the secondary particles from neutron-induced reactions that is based on the use of data from the ENDF-based MCNP data libraries. Because this data does not always contain a full description of the secondary photons that are generated in neutron interactions, approximations have been made. The guiding principle is the conservation of energy at each interaction.

A similar approach was adopted in the modifications for the simulation of photo-nuclear interactions. Here, the simulations are performed in two steps. First, a modified version of MCNP-X transports the photons to determine the position and type of photo-nuclear interaction that has occurred in any given cell of the problem considered. Then, MCNP-PoliMi transports the secondary particles that arise from the interactions and simulates the detector response.

The primary photo-nuclear interactions that occur in actinides are photo-fission, (Γ, *n)* and (Γ, 2*n*) (we denote with Γ the incident photon and with γ the secondary photons). All of these interactions can be accompanied by γ-ray de-excitation. Currently, in MCNP-X the photonuclear events in actinides are described by the *Bofod01u* library, which contains information on the outgoing neutrons but no description of secondary photons from any of the above-mentioned photo-nuclear interactions. However, the *Q*-values of the interactions are given in the data library. We used this information to determine the multiplicity and energy spectra of the outgoing neutrons and photons as follows.

In the case of (Γ, *n)* interactions, the energy and direction of the outgoing neutron is sampled from the data in the library. The total energy of the outgoing photon(s) $E_\gamma$ is determined by an energy balance:

$$E_\gamma = E_\Gamma - E_n + Q \,,$$

where $E_\Gamma$ is the energy of the incoming photon, $E_n$ is the energy of the outgoing neutron, and $Q$ is the $Q$-value of the reaction.

A similar expression is obtained for the total energy of the outgoing photon(s) $E_\gamma$ in the case of (Γ, 2*n)* interactions. In this case we have

$$E_\gamma = E_\Gamma - E_{n1} - E_{n2} + Q \,,$$

where $E_{n1}$ and $E_{n2}$ are the known energies of the two outgoing neutrons.

Knowledge of the total available energy for photon de-excitation does not, of course, imply any information on the multiplicity of the photons that are emitted in any of the previously described interactions. Because this information is missing from the data libraries, the user can set an input parameter that controls the multiplicity of photons emitted in these cases.

In the case of photo-fission, the neutrons are emitted according to the average number $\overline{\nu}$, which is present in the data libraries. The distribution of the neutrons *P(v)* is then determined according to Terrell's formula, similarly to what is done in MCNP-PoliMi for neutron-induced fission. The number of neutrons *v* ranges from 0 to 10.

The average number of photons emitted in photofission $\overline{\mu}$ is determined by evaluating a semi-empirical model that was determined for neutron-induced fission. The model is evaluated for fission induced on a nucleus of mass A-1. This approximation is justified in part by the physics of fission: it is assumed that the fission fragments carry no memory of the type of interaction that produced them. The average number of photons is then used to determine the distribution from which the number of photons is sampled. The number of photons $\mu$ ranges from 0 to 23.

The modified versions of MCNP-X and MCNP-PoliMi were then used to simulate the transport of photons from a linear accelerator to interrogate shielded highly enriched uranium in a variety of scenarios. The results of this research were presented at various international conferences, in one accepted journal article, and in two journal articles that are in progress.

# *Physics*

# *Director's R&D Fund*

# Probing Explosive Nucleosynthesis through Measurements at the Holifield Radioactive Ion Beam Facility

D. W. Bardayan, J. C. Blackmon, and M. S. Smith
*Physics Division*

Unstable nuclei play an influential role in many astrophysical processes occurring in exploding stars such as novae, supernovae, and X-ray bursts. To understand these events, we must understand the reactions involving unstable, radioactive nuclei. The best way to probe such reactions is by using beams like those available at the Holifield Radioactive Ion Beam Facility (HRIBF). We investigated proton-induced reactions on radioactive fluorine and phosphorus nuclei and neutron-induced reactions on radioactive neutron-rich nuclei, using the large detector arrays and the ion beams at the HRIBF.

## Introduction

Unstable nuclei play an influential, and in some cases dominant, role in many phenomena in the cosmos such as novae, supernovae, X-ray bursts, and other stellar explosions. In the extremely high temperatures (greater than 0.1 GK) of these astrophysical environments, the interaction times between nuclei can be so short (~seconds) that unstable nuclei formed in a nuclear reaction can undergo subsequent reactions before they decay. Sequences of (predominantly unmeasured) nuclear reactions occurring in exploding stars are therefore quite different from sequences occurring at lower temperatures characteristic of, for example, our Sun. Measurements of the structure and reactions of unstable nuclei are therefore required to improve our understanding of the astrophysical origin of atomic nuclei and the evolution of stars and their (sometimes explosive) deaths.

One important issue is understanding the flux of gamma rays originating from the decay of fluorine-18 ($^{18}$F) in the remnants of nova explosions. This is an especially timely issue as the recently launched INTEGRAL observatory promises to provide us with the most detailed pictures of the gamma-ray emission from novae ever available. To understand these observations, we must understand the astrophysical rate of the

$^{18}\mathrm{F} + {}^{1}\mathrm{H} \rightarrow {}^{15}\mathrm{O} + {}^{4}\mathrm{He}$ reaction

that destroys $^{18}$F in nova explosions. We have carried out a variety of studies using radioactive $^{18}$F beams at the HRIBF and combined these data with improved analyses of previously taken data to better determine this rate.

Another important problem is the understanding of the production of elements from Si to Ca in nova explosions. Recently, grains of stardust have been extracted from meteorites that survived the journey from stellar sources to Earth. Several of these grains are thought to have been formed in nova explosions, and detailed studies of their isotopic ratios have shown significant deviations from solar system abundances in the Si-to-Ca mass range (e.g., the $^{30}$Si/$^{28}$Si ratio was found to be twice the solar system value). Understanding these detailed observations and, in particular, the $^{30}$Si observations requires a better knowledge of the proton-capture rates of $^{29}$P and $^{30}$P which form $^{30}$S and $^{31}$S, respectively. These produced radioactive nuclei subsequently decay and ultimately determine, in part, the abundance ratios observed such as $^{30}$Si/$^{28}$Si mentioned above. New measurements of the

$^{32}\mathrm{S} + p \rightarrow t + {}^{30}\mathrm{S}$ and $^{32}\mathrm{S} + p \rightarrow d + {}^{31}\mathrm{S}$ reactions

have been made at the HRIBF to probe the properties of the $^{30}$S and $^{31}$S compound nuclei, which in turn determine the stellar rates of proton-capture reactions on $^{29}$P and $^{30}$P, respectively.

The production of elements in supernova explosions is another important problem studied with experiments at the HRIBF. The rapid neutron-capture process (r-process) is thought to occur in supernova explosions via a series of neutron-capture and beta-decay reactions on extremely neutron-rich radioactive nuclei. Comparisons of measured abundances with calculations can constrain the astrophysical conditions in which the r process occurs as well as the age of the Galaxy. These calculations, however, use as critical input the properties of extremely neutron-rich nuclei, many of which have never been studied in the laboratory. A series of groundbreaking experiments have been performed at the HRIBF to study properties of several neutron-rich nuclei of astrophysical importance. These studies used unique beams of neutron-rich radioactive nuclei from the HRIBF to bombard deuterated-polypropylene targets, transferring a single neutron to the heavy beam nuclei. Properties of the even more neutron-rich compound nucleus have be deduced from the energy and angular distributions of protons emitted from these single-neutron transfer reactions.

## Technical Approach

The research described above was carried out at the HRIBF, using the standard PAC-reviewed proposal mechanism to obtain beam time. The HRIBF is one of only a few facilities in the world that can create radioactive beams of the high quality needed for astrophysics research. Such research with radioactive beams has been endorsed in the 2001 Nuclear Science Advisory Committee Long Range Plan as having one of the highest priorities for future development. Nearly all apparatus needed exists in the DRS target hall. Experiments were scheduled as part of regular HRIBF running, and data taking and analysis was carried out using HRIBF facilities. The experiments generally involved bombarding hydrogen-containing targets with energetic radioactive beams. The only exceptions were for the studies of $^{30}$S and $^{31}$S, for which sulfide targets were bombarded with hydrogen beams. Elemental sulfur targets, however, are not stable under vacuum, so a suitable sulfur compound had to be used as a sulfur target. ZnS and FeS were both investigated with ZnS ultimately chosen and developed. Charged particle products from the reactions of interest were detected and identified in the Silicon Detector Array (SIDAR). The SIDAR array is a collection of silicon strip detectors specifically developed for the task of studying reactions of astrophysical interest using radioactive beams at the HRIBF. Various pieces of information can be extracted from the SIDAR data including the energies, angles of emission, and species of detected particles coming from the reaction. This information is used to determine the properties of compound nuclei and ultimately the rates at which nuclear reactions occur in stars and stellar explosions.

## Results and Discussion

Several measurements have been made at the HRIBF to determine the astrophysical rate of the

$^{18}$F + $^{1}$H → $^{15}$O + $^{4}$He reaction.

The energy dependence of the

$^{18}$F + $^{1}$H → $^{18}$F + $^{1}$H reaction rate

was measured for the first time over the entire energy range of interest for astrophysics (Bardayan 2004). A new quantum level of $^{19}$Ne was observed that significantly affects the astrophysical rate of the

$^{18}$F + $^{1}$H → $^{15}$O + $^{4}$He reaction

at stellar temperatures above 1 GK. The

$^{18}$F + $^{2}$H → $^{19}$F + $^{1}$H reaction

was also studied at the HRIBF to better understand quantum levels in $^{19}$F (Kozub 2005). While $^{19}$F does not directly entire into the astrophysical scenarios, knowledge of the $^{19}$F nucleus helps in the estimation of properties of the (isospin mirror) nucleus, $^{19}$Ne. After this study, the role of very-low energy resonances in the

$^{18}$F + $^{1}$H → $^{15}$O + $^{4}$He reaction

were better determined. An additional study of the (isospin mirror) nucleus, $^{19}$F, involved the reevaluation of data taken previously at Columbia University on the

$^{15}$N + $^{4}$He → $^{15}$N + $^{4}$He reaction.

These data provide the only experimental measurements of the widths of several quantum levels of $^{19}$F. We found that the previous analysis had been insufficient to accurately describe the data, and we extracted much improved nuclear properties using modern approaches (Bardayan 2005). This analysis was critical to describing the interference between $^{19}$Ne resonances in the

$^{18}$F + $^{1}$H → $^{15}$O + $^{4}$He reaction.

Finally, the rate of the

$^{18}$F + $^{1}$H → $^{15}$O + $^{4}$He reaction

has been measured directly at several energies during July–August 2005. These data are still in a preliminary state of analysis but will form, in part, the basis for a Ph.D. thesis for University of Tennessee graduate student K. Chae.

Another set of important astrophysical reaction rates that we have studied at the HRIBF are the proton-capture rates on $^{29}$P and $^{30}$P leading to compound nuclei $^{30}$S and $^{31}$S. Knowledge of the proton-capture reactions on these nuclei is critical for determining the nucleosynthesis of nuclei from Si to Ca in nova explosions. In fact, the proton capture on $^{30}$P has been highlighted as a gateway reaction to producing heavier elements. To study the properties of levels in $^{30}$S and $^{31}$S that determine the astrophysical reaction rates, we have studied at the HRIBF the

$^{32}$S + $p$ → $^{3}$H + $^{30}$S

and

$^{32}$S + $p$ → $^{2}$H + $^{31}$S reactions.

To perform these studies, we had to develop thin films of sulfide materials to be used as targets. ZnS targets were ultimately found to be the most stable containing the highest density of sulfur. The $^{2}$H and $^{3}$H atoms emitted from these reactions were detected and identified in the SIDAR array. From the energy and angular distributions of these ions, we have been able to determine properties of important quantum levels of $^{30}$S and $^{31}$S (Ma 2004).

The production of elements in supernova explosions is another important problem studied with experiments at the HRIBF. The rapid neutron-capture process (r-process)

is thought to occur in supernova explosions via a series of neutron-capture and beta-decay reactions on extremely neutron-rich radioactive nuclei. The HRIBF is the only facility world-wide that produces beams of r-process nuclei and can accelerate them to energies sufficient for reaction studies. These neutron-rich beams are radioactive, however, and so the rate of neutron-capture reactions on them can not be measured directly. Instead, we transfer a neutron to the nuclide of interest from a stable $^{2}$H target. The proton emitted from the neutron-transfer reaction provides important information about nuclei along the r-process path.

This technique was used to study the

$^{82}Ge + {}^{2}H \rightarrow {}^{83}Ge + {}^{1}H$ reaction

at the HRIBF (Thomas 2005). This was the first neutron-transfer reaction measured on an r-process nucleus and for this an ORNL Significant Event Award was received. $^{82}$Ge is on the r-process path and contains 50 neutrons (N=50), making it a "singly magic" nucleus resulting in extra stability. This "singly magic" nature means that the neutron-capture reaction will be determined by the properties of a few quantum levels of $^{83}$Ge. These quantum levels are selectively studied in the

$^{82}Ge + {}^{2}H \rightarrow {}^{83}Ge + {}^{1}H$ reaction,

and our measurement provided the first spectroscopic information on $^{83}$Ge and actually the first measurement of its mass. This was a groundbreaking study that provides a roadmap to future studies at facilities such as the proposed billion-dollar Rare Isotope Accelerator. This study has now been augmented with a second neutron-transfer measurement on a N=50 nucleus, $^{84}$Se (Thomas 2005). The combination of these experiments formed the basis of a Ph.D. thesis for Rutgers University graduate student J. Thomas.

We have also developed techniques to extend our measurements to heavier neutron-rich beams at the next neutron closed shell, N=82. In particular, we are preparing to study the

$^{132}Sn + {}^{2}H \rightarrow {}^{133}Sn + {}^{1}H$ reaction

to understand nuclei around "doubly-magic" (i.e., a nucleus with magic numbers of protons and neutrons) $^{132}$Sn. Similar to the $^{82}$Ge case, the neutron capture reaction rate on $^{132}$Sn is expected to be dominated by direct capture, and to calculate this rate, one must know the properties of low-lying quantum levels in the compound nucleus. These low-lying quantum levels are selectively populated in the neutron-transfer reaction, and thus these measurements are an ideal probe of the nucleus of interest. The reaction measurement for this heavier beam is more difficult, however, because reaction products must be detected at laboratory positions nearly perpendicular to the beam direction and, thus, detector arrays had to be developed that could be placed at these positions. Furthermore, because of the relatively low energies available for these heavy mass beams, it was not clear that all of the required nuclear information could be reliably extracted. We therefore performed a stable beam test of the developed detector array and technique using a stable $^{124}$Sn beam (Jones 2004). This test proved to be quite successful, and we are poised to perform our measurement with the radioactive $^{132}$Sn beam.

## Benefits

The HRIBF provides a unique facility to study reactions occurring in stellar explosions such as novae and supernovae. A variety of techniques have been developed and used to study those unstable nuclei produced in these extreme astrophysical conditions. In addition to providing important astrophysical information, the techniques developed pave the way for future studies at advanced facilities such as the Rare Isotope Accelerator (RIA).

The DOE Office of Nuclear Physics supports research in low-energy nuclear physics (e.g., research performed at the HRIBF) with a new component involving reactions of astrophysical interest. This component is on a steady growth curve due to the recent availability of post-accelerated beams of unstable nuclei such as those available at the HRIBF. This project is central to DOE's desire to continue growth in that area and to develop techniques applicable for use at future facilities such as RIA. This project also advances goals of the National Science Foundation (NSF), which supports nuclear measurements of astrophysical interest mainly through its support of facilities such as at the University of Notre Dame and the National Superconducting Cyclotron Laboratory at Michigan State University. NASA benefits through improved interpretations of the gamma-ray fluxes emitted by stellar explosions and better estimates of the required sensitivities of telescopes. The NNSA is also interested in neutron-capture reaction rates on unstable nuclei so a better understanding of these types of reactions benefits them.

## References


Bardayan, D. W., R. L. Kozub, and M. S. Smith. 2005. "$^{19}$F $\alpha$ widths and the $^{18}$F+$p$ reaction rates," *Phys. Rev. C* **71**, 018801.

Bardayan, D. W., J. C. Blackmon, J. Gómez del Campo, R. L. Kozub, J. F. Liang, Z. Ma, L. Sahin, D. Shapira, and M. S. Smith. 2004. "Search for astrophysically important $^{19}$Ne levels with a thick-target $^{18}$F($p$,$p$)$^{18}$F measurement," *Phys. Rev. C* **70**, 015804.

Jones, K. L., R. L. Kozub, C. Baktash, D. W. Bardayan, J. C. Blackmon, W. C. Catford, J. A. Cizewski, R. P. Fitzgerald, M. Johnson, R. J. Livesay, Z. Ma, C. D. Nesaraja, D. Shapira, M. S. Smith, J. S. Thomas, and D. W. Visser. 2004. "Study of the

$^{124}$Sn(*d,p*) reaction in inverse kinematics close to the Coulomb barrier," *Phys. Rev. C* **70**, 067602.

Kozub, R. L., D. W. Bardayan, J. C. Batchelder, J. C. Blackmon, C. R. Brune, A. E. Champagne, J. A. Cizewski, T. Davinson, U. Greife, C. J. Gross, C. C. Jewett, R. J. Livesay, Z. Ma, B. H. Moazen, C. D. Nesaraja, L. Sahin, J. P. Scott, D. Shapira, M. S. Smith, J. S. Thomas, and P. J. Woods. 2005. "New constraints on the $^{18}$F(*p,α*)$^{15}$O rate in novae from the (*d,p*) reaction," *Phys. Rev. C* **71**, 032801(R).

Ma, Z., M. W. Guidry, D. W. Bardayan, J. C. Blackmon, M. S. Smith, R. L. Kozub, K. L. Jones, J. S. Thomas, R. Fitzgerald, D. W. Visser, M. S. Johnson, R. J. Livesay, T. Davinson, and P. J. Woods. 2004. "Measurement of the $^{32}$S(*p,d*)$^{31}$S Reaction for $^{30}$P(*p,γ*)$^{31}$S Nova Nucleosynthesis Study," *Bull. Amer. Phys. Soc*. **49**(7), 38.

Thomas, J. S., D. W. Bardayan, J. C. Blackmon, J. A. Cizewski, U. Greife, C. J. Gross, M. S. Johnson, K. L. Jones, R. L. Kozub, J. F. Liang, R. J. Livesay, Z. Ma, B. H. Moazen, C. D. Nesaraja, D. Shapira, and M. S. Smith. 2005. "First study of the r-process nucleus $^{83}$Ge," *Phys. Rev. C* **71**, 021302(R); Thomas, J. S. 2005. Ph.D. thesis, Rutgers University.

# $H^-$ Laser Stripping Proof-of-Principle Experiment for the Spallation Neutron Source Power Upgrade Proposal

Y. Braiman,[1] S. Henderson,[2] A. Aleksandrov,[2] S. Assadi,[2] J. Barhen,[1]
V. Danilov,[2] W. Grice,[1] and Y. Liu[1]
[1]*Computer Science and Mathematics Division*
[2]*Accelerator Systems Division, Spallation Neutron Source*

Our group formulated a practical method to achieve $H^-$ stripping with good efficiency using a narrowband laser. Such a scheme would provide a clear path forward for the SNS Power Upgrade by eliminating foil lifetime issues and providing a lower-beamloss approach for charge-exchange injection. The goal of this project is to perform a proof-of-principle experiment to test this promising idea. The goal of this experiment is to prove an approach that would point the way towards a viable laser-based charge-exchange injection method, having application at the SNS and other future high-power accelerators under consideration throughout the world.

The Spallation Neutron Source (SNS) uses charge-exchange injection to "stack" a high-intensity proton beam in the accumulator ring for short-pulse neutron production. In this process, a 1-msec-long, 1-GeV $H^-$ beam-pulse is transported to a stripping foil located at the injection point of the ring. Both electrons are foil-stripped, and the resulting proton is merged with the previously accumulated beam. As the beam power of the SNS accelerator complex is increased from the baseline 1.44 MW to beyond 3 MW as envisioned in the SNS Power Upgrade Proposal, the traditional foil-stripping scheme will become a severe limitation. It is expected that the lifetime of carbon foils at such high beam powers will be too short to be of practical use due to foil damage by extreme temperatures. Furthermore, the use of stripping foils carries undesirable side effects for high-power operation: principally, the uncontrolled beam loss associated with multiple traversals of the foil by the accumulated beam.

We developed a novel approach for laser stripping of a 1-GeV $H^-$ beam that uses a three-step method employing a narrowband laser. In the first step, the beam traverses a strong magnetic field in which the $H^-$ ions are stripped to $H^0$ ($H^- \rightarrow H^0 + e^-$) by the Lorentz-stripping mechanism. In the second step, the $H^0$ beam is excited to the $n = 3$ state by colliding a laser beam with the neutral hydrogen beam at an angle chosen to provide the necessary transition frequency in the hydrogen atom's rest-frame. In the final step, the excited hydrogen is readily stripped ($H^{0*} \rightarrow p + e^-$) in a second high-field magnet.

To test this idea, we will use the third harmonic beam from a Nd:YAG laser with 650-mJ pulse energy (at 1064 nm wavelength), 6–8 ns pulse width, and 30-Hz repetition rate. Using the injection seed, the linewidth can be reduced to 0.003 $cm^{-1}$ (90 MHz). Frequency-tripled light has been obtained from the laser system, and the required pulse energy of 150 mJ was initially measured, as were the laser beam profiles. The optical system design involves multiple stages beginning with the third harmonic output from the laser which is housed in an auxiliary building outside the SNS linac tunnel and terminating with the laser-particle interaction region inside the vacuum. The laser light is transported about 100 m to the experimental setup in a laser transport line that has been installed and tested.

We completed the FY 2005 deliverables outlined in the initial proposal. The following has been accomplished:

(a) We have optimized the parameter set, optics design, and beamline insertion layout design.
(b) The magnet design work was completed, and the magnets were manufactured, tested and delivered.
(c) The design work for laser beam optics and diagnostics, as well as the actual vacuum hardware, laser optics, and diagnostics hardware, has been completed and all the components are in-hand.
(d) Several tasks associated with the deployment of this experiment in the linac tunnel have been completed, including the installation of (i) the laser-transport system, (ii) the high-current magnet cables, (iii) the low-current controls cables, (iv) the magnet assembly stand, and (v) the fiducialization and mounting of the magnets on their stand.

Installation of equipment in the beamline and magnet testing in situ is complete. First beam tests are scheduled for December 2005.

# Applications of Ultrafast/Ultra-Intense Lasers to Radioactive Ion Beam Production and Diagnostics

D. R. Schultz,[1] C. R. Vane,[1] J. R. Beene,[1] D. W. Stracener,[1] C. C. Havener,[1] H. F. Krause,[1]
J. Liang,[1] R. W. Shaw,[2] W. P. Grice,[3] A. Maksimchuk,[4] and D. P. Umstadter[5]
[1]*Physics Division*
[2]*Chemical Sciences Division*
[3]*Computer Science and Mathematics Division*
[4]*University of Michigan*
[5]*University of Nebraska*

Enabled by extremely rapid advances in ultrafast, ultraintense laser (UUL) technology, we are pursuing development of innovative methods for laser acceleration of charged particles, particularly electrons, to relativistic energies as a means for producing radioactive ions for nuclear physics research and catalyzing other high-priority ORNL applications. Specifically, we are investigating and developing the necessary stages of proof-of-concept to produce neutron-rich ion beams and diagnostics for those beams, utilizing UUL pulses. In addition, many novel features of these high-power density light pulses are being explored with respect to enabling applications aiding other key ORNL objectives, such as providing a compact ultrafast X-ray light source complementing neutron scattering capabilities for nanophase, chemical, biological, and material sciences.

The technical and commercial advancement of ultrafast, ultraintense lasers is currently proceeding extraordinarily rapidly. The intense electromagnetic light pulses from these laser systems can be used in a number of innovative applications, including exceptionally compact accelerators of charged particles. In this research project, we are developing these rapidly evolving capabilities toward implementation of new methods for the production and diagnostics of radioactive isotopes, especially for use in nuclear physics research, and other ORNL objectives such as realization of a compact, cost-effective, X-ray light source.

Recently discovered methodologies for efficient laser production of electrons at relativistic energies through laser wake field acceleration have been implemented in a number of laboratories (Mangles et al. 2004, Geddes et al. 2004, Faure et al. 2004) to generate approximately 1 nano-Coulomb pulse per laser shot of very forward directed electrons at up to 300 MeV. The method requires matching of intense ultrafast laser pulse timing characteristics to plasma frequencies created in gas targets. Using this specific regime of laser-gas target parameters, we carried out photo-nuclear production tests in 2005 at the HERCULES laser facility at the University of Michigan in collaboration with Anatoly Maksimchuk and colleagues. The HERCULES laser, firing 30-TW, 30-fs pulses at about one shot per minute, was used to generate pulses of relativistic electrons by laser interaction with a dense helium gas-jet target. The repetition rate was limited primarily by the ability to pump the residual gas from the target vacuum chamber. The combination of helium target density, plasma length, laser pulse length, and laser intensity was chosen to reach the "wave-breaking" regime demonstrated recently to yield quasi-monoenergetic electron distributions peaked near 150 MeV (e.g., Faure et al. 2004). The highly relativistic electrons produced by the laser-plasma interaction were then used to produce high-energy bremsstrahlung radiation in tantalum or uranium conversion targets.

Emittance and energy characteristics of these electron pulses were studied by magnetic analysis and imaging methods, and independently, by measuring the formation rates of specific radioactive isotopes from various secondary targets via a number of well-known photo-nuclear processes. These included photo-emission of neutrons and photo-fission reactions, that is, ($\gamma$, n), ($\gamma$, 2n), and ($\gamma$, fission) channels of $^{12}C$, $^{63}Cu$, and $^{238}U$ targets. Yields of several unstable isotopes were obtained after exposure to bremsstrahlung from the laser-electron pulses through calibrated off-line time-dependent detection and spectroscopy of nuclear gammas emitted by the photo-nuclear-reaction-generated radioactive species. Our goal in this set of test exposures was to quantify enhancements made available by the new regime of electron laser-acceleration over previously published results for photo-nuclear production in similar targets. As anticipated, significant improvements in average radioisotope production yields resulted for all

the targets. For example, compared to results using a similar laser (LOA— Laboratoire d'Optique Appliquée, "Salle Jaune" laser, 2-J, 30-fs pulse), in 2002 (Malka et al. 2002), our HERCULES tests indicated an enhancement of approximately a factor 100, giving ~106 $^{238}$U gamma-induced fissions per HERCULES laser shot. As in other studies, significant shot-to-shot variation of the high-energy electron yield was observed, indicating continued need for development of tighter controls on laser and gas target parameters. For example, comparison of measured production rates for $^{61}$Cu and $^{62}$Cu, from $^{63}$Cu($\gamma$,2n)$^{61}$Cu and $^{63}$Cu($\gamma$,n)$^{62}$Cu reactions, indicated through comparison with GEANT code calculations carried out by J. Beene at ORNL that the electron energy averaged over all laser shots during a ~ 20-min exposure was 30–50 MeV. However, imaging measurements of magnetically analyzed electrons taken immediately before the Cu target exposure showed that individual laser shots produced electron pulses with peak energies up to 300 MeV. In work in 2006 and 2007, we will resolve and correct these variations through a set of improvements in laser and target parameter controls.

Many technical applications of ultrafast, ultraintense lasers require reliable laser operation at higher average power than available up to now. In collaboration with Professor Donald Umstadter, now at the University of Nebraska at Lincoln, where a new commercial 100-TW, 30-fs, 10-Hz laser (DIOCLES) is being installed, a shielded target facility for production and diagnostics of high-energy electrons is being developed and constructed and will be ready for use in 2006. We have designed, purchased components, and constructed a high-density gas jet target apparatus at ORNL that will be relocated and installed at the DIOCLES facility in FY 2006. Testing of fluorescence methods for measuring the time and spatial profiles of the gas target is being developed at ORNL and will be implemented at DIOCLES along with existing laser interference techniques for on-line diagnostics and control of the critical target density parameters to optimize and maintain precise laser-target stability. Similarly, magnetic analyzers and detector arrays for on-line diagnosis of relativistic electron production and radioisotope remote-handling and gamma and neutron counting detectors are being developed for use in yield optimization experiments at DIOCLES in FY 2006 and FY 2007. We are also exploring methods for laser production of pulsed X-rays that can be used for real time diagnosis of the specific radioisotopes of interest.

## References


Faure, J., Y. Glinec, A. Pukhov, S. Kiselev, S. Gordienko, E. Lefebvre, J.-P. Rousseau, F. Burgy, and V. Malka. 2004. *Nature* **431**, 541.

Geddes, C. G. R., C. Toth, J. van Tilborg, E. Esarey, C. B. Schroeder, D. Bruhwiller, C. Nieter, J. Cary, and W. P. Leemans. 2004. *Nature* **431**, 538.

Malka, V., S. Fritzler, E. Lefebvre, M.-M. Aleonard, F. Burgy, J.-P. Chambaret, J.-F. Chemin, K. Krushelnick, G. Malka, S. P. D. Mangles, Z. Najmudin, M. Pittman, J.-P. Rousseau, J.-N. Scheurer, B. Walton, and A. E. Dangor. 2002. *Science* **298**, 1596.

Mangles, S. P. D., C. D. Murphy, Z. Najmudin, A. G. R. Thomas, J. L. Collier, A. E. Dangor, E. J. Divall, P. S. Foster, J. G. Gallacher, C. J. Hooker, D. A. Jaroszynski, A. J. Langley, W. B. Mori, P. A. Norreys, F. S. Tsung, R. Viskup, B. R. Walton, and K. Krushelnick. 2004. *Nature* **431**, 535.

# *Physics*

# *Seed Money Fund*

# Coupled-Cluster Theory with Effective Three-Body Forces

T. Papenbrock,[1] D. J. Dean,[1] D. E. Bernholdt,[2] and R. J. Harrison[2]
[1]*Physics Division*
[2]*Computer Science and Mathematics Division*

The aim of this project is to develop coupled cluster theory for systems with effective three-body forces and to perform a proof-of-principle calculation for a light nucleus. To date, we have diagrammatically and algebraically derived coupled cluster equations for three-body forces in the one- and two-particle cluster approximation (CCSD). We have also started to write a FORTRAN program that solves the coupled cluster equations numerically. The final program will be ready on time in a few months for the proof-of-principle calculation.

Coupled cluster theory is one of the most widely applied methods to numerically solve the quantum many-body problem. So far, this method has only been able to deal with two-body forces. However, modern nuclear physics and quantum chemistry introduce three-body forces through restrictions and renormalizations of the underlying model space. It is thus imperative to extend coupled cluster theory to deal with such forces. This is the objective of this project.

This task can be divided into three steps, namely (i) the derivation of the coupled cluster equations, (ii) the development of a computer program that solves these equations, and (iii) the test of the computer code in a proof-of principle calculation. The first step is done via diagrammatic means using and extending standard techniques of coupled cluster theory. The second step is done by developing a FORTRAN program that implements the solution of the coupled cluster equations in a most efficient way. Here, the experience with the tensor contraction engine is employed. For the third step, one tailors a modern free-space three-body force to the model space and performs the calculation numerically.

To date, we have finished the first step completely and have derived coupled cluster equations in diagrammatic and algebraic form within the commonly used CCSD approximation. Step two has partially been solved. Presently, we are able to compute the energy-corrections due to the three-body forces for given one- and two-particle cluster amplitudes. The remaining task of the second step consists of the full numerical implementation of the coupled cluster equations and is presently under way. In collaboration with Achim Schwenk (University of Washington, Seattle, WA) and Andreas Nogga (Julich, Germany), we tailored a modern three-body interaction into our model space.

In summary, the derived coupled cluster equations have been formulated, and the program development for their numerical solution is under way. By the end of this project, we will have the first coupled-cluster solution of a quantum many-body problem with three-body forces! This will enhance DOE's leadership in solving the quantum many-body problem and has the potential for wide-spread application in quantum chemistry and nuclear structure physics.

# Excited-State Quantum-Classical Molecular Dynamics

P. S. Krstić,[1] R. J. Harrison,[2] and B. Sumpter[2]
[1]*Physics Division*
[2]*Computer Science and Mathematics Division*

There is a strong interest for better understanding and characterization of molecular dynamics with excited electronic states in chemistry, nano-science, molecular photonics, molecular biology, and various applications of particle-cluster interactions (fusion energy research, semiconductor industry). The objective of this project is the development of a theoretical, algorithmic, and computational framework describing the corresponding excited-state many-body dynamics by applying multiphysics described by quantum-classical Liouville equation and multiresolution technique for solving the quantum part of the problem. The aim is to prototype these ideas in a suite of computer codes for excited-state, quantum-classical molecular dynamics.

Molecular dynamics (MD) has become an irreplaceable tool for studying dynamical phenomena in multi-atom systems, whether these are large molecules, nano-size devices, particle-surface scattering, biological or biotechnical processes involving proteins, monomer or polymer growth on a substrate, and whether interaction involves reaction dynamics of various parts of the system or perturbation by an external electromagnetic field. The most prominent approaches in MD are based on the Born-Oppenheimer (BO) model, which leads to entirely wrong descriptions whenever transitions between electronic states of the system become measurable; that is, if the system is significantly nonadiabatic. The most important reasons for nonadiabaticity are energy term avoided crossings and conical intersections. There is a growing interest in MD applications in consistent and systematic inclusion of nonadiabatic effects into the description of large molecular systems.

The main goal of this project is the development and realization of the numerical techniques for computational treatment of the time-dependent dynamics which includes electronically excited states in large molecular systems, containing hundreds of atoms, with slow heavy (atomic nuclei, treated classically) and light (electrons) particles. The core problem of the project—multi-electron, excited-state dynamics of the light subsystem—is the main scientific challenge of the project: Solving the multielectron Schrodinger equation, with the time-dependent Hamiltonian. Our approaches are based on the time-dependent versions of the mean-field theories (Hartree-Foc, Density Functional Theory, Multi-Configuration Hartree-Fock (MCTDHF), and Single-Excited Configuration Interaction). Important components of our computer simulations are the recently developed multiresolution analysis (MRA) numerical techniques, which are developed at ORNL by Harrison and Fann, which have several significant advantages for our simulations: The basis can systematically and robustly approach completeness, it is adaptive, and it enables fast application of integral operators. As needed, we use NWChem for many-body simulations.

Thus far there have been two important achievements of the project. In order to implement electron transition dynamics consistent with accuracy and stability of the MRA spatial discretization, the numerical solvers were implemented, describing the system time evolution. We have developed a series of solvers, based on Lanczos-Arnoldi algorithms, with Krylov subspace projection, as well as on combination of Pade and integral techniques. Numerically stable and accurate are the higher orders Runge-Kutta solvers, where we were able to keep, during the time evolution, accuracy of normalization and energy at six significant digits. Another achievement is development of the MCTDHF theory, compatible to MRA, which is being adapted and tested with the time-dependent solvers.

This new capability at ORNL, contained in development and realization of computer simulation of excited-state, quantum-classical molecular dynamics in large molecular systems, will greatly increase our competitiveness in what we see as a central theme for future research in physics, chemistry, and computational science to the DOE, ONR, AFOSR, and other agencies. The research provides a foundation for further development of excited-state molecular dynamics, consistently described by the quantum-classical Liouville approach and MCTDHF, with potential for opening a new, long-term program in ORNL that would raise the theoretical studies of dynamically perturbed large systems to a significantly higher quality.

# Development of Readout Electronics for the ALICE Electromagnetic Calorimeter

D. Silvermyr,[1] T. Awes,[1] V. Cianciolo,[1] Y. Efremenko,[1] K. F. Read,[1] P. Stankus,[1] G. R. Young,[1]
M. Bobrek,[2] C. L. Britton,[2] W. L. Bryan,[2] K. N. Castleberry,[2] and M. S. Emery[2]
[1]*Physics Division*
[2]*Engineering Science and Technology Division*

The goal of this project is to develop a system design for readout of the Electro-Magnetic Calorimeter (EMCal) in the ALICE ("A Large Ion Collider Experiment") experiment at the Large Hadron Collider. We will address issues of signal shaping, noise issues, and data acquisition interfacing requirements, and adapting certain components from the ALICE photon spectrometer (PHOS). We will also perform a beam test with the first EMCal modules, which are being assembled.

The proposed Electro-Magnetic Calorimeter (EMCal) will measure the energy of individual particles with a sufficient resolution for so-called jet reconstruction even in the high-multiplicity environment of a head-on heavy-ion collision. The jet reconstruction is a necessary requirement to characterize the produced state of matter in these collisions. We are looking into the readout electronics for this detector.

Since the start of this project half a year ago, and with help from CERN and elsewhere, we have assembled a test setup with a working data acquisition and readout system. This involved locating and adapting many different pieces of both custom hardware and software. We have also made a preliminary study of the EMCal electronics design to determine which modifications of the PHOS electronics are needed. Most components, including the avalanche photo-diode (APD) and pre-amplifier, seem well suited for the EMCal too. However, some changes are needed; for example, different signal shaping options have been studied. It seems desirable to go from a 2-μs shaping time to a 100-ns shaping time. In the bench tests so far, this does not seem to worsen the electronics noise significantly, which is good news.

Another change from the PHOS readout scheme that has been identified is the need for new so-called transition cards that need to drive the signals over longer distances between the electronics and the detector. This will be pursued after the beam tests, when we will hopefully know if other bigger changes are needed or not. We also need to map out how the front-end modules will be used in a jet trigger setup to achieve the best trigger performance.

We have now arranged for a first beam test with EMCal prototype modules. This will take place at FNAL (Chicago) from November 4 to November 28.

The hope is that we should have first preliminary results ready from the beam tests, regarding noise, resolution and efficiency, for a DOE review in mid-December of the U.S. involvement in ALICE.

For FY 2006, the remaining main identified items are as follows:

1. Beam test at FNAL in November, and subsequent analysis of the obtained data.
2. Design and testing of the transition cards, and perhaps a larger scale follow-up second beam test at CERN in the spring/summer of 2006.

## AUTHOR INDEX

## INDEX OF PROJECT NUMBERS

## DIRECTOR'S R&D FUND PROJECTS BY INITIATIVE

**Systems Biology**



**Terascale Computing and Simulation Science**



**General**

# FY 2005

ORNL 2006-G00324/asg